SEARCH OF NEW PHYSICS WITH BOOSTED HIGGS BOSON IN HADRONIC FINAL STATES WITH ATLAS DETECTOR

A DISSERTATION
SUBMITTED TO THE DEPARTMENT OF PHYSICS
AND THE COMMITTEE ON GRADUATE STUDIES
OF STANFORD UNIVERSITY
IN PARTIAL FULFILLMENT OF THE REQUIREMENTS
FOR THE DEGREE OF
DOCTOR OF PHILOSOPHY

Qi Zeng
June 2017

CERN-THESIS-2017-124
01/05/2017

© 2017 by Qi Zeng. All Rights Reserved.

Re-distributed by Stanford University under license with the author.



This work is licensed under a Creative Commons Attribution-Noncommercial 3.0 United States License.
http://creativecommons.org/licenses/by-nc/3.0/us/

This dissertation is online at: http://purl.stanford.edu/kt719mz9192

I certify that I have read this dissertation and that, in my opinion, it is fully adequate in scope and quality as a dissertation for the degree of Doctor of Philosophy.

Dong Su, Primary Adviser

I certify that I have read this dissertation and that, in my opinion, it is fully adequate in scope and quality as a dissertation for the degree of Doctor of Philosophy.

Peter Graham

I certify that I have read this dissertation and that, in my opinion, it is fully adequate in scope and quality as a dissertation for the degree of Doctor of Philosophy.

Ariel Schwartzman

I certify that I have read this dissertation and that, in my opinion, it is fully adequate in scope and quality as a dissertation for the degree of Doctor of Philosophy.

Lauren Tompkins

Approved for the Stanford University Committee on Graduate Studies.

Patricia J. Gumport, Vice Provost for Graduate Education

This signature page was generated electronically upon submission of this dissertation in electronic format. An original signed hard copy of the signature page is on file in University Archives.

Abstract

The discovery of a Higgs boson at the Large Hadron Collider (LHC) confirms the validity of the Standard Model (SM) in the description of particle interactions at electroweak scale. However, radioactive corrections to the Higgs mass drives its value to the model's validity limit, indicating either extreme fine-tuning or the presence of new physics at higher energy scale. Since 2015, the LHC starts its Run 2 journey with unprecedented center of mass energy of 13 TeV. Along with increase in luminosity, this greatly extends the sensitivity of ATLAS experiment to heavy new particles at TeV scale. In particular, many new physics models beyond the Standard Model manifest themselves through significant coupling to the Higgs boson in decays of new particles to a Higgs boson and other SM particles.

In this work, two searches for resonances decaying to either pair of Higgs bosons or a Higgs boson associated with another SM vector boson in all hadronic final states are presented using data collected by ATLAS during Run 2. Due to the heavy mass of new resonance, Higgs boson and W/Z boson can be boosted to large momentum, causing their decay products to be collimated. The dominant $H \to b\bar{b}$ decay mode also provides a clear signature through displaced vertices. A powerful boosted boson identification technique fully exploiting such jet substructure and heavy flavor information is therefore developed and used in both searches to suppress the dominant multijet backgrounds and largely enhance search sensitivity in particular for very high resonance mass. In the absence of significant excess, new exclusion limits are set on benchmark new physics models.

Acknowledgments

The ATLAS experiment is a giant scientific project in terms of both the size of collaboration and the complexity of experiment itself. I can clearly remember how hopeless I felt when I was first exposed to this brand new territory. It is impossible to get through the whole graduate life and finish this dissertation without the supports and helps from numerous people, to whom I would like to express my gratitude here.

First of all, I would like to thank my supervisor, Su Dong, for your dedicated supervision in my Ph.D. career. I would also like to thank Ariel Schwartzman for all the guidance. I literally grow from knowing nothing to knowing something now thanks to all the knowledge passed by you. I also would like to thank my defense committee and reader committee, including Su Dong, Ariel Schwartzman, Lauren Tompkins, Peter Graham and Jerome Friedman, for their time and efforts in this.

I also want to thank Michael Kagan, who joined SLAC ATLAS group as a postdoc at the same year as I joined in as graduate student, for the close collaboration for all five years. We worked together on almost every project and it is really a great pleasure working with you.

I want to thank the SLAC / Stanford ATLAS group which hosts like a family in my research. In particular, I would like to thank Charlie Young, Lauren Tompkins, Giacinto Piacquadio, Francesco Rubbo, Pascal Nef, Zihao Jiang, Ben Nachman, Maximilian Swiatlowski, Aviv Cukierman, Philippe Grenier, Rainer Bartoldus, Tim Barklow, Martin Kocian etc. for all the help and fun. This is really an excellent research group with very open environment where everybody is willing to discuss and collaborate on any problem, as well as share their knowledge and experience to each other.

I should also thank my colleagues in the ATLAS collaboration across the whole high energy physics community. There are more than 3000 collaborators around the world and every progress that we make strongly depends on each other's joint effort. In particular, I would like to thank some of my colleagues who I used to work with directly during my research: Ines Ocha, Baojia Tong, John Alison, Patrick Bryant, Reina Camacho, Nikola Whallon, Shih-Chieh Hsu, Jie Yu and Soshi Tsuno etc.. There is no way to make many work in this thesis happen without the collaboration with these people.

And in the last, I would like to thank my beloved wife, Liangjing Zhu. There is no way I can get through all the difficulties and make it today without you. Thank you for being there for me.

I should also thank my parents, my family and my wife's family for all your supports and patience with me.

Contents

Abstract **iv**

Acknowledgments **v**

1 Introduction **1**

2 Theoretical Considerations **4**

2.1 The Standard Model 6

2.1.1 Introduction 6

2.1.2 Fields 7

2.1.3 Gauge Theory 9

2.1.4 Quantum Chromodynamics 12

2.1.5 Electroweak Sector and the Higgs Mechanism 12

2.2 Physics beyond Standard Model 19

2.2.1 Difficulties of the Standard Model 19

2.2.2 The Randall-Sundrum Model 21

2.2.3 Bridging Theory and Data 24

3 The Large Hadron Collider **28**

3.1 Machine Design 29

3.2 Limitations 32

3.2.1 Luminosity 32

3.2.2 Energy 32

3.2.3 Luminosity Lifetime 33

3.3 Performance 34

4 ATLAS Detector **37**

4.1 Inner Detector 39

4.1.1 Silicon Pixel Detector 41

4.1.2 Semiconductor Microstrip Tracker . . . 45
4.1.3 Transition Radiation Tracker . . . 46
4.2 Calorimeter . . . 46
4.2.1 Liquid Argon Electromagnetic Calorimeter . . . 48
4.2.2 Hadronic Calorimeter . . . 50
4.3 Muon Spectrometer . . . 52
4.3.1 Precision-tracking Chambers . . . 55
4.3.2 Trigger Chambers . . . 56
4.4 Forward Detectors . . . 58
4.5 TDAQ System . . . 59
4.5.1 Level 1 Trigger . . . 61
4.5.2 High Level Trigger and Data Acquisition System . . . 63
4.5.3 Data Streams . . . 64

5 Physics Objects Reconstruction 65
5.1 Inner Detector Tracks . . . 65
5.2 Primary Vertex . . . 69
5.3 Jets . . . 70
5.4 Flavor Tagging . . . 76
5.5 Track Jets . . . 81
5.5.1 Motivation . . . 82
5.5.2 Track Selection . . . 83
5.5.3 Track Jet Properties . . . 85
5.5.4 Track Jet based b-Tagging . . . 87

6 Boosted Bosons Identification 91
6.1 Introduction . . . 92
6.1.1 Jet Grooming . . . 92
6.1.2 Jet Substructure Variables . . . 94
6.2 Boosted W/Z Tagging . . . 96
6.3 Boosted $H \to b\bar{b}$ Identification . . . 96
6.3.1 Higgs Candidate Jet . . . 98
6.3.2 Small Radius Track Jet b-Tagging . . . 98
6.3.3 Mass Window . . . 103
6.3.4 Jet Substructure Variables for $H \to b\bar{b}$ . . . 105
6.3.5 Benchmark Tagging Performance . . . 109

7 Search of Pair Production of Higgs Bosons in $b\bar{b}b\bar{b}$ Final States **111**
7.1 Introduction . . . 111
7.2 Data and Simulation Samples . . . 113
7.2.1 Data . . . 113
7.2.2 Simulated Signal and Background Samples . . . 113
7.3 Selections . . . 114
7.3.1 Event Reconstruction . . . 114
7.3.2 Trigger . . . 115
7.3.3 Preselection . . . 116
7.3.4 Signal Regions . . . 120
7.3.5 Cut Flow . . . 125
7.4 Background Estimations . . . 129
7.4.1 Multijet Background . . . 130
7.4.2 $t\bar{t}$ Background . . . 133
7.4.3 Fitting Procedure for Multijet and $t\bar{t}$ Normalization . . . 134
7.4.4 Validation in Control Region . . . 137
7.4.5 Prediction in Signal Region . . . 142
7.4.6 Event Yields . . . 144
7.5 Systematic Uncertainties . . . 146
7.5.1 MC Uncertainties . . . 146
7.5.2 Theoretical Uncertainties . . . 148
7.5.3 Background Prediction Uncertainties . . . 149
7.5.4 Summary of Systematics . . . 163
7.6 Results . . . 165
7.6.1 Unblinded Results in Signal Region . . . 165
7.6.2 Statistical Analysis . . . 165
7.6.3 Conclusion . . . 177
7.7 Improved Search and Results . . . 178
7.7.1 Data and Trigger . . . 178
7.7.2 Selections . . . 178
7.7.3 Background Estimation . . . 179
7.7.4 Results . . . 181

8 Search for Heavy Resonance Decaying to W/Z Boson and Higgs Boson in qqbb Final States **184**
8.1 Introduction . . . 184
8.2 Data and Simulation Samples . . . 186
8.2.1 Data . . . 186

8.2.2 Simulated Signal and Background Samples . . . 186
8.3 Selections . . . 188
8.3.1 Event Reconstruction . . . 188
8.3.2 Trigger and Preselection . . . 189
8.3.3 Event Selection . . . 191
8.3.4 Signal Regions . . . 195
8.4 Background Estimations . . . 199
8.4.1 0-Tag Extrapolation Method . . . 199
8.4.2 Definition of Various Regions . . . 201
8.4.3 Normalization Estimation . . . 202
8.4.4 Kinematic Re-weighting . . . 203
8.4.5 Cross-check in Validation Region . . . 208
8.4.6 Prediction in Signal Region . . . 213
8.4.7 Yields . . . 222
8.5 Systematic Uncertainties . . . 222
8.5.1 Theoretical and Experimental Uncertainties . . . 222
8.5.2 Background Estimation Uncertainties . . . 224
8.5.3 Systematics Summary . . . 233
8.6 Results . . . 235
8.6.1 Statistical Analysis . . . 235
8.6.2 Conclusion . . . 247

9 Summaries and Future Prospects **248**

A Improved Simulation of Particles Interacting with Pixel Detectors **251**
A.1 Introduction . . . 251
A.2 The Bichsel Model . . . 252
A.3 Implementations . . . 255
A.4 Effect on ATLAS Reconstruction Performance . . . 258
A.4.1 Setup . . . 258
A.4.2 Pixel Cluster Shapes . . . 259
A.4.3 Tracking Performance . . . 260
A.5 Computation Optimization . . . 262

B Double *b*-Tagging for Small Angular Separation **269**
B.1 Introduction . . . 269
B.2 Exclusive-k_t Algorithm . . . 271
B.3 *k-means* Clustering Algorithm . . . 278

Bibliography **285**

List of Tables

7.1 HLT triggers, and their L1 seeds, considered for use in the boosted regime. 115
7.2 List of kinematic pre-selection used in the boosted analysis. These cuts are generally efficient for signal. 118
7.3 Cutflow of data, signal samples of two particular mass points, $t\bar{t}$ and $Z + jets$ 126
7.4 The selection efficiency for $G^*_{KK} \to hh \to b\bar{b}b\bar{b}$ events ($c = 1.0$) at each stage of the event selection. 127
7.5 The selection efficiency for $H \to hh \to b\bar{b}b\bar{b}$ events at each stage of the event selection. 128
7.6 Definitions of the Signal (SR), Sideband (SB) and Control (CR) regions. X_{hh} is defined in Section 7.3.4 and R_{hh} is defined as $R_{hh} = \sqrt{(m_{J_1} - 124)^2 + (m_{J_2} - 115)^2}$. 131
7.7 Background normalization transfer parameters (μ_{Multijet} and $\alpha_{t\bar{t}}$) estimated from fits in the leading jet mass distributions in $4b$ and $3b$ sideband regions. 136
7.8 Fited μ_{Multijet} and $\alpha_{t\bar{t}}$ for different binning of leading large-R jet mass spectrum for boosted "4-tag" region 136
7.9 Fited μ_{Multijet} and $\alpha_{t\bar{t}}$ for different binning of leading large-R jet mass spectrum for boosted "3-tag" region 136
7.10 Expected yields for backgrounds in the $4b$ signal region, control region, and sideband region, along with the observed number of data events. The signal predictions for RS $m = 1.0, 1.5, 2.0$ TeV of both $c = 1.0$ and $c = 2.0$, and for narrow width heavy Higgs of $m = 1.0, 1.5, 2.0$ TeV are also listed. For each predicted value, the first uncertainty listed is statistical, and the second is the sum in quadrature of all systematic uncertainties. 145
7.11 Expected yields for backgrounds in the $3b$ signal region, control region, and sideband region, along with the observed number of data events. The signal predictions for $m = 1.0, 1.5, 2.0$ TeV of both $c = 1.0$ and $c = 2.0$, and for narrow width heavy Higgs of $m = 1.0, 1.5, 2.0$ TeV are also listed. For each predicted value, the first uncertainty listed is statistical, and the second is the sum in quadrature of all systematic uncertainties. 145
7.12 Background prediction in SR/CR/SB for nominal CR definition in 4 b-tag region . . 151
7.13 Background prediction in SR/CR/SB for high mass CR definition in 4 b-tag region . 151

7.14 Background prediction in SR/CR/SB for low mass CR definition in 4 b-tag region . 151
7.15 Background prediction in SR/CR/SB for signal depleted CR definition in 4 b-tag region 153
7.16 Background prediction in SR/CR/SB for sideband restricted CR definition in 4 b-tag region 153
7.17 Background prediction in SR/CR/SB for nominal CR definition in 3 b-tag region . . 153
7.18 Background prediction in SR/CR/SB for high mass CR definition in 3 b-tag region . 153
7.19 Background prediction in SR/CR/SB for low mass CR definition in 3 b-tag region . 153
7.20 Background prediction in SR/CR/SB for signal depleted CR definition in 3 b-tag region 153
7.21 Background prediction in SR/CR/SB for sideband restricted CR definition in 3 b-tag region 155
7.22 Variation of prediction in 4 b-tag SR 155
7.23 Variation of prediction in 3 b-tag SR 155
7.24 Agreement between data and prediction in 4 b-tag CR 155
7.25 Agreement between data and prediction in 3 b-tag CR 156
7.26 Background prediction in SR/CR/SB for ZZ SR in 4 b-tag region 157
7.27 Background prediction in SR/CR/SB for ZZ SR in 3 b-tag region 157
7.28 Agreement between data and prediction in ZZ SR in 4 b-tag region 157
7.29 Agreement between data and prediction in ZZ SR in 3 b-tag region 157
7.30 Functions used to fit the multijet dijet mass distributions, where $x = m_{JJ}/\sqrt{s}$. . . . 161
7.31 Percent impact of the dominant systematics on the background acceptance and on the signal acceptance of RS $c = 1.0$ graviton predictions in the $4b$ signal region. . . . 164
7.32 Percent impact of the dominant systematics on the signal acceptance of RS $c = 2.0$ graviton and 2HDM predictions in the $4b$ signal region. 164
7.33 Percent impact of the dominant systematics on the background acceptance and on the signal acceptance of RS $c = 1.0$ graviton predictions in the $3b$ signal region. . . . 164
7.34 Percent impact of the dominant systematics on the signal acceptance of RS $c = 2.0$ graviton and 2HDM predictions in the $3b$ signal region. 164
7.35 The number of predicted background events in the hh 3-tag and 4-tag signal regions, compared to the data for the boosted analysis. Errors correspond to the total uncertainties in the predicted event yields. The yields for a 1000 GeV G^*_{KK}in the bulk RS model with $k/\bar{M}_{\mathrm{Pl}}$= 1 is also given. 167
7.36 Minimum local and global p_0 values along with the corresponding significances and the trial factors for the different analyses and for the KK graviton model with $c \equiv k/\bar{M}_P = 1.0$. The trial factor is computed only when a local significance greater then 2 *sigma* is observed. 174

7.37 Minimum local and global p_0 values along with the corresponding significances and the trial factors for the different analyses and for the KK graviton model with $c \equiv k/\bar{M}_P = 2.0$. The trial factor is computed only when a local significance greater then 2 *sigma* is observed. 174
7.38 Minimum local and global p_0 values along with the corresponding significances and the trial factors for the different analyses and for the 2HDM model. The trial factor is computed only when a local significance greater then 2 *sigma* is observed. 175
7.39 Number of predicted background events in signal region compared to data. Quoted errors include both statistical and systematic uncertainties. Anti-correlation between multijet and $t\bar{t}$ yield is accounted for. 181

8.1 Number of events in signal region for WH signal sample with resonance mass being 2 TeV. 193
8.2 Summary of event selection criteria. 195
8.3 Cutflow of events for the 2015 and 2016 datasets. 196
8.4 Definition of signal region, sidebands and validation regions. 202
8.5 μ_{qcd} of both 1-tag and 2-tag derived for inclusive, "WH"-only and "ZH"-only signals. Only statistical uncertainties are shown. 203
8.6 Yields in the SB and various validation regions for both 1-tag and 2-tag cases. Only statistical uncertainties are shown on this table. 222
8.7 Yields in both 1-tag and 2-tag SR, for both WH and ZH signal samples. Yields for signal sample with $M = 2000$ GeV are also shown. Uncertainties shown on this table is the combination of statistical and systematic uncertainties. 223
8.8 Agreement between data and prediction in various 1-tag validation regions. The "data" denoted in this table is the data after subtraction of $t\bar{t}$ and V+jets MC contributions. The "Pred" denoted in this table is the normalization prediction of multijet component. 225
8.9 Agreement between data and prediction in various 2-tag validation regions. The "data" denoted in this table is the data with $t\bar{t}$ and V+jets MC subtracted. The "Pred" denoted in this table is the normalization prediction of multijet component. . 225
8.10 Impact of difference sources of systematic uncertainties in percentage on the background and signal process in 1-tag signal region of WH signal sample. 235
8.11 Impact of difference sources of systematic uncertainties in percentage on the background and signal process in 2-tag signal region of WH signal sample. 235
8.12 Impact of difference sources of systematic uncertainties in percentage on the background and signal process in 1-tag signal region of ZH signal sample. 236
8.13 Impact of difference sources of systematic uncertainties in percentage on the background and signal process in 2-tag signal region of ZH signal sample. 236

8.14 Impact of difference sources of systematic uncertainties in percentage on the background and signal process in all signal regions. 237
8.15 Summary of systematic uncertainties (expressed in percentage yield) in the background and signal event yields in the 1-tag and 2-tag signal regions. The values for the JES and b-tagging efficiency uncertainties represent the sum in quadrature of the values from the dominant components. The JES, JMR, b-tagging efficiency, luminosity and MC statistics uncertainties do not apply to the multijet contribution, which is determined from data. Uncertainties are provided for a resonance mass of 2 TeV in the context of the HVT *Model A*, for both $V' \to WH$ and $V' \to ZH$ resonances. . . 241

List of Figures

2.1 Schematic overview of the Standard Model 6
2.2 Illustration of Higgs potential 15
2.3 The generation of an exponential hierarchy 23
2.4 Branching ratio of KK graviton of various resonance mass for RS1 (left) and bulk (right) scenario. "MGr" on the plot is the KK graviton resonance mass; Symbol q represents sum of all flavors of quarks except top quark; Symbol l represents sum of all flavors of charged leptons (e, μ, τ) or neutrinos; Dashed line and solid line on the right plot represents bulk scenario in two difference cases: coupling of KK graviton to top quark is ignored in the dashed line, while a fully elementary top quark is considered in solid line. 24
2.5 Pictorial view of how to connect experiment and theory. $\vec{c}$ represents the parameters of phenomenological Lagrangian; $L(\vec{c})$ represents the likelihood function or exclusion limits as function of these parameters as extracted from the data; $\vec{p}$ represents the free parameters in explicit models; $\vec{c}(\vec{p})$ represents the relationship between parameters in phenomenological and explicit models 26
2.6 Branching ratios (upper row) and total width (lower row) for the two body decays of the neutral vector V^0 for the benchmarks $A_{gV} = 1$ (left) and $B_{gV} = 3$ (right). . . . 27

3.1 Schematic layout of LHC 29
3.2 Schematic illustration of LHC injection chains 31
3.3 Cross-section of cryodipole 31
3.4 Integrated (left) and peek instantaneous (right) luminosity delivered to ATLAS in Run 1 34
3.5 Integrated luminosity recorded by ATLAS in 2015 (top left), 2016 (top right) and a comparison across all years (bottom) 35
3.6 Peek instantaneous luminosity recorded by ATLAS in 2015 (left) and 2016 (right) . 36
3.7 Average number of interactions per bunch crossing in 2015 (left) and 2015+2016 (right) 36

4.1 Cut-away view of the ATLAS detector 38

4.2 Cut-away view of the ATLAS inner detector . . . 39
4.3 Plan view of a quarter-section of the ATLAS inner detector showing each of the major detector elements with its active dimensions and envelopes. The labels PP1, PPB1 and PPF1 indicate the patch-panels for the ID services . . . 40
4.4 A schematic view of the active region of the Pixel detector consisting of barrel and endcap layers . . . 41
4.5 Elements of a pixel barrel module . . . 42
4.6 Illustration of sensor design on pixel layers before (a) and after (b) type inversion . 43
4.7 Schematic Cross-section view of double-sided 3D sensor design of FBK (a) and CNM (b) . . . 44
4.8 Left: layout of the four sensors in the SCT barrel module (two on the upper surface, two on the lower surface, with 40 mrad stereo rotation). Right: modules mounted on the outermost barrel layer of ATLAS SCT detector . . . 45
4.9 Cut-away view of ATLAS calorimeter system . . . 47
4.10 Sketch of barrel module showing both accordion structure and granularity in $\eta - \phi$ of the cells on each of layer . . . 49
4.11 Illustration of how tile calorimeter is structured . . . 51
4.12 Cut-away view of ATLAS muon system . . . 53
4.13 Geometric layout of muon sub-detectors in barrel (up) and end-cap (down) region . 54
4.14 Cross-section view of a MDT tube . . . 55
4.15 Structure of RPC in ATLAS . . . 57
4.16 Location of forward detector along beam pipe with respect to interaction point in ATLAS . . . 58
4.17 Cross section of physics processes produced by hadron colliders . . . 59
4.18 Schematic overview of ATLAS TDAQ system with emphasis on trigger part . . . 60
4.19 Illustration of the decomposition of L1 latency . . . 62
4.20 Schematic view of trigger towers used in L1Calo algorithms . . . 63

5.1 Illustration of perigee parametrization of track trajectory in ATLAS . . . 66
5.2 Illustration of typical QCD processes involved in a hadron collider, including parton shower, hadronization and underlying events (multiple parton interactions, initial state radiation) . . . 71
5.3 A sample parton-level event clustered with different jet algorithms . . . 74
5.4 Calibration stages for reconstructed jets. Other than the origin correction, each stage is applied to the four-momentum of the jet . . . 75
5.5 The transverse (left) and longitudinal (right) signed impact parameter significance of tracks associated with b (solid green), c (dashed blue) and *light*-flavour (dotted red) jets . . . 78

5.6 Secondary vertex reconstruction rate as function of jet p_{T} (left) and η (right) for b (green), c (blue) and *light*-flavour (red) jets. 79
5.7 *Light*-jet rejection (left) or c-jet rejection (right) versus b-jet efficiency for the previous (2015 config) and the current configuration (2016 config) of the MV2 b-tagging algorithm evaluated on $t\bar{t}$ events. MV2c00 denotes the MV2 algorithm where no c-jet contribution was present in the training. MV2c10 (MV2c20) denote the MV2 outputs where a 7% (15%) c-jet fractions was present in the background sample (for the 2016 configuration). 80
5.8 The light (left) and c-jet rejection (right) versus b-jet efficiency for the MV1c b-tagging algorithm using the Run 1 detector and reconstruction software (blue) compared to the MV2c20 b-tagging algorithm using the Run 2 setup (red). 81
5.9 The b-tagging efficiency of MV1 tagger as function of angular distance between jet axis and b-hadron flight direction 83
5.10 Normalized distribution of tracks from pile-up vertices and b-hadron decays in transverse impact parameter significance with respect to hard scatter primary vertex (top left), track-to-vertex association weight (top right) and longitudinal impact parameter with respect to hard scatter primary vertex (bottom). Track-to-vertex association weight shows the compatibility between track and vertex where it originates from during reconstruction, while negative value represents tracks not associated to any reconstructed primary vertices. 84
5.11 Probability of a b-hadron being associated to calorimeter jets and track jets of various radius. 86
5.12 (Left) Distribution of angular separation between jet axis and b-hadron flight direction for various jet collections. (Right) Dependency of mean of angular separation on b-hadron p_{T} 86
5.13 (Left) b-jet identification efficiency as function of *light*-jet rejection for various jet collection in inclusive p_{T} range with track jet p_{T} threshold of 7 GeV (left) and 10 GeV(right) 87
5.14 b-tagging efficiencies for b, c and *light* components as function of jet p_{T} for anti-k_t track jet with radius parameter 0.2 (left) and 0.3 (right). Efficiencies are evaluated at a working point such that overall b-jet identification efficiency is 70%. 88
5.15 Probability of at least one track jets matched to calorimeter jet as function of p_{T} for various track jet collections. The matching is done through ghost association technique. 88
5.16 p_{T} correlation between b-labelled track jets of various radius (top left 0.2, top right 0.3 and bottom 0.4) and calorimeter jets. 89

5.17 b-tagging efficiencies for b, c and *light* components as function of matched calorimeter jet p_{T} for anti-k_t track jet with radius parameter 0.2 (left), 0.3 (right) and 0.4 (bottom). Matching efficiency between track jets and calorimeter jets are included. Efficiencies are evaluated at a working point such that overall b-jet identification efficiency is 70%. 90

6.1 The angular distance between light quark and anti-quark decayed from W boson. Distributions are at the generator level, without including effects due to initial and final-state radiation or the underlying event. 92

6.2 Leading p_{T} jet mass for simulated Herwig+Jimmy $Z \to qq$ signal events (red) compared to Powheg+Pythia dijet background event (black) for jets in the range of $600 < p_{\mathrm{T}} < 800$ GeV. The dotted lines show the ungroomed jet distribution wheres the solid lines shows the trimmed jet distribution with parameter $f_{cut} = 0.05$ and $R_{sub} = 0.3$. All distributions are normalized to unity. 94

6.3 W-jet efficiency versus multijet background rejection curve for the leading reconstructed jet for various substructure variables. Events are categorized in the leading ungroomed C/A truth jet with $200 < p_{\mathrm{T}}^{Truth} < 350$ GeV (left) and $1500 < p_{\mathrm{T}}^{Truth} < 2000$ GeV. The "Medium" (50%) and "Tight" (25%) signal efficiency working points are indicated. 97

6.4 Multijet rejection for W-jet (left) and Z-jet (right) as function of p_{T} for "Medium" and "Tight" flat efficiency working point. 97

6.5 Distribution of p_{T} (left) and number of associated $R = 0.2$ track jets (right) of large-R jet passing basic kinematic cuts in multijet, hadronic top and RSG Higgs-jet signal samples for three resonance masses of 500, 1000 and 1500 GeV. 98

6.6 Number of truth b-flavor labeled subjets associated to the leading large-R jet in an RSG sample with mass of 1000 GeV (top left), 1500 GeV (top right) and 2000 GeV (bottom left). Efficiency to find two b-tagged track jets / subjets in both large-R jets for RSG mass points are also shown in the bottom right. 100

6.7 (left) The rejection of inclusive multijets versus Higgs-jet efficiency using all large-R jets with $p_{\mathrm{T}} > 250$ GeV for (single / double / asymmetric) b-tagging requirements. (Right) Multijet rejection versus Higgs-jet efficiency using all large-R jets with $p_{\mathrm{T}} > 250$ GeV, broken down by multijet flavor composition, using double b-tagging. The stars correspond to a 70% b-tagging WP. The bands represent the statistical uncertainties. None of the curves reach a Higgs-jet efficiency of 100% due to the imperfect efficiency to reconstruct the track jets needed for b-tagging and in the case of asymmetric b-tagging the 70% b-tagging working point requirement on one of the track jets. 101

6.8 (left) The rejection of inclusive hadronic top jets versus Higgs-jet efficiency using all large-R jets with $p_{\mathrm{T}} > 250$ GeV, for (single / double / asymmetric) b-tagging requirements. (right) Hadronic top jet rejection versus Higgs-jet efficiency using all large-R jets with $p_{\mathrm{T}} > 250$ GeV, broken down by hadronic top jet flavor composition, using double b-tagging. The stars correspond to a 70% b-tagging WP. The bands represent the statistical uncertainties. No star is seen for the light-flavor curve as the statistics of the sample were not sufficient to reach this point. Note that none of the curves reach a Higgs-jet efficiency of 100% due to the imperfect efficiency to reconstruct the track jets needed for b-tagging and in the case of asymmetric b-tagging the 70% b-tagging working point requirement on one of the track jets. 103

6.9 The calibrated mass distribution for large-R trimmed double b-tagged jets before and after the muon correction for Higgs-jets is shown in the large-R jet transverse momentum ranges $350 < p_{\mathrm{T}} < 500$ GeV and $1000 < p_{\mathrm{T}} < 1500$ GeV. Higgs bosons are simulated with a mass of 125 GeV. All jets, whether they have a close-by muon or not, are used. 104

6.10 Mass distribution, after the muon correction, in the large-R jet transverse momentum ranges $350 < p_{\mathrm{T}} < 500$ GeV (left) and $1000 < p_{\mathrm{T}} < 1500$ GeV (right) for Higgs-jets and multijet and hadronic top backgrounds. Higgs bosons are simulated with a mass of 125 GeV. 105

6.11 Distributions of $D_2^{(\beta=1)}$ (top left), $C_2^{(\beta=1)}$ (top right) and τ_{21}^{wta} (bottom) for Higgs-jets (black), multijet (red) and hadronic top (blue) in Monte Carlo after the 68% mass window selection and after applying double b-tagging at the 70% efficiency WP. . . 106

6.12 The Higgs-jet efficiency versus multijet background rejection power, in large-R jet transverse momentum ranges of $350 < p_{\mathrm{T}} < 500$ GeV (left) and $1000 < p_{\mathrm{T}} < 1500$ GeV (right), for selected tagging variables (combined with the calibrated groomed 68% mass window and double b-tagging using 70% in (top) and 85% WP in (bottom)). The high end point of the Higgs-jet efficiency curves are a result of the 68% mass window requirement. The stars correspond to the nominal 70% (top) and the 85% (bottom) b-tagging working points. The bands represent the statistical uncertainties. 107

6.13 The Higgs-jet efficiency versus hadronic top rejection power, in large-R jet transverse momentum ranges of $350 < p_{\mathrm{T}} < 500$ GeV (left) and $1000 < p_{\mathrm{T}} < 1500$ GeV (right), for selected tagging variables (combined with the calibrated groomed 68% mass window and double b-tagging using 70% in (top) and 85% WP in (bottom)). The high end point of the Higgs-jet efficiency curves are a result of the 68% mass window requirement. The stars correspond to the nominal 70% (top) and the 85% (bottom) b-tagging working points. The bands represent the statistical uncertainties. 108

6.14 Criteria used for the different Higgs-jet tagging selections. 109
6.15 Higgs-jet efficiency versus large-R jet p_{T} (top) and multijet (bottom left) and hadronic top (bottom right) background rejection for different benchmark Higgs-jet taggers. The plots correspond to a nominal b-tagging working point of 70%. 110

7.1 L1 trigger efficiencies as a function of the signal resonance mass with no selection applied. The lowest unprescaled single jet trigger (`L1_J100`) has good efficiency across the entire mass range. 116
7.2 HLT trigger efficiencies as a function of the signal resonance mass with no selection (left) and after leading jet p_T requirement (right). 117
7.3 HLT trigger efficiencies as a function of the signal resonance mass for events in 3b (left) and 4b (right) signal regions. The lowest unprescaled large-R jet trigger (`HLT_j360_a10r`) has good efficiency across the entire mass range and is fully efficient above ~ 1 TeV in the signal region selection. 117
7.4 `HLT_j360_a10r` trigger efficiency measured as function of large-R jet p_{T}. Data and MC show good agreement. 118
7.5 Distribution of $\Delta\eta$ for RSG signal samples of various mass with $c = 1.0$ (left) and heavy neutral Higgs in 2HDM model (right) 119
7.6 Distribution of selected signal kinematics for RSG signal resonance masses with $c = 1.0$ in "4-tag" (left) and "3-tag" (right) category. Definition of "4-tag" and "3-tag" can be found in Section 7.3.4. First row is the leading large-R jet p_{T}. Second row is the leading large-R jet mass. Third row is the angular separation between two leading large-R jets in ϕ direction. Last row is the invariant mass of dijet system. 121
7.7 Kinematics of 1 TeV signal before and after muon-in-jet corrections. Both leading (top left) and subleading (top right) large-R jet mass, as well as invariant mass of dijet system (bottom left) gets improved mass resolution after the muon-in-jet correction. Events are therefore able to migrate from sideband / control region to the signal region, improving signal efficiency. 122
7.8 Median mass of leading (black) and sub-leading (red) large-R jet mass distribution for signal samples of different resonance masses, after 4 b-tag (left) and 3 b-tag (right) selection 123
7.9 Values of the X_{hh} variables, which are shapes in the two-dimensional plane of the large-R jet masses used to defined signal region. A smaller value of X_{hh} indicates the jets are closer to the Higgs mass. 124
7.10 The selection efficiency as a function of resonance mass at each stage of the event selection for (left) $G^*_{\mathrm{KK}} \to hh \to b\bar{b}b\bar{b}$ and (right) $H \to hh \to b\bar{b}b\bar{b}$ decays in the boosted analysis. The "2 large-R Jets" curve includes the requirements that the leading jet has $p_{\mathrm{T}} > 350$GeV and that the large-R jets have a mass greater than 50 GeV. . . . 124

7.11 The selection efficiency as a function of resonance mass after the full event selection for G*KKhhbanti-bbanti-b decays in the resolved analysis as well as in the boosted analysis for the 3-tag and 4-tag selections. 125
7.12 The m_J^{subl} vs. m_J^{lead} distribution for the 2-tag data sample used to model the multijet background in the boosted analysis. The signal region is the area surrounded by the inner black contour line, centered on $m_J^{subl} = 124$ GeV, $m_J^{lead} = 115$ GeV. The control region is the area inside the outer black contour line, excluding the signal region. The sideband region is the area outside the outer contour line. The kinematic region enriched in $t\bar{t}$ events is indicated by the dashed white contour line. 130
7.13 (Left) Regions defining different areas of the sideband. The white box is the control region, while the red area is the signal region. The regions used for the middle mass region method are shown with orange lines and labels. E_{CR} used in Equation 7.2 corresponds to the number of $2b$ events in the portion of the white control region contained within region E. (Right) Fractional difference between normalization transfer factor derived in the sideband and $2b$ to $4b$ ratio in the control region, versus the difference in medium mass events in the sideband and medium mass events in the control region. 133
7.14 comparison between the $3b$ and $4b$ shapes for the dijet invariant mass distributions (the final discriminant) in the SR 134
7.15 The leading large-R jet mass distribution in the hh sideband region for data (points) and background estimate (histograms) in the boosted analysis for events in the (left) 3-tag and (right) 4-tag categories. The shape of the multijet distributions is taken from the 2-tag region and is fitted to the data. The hatched bands represent the statistical uncertainty in the total background estimate. 135
7.16 Distribution of leading large-R jet p_{T} (first row), leading large-R jet mass (second row), subleading large-R jet p_{T} (third row) and subleading large-R jet mass (fourth row) between data and prediction in "4-tag" (left) and "3-tag" (right) sideband. . . 138
7.17 Distribution of dijet invariant mass (first row), ΔR between dijet (second row), $\Delta\eta$ between dijet (third row) and ΔR between two leading track jets associated with leading large-R jet (fourth row) between data and prediction in "4-tag" (left) and "3-tag" (right) sideband. 139
7.18 Distribution of leading large-R jet p_{T} (first row), leading large-R jet mass (second row), subleading large-R jet p_{T} (third row) and subleading large-R jet mass (fourth row) between data and prediction in "4-tag" (left) and "3-tag" (right) control region. 140

7.19 Distribution of dijet invariant mass (first row), ΔR between dijet (second row), $\Delta\eta$ between dijet (third row) and ΔR between two leading track jets associated with leading large-R jet (fourth row) between data and prediction in "4-tag" (left) and "3-tag" (right) control region. 141
7.20 Scaled invariant mass of dijet system for the $4b$ (left) and $3b$ (right) signal regions. For comparison, the unscaled distributions are shown on the same plot 142
7.21 Smoothed background estimations for the $4b$ (left) and $3b$ (right) signal regions. Multijet is shown on top, and $t\bar{t}$ is on bottom. Only smoothing statistical uncertainties are shown here. 143
7.22 Background prediction for $4b$ (left) and $3b$ (right) signal region using scaled dijet invariant mass before smoothing. The uncertainty band includes all statistical and systematic uncertainties. 144
7.23 Background prediction for $4b$ (left) and $3b$ (right) signal region using scaled dijet invariant mass after smoothing. The uncertainty band includes all statistical and systematic uncertainties. 144
7.24 Illustration of all variation of control regions (CR) and sideband regions (SB) under consideration. Left top is the nominal CR. Right top is low-mass CR. Bottom left is High-mass CR. Bottom right is signal-depletion CR. Bottom is sideband-restricted region 152
7.25 Comparisons of the nominal multijet shape prediction (black points) with the results of Control and Sideband Region definition variations (red points). The ratio of the shape from each variation to the nominal shape is shown in the lower panel, with the nominal shape uncertainty shown as the black-outlined band. The first row shows the high-mass CR variation; the second row shows the low-mass CR variation; and the third row shows the sideband restricted CR variation. The left column shows the relevant distributions for the 4 b-tag Signal Region and the right column is for the 3 b-tag Signal Region. 154
7.26 Illustration of ZZ signal region as shown in blue shaded region 156
7.27 Distribution of di-jet mass (left column) and leading large-R jet mass (right column) in ZZ SR, for 4 b-tag (first row) and 3 b-tag (second row) 158
7.28 (left) Shape of the $t\bar{t}$ di-large-R-jet mass in the signal region, comparing various b-tag bins. (right) The ratio of $4b$ to $3b$ shapes, with a linear fit to the ratio. The same fit with negative slope is also shown on the figure. 159
7.29 The ratio of $4b$ to $3b$ shapes of the $t\bar{t}$ scaled di-large-R-jet mass in the signal region, with a linear fit to the ratio. The same fit with negative slope is also shown on the figure. 160

7.30 Dijet mass ratio of total background to 4b (left) and 3b (right) data in the control region, fit (red line), and $\pm 1\sigma$ variation of the slope parameter (blue lines). 160
7.31 Effect of the up/down variation of the $2b$ multijet shape in the $4b$ (left) and $3b$ (right) signal regions. Gray lines show the upwards and downwards variations. 161
7.32 The ratio of the nominal exponential multijet prediction of the scaled dijet mass distribution (with hashed band statistical uncertainties) to the predictions when fit with different upper bounds, in the $4b$ (left) and $3b$ (right) signal regions. 162
7.33 The multijet prediction of the scaled dijet mass distribution in the $4b$ (left) and $3b$ (right) signal regions, showing the nominal exponential fit (with has band statistical uncertainties) and the additional fits from Table 7.30. 162
7.34 The ratio of the nominal exponential QCD prediction of the scaled dijet mass distribution (with hashed band statistical uncertainties) to the predictions of the additional fit functions of Table 7.30 in the $4b$ (left) and $3b$ (right) signal regions. 163
7.35 Impact of each systematic on the signal prediction as a function of the signal mass, in the $4b$ (left) and $3b$ (right) signal regions. 165
7.36 The systematic uncertainty from QCD shape variation as well as smoothing procedure for scaled dijet mass, in $4b$ (left) and $3b$ (right) signal region. The only difference between top and bottom is the range of y-axis. 166
7.37 The total background estimation in $4b$ (left) and $3b$ (right) signal region, along with total uncertainties (stats.+systematic) variation up and down 166
7.38 Dijet mass distribution in signal region for 3-tag (left) and 4-tag (right) category. The uncertainty band includes both the statistical and systematic uncertainties in the background estimate. 167
7.39 Distribution of leading large-R jet p_{T} (first row), leading large-R jet mass (second row), subleading large-R jet p_{T} (third row) and subleading large-R jet mass (fourth row) between data and prediction in "4-tag" (left) and "3-tag" (right) signal region. 168
7.40 Distribution of ΔR between dijet (first row), $\Delta\eta$ between dijet (second row), ΔR between two leading track jets associated with leading large-R jet (third row) and ΔR between two leading track jets associated with subleading large-R jet (fourth row) between data and prediction in "4-tag" (left) and "3-tag" (right) signal region. 169
7.41 The individual relative impact of the systematic uncertainties considered in the $4b$ (top left), $3b$ (top right) and combined boosted analysis on the G^*_{KK} $k/\bar{M}_{\mathrm{Pl}} = 1.0$ expected 95% confidence level exclusion limit, as a function of KK graviton mass. The impact is the ratio of the limit calculated using all systematic uncertainties sources to the limit calculated using all systematic uncertainty sources excluding those under investigation. 171

7.42 Pulls (top left) and correlation (top right) of nuisance parameters and post-fit distributions in linear (second row) and log (third row) scale obtained from the unconditional likelihood fits combining $3b$ and $4b$ channels. The signal is the KK graviton model with $c \equiv k/\bar{M}_P = 1.0$ and mass set to 1500 GeV. In second and third rows, left column is the post-fit distribution in $3b$ channel and right column is the post-fit distribution in $4b$ channel 172
7.43 Local p_0 value for the $3b$ (left) and $4b$ (right) boosted analysis as a function of the resonance mass for G^*_{KK} with $k/\bar{M}_{\mathrm{Pl}} = 1.0$ (first row), $k/\bar{M}_{\mathrm{Pl}} = 2.0$ (second row) and heavy neutral Higgs from 2HDM model (third row) 173
7.44 Local p_0 value for boosted $3b$+$4b$ analysis as a function of resonance mass for G^*_{KK} with $k/\bar{M}_{\mathrm{Pl}} = 1.0$ (top left), $k/\bar{M}_{\mathrm{Pl}} = 2.0$ (top right) and heavy neutral Higgs from 2HDM model (bottom) 174
7.45 The expected and observed limits for $G^*_{\mathrm{KK}} \to hh \to b\bar{b}b\bar{b}$ in the bulk RS model with $k/\bar{M}_{\mathrm{Pl}} = 1.0$ for combined 3b and 4b boosted analysis (left) and individual component from 3b and 4b alone (right). 175
7.46 The expected and observed upper limit on $G^*_{\mathrm{KK}} \to hh \to b\bar{b}b\bar{b}$ in the bulk RS model with $k/\bar{M}_{\mathrm{Pl}} = 1.0$ (first row) and $k/\bar{M}_{\mathrm{Pl}} = 2.0$ (second row) as well as $H \to hh \to b\bar{b}b\bar{b}$ with fixed $\Gamma_H = 1$ GeV (third row), at 95% confidence level. The results of the resolved analysis are used up to a mass of 1100 GeV and those of the boosted analysis are used at higher mass where its expected sensitivity is higher. The red curves show the predicted cross sections as a function of resonance mass for the models considered. 176
7.47 The expected and observed 95% CL upper limits on the $G^*_{\mathrm{KK}} \to hh \to b\bar{b}b\bar{b}$ cross section strength modifier μ ($\sigma = \mu\sigma(G^*_{\mathrm{KK}})$) in the bulk RS model with $k/\bar{M}_{\mathrm{Pl}} = 1.0$ for the combination of resolved and boosted analyses at $\sqrt{s} = 8$ and 13 TeV. The search sensitivity of the analysis at $\sqrt{s} = 13$ TeV is similar to that achieved at $\sqrt{s} = 8$ TeV with 19.5 fb^{-1} for resonance masses below 1350 GeV but exceeds it above that mass by factors of 1.4 at 1500 GeV and 12 at 2000 GeV. The vertical blue line at a mass of 2000 GeV indicates the upper end of the search region for the 8 TeV analysis. . . 177
7.48 (Left) The absolute selection efficiency as function of G^*_{KK} mass at eacg stage of the event selection. Trigger efficiency is 100% after requiring two large-R jets, hence now shown on the plot. (Right) The selection efficiency of in each b-tag categorization after requiring $X_{hh} < 1.6$ as function of G^*_{KK} mass. 180
7.49 Distribution of m_{2J} in the signal region for "2-tag-split" (top left), "3-tag" (top right) and "4-tag" (bottom) 182

7.50 The expected and observed uppser limit for $G^*_{\mathrm{KK}} \to hh \to b\bar{b}b\bar{b}$ in the bulk RS model with $kMPl = 1.0$ at 95% confidence level. Transition point from resolved analysis to boosted analysis is at 1000 GeVsuch that maximal sensitivity is used for each mass point. Blue curve corresponds to the results from first stage of analysis. 183

8.1 Trigger efficiency of `HLT_j420_a10_lcw_L1J100` with respect to `HLT_j240_a10_lcw_L1J75` as function of leading large-R jet p_{T} (left) and dijet mass of two leading large-R jet. 190
8.2 (Left) $E_{\mathrm{T}}^{\mathrm{miss}}$ distribution for various VH signal samples; (Right) Correlation between $E_{\mathrm{T}}^{\mathrm{miss}}$ and $\Delta\phi$ between $E_{\mathrm{T}}^{\mathrm{miss}}$ direction and Higgs candidate jet direction for a WH resonance mass of 2 TeVin 2-tag signal region. 192
8.3 Fraction of events that are correctly matched with V/H assignment by checking if jets chosen for V/H candidates are consistent with the truth-level boson in signal samples. Only basic jet kinematic cuts are applied here. 192
8.4 Ratio of sensitivity of various V/H assignment scheme over the reference scheme "V-preferred", as function of resonance mass points, for both WH(left) and ZH(right) signal samples. Sensitivity here is the combined sensitivity from 1-tag and 2-tag signal regions which will be defined below. 194
8.5 Parameterization of vector boson mass cut and D_2 cut as function of jet p_{T} in the 50% medium working point. 195
8.6 Signal acceptance×efficiency as a function of resonance mass 196
8.7 Signal efficiency of the total MET cut and of each of its sub-cuts (on the magnitude and azimuthal angle) as a function of the resonance mass, measured in WH and ZH signal samples. The "ME" line corresponds to an OR of the other cuts, i.e., an event is only kept if it has low MET or small $\Delta\phi$. 197
8.8 Signal efficiency at various stages of the event selection as a function of resonance mass for the WH (left) and ZH (right) selections (applied to the corresponding sample). The "large-R jet" curve includes the preselection cuts, such as lepton and MET vetoes. 197
8.9 Background efficiencies at various stages of the event selection for the dijet, top and V+jets MC. The 1-tag and 2-tag regions correspond to the combined $V = W, Z$ signal regions. 198
8.10 Illustration of 0-tag extrapolation method for multijet backgrounds. Such extrapolation is not only limited in SR, but can be applied on all mass regions such as sidebands and validation regions. The sideband illustrated here is for normalization estimation purpose as will be discussed in Section 8.4.3 200
8.11 Comparison of 0-tag SR shape to the 1-tag (left) and 2-tag (right) SR shapes in multijet MC simulation. 200

8.12 Illustration of orthogonal mass regions on the 2D H-jet / V-jet mass plane. Left is the illustration using 0-tag data sample and right is a schematic illustration of the divisions. Exact definition of regions in Table 8.4. 201
8.13 Post-fit distribution of m_{JJ} of VH di-jet system in 1-tag (left) and 2-tag (right) SB. No kinematic re-weighting applied here yet. 203
8.14 Distribution of track jet p_{T} ratio (left) and subleading track jet p_{T} associated to H-jet in 2-tag (first row) and 1-tag (second row) before kinematic re-weighting 205
8.15 The weights applied for the track jet p_{T} ratio distribution (left) and sub-leading track jet p_{T} (right) in the 2-tag region at first iteration. Weights are smoothed with polynomial function in certain range with enough statistics. If kinematic variable is above (below) the fit range, then value evaluated at upper bound (lower bound) of fit range is used. Weight is also not allowed to fall below 0.1 to prevent events from receiving negative or zero weight due to the kinematic re-weighting. 205
8.16 The weights applied for the track jet p_{T} ratio distribution (left) and sub-leading track jet p_{T} (right) in the 2-tag region at last (8th) iteration. Weights are smoothed with polynomial function in certain range with enough statistics. If kinematic variable is above (below) the fit range, then value evaluated at upper bound (lower bound) of fit range is used. Weight is also not allowed to fall below 0.1 to prevent events from receiving negative or zero weight due to the kinematic re-weighting. 206
8.17 The total weights applied for the track jet p_{T} ratio distribution (left) and sub-leading track jet p_{T} (right) in the 2-tag region after all iteration. 207
8.18 Distribution of invariant mass of VH di-jet system m_{JJ} in 1-tag (left) and 2-tag (right) SB. Kinematic re-weighting has been applied to the 2-tag region only. 207
8.19 Distribution of dijet system invariant mass (first row), H-jet p_{T} (second row), Δy_{12} of dijet system (third row) and ΔR between dijet (last row) in 1-tag (left) and 2-tag (right) VR-SR. Kinematic re-weighting is applied for 2-tag only. 209
8.20 Distribution of H-jet mass (first row), track jet p_{T} ratio associated to H-jet (second row), V-jet D_2 (third row) and V-jet mass (last row) in 1-tag (left) and 2-tag (right) VR-SR. Kinematic re-weighting is applied for 2-tag only. 210
8.21 Distribution of dijet system invariant mass (first row), H-jet p_{T} (second row), Δy_{12} of dijet system (third row) and ΔR between dijet (last row) in 1-tag (left) and 2-tag (right) VR-SB. Kinematic re-weighting is applied for 2-tag only. 211
8.22 Distribution of H-jet mass (first row), track jet p_{T} ratio associated to H-jet (second row), V-jet D_2 (third row) and V-jet mass (last row) in 1-tag (left) and 2-tag (right) VR-SB. Kinematic re-weighting is applied for 2-tag only. 212

8.23 Distribution of dijet system invariant mass (first row), H-jet p_{T} (second row), Δy_{12} of dijet system (third row) and ΔR between dijet (last row) in 1-tag (left) and 2-tag (right) WH signal region. Kinematic re-weighting is applied for 2-tag only. 214
8.24 Distribution of H-jet mass (first row), track jet p_{T} ratio associated to H-jet (second row), V-jet D_2 (third row) and V-jet mass (last row) in 1-tag (left) and 2-tag (right) WH signal region. Kinematic re-weighting is applied for 2-tag only. 215
8.25 Distribution of dijet system invariant mass (first row), H-jet p_{T} (second row), Δy_{12} of dijet system (third row) and ΔR between dijet (last row) in 1-tag (left) and 2-tag (right) ZH signal region. Kinematic re-weighting is applied for 2-tag only. 216
8.26 Distribution of H-jet mass (first row), track jet p_{T} ratio associated to H-jet (second row), V-jet D_2 (third row) and V-jet mass (last row) in 1-tag (left) and 2-tag (right) ZH signal region. Kinematic re-weighting is applied for 2-tag only. 217
8.27 Smoothing fit using MJ5 function for multijet background prediction in WH (first row) and ZH (second row) signal regions of 1-tag (left) and 2-tag (right). Statistical smoothing uncertainties ("Fit Variations") are determined by varying fit parameters within uncertainties in a correlated way. The ratio panel shows the significance of the points with respect to the fit result. 219
8.28 Smoothing fit using dijet/exponential functions for non-multijet background prediction in WH (first row) and ZH (second row) signal regions of 1-tag (left) and 2-tag (right). Statistical smoothing uncertainties ("Fit Variations") are determined by varying fit parameters within uncertainties in a correlated way. The ratio panel shows the significance of the points with respect to the fit result. 220
8.29 Pre-fit m_{VH} distributions in WH (top) and ZH (bottom), 1-tag (left) and 2-tag (right) signal regions. 221
8.30 Smoothing fit on data with $t\bar{t}$ and V+jets MC subtracted (first row) and multijet prediction (second row) in 1-tag (left) and 2-tag (right) VRSR. 226
8.31 Smoothing fit on data with $t\bar{t}$ and V+jets MC subtracted (first row) and multijet prediction (second row) in 1-tag (left) and 2-tag (right) VRSR with the D_2 requirement. 227
8.32 Smoothing fit on data with $t\bar{t}$ and V+jets MC subtracted (first row) and multijet prediction (second row) in 1-tag (left) and 2-tag (right) VRSB. 228
8.33 Smoothing fit on data with $t\bar{t}$ and V+jets MC subtracted (first row) and multijet prediction (second row) in 1-tag (left) and 2-tag (right) VRSB with the D_2 requirement. 229
8.34 Fitted smoothing function ratio between multijet prediction over (subtracted) data as function of m_{JJ}, in 1-tag (left) and 2-tag (right) VRSR. The ratio of data eigenvariations from smoothing fit statistical fluctuation over data nominal fit is also shown for comparison. 230

8.35 Fitted smoothing function ratio between multijet prediction over (subtracted) data as function of m_{JJ}, in 1-tag (left) and 2-tag (right) VRSR with the D_2 requirement. The ratio of data eigenvariations from smoothing fit statistical fluctuation over data nominal fit is also shown for comparison. 231
8.36 Fitted smoothing function ratio between multijet prediction over (subtracted) data as function of m_{JJ}, in 1-tag (left) and 2-tag (right) VRSB. The ratio of data eigenvariations from smoothing fit statistical fluctuation over data nominal fit is also shown for comparison. 231
8.37 Fitted smoothing function ratio between multijet prediction over (subtracted) data as function of m_{JJ}, in 1-tag (left) and 2-tag (right) VRSB with the D_2 requirement. The ratio of data eigenvariations from smoothing fit statistical fluctuation over data nominal fit is also shown for comparison. 232
8.38 Ratio of fitted multijet predictions obtained with the dijet and MJ3-8 functions with respect to the nominal MJ5 function, in each signal region. 232
8.39 Ratio of multijet predictions obtained by fitting the dijet function to different ranges of the m_{JJ} distribution with respect to the nominal range, in each signal region. . . 233
8.40 Impact of different experimental systematic uncertainties on the signal yields of the (top left) WH 1-tag, (top right) WH 2-tag, (bottom left) ZH 1-tag and (bottom right) ZH 2-tag signal regions, as a function of the resonance mass. Of the up and down variations, the one with the largest impact is plotted. 234
8.41 Post-fit m_{JJ} distribution in WH (top) and ZH (bottom) signal regions for 1-tag (left) and 2-tag (right) respectively. 238
8.42 Pulls and constrains on nuisance parameters in the combined fit to the full dataset, in the 2 TeV mass point, shown for the WH (top) and ZH (bottom) channels, comparing observed (black) with the Asimov dataset (red). 239
8.43 Pulls and constrains on nuisance parameters in the combined fit to the full dataset, in the 3 TeV mass point, shown for the WH channels, comparing observed (black) with the Asimov dataset (red). 240
8.44 Ranking of nuisance parameters in terms of post-fit impact on $\hat{\mu}$ for the WH (left) and ZH (right) channels, for the 2 TeV S+B fit. The best-fit μ and associated statistical uncertainties are (left) $\mu = 0.145033 + 0.188445/-0.171449$ (stat.) and (right) $\mu = -0.143086 + 0.287485/-0.237264$ (stat.). 242
8.45 Ranking of nuisance parameters in terms of post-fit impact on $\hat{\mu}$ for the WH (left) and ZH (right) channels, for the 3 TeV S+B fit. The best-fit μ and associated statistical uncertainties are (left) $\mu = 3.77929 + 1.41278/-1.25674$ (stat.) and (right) $\mu = 6.89471 + 2.54038/-2.22707$ (stat.). 243

8.46 The number of predicted background events in the VH 1-tag and 2-tag signal regions after the fit, compared to the data. The "Other Backgrounds" entries include both $t\bar{t}$ and V+jets. Uncertainties correspond to the total uncertainties in the predicted event yields, and are smaller for the total than for the individual contributions because the latter are anti-correlated. The yields for m =2 TeV V' bosons decaying to VH in *Model A* are also given. Due to rounding the totals can differ from the sums of components. 244
8.47 Observed p_0 values shown for the WH (left) and ZH (right) channels. 245
8.48 Observed p_0 values shown for the (top left) WH 1-tag, (top right) WH 2-tag, (bottom left) ZH 1-tag and (bottom right) ZH 2-tag regions. 245
8.49 The observed and expected cross-section upper limits at the 95% confidence level for $pp \to V' \to VH \to q\bar{q}'(b\bar{b} + c\bar{c})$ in *Model A* and *Model B* in the (left) ZH and (right) WH signal regions. The red and magenta curves show the predicted cross-sections as a function of resonance mass for the models considered. 246

A.1 Pipeline of pixel detector simulation and digitization chain 252
A.2 Differential (left) and Integrated (right) cross section as function of energy loss for single collision between 45 GeV pion and silicon material. The differential cross section is expressed in the form of $E^2\sigma(E)$, while the integrated cross section is expressed in the form of moments defined as $M_v = N_a \int_0^\infty E^v \sigma(E) dE$. 254
A.3 (Left) Total energy loss per micro-meter for muon of 1 GeV transpassing silicon layers of different thickness, convoluted from single collisions cross-section ; (Right) Total lenergy loss spectrum for 1 GeV passing through a silicon detector of thickness 10 μm as calcualted under different models. Curve a is the one from Bichsel Model; Curves b,c and d are from Shulek function 254
A.4 Sketch of implementation workflow of the Bichsel Model in ATLAS 256
A.5 Normalized distribution of deposited energy for different type of incoming particles of different selected beta-gamma ranges. From top to bottom it corresponds to proton, kaon, pion, muon and electron 257
A.6 Fraction of total energy deposited in the pixel layer. The flight path in pixel layer is divided into 20 segments evenly and sorted by the amount of energy deposited in each of them. Black curve corresponds to the fraction of deposited energy in first segment over total deposited energy and red curve corresponds to the fraction of deposited energy in first two segments over total deposited energy. 258
A.7 Normalized distribution of p_{T} and η for tracks selected as candidates for $Z \to \mu\mu$ decay in both data and MC samples. The red curve represents the uniform model and blue dashed line represents the Bichsel Model. 260

A.8 Normalized distribution of pixel cluster size in transverse direction (first row) and longitudinal direction (second row) for IBL (left) and b-layer (right), measured on clusters associated to $Z \to \mu\mu$ tracks. The red curve represents the uniform model and blue dashed line represents the Bichsel Model. 261
A.9 Normalized distribution of pixel cluster maximal charge fraction in IBL (left) and b-layer (right) for $Z \to \mu\mu$ tracks. The red curve represents the uniform model and blue dashed line represents the Bichsel Model. 261
A.10 Normalized distribution of track-hit residuals in transverse (left) and longitudinal (right) direction in IBL (first row), b-layer (second row), and other pixel layers (third row) for $Z \to \mu\mu$ tracks of $p_{\mathrm{T}} > 25$ GeV and $|\eta| < 1.5$. The red curve represents the uniform model and blue dashed line represents the Bichsel Model. 263
A.11 Pull of track-hit residuals in transverse (left) and longitudinal (right) direction as function of track p_{T} (up) and η (down). Hits from all tracks in $Z \to \mu\mu$ track collection with $p_{\mathrm{T}} > 1$ GeV on all pixel layers are used. The red curve represents the uniform model and blue dashed line represents the Bichsel Model. 264
A.12 Normalized distribution of track-hit residuals in transverse (left) and longitudinal (right) direction in end-caps for $Z \to \mu\mu$ tracks of $p_{\mathrm{T}} > 25$ GeV. The red curve represents the uniform model and blue dashed line represents the Bichsel Model. . . 264
A.13 Normalized distribution of track impact parameter in transverse (d_0, left) and longitudinal (z_0, right) direction for $Z \to \mu\mu$ tracks of $p_{\mathrm{T}} > 25$ GeV. The red curve represents the uniform model and blue dashed line represents the Bichsel Model. . . 265
A.14 Resolution of impact parameter in transverse (d_0, left) and longitudinal (z_0, right) direction as function of track p_{T} (up) and η (down). Hits from all tracks in $Z \to \mu\mu$ track collection with $p_{\mathrm{T}} > 1$ GeV on all pixel layers are used. The red curve represents the uniform model and blue dashed line represents the Bichsel Model. 265
A.15 CPU time per *HIT* spent on simulating charge distribution along flight path (left) and on simulating drift of ionized charges to diodes (right). In the left plot, the reduction sequence is red, blue and purple. 267
A.16 (Left) CPU time as function of pile-up with Bichsel Model turned on and off; (Right) the percentage of CPU time increase as function of pile-up 267
A.17 Effect of approximations introduced during computing time optimization on selected pixel cluster and tracking observables: Pixel cluster size in transverse direction (top left), charge fraction (top right), track-hit residual in transverse direction (bottom left), track-hit residual in longitudinal direction (bottom right). Red curve represents the nominal uniform model; Dashed blue line represents the Bichsel Model before approximations; Dashed purple line represents the Bichsel Model after approximations. 268

B.1 ΔR between two b-hadrons in truth records for $h \to b\bar{b}$ jets and $g \to b\bar{b}$ jets in $600 < p_{\mathrm{T}} < 1000$ GeV (left) and $1250 < p_{\mathrm{T}} < 2000$ GeV (right) 270
B.2 LO and NLO Feynman diagram for $b\bar{b}$ production 270
B.3 Illustration of exclusive-k_t algorithm 272
B.4 Normalized distribution of ΔR between subjets (left) and reconstructed secondary vertices (right) for $g \to b\bar{b}$ jet with $150 < p_{\mathrm{T}} < 300$ GeV and $|\eta| < 2.5$ 272
B.5 Normalized distribution of "Second-MV1" (top left), "NtrksDiff" (top right), "Combined SV Mass" (bottom left) and correlation between "NtrksDiff" and "Combined SV Mass" (bottom right) 274
B.6 Background single b-jet rejection as function of signal double b-jet efficiency using different combination schemes. The efficiency of having two secondary vertices passing quality cut is already included here. 275
B.7 Probability of finding double secondary vertices in signal sample as function of ΔR under different conditions. Black curve is the inclusive efficiency; Blue dashed line is the same efficiency but requiring both b-hadrons to be $p_{\mathrm{T}} > 5$ GeV, $|\eta| < 2.5$; Red line represents the efficiency under same condition as dashed blue line, but additionally requiring each b-hadron should be assigned to separate subjet; Purple line represents the efficiency under same condition as red line, but additionally requiring distance between b-hadron to corresponding subjet less than 0.2 276
B.8 Illustration of $N = 3$ splitting in exclusive-k_t when $N = 2$ splitting fails. 277
B.9 Background single b-jet rejection as function of signal double b-jet efficiency after combining $N = 3$ and $N = 2$ configuration when 1) (left) compared to $N = 2$ only configuration 2) (right) compared across different p_{T} bins 277
B.10 Correlation between reconstructed and truth ΔR between secondary vertices in signal double b-jets using exclusive-k_t algorithm for $60 < p_{\mathrm{T}} < 100$ GeV (top left), $100 < p_{\mathrm{T}} < 150$ GeV (top right), $150 < p_{\mathrm{T}} < 300$ GeV (bottom left) and $300 < p_{\mathrm{T}} < 500$ GeV (bottom right). The z-axis is in log-scale. 278
B.11 Illustration of workflow of *k-means* clustering algorithm for $g \to b\bar{b}$ tagging 280
B.12 Normalized distribution of "ΔR Significance" (top left), "NtrksDiff" (top right) and "Combined SV Mass" (bottom left) between signal double b-jets and background single b-jets. The background jet rejection as function of signal jet efficiency using different algorithm configurations are also shown in the bottom right: Blue curve represents the case using two-track vertices as input primitive vertices; Red curve represents the case using MSV as input primitive vertices; Black curve represents the case using MSV as input, and with outliers being removed in an iterative way as described above. 281

B.13 Background single b-jet rejection as function of double b-jet efficiency between *k-means* and exclusive-k_t algorithms in $60 < p_{\mathrm{T}} < 100$ GeV (top left), $100 < p_{\mathrm{T}} < 150$ GeV (top right), $150 < p_{\mathrm{T}} < 300$ GeV (bottom left) and $300 < p_{\mathrm{T}} < 500$ GeV (bottom right) 282
B.14 Correlation between reconstructed and truth ΔR between secondary vertices in signal double b-jets using *k-means* algorithm for $60 < p_{\mathrm{T}} < 100$ GeV (top left), $100 < p_{\mathrm{T}} < 150$ GeV (top right), $150 < p_{\mathrm{T}} < 300$ GeV (bottom left) and $300 < p_{\mathrm{T}} < 500$ GeV (bottom right). The z-axis is in log-scale. 283
B.15 RMS of the distribution of $\Delta R_{recon} - \Delta R_{truth}$ in signal double b-jets for $60 < p_{\mathrm{T}} < 100$ GeV (top left), $100 < p_{\mathrm{T}} < 150$ GeV (top right), $150 < p_{\mathrm{T}} < 300$ GeV (bottom left) and $300 < p_{\mathrm{T}} < 500$ GeV (bottom right) 284

Chapter 1

Introduction

Everything not forbidden is compulsory

— Murray Gell-Mann

Over 20th century, especially the last few decades, the Standard Model has been established to be highly successful in describing our world at the most fundamental level. It tells us that our seemingly complex world full of variations is made of two types of fermions, quarks and leptons, each of which has three generations and six flavors in total. The dynamics and interaction of these particles is governed by only a handful of basic physics principles, based on which three most fundamental interactions between particles are found: electromagnetic, weak and strong interaction[1]. To make the picture even more elegant, all these three interactions can be unified through a gauge symmetry under $SU(3) \times SU(2) \times U(1)$.

However, what makes the Standard Model truly remarkable is that all its predictions are confirmed by experimental high energy physics at precision levels. In particular, all force carriers, the so-called *gauge bosons*, predicted by the Standard Model are found by humans one by one as we extend our particle colliders to the corresponding energy scale. The last element of the Standard Model, the Higgs boson, which is playing a central role in the whole picture through so-called *spontaneous symmetry breaking* (or *Higgs mechanism*), was just discovered by ATLAS and CMS collaborations in 2012 using proton-proton collisions produced by the Large Hadron Collider (LHC) at a confidence level beyond 5σ [1, 2].

Despite of great success of the Standard Model, several disturbing issues also arise at the same time. One of the most disturbing problems is probably the so-called *hierarchy problem*. While the hierarchy problem typically manifests itself as the divergence of Higgs mass from radioactive correction, this is more a tip of iceberg among a series fundamental questions of *why so* on our

[1] There is an additional interaction between any massive particles, which is the gravity. However, it is not included under the Standard Model framework and is significantly weaker than other three interactions.

universe: Why is gravity so weak? Why is there a huge gap between electroweak scale and Planck scale? Is the Standard Model truly fundamental?... The list of *why* can simply keep extending as we are diving further into it. However, just like the situation at the beginning of 20th century when "*The beauty and clearness of the dynamical theory, which asserts heat and light to be modes of motion, is at present obscured by two clouds*"[2], these myths are the opportunities for us to discover brand new world. Numerous new theories or frameworks beyond the Standard Model are proposed, from supersymmetry to extra dimensions, trying to answer these questions. Nevertheless, nobody knows the true answer unless proved by the experiment.

In this thesis, we are trying to tackle these fundamental problems in the nature from an experimental point of view. In order to probe new physics beyond the Standard Model at an energy scale higher than the already discovered electroweak scale, proton-proton collisions with unprecedented collision energy of 13 TeV at the LHC, the largest and most energetic particle collider ever built by human beings, are exploited. By tracing the particles created from collisions using ATLAS detector, one is able to infer the physics at short distances, thus either testing existing theories or discovering new physics. In particular, many new models beyond the Standard Model predicts heavy resonances of narrow width at TeV scale, which is an excellent phenomena for the LHC. Furthermore, these heavy resonances can have large coupling to the Standard Model sector via electroweak bosons and the Higgs boson, which can provide various signature in experiment through these Standard Model bosons' decays. Two searches are therefore presented in this thesis trying to cover a wide range of heavy resonances in spin-0, spin-1 or spin-2, with masses above 1 TeV. Searches are conducted in the channel where these heavy resonances decay to either a pair of Higgs boson or a Higgs boson associated with another Standard Model gauge boson. Although these heavy resonances are predicted by different specific models, the experiment result itself is model-independent to a large extent, making our results generic enough.

All searches presented in this thesis are done in the all-hadronic channel, meaning Higgs bosons and electroweak gauge bosons decay hadronically. While this has the advantage of high branching ratio, it was traditionally regarded as insensitive channel due to dominant multijet background produced at hadron colliders. However, due to the heavy mass of resonances being hunted for, Higgs boson and W/Z boson are so boosted that their decay products get collimated. This observation turns out to be a crucial leverage point through various techniques developed in the so-called *jet substructure*, a field being very active in last ten years on LHC [3, 4, 5, 6]. In addition, since Higgs particle decays dominantly to $b\bar{b}$ final state, displaced vertices left by b-hadrons can provide a unique signature which can strongly suppresses background process. In the thesis, development of a powerful boosted boson identification techniques fully exploiting these two aspects is presented as well. It turns out this techniques can significantly extend our search sensitivity to very boosted phase space that was never able to be reached before.

[2]By Lord Kelvin in the speech "Nineteenth-Century Clouds over the Dynamical Theory of Heat and Light"

The thesis is organized in following way. An introduction to the theoretical considerations, especially the new physics models beyond Standard Model being searched for, is presented in Chapter 2; A general introduction to the LHC as well as ATLAS detector can be found in Chapter 3 and 4; Reconstruction of physics objects that are relevant to the searches in this thesis are presented in Chapter 5; The techniques being developed for boosted boson identification can be found in Chapter 6; Two searches for the heavy resonances can be found in Chapter 7 and 8, one being pair production of Higgs boson and another being production of Higgs boson associated with a W/Z boson respectively; Summaries and future prospects of searches in this thesis can be found in Chapter 9; In the last, two studies that are not directly related to this thesis can be found in Appendix A and B. The first one discusses an improved simulation of interactions between particles and pixel detectors which has already been implemented into ATLAS official simulation. The second one discusses several advanced techniques that was explored to resolved two close-by b-hadrons beyond the limit of existing techniques.

Chapter 2

Theoretical Considerations

Particle physics is essentially trying to answer two very fundamental questions: what the most fundamental particles that constituent our matter world are, and how these particles interact with each other. The quest for these two questions can originate from as early as the ancient Greek era when people concluded that elements of nature was composed from some fundamental unit from pure philosophy point of view. By the 20th century, especially since the discovery of electromagnetic phenomena and radioactive elements, people started to probe the particle worlds in real sense with solid concept of *atoms*.

Fundamental breakthrough on theoretical side was made in early 20th century with the establishment of relativity and quantum mechanism which completely replaced Newtonian laws of motion. Later by 1960, a more sophisticated quantum field theory was gradually developed, becoming a really powerful tool in describing particles as well as interactions between them (electromagnetic and weak interaction then). At the same time, numerous experimental techniques, most of which are the prototypes of modern experimental methods, were developed enabling either creation or detection of subatomic particles, including the utilization of high energy cosmic ray, bubble chambers, spectrometers, synchrotrons etc.. Such coherent effort from both theory and experiment advancement led to the discovery of various subatomic particles such as neutron (1931), muon (1937), pions (1947), kaons (1949), and eventually the eruption of discoveries of mesons and baryons in 1950s and 1960s, called "particle zoo" at that time.

By the mid 1960s, physicists further realized that there should be even more basic level than protons and neutrons in order to explain the wide spectrum of new particles being discovered. The idea of *quarks* was then proposed in 1964 by Murray Gell-Mann [7] and George Zweig [8] tentatively under this context. In 1973-1974, this idea evolved to a more formal theory called quantum chromodynamics (QCD), in which the quarks were determined to be real particles carrying color charge and interact with each other through strong interactions by exchange of gluons. An unique property of QCD, now called *asymptotic freedom*, was also identified which is essential in

understanding how hadrons are composed of fractionally charged quarks. On parallel, people also started to unify various interactions observed previously under a common framework. The first step was an attempt to combine electromagnetic and weak interactions by Sheldon Glashow [9] in 1961. In 1964, spontaneous symmetry breaking (also called *Higgs mechanism*) was proposed to explain masses of gauge bosons [10, 11, 12]. In 1967, Steven Weinberg [13] and Abdus Salam [14] was able to incorporate Higgs mechanism into the electroweak interaction framework developed by Sheldon Glashow earlier. The formulation of QCD as mentioned above in 1973 was in a similar structure as the unified electroweak theory [15, 16, 17]. Combined with all these efforts, the grand view of the *Standard Model* that people are familiar with today were first presented by John Iliopoulos in a summary talk for a conference in 1974.

The Standard Model turns out to be a great success, since all particles, both fermions and force-mediating gauge bosons, were discovered by high energy physics experiments. The latest example of this, which is also the last piece of the Standard Model, is the discovery of Higgs boson by ATLAS and CMS collaboration using the Large Hadron Colliders (LHC) at the European Organization for Nuclear Research (CERN) [1, 2]. As a matter of fact, high energy particle colliders with higher and higher collision energy were playing a key role in this discovery path: J/ψ particle, a charm-anticharm meson, was discovered at SLAC and Brookhaven by Burton Richter and Samuel Ting independently in 1974; Tau lepton was discovered at SLAC in 1976; Bottom quark was discovered at Fermilab in 1977; Strong evidence for a gluon radiated from initial quark and anti-quark was found in PETRA at DESY and several other experiments; W and Z bosons were discovered by UA1 and UA2 collaborations at CERN in 1983; Precise measurement of Z resonance width carried out at CERN's Large Electron-Positron Collider (LEP) in 1989 strongly suggested there are three and only three generations of fundamental particles; Top quark was discovered by CDF and D0 collaborations at Fermilab in 1995; Higgs boson was discovered by ATLAS and CMS collaborations at CERN using LHC in 2012.

However, the quest of the very first questions people ask in particle physics never ends, even with the discovery of Higgs boson. It turns out there are still many problems – some are even very fundamental – that cannot be explained by the Standard Model. Therefore, the search of physics beyond Standard Model is still ongoing today in both theory and experiment side in all aspects of particle physics.

In this chapter, an overview of the theoretical framework that the work of this thesis resides in is presented. A formal description of the Standard Model is presented in Section 2.1; An overview of the physics beyond Standard Model with focus on the models that searches presented in this thesis are hunting for can be found in Section 2.2. Since this is a very broad topics, it is impractical to cover all aspects here. However, there are numerous excellent pedagogical materials available for readers who wish to know more details. Selected examples include [18] and [19] which are typically used as text book. Examples of short introductions to these topics can also be found in [20] where

part of this chapter is adapted from.

2.1 The Standard Model

2.1.1 Introduction

The Standard Model of particle physics is a framework that can describe three of four known fundamental interactions in the universe as well as all known elementary particles as constituents of the matter world. As summarized in Figure 2.1, all elementary particles are composed of three parts: The spin-1/2 fermions as the building block of matters; The spin-1 gauge bosons as intermediator of fundamental interactions; The spin-0 scalar Higgs boson explaining the origin of mass of other elementary particles.

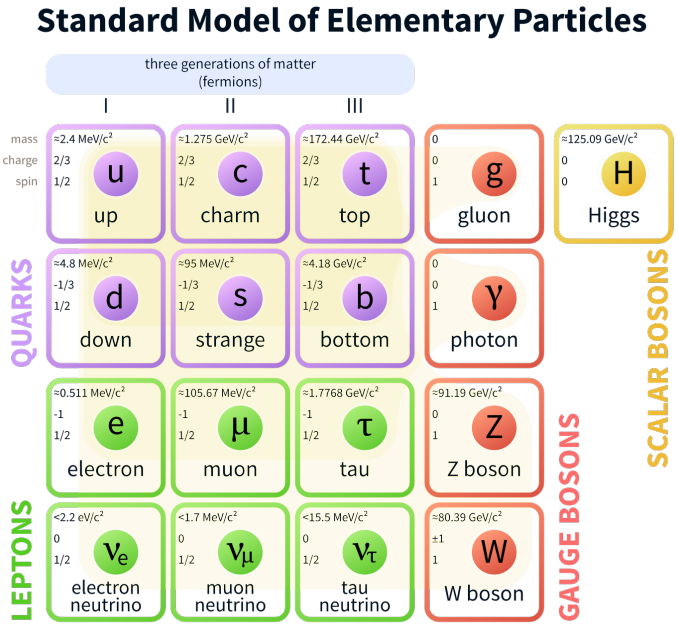


Figure 2.1: Schematic overview of the Standard Model [21]

Fermions are further divided into two categories, quarks and leptons. There are six flavors of quarks, organized in three generations with *up*-type and *down*-type for each generation: *up* and *down*, *charm* and *strange*, *top* and *bottom*. The defining feature of quarks is that they carry the color charge, thus interact via strong interaction. Due to asymptotic freedom as revealed in QCD, quarks cannot exist in standalone form – instead they must bind with each other in the color-neutral form as either *baryons* or *mesons*, collectively called *hadrons*. Common examples of baryons are protons and neutrons, while a common example of meson is pion. Baryons are further bound to

each other through the *nuclear force*, which can be regarded as residual strong interaction, forming the nucleus, which is the central core of an atom. All quarks also take fraction of electric charge. The *up*-type takes +2/3 electric charge and *down*-type takes -1/3 electric charge. Furthermore, quarks carry weak isospin. Therefore, quarks can also couple with the electroweak sector just as any fermion. Similarly, there are also six flavors of leptons, organized in three generations, each of which has a charged particle and electrically neutral neutrinos. All leptons carry weak isospin, and charged leptons also carry electric charge. Therefore they have coupling with the electroweak sector. However, leptons do not carry color charge, hence do not couple via strong interactions. Neutrinos can only interact through weak interactions, making them extremely hard to be detected in experiment.

Gauge bosons are treated as propagator of the fundamental interactions in the Standard Model. In particular, electromagnetic force is carried by the massless photons; weak interaction is intermediated by massive $W^{\pm}/Z$ bosons; Strong interaction is propagated via massless gluons. As we will see, all these interactions can be described by a unified framework of non-Abelian gauge symmetry under symmetry group $SU(3) \times SU(2) \times U(1)$. However, these gauge bosons were supposed to be massless as constrained by the gauge symmetry. As a result, a spontaneous symmetry breaking, also called Higgs mechanism, is developed to explain the origin of mass of W/Z through the introduction of Higgs field in gauge invariant way. Furthermore, mass of fermions is acquired through Yukawa coupling between fermions and Higgs field. Hence, the spin-0 scalar neutral Higgs particle is playing a central role in the Standard Model.

In summary, the Standard Model starts with the relativistic quantum field theory as the basic theoretical framework to describe particles and their interactions through fields. The local gauge symmetry provides an elegant way to formulate the Lagrangian and thus is able to unify all three basic interactions. This is then supplemented by spontaneous symmetry breaking to embed massive particles in a gauge-invariant way. With model being built, quantum field theory also provides a powerful tool to calculate the observables such as cross-sections for any process in order to compare with the experiment data. However, before predictions can be made from the Standard Model there are a few input parameters that have to be predetermined from experiments.

2.1.2 Fields

Natural unit ($\hbar = 1$ and $c = 1$) is used in this section, and throughout the whole chapter. The convention of metric being used here is

$$g_{\mu\nu} = \begin{pmatrix} 1 & 0 & 0 & 0 \\ 0 & -1 & 0 & 0 \\ 0 & 0 & -1 & 0 \\ 0 & 0 & 0 & -1 \end{pmatrix} \tag{2.1}$$

In quantum field theory, particles are described by fields, which act as operators in the quantum mechanics on the particle state in Hilbert space through creating and annihilation operators for particles and anti-particles. For particles in the Standard Model, they are described by different kind of fields depending on the spin. Spin-0 particles are described by scalar (complex) fields, usually denoted by $\phi(x)$; Spin-1 particles are described by vector field, usually denoted by $A_\mu(x)$; Spin-1/2 particles are described by spinor field, usually denoted by $\psi(x)$.

The dynamics of particles are then described through Lagrangian $\mathcal{L} = \mathcal{L}(\phi(x), \partial_\mu\phi(x))$ which yields the action

$$S = \int d^4x \mathcal{L}(\phi(x), \partial_\mu\phi(x)) \tag{2.2}$$

. Then following the Euler-Lagrangian equations based on Hamilton's principle, one can get the equation of motions as

$$\partial_\mu \frac{\partial\mathcal{L}}{\partial(\partial_\mu\phi)} - \frac{\partial\mathcal{L}}{\partial\phi} = 0 \tag{2.3}$$

where ϕ represents any generic field or its components here.

Scalar Complex Fields

The Lagrangian for a free scalar complex field is

$$\mathcal{L} = (\partial_\mu\phi)^\dagger(\partial^\mu\phi) - m^2\phi^\dagger\phi \tag{2.4}$$

which could lead to the Klein-Gordon equation:

$$(\partial_\mu\partial^\mu + m^2)\phi = 0 \tag{2.5}$$

Vector Fields

Vector field $A_\mu(x)$ is used to describe spin-1 particles. Compared to the scalar field, it has another degree of freedom in terms of helicity for both the annihilation / creation operators and the particle states. Vector fields can be further divided into massive case and massless case.

For massive vector fields, free Lagrangian can be written as

$$\mathcal{L} = -\frac{1}{4}F_{\mu\nu}F^{\mu\nu} - \frac{m^2}{2}A_\mu A^\mu \tag{2.6}$$

where $F_{\mu\nu} = \partial_\mu A_\nu - \partial_\nu A_\mu$. The equation of motion to it is:

$$[(\partial_\mu\partial^\mu + m^2)g^{\mu\nu} - \partial^\mu\partial^\nu]A_\nu = 0 \tag{2.7}$$

Its solution in momentum space is

$$\epsilon_\mu^{(\lambda)} e^{\pm ikx} \tag{2.8}$$

where there are three independent *polarization* vectors $\epsilon_\mu^{(\lambda)}$, corresponding to $\lambda = \pm 1, 0$. All these polarization vectors are transverse to the propagation direction k in 4-dimension and can be chosen to be orthogonal and normalized through proper choice of basis.

For massless term, the free Lagrangian is the same as above but without the quadratic mass term. Therefore the equation of motion is also similar to massive one by setting $m = 0$. However, being massless has an important physical consequence on its solution, that only two polarization vectors are transverse while the third one being longitudinal polarization vector is unphysical. This is because such longitudinal polarization can always be removed by a gauge transformation.

Dirac Fields

Spin-1/2 fermions are described by 4-component spinor field

$$\psi(x) = \begin{pmatrix} \psi_1(x) \\ \psi_2(x) \\ \psi_3(x) \\ \psi_4(x) \end{pmatrix} \tag{2.9}$$

The free Lagrangian for spinor field is

$$\mathcal{L} = \bar{\psi}(i\gamma^\mu \partial_\mu - m)\psi \tag{2.10}$$

where

$$\bar{\psi} = \psi^\dagger \gamma^0 \tag{2.11}$$

where γ_μ are the Dirac matrices written in terms of Pauli matrices.

2.1.3 Gauge Theory

As one might notice only free Lagrangian is discussed above, while the interaction term is missing. It turns out the structure of interactions between vector bosons and fermions, as well as vector boson self-coupling can be dictated by the principle of gauge invariance. In particular, the Quantum Electrodynamics (QED) is determined by the Abelian gauge symmetry, while non-Abelian gauge symmetry is needed when it comes to more generalized electroweak and strong interactions.

Abelian Gauge Symmetry

QED is dictated by the U(1) symmetry, which requires invariance of Lagrangian

$$\mathcal{L}_0 = \bar{\psi}(\gamma^\mu \partial_\mu - m)\psi \tag{2.12}$$

under the local transformation

$$\psi(x) \to \psi'(x) = e^{i\alpha(x)}\psi(x) \tag{2.13}$$

for arbitrary real $\alpha(x)$. This requirement leads to the introduction of covariant derivative in place of normal partial derivative:

$$\partial_\mu \to D_\mu = \partial_\mu - ieA_\mu \tag{2.14}$$

where A_μ is the vector field as introduced earlier which transforms as

$$A_\mu(x) \to A'_\mu(x) = A_\mu(x) + \frac{1}{e}\partial_\mu\alpha(x) \tag{2.15}$$

under U(1) symmetry. The *local* transformation is really the key here since otherwise it would be simply a global phase transformation and the original free Lagrangian is invariant under such global transformation automatically without the need of covariant derivative. As a result, the interaction term between fermion and vector field naturally arises after this substitution:

$$\mathcal{L} = \bar{\psi}(i\gamma^\mu D_\mu - m)\psi = \mathcal{L}_0 + e\bar{\psi}\gamma^\mu\psi A_\mu = \mathcal{L}_0 + \mathcal{L}_{int} \tag{2.16}$$

Of course, there should be another term in the Lagrangian which is the kinematic term for vector field

$$\mathcal{L}_A = -\frac{1}{4}F_{\mu\nu}F^{\mu\nu} \tag{2.17}$$

where $F_{\mu\nu} = \partial_\mu A_\nu - \partial_\nu A_\mu$. In the definition of $F_{\mu\nu}$, there is no need to replace normal derivative with covariant derivative since it is already invariant under the local gauge transformation. Vector field A_μ can be identified as photon since the equation of motion from this Lagrangian would be Maxwell's equation. As we can see, one is able to formulate QED with the only requirement of local U(1) gauge symmetry.

Non-Abelian Gauge Symmetry

The formulation of Abelian gauge symmetry can be generalized to non-Abelian gauge symmetry, where a multiplet of fermion fields $\Psi = (\psi_1, \psi_2, ..., \psi_n)^T$ is considered. Similar to the Abelian case, one can start with free Lagrangian and realize it is invariant under global transformation

$$\Psi(x) \to U(\alpha^1, \alpha^2, ..., \alpha^N)\Psi(x) \tag{2.18}$$

where U is unitary matrices from n-dimension representation of non-Abelian Lie group G of rank N. As we will see later, only $SU(2)$ and $SU(3)$ with $n = 2$ and $n = 3$ representation are relevant for the Standard Model. The transformation can be written as

$$U = e^{i(\alpha^1 T_1 + ... + \alpha^N T_N)} \tag{2.19}$$

where T_i is the generator of Lie group, a set of Hermitian matrices following Lie algebra

$$[T_a, T_b] = if_{abc}T_c \tag{2.20}$$

where f_{abc} is structure constant.

Now, similar to the case in QED, we put a further requirement that such transformation should be local, i.e. $\alpha^i = \alpha_i(x)$. As a result, normal derivative needs to be replaced by the covariant derivative in free Lagrangian in order to make it invariant under such local transformation:

$$\partial_\mu \to D_\mu = \partial_\mu - ig\boldsymbol{W}_\mu \tag{2.21}$$

where vector field is introduced again together with coupling constant g (in QED as formulated above, e is the coupling constant). Since D_μ is supposed to be applied on the n-dimension multiplet $\Psi(x)$, vector field $\boldsymbol{W}_\mu$ here has to be a $n \times n$ matrix as well. Therefore, we can express it as a linear combination of the generators:

$$\boldsymbol{W}_\mu(x) = T_a W_\mu^a(x) \tag{2.22}$$

where $W_\mu^a(x)$ here is no longer a matrix, but rather acts like a coefficient. However, since all $\boldsymbol{W}_\mu(x)$ can be decomposed in this way, we will refer *vector fields* to these coefficient $W_\mu^a(x)$ from now since that is the one we will be more focused on later on. Now under local gauge transformation that leaves $\mathcal{L}$ invariant, fields would transform as following:

$$\begin{aligned} \Psi &\to \Psi' = U\Psi \\ W_\mu^a &\to W_\mu'^{\,a} = W_\mu^a + \frac{1}{g}\partial_\mu \alpha^a + f_{abc}W_\mu^b \alpha^c \end{aligned} \tag{2.23}$$

Compared to the Abelian case, there is an additional term for vector field at the end which is pure effect from non-Abelian group.

Consequently, the reformulation of Lagrangian directly leads to the interaction term between fermion and vector field

$$\mathcal{L}_{int} = j_a^\mu W_\mu^a = g\bar{\Psi}\gamma^\mu T_a \Psi W_\mu^a \tag{2.24}$$

which can be regarded as a coupling between N vector fields and currents.

As we see in QED, there is no tree-level interaction between photons. However this is no longer the case for non-Abelian gauge symmetry. The field strength tensor $\boldsymbol{F}_{\mu\nu}$ now is

$$\boldsymbol{F}_{\mu\nu} = T_a F_{\mu\nu}^a \tag{2.25}$$

where $F_{\mu\nu}^a = \partial_\mu W_\nu^a - \partial_\nu W_\mu^a + g f_{abc} W_\mu^b W_\nu^c$. This can be seen as a generalization of field strength tensor in QED to $n \times n$ matrices decomposed with generators as basis.

To construct a gauge invariant and scalar Lagrangian term for vector field kinematics, the trace is used:

$$\mathcal{L}_W = -\frac{1}{2}Tr(\boldsymbol{F}_{\mu\nu}\boldsymbol{F}^{\mu\nu}) = -\frac{1}{4}F^a_{\mu\nu}F^{a,\mu\nu} \tag{2.26}$$

By putting the expression of $F^a_{\mu\nu}$ into this kinematic term, one can immediately identify the quadratic and cubic coupling term between vector fields in addition to the familiar kinematic term. Therefore, the vector field self coupling is a direct consequence of non-Abelian transformation.

One should notice that mass term $\frac{m^2}{2}W^a_\mu W^{a,\mu}$ is not included since they are not invariant under gauge transformation. As a result, these vector fields are massless by construction. This peculiar feature has a significant consequence on the electroweak sector as we will discuss later on.

2.1.4 Quantum Chromodynamics

The formulation of Quantum Chromodynamics (QCD) is fairly straightforward following the non-Abelian gauge transformation invariance formality as discussed with the Lie group being $SU(3)$. Fermions are identified as quarks in a triplet with each component representing a color state (R, G, B), thus forming the fundamental $n = 3$ representation of the group. For Lie group $SU(3)$, there are eight generators, which can be expressed under fundamental representation as:

$$T_a = \frac{1}{2}\lambda_a \tag{2.27}$$

where λ_a is 3×3 Gell-Mann matrices. Consequently, there are eight different vector fields G^a_μ, corresponding to eight different kind of intermeidating gluons. Then all the formulations discussed above applies here, with g_s identified as QCD coupling constant.

As a summary the Lagrangian for QCD is

$$\mathcal{L}_{QCD} = \bar{\Psi}(i\gamma^\mu\partial_\mu - m)\Psi + g_s\bar{\Psi}\gamma^\mu\frac{\lambda_a}{2}\Psi G^a_\mu - \frac{1}{4}G^a_{\mu\nu}G^{a,\mu\nu} \tag{2.28}$$

where first term is the free Lagrangian for quarks, second term is coupling between quarks and gluons and third term is a combination of gluon kinematics and self-couplings.

One thing important is that the Lagrangian above only consider one flavor. In the Standard Model we already know there are six different flavors of quarks and the mass for each quark is different. In that case, quark of each flavor is described by a color triplet and a summation of Lagrangians for each flavor following same structure is needed.

2.1.5 Electroweak Sector and the Higgs Mechanism

For electroweak interaction, same formulation as general non-Abelian gauge symmetry discussed earlier can be applied, but using Lie group $SU(2) \times U(1)$. Therefore, there are four generators,

corresponding to three isospin operators and one Abelian hypercharge operator: I_a $(a = 1, 2, 3)$ and $T_4 = Y$ respectively. They form the Lie algebra

$$[I_a, I_b] = i\epsilon_{abc} I_c, \ [I_a, Y] = 0 \tag{2.29}$$

Furthermore, these operators would also correspond to a set of quantum numbers that are supposed to be conserved due to the symmetry: weak isospin I, I_3 and weak hypercharge Y. These quantum numbers are related to the electric charge through $Q = I_3 + Y/2$.

Each of these generators in $SU(2) \times U(1)$ Lie group is associated with a vector field, as we have already seen in the general non-Abelian gauge symmetry above: isotroplet W^a_μ with I_a for $a = 1, 2, 3$ and isosinglet B_μ for Y. Following the same non-Abelian gauge symmetry discussion, Lagrangian for these vector fields are

$$\mathcal{L}_G = -\frac{1}{4} W^a_{\mu\nu} W^{a,\mu\nu} - \frac{1}{4} B_{\mu\nu} B^{\mu\nu} \tag{2.30}$$

where $W^a_{\mu\nu}$ and $B_{\mu\nu}$ are the field strength tensors corresponding to non-Abelian SU(2) and Abelian U(1) respectively. In this pure gauge field Lagrangian, both kinematic terms and gauge self-coupling terms are already included (W^a_μ only). Explicit mass term for gauge fields is forbidden since it would violate gauge symmetry.

Things would get a bit complicated when it comes to the fermion fields. Unlike the case in $SU(3)$, two different representations are used for fermions, depends on its chirality. Left-hand fermions spinor fields have $I = 1/2$ and thus are grouped into $SU(2)$ doublet, while right-handed fermions have $I = 0$ and thus form singlet:

$$\psi^j_L = \begin{pmatrix} \psi^j_{L+} \\ \psi^j_{L-} \end{pmatrix}, \quad \psi^j_{R\sigma} \tag{2.31}$$

where j is the generation index and σ represents each component in the doublet. In the case of lepton, $\sigma = +$ represents neutrino and $\sigma = -$ represents charged lepton. In the case of quarks, $\sigma = +$ represents up-type quark (the one with charge +2/3) and $\sigma = -$ represents down-type quark (the one with charge -1/3). In the original version of the Standard Model, neutrinos are considered to be massless, and there are no right-handed neutrino fields. Therefore, there are in total three doublets for left-hand leptons corresponding to three generations and three singlets for right-hand neutrino; Three doublets for left-hand quarks corresponding to three generations and six singlets for right-hand quarks corresponding to six flavors.

Coupling between fermions and vector fields is realized through covariant derivative

$$\begin{aligned} D^{L,R}_\mu &= \partial_\mu - i g_2 I^{L,R}_a W^a_\mu + i g_1 \frac{Y}{2} B_\mu \\ \mathcal{L}_F &= \sum_j \bar{\psi}^j_L i\gamma^\mu D^L_\mu \psi^j_L + \sum_{j,\sigma} \bar{\psi}^j_{R\sigma} i\gamma^\mu D^R_\mu \psi^j_{R\sigma} \end{aligned} \tag{2.32}$$

where $I_a^L = \frac{1}{2}\sigma_a$ and $I_a^R = 0$. Weak isospin is different under different representations while other parts are the same. There are two coupling constants here one for the $SU(2)$ part and one for $U(1)$ part. Furthermore, mass term for fermions are avoided since an explicit mass term would mix left and right-hand components and hence violate gauge symmetry.

So far, the legitimate Lagrangian for fermion and vector fields under $SU(2) \times U(1)$ are all massless. However, this is inconsistent with the observation on massive W/Z bosons, quarks and charged leptons. Therefore, the Higgs mechanism is introduced to solve this problem through a spontaneous symmetry breaking of $SU(2) \times U(1)$ leaving electromagnetic $U(1)_{em}$ unbroken.

Here a isospin doublet of complex scalar field with hypercharge $Y = 1$, is introduced as

$$\Phi(x) = \begin{pmatrix} \phi^+(x) \\ \phi^0(x) \end{pmatrix} \tag{2.33}$$

Similar to the procedure how we formulate Lagrangian in gauge invariant way, we can start with a free Lagrangian for complex scalar field as discussed in Section 2.1.2, and then replace the partial derivative with covaraint derivative:

$$\mathcal{L}_H = (D_\mu \Phi)^\dagger (D^\mu \Phi) - V(\Phi) \tag{2.34}$$

where

$$D_\mu = \partial_\mu - ig_2 I_a W_\mu^a + ig_1 \frac{Y}{2} B_\mu \tag{2.35}$$

Obviously, $I = 1/2$ representation is used here. The interaction term between vector fields and this scalar complex field arises naturally when we are trying to write out the Lagrangian for it. Next, the Higgs potential, $V(\Phi)$, is defined as

$$V(\Phi) = -\mu^2 \Phi^\dagger \Phi + \frac{\lambda}{4}(\Phi^\dagger \Phi)^2 \tag{2.36}$$

For $\mu^2, \lambda > 0$, this Higgs potential has the shape of famous "Mexican hat" or "wine bottle", as shown in Figure 2.2, where the minimum does not happen at $\Phi = 0$. Instead, it is minimized by a non-vanishing field configurations where $\Phi^\dagger \Phi = 2\mu^2/\lambda$, which is a circle on the complex plane. Now we can select the one that is the eigenstate of electric charge operator such that $Q\Phi = 0$ where

$$Q = I_3 + \frac{Y}{2} = \begin{pmatrix} 1 & 0 \\ 0 & 0 \end{pmatrix} \tag{2.37}$$

This would set $\Phi^+(x) = 0$. Then by choosing Φ^0 to be real, one can get the vacuum expectation value (VEV)

$$< \Phi >= \frac{1}{\sqrt{2}} \begin{pmatrix} 0 \\ v \end{pmatrix} \tag{2.38}$$

where $v = 2\mu/\sqrt{\lambda}$. Although our Lagrangian for this scalar complex field is gauge symmetric, VEV is not, which is the reason why we say gauge symmetry has been *spontaneously broken*.

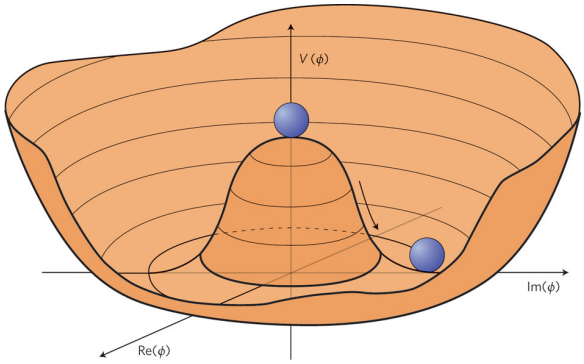


Figure 2.2: Illustration of Higgs potential [22]

Now the complex scalar field can be expanded around the VEV:

$$\Phi(x) = \begin{pmatrix} \phi^+(x) \\ (v + H(x) + i\chi(x))/\sqrt{(2)} \end{pmatrix} \tag{2.39}$$

By expanding the Higgs potential around VEV in this form, one could get a mass term for $H(x)$, while $\phi^+(x)$ and $\chi(x)$ are massless. As a matter of fact, the components ϕ^+ and χ are unphysical degree of freedom since one can always choose a particular gauge such that they vanish. As a result, we have a much simpler expression for Higgs doublet field

$$\Phi(x) = \frac{1}{\sqrt{2}} \begin{pmatrix} 0 \\ v + H(x) \end{pmatrix} \tag{2.40}$$

Consequently, the Higgs potential becomes

$$V = \mu^2 H^2 + \frac{\mu^2}{v} H^3 + \frac{\mu^2}{4v^2} H^4 \tag{2.41}$$

Now the real field $H(x)$ is able to be associated with a physical neutral scalar particle, the Higgs boson, with mass being identified as $M_H = \sqrt{2}\mu$. The triple and quartic self-coupling term is also identified with coupling constant proportional to M_H^2.

Next we put this simplified complex scalar field into the gauge invaraint Lagrangian in order to see the interaction with vector fields. Since the non-zero part of Higgs doublet is $v + H(x)$, the interaction terms break into two parts: one part has the direct trilinear and quadrilinear coupling between $H(x)$ and vector fields; The other part only has the interaction between vector fields with constant v mixed in. The first part is more related to the HWW, HZZ, $HHWW$ and $HHZZ$ coupling, while the second part is the main focus here, which is related to the origin of electroweak

boson mass.

By writing out second term explicitly, one can get

$$\frac{1}{2}(\frac{g_2}{2}v)^2(W_1^2+W_2^2)+\frac{1}{2}(\frac{v}{2})^2\begin{pmatrix} W_\mu^3 & B_\mu \end{pmatrix}\begin{pmatrix} g_2^2 & g_1g_2 \\ g_1g_2 & g_1^2 \end{pmatrix}\begin{pmatrix} W^{3,\mu} \\ B^\mu \end{pmatrix} \tag{2.42}$$

It is unfortunately not very clear on the physics meaning behind it since there are off-diagonal terms. However, this can be easily diagonalized through a proper linear transformation:

$$\begin{aligned} W_\mu^\pm &= \frac{1}{\sqrt{2}}(W_\mu^1 \mp iW_\mu^2) \\ \begin{pmatrix} Z_\mu \\ A_\mu \end{pmatrix} &= \begin{pmatrix} \cos\theta_W & \sin\theta_W \\ -\sin\theta_W & \cos\theta_W \end{pmatrix}\begin{pmatrix} W_\mu^3 \\ B_\mu \end{pmatrix} \end{aligned} \tag{2.43}$$

Now the expression has very clear physics meaning, that it is nothing but quadratic mass term for each vector field after the linear combination. Therefore, we associate $W_\mu^\pm$ with the charged W boson, Z_μ with the neutral Z boson and A_μ with the photon under $U(1)_{em}$. In particular, the mass of each boson can be identified as following

$$\begin{aligned} M_W &= \frac{1}{2}g_2v \\ M_Z &= \frac{1}{2}\sqrt{g_1^2+g_2^2}v \end{aligned} \tag{2.44}$$

In addition, there is a mixing angle during the linear transformation:

$$\cos\theta_W = \frac{g_2}{\sqrt{g_1^2+g_2^2}} = \frac{M_W}{M_Z} \tag{2.45}$$

The mixing angle is a very important parameter to be determined by experiment since it is able to relate coupling constant g_1 and g_2, as well as the relation between W/Z mass. Furthermore, if we plug the linear transformation into the part of Lagrangian where vector fields interact with fermions, one is able to express gauge couplings in terms of electric charge:

$$g_1 = \frac{e}{\cos\theta_W},\ g_2 = \frac{e}{\sin\theta_W} \tag{2.46}$$

While this can successfully solve the mass of electroweak bosons, one needs an additional mechanism for mass of fermions. This is handled through the introduction of coupling between Higgs field and fermion fields, called *Yukawa coupling*:

$$\mathcal{L}_Y = -G_l\bar{L}_L\Phi l_R - G_d\bar{Q}_L\Phi d_R - G_u\bar{Q}_L\Phi^c u_R + h.c. \tag{2.47}$$

Again we plug the simplified Higgs doublet into it, and this can be reduced to

$$\mathcal{L}_Y = -\sum_f m_f \bar{\psi}_f \psi_f - \sum_f \frac{m_f}{v} \bar{\psi}_f \psi_f H \tag{2.48}$$

where $m_f = G_f v/\sqrt{2}$. Here G_f is the Yukawa coupling constants which could be different value for different fermions. In this way, the fermion mass is able to be incorporated to the SM Lagrangian[1]. Additionally, the real Hff coupling is also shown in the reduced Lagrangian, with a coupling proportional to the fermion mass.

But this is not the end of story yet. One complication is that there is more than one generation of fermions, while the formulation above only consider coupling within same generation. For the lepton sector, lepton number is conserved and thus coupling between different generations is forbidden. However, mixing between quark generations is induced by the same Yukawa coupling mechanism as before, but with the coupling now being matrices in the generation space with complex entries:

$$\mathcal{L}_Y^{quarks} = -G_{ij}^d \bar{Q}_L^i \Phi d_R^j - G_{ij}^u \bar{Q}_L^i \Phi^c u_R^j \tag{2.49}$$

where index i, j are generation index. Then we again plug in the simplified complex scalar field. Similar to the case in gauge boson, there would be many off-diagonal items mixing different generations. Therefore a diagonalization is applied here through linear transformation on the fermion fields, leading to mass eigenstates as following:

$$\begin{aligned} \tilde{u}_{L,R}^i &= (V_{L,R}^u)_{ik} u_{L,R}^k \\ \tilde{d}_{L,R}^i &= (V_{L,R}^d)_{ik} d_{L,R}^k \end{aligned} \tag{2.50}$$

And the diagonalized mass matrix becomes:

$$\frac{v}{\sqrt{2}} V_L^q G_q V_R^{q\dagger} \tag{2.51}$$

where $q = u, d$. Here, one would get a 3×3 diagonal matrix for up-type or down-type, thus masses for all six flavors.

Furthermore, this linear transformation introduce a unitary CKM matrix through the flavor-changing quark interaction with charged vector boson

$$V_L^u V_L^{d\dagger} \equiv V_{CKM} \tag{2.52}$$

Due to constraints from unitary, CKM matrix has four independent physical parameters, three real angles and one complex phase. The CKM matrix plays an essential role in the so-called *flavor*

[1] While this relabels the fermion mass as Yukawa coupling, it can hardly explain the origin of huge difference between observed fermion mass, which is sometimes called *flavor hierarchy problem*

physics.

Now with all parts in hand, we are able to write the full Lagrangian as

$$\mathcal{L}_{EW} = \mathcal{L}_G + \mathcal{L}_F + \mathcal{L}_H + \mathcal{L}_Y \tag{2.53}$$

But from discussion above we can see that certain linear transformation on the original fields – both vector fields and fermion spinor fields – is needed in order to be associated with the physical fields and parameters. Therefore, we replace the original vector fields with W/Z and photon field, fermion spinor field with the mass eigenstates. As a result, the fermion-gauge interaction term can be re-written as

$$\mathcal{L}_{FG} = J^\mu_{em} A_\mu + J^\mu_{NC} Z_\mu + J^\mu_{CC} W^+_\mu J^{\mu\dagger}_{CC} W^-_\mu \tag{2.54}$$

which is in a uniform structure that current interacts with electroweak bosons. The current interacting with photon is the EM-current that we have already seen when deriving QED. The current coupling with Z is called *neutral current* and the one coupling with W is called *charged current*. Expressions for these currents are summarized below

$$\begin{aligned} J^\mu_{em} &= -e \sum_{f=l,q} Q_f \bar{\psi}_f \gamma^\mu \psi_f \\ J^\mu_{NC} &= \frac{g_2}{2\cos\theta_W} \sum_{f=l,q} (\bar{\psi}_f (v_f \gamma^\mu - a_f \gamma^\mu \gamma_5) \psi_f) \\ J^\mu_{CC} &= \frac{g_2}{\sqrt{2}} \left(\sum_{i=1,2,3} \bar{\nu}^i \gamma^\mu \frac{1-\gamma_5}{2} e^i + \sum_{i,j=1,2,3} \bar{u}^i \gamma^\mu \frac{1-\gamma_5}{2} V_{ij} d^j \right) \end{aligned} \tag{2.55}$$

In the neutral current, coupling constant are determined by electric charge and isospin:

$$\begin{aligned} v_f &= I^f_3 - 2Q_f \sin^2\theta_W \\ a_f &= I^f_3 \end{aligned} \tag{2.56}$$

One can notice that in electromagnetic current and neutral current, there is no flavor mixing – all fermions only couple to themselves. Thus flavor-changing neutral current can only happen beyond the leading order. On the other hand, flavor mixing happens in the charged current. For lepton sector, this is the mixing between charged lepton and neutrino withint same generation; For quarks, this is the mixing between any two flavors controlled by the CKM matrix. The CKM matrix in charged current is a direct consequence of flavor mixing Yukawa coupling and the diagonalization that we perform in order to move to mass eigenstates.

In addition to the fermion-gauge coupling, there are also gauge boson self-couplings which is entirely contained in the gauge-field part of Lagrangian. This is a direct consequence of the non-Abelian structure of Lie group under which the physics is invariant.

While the Standard Model provides a beautiful framework to incorporate all known particles and interactions, it does contain some parameters that needs to be predetermined from experiment before making any prediction. In the original representation where we formulate the structure, sets of parameters are $g_1, g_2, \lambda, \mu^2, G_f$. However, with all the transformation we have just been through, this can be equivalently replaced by another set of more physical parameters $e, M_W, M_Z, M_H, m_f, V_{CKM}$. Indeed, with the discovery of Higgs boson in 2012, all parameters are known now.

2.2 Physics beyond Standard Model

2.2.1 Difficulties of the Standard Model

Despite of its great success as examined by various high energy physics experiments, the Standard Model is still not a complete theory. For one thing, there are already several very solid experimental observations that cannot be explained by the Standard Model, which are listed below; For another, several theoretical considerations strongly suggest the Standard Model might be an low-energy approximation of a complete theory at higher energy scale.

For the first issue, below is a selected list of the observations that cannot be explained by the Standard Model

- Neutrino mass and oscillation
  As discussed in Section 2.1, in particular in the Higgs mechanism, fermions acquire mass by interacting with the Higgs field through Yukawa coupling. In particular, such coupling is possible because these fermions can be both left-handed and right-handed. However, neutrino is an exception here. In the Standard Model, neutrinos are assumed to be massless, which comes from the assumption that there is only left-handed neutrino. As a matter of fact, such assumption is fairly solid as shown in the famous *Wu Experiment* conducted by Chien-Shiung Wu as well as many other experiments that only left-handed neutrinos are observed. However, this picture kinds of change as people find that flux of neutrinos in certain flavor originated from the Sun was detected to be much less than expected in 1960s. Later people realize that if neutrinos are allowed to oscillate between three different flavors, then those "missing" flux can be attributed to neutrinos oscillated to other flavors. Such hypothesis was later confirmed by numerous experiments with neutrinos from all kinds of sources like sun, atmosphere and nuclear reactors. Nowadays, we already have precision measurement of neutrino oscillation, characterized by the mixing angle θ_{13}, with more than 5σ confidence, for instance, in the *Daya Bay Reactor Neutrino Experiment*. The oscillation of neutrino flavor arises from the mixture of flavor eigenstates and mass eigenstates. When being produced through electroweak interactions, neutrinos start with some pure flavor eigenstate, which is a superposition of mass eigenstates of three flavors. During propagation, the mass eigenstates evolves with different

rate due to the difference of masses between three flavors – in other words, the relative phase between mass eigenstates changes over the time. As a result, their superposition would no longer be the original pure flavor eigenstate, but instead a superposition of three flavor eigenstates now. Since neutrinos can only be observed through electroweak interaction, any observation might collapse to different flavor eigenstate with certain probability. Since the phase changes in a periodic manner, neutrino would go through an oscillation between different pure flavor eigenstates with mixture states in-between. Apparently, neutrino cannot be massless with the experimental observation of oscillation. Nevertheless, further experiment suggest that mass of neutrinos should be very small. However, a massive neutrino would indicate the existence of right-handed neutrino, which has not be found yet.

- Dark matter
  The existence of dark matter is established from numerous astrophysics observations. For example, the spiral galaxy rotation curve does not decrease as one goes further from galaxy center, which is expected by assuming luminous mass were all the masses; Estimation of galaxy cluster mass through galaxy dynamics, X-ray emission and gravitational lensing suggest there is a significant part of invisible mass that is outweighing the visible part with a ratio of approximately $5:1$. All these observations strongly suggest the existence of dark matter and the proportion of these dark matter in our universe is estimated to be about 27%. Unfortunately, for such a big portion of our universe, we have no idea what they really are – in the Standard Model, there is simply no place reserved for the dark matter at all. As a matter of fact, dark matters are neutral, colorless, non-baryonic and massive. Most properties of the dark matter that people know today are inferred from gravitational effect.

- Abundance of matter over anti-matter
  This is also sometimes referred to as *baryon asymmetry* that there is a huge imbalance between baryonic matter and anti-matter in our observed universe. The Standard Model is unable to provide explanation over this, while it is naturally assumed that matters and anti-matters are equally created during the Big Bang. There are several hypotheses trying to explain this, but they are either insufficient to explain the observed imbalance (CP violation), or have not found any experimental support yet.

Furthermore, there are several serious concerns over the Standard Model from theoretical considerations, including hierarchy problem, strong CP problem and so on. Here we would only discuss the hierarchy problem briefly, which is most relevant to the studies of this thesis.

Generally speaking, the hierarchy problem refers to the huge gap between electroweak scale of 246 GeV and huge Planck scale of 10^{19} GeV (weakness of gravity). Technically this is often expressed in terms of the Higgs mass. Experimental observation by ATLAS and CMS has determined the Higgs mass to be 125 GeV. However, due to the coupling between Higgs to fermions, gauge bosons and

themselves, one can imagine loop corrections for the Higgs mass in quantum field theory, and indeed the one-loop correction for Higgs mass is at the order $\delta_m \sim g\Lambda^2$. Here the Λ is the UV cut-off. The correction would diverge as we integrate all momentum in the loop up to infinity. However, such divergence is not really the problem, since people already know how to address them through *renormalization* trick. Roughly speaking, in the normalization theory, parameters such as mass and couplings are re-defined by absorbing those infinities into the corresponding *bare* parameters, yielding a finite value as observed. This leads to the picture of running couplings and masses where one starts with the bare value at some very high energy scale and then let them flow down to the energy scale where we observe them. In this scheme, the Standard Model can be regarded as a low-energy effective field theory as an approximation of a UV complete theory at cut-off scale.

The UV divergences that Higgs mass experiences also happen to other particles like fermions and gauge bosons. However, what makes Higgs unique is that it does not have the "protection mechanism" as fermions and gauge bosons. For fermions, such protection is provided by chiral symmetry and for gauge bosons this comes from gauge invariance. For example, in the case of fermions, the loop correction is $\delta_m \sim g^2 m log(\Lambda/m))$. This has two very special features: 1) log-divergence is much slower than quadratic one as in the case of Higgs; 2) the correction is proportional to mass. Now if we resort to the renormalization flow picture as mentioned above, one needs to make sure that correction being canceled has an uncertainty less than the low-energy scale parameter to be consistent with experiment results: $\Delta(\delta) < m$, or equivalently, $\Delta(\delta)/\delta < m/\delta_m$. For fermion, this is not a serious problem since correction is proportional to m and it is only log-divergent. However, it would be a disaster for Higgs mass as that means the cancellation to divergences must be extremely accurate due to the quadratic divergence. In other words, it requires an extreme fine-tuning of the theories to make sure one get results compatible with observations if we believe the Standard Model is valid all the way up to the Planck scale (setting $\Lambda = \Lambda_{pl}$).

As we have seen, the hierarchy problem is more a *naturalness* problem instead of *inconsistency* problem, as it involves a fundamental question on *why so small*. Various models or frameworks have been developed trying to address this in various aspects, including *supersymmetry*, *extra dimensions*, *composite Higgs* and so on. In the following sections we would only focus on the models that will be searched in the work of this thesis.

2.2.2 The Randall-Sundrum Model

Among various methods to address the hierarchy problem, the Randall-Sundrum (RS) [23] model is a very appealing one due to its simplicity. In the RS model, an extra dimension in addition to the ordinary 4-dimensional space-time that we are familiar with is proposed. Different from a similar extra dimension model as proposed by Arkani-Hamed, Dimopoulos and Dvali (ADD) [24] with a large volume for the extra dimensions, RS model considers only one extra dimensions where the metric cannot be factorized, but rather the 4-d metric is multiplied by a "wrap" factor that is

changing rapidly along the extra dimension:

$$ds^2 = e^{-2\sigma(\phi)}\eta_{\mu\nu}dx^\mu dx^\nu + r_c^2 d\phi^2 \tag{2.57}$$

where ϕ represents the extra dimension and r_c is a free parameter here independent of ϕ characterizing the size of extra dimension. In this setup, a boundary condition that ϕ is periodic is applied. The domain of ϕ is therefore determined to be $0 \leq \phi \leq \pi$, with two end-points being identified as where the 3-brane, the place that support (3+1)-dimension field theories, locates. In particular, $\phi = \pi$ corresponds to the *visible brane* (or sometimes called *TeV-brane*) where we are living in, and $\phi = 0$ corresponds to the *hidden brane* (or sometimes called *Planck-brane*).

The metric can be determined by solving five-dimensional Einstein's equation:

$$ds^2 = e^{-2kr_c|\phi|}\eta_{\mu\nu}dx^\mu dx^\nu + r_c^2 d\phi^2 \tag{2.58}$$

where k is a scale variable. In particular, it is assumed that r_c is small but larger than $1/k$ such that the fifth dimension cannot be resolved in practice. Therefore one would want to build the relation between high-dimensional fundamental theory and the four-dimensional effective field theory as we observed in the 3-brane. This involves two important scales – the Planck scale M and VEV scale m_0 in the five-dimensional fundamental theory – and how these two scales in the high-dimensional fundamental theory appears to be in 3-brane, especially the TeV-brane.

For the Planck scale, it turns out there is not much difference as indicated by the results:

$$M_{pl}^2 = \frac{M^3}{k}[1 - e^{-2kr_c\pi}] \tag{2.59}$$

Since kr_c is large in general, the Planck scale in TeV-brane is therefore at the same order as one in fundamental theory. However, things are different for the VEV scale:

$$v = e^{-kr_c\pi}v_0 \tag{2.60}$$

where v_0 is the VEV scale in five-dimensional fundamental theory and v is the VEV we are familiar with in spontaneous symmetry breaking. Due to the Higgs mechanism, the mass of particles are in general determined by VEV scale. Therefore, this conclusion is very general for any mass scale

$$m = e^{-kr_c\pi}m_0 \tag{2.61}$$

In the five-dimensional fundamental theory, v_0 is at the same scale as M. However, the mass scale as observed in TeV-brane is exponentially suppressed even for the given extra dimension size r_c, while the Planck scale is not sensitive to the size of extra dimension. This naturally solves the hierarchy problem since there is no longer large hierarchies in the fundamental theory M and v_0, while the huge

hierarchies in TeV-brane is a nature result of the warped extra dimension. This can be illustrated by Figure 2.3 showing how the Planck scale and mass scale diverges. This also explains the weakness of gravity with graviton localized at the Planck-brane: The overlap of graviton wavefunction with our brane decays exponentially along the extra dimension.

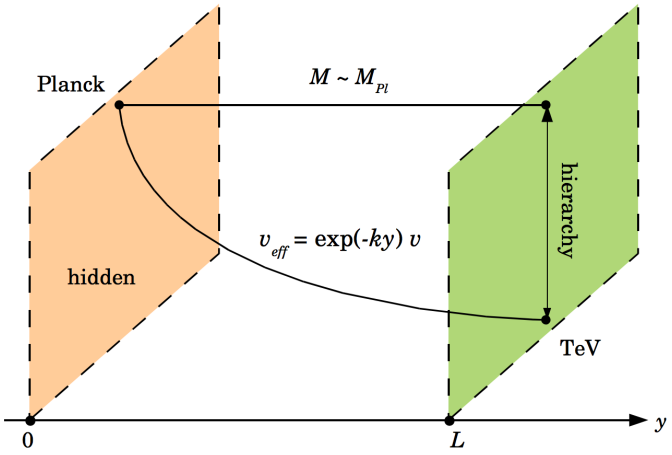


Figure 2.3: The generation of an exponential hierarchy [25]

So far r_c is a free parameter that we just tune it to be whatever value that needs to solve the hierarchy problem as shown above. This is still not ideal, since we are essentially transfering the hierarchy problem to explaining why r_c is that particular (small) value. One way to address this is the so-called Goldberger-Wise mechanism. Reader might find more details on this in [26].

In the original RS model as shown above, all Standard Model particles are confined on the TeV-brane. However, it does not solve the flavor hierarchy problem that there is large difference on quark mass of different flavors (e.g. top quark mass is significantly larger than other quarks). Therefore, the RS model is later modifed to the so-called "bulk" version, in which only Higgs particle is confined to TeV-brane while gauge bosons and matter fields can propogate in the bulk (i.e. extra dimension) [27]. The original version of the RS model as described above is called "RS1"[2]. In such scenario, 1st and 2nd generation of quarks can be localized near the Planck-brane while top quark can be closer to the TeV-brane. Due to the exponential decay from warped extra dimension, Yukawa coupling between top quark and Higgs which is confined at TeV-brane is much larger than the other quarks, leading to the flavor hierarchy as observed (remember that fermion acquires mass through Yukawa coupling with the Higgs).

One important reason for RS model being appealing is its distinctive phenomenological implication on the LHC. In RS scenario, there exists spin-2 Kaluza-Klein (KK) gravitons whose masses and

[2]There is another so-called "RS2" where there is no TeV-brane by allowing r_c to be infinite. Particles of the Standard Model are presumed to be on Planck-brane. This model is more of interest for studies of Ads/CFT conjecture.

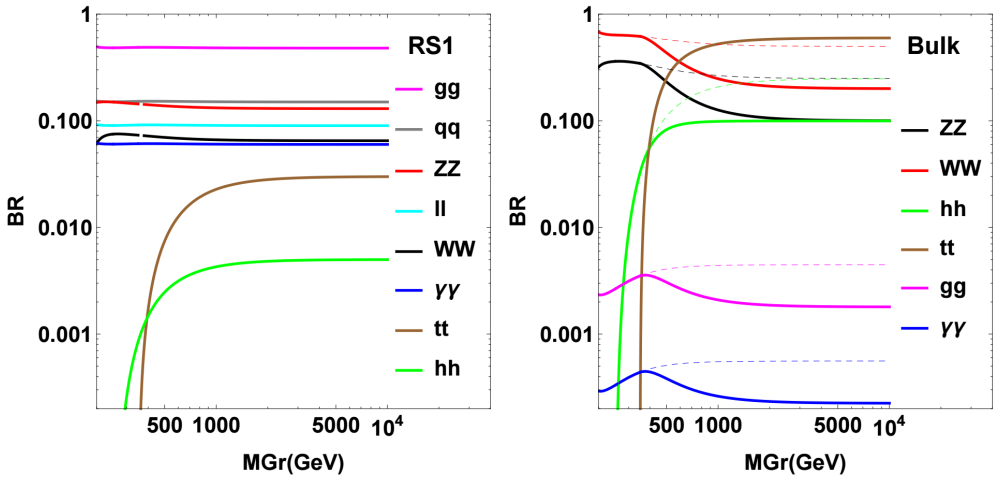


Figure 2.4: Branching ratio of KK graviton of various resonance mass for RS1 (left) and bulk (right) scenario. "MGr" on the plot is the KK graviton resonance mass; Symbol q represents sum of all flavors of quarks except top quark; Symbol l represents sum of all flavors of charged leptons (e, μ, τ) or neutrinos; Dashed line and solid line on the right plot represents bulk scenario in two difference cases: coupling of KK graviton to top quark is ignored in the dashed line, while a fully elementary top quark is considered in solid line. [28]

couplings to the SM particles are set by the TeV scale rather than the Planck scale. Furthermore, each excited state can be individually detected through their decay products. In the RS1 scenario, the KK graviton mainly couples to the light components like $q\bar{q}$ and gg. However, this is flipped in the bulk scenario since KK gravitons are localized near the TeV-brane while light quarks are closer to the Planck-brane. As a result, coupling to light quarks are highly suppressed in the bulk scenario. Instead, decays of KK gravitons are dominated by top quarks and Higgs due to their profile being near TeV-brane. A comparison of KK graviton branching ratio in two scenarios can be found in Figure 2.4.

In one of the searches as presented in this thesis, we would focus on the KK graviton of TeV mass from RS model in bulk scenario. As discussed above, the KK graviton has very large coupling to the Higgs boson, making the di-Higgs channel plausible. Although this channel was traditionally regarded as challenging [29], dedicated techniques are developed to fully exploit the potential in this channel, as will be elaborated in details throughout this thesis.

2.2.3 Bridging Theory and Data

While the RS model above is an appealing possibility for new physics beyond the Standard Model, it is not the only one. Depending on the underlying assumptions, various models have been proposed to solve the problems in the Standard Model more or less from different aspects, and at this moment it is hard to say which one is more compelling than others. Many of them are actually *framework* instead

of a concrete models. These generic frameworks are usually defined as a set of broad assumptions on the new physics and it could be mapped into many concrete models depending on the scenarios being adopted. To make things more complicated, even we are able to pin down a specific model, it usually contains many free parameters that should be determined from experiment. Such complication leads to two practical challenges when comparing experiment data and the thoery: 1) All models should be tested in principle since we simply do not know which one is better; 2) A multi-dimensional scan on parameter space is needed to properly interpret data. For the first issue, different scenarios may lead to completely different final states and thus numerous search efforts are needed in experiment collaboration; The second issue would require massive computation resources, if ever possible, since MC simulation is needed for the whole parameter space.

While in practice it probably would never be possible to fully explore all possibilities, progress can be made using the so-called "Simplified Model" strategy [30]. The main idea is that searches for narrow-width resonance, as predicted in many models, are not really sensitive to all the parameters or scenarios, but instead only to a limited number of combination of parameters controlling the resonance mass and its coupling with decay products. Therefore, one can construct a phenomenological Lagrangians only with relevant parameters in it. An important disclaimer is that these Lagrangians are by no means complete theories – they are simply a way to parameterize a broad set of explicit models. Therefore, many theoretical requirements as imposed on explicit models can be relaxed in the Simplified Model.

With the introduction of Simplified Model, comparison between data and theory gets much easier, as illustrated in Figure 2.5. For the experimentalists, they only need to interpret the data based on phenomenological Lagrangians in the Simplified Model as $L(\vec{c})$. This would usually be expressed as, for instance, an exclusion limit on parameter space of just single on or a few dimensions. Then, a mapping from explicit theory to the Simplified Model can be built *analytically* as $\vec{c}(\vec{p})$, when writing down the phenomenological Lagrangian. With this mapping, limits can be imposed on the explicit models instantaneously since only analytic calculation is needed here. In this way, the Simplified Model serves as a bridge connecting the data and theory in an efficient way.

However, some care must be taken when adopting this "bridging" strategy. As mentioned earlier, the Simplified Model is by no means a complete theory and any prediction from it should be restricted to its realm. In particular, it should only describe the *on-shell* resonance production and decay, while any off-shell behavior should depend on the explicit models. Since off-shell behaviors can present in the tail of distributions, or manifest them selves through a very broad distribution, predictions from Simplified Model are reliable only around the resonance peak. Such constraint also requires that resonance searches using Simplified Model should only cut on "on-shell variables" which are only sensitive to the resonance formation and decay, such as dijet system invariant mass. Besides the concern of Simplified Model validity, on-shell variables also have the nice feature that they can be easily converted to the phenomenological Lagrangian parameter spaces. In experiment searches, the

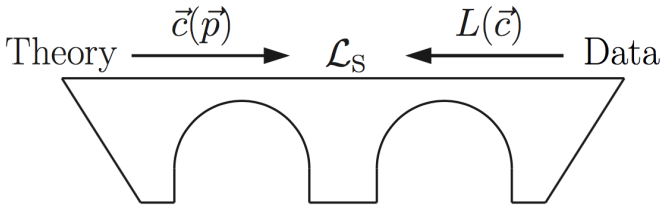


Figure 2.5: Pictorial view of how to connect experiment and theory. $\vec{c}$ represents the parameters of phenomenological Lagrangian; $L(\vec{c})$ represents the likelihood function or exclusion limits as function of these parameters as extracted from the data; $\vec{p}$ represents the free parameters in explicit models; $\vec{c}(\vec{p})$ represents the relationship between parameters in phenomenological and explicit models [31]

exclusion limits are usually set on the production cross-section and decay branching ratios as function of resonance mass. Since the cross-sections and branching ratios are usually a simple function of the Simplified Model parameters, mass-dependent limits can be easily converted to phenomenological parameter space *analytically*.

In the second search presented in this thesis, we would focus on a particular Simplified Model, called *Heavy Vector Triplets* (HVT) [31], where electroweak-charged spin-1 heavy resonances of TeV scale, W' and Z', are predicted. Such resonances are common predictions from many new physics models. Depending on the underlying assumptions, this can be further split to *Model A* [32] and *Model B* [33]. In the Model A, vector triplet emerges from the symmetry breaking pattern $SU(2)_1 \times SU(2)_2 \times U(1)_Y \to SU(2)_L \times U(1)_Y$ achieved through a linear σ-model. In the Model B, Higgs boson emerges as a light state from some underlying strong dynamics predicting the existence of heavy vector resonances. An example of the explicit model behind this scenario is the Minimal Composite Higgs Model where the Higgs doublet emerges from the spontaneous breaking of a global $SO(5)$ symmetry to an $SO(4)$ subgroup. More details on the HVT can be found in [31].

Phenomenologically, a major difference between Model A and Model B is their relative couplings with the Standard Model gauge bosons and fermions, as shown in Figure 2.6. In Model A, the coupling relation is

$$g_V c_H \simeq g^2 c_F / g_V \simeq g^2 / g_V \tag{2.62}$$

where g is the SM SU(2) coupling constant, g_V is the typical strength of heavy vector boson coupling and c_H (c_F) parameterize coupling of heavy vector boson with Higgs boson (fermions). In this case, it has comparable branching ratio to fermions and bosons. The total width decreases as g_V increases due to the suppression from g^2/g_V. On the other hand, c_H in Model B is no longer suppressed so that

$$g_V c_H \simeq -g_V, \; g^2 c_F / g_V \simeq g^2 / g_V \tag{2.63}$$

As a result, the dominant decay mode in Model B is di-bosons while fermionic decays are extremely

suppressed or the order of one percent or even smaller. The total width increases as g_V increases since the dominant di-boson coupling is proportional to g_V as shown above. Therefore, for Model B, a very large g_V (like $g_V = 8$) coupling is no longer meaningful since the resonance width is so broad ($\Gamma/M \gg 0.1$) that the experimental searches for a narrow width resonance are no longer motivated.

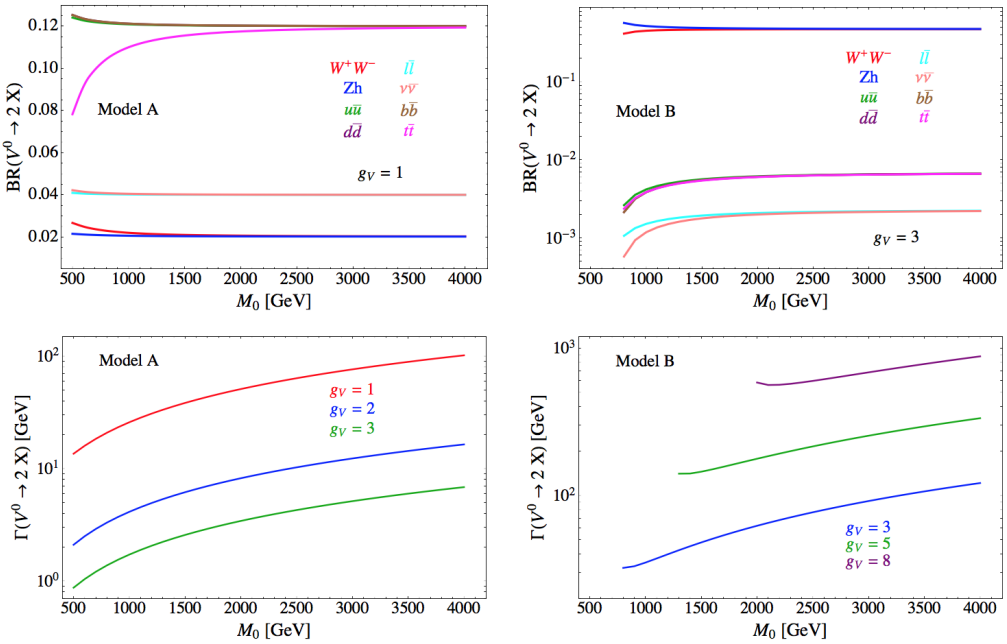


Figure 2.6: Branching ratios (upper row) and total width (lower row) for the two body decays of the neutral vector V^0 for the benchmarks $A_{g_V} = 1$ (left) and $B_{g_V} = 3$ (right). [31]

Chapter 3

The Large Hadron Collider

The Large Hadron Collider (LHC) is a circular superconducting hadron collider with approximately 27 km circumference, operated by the *European Organization for Nuclear Research* (CERN). It is located across the boundary between *Geneva, Switzerland* and *France*, underneath the surface by 45 m to 170 m on a plane inclined at 1.4% sloping toward the Geneva Lake [34]. The machine is primarily designed as a proton-proton collider, which is expected to accelerate each of two proton beams to an energy of 7 TeV and thus collides at a center-of-mass energy of $\sqrt{s} = 14$ TeV with unprecedented luminosity of $10^{34}\ cm^{-2}s^{-1}$, making them the world's largest and most powerful particle accelerator. In addition, it can also collide heavy ions (Pb) with an energy of 2.76 TeV per nucleon (total center-of-mass energy of 1.15 PeV) and a peak luminosity of $10^{27}\ cm^{-2}s^{-1}$ [34]. The unprecedented energy and luminosity of LHC not only allows physicists to test the Standard Model, including the discovery and measurement of Higgs boson, but also opens an window toward the potential new physics at TeV scale.

The physics motivation of building LHC was fairly obvious when it was first discussed in 1984, a time that colliders with even higher energy were actively proposed. Superconducting Super Collider (SSC) near Waxahachie, Texas, was considered a main competitor to LHC at that time due to its much higher collision energy of 40 TeV . However, SSC was eventually canceled in 1993 due to budget problem, while LHC was approved by the CERN Council in December 1994, marking a shift of experimental high energy physics center to Europe until now.

The decision to build LHC at CERN was strongly influenced by the cost saving to be made by re-using the LEP tunnel and its injection chain [34], whose construction was completed in 1988. Furthermore, broad international collaboration, especially the CERN non-member state agreement with financial contributions, not only spread the budget load of the project, but also proves to be an extremely successful way for a big physics experiment as LHC.

This chapter is only intended as a very brief introduction to the machine design (Section 3.1) as well as its performance (Section 3.3) until now. A brief discussion on the physics and engineering

limitations of LHC designed energy and luminosity is also presented in Section 3.2. Readers with interests in details can find more information in *LHC Conceptual Design* [35], *LHC Design Report* [36] and *LHC Machine* [34].

3.1 Machine Design

The design of LHC is largely constrained by the LEP layout, though LHC adopts many latest technology as much as possible. A schematic layout of the LHC can be found in Figure 3.1. Following the LEP layout, there are eight arcs and eight straight sections, composing in total 8 octanes. Each straight section is about 528 m in length and can be used as either experimental or utility insertion. During the LEP era, these eight straight sections are mainly designed for Radio-frequency (RF) cavities in order to compensate the high synchrotron radiation losses due to electron (and position). However, for LHC, this is much less a problem as a proton accelerator. While it is ideal to have a longer arc and shorter straight section for the same circumference for LHC, it is eventually decided to use the tunnel "as built" which was the most cost-effective solution. Nevertheless, only four straight sections are used in LHC, with the other four straight sections suppressed for beam crossings.

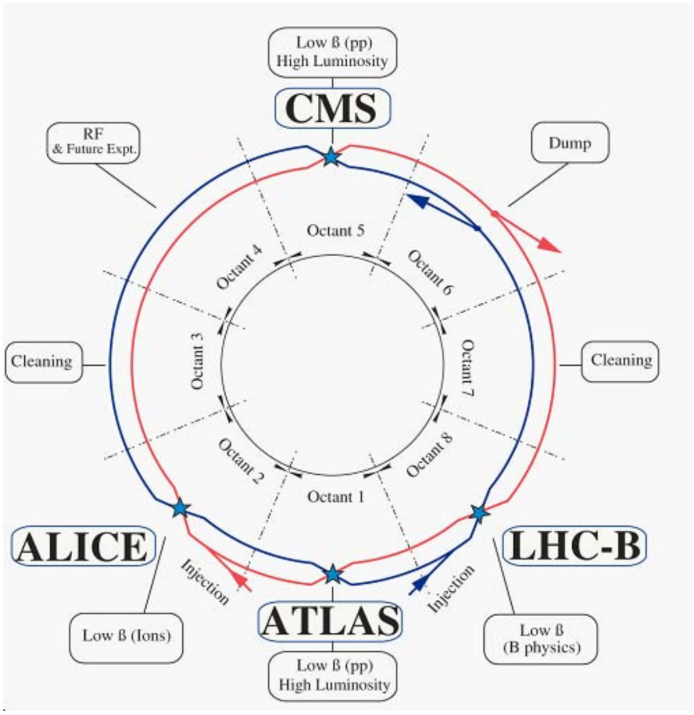


Figure 3.1: Schematic layout of LHC [34]

All these four "activated" straight sections are reserved for high energy experiment detectors:

ATLAS and CMS are located at Point 1 and Point 5 respectively, diametrically opposed to each other, both of which serve as high luminosity experiment using proton-proton collision data; ALICE is located at Point 2 and is mainly used for heavy ion studies; LHCb is located at Point 8 as a low-luminosity proton-proton collision detector, mainly for b-physics studies.

As a proton-proton collider, there are two rings with counter-rotating beams in LHC , instead of both beams sharing a single ring in the case of particle-antiparticle colliders such as Tevatron. However, the tunnel left from LEP only has an internal diameter of 3.7 m, making it very difficult to deploy two separate proton rings. Such limit directly lead to the adoption of so-called "two-in-one" super-conducting magnet design [37]. Such two-in-one design accommodates the windings of both beam channels in a common supporting system, with dipole magnetic flux circulating in opposites direction through both beam channels. The clear disadvantage of such design is that it makes two rings magnetically coupled to each other, and thus makes it much less flexible.

The protons in LHC are accelerated step by step through chains of injection facilities (injection chain), as illustrated in Figure 3.2. Initially the proton source is just a bottle of hydrogen gas, with proton extracted out using electric field. Then these protons are accelerated to an energy of 50 MeV through Linac2. Beam of protons are then injected into Proton Synchrotron Booster (PSB) to be accelerated to 1.4 GeV, followed by the Proton Synchrotron (PS) with energy further increased to 25 GeV. Before sending to the next step of Super Proton Synchrotron (SPS) which will increase proton energy to 450 GeV LHC bunch train with 25 ns spacing is also generated in the PS. Finally, protons are injected into two LHC beam pipes circulating in opposite direction from SPS. The injection point is at Point 2 and Point 8 for each proton beam respectively, as shown in Figure 3.1. The injection happens in the vertical direction from below the LHC reference plane. Then two proton beams will only cross over each other in the four interaction points as mentioned above, where the proton in one beam pipe will be transferred to the other one after each cross-over. In the interaction region, two beams share a common beam pipe of approximately 130 m in length. Considering that there are 2808 bunches per proton beam, and the bunch spacing is nominally 25 ns, one can expect about 34 parasitic collision points in each interaction region, which would be undesirable for the experiment there. As a result, dedicated crossing angle between proton beams from both direction is designed to avoid these parasitic collisions, which reduces the pile-up in detectors. In the end, proton beams will be dumped at Point 6 using a both horizontally and vertically deflecting magnet complex ("kicker").

In order to bend proton with energy as high as 7 TeV in a tunnel with 27 km circumference, strong magnetic field is needed, which can only be achieved with superconductivity. The LHC uses classical NbTi superconductors for generating magnetic field, which is a well-proven techniques as applied on other large superconducting colliders such as Tevatron, DESY and RHIC. However, instead of being cooled by supercritical helium at temperature slightly above 4.2K with fields around only 5 T as done in the other large colliders, LHC is able to cool the magnets down to 2 K using superfluid

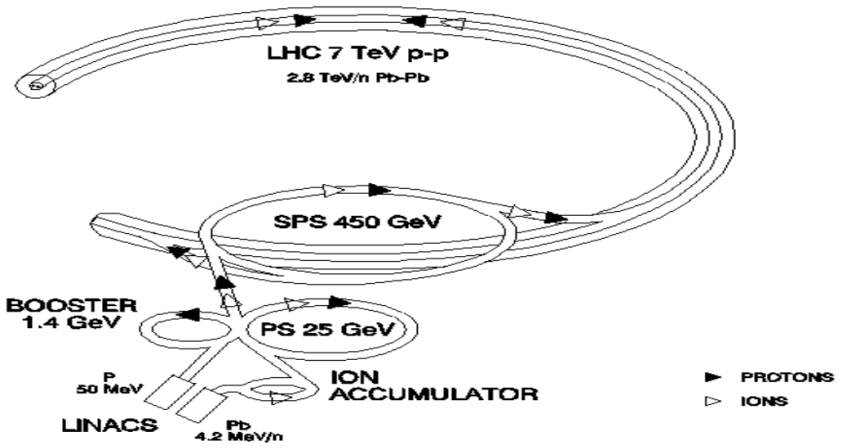


Figure 3.2: Schematic illustration of LHC injection chains [34]

helium, hence generate magnetic field above 8 T. Along the LHC ring, 1232 main dipoles, which are the most critical part of the machine, are accommodated with the same basic design, as shown in Figure 3.3.

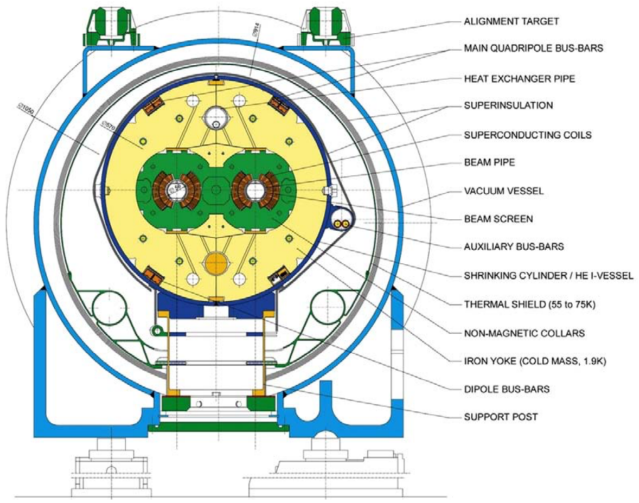


Figure 3.3: Cross-section of cryodipole [34]

3.2 Limitations

From particle physicists' point of view, two parameters of LHC are probably the most relevant: collision energy and luminosity. In order to explore new physics beyond the Standard Model, center of mass energy as high as TeV scale is necessary to open the phase space of potential new physics. Luminosity, on the other hand, is directly proportional to the number of events produced for any fixed physics process, hence critical for sensitivity of any measurement and discovery. The number of events produced from LHC collision is given by:

$$N = L_{int}\sigma = (\int Ldt)\sigma \tag{3.1}$$

where L_{int} is the integrated luminosity, L is the instantaneous luminosity (luminosity for short below) and σ is the cross section of physics process of interest, which is usually collision energy dependent. For LHC, the design colllision energy is 14 TeV and designed luminosity is $10^{34}cm^{-2}s^{-1}$. Such performance goal poses a great challenge to the design of LHC and, on the other hand, is also heavily constrained by the existing technology owned by human being. In this section, we will go through briefly how the energy and luminosity of LHC is limited by both physics and technology considerations.

3.2.1 Luminosity

For a Gaussian beam distribution, luminosity depends only on beam parameters and can be written as [34]:

$$L = \frac{N_b^2 n_b f_{rev} \gamma_r}{4\pi\epsilon_n \beta^*} F \tag{3.2}$$

where N_b is the number of particles per bunch, n_b is the number of bunches per beam, f_{rev} is the revolution frequency, γ_r is the relativistic gamma factor, ϵ_n is the normalized transverse beam emittance, β^* is the beta function at collision point, and F is the geometric luminosity reduction factor due to the cross angle at interaction point (IP).

N_b, the particle density per bunch, is mainly constrained by the nonlinear beam-beam interaction and LHC mechanical aperture such that $N_b < 1.15 \times 10^{11}$. Furthermore, mechanical aperture of the triplet magnets imposes a minimum on the attainable β^* and maximum on crossing angle at interaction region [34].

3.2.2 Energy

The maximum energy of proton beam is directly determined by the tunnel circumference and magnetic field bending proton beams in the storage ring. Inherited from LEP, tunnel circumference is

fixed at 27 km. Dipole field is mainly constrained by the superconductivity technology as mentioned earlier. In LHC, the nominal field is 8.33 T, corresponding to an energy of 7 TeV [34].

However, there are several further practical limitations on the actual attainable field strength. One can imagine the LHC as a super big circuit, with beam current being 0.584 A. Considering the complicated magnetic field in this circuit, total electromagnetic energy stored in circulating beams can be as high as more than 1 GJ. In case of beam dump, malfunction, or any kind of emergency, such huge amount of energy needs to be absorbed safely to avoid explosion. Therefore, beam dumping system provide additional limits on the maximal attainable beam energies and intensities.

Head load is another source of limitations on the beam energy and intensity. For one thing, this comes from the synchrotron radiation in circulating beams (although this is already much less then electron rings). For another, there are also heat deposition from luminosity-induced losses, impedance-induced losses and electron-cloud bombardment [34]. All these heat losses have to be absorbed by the LHC cryogenic system, whose capacity can also impose an upper limit on the beam energy and intensity.

3.2.3 Luminosity Lifetime

It should be noted that luminosity is not a constant during a physics run, but decaying over the time. Therefore, a long luminosity lifetime is also essential for high integrated luminosity. Intrinsically, such decay is due to the beam loss from proton-proton collision at interaction point for the experiments. It can be calculated that the luminosity decay time, defined as the time needed for luminosity to drop to $1/e$ of its original value, from this factor alone is about 29 h. However, other effects such as synchrotron radiation damping and emmitance blow-up can further bring lifetime down to about 14.9 h.

In practice, detectors would only take a fraction of the luminosity lifetime during a stable physics run. This is because people can actually gain more data by stopping the run early and starting a new fill with much higher luminosity than collecting the tail of luminosity decay in previous run. However, there is an non-negligible turnaround time for LHC between two fills: minimum LHC injection time is 16 minutes, minimum time required to ramp up beam energy in LHC ring from 450 GeV to 7 TeV is about 20 minutes (and similar for ramping down), time for routined system checks is about 10 minutes. All these lead to approximately 70 minutes turnaround time for LHC between two fills. Therefore, one needs to find an optimal run time depending on the turnaround time, in order to maximize the integrated luminosity over a long period. Quick estimation shows that an integrated luminosity of 80 fb^{-1} (120 fb^{-1}) per year is achievable by setting run time to be 12 (5.5) hours for average turnaround time of 7 (1.15) hours, assuming the machine can be operated for 200 days per year with luminosity lifetime of 15 hours as estimated above [34]. Such assumption, however, could be too optimal in reality, since LHC is composed of a large set of hardware that needs to be *all* in good status. Many single failure among the system can wipe out the beam and

thus result in loss of luminosity.

3.3 Performance

LHC successfully starts its first proton beam in September 10, 2008. Unfortunately, this milestone success was soon shadowed by the incident 9 days later resulting in "mechanical damage and release of helium from magnet cold mass" [38]. After about 1-year repairment, beam is back to LHC at the end of 2009. On March 30 2010, first LHC collision of 7 TeV was observed on ATLAS, marking the the begin of physics data harvest.

Data taking between 2010 to 2012 is called Run 1 [39], in which collision energy is 7 TeV in 2010 and 2011 and 8 TeV in 2012. The integrated and peek instantaneous luminosity delivered to ATLAS during Run 1 can be found in Figure 3.4. While 2010 and 2011 was more devoted to establishing the confidence in LHC operation, 2012 was more a production year with slightly higher collision energy, and a much higher luminosity. In particular, the increase in luminosity was due to the use of high bunch intensity with 50 ns bunch spacing, though at the cost of high pile-up: In 2012, the mean number of collisions per bunch crossing (mu) reached 30 events with tails up to 40. At the end of Run 1, approximately 23.1 fb^{-1} integrated luminosity is accumulated at an center of mass energy of 8 TeV. The maximal peek instantaneous luminosity attained during Run 1 data taking is about $0.8 \times 10^{34} cm^{-2} s^{-1}$.

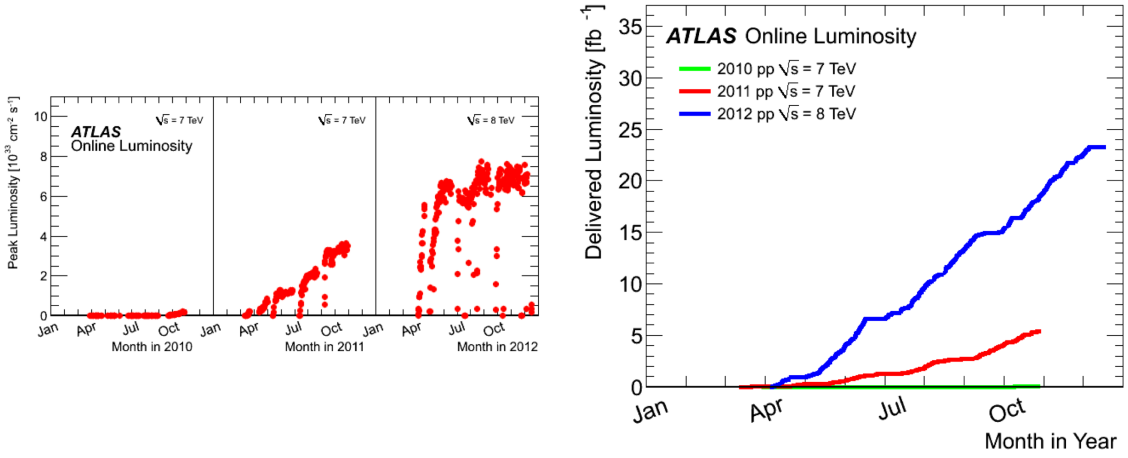


Figure 3.4: Integrated (left) and peek instantaneous (right) luminosity delivered to ATLAS in Run 1 [40]

After a 27-month Long Shutdown 1 (LS1) for both accelerator and experiment detectors upgrades following the conclusion of Run 1, LHC got back online with an unprecedented collision energy of

13 TeV, marking the highest energy achieved by particle accelerators ever built. Data taking period from 2015 to 2018 is called Run 2 [41], after which LHC will go into Long Shutdown 2 (LS2) phase. Data taking in 2015 was more considered a commission year, aiming to validate the updates during LS1. LHC first circulate proton beams with 50 ns spacing as Run 1 in April, but soon moved to 25 ns operation in August. However, a relaxed set of machine parameters were chosen for 2015 operation to ease commissioning, leading to a relatively low luminosity. In 2016, a significant increase in luminosity was achieved by a much tighter tuning of machine parameters such as β^* and geometric factor F, and a more stable operation with longer run time per fill. As a result, the LHC data collection rate in 2016 was faster than any previous year with more than 2 fb^{-1} per week. A summary of integrated and peek instantaneous luminosity in Run 2 so far can be found in Figure 3.5 and 3.6. Up to the end of 2016, accumulated luminosity in 13 TeV is 39.5 fb^{-1} as recorded by ATLAS, with peek instantaneous luminosity $1.38 \times 10^{34} cm^{-2} s^{-1}$, reaching the original LHC design.

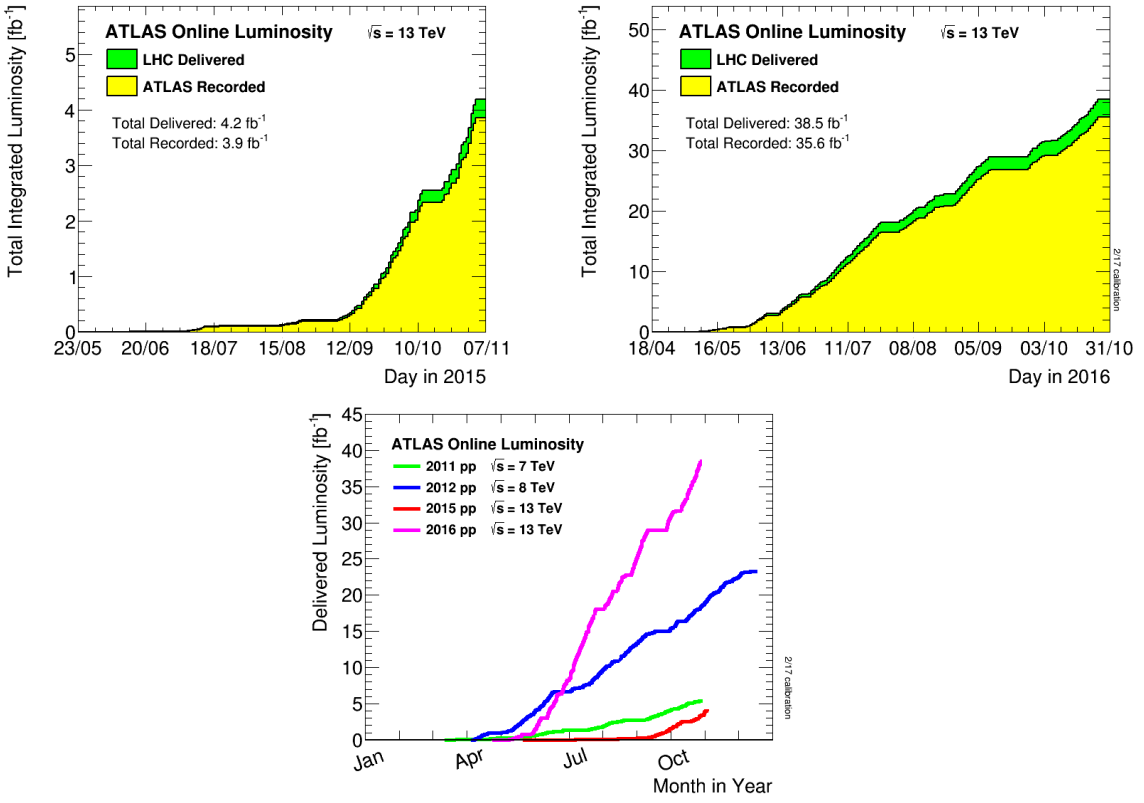


Figure 3.5: Integrated luminosity recorded by ATLAS in 2015 (top left), 2016 (top right) and a comparison across all years (bottom) [42]

One distinct feature of the proton-proton collisions produced by LHC from previous colliders is the "pile-up" effect. Despite of large number of protons per bunch, protons would either just pass

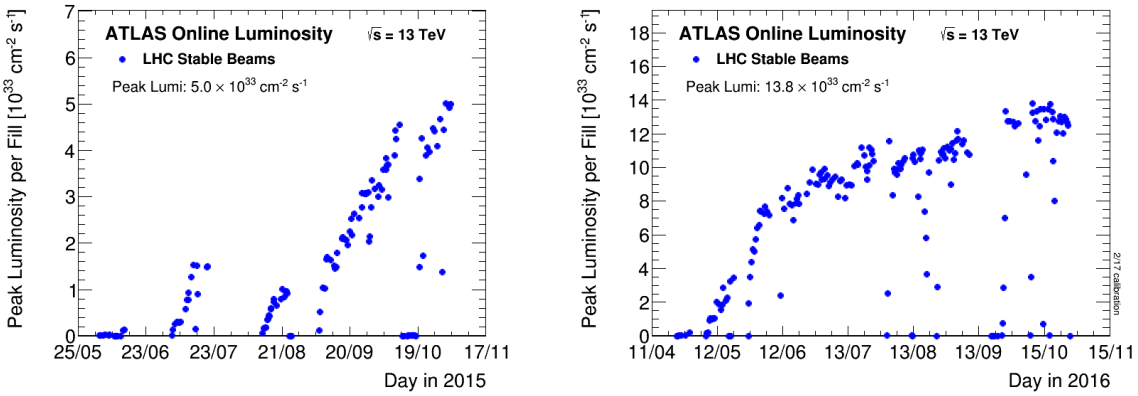


Figure 3.6: Peek instantaneous luminosity recorded by ATLAS in 2015 (left) and 2016 (right) [42]

by each other or only interact softly due to much lower cross section of hard interaction with respect to the total cross section, leading to at most one hard interaction per bunch crossing in previous colliders. In the case of LHC, however, one has to increase the proton density significantly in order to achieve the unprecedented luminosity, leading to more than one interaction per bunch crossing, which is called *in-time pile-up*. In addition, since the bunch spacing is as small as 25 ns now, fractions of energy from bunch crossings before or after current one can still be left in the read-outs of current bunch crossing, which is called *out-of-time pile-up*. A summary of average number of interactions per bunch crossing can be found in Figure 3.7.

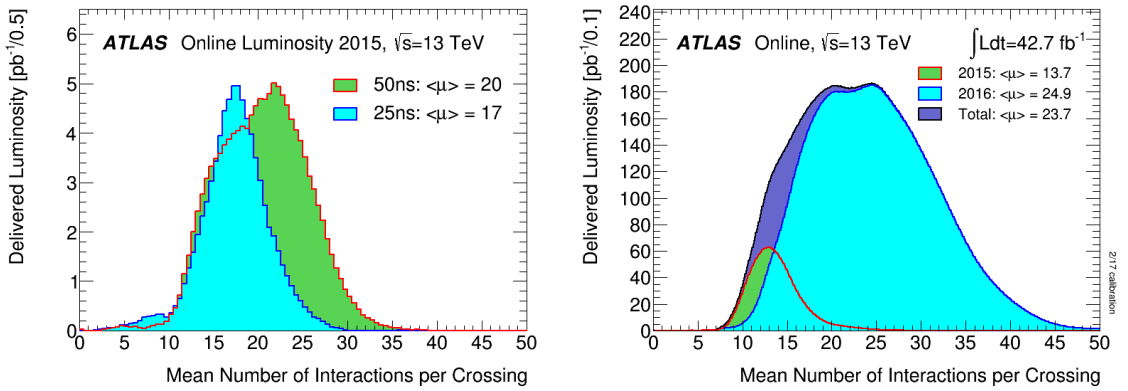


Figure 3.7: Average number of interactions per bunch crossing in 2015 (left) and 2015+2016 (right) [42]

All the analysis as presented in this thesis is done with LHC data produced in Run 2 with 13 TeV.

Chapter 4

ATLAS Detector

The ATLAS (**A T**oroidal **L**HC **A**pparatu**S**) detector [43] is a general-purpose particle detector used to investigate a broad range of physics processes produced by LHC. It is one of the two general purpose detectors built, with the other one naming CMS (Compact Muon Solenoid), around LHC ring for probing both proton-proton collisions and pb-pb collisions. Located at Point 1 of LHC ring about 92 m below ground, ATLAS has a cylinder shape in general, with 46 m long in length, 25 m in diameter and weights of over 7000 tons. ATLAS is also a huge experiment collaboration with roughly 3000 physicists , including around 1000 students, from 174 universities / labs and 38 countires [44].

Before the description of ATLAS detector along with its sub-systems, it is necessary to summarize the coordinate system which would be used repeatedly in this thesis. The coordinate origin is defined at the geometric center of the ATLAS detector, with z-axis defined as the direction of beam pipe[1]. Plane perpendicular to z-axis is defined as x-y plane, with x pointing from origin point to the center of LHC ring and y pointing upward. Therefore, polar angle θ is defined with respect to z-axis and azimuthal angle ϕ is measured around beam axis. Pseudorapidity is defined as $\eta = -\ln\tan(\theta/2)$. Transverse momentum p_{T}, transverse energy E_{T} and missing transverse energy $E_{\mathrm{T}}^{\mathrm{miss}}$ are all defined in x-y plane unless explicitly defined otherwise. The distance ΔR in the pseudorapidity-azimuthal plane is defined as $\Delta R = \sqrt{\Delta\eta^2 + \Delta\phi^2}$.

A cut-away view of ATLAS detector can be found in Figure 4.1. It includes inner tracking system surrounded by a 2.3 m diameter superconducting solenoid, electromagnetic and hadronic calorimeters and a muon spectrometer with a toroidal magnetic field. The inner detector, immersed in a 2 T solenoid field, consists of a high-granularity silicon pixel detector (Pixel), including the Insertable B-Layer (IBL) installed after Run 1 of the LHC, a semiconductor microstrip detector (SCT), and a straw-tube transition radiation tracker (TRT). Combining all these layers, inner detector is able

[1]The nominal interaction region location, on the other hand, is determined from each 30s lumi-block. Although it is close to the coordinate origin, the interaction region point has to be determined more precisely for many purposes

to perform pattern recognition for track reconstruction, momentum measurement, vertex (primary and secondary) reconstruction, and particle identification with extremely high precision for charge particles with pseudorapidity coverage $|\eta| < 2.51$. The calorimeter system consists of electromagnetic and hadronic calorimeters. Electromagnetic calorimeter is a finely segmented sampling calorimeter with lead as absorber and liquid-argon (LAr) as active medium for the detection of electromagnetic showers up to $|\eta| < 3.2$, providing excellent performance in terms of energy and position resolution for electron and photons. LAr technology is also used for part of hadronic calorimeters at the end-cap with copper or rungsten as absorber in order to detect hadronic showers between $1.5 < |\eta| < 4.9$. Surrounding the LAr electromagnetic calorimeters, a steel/scintillator hadronic calorimeter is used for hadronic showers at the central with pseudorapidity coverage $|\eta| < 1.7$ in order to detect energy of hadronic jets and missing energy. Outside the calorimeters, the muon system incorporates multiple layers of trigger and tracking chambers within a magnetic field produced by a system of superconducting toroids, enabling an independent precise measurement of muon track momenta for $|\eta| < 2.7$.

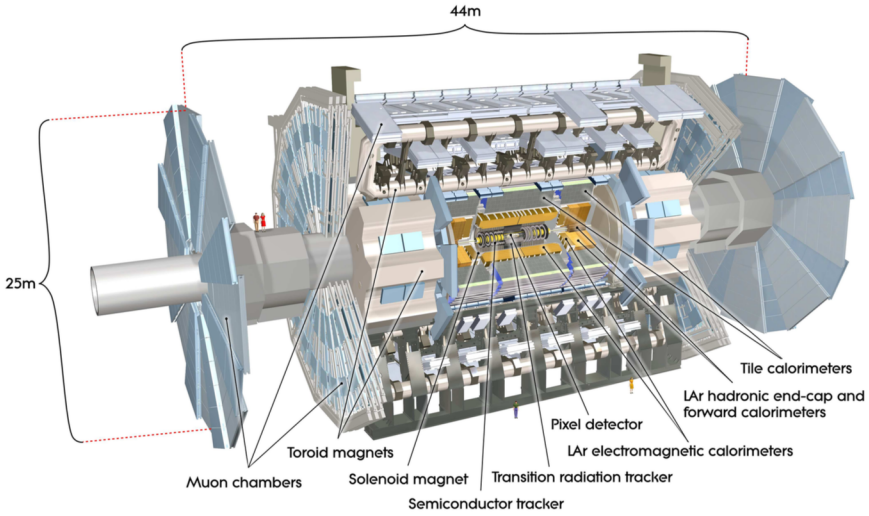


Figure 4.1: Cut-away view of the ATLAS detector [43]

Due to the nominal 25 ns bunch spacing, proton-proton collision happens at a rate of 40 MHz. With millions of read-out channels across the ATLAS detector, recording all these collision events is far beyond bandwidth provided by existing technology. Therefore, a dedicated trigger system is used to select events. The first-level trigger (Level 1) is implemented in hardware and uses the calorimeter and muon detectors to reduce the accepted rate to 100 kHz. This is followed by a software-based high-level trigger (HLT), which is a combination of the previous Level 2 and Event Filter in Run 1, that reduces the accepted event rate to 1 kHz on average. Events passing through the trigger system

are first streamed to CERN Tier-0 data center, and then further distributed worldwide to Tier-1 composed of 11 large data center, where the data reconstruction also happens. There are even more computing clusters around the world at Tier-2 and Tier-3: Tier-2 mainly hosts the simulations, while Tier-3 is used for data analysis.

This chapter is intended as a brief introduction to the ATLAS sub-systems, including Inner detector in Section 4.1, calorimeters in Section 4.2, muon system in Section 4.3, forward detectors in Section 4.4, and trigger / data acquisition system in Section 4.5. Readers with interest can find more technical details in reference [43, 45, 46, 47] and other references therein.

4.1 Inner Detector

ATLAS inner detector (ID) is designed to provide pattern recognition, momentum measurement and both primary and secondary vertex reconstruction for charged particles above hundreds of MeV and within pseudorapidity range $|\eta| < 2.5$. As illustrated in Figure 4.2, the whole ID is contained inside a cylinder of length ± 3512 mm and of diameter 1150 mm.

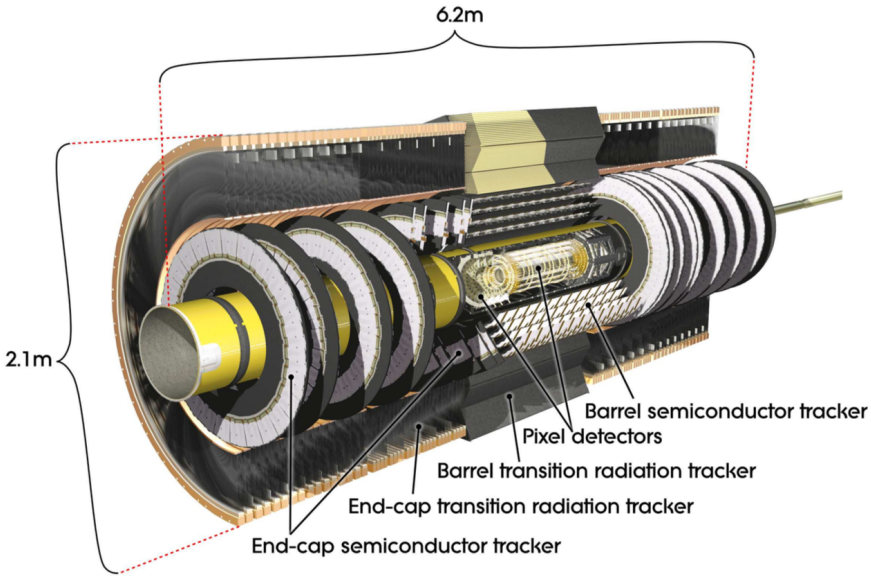


Figure 4.2: Cut-away view of the ATLAS inner detector [43]

The ID consists of three independent but complementary sub-detectors. In the innermost radii, silicon pixel detectors (Pixel) and silicon microstrip layers (SCT) are arranged on concentric cylinders with multiple layers around the beam axis in barrel regions while in the end-cap they are arranged

as separate disks perpendicular to the beam axis. Both Pixel and SCT are able to provide high-resolution pattern recognition capabilities using 3D space-points[2] Since Pixel and SCT layers are the detectors closest to beam pipe, precise hit point measurements left from charged particle transversing through them are critical for extrapolation of track trajectory to interaction points, thus essential for the reconstruction of primary and secondary vertex, and b-jet tagging. At larger radii, the transition radiation tracker (TRT) comprises many layers of gaseous straw tube elements interleaved with transition radiation material. Being far away from the interaction point, these straw tubes are able to depict the curvature of charged particle trajectory under solenoid field, with about 36 hits per track. As a result, TRT is able to provide an enhanced pattern recognition capability as well as improved momentum resolution in $|\eta| < 2.0$. Furthermore, by exploiting the ionization dE/dx feature, TRT is able to provide additional electron identification power complementary to that of calorimeters over a wide range of energies [48]. An illustration of each sub-system coverage can be found in Figure 4.3.

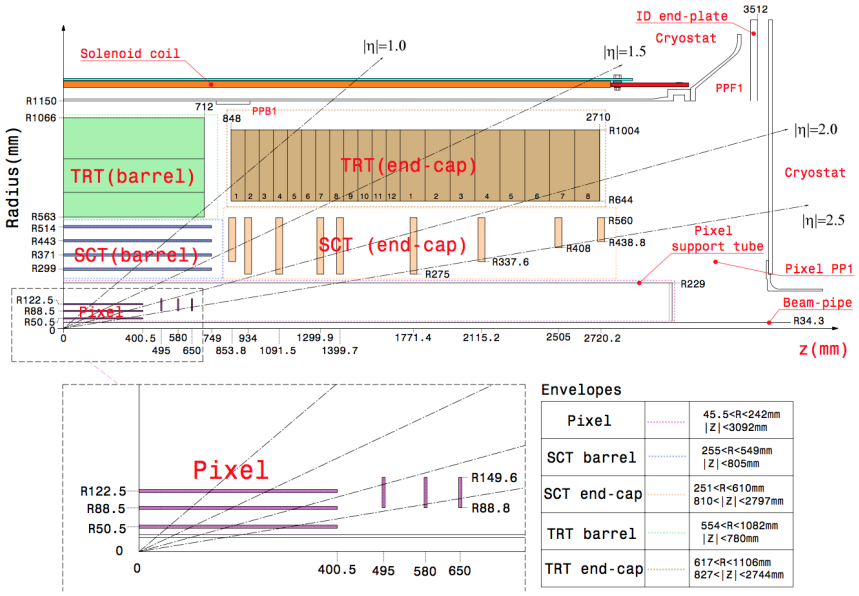


Figure 4.3: Plan view of a quarter-section of the ATLAS inner detector showing each of the major detector elements with its active dimensions and envelopes. The labels PP1, PPB1 and PPF1 indicate the patch-panels for the ID services [43]

[2]The 3D space-points provided by two systems are not completely the same though. Pixel hits are discrete 3D hit points, while SCT space points are derived from two strips with small stereo angle. The latter one might be ambiguous when close-by hits present.

4.1.1 Silicon Pixel Detector

The Pixel detector [49] is the innermost element of the Inner Detector, playing an critical role for the identification and reconstruction of secondary verticies from the decay of b-quarks or other long lived particles. In addition, it provides excellent spatial resolution for reconstructing primary vertices, which is essential for pile-up suppression in the presence of multiple interactions for LHC.

Pixel detector consists of three layers in the barrel regions arranged as cylinder with radius of 50.5 mm, 88.5 mm and 122.5 mm respectively, and two identical end-cap regions, each with three disk layers, with total coverage of $|\eta| < 2.5$. During LS1, a fourth layer (or 0-th layer) [50, 51], the Insertable B-Layer (IBL), is added to the existing Pixel detector between new beam pipe and the inner most layer ($R = 25.7\ mm$) for further improvement of tracking performance. The pseudorapidity coverage of IBL extends to $|\eta| < 3.0$ due to its closeness to the beam pipe. A schematic view of the active region of the Pixel detector consisting of barrel and endcap layers can be found in Figure 4.4. To avoid confusion, we refer to the three layers that were installed before Run 2 as "pixel layers" and the newly inserted layer as "IBL", while the whole sub-system called "Pixel detector", in all descriptions below.

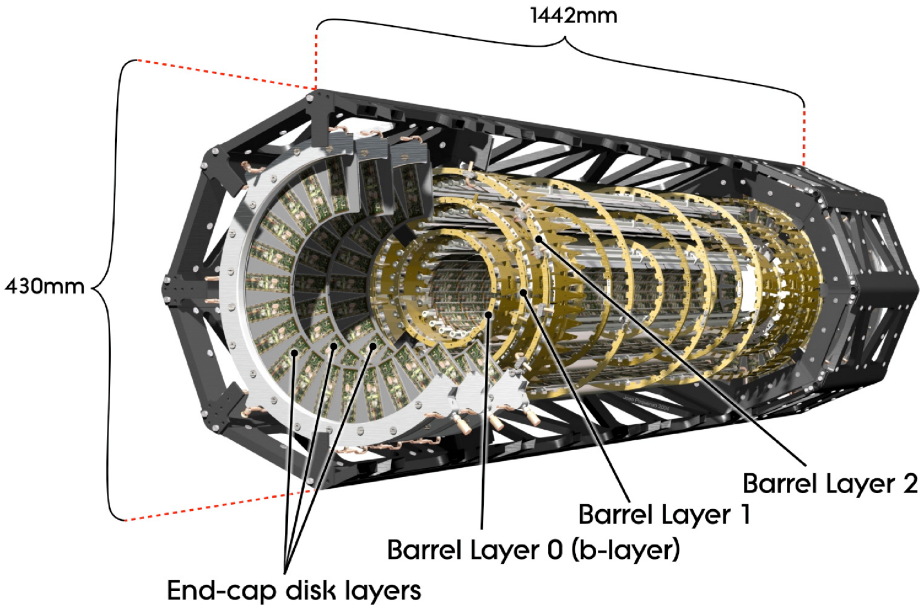


Figure 4.4: A schematic view of the active region of the Pixel detector consisting of barrel and endcap layers [50]

The high granularity of pixel layers is achieved through a very fine segmentation in both $R-\phi$ and z direction, with the basic detection unit down to a silicon sensor with minimum size in $R-\phi \times z$ of $50 \times 400\ \mu m^2$ ($50 \times 250\ \mu m^2$) for pixel layers (IBL). Some silicon sensors at the edge might have a dimension larger than this in order to allow for a continuous sensitive area between chip boundaries

in the long pixel direction. As a result, the intrinsic accuracies of track-hit measurement in the barrel of pixel layers are 10 μm $(R-\phi)$ and 115 μm (z) and in the disks are 10 μm $(R-\phi)$ and 115 μm (R) [49]. For IBL, the resolution at z direction can be 72 μm due to shorter pixel length [50].

In practice, silicon sensors are grouped into modules along with front-end electronics and control circuits, which is the building block of Pixel detector. There are 1744 identical modules covering all pixel layers and disks, making a sensitive area of in total about 1.7 m^2. Each module has an active surface of 6.08×1.64 cm^2. It has 1 sensor tile containing 47232 pixels, covered by 16 front end electronics chips (FE) connected by means of bump-bonding [49]. Illustration of elements of a pixel barrel module can be found in Figure 4.5.

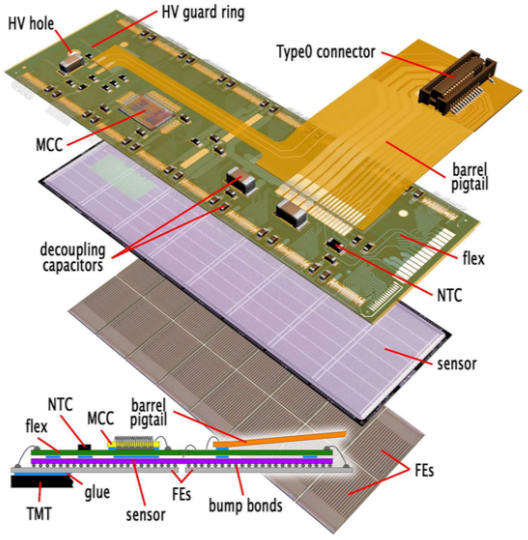


Figure 4.5: Elements of a pixel barrel module [49]

Modules are then further mounted on mechanical and cooling supports, called staves (disk sectors), for barrel (end-cap) region, covering a certain $R-\phi$ region. Multiple Staves (disk sectors) are further arranged along a cylinder (disk) such that full ϕ-plane can be covered. During installation, stave is not perpendicular to the radius direction, hence leaving a small tilt angle between radius axis and sensor surface. The tilt angle in ϕ direction is mainly due to the space constraints. However, sign and exact value of tilt angle is selected to compensate the Lorentz angle [49].

Pixel Layer Sensor Design

As a silicon detector [52], ATLAS pixel sensor is essentially a p-n junction with reverse bias voltage applied to expand the depletion region, where ionization and charge collection happens. The pixel sensor consists of a 256 ± 3 μm thick n-type bulk that is weekly doped close to its intrinsic charge concentration. p-n junction is formed at the back side of the n-bulk by implanting high positive (p^+)

dose regions on the surface. High negative (n^+) dose implantation is placed on the other side of the n-bulk, connected to the read-out. While the n-bulk and p^+ implant comes with a whole wafer, pixel implants (the n^+ side) are segmented into 144 columns and 328 rows, each of which with a pixel pitch as mentioned above. The p^+ implant is connected to a negative high voltage, with the n^+ side grounded, such that a reverse bias can be applied. Since the charge concentration in n-bulk is much less than the p^+ implant, depletion region will grow from the back side to the pixel (front end) if fully depleted, making the whole bulk being active detection medium [52]. One advantage of such $n^+ - in - n$ design is that the sensor can still operate in case of being irradiated to even type-inversed, in which case the n-bulk effectively becomes p-bulk. In case of such type inversion, p-n junction forms at the n^+ implant surface now and depletion zone would grow from the pixel implant to most of the bulk, keeping the sensor still functional. An illustration of the pixel sensor design can be found in Figure 4.6. This is very important, in particular in Run 2, when the ATLAS Pixel detector has already experienced large radiation dose.

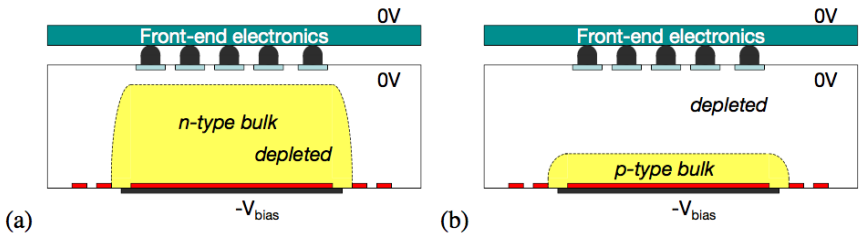


Figure 4.6: Illustration of sensor design on pixel layers before (a) and after (b) type inversion [49]

IBL Sensor Design

For IBL, more than one type of technology are available for pixel sensors: planar sensors, 3D sensors and diamond sensors [50]. In the end, a "mixed scenario" is adopted, in which the planar sensors occupy central region and 3D technology populates the higher eta region of IBL where the tracking could benefit from the electrode orientation interms of better z-resolution after heavy irradiation [51]. In addition, a Diamond Beam Monitor [53] is developed and installed as an upgrade to the existing luminosity monitor, Beam Condition Monitor (BCM) [54, 55], in the forward region of ATLAS detector close to tbe beam pipe to monitor the instantaneous luminosity and beam spot position bunch-by-bunch.

For the planar pixel sensor, a slim-edge n-in-n design [50] is adopted. The design in general follows that of the proven and reliable pixel sensors as commissioned during Run 1. However, in the design of IBL, length of inactive edge can shrink to only 100 μm, much smaller than IBL design requirement of 450 μm, hence lowering geometric inefficiency to 0.5%. Because the guard rings of n-in-n design are located on the p-side of sensor, a partial overlap between the guard rings and

outermost pixel rows, which are implanted on n-side of sensor, makes such slim edge design possible, as shown in Figure 46 of [50]. Further simulation [56] shows that the field distortion at the edge due to such partial overlap is negligible after irradiation.

The 3D silicon sensor, originally proposed in [57], is studied inside ATLAS as an alternative to the planar sensor to deal with heavy radiation environment in LHC collisions. It is suitable for high doses of nuclear interacting particles mainly because of shorter distance between electrodes than the planar design [58]. In 3D design, the electrode along with pn junction surface forms as columns perpendicular to the wafer surface, instead of being parallel as in planar design. As a result, electric field is defined between the columns, which has a much shorter distance than between the planar surfaces. After heavy irradiation damage, there is an increase of the full depletion voltage and decrease of charge collection efficiency due to carrier trapping [58]. Reducing distance can lower depletion voltage [52], and increase charge collection efficiency.

While various designs are proposed originally as candidates for IBL [50], the "double-sided thin edge" 3D sensor is adopted from consideration of both technology advancement and manufacturing maturity [51]. A schematic cross-section of the double-sided 3D sensor can be found in Figure 4.7. In such double-sided design, n^+-columns are etched from the front wafer side (bump-bonding side) and p^+-columns are etched from the back side. There are two manufacturing process, determined by the manufacturer, FBK[3] and CNM[4]: In FBK processing columns pass all the way through wafer [59]; In CNM processing, the columns stop at a short distance from the surface of opposite side [60].

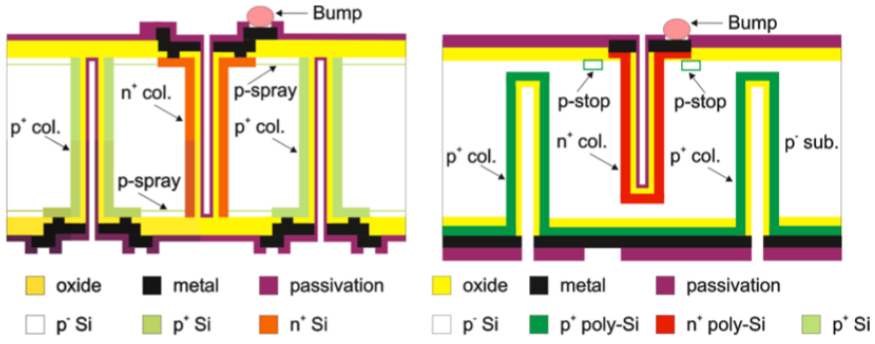


Figure 4.7: Schematic Cross-section view of double-sided 3D sensor design of FBK (a) and CNM (b) [61]

[3]Centro Nacional de Microelectronica, CNM-IMB (CSIC), Barcelona E-08193, Spain
[4]Fondazione Bruno Kessler, FBK-CMM, Via Sommarive 18, I-38123 Trento, Italy

4.1.2 Semiconductor Microstrip Tracker

Similar to the Pixel detector, SCT detector [62] also uses semiconductor technology to provide precision space-point coordinates. In SCT there are 4 cylinders in the barrel and 9 disks at each side of end-cap. Each layer is able to read out a position in two dimension. There are in total 8448 identical rectangular sensors installed in the barrel SCT and 6944 senors, of 5 different wedge-shaped geometries, in the end-cap SCT [62], covering a surface of 63 m^2 of silicon [43]. The total number of readout channels in SCT is approximately 6.3 millions [43].

The building block of SCT detector is a module, which in most cases consists of four single-sided p-in-n sensors along with electronics front ends. On each side of a module, there are two sensors, glued to each other back-to-back around a high thermal conductivity substrate, as illustrated in Figure 4.8. In addition to a 80 μm strip pitch on each sensor, there is a 40 mrad stereo rotation between the two sensors on upper and lower surface, in order to measure both coordinates of a space-point [62]. As a result, the intrinsic accuracies per module in the barrel are 17 μm $(R-\phi)$ and 580 μm (z) and in the disks are 17 μm $(R-\phi)$ and 580 μm (R) [43].

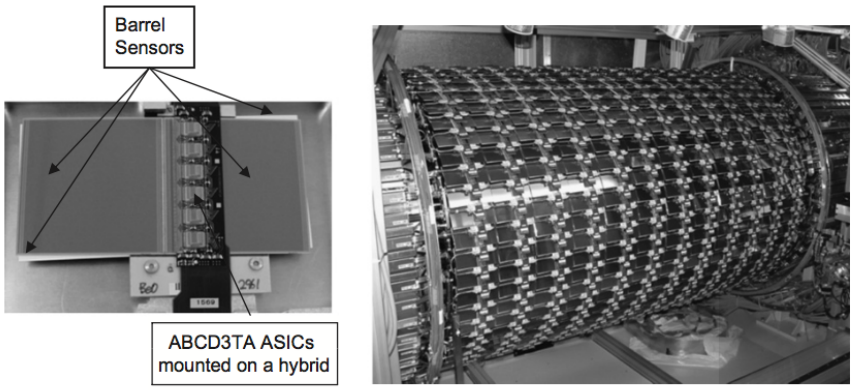


Figure 4.8: Left: layout of the four sensors in the SCT barrel module (two on the upper surface, two on the lower surface, with 40 mrad stereo rotation). Right: modules mounted on the outermost barrel layer of ATLAS SCT detector [62]

As one of the largest silicon tracker to date for a particle physics experiment, SCT has a very large surface area. Since silicon sensors are expensive, one has to take the economic consideration into account, requiring the design to be relatively simple yet meeting all physics requirements. Therefore, instead of complicated double-sided design, classic single-sided p-in-n sensor with AC-coupled readout strips is adopted [62, 43]. The sensor has thickness of 285 ± 15 μm and a strip pitch of 80 μm. Sensors would initially operate at about 150 V bias voltage, but in practice might need $250 \sim 350$ V for a good charge collection efficiency due to irradiation.

4.1.3 Transition Radiation Tracker

The TRT detector [43, 63] locates at the outermost part of ATLAS inner detector, providing a large number of hits left by track curvature through arrays of 4 mm diameter star tubes of the TRT up to $|\eta| = 2.0$. The TRT only provides measurements at $R-\phi$ direction with intrinsic accuracy of 130 μm per straw. In barrel region, straws are parallel to the beam pipe with 144 cm long; In end-cap region, straws are arranged radially in wheels with 37 cm long. The total number of TRT readout channel is approximately 351000. All charged particles with $p_T > 0.5$GeV and $|\eta| < 2.0$ are expected to transverse at least 36 straws, except in the barrel-end-cap transition region ($0.8 < |\eta| < 1.0$) where at least 22 hits are expected. In addition, 7 to 10 high-threshold hits from transition radiation are expected for electrons with energies above 2GeV [43].

The TRT contains up to 73 layers of straws interleaved with fibers (barrel) and 160 straw planes interleaved with foils (end-cap). While the tube is filled with gas as a proportional counter, interleaved materials provide transition radiation for electron identification. The barrel TRT is divided into three rings, each of which contains 32 modules. Each module contains an array of straws parallel to the beam pipe with a mean spacing of about 7 mm. The TRT end-caps each consist of two set of independent wheels: The one closer to interaction point has 12 wheels , each with 8 layers spaced 8 mm apart; The one further has 8 wheels with 8 layers spaced 15 mm apart. Each layer contains 768 radially oriented straws, azimuthally spaced uniformly.

Polyimide drft (straw) tubes of 4 mm diameter are the basic TRT detector elements [63]. Around the tube a wall is formed from two layers of 35 μm thick multilayer film. Inside the tube it is filled with gas mixture which are required to have efficient transition radiation absorption, high electron drift velocity and operation safety / reliability. Eventually, a gas mixture Xe-CO_2-O_2 70/27/3 is chosen for operation given its good high-rate performance and ageing behavior [63].

4.2 Calorimeter

ATLAS calorimeter system [43], as illustrated in Figure 4.9, consists of various sub-systems using different techniques suited to the widely varying requirements of physics processes over large pseudorapdity range of $|\eta| < 4.9$. In the pseudorapidity range matched to inner detector, electromagnetic (EM) calorimeter is finely segmented for precise identification and measurement of electrons and protons. The relatively coarser granularity of the rest hadronic calorimeters is sufficient for reconstruction and measurements of the dominant jets in LHC environment and $E_{\mathrm{T}}^{\mathrm{miss}}$. A detailed tabulation of pseudorapidity coverage of each sub-system can be found in Table 1.3 of [43].

The primary objective of calorimeter is to measure the energy of incoming particles as accurately as possible – both charged and neutral (including neutrinos through $E_{\mathrm{T}}^{\mathrm{miss}}$) [64]. Besides energy, it is also able to measure the position, angle of incidence as well as arrival time through fine segmentation. As a destructive detector, calorimeters would induce either EM shower (electron, photon) or hadronic

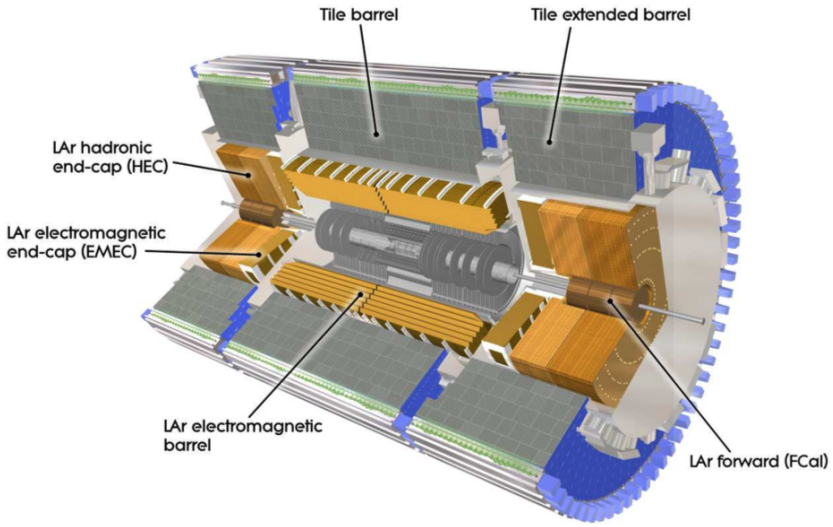


Figure 4.9: Cut-away view of ATLAS calorimeter system [43]

shower (proton, neutron, pion, etc.) by having incoming particle interacting with passive absorber, which is usually made of dense materials such as lead or steel. Such shower would grow both longitudinally and laterally through cascade chains since outgoing high energy particles from each collision in dense medium can interact with the absorber again as it flys on, until energies of these outgoing particles are lower than a critical energy where ionization becomes dominant instead of radiation. These final state particles would then either be absorbed as phonons (heat), or induce ionization or scintillation in the active detection medium, depending on technology being used, so that their energy can be read out and measured. There are two kinds of calorimeters: homogeneous and sampling. The sampling calorimeter has alternative layers between absorber and active detection medium, while homogeneous a single dense medium would serve as both. Homogeneous calorimeters have the advantage of better energy resolution (stochastic term) and good linearity, but suffers from high cost and limited segmentation. For ATLAS, all calorimeters are sampling calorimeter.

Ideally, if all showers are counted, measured energy would be proportional to the signal strength (number of electron-hole pair for example), and thus measurement error is proportional to $\sqrt{E}$. In practice, the energy resolution of calorimeters have three terms:

$$\frac{\sigma(E)}{E} = \frac{a}{\sqrt{E}} \oplus \frac{b}{E} \oplus c \tag{4.1}$$

where a is stochastic term representing the intrinsic statistical shower and sampling fluctuation, b is noise term representing readout electronics noise and c is constant term representing any

inhomogeneities [64]. As one can see from this equation, the energy resolution improves with increasing energy in general, which is not the case in spectrometers (inner detector for example) which would get worse for very high momentum due to larger uncertainty in track trajectory curvature measurement.

For calorimeter, shower shape is one of the most important specifics, not only because it is essential in understanding detector performance, particle reconstruction and identification, but also because the size of whole calorimeter is limited by it. Radiation length, X_0, (interactive length, λ) is defined as the thickness of material in EM (hadronic) calorimeter that can reduce the mean energy of incoming particle by a factor of e. For cascade decay, it is easy to estimate that longitudinal shower spread increases with energy logarithmically, which makes calorimeters compact in general [64]. Therefore calorimeters must provide good containment for both EM and hadronic showers to limit punch-through into the muon system. The total thickness of ATLAS EM calorimeter is $> 22\ X_0$ in barrel and $> 24\ X_0$ in end-caps. For hadronic calorimeters, total thickness is approximately $9.7\ \lambda$ in barrel and $10\ \lambda$ in end-caps. It has been shown by measurements and simulations to be sufficient to reduce punch-through to the muon system well below irreducible level of prompt or decay muons, as well as be adequate for high-energy jet measurements. The large η, along with sufficient thickness, also ensure a good $E_{\mathrm{T}}^{\mathrm{miss}}$ measurement [43].

4.2.1 Liquid Argon Electromagnetic Calorimeter

The LAr EM Calorimeter [43, 65] is composed of the barrel part (EM barrel), covering $|\eta| < 1.475$, and two end-caps (EMEC) on each side, covering $1.375 < |\eta| < 3.2$. The barrel is further split into two half-barrels at $z = 0$ with a small gap of 4 mm. Each end-cap is also divided into two coaxial wheels: one covering $1.375 < |\eta| < 2.5$ and one covering $2.5 < |\eta| < 3.2$. Ahead of EM calorimeter, there is also a presampler detector in the region of $|\eta| < 1.8$ used to correct for the energy lost by electrons and photons upstream of the calorimeter.

The EM calorimeter has a complicated segmentation in terms of both depth and lateral direction, in order to meet different physics requirement at different pseudorapidity. A complete overview of segmentation can be found on Table 1.3 of [43]. In the central region, $|\eta| < 2.5$, devoted to precision physics, EM calorimeter is segmented in three layers in depth, regardless of barrel of end-cap, with very fine yet different lateral granularity on $\eta - \phi$ plane depending on both layer and η. In the forward region where $|\eta| > 2.5$, calorimeter is segmented into two layers in terms of depth and has a coarser lateral granularity on $\eta - \phi$ plane in order to provide as complete coverage as possible.

An accordion geometry has been chosen for both absorbers and electrodes (detection medium) in both barrel and end-cap EM calorimeters, as illustrated in Figure 4.10. In barrel, the accordion wave "propagates" in depth direction with folding angle varying in radius, while the waves are laid on each other in ϕ direction. In end-cap, the accordion wave "propagates" in beam direction and laid on each other in ϕ direction. A good visualization of the accordion layout for both barrel and

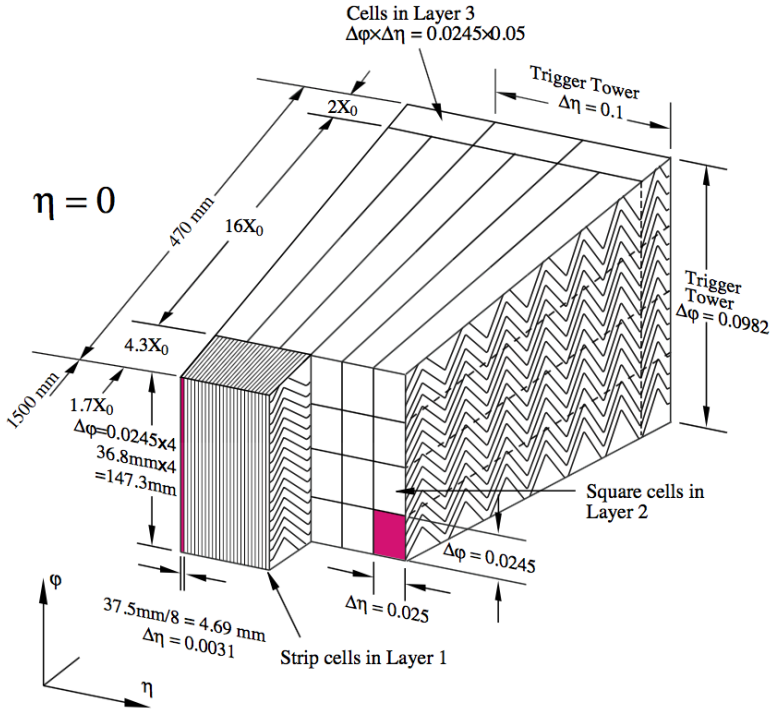


Figure 4.10: Sketch of barrel module showing both accordion structure and granularity in $\eta - \phi$ of the cells on each of layer [43].

end-cap can be found in Figure 5.5 and Figure 5.6 of [43]. Such accordion geometry can make sure a full ϕ coverage without cracks between modules, thus leading to uniform performance in terms of linearity and resolution as function of ϕ.

The absorbers of ATLAS EM calorimeter are made of lead plates. As suggested by its name, liquid Argon is used as the active detector medium. Liquid argon has been chosen for its intrinsic linear behavior, stability of response over time and radiation-hardness [43]. Furthermore, since signal is produced through ionization in liquid argon, its high number of electron-ion pairs per MeV deposited can help reduce statistical uncertainty of electronic signals, thus providing good energy resolution [64]. A dedicated cryogenic system, on the other hand, is needed since temperature required to turn Argon into liquid state is -183°C and also because the performance would be sensitive to temperature change [64].

4.2.2 Hadronic Calorimeter

The ATLAS hadronic caloirmeter [43, 65, 66] is composed of three sub-systems, located at different location with varying technology in order to reconstruct and measure jets and $E_{\mathrm{T}}^{\mathrm{miss}}$: Tile calorimeter, LAr hadronic end-cap calorimeter and LAr forward calorimeter. Unlike electron and photon, hadrons such as protons or neutrons would induce hadronic shower through interaction with materials, which is much more complicated than the EM shower. A typical hadronic shower would contain both electromagnetic and hadronic components. This would lead to the non-compensation issue for hadronic calorimeter, that the efficiency of detecting hadronic component is typically far lower than the EM component [64]. As a result, energy resolution in hadronic calorimeters are relative poorer (Table 1.1 of [43]), and would also suffer from non-linearity and non-Gaussian response [64]. Interaction length λ, a characteristic length defined for hadronic shower, is typically much larger than the radiation length X_0, a counterpart of interaction length for EM shower. This has several consequences: Hadronic calorimeters need to be placed after the EM calorimeter since EM shower would be fully contained at whatever detector that comes the first; The absorber for hadronic calorimeters is usually different from EM calorimeter to ensure λ is not too large; The depth of hadronic calorimeter is also typically very big [64].

Tile Calorimeter

The tile calorimeter [43, 66] is placed directly outside the EM calorimeter. It doesn't have the end-cap part, as illustrated in Figure 4.9, but has a central barrel with 5.8 m long in length covering $|\eta| < 1.0$, and two extended barrel (one on each side) with 2.6 m long in length for each, covering $0.8 < |\eta| < 1.7$. Both barrel and extended barrels have an inner radius of 2.28 m and outer radius of 4.25 m. In depth direction, it is segmented into three layers: For barrel, three layers are approximately 1.5, 4.1 and 1.8 λ thick; For extended barrel, three layers are approximately 1.5,

2.6 and 3.3 λ. At lateral direction, barrel is segmented into 64 modules, each of wich has a size $\Delta\phi \sim 0.1$ [43].

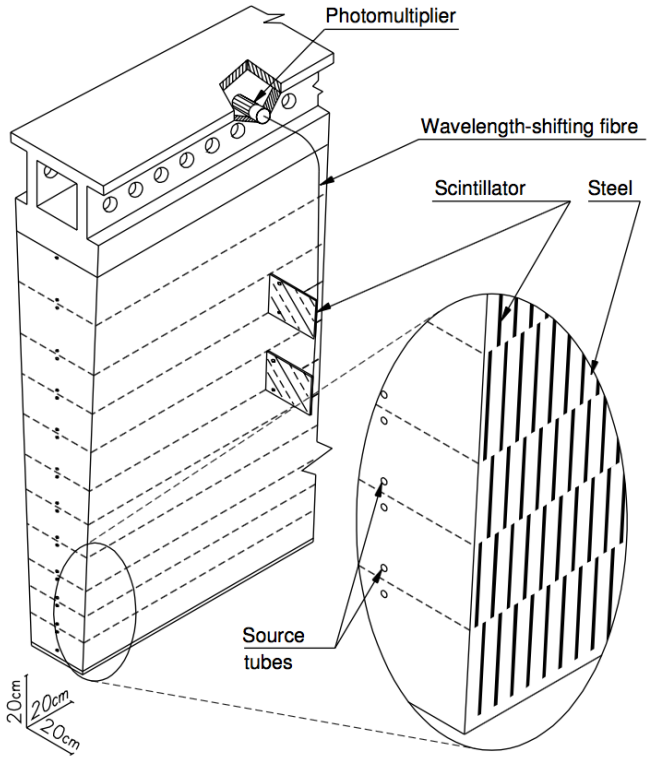


Figure 4.11: Illustration of how tile calorimeter is structured [43].

Tile calorimeter is a sampling calorimeter using steel as absorber and scintillator as active detection medium, with volume ratio of approximately 4.7:1. A geometric sketch of how the steel-scintillator structure is mechanically assembled can be found in Figure 4.11. Scintillator tiles are oriented radially (normal to the beam line), with wavelength-shifting fiber readout connected at the tile edge, allows a full coverage on azimuthal direction. Readout fibers are then grouped together, connecting to the readout photomultiplier tubes (PMT). The gap between barrel and extended barrels are filled with a special modules made of steel-scintillator alternative layers with the same sampling fraction just like the rest of tile calorimeters, allowing partial energy recovery in the crack.

LAr Hadronic End-cap Calorimeter

The LAr Hadronic End-cap Calorimeter [43, 65] (HEC) is made of two independent wheels for each end-cap, located at the forward region of the EM calorimeter, but even further away than the EMEC. While it also uses liquid Argon as active detection medium (and therefore it is able to share the same

LAr cryostats as the EMEC), copper plates are interleaved with the 8.5 mm LAr gap as absorber. To reduce the material density drop at the transition region between HEC and other detectors, the lower bound of its pseudorapidity coverage is $|\eta| > 1.5$, slightly lower than the tile calorimeter (1.7), and upper bound of HEC is $|\eta| < 3.2$, slightly larger than the forward calorimeter (3.1). Each wheel of HEC is segmented into two parts in depth, thus a total of 4 layers in depth for one end-cap. The segmentation on $\eta - \phi$ plane is 0.1×0.1 when $|\eta| < 2.5$ and 0.2×0.2 for larger η.

LAr Forward Calorimeter

LAr Forward Calorimeter [43, 65] (FCal) is a dual-use, both electromagnetic and hadronic, calorimeter, covering the most forward region in the calorimeter system. Due to the neutron albedo from inner detector cavity, FCal has to be recessed by 1.2 m with respect to the EM calorimeter front face, heavily limiting the possible depth of FCal. As a result, a high-density absorber has to be considered, while the liquid Argon, same as EM calorimeter and HEC, technology is used as active detection medium. Each end-cap of FCal is segmented into three modules: First one is made of copper optimized for the electromagnetic measurements; The other two are made of tungsten, a material with much shorter interaction length, for the measurements of hadronic interactions.

4.3 Muon Spectrometer

Muon system [43, 67], as illustrated in Figure 4.12, is the outermost part of ATLAS detector, also being the largest one which defines the total size of ATLAS detector. Its purpose is to provide precision measurement of the trajectory left by transversing muons, as well as provide online muon trigger using separate sets of detection chambers.

Building the muon system at the outermost part of detector, especially after the calorimeter system, takes fully advantage of some features of muons [68]: Muon has a much smaller energy loss during ionization (dE/dx) due to its higher mass than electron, which makes it able to pass through a lot of materials; With mean life time of 2.197×10^{-6} s, it vary rarely decays within ATLAS detector. Therefore, muon detectors are usually placed after the calorimeters, which can absorb almost all particles except muon, leaving an unambiguous signature.

The reconstruction and momentum measurement of muon is then performed with a spectrometer system. Being located farthest from interaction point, the muon system has to be very large to realize full coverage. Due to low occupancy, large cell is possible in muon system (though this would be less true for HL-LHC). The radiation level is typically smaller in the muon system (than ID). Also, it should be able to perform stand-alone measurement of high-momentum muon [68]. The driving performance goal is a stand-alone transverse momentum resolution of approximately 10% for 1 TeV tracks, which translates into a sagitta along the z (beam) axis of about 500 μm, to be measured with a resolution of ~ 50 μm. Momentum down to a few GeV(~ 3 GeV due to energy loss in calorimeters)

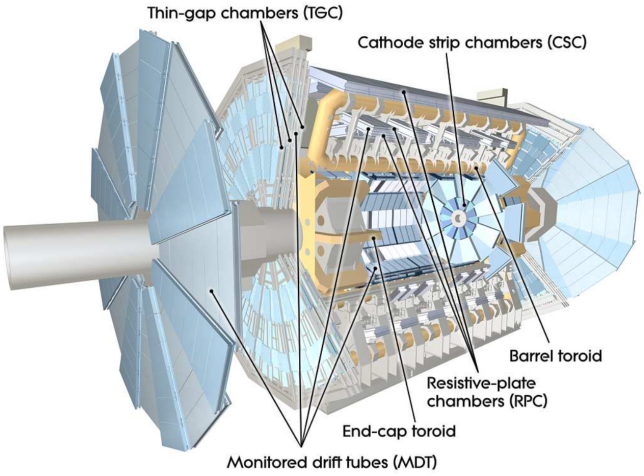


Figure 4.12: Cut-away view of ATLAS muon system [43]

may also be measured by spectrometer alone [43].

The main technology used in ATLAS muon system is gas-filled detector operating as proportional chamber [68]. There are many advantages for gas detector: gas material usually has large X_0, reducing multiple scattering; Large volume is easily achievable with gas which is relatively inexpensive. Muon interact with gas detector mainly through ionization, although bremsstrahlung radiation would gradually become dominant when muon energy is large than 900 GeV. As muon transverse gas detector, ionized electron-ion pair would fly toward anode and cathode . Most muon detector in ATLAS uses anode wire design so that the electric field would increase dramatically as it is closer to the anode wire, inducing avalanche effect in order to amplify the signal with generated ionization electrons. This is different from the process as described in silicon detector in Section 4.1 which has a much lower ionization energy. The electric signal from front-end is formed as electrons (ions) approach and get collected by anode (cathode). Since drift speed of electron is much faster than ion due to smaller mass, an uprising electric signal would be first formed as electrons are collected, then a very long tail dropping signal follows as ions are being collected slowly, which could take as much as 10 bunch-crossing [68].

As a spectrometer, it needs a magnetic system to bend muon trajectory in order to measure its momentum from curvature. A system of three large air-core toroids generates the magnetic field for muon spectrometer: The barrel mainly covers a region of $|\eta| < 1.4$; Two end-cap toroids are inserted in the barrel toroid at each end and line up with the central solenoid in ID system, mainly covering region of $1.6 < |\eta| < 2.7$. Over region of $1.4 < |\eta| < 1.6$, which is also called transition region, magnetic field is provided by a combination of barrel and end-cap fields. The adoption of air-core toroids, instead of solenoid, can reduce multiple scattering and hence improve low-p_{T}

momentum measurement resolution significantly, as a yoke iron for bending magnetic field back as adopted in CMS is saved. Furthermore, B-field is more homogeneous in the high η region with toroid configuration [68]. Toroids configuration means the bending plane is in the $r-z$ configuration while, while $r-\phi$ plane is now non-bending plane, which is different from the ID system.

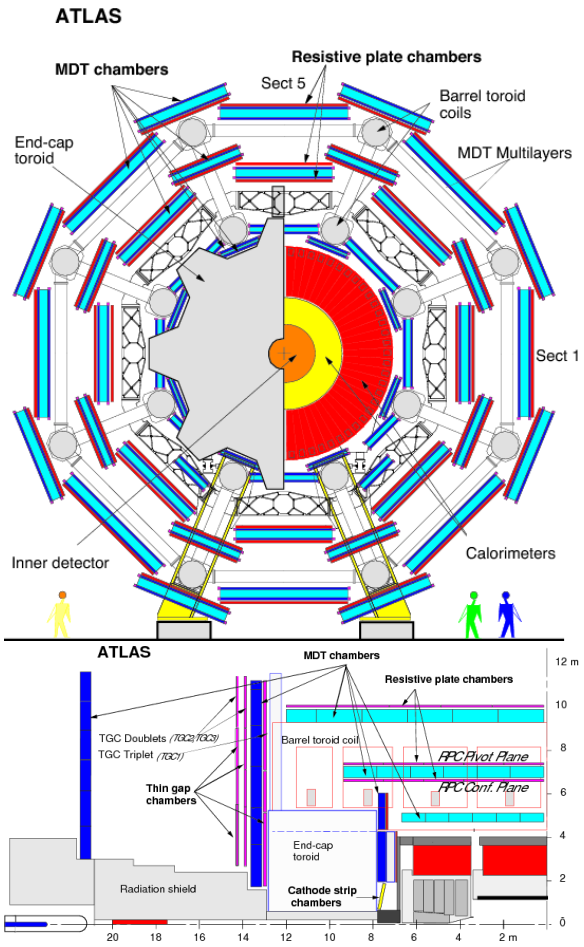


Figure 4.13: Geometric layout of muon sub-detectors in barrel (up) and end-cap (down) region [69]

Muon system is composed of barrel part and end-cap part, each of which has three layers. For the barrel, each layer is a cylinder around the beam pipe, with increasing radius. Each layer is further divided to 8 octanes filled with plates. Each layer of end-cap is a disk, or more often referred to as wheel. Based on the distance to interaction point, three layers in end-cap are called "Inner" (EI), "Middle" (EM) and "Outer" (EO) Wheel. There are four different types of chambers in muon system, for two different purposes. One set of chambers are for precision tracking, which consists of Monitored Drift Chamber (MDT) and Chathode Strip Chamber (CSC). MDT is laid on all layers in both barrel and end-cap, except part of EI, covering a range of $|\eta| < 2.7$, providing

measurement of track-hit in bending plane. CSC is only laid on part of EI, covering a range of $2.0 < |\eta| < 2.7$, to withstand demanding rate and background conditions beyond MDT capability. Another set of chambers consists of Resistive Plate Chambers (RPC) and Thin Gap Chambers (TGC), providing trigger function and second coordinate measurement complementary to precision measurement. RPC is laid at the barrel region while TGC is laid at the end-caps. The trigger system can cover pseudorapidity range of $|\eta| < 2.4$. An illustration of the cut-away view of muon system, as well as geometric layout of each sub-system can be found in Figure 4.12 and 4.13.

4.3.1 Precision-tracking Chambers

Monitored Drift Tube Chambers

MDT [43] is deployed on all layers of both barrel and end-cap to cover most of the acceptance $|\eta| < 2.7$, except for part of innermost end-cap wheel at the range of $2 < |\eta| < 2.7$ due to higher background rate, as illustrated in Figure 4.13. These chambers consist of three to eight layers of drift tubes, operated at an absolute pressure of 3 bar, which achieve an average spacing resolution of 80 μm per tube, or about 35 μm per chamber. The gas mixture used is 93% Ar and 7% CO_2 with a small admixture of water vapor. The drift velocity is not saturated and the total drift time is about 700 ns [69]. While determined by the intrinsic wire spacing, tube resolution can be further improved in two ways: By measuring the drift time, exact distance of ionization collision from anode wire can be inferred; The deleterious effect of diffusion can be reduce with pressured air in the tube [43]. An illustration of the cross-section of the tube can be found in Figure 4.14. The orientation of tube is perpendicular to the beam pipe. As a result, precision measurement is possible only in the $r - z$ plane, the bending plane.

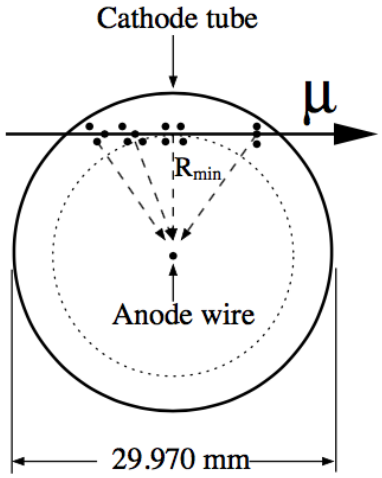


Figure 4.14: Cross-section view of a MDT tube [43]

Cathode-Strip Chamber

The limit for safe operation of the MDT is at counting rates of about 150 Hz/cm^2, which will be exceeded in the region $|\eta| > 2$ in the innermost layer of end-cap. Therefore, MDT is replaced by CSC, which is able to provide precision measurement of 2D coordinates with high-rate capability [43]. Installation location of CSC can be found in Figure 4.13. The whole CSC consists of 2 disks (one disk per end-cap) with 16 chambers on each disk (eight large chambesr plus eight small chambers). Each chamber contains four CSC planes as described below giving 4 independent measurement.

The CSC is essentially a multiwire proportional chamber with wires oriented in radial direction. Both cathodes (above and below the wire) are segmented but in orthogonal direction: one perpendicular to the wire providing precision measurement in bending plane, one parallel to the wire providing measurement in non-bending plane (ϕ direction) with 1/4 coarser segmentation. It should be noticed that CSC wire signals are not read out. Therefore, the 2D position of track-hit is obtained by interpolation between charges induced on the orthogonal cathode strips. A typical resolution obtained with this scheme is 50 μm [69].

4.3.2 Trigger Chambers

While MDT and CSC are good in terms of precision measurement of track-hit, they cannot be used for current ATLAS trigger system since the detector response time due to ion drifting in gas chamber does not fit into L1 latency[5]. The main requirement for trigger system includes: Discrimination on muon p_{T}; Bunch-crossing identification; Fast and coarse track reconstruction for high-level trigger; Second coordinate measurement in non-bending plane to complement MDT measurements [43]. Furthermore, while trigger detector needs to cover $|\eta| < 2.4$ and full ϕ, requirements are different between barrel and end-cap: For fixed p_{T}, momentum at end-cap of high η is much larger than barrel, requiring a finer granularity at end-cap; Radiation level at end-cap is also a factor of 10 higher than barrel [43]. As a result, two different technology, Resistive Plate Chamber (RPC) and Thin Gap Chambers (TGC), are used for barrel and end-cap respectively.

Besides trigger purpose, trigger chambers are also used to measure second coordinate complementary to MDT: After matching of MDT and trigger chamber hits in the bending plane, trigger chamber's coordinate in non-bending plane is adopted as second coordinate of the MDT measurement [43].

Resistive Plate Chambers

As illustrated on Figure 4.13, there are three layers of RPC in barrel region: 2 layers are located at the up and down surface of MDT of second layer, and 1 layer is located at the upper surface of MDT of third layer. RPC is able to provide first level muon trigger: Two RPC chamber installed

[5]The same MDT would become very optimal for Phase-II when the L1 latency gets extended to 6-12 μs, enabling higher precision L1 muon trigger then.

together on middle barrel layer provides low-p_{T} trigger information by requiring coincidence of hits in these two layers for muon p_{T} in range $6 \sim 9$GeV; High-p_{T} trigger is provided by requiring a third coincident hit at the RPC in outmost layer for muon p_{T} in range $9 \sim 35$GeV [43, 70].

RPC is a gaseous parallel electrode-plate (i.e.no wire) detector [43]. Two resistive plates are kept parallel to each other at distance of 2 mm by insulating spacers. The E-field in-between plates is $4.9kV/mm$ allowing avalanche to form from ionization collision. The signal is read out from strips. Read-out strips have a typical width of about 30 mm and grouped into two read-out panels orthogonal to each other (one in η direction and one in ϕ direction) in order to provide 2D position measurement [70]. An illustration of RPC structure can be found in Figure 4.15.

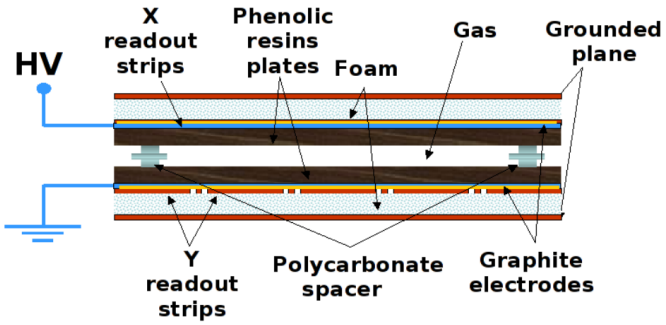


Figure 4.15: Structure of RPC in ATLAS [70]

In ATLAS, the RPC works under avalanche mode (instead of streamer mode) by choosing appropriate voltage and gas mixture. Due to the high voltage and small gas gap, avalanche is roughly grown at a fixed time. The signal at any time is the sum of simultaneous contributions from all primary clusters multiplications. As a result, time jitters for detectable signals is always < 2 ns, making it a very good candidate for trigger detector [70].

Thin Gap Chambers

TGC [43] is essentially a multi-wire proportional chamber, just like CSC, but with a very small wire-to-cathode distance of 1.4 mm, which is smaller than wire-to-wire distance of 1.8 mm. The high electric field around TGC wire as well as such small wire-to-cathode and wire-to-wire distance leads to very good time resolution for trigger purpose. It is installed in the end-cap region of muon system, as illustrated in Figure 4.13: the middle layer of MDT in end-cap is complemented by 7 layers of TGC, while inner layer is complemented by 2 layer of TGC (not shown on the plot). Thought not installed in the outermost wheel, azimuthal coordinate there can be inferred through extrapolation of tracks at middle wheel since there is no magnetic field between middle wheel and outermost wheel. As a multi-wire proportional chamber, TGC is able to provide measurements of both coordinates: the coordinate in bending plane is provided through TGC wire groups and

coordinate in non-bending plane is provided by strip oriented in radial direction. As mentioned above, a finer granularity is desired in end-cap region. Therefore, the size of wire group varies from 6 to 31 as a function of η, corresponding to a variation in width from 10.8 mm to 55.8 mm.

4.4 Forward Detectors

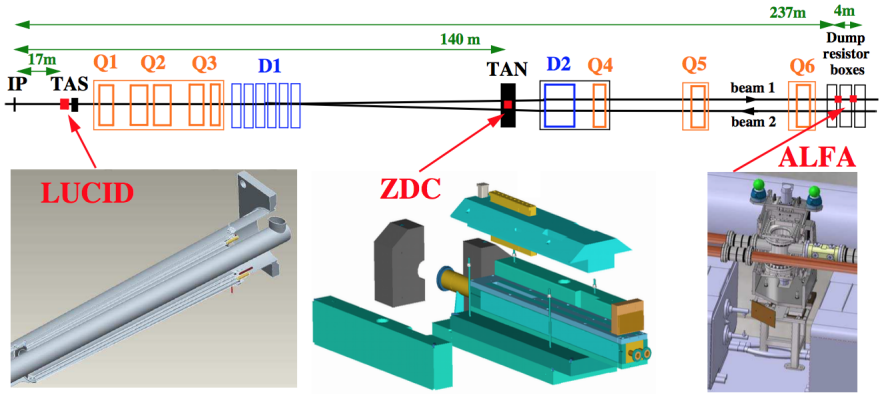


Figure 4.16: Location of forward detector along beam pipe with respect to interaction point in ATLAS [43]

Three small detectors, collectively called Forward Detector [43], are placed along the beam pipe in the very forward region to measure the luminosity delivered to ATLAS. Readers should not confuse these forward detectors with the FCal in calorimeter system. There are three different detectors using different technologies: LUCID (LUminosity measurement using Cerenkov Integrating Detector) [71], ALFA (Absolute Luminosity For ATLAS) [72] and ZDC (Zero-Degree Calorimeter) [73]. LUCID locates at ± 17 m from interaction point, used to detect inelastic p-p scattering in forward region, serving as main online relative luminosity monitor for ATLAS. ALFA locates at ± 240 m from interaction point, used to determine absolute luminosity via elastic scattering at small angles – The optical theorem connects the elastic-scattering amplitude in the forward direction to the total cross-section and can be used to extract luminosity. ZDC locates at ± 140 m from interaction point, playing a key role in determining the centrality of heavy-ion collisions. An illustration of the location of these three detectors can be found in Figure 4.16.

Since luminosity measurement and its uncertainty is not the major concern of the work of this thesis, I do not plan to expand on this part. Readers with interests can find more details in mentioned references. Furthermore, since these detectors are mainly used for luminosity measurement, readers with interest can also find ATLAS publications on luminosity measurements at [74, 75].

4.5 TDAQ System

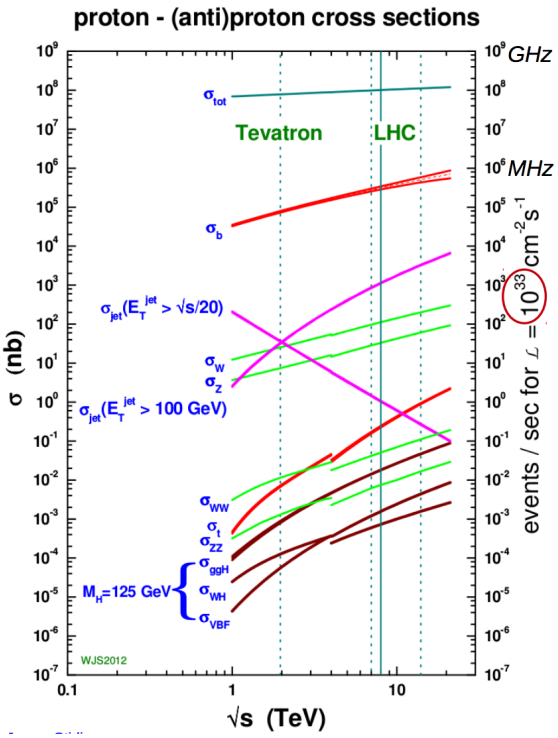


Figure 4.17: Cross section of physics processes produced by hadron colliders [76]

While the unprecedented high energy and luminosity of LHC can greatly push forward the front line of discovery, it is also a great challenge to existing technology for data taking and processing. Such challenge comes from two aspects: For one thing, the collision event happens extremely frequently, at a rate of 40 MHz due to the design bunch spacing of 25 ns; For another, as we have seen above, with millions of sensors across the ATLAS detector, there are in total about 100 millions read-out channels, contributing to about 1 MB of raw data for each collision event. As a result, the total demanded bandwidth is 40 TB per second, which is beyond the bandwidth that can provided by any existing data transfer technology[6], if we want to take all the data, not to mention the huge amount of mass storage needed for them. Therefore, a dedicated trigger and data acquisition system (TDAQ) [43] is designed for ATLAS in order to perform fast online selection of a fraction of events without loss of sensitivity to interested physics processes and high quality data flow control.

The main physics motivation behind such a trigger system is that almost all physics processes of interest at LHC is only a tiny fraction of the total interaction cross section, as illustrated in

[6] Interestingly, the probably largest bandwidth provided by existing technology is about 255 Tbit per second [77], corresponding to 32 TB per second, which is almost enough for ATLAS. Even so, one also needs to take technology cost and maturity into account since ATLAS needs to deploy such system on a large scale with reasonable budget

Figure 4.17. For Standard Model electroweak and top physics, cross section is 6 to 8 order of magnitude lower than total cross section; For Higgs production it is less than 9 order of magnitude rarer; For potential new physics beyond Standard Model, which is the main focus of this thesis, it could be more than 10 order of magnitude lower. Therefore, even if we could, saving all events at hadron colliders are not necessary [76].

During Run 1, ATLAS trigger system operated efficiently at instantaneous luminosity of up to $8 \times 10^{33}\ cm^{-2}s^{-1}$ with center-of-mass energy of 7 TeV and 8TeV. In Run 2 since 2015, due to the LHC condition as mentioned in Section 3.3 (increased center-of-mass energy to 13 TeV, higher luminosity and increased pile-up level), trigger rate would exceed the maximal allowed bandwidth limit without increasing trigger threshold at the cost of losing efficiency for physics of interest. Therefore, substantial upgrades [78] on ATLAS trigger system was performed in almost all aspects during LS1 to accommodate such situation. Since all the data used by the work of this thesis is taken from Run 2, only trigger system after LS1 upgrade would be described here [79, 80], while details about trigger system at Run 1 can be found in [43, 81, 82].

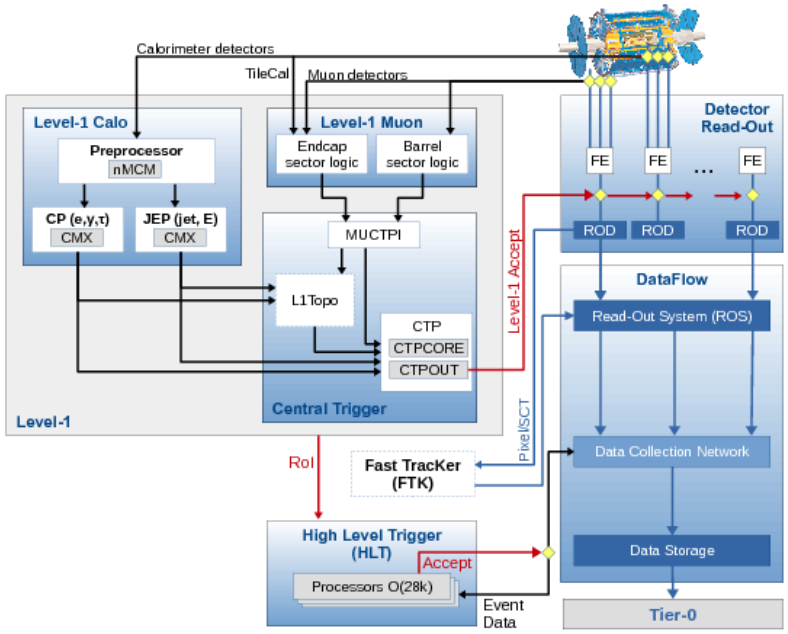


Figure 4.18: Schematic overview of ATLAS TDAQ system with emphasis on trigger part [79]

As shown in Figure 4.18, the trigger system consists of a hard-ware based first-level trigger (L1) and a soft-ware based high-level trigger (HLT). With input collision rate of 40 MHz, L1 trigger would first reduce event rate down to around 100 kHz within 2.5 μs using customized hardware installed on front-end using very coarse granularity and local detector information. If accepted by L1, events would be further streamed down for HLT, which would make further decision with finer granularity and global detector information, in the time scale of hundreds of milliseconds. HLT will further bring event rate down to 1 kHz before streaming them to data center at CERN and distributed to Worldwide LHC Computing Grid (WLCG). The L1 rate is more constrained by readout capability (bandwidth), while HLT rate is more constrained by offline computing model (computing farm resources, algorithms, etc.) [79].

4.5.1 Level 1 Trigger

L1 trigger is probably the most challenging part of trigger system since it requires extremely fast decision on average in order to catch up with the collision rate. While some events can be rejected (or accepted) in very short amount of time, some might take significantly longer time to decide. Therefore, data is buffered when trigger decision is taking place. The buffer size directly defines the maximal trigger latency, and is very hard to change once decided (for example, change of data buffer on-detector requires replacement of all front-end electronics). In ATLAS L1, the buffer size is 100 bunch crossing, leading to 2.5 μs in case of 40 MHz collision rate [76]. The L1 trigger latency is defined as the time between collision and arrival of L1 decision, and can be broken down into three parts as shown in Figure 4.19: L1 algorithm execution time; Signal transmission time; Synchronization delay since it takes different time for signals coming from different part of detector.

After electronic signal is formed in detector sensors, signals are split in two as shown in Figure 4.18: One heading toward front end and get buffered, waiting for the other one heading to L1 trigger. Due to the time limit, only calorimeters and muon system have L1 trigger system: signals detected in calorimeters are sent to L1Calo located off-detector in the service cavern USA15 and signals formed in muon system are sent to L1Muon on-detector located at each muon trigger station as mentioned in Section 4.3.2 [43] before combined in USA15 counting room. Trigger information from L1-Calo and L1-Muon are then sent to L1 Central Trigger (CTP) located at USA15 counting room, which would generate a pre-scale and final L1 decision (L1A). L1A is sent back to the front-end of each sub-detector, allowing the data to keep flowing down if accepted.

L1Calo [83] algorithms are based on a very coarse granularity on calorimeters called trigger tower, which is formed from groups of calorimeter cells into fixed size of 0.1×0.1 ($\Delta\eta \times \Delta\phi$). Energy of trigger towers is calibrated at electromagnetic energy scale (EM scale), which correctly reconstruct the energy deposition in EM calorimeter, though energy deposition from hadrons would be underestimated. For electron, photon and taus, trigger algorithm identifies a Region-of-Interest (RoI) as an 2×2 trigger tower cluster in the EM calorimeter for which the sum of the transverse

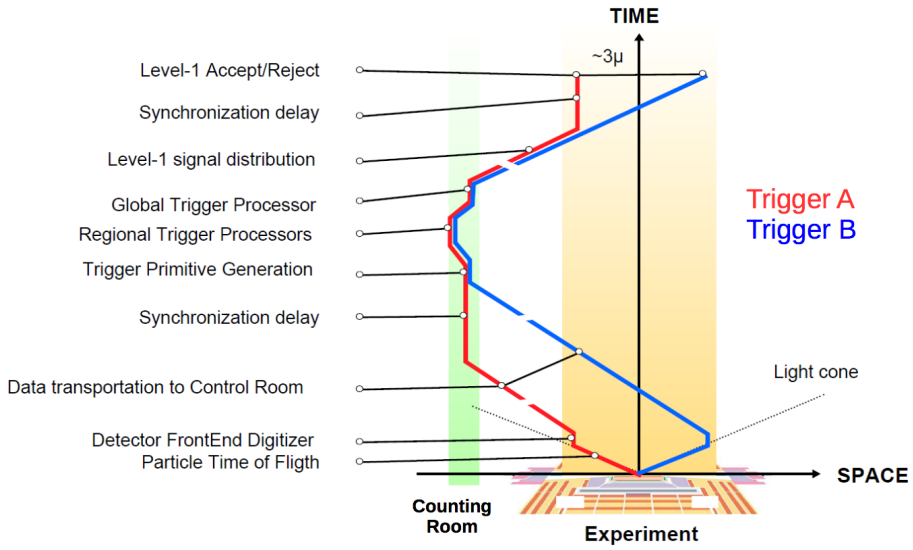


Figure 4.19: Illustration of the decomposition of L1 latency [76]

energy from at least one of the four possible pairs of nearest neighbor towers (1×2 or 2×1) exceeds a predefined threshold. For jets, RoIs are defined as 4×4 or 8×8 trigger tower windows for which the summed electromagnetic and hadronic energy exceeds predefined threshold and which surround a 2×2 trigger tower core as local maximum. The location of this local maximum also defines the coordinate of jet RoI [79]. An illustration of L1Calo RoI can be found in Figure 4.20.

L1 muon trigger [43] is directly based on the trigger chambers in muon system, RPC and TGC, which has fine granularity and fast time resolution optimized for trigger purpose. The basic principle of the algorithm is to require a coincidence of hits in the different trigger station within a "road", which basically is the trajectory of muon from interaction pointing through detector. The width of the road is related to the p_{T} threshold to be applied. A system of coincidence logic allows concurrent operation with a total of 6 thresholds, 3 related to low-p_{T} trigger and 3 related to high-p_{T} trigger as mentioned in Section 4.3.2. Trigger signals from both barrel and end-caps are combined before sending to CTP [43].

The Central Trigger Processor (CTP) [84] receives trigger information from L1Calo and L1Muon, which consists of multiplicities of electron/photon/tau/jet/muon and flags indication which threshold is passed for of jet transverse energy and $E_{\mathrm{T}}^{\mathrm{miss}}$. Additional inputs are provided for special triggers such as a filled-bunch trigger based on beam-pickup monitors, and a minimum-bias trigger based on scintillation counters [43]. In Run 2, a new topological trigger (L1Topo) consisting of two FPGA-based (Field-Programmable Gate Arrays) processor modules is added in, to perform selections based on geometric and kinematic association between objects received from L1Calo and L1Muon, as well as refined calculation of global quantities such as $E_{\mathrm{T}}^{\mathrm{miss}}$ [79]. In addition to its function as selection,

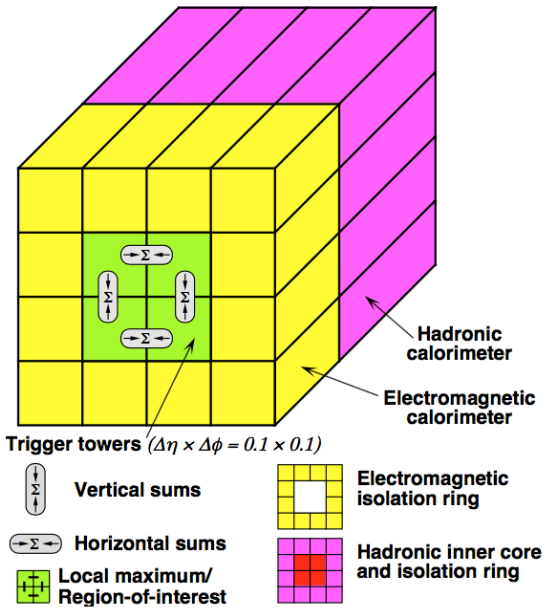


Figure 4.20: Schematic view of trigger towers used in L1Calo algorithms [79]

CTP is also the timing master of whole detector: The clock signal synchronized to LHC beams arrives at CTP and gets distributed from here to all sub-systems along with L1A and other timing signals [43].

4.5.2 High Level Trigger and Data Acquisition System

After an event is accepted at L1, it would be further streamed down and processed by HLT, using finer granularity of calorimeters, precision measurements from muon system (MDT and CSC) as well as tracking information from ID, all of which are not possible in L1 due to limit of time. Furthermore, the RoI as defined in L1 is passed down to HLT as seed for further reconstruction as shown in Figure 4.18, although access to full detector information at HLT is also possible if needed. While HLT consists of L2 and Event Filter back in Run 1, they are all merged to a single homogeneous concept of HLT in Run 2 for better resource sharing and simplification on both hardware and software side. However, a multi-stage strategy same as Run 1 is adopted in Run 2: most HLT triggers have two stages with a fast first-pass reconstruction to reject majority of events and a slower precision reconstruction for remaining events. A detailed description of reconstruction algorithm for ID, calorimeter and muon in HLT can be found in [79]. To achieve higher readout and output rates, the ROS, data storage system and the data collection network were upgraded. On-detector front-end and detector-specific read-out drivers (ROD) did not change dramatically from conceptual point of view, while certain sub-systems such as CSC ROD adopts completely new

technology for better performance during LS1.

In the offline physics analysis, the way to interact with trigger system is through so-called "trigger menu", which consists of a list of "trigger lines" containing L1 and HLT signatures, thresholds and pre-scales (if available). Trigger menu composition and thresholds may change in time for several luminosity range, in order to maximize the physics output under the constraints of detector rate and bandwidths.

4.5.3 Data Streams

Event accepted by HLT are written into separate data streams. In Run 1, data streams are separated by the major trigger signature into three streams (*Egamma*, *Muons* and *JetTauEtMiss*). In Run 2, these are merged into a single stream called *PhysicsMain* in order to reduce data duplication and therefore reduce storage and CPU resource by 10% [79]. Even so, the amount of time needed for Tier-0 reconstruction of *PhysicsMain* is typically 36 hours after data taking. A small fraction of them at rate of 10 to 20 Hz is streamed into *Express* stream, for calibration and data quality monitor purpose. Furthermore, events with only HLT object information but without ATLAS detector information is recorded into a new type of stream, for Trigger-Level Analysis purpose. An example of such kind of analysis can be found in [85]. It can be used as front line of new physics discovery since the amount of data in HLT is more than offline level. In the last, events that cannot be properly processed by HLT or have some DAQ-related problem are written to *debug* stream. These events can be restored through offline reprocessing using the same configuration as HLT. Therefore, most physics analysis would need to check these *debug* stream since they are just the same as other events in *PhysicsMain* after reconstruction.

Chapter 5

Physics Objects Reconstruction

After signals are read out from ATLAS detectors (and accepted by trigger system), dedicated algorithms are needed to reconstruct them into meaningful physics objects such as tracks, jets, electrons etc.. For simulation, events are in the same format as data byte-stream after digitization and trigger simulation step (technically, *RDO* or *RDOTrigger* format in Athena terminology) and thus same reconstruction algorithms are applied on them. Furthermore, these physics objects need to be calibrated before being used in any physics analysis.

Since all physics searches presented in this thesis are in hadronic final states, the most important physics objects would be jets. A generic introduction to jet reconstruction is in Section 5.3, while jet reconstruction for jet substructure and boosted object identification, which is more relevant to the work in this thesis, is presented in Chapter 6. Track jets, which is playing a key role in the boosted topology reconstruction in the work of this thesis, will be presented in Section 5.5, while the ingredients of building track jets – tracks – along with primary vertex reconstruction is in Section 5.1 and 5.2. Furthermore, flavor tagging which is essential to background suppression in both searches presented in this thesis is in Section 5.4. Since electrons, muons and missing transverse energy are not playing any fundamental role in the work of this thesis, they are omitted here. Readers with interest in this topic can refer to [86, 87, 88].

5.1 Inner Detector Tracks

Due to the solenoid magnetic field filled in ATLAS tracking system, charged particle would follow a helix-like trajectory before leaving the ID system. The convention used by ATLAS to parameterize track trajectory is the so-called *perigee parametrization*, as illustrated in Figure 5.1. In this representation, a reference point needs to be first chosen: Although it could be any point, the ATLAS convention is either the geometric center $(0, 0, 0)$ or beam spot center. A Cartesian coordinate system as defined in the beginning of Chapter 4 is built centered at this reference point. Then every

point on the trajectory can be described by a five dimension vector, $(d_0, z_0, \theta, \phi, \frac{q}{p})$ with respect to the chosen reference point. d_0 and ϕ are defined on the transverse plane: d_0 (also called *transverse impact parameter*) is the distance to reference point and ϕ is the angle between momentum direction and x-axis direction. z_0 (also called *longitudinal impact parameter*) and θ are defined on the longitudinal plane ($r - z$ plane): z_0 is defined as the distance along z-axis between reference point and cross point between z-axis and projected straight line in momentum direction in $r - z$ plane, while θ is defined as the angle between this projected line and z axis. Furthermore, the representation point along trajectory is usually chosen to be *perigee*, which is defined as the point that is closest to reference point in transverse plane: Since the trajectory on transverse plane is a circle, perigee is simply the cross point between circle and connected line between reference point and circle center.

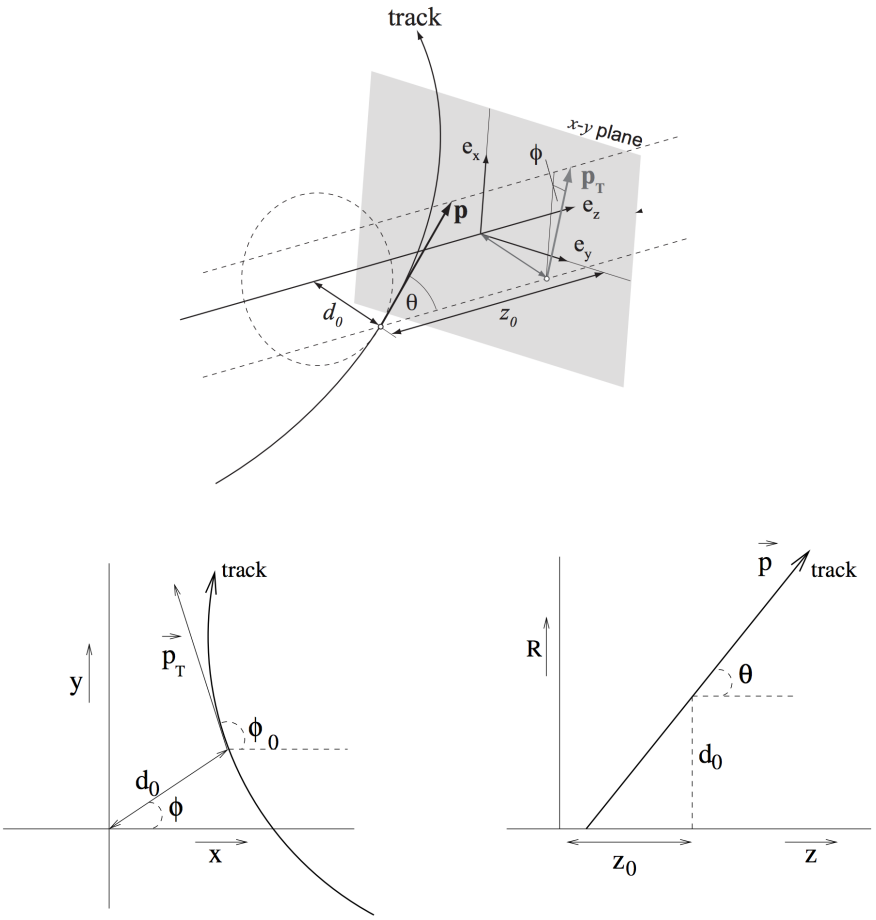


Figure 5.1: Illustration of perigee parametrization of track trajectory in ATLAS [89, 90]

The first step toward track reconstruction is reconstruction of 3D space-point measurement on silicon detectors (TRT can only form measurement in transverse direction). For pixel detector, pixels

naturally gives a 3D measurement through knowledge of pixel position on the layer and position of its layer. However, as particle transverses a pixel layer, its energy deposition is usually collected in more than pixels: The particle itself might pass through more than one pixel due to incident angle; Drift of ionized electron-ion pair to neighborhood pixels; Kicked-out δ-ray can further deposit energy in neighborhood pixels etc.. As a result, a connected component analysis (CCA) algorithm [91] is used to group pixels with common edge and corner together. Such *cluster* is the fundamental unit for any further pattern recognition and track fitting. Position as well as its covariant matrix is obtained through a linear interpolation exploiting the charge distribution between pixels within the cluster [92]. For SCT, a space-point is formed by combining measurements from pair of strips from a SCT module consisting of two pairs of sensors glued back-to-back at stereo angle of 40 mrad as described in Section 4.1.2.

Naively, the track reconstruction would be a pattern recognition which identifies groups of space points as track candidates, followed by a global χ^2 fit. Unfortunately such classical picture does not work anymore in modern track reconstruction. Instead, Local pattern recognition strategies are used in that track fitting and track finding happens simultaneously in a progressive way now [93]. Under this context, ATLAS New Tracking (NEWT) [94] is designed for ATLAS track reconstruction. Track candidate is first obtained using iterative track-finding algorithm seeded on combinations of space points from silicon detectors (with additional methods to recover non-prompt tracks [94]). Then a loose track candidate search allowing combinatorial track candidates is followed by a stringent ambiguity solver to only keep tracks with high quality.

Track seeds are found from three space points on silicon detectors, in four possible types of combinations: All on Pixel; All on SCT; Two on Pixel one on SCT; One on Pixel two on SCT. A number of requirements are then imposed on these seeds to improve purity such as type-dependent minimum momentum and maximum impact parameters etc. [95, 96]. Then a combinatorial Kalman filter [97] assuming a perfect helix trajectory is used to get first crude estimation of track parameters for each track seed, which is also called *track candidate*. During the propagation step in Kalman filter, any compatible hit in next layer that is within certain window can be used to build a separate track candidate. Therefore, multiple track candidates might be built from a seed. This strategy would result in very high efficiency in reconstructing primary particles with tracks purely from random combination suppressed, but at the cost of incorrect (multiple) association between space points (or sometimes called *hits*) and track candidates. This necessitates a stringent ambiguity solving stage afterwards.

In ambiguity solving stage, track candidate might be rejected if some minimal requirements are not met such as minimum momentum cut or hit/hole multiplicity requirements. Then each survived track candidate would get a track score, based on multiple measures of track quality including intrinsic resolution of clusters, cluster multiplicities in different sub-detectors, number of holes, χ_2 of fit and so on [96]. Tracks are processed in the descending order of track score, ensuring tracks

with high quality gets preference. For track candidate being processed, if a cluster has been used by accepted track candidates, dedicated algorithm would be decided if such cluster is *shareable*, shared-with-penalty, or not shareable at all (see next paragraph). In case of shareable, nothing would happen; In case of shared-with-penalty, track can not have more than one such hit and such cluster cannot be shared by more than two tracks; In case of not shareable at all, cluster should be removed from track candidate being processed. Furthermore, in any case, if adding such cluster would make current track candidate or accepted track candidate fail the shared cluster limit, it should be removed from current track candidate. Since clusters associated with current track candidate might be changed by following this procedure, current track candidate needs to be re-scored and returned to the ordered list of remaining candidates. If they are too low in the list or fail basic track quality requirement, track candidate might be further rejected.

One of the main goals of ambiguity solver is making correct assignment between hits and track candidates in case hits are shared by multiple track candidates. While such sharing can come from pure combinatorics effect, it can also come from the fact that multiple particles are so close to each other that clusters left from them on Pixel detector get connected, resulting in merged clusters. Such merge clusters would not only complicate the ambiguity solving, but smear out the track-hit measurement resolution as well. A novel artificial neural network (NN) approach [92] is developed in ATLAS to identify these merged clusters based on charge measurements pixel-by-pixel in the cluster, incident angle of incoming particle and other geometric information. Probability of a cluster being 1-particle, 2-particle or 3-particle originated can be estimated from NN. Furthermore, separate sets of NN are used to estimate the cluster position and its covariant matrix for each hypothesis on number of transversing particles. While such NN technique is used to split clusters into multiple ones in Run 1, it is decided to be moved to ambiguity solving stage to fully exploit the incident angle information and optimizate track reconstruction in dense environments [96] in Run 2. As a result, NN is consulted only when a cluster is contained in multiple track candidates. If output of NN is over the tunable threshold, cluster is identified as *shareable* and thus can be shared across track candidates without any penalty. Furthermore, clusters used by multiple track candidates failing the NN cuts can still be shareable if the track candidates use a shareable cluster on the next layer. Clusters with two-particle hypothesis more than 0.05 but failing above cuts can be shared, but with certain penalty, while those less than 0.05 are forbidden to be shared at all. To control the fake rate, a track cluster must have at least 9 silicon clusters before any sharing is allowed. Furthermore, a track with p_{T} less than 1 GeV cannot have shareable cluster and every track is required to have at least 4 unique SCT hits.

Survived track candidates are extended to TRT to find consistent TRT hits; When associated TRT hits are identified, track would be refit for final track parametrization [95]. Kalman filter is also used in both the extension search and refit procedure, as it can naturally incorporate various stochastic process such as multiple scattering. Furthermore, due to the energy loss in material

and distribution of B-field in solenoid, particle is not following a strict helix, which also can be naturally handled in Kalman filter framework by incorporating them in propagation function. Steps mentioned above is the main sequence called *inside-out* sequence, while a second *outside-in* sequence is similarly done, but starting from Hough transformation in TRT track segment search backward to the silicon layers. Such backtracking is important for particles with vertices away from primary vertices. A complementary third step is followed for these photon conversion / V0 (long-lived neutral particles) reconstruction [93]. More implementation details in ATLAS track reconstruction can be found in [94]

5.2 Primary Vertex

After tracks are reconstructed, primary vertices representing the collision interaction regions are reconstructed from them. It should be noticed that in high-luminosity case such as LHC, more than one primary vertices is common, which also needs to be taken into account during primary vertices reconstruction. The reconstruction of primary vertices in ATLAS can be organized in two steps: *vertex finding* step where associated between tracks and vertices are established; *vertex fitting* step where vertex position along with its covariant matrix is determined from associated tracks [98]. While in general these two steps are sequential, the boundary between them is not strictly evident since there are some back-and-forth iterations between them.

Reconstructed tracks first need to be of good quality [99]: $p_{\mathrm{T}} > 400$ MeV and $|\eta| < 2.5$; At least 9 (11) silicon hits for $|\eta|$ less (larger) than 1.65; At least of 1 hits on either IBL or B-layer; At most 1 shared module (1 shared hit on Pixel or 2 shared hit on SCT); No holes in Pixel; At most 1 holes on SCT. Furthermore, these tracks need to be compatible with interaction region by requiring [98]: $|d_0| < 4\ mm$, $\sigma(d_0) < 5\ mm$ and $\sigma(z_0) < 10\ mm$. All these impact parameters are estimated with respect to the luminous region (beam-spot), which is determined online using same algorithm described in this section, but without constraints of beam-spot. Then a vertex seed is found by looking for global maximum in the distribution of z among these selected tracks with respect to beam-spot. Such vertex seed will be used as initial point for any iterative procedure described below.

The vertex fitting problem can essentially be regarded as a chi-square minimization problem. However, a direct global χ^2 minimization in the spacial representation has a computing complexity of $O(N_{trk}^3)$, which limits its application in ATLAS. This can be significantly sped up through Billoir method, which re-write χ^2 in helix representation and linearize residual term in χ^2 as function of vertex spacial position. While this can reduce computing complexity to $O(N_{trk})$, it can be more efficiently implemented through iterative way such as Kalman Filter. In Kalman Filter approach, vertex spacial position and a virtual momentum vector is taken as system state (so that propagation

function is trivial) and measurement function is simply the transformation from spacial representation to helix representation. Then the vertex fitting can be naturally incorporated into Kalman Filter by regarding the addition of a new track to vertex fitting as a system transition. Readers can find more details on the mathematics formalism in [100].

However, all these approaches suffer from robustness issue when there is outlying tracks or poorly measured tracks. This is particular urgent when it comes to ATLAS experiment due to the pile-up collisions in which case outlying tracks would surely exist. This is handled using *adaptive vertex fitting* algorithm [101], which deals with outlying track measurements by down-weighting their contribution to the overall vertex χ_2. Formally, each track would have a χ^2-dependent weight term:

$$w_i(\chi_i^2) = \frac{\exp(-\chi_i^2)/2T}{\exp(-\chi_i^2)/2T + \exp(-\chi_c^2)/2T} \tag{5.1}$$

where χ_i^2 is the chi-square contribution from each track, χ_c is a critical value representing the cut where weight is $1/2$ and T is a tunable parameter defining the function. Such weight term is directly added to the derivation of chi-square over vertex position for each track. As a result, the Kalman Filter also needs to be changed accordingly. $\chi_c = 3$ is chosen and T is used to employ a deterministic annealing approach that helps to avoid falling into local minimum [101].

After the adaptive vertex fit, tracks incompatible with the vertex by more than 7σ ($\chi^2 > 49$) are removed and used to seed new vertex. Such procedure is repeated until all tracks are exploited, or no additional vertex can be found.

Typically more than one primary vertices can be found per event due to pile-up. In most physics analysis, including searches presented in the work of this thesis, primary vertex with highest $\sum p_{\mathrm{T}}^2$ is taken as the hard-scattering vertex while the rest are taken as pile-up vertices. This is based on the argument that hard-scattering collision of interest usually comes with high momentum transfer while most pile-up activities are just soft inelastic, or even elastic, collision. However, this could be analysis-dependent since some analysis, such as $H \to \gamma\gamma$ analysis, use different criteria due to less production in charged particles. Readers can find more details on latest primary vertex reconstruction performance in [99, 102].

5.3 Jets

As a hadron collider, QCD process is predominant in LHC with partons (quarks and gluons) produced from proton-proton collisions, either hard-scattering or not. Furthermore, partons could also come from the hadronic decay of electroweak bosons. However, partons are not observable due to the asymptotic freedom. Instead, partons would be first transitioned to a spray of particles, also known as *jets*, depositing energies in detectors, from which one can infer back the quantum states of initial partons and the physics processes behind it.

Quantum chromodynamics is the essential tool to understand these parton productions as well

as their evolution afterwards. There are in general two main approaches to solve the QCD, either numeric solution with lattice QCD or perturbation theory, while none of them is able to provide a full solution due to the non-perturbation nature at energy scale lower than Λ_{QCD} (≈ 200 MeV). In hadron collider physics community, the basic approach is perturbative QCD followed by non-perturbative phenomenological modeling.

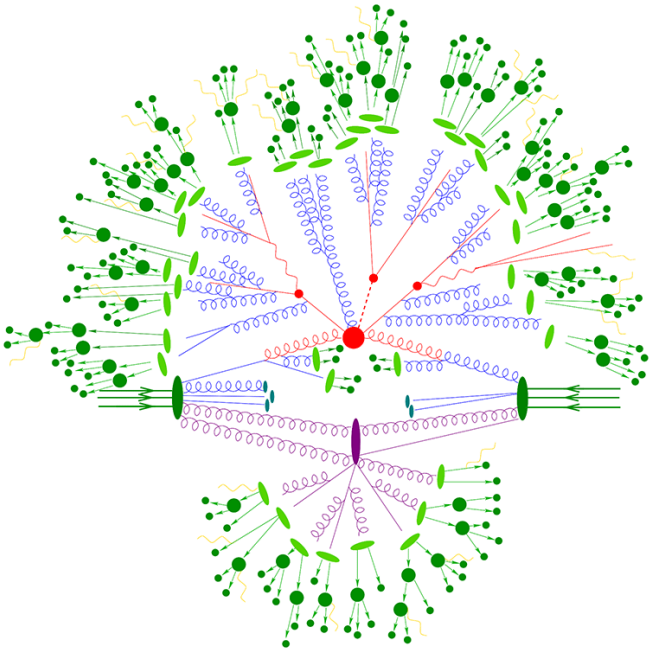


Figure 5.2: Illustration of typical QCD processes involved in a hadron collider, including parton shower, hadronization and underlying events (multiple parton interactions, initial state radiation) [103]

During evolution of a parton, gluons can be emitted dominantly at small splitting angle and/or small energy scale, which is a universal property in QCD called *soft-collinear divergences*:

$$\begin{aligned} P(gluon\ emission\ from\ quark) &\sim \frac{2\alpha_s C_F}{\pi}\frac{dE}{E}\frac{d\theta}{\theta} \\ P(gluon\ emission\ from\ gluon) &\sim \frac{2\alpha_s C_A}{\pi}\frac{dE}{E}\frac{d\theta}{\theta} \end{aligned} \tag{5.2}$$

Gluon emission from quark or gluon shares the same structure with only difference in the color factor ($C_F = 4/3$, $C_A = 3$). Therefore, a practical way to compute observables in QCD would be summation over all orders in soft/collinear approximation with regularization of divergences by cutting off near Λ_{QCD}. A pictorial illustration of this idea is the so-called *parton shower*, which also turns out to be a very powerful tool to describe the evolution of partons after being produced

in Monte Carlo simulation, as illustrated in Figure 5.2. Starting from initial parton produced from hard scattering, every parton can be split into two by emitting a gluon, and thus form cascades of parton shower by repeating this procedure. The splitting is in the descending order of either angle or energy scale, depending on the MC, controlled by *Sudakov Form Factor*, which is essentially a cumulative distribution function giving the probability of not radiating a gluon above certain energy or angle scale. The splitting would not stop until one reaches non-perturbative cutoff scale Λ_{QCD}, after which a phenomenological model would be used to simulate hadronization process and output a bunch of observable hadrons.

Despite the success of parton shower (and hadronization model) in describing parton evolution, individual hadrons are not good candidates for QCD precision measurement, or as basic physics objects in searches. For one thing, one is more interested in the initially produced partons, which should correspond to a collection of final state hadrons. For another, which might be more important, this is too sensitive to the detailed description of soft/collinear splitting, which is considered unsafe theoretically. More in general, for any observable whose distribution can be perturbatively calculated, it should be insensitive to the emission of soft or collinear gluons, which is the famous *infrared/collinear-safety (IRC safety)*.This is based on the argument that if an observable is to be calculated in perturbative QCD, soft-collinear divergence contribution from real branching and virtual corrections must cancel at all orders in order to give meaningful finite results. As a result, if one wants to do a reasonable comparison between experiment result and theoretical prediction, the observable has to be IRC-safe. Such IRC-safety principle strongly influences the choice of jet definition in LHC physics, which would be described in details later.

In this section, calorimeter jet reconstruction in ATLAS would be briefly reviewed. However, it should be noticed that the concept of jet applies to any type of input ranging from truth level partons or hadrons to detector level topoclusters or tracks. More details on jet reconstructed from tracks (track jets) can be found in Section 5.5.

Topological Clusters

As incoming particle deposits energy in calorimeters, a particle shower in both lateral and depth direction would be formed, as described in Section 4.2. Due to very fine segmentation in calorimeters, cells need to be clustered together into the so-called *topological clusters* (*topocluster* for short) [104] to reconstruct such particle shower. However, due to the complication of particle showering process (for example the difference between EM shower and hadronic shower), individual topocluster might represent the full or partial response to single particle (full shower or partial shower), or combination of several complete/partial showers induced by more than one particles, depending on incoming particle type, energies, spatial separation and cell signal formation.

The 3-dimension topocluster reconstruction is based on cell signal significance, which is defined as the ratio of cell energy at electromagnetic (EM) energy scale over average expected noise. Seeds

for topocluster growing are first identified from cells with signal significance over $S = 4$. Each seed forms a *proto-cluster*. Then the proto-cluster would keep growing as long as signal significance of neighbouring cells is over $N = 2$. Such growing would stop when the signal significance of neighbouring cells is over $P = 0$ but less then $N = 2$ (these cells would still be collected but then growing stops). different proto-clusters might merge if they touch each other during growing. Then proto-clusters with two or more local maximum would be split between corresponding signal peaks in all three spatial dimensions. After the split, each cell should be uniquely assigned to one cluster without any sharing.

Topocluster at this stage is in the *EM* scale. Although it can correctly estimate energies deposited by electrons and photons, it would underestimate the energy of hadronic particles due to non-compensation effect. Further correction might be needed due to signal inefficiencies coming from signal loses in clustering process or energy lost in inactive material. Therefore, a local hadronic calibration (LCW) can be applied at cluster-by-cluster level to correct for these effects [105]. While LCW scale is used as default for all calorimeter jets in Run 1, EM scale becomes the default for small radius calorimeter for ATLAS in Run 2 (LCW scale is still the default for large radius calorimeter jets) [106, 107].

Jet Clustering Algorithms

There are two kinds of mainstream jet clustering algorithms: cone-type algorithm and sequential clustering algorithm. Except for a few cases, cone-type algorithms do not meet the IRC-safety requirement, mainly due to the need of a seed: if any seed is allowed, it would be infrared-unsafe; If a minimum momentum cut is applied on seed, it would be collinear-unsafe. Therefore, cone-type algorithms are strongly disfavored by theorists. On the other hand, sequential clustering algorithm is IRC-safe by construction, and thus adopted in both ATALS and CMS experiment.

A typical sequential algorithm can be summarized as following:

1. A distance metric d_{ij} first needs to be defined between any two constituent. Furthermore, the distance between each constituent and beamline d_{iB} should also be defined.

2. Compute d_{ij} and d_{iB} for all existing particles in the list in current stage and get the minimal one.

3. If the minimum is some d_{ij}, combine particle i and j and replace them with the merged one. Then go back to second step.

4. If the minimum is d_{iB}, remove particle i out of the list and tag it as a jet. Then go back to second step.

5. Do the iteration until all constituents are tagged as jet and nothing left in the list.

A generic implementation with optimization on computing time is provided by FastJet package [108], which also includes various kinds of other jet clustering algorithms. A commonly used metric is the so-called *generalized* k_t metric:

$$\begin{aligned} d_{ij} &= \min(k_{Ti}^{2p}, k_{Tj}^{2p})\frac{\Delta R_{ij}}{R} \\ d_{iB} &= k_{Ti}^{2p} \end{aligned} \tag{5.3}$$

where ΔR_{ij} is the distance on $\eta - \phi$ plane and D is a tunable parameter, called *jet radius*, representing the characteristic size of jets.

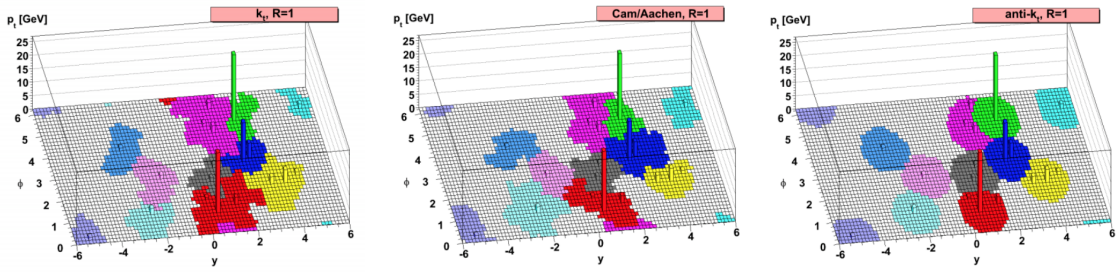


Figure 5.3: A sample parton-level event clustered with different jet algorithms [109]

Three different values of p are used: $p = 1$ for k_t algorithm [110, 111], $p = 0$ for Cambridge/Aachen (C/A) algorithm [112, 113] and $p = -1$ for anti-k_t algorithm [109]. For k_t algorithm, it would typically starts from soft particles and merge them into harder ones. Furthermore, the k_t distance metric are closely related to the structure of divergences in gluon emission. As a result, k_t algorithm would attempt to reverse the QCD branching procedure in parton shower, which itself could be very informative by looking through the clustering history. However, since activities from pile-up or underlying events are also predominantly soft, k_t algorithm would unnecessarily include many unrelated components, making it relatively more pile-up sensitive. The C/A algorithm remove such kinematic dependency since it is purely based on spatial separation. The anti-k_t algorithm instead push toward the opposite direction as k_t algorithm. It will typically starts with hardest one during iteration and then try to "grab" the nearby softer components to merge. Such feature leads to much more regular jet area [114] for anti-k_t jets compared to the other two, as illustrated in Figure 5.3: A hard jet without other hard neighbours within distance of $2R$ will form a conical jet; If two another hard jet is present within $R < \Delta R_{12} < 2R$, both would not be perfectly circle with overlapping region partially clipped; If the close-by jet is much softer than first one, the harder one will have a perfect circle jet area while the jet area of softer one would lose the part overlapping with first one. The feature of prioritizing hard component in anti-k_t algorithm would make it less sensitive to the pile-up activities. In ATLAS, the default jet clustering algorithm is anti-k_t with

$R = 0.4$.

Jet Energy Scale Calibration

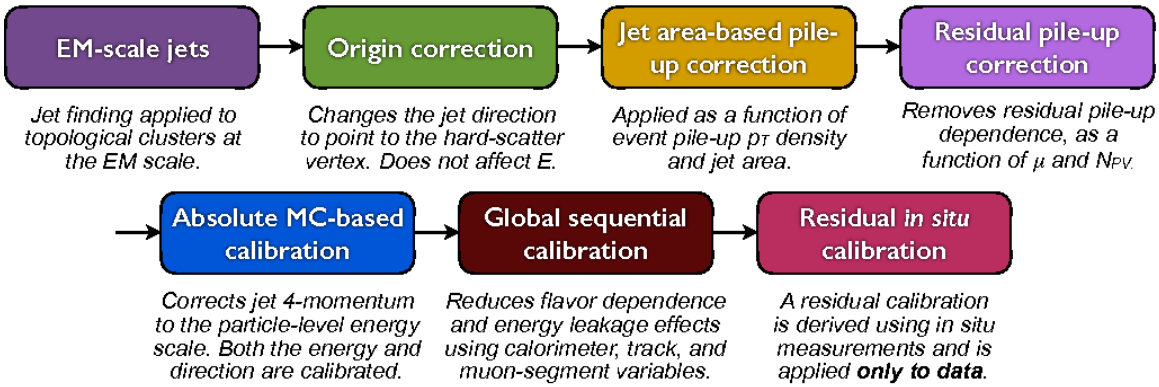


Figure 5.4: Calibration stages for reconstructed jets. Other than the origin correction, each stage is applied to the four-momentum of the jet [106]

After a jets are reconstructed, calibration needs to be applied on the four momentum of reconstructed jet in order to restore it back to particle-level energy scale. As illustrated in Figure 5.4, calibration has various steps:

Origin correction In this step, the η of jet is re-calculated with origin being the hard-scattering primary vertex as reconstructed in Section 5.2, with jet energy remains the same. Therefore, only η resolution can be improved in this step.

Jet area-based pile-up correction This step, along with next step, aims at removing the excess energy from pile-up as well as afterward residual correction. First an area-based p_{T} density subtraction is applied event-by-event [115]. The p_{T} density, ρ, is estimated by taking the medium of p_{T} density of all jets in the event, p_{T}/A, where A is the jet area estimated using *ghost particles*. Medium instead of average is taken for ρ to reduce bias from high-p_{T} activity.

Residual pile-up correction After the area-based subtraction, a residual p_{T} dependency on N_{PV} (in-time pile-up) and μ (out-of-time pile-up) is observed to be fairly linear. Thus linear correction with coefficients derived from MC simulation is applied. This step, along with jet area-based pile-up correction can be expressed as:

$$p_{\mathrm{T}}^{corr} = p_{\mathrm{T}}^{reco} - \rho \times A - \alpha \times (N_{PV} - 1) - \beta \times \mu \tag{5.4}$$

Absolute MC-based calibration In this step, an absolute jet energy scale as well as η correction, derived from MC, is applied on four-momentum of jets to account for biases. The average

energy response is defined as mean of E^{reco}/E^{truth} binned in E^{truth} and η_{det}. This can be numerically inverted to be a calibration factor, the inverse of average response, as function of E^{reco}. Similar correction is also derived for η and applied on jets.

Global sequential calibration Following the absolute JES in last step, residual dependencies of JES on other features of jets are observed. This mainly comes from the fluctuations in jet particle compositions and distributions within the jet: average response is different between quark- and gluon-initiated jets; Response could be different between light and heavy flavor jets, etc.. Therefore, a global sequential calibration (GSC) method [105] is applied to further improve resolution of JES. In GSC, five observables accounting for different aspects that JES is dependent on are identified. Calibration factor is derived from MC following similar procedure as the absolute JES, but with additional dependency on these extra observables.

Residual *in situ* calibration In the last, a residual *in situ* calibration is applied to correct jets in the data only. This steps aims at correcting any difference between data and MC due to imperfect simulation. For jets up to 950 GeV and with $|\eta| < 0.8$, Z+jet and γ+jet balance is used, while multijet balance is used for high-p_{T} jet up to 2 TeV.

Latest measurement using 2015 data indicates that an uncertainty of 4.5%, 1% and 2% is achieved for p_{T} of 20 GeV, 200 GeV and 2 TeV respectively by following this calibration procedure. More details about the jet energy calibration and measurement can be found in [106, 107, 105]

5.4 Flavor Tagging

The identification of b-quark initiated jets, typically referred to as b-tagging or flavor tagging, plays an important role in ATLAS physics. In particular, as we will see soon, it is also playing a central role in both searches presented in this thesis as well. After the fragmentation of b-quarks, most of original b-quark energy ($\sim 70\%$) goes into the weakly decaying b-hadrons (about 5 GeV), whose intrinsic life-time is about 1.5×10^{-12} s. Therefore, for b-hadrons of 30 GeV, the average decay length could be about 3 mm, a quantity large enough to be measured by ATLAS high-precision tracking system. In addition to b-hadron decay, the c-hadrons out of decay of b-hadrons also have similar average lifetime, thus leading to an additional decay afterward. As a result, several b-tagging algorithms are developed by taking advantage of different aspects of the decay patterns.

All these b-tagging algorithms use the tracks reconstructed from inner detector, representing the charged particles from decays, as input to discriminate between different jet flavors. This is because only tracking system is able to provide enough precision to resolved the secondary vertices from primary vertex in hadron collider. Tracks are selected for each jet within certain p_{T}-dependent ΔR criteria. In case tracks are shared by two close-by jets, tracks are assigned to the closer jet[1]. These

[1] Although there is an option of allowing tracks to be shared

tracks would further need to pass some basic quality cuts, which depends on the b-tagging algorithm. Then three different b-tagging algorithms would be run, providing complementary information to each other:

1. Impact parameter based algorithm
2. Inclusive secondary vertex reconstruction algorithm
3. Decay chain multi-vertex reconstruction algorithm

Later, these three algorithms would be combined appropriately using *boosted decision tree* (BDT) providing the best separation between different flavors.

This section only aims to provide a basic introduction to this topic, while readers with interest can find great details in [100, 116, 117, 118]. However, it should be noticed that there might be subtle difference across references since the b-tagging algorithm is updating from time to time constantly.

Impact Parameter Based Algorithm

The IP2D and IP3D algorithm make used of the signed impact parameter significance of tracks associated to jet to discriminate between different flavors. This comes from the observation that tracks from a displaced vertex should have larger impact parameter than those coming from primary vertex, as shown in Figure 5.5. Furthermore, tracks are categorized based on a set of rules, most of which are quality requirements on hit multiplicities in inner detector. The template distribution for tracks in each category from each flavor is built using the training MC sample. Then, for all the tracks associated with a given jet, one is able to build likelihood profile for each flavor hypothesis through the product of likelihood of each track based on its template. Then the final output score is calculated from likelihood ratio between different hypothesis to be tested. The main difference between IP2D and IP3D is that IP3D uses the 2D template with correlation between transverse and longitudinal direction taken into account, while IP2D only uses transverse impact parameter. Compared to IP3D, IP2D is more robust against the effects of pile-up, as it does not take account of the longitudinal impact parameter significance, which will typically be large for tracks from pile-up jet.

As one may already notice, the underlying assumption in either IP2D or IP3D is that tracks are independent to each other. In other words, it is essentially a *naive Bayesian model*. However, this is a very crude approximation since tracks are actually correlated to each other. For example, given a track from secondary vertex, one can immediately infer that probability of other tracks from the same secondary vertex at high impact parameter region would be higher than the unconditional probability. Therefore one would expect to have better performance by taking these track-by-track correlation into account. Another important comment on IP3D/IP2D algorithm is that they are not scalable in the sense that it is hard to encode too many variables at the same time. This is due

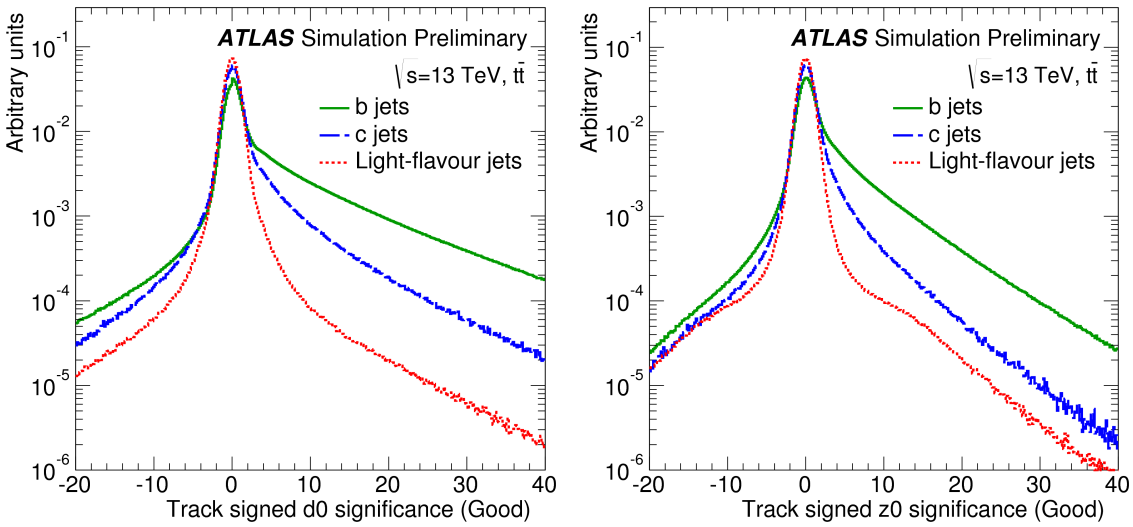


Figure 5.5: The transverse (left) and longitudinal (right) signed impact parameter significance of tracks associated with b (solid green), c (dashed blue) and *light*-flavour (dotted red) jets [116]

to the use of a template histogram. While it is not so hard to build 2D or 3D template histogram, higher dimension would become challenging both from technical side and from statistics side.

To overcome these two difficulties, a novel technique leveraging the *recurrent neural network* in natural language processing is used in ATLAS b-tagging and significant imporvement is indeed found. For more details on this readers can refer to [119].

Inclusive Secondary Vertex Reconstruction Algorithm

The secondary vertex based algorithm aims to explicitly reconstruct an inclusive displaced vertex within the jet. Tracks passing certain quality cuts would be paired up to form the so-called *two-track vertices*. These two-track vertices would be filtered at the beginning to reject those coming from decay of long-lived particles such as K_s, Λ, photon conversion or hadronic interaction with detector materials. Tracks associated to these rejected two-track vertices would also be discarded. Then an inclusive secondary vertex would be fit using survived tracks using Kalman filter in an iterative way similar to how we reconstruct primary vertex. These reconstructed displaced vertex would further be required to pass certain quality cuts. The probability of successfully finding inclusive secondary vertex within a jet as function of p_{T} and η can be found in Figure 5.6.

After inclusive secondary vertex is successfully reconstructed, various aspects of the kinematic variables such as vertex mass, decay length would be extracted from it to provide discrimination power.

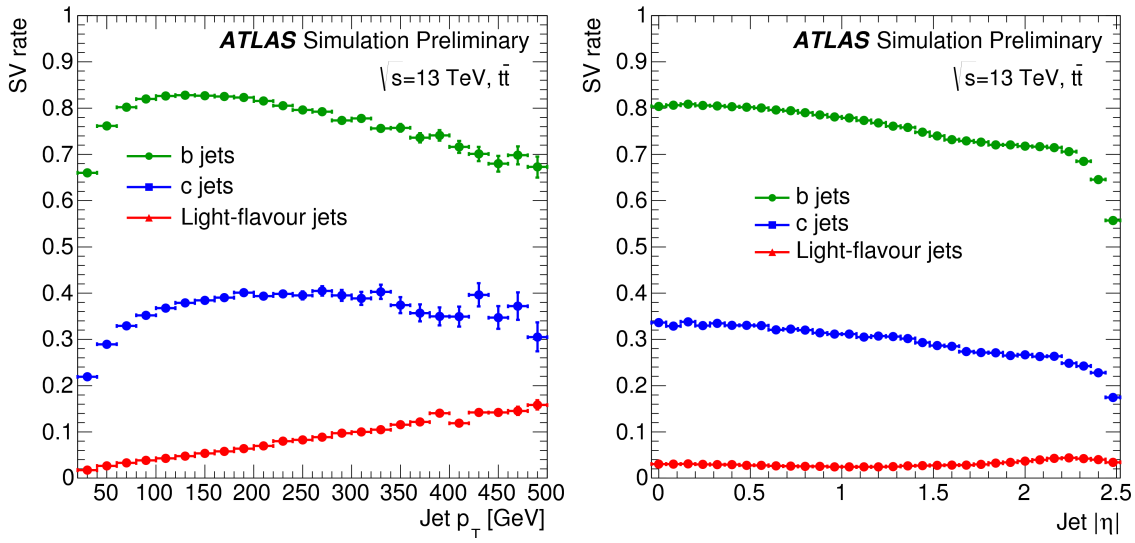


Figure 5.6: Secondary vertex reconstruction rate as function of jet p_{T} (left) and η (right) for b (green), c (blue) and *light*-flavour (red) jets. [116]

Decay Chain Multi-vertex Reconstruction Algorithm

The decay chain multi-vertex reconstruction algorithm, also called *JetFitter* in ATLAS, exploits the cascade decay structure of b-hadron and c-hadron out of it in order to reconstruct the full PV$\rightarrow b\rightarrow c$-hadron decay chain. A Kalman filter with the flight direction as system state to be estimated is used by treating the addition of tracks one by one as "state transition". More details on mathematical formalism of the JetFitter can be found in [100].

In JetFitter, vertex is a rather loose concept. Since it roughly refers to the intersection between tracks and estimated decay chain direction, a vertex could have even only one track associated to it, which is forbidden in inclusive secondary vertex reconstruction algorithm. Therefore, JetFitter typically has a much higher reconstruction efficiency. However, this comes at the cost of a higher fake rate where vertices are also built in light jets. Therefore a set of topological variables are built in JetFitter for discrimination purpose.

b-tagging Performance

After each b-tagging algorithms mentioned above have been run on input track collections independently, discriminative variables summarized from each algorithm would be combined using BDT. Kinematic properties, in particular the p_{T} and η, of jets are also included in the training in order to capture the kinematic dependency of discriminative variables. However, p_{T} and η joint distribution between signal and background jets in the training procedure is re-weighted to match each other so that these kinematic variables are not treated as discriminative variables – after all, the kinematics

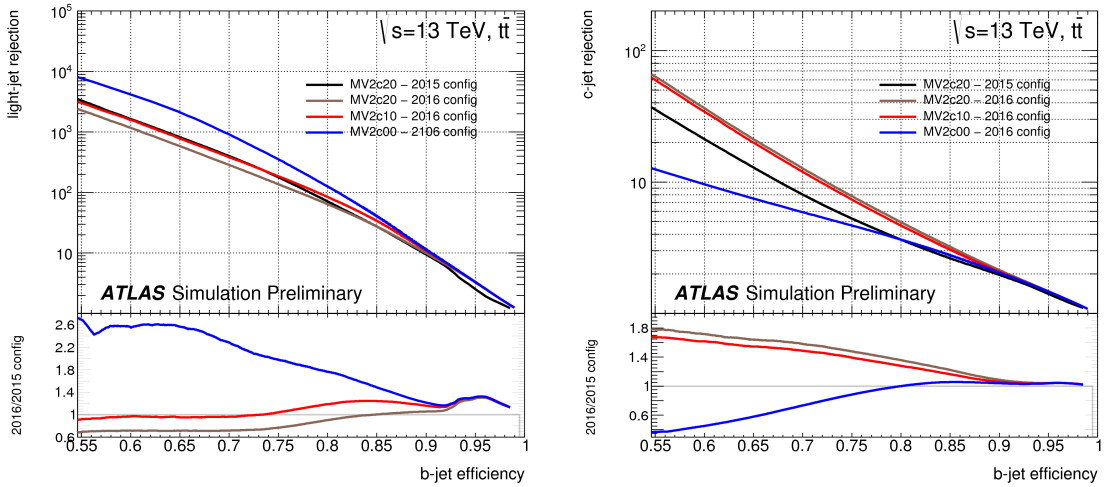


Figure 5.7: *Light*-jet rejection (left) or c-jet rejection (right) versus b-jet efficiency for the previous (2015 config) and the current configuration (2016 config) of the MV2 b-tagging algorithm evaluated on $t\bar{t}$ events. MV2c00 denotes the MV2 algorithm where no c-jet contribution was present in the training. MV2c10 (MV2c20) denote the MV2 outputs where a 7% (15%) c-jet fractions was present in the background sample (for the 2016 configuration). [117]

could strongly depend on the physics process.

Training procedure is done on $t\bar{t}$ MC samples, typically with at least millions of events. The signal jets are always the b-jets, while background is a mixture of c-jets and *light*-jets. Such mixture makes sure one can gain discrimination power between b-c, in addition to the more commonly used b-*light*. Three versions of mixture are available at ATLAS: MV2c00, MV2c10 and MV2c20. The number after character "c" represents the rounded percentage of c-jets in background sample (exact mixture percentage can vary depending on configuration). Depending on the physics processes considered in a physics analysis, user can choose the any of these three version: MV2c20 has the best discrimination power against c-jets though at the cost of less *light*-jet rejection; MV2c00 has best *light*-jet rejection but worst rejection on c-jet; MV2c10 is recommended for general purpose due to its balance between *light*-jets and c-jets. The performance of each tagger for discrimination against *light*-jet and c-jets can be found in Figure 5.7.

One important remark is that b-tagging performance does not only depend on the algorithm itself, but also relies on the underlying detector capability. The more precise one is able to reconstruct tracks near primary vertex, the better b-tagging performance one can get in general. In particular, since secondary vertex reconstruction depends on precise extrapolation of tracks to the interaction point, precision measurement close to primary vertex is much more important than the curvature measurement far away from interaction point. An example is the installation of IBL in ATLAS pixel detector during LS1. Due to the additional layer closer to interaction points, ATLAS gain a significant improvement on b-tagging performance in Run 2 with respect to one in Run 1, as shown

in Figure 5.8.

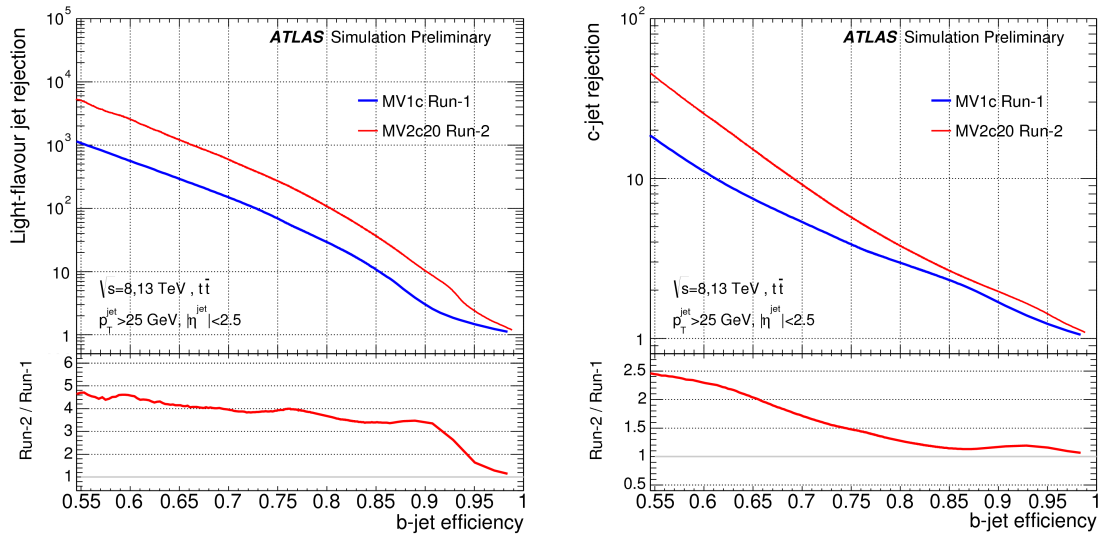


Figure 5.8: The light (left) and c-jet rejection (right) versus b-jet efficiency for the MV1c b-tagging algorithm using the Run 1 detector and reconstruction software (blue) compared to the MV2c20 b-tagging algorithm using the Run 2 setup (red). [116]

5.5 Track Jets

While only calorimeter jets are discussed in Section 5.3, the jet reconstruction algorithm is universal in that any type of inputs can be used. In ATLAS, there is another class of jets built entirely from tracks reconstructed in inner detector, called *track jet*, using the same clustering algorithm as calorimeter jets. While track jets are mainly used as proxy for jet property measurement at the beginning [120], it gains more and more attention in terms of b-tagging starting from the end of Run 1, in particular in the boosted topologies [121, 122]. In the Run 2, track jet b-tagging has already become the standard approach to resolve close-by heavy flavor components in the decay products from boosted decay of heavy resonances [123, 124]. Nevertheless, the idea of track jet b-tagging itself arises as a general alternative to the traditional calorimeter jet based b-tagging, which does not necessarily have to be in boosted topology at the beginning. In this section, an overview of the track jet b-tagging is presented, with more details on performance and optimization found in [125]. Studies of track jet calibration can be found in [126].Discussion in this section will be more focused on the general aspects of track jet b-tagging while its specific application in boosted topology in Run 2 would be shown in Chapter 6.

5.5.1 Motivation

The motivation of using track jets comes with several advantages of track jet coming by construction:

- In the traditional calorimeter jet based b-tagging, calorimeter jet four momentum is used as the seed in most flavor tagging pattern recognition algorithms. However, since all these algorithms only use information from the inner detector, they can be decoupled from calorimeter system in principle to identify b-jets. Track jet naturally provides such decoupling so that the whole flavor tagging procedure can rely only on the high precision tracking system, making both flavor tagging algorithm and their calibration free from constraints of calorimeter system resolution.

- As shown in Section 5.3, calorimeter jets calibration is a very complicated procedure for a good measurement of the hadronic activities in calorimeter system. As an independent jet collection, track jets can be optimized and calibrated specifically for b-tagging purpose, since track jets are not to be used for precision measurements of hadronic physics as calorimeter jets do.

- While calorimeter jets are sensitive to pile-up activities, track jets are intrinsically insensitive to the pile-up activity by rejecting tracks coming from pile-up vertices as input to the jet reconstruction, thanks to the excellent resolution provided by tracking system. This could be particularly important to the low-p_{T} b-hadrons that can still be present even in highly boosted environment if b-hadron decays in the direction opposite direction to boost direction. These low-p_{T} b-hadron might be otherwise lost due to the higher p_{T}-threshold imposed by calorimeter jets for pile-up rejection. Besides, resistivity of track jets against pile-up allows a smaller jet cone size than usual (0.4) which is hard for calorimeter jets due to large fake rate from pile-up interactions in the event calorimeter system resolution effect.

- Although being an independent system from calorimeter jets, track jets b-tagging can still be combined with the calorimeter jets through ghost association techniques [115] in order to fully take advantage of the full reconstruction of hadronic activities in calorimeter jets. The easy association between track jets and calorimeter jets also make the usage of track jet extremely flexible: Once a set of track jets along with its b-tagging are well defined and calibrated independently, it can be applied on any calorimeter jet collection to provide b-tagging information. This used to be a painful process in ATLAS since for every new definition of calorimeter jets (radius, clustering algorithm, etc.) one needs to go through the complex pipeline of calorimeter jet energy scale calibration and b-tagging efficiency calibration before using them in physics analysis. More details in track jet b-tagging calibration can be found in [126].

- Last, the current ATLAS b-tagging algorithm looks for a b-hadron locally around a direction

seeded by jet axis. Track jets can provide good angular resolution with respect to the b-hadron especially in dense environments. As shown in [127], an important reason for degraded b-tagging performance in dense environment is the shift of jet axis away from b-hadron as shown in Figure 5.9. Such shift has several consequences on b-tagging: If the shift is too large, track-to-jet associator would fail to find enough tracks coming from decay of b-hadron for secondary vertex reconstruction and identification; Furthermore, shift of jet axis may also lead to flipped sign of impact parameter significance or decay length, hence degrading secondary vertex finding efficiency. As we will see, track jets are able to provide better b-hadron flight direction estimation than calorimeter jets in general.

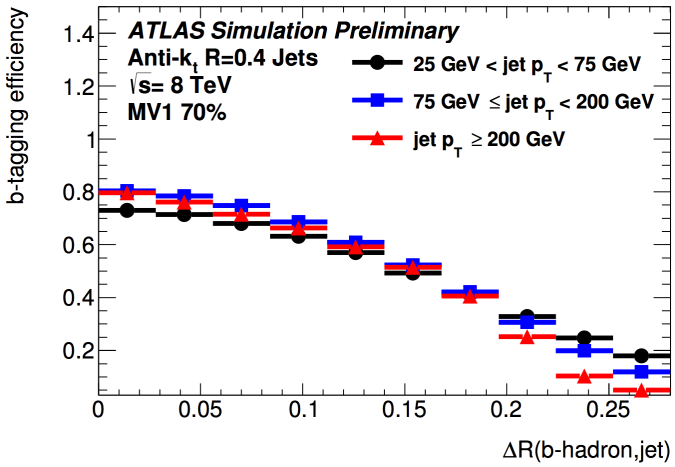


Figure 5.9: The b-tagging efficiency of MV1 tagger as function of angular distance between jet axis and b-hadron flight direction [127]

5.5.2 Track Selection

As mentioned above, one advantage of using track jets is the good alignment between jet axis and b-hadron flight direction. An optimization of track selection for track jet reconstruction was performed for Run 2 for this purpose. During optimization, the main idea is to keep as much tracks out of b-hadrons as possible, while still maintaining good rejection of tracks from pile-up vertices.

The first step is to understand difference between tracks coming from b-hadrons and pile-up. Naively, one would expect to simply take tracks from hard scatter primary vertex during reconstruction, or a tight cut with respect to hard scatter primary vertex as done in Run 1 [121]. While this simple approach can help suppress tracks from pile-up, it comes at the cost of losing some tracks from b-hadrons. This is mainly due to the displaced vertices from b-hadron decays that do not merge with primary vertices, as shown in Figure 5.10 that many tracks coming from b-hadron

are not associated to any primary vertex during reconstruction at all. Therefore, cuts on impact parameter has to be resorted to for these tracks. As suggested by Figure 5.10, secondary vertex displacement mainly happens in the transverse direction while it is still quite compatible with hard scatter primary vertex in longitudinal direction. Tracks from pile-up, on the other hand, are more uniformly spread out in longitudinal direction by definition. This observation leads a loose cut on longitudinal impact parameter for discrimination between tracks from b-hadrons and pile-up with priority on b-tracks efficiency. The fake rate of tracks from pile-up is controlled by requiring only tracks not compatible with any primary vertex can be considered for this second cut. This simple track-vertex association rule is able to greatly improve efficiency of getting tracks from b-hadron from 83.1% to 97.7% compared to the track selection used in Run 1.

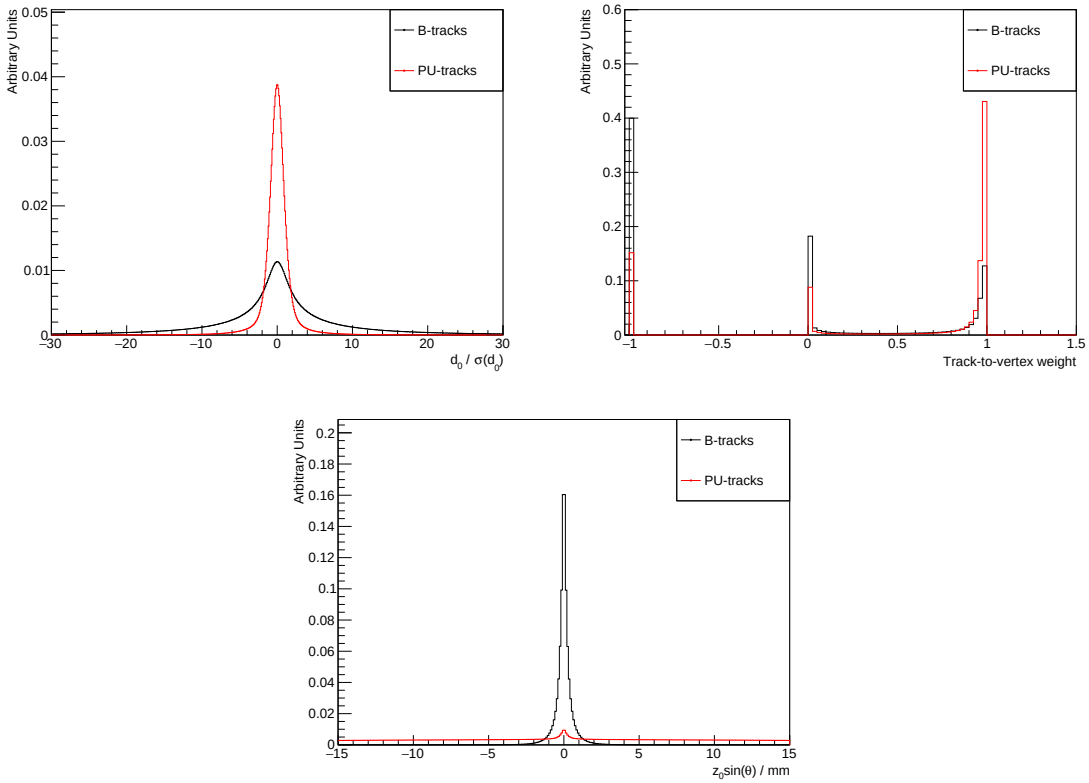


Figure 5.10: Normalized distribution of tracks from pile-up vertices and b-hadron decays in transverse impact parameter significance with respect to hard scatter primary vertex (top left), track-to-vertex association weight (top right) and longitudinal impact parameter with respect to hard scatter primary vertex (bottom). Track-to-vertex association weight shows the compatibility between track and vertex where it originates from during reconstruction, while negative value represents tracks not associated to any reconstructed primary vertices.

Combined with the *loose* criteria of track quality cuts [128], track selection for track jet reconstruction in Run 2 is as following:

- $p_{\mathrm{T}} > 0.4$ GeV and $|\eta| < 2.5$
- At least 7 hits in silicon detector (Pixel + SCT)
- No more than one hit in the Pixel detector that is shared by multiple tracks
- No more than one hole in the Pixel detector, and no more than two holes in silicon detectors
- Tight match to the hard scattering primary vertex by requiring track should be constituent of reconstructed hard scatter primary vertex. If track is not associated to any primary vertex, it should satisfy $|z_0 \sin\theta| < 3\ mm$ with respect to hard scatter primary vertex.

As a side note, the track-vertex association developed in track jet studies turns out to be a quite general way of selecting tracks from hard scatter activity. Indeed, it was later soon adapted to the new pile-up jet tagging and suppression techniques in ATLAS [129], and shows a significantly better performance for b-quark initiated jets than previous one [130].

5.5.3 Track Jet Properties

Track jets are then built by applying anti-k_t algorithm with $R = \{0.4, 0.3, 0.2\}$ on selected tracks following selection described above. Only jets in fiducial region $p_{\mathrm{T}} > 7$ GeV and $|\eta| < 2.5$ are accepted. Track jets with $p_{\mathrm{T}} < 7$ GeV are not used since they are dominated by light jets and rejection of these jets by b-tagging algorithm is low [121]. As a reference point, calorimeter jets reconstructed using anti-k_t algorithm with $R = 0.4$ are also reconstructed, followed by $p_{\mathrm{T}} > 20$ GeV, $|\eta| < 2.5$ and pile-up suppression.

The probability of reconstructing b-hadron by various collections of jets can be found in Figure 5.11. Reconstruction efficiency can reach more than 95% as p_{T} of b-hadron is above 40 GeV, below which is a sharp turn-on curve. Several reasons contribute to the efficiency drop at low p_{T}. For one thing, the p_{T} threshold would naturally lead to inefficiency below it. Furthermore, since track jets can only measure charged fraction of b-hadron decay products and the fluctuation of such fraction is very big in general, the turn-on curve is wider than a simple step function. For another, decay products from low-p_{T} b-hadron are no longer well collimated in flight direction but instead experience a spread-out on $\eta - \phi$ plane, leading to a low reconstruction efficiency, especially for small radius track jets. While the first reason can be easily addressed through a lower p_{T} threshold, the second one implies that a higher p_{T} threshold might be better for small radius track jets so that one can be more focused on well reconstructed objects instead of fragments of decay products, which tends to be identified as light jets regardless of the truth origin.

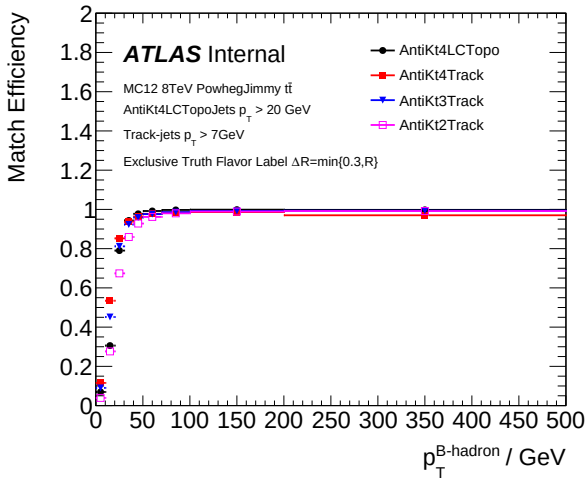


Figure 5.11: Probability of a b-hadron being associated to calorimeter jets and track jets of various radius.

As mentioned above, one feature of track jets is the better angular alignment between jet axis and b-hadron flight direction, as shown in Figure 5.12. By comparing between calorimeter jets and track jets of same radius parameter, improvement in track jets can be observed across full p_{T} range, with effect more evident for boosted b-hadrons. The improvement mainly comes from usage of tracks, which can provide a better spacial resolution on particle direction than calorimeter system. As cone size of track jets further shrinks, angular resolution improves naturally. This is particular important for high p_{T} b-hadron case, where smaller radius track jets have the same reconstruction efficiency as larger radius track jets.

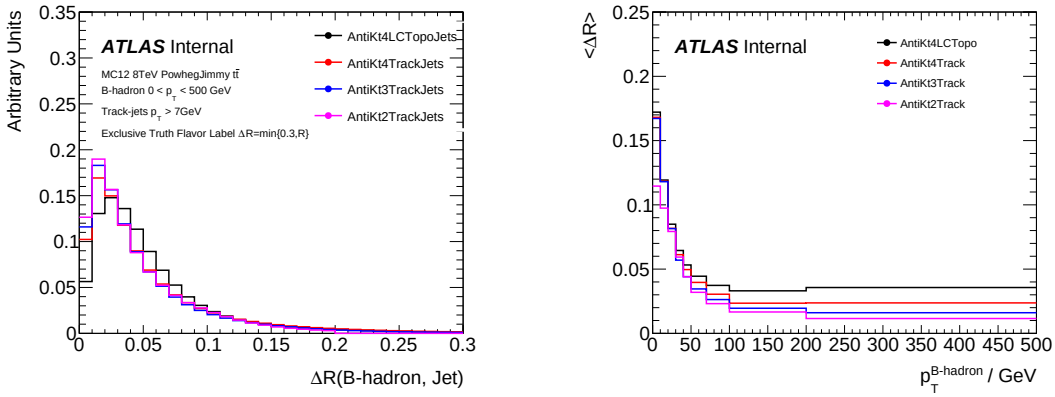


Figure 5.12: (Left) Distribution of angular separation between jet axis and b-hadron flight direction for various jet collections. (Right) Dependency of mean of angular separation on b-hadron p_{T}

5.5.4 Track Jet based *b*-Tagging

After track jets are reconstructed and selected, b-tagging algorithms can be applied on them using tracks found in a cone of p_{T}-dependent size around track jet axis with. Track selection for b-tagging is independent of the one for track jet reconstruction since they are optimized for each b-tagging algorithm.

An inclusive b-tagging performance of track jets (as well as calorimeter jet as reference) can be found in the left plot of Figure 5.13. While track jets with radius of 0.3 and 0.4 have similar tagging performance as calorimeter jets, track jets with radius of 0.2 are significantly worse than others. By comparing the p_{T} dependency of tagging efficiency, as shown in Figure 5.14, track jets with radius 0.2 and 0.3 are very similar to each other, except for *light*-jet efficiency at $p_{\mathrm{T}} < 20$ GeV where track jet with radius 0.2 is much worse. This is mainly due to the bad reconstruction of b-hadron at such low p_{T}, where it is hard to capture all decay particles with a radius of only 0.2. As a result, more than one track jets of radius 0.2 can be formed for one b-hadron, each of which takes a fraction of tracks. While the track jet closest to b-hadron would be labeled as b-jet, others around it will be mislabeled as *light*-jet. These fake *light*-jets could still get a high flavor tagging weight due to the presence of displaced tracks around them from b-hadron, hence leading to larger acceptance rate as observed. Therefore, it is decided to increase p_{T} threshold of track jets with radius 0.2 to 10 GeV from 7 GeV in Run 2. The overall b-tagging performance for anti-k_t $R = 0.2$ track jets is largely improved as shown on right plot of Figure 5.13.

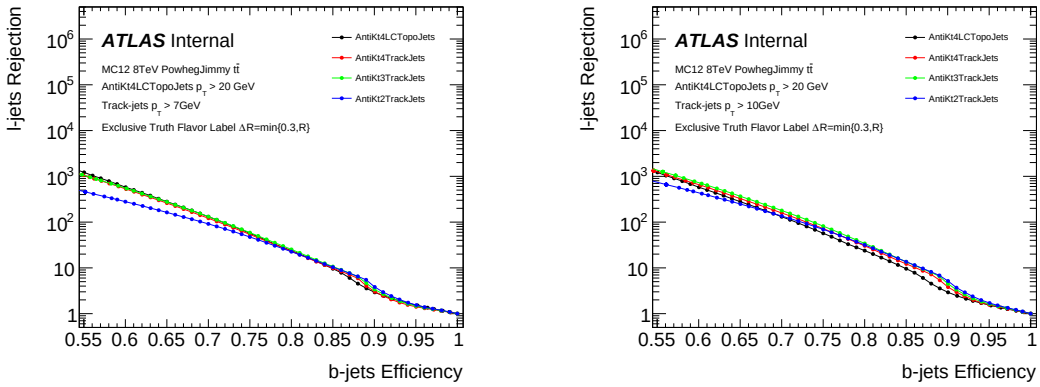


Figure 5.13: (Left) b-jet identification efficiency as function of *light*-jet rejection for various jet collection in inclusive p_{T} range with track jet p_{T} threshold of 7 GeV (left) and 10 GeV(right)

In practice, track jets are seldom used alone for object reconstruction, since it is only able to measure the charged fraction of a jet. Instead, it is usually used along with the calorimeter jets: calorimeter jets are in charge of jet reconstruction (four momentum etc.) while track jets are in charge of providing b-tagging information. Therefore, one needs to first match track jets to calorimeter jets as first step for b-tagging. As shown in Figure 5.15. The matching efficiency reaches $> 95\%$ when

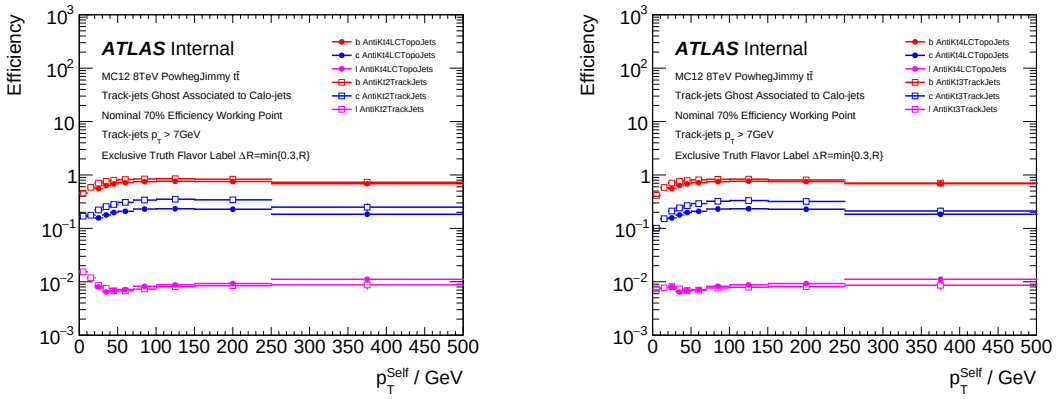


Figure 5.14: b-tagging efficiencies for b, c and *light* components as function of jet p_{T} for anti-k_t track jet with radius parameter 0.2 (left) and 0.3 (right). Efficiencies are evaluated at a working point such that overall b-jet identification efficiency is 70%.

$p_{\mathrm{T}} > 40$GeV. Inefficiency mainly comes from the charge fraction fluctuation and p_{T} threshold on track jets as shown on Figure 5.16. Furthermore, as track jet radius shrinks, p_{T} allocated on each track jet would be naturally smaller due to less constituent, leading to a worse matching efficiency compared with others of larger radius with same p_{T} threshold.

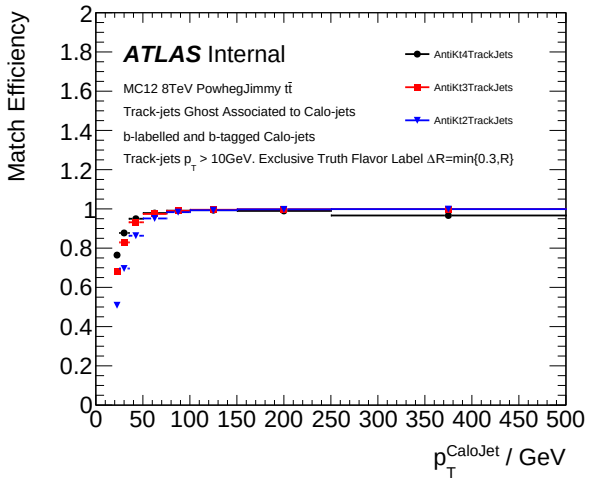


Figure 5.15: Probability of at least one track jets matched to calorimeter jet as function of p_{T} for various track jet collections. The matching is done through ghost association technique.

While matching inefficiency would hurt the b-jet identification, it is actually beneficial for *light*-jet rejection since un-matched track jets are predominantly low p_{T} *light*-jets. The overall performance can therefore be better if an appropriately tight p_{T} threshold is used to reject those low p_{T} backgrounds without much hurt on efficiency, as shown in Figure 5.17, where the p_{T} threshold is chosen

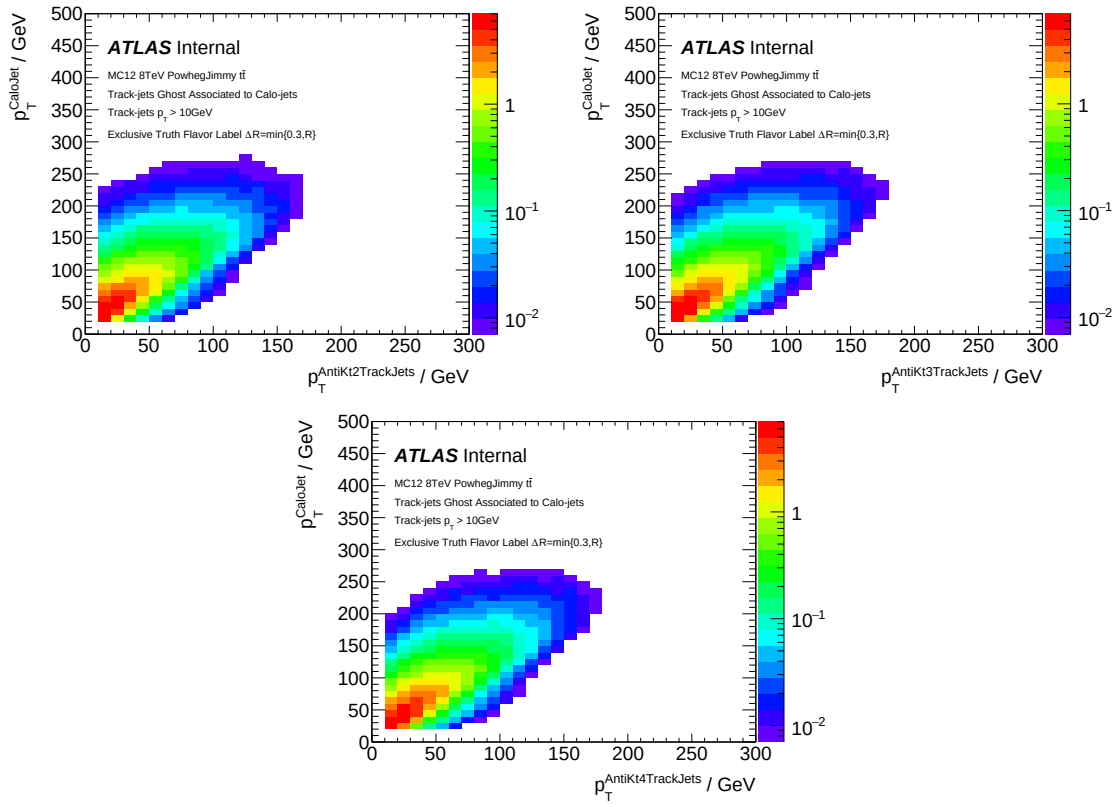


Figure 5.16: p_{T} correlation between b-labelled track jets of various radius (top left 0.2, top right 0.3 and bottom 0.4) and calorimeter jets.

to be 10 GeV. For all track jet collections, a *light*-jet rejection higher than calorimeter jets is achieved with a working point chosen such that b-jet efficiency is overall 70%. Such improvement is a combined effect of track selection, p_{T} threshold as well as many other detailed factors [125]. Furthermore, it can be noticed that there is no single choice of radius that can reach optimal performance across whole p_{T} range: $R = 0.3$ is clearly preferred when $p_{\mathrm{T}} < 100$GeV, while $R = 0.2$ has higher rejection power when $p_{\mathrm{T}} > 150$GeV. Such observation is consistent with the intuition that jets are more and more collimated in the boosted region.

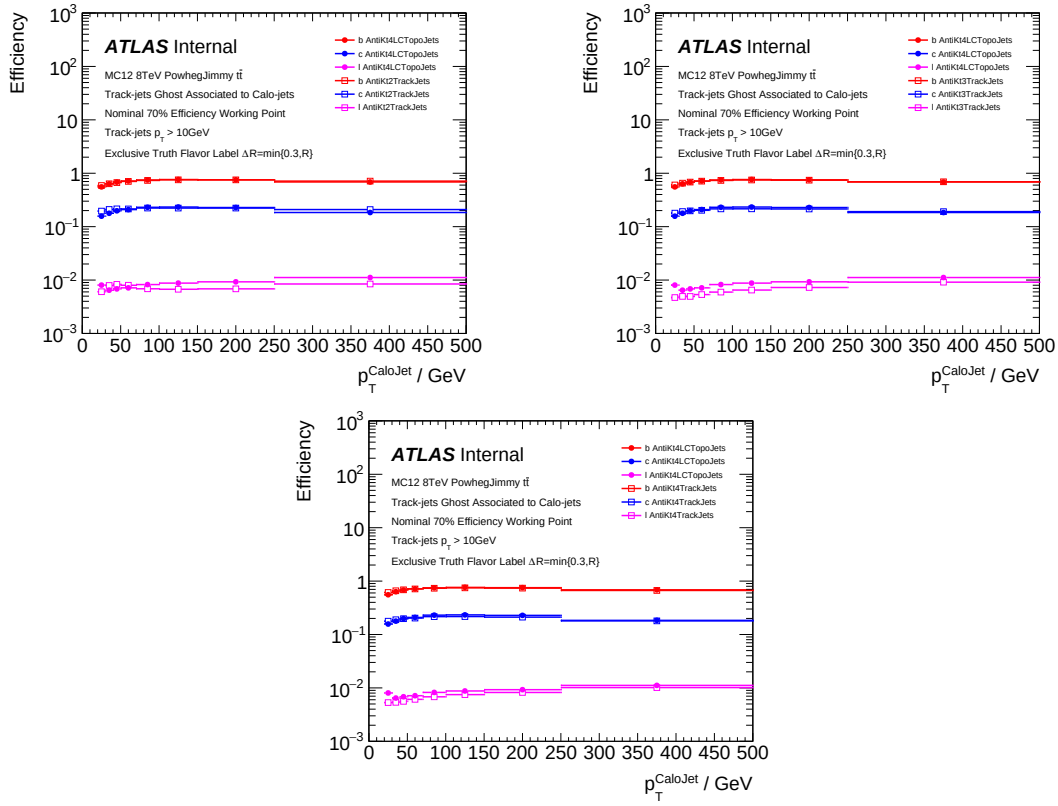


Figure 5.17: b-tagging efficiencies for b, c and *light* components as function of matched calorimeter jet p_{T} for anti-k_t track jet with radius parameter 0.2 (left), 0.3 (right) and 0.4 (bottom). Matching efficiency between track jets and calorimeter jets are included. Efficiencies are evaluated at a working point such that overall b-jet identification efficiency is 70%.

Chapter 6

Boosted Bosons Identification

In the Standard Model, hadronic decay mode has the largest branching ratio for vector bosons and Higgs boson: $W \to qq$ is 67.4%, $Z \to qq$ is 69.9% and $H \to b\bar{b}$ is 57.7%. Nevertheless, these hadronic decay mode were often seen as insensitive since they can be easily buried in the predominant multijet backgrounds. However, this situation could change when it comes to the boosted regime, where cross-section for W/Z/H production typically falls less rapidly than multijet background as p_{T} goes up. Fortunately, this is exactly the case in LHC era with unprecedented high collision energy.

In this chapter, we will present the techniques used for boosted hadronically decaying boson identification, which is the key part of both searches in this thesis. Traditionally, vector bosons and Higgs boson were reconstructed by first reconstructing each individual decay product out of bosons first. However, as p_{T} of the heavy bosons gets so large that decay products get highly collimated, new reconstruction technique is needed. As a result, the so-called *boosted physics* [3, 4, 5, 6] gains more and more attention over past ten years where people begin to study how to reconstruct and identify the boosted bosons in such high p_{T} case in terms of both phenomenology and experiment. In particular, it is further realized that these techniques enables powerful discrimination of all hadronic decay mode of W/Z/H against q/g-initiated jets, which is predominant in QCD backgrounds. This has a remarkable consequence that it can significantly enhance the sensitivity of searches in boosted phase space, as we will see in Chapter 7 and 8.

This chapter is organized as following. A brief introduction to the boosted topology and jet reconstruction for boosted bosons can be found in Section 6.1; Boosted W/Z tagging is then discussed in Section 6.2; Then a detailed discussion on boosted $H \to b\bar{b}$ identification, which provides a key signature to the searches in this thesis, can be found in Section 6.3.

6.1 Introduction

6.1.1 Jet Grooming

For massive particles produced with high p_{T}, angular separation of decay products is approximately $\Delta R \sim 2M/p_{\mathrm{T}}$, where M and p_{T} are the mass and transverse momentum of boosted massive parent particle, as shown in Figure 6.1. As a result, large radius is typically used for boosted boson reconstruction so that all decay products can be contained inside one single jet. For example, for $H \to b\bar{b}$ jets, a jet radius of 1.0 is needed for Higgs of $p_{\mathrm{T}} > 250$ GeV.

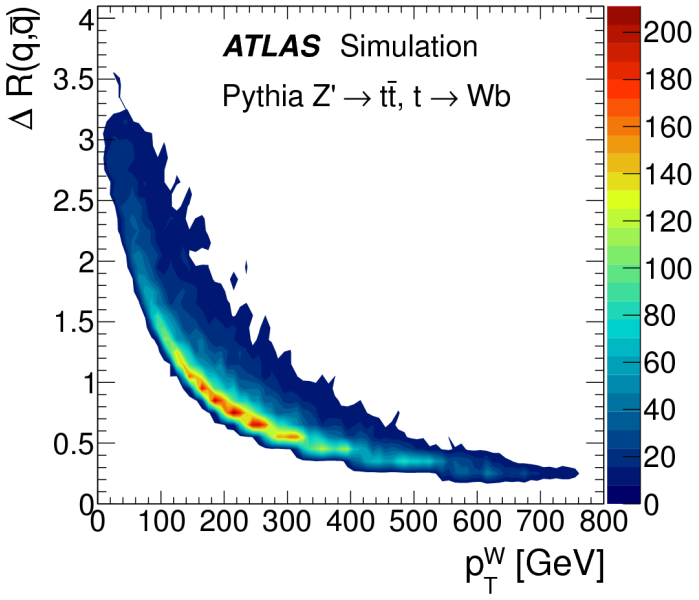


Figure 6.1: The angular distance between light quark and anti-quark decayed from W boson. Distributions are at the generator level, without including effects due to initial and final-state radiation or the underlying event. [131]

However, simply a jet reconstruction as described in Section 5.3 but with larger radius is not enough. When jet radius gets much larger, reconstructed jet also get sensitive to various soft components accompanying the jet production in LHC. This includes contributions from pile-up acitivity, underlying events and soft component of the radiations. Therefore, an additional step called *jet grooming* is applied to remove these soft parts so that a real hard substructure within jets from massive particle decays can be revealled. There are three major categories of jet grooming algorithms as described below [132]:

- **Trimming** [133]: The trimming algorithm takes advantage of the fact that contamination from pil-up, multiple parton interactions (MPI) and initial state radiation (ISR) in reconstructed jet is usually much softer than the partons from hard-scattering or final state radiation (FSR)

process. large-R jets are first built with C/A or anti-k_t algorithm. Then small subjets are built by reconstructing constituents of un-groomed large-R jet with k_t algorithm with a smaller radius parameter $R = R_{sub}$. Then subjets are removed if they carry less than a fraction f_{cut} of the original un-groomed large-R jet p_{T}.

- **Pruning** [134]: The pruning algorithm is similar to trimming in that it also removes constituents with small relative p_{T}, but additionally utilizes a wide-angle radiation veto. large-R jets are first built with C/A or anti-k_t algorithm. Constituents of un-groomed large-R jet is then re-clustered with C/A algorithm with two parameters: R_{cut} and Z_{cut}. In each pairwise clustering step, secondary constituent is discarded if it is wide-angled or soft: Definition of being wide-angled is that $\Delta R_{12} > R_{cut} \times 2M/p_{\mathrm{T}}$; Definition of being soft is that $f_2 < Z_{cut}$ where f_2 is the p_{T} fraction of softer constituent with respect to p_{T} of the pair.

- **Split-filtering** [135]: This was also historically called *BDRS* algorithm which is named after the authors proposing this method. It seeks to isolate concentrations of energy within a jet by identifying relatively symmetric subjets, each with a significantly smaller mass than that of their sum (i.e. *mass-drop*). large-R jets are first built with C/A algorithm. This algorithm has two stages, the splitting and filtering as name suggests. Splitting stage is trying to find the hard two-prong splitting substructure from massive parent particle. In this stage, C/A jets are de-clustered by reversing the C/A clustering procedure which can be thought of as splitting jet into two pieces. In each step of de-clustering, if the requirements on mass-drop $\mu_{12} < \mu_{\max}$ and momentum balance $\sqrt{y_{12}} > \sqrt{y_{\min}}$ are met then such splitting is accepted as the desired hard splitting so that one can proceed to filtering step. Otherwise, de-clustering procedure continues with the highest mass piece. The momentum balance is defined as:

$$\sqrt{y_{12}} = \frac{\min(p_{T1}, p_{T2})}{m_{12}} \Delta R_{12} \tag{6.1}$$

  and mass-drop is defined as

$$\mu_{12} = \frac{\max(m_1, m_2)}{m_{12}} \tag{6.2}$$

  where m_{12} is the invariant mass of two pieces. The filtering stage aims at removing soft radiations that is irrelevant to the hard splitting process. In filtering stage, constituents of surviving jet are reclsutered with subjet size of $R_{sub} = \min(0.3, \Delta R_{12})$ where ΔR_{12} is taken from splitting stage. Only three hardest subjets would be kept while all other subjets would be discarded.

Studies show that all these jet grooming algorithms are very effective in removing irrelevant soft components inside the large-R jet. Jets after grooming is able to better represent the hard splitting processing from heavy particle decays. As illustrated in Figure 6.2, jet after grooming is able to

reconstruct Z boson mass without bias and better resolution, and thus provide better discrimination against the multijet background.

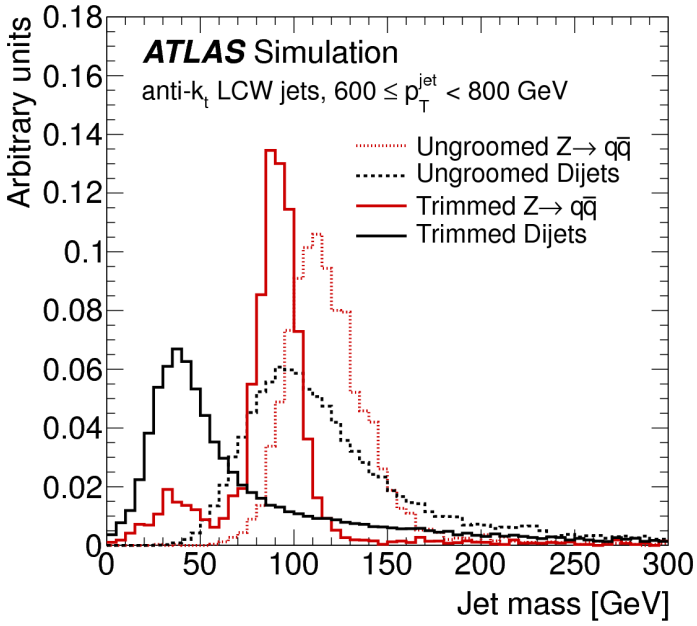


Figure 6.2: Leading p_{T} jet mass for simulated Herwig+Jimmy $Z \to qq$ signal events (red) compared to Powheg+Pythia dijet background event (black) for jets in the range of $600 < p_{\mathrm{T}} < 800$ GeV. The dotted lines show the ungroomed jet distribution wheres the solid lines shows the trimmed jet distribution with parameter $f_{cut} = 0.05$ and $R_{sub} = 0.3$. All distributions are normalized to unity. [131]

Due to similar performances, people can use different algorithms / parameters during large-R jet reconstruction and grooming, as long as the one being adopted is optimized for their own purpose. In ATLAS, large-R jet radius is chosen to be $R = 1.0$ and trimming algorithm is used with $R_{sub} = 0.2$ and $f_{cut} = 5\%$ in Run 2. Such configuration is found to be optimal among a wide range of configuration scans for W-jet in terms of providing best multijet background rejection and least sensitive to pile-up effect [132].

6.1.2 Jet Substructure Variables

Jet substructure variables are a set of jet properties for uncovering hard substructure within jets. There are too many different jet substructure variables that it is impractical to enumerate all of them. However, these jet substructure techniques can be roughly categorized as following [132]

- **Jet Shapes**: This uses the relative position and momentum of jet constituents with respect to each other without defining subjets. This includes a broad list of variables, most of which

are actually used in ths boosted boson taggers in the work of this thesis: jet mass, energy correlation ratios $C_2^{(\beta)}$ [136] and $D_2^{(\beta)}$ [137, 138], planar flow [139] etc.

- **Splitting Scales**: This uses the clustering history of jet to define substructures. This includes, for instances, $\sqrt{d_{12}}$ [140], momentum balance and mass-drop as defined above.
- **Subjettiness** [141, 142]: This forces the constituents into substructure templates to see if they fit with the hypothesis of n-subjets. Examples are 2-subjettiness τ_2, τ_2^{wta}, corresponding ratios τ_{21}, τ_{21}^{wta}, their counterpart for 3-subjettiness, and dipolarity [143].
- **Centre-of-mass Jet Shapes**: This transforms constituents and then use them with respect to the jet axis. Examples are thrust, sphericity and aplanarity, which have been used in previous ATLAS measurement [144].
- **Quantum-jet Variables**: This is mainly the "Q-jets", which uses a non-deterministic approach to jet reconstruction [145, 146].

In particular, the $D_2^{(\beta)}$ variable which would be ultimately used in the analysis, is defined as below [132]. The 1-point, 2-point and 3-point energy correlation functions for a jet J are given by:

$$\begin{aligned} E_{CF0}(\beta) &= 1 \\ E_{CF1}(\beta) &= \sum_{i \in J} p_{T_i} \\ E_{CF2}(\beta) &= \sum_{i<j \in J} p_{T_i} p_{T_j} (\Delta R_{ij})^{\beta} \\ E_{CF3}(\beta) &= \sum_{i<j<k \in J} p_{T_i} p_{T_j} p_{T_k} (\Delta R_{ij} \Delta R_{ik} \Delta R_{jk})^{\beta} \end{aligned} \tag{6.3}$$

where parameter β is used to give weights on angular separation between jet constituents. Intuitively, 1-point correlation function is approximately the jet p_{T}, while 2-poitn correlation function is roughly the mass of a particle undergoing two-body decay. These can be combined in an appropriate way:

$$\begin{aligned} e_2^{(\beta)} &= \frac{E_{CF2}(\beta)}{E_{CF1}(\beta)^2} \\ e_3^{(\beta)} &= \frac{E_{CF3}(\beta)}{E_{CF1}(\beta)^3} \end{aligned} \tag{6.4}$$

These ratios can be used to generate dimensionless variable $C_2^{(\beta)}$ or a modified version $D_2^{(\beta)}$ that have been shown in particle-level MC to be particularly useful in identifying two-body structures

within jets:

$$C_2^{(\beta)} = \frac{e_3^{(\beta)}}{(e_2^{(\beta)})^2}$$
$$D_2^{(\beta)} = \frac{e_3^{(\beta)}}{(e_2^{(\beta)})^3} \tag{6.5}$$

Value of $\beta = 1$ are used in ATLAS W/Z/H tagger as will be described below.

6.2 Boosted W/Z Tagging

With all the tools available as described in Section 6.1, it becomes fairly straightforward to do the vector boson (W/Z) tagging, which is basically cutting on jet mass and jet substructure vairables. Furthermore, extensive studies have been done in ATLAS to understand the performance of each jet grooming algorithm and each jet substructure variables, as well as the optimized combination between grooming algorithm and jet substructure variables, as found in [132, 147]. These studies show that the optimial combination for ATLAS is jet trimming with $R_{sub} = 0.2$ and $f_{cut} = 5\%$ along with use of $D_2^{(\beta=1)}$ substructure variable, due to its good performance in terms of both multijet background rejection and pile-up dependency [147].

Background rejection as function of W-jet efficiency in different p_{T} bins can be found in Figure 6.3. For final efficiency of 50% (25%), a rejection of $30 \sim 50$ (~ 200) is achievable. Furthermore, as one may notice the performance is p_{T} dependent, not just in substructure, but in the jet mass as well due to the p_{T}-dependency of detector resolution. Therefore, A p_{T}-dependent cut on both mass window and substructure variables are applied ensuring the final tagging efficiency is flat at some fixed value: "Medium" working point is defined for 50% flat efficiency and "Tight" working point is defined for 25% flat efficiency. For these pre-defined working point, multijet rejection power as function of p_{T} for both W and Z can be found in Figure 6.4.

6.3 Boosted $H \to b\bar{b}$ Identification

For $H \to b\bar{b}$ jet, conclusion in terms of jet grooming and substructure variables from W/Z-tagging studies can be applied directly. However, the unique signature from double close-by b-hadrons inside large-R jet provides an additional extremely powerful handle to this phenomena. In particular, the track jet b-tagging techniques as introduced in Section 5.5 plays a central role in the $H \to b\bar{b}$ identification. The idea of using small radius track jet b-tagging was first discussed during Run 1 [121] and is further developed and optimized at Run 2 [123, 124]. Due to its excellent rejection against the multijet backgrounds, this $H \to b\bar{b}$ tagger has not only been used in the two searches as

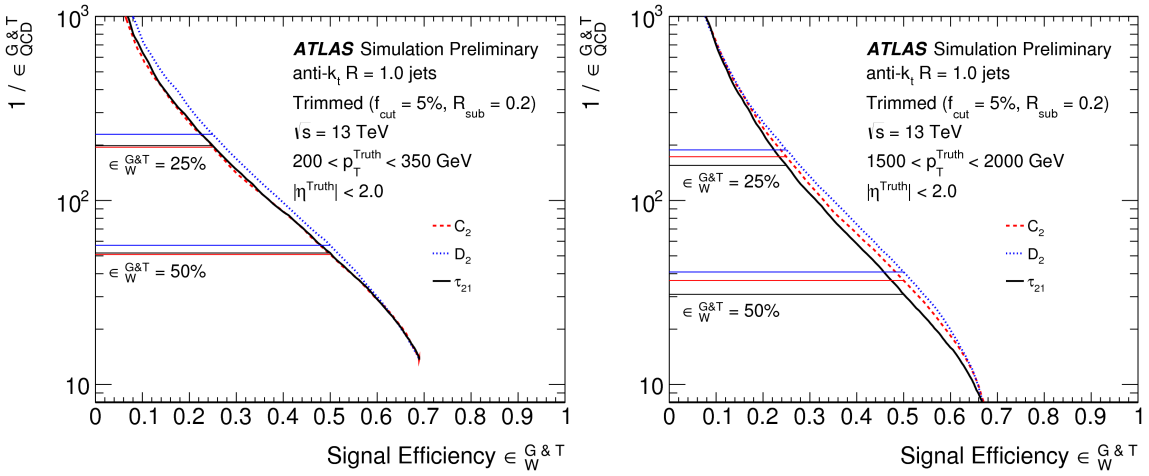


Figure 6.3: W-jet efficiency versus multijet background rejection curve for the leading reconstructed jet for various substructure variables. Events are categorized in the leading ungroomed C/A truth jet with $200 < p_{\mathrm{T}}^{Truth} < 350$ GeV (left) and $1500 < p_{\mathrm{T}}^{Truth} < 2000$ GeV. The "Medium" (50%) and "Tight" (25%) signal efficiency working points are indicated. [147]

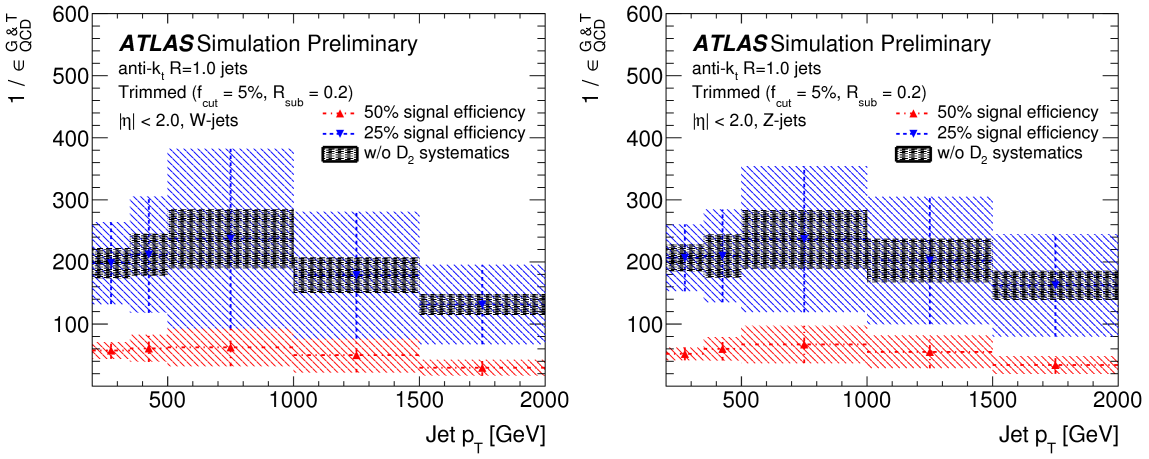


Figure 6.4: Multijet rejection for W-jet (left) and Z-jet (right) as function of p_{T} for "Medium" and "Tight" flat efficiency working point. [147]

presented in this thesis, but also in various boost physics searches such as mono-Higgs search [148] and leptonic VH searches [149]. This section adapts from [123] but with more focus on the tagging strategy and its performance in MC. There is also a follow-up studies in ATLAS [124] which is following exactly same strategy as [123] but using latest performance recommendations. Studies validating $H \to b\bar{b}$ identification techniques using data enriched of $g \to b\bar{b}$ can also be found in [124].

6.3.1 Higgs Candidate Jet

The first step in identifying boosted Higgs boson is the large-R jet reconstruction. Following W/Z-tagging, Higgs candidate jet is reconstructed using anti-k_t algorithm with $R = 1.0$ with topological clusters calibrated using local cluster weight (LCW) method as inputs. Jets are further trimmed using k_t subjets with $R_{sub} = 0.2$ and $f_{cut} = 0.05$. After the jet grooming procedure, jet energy and mass are calibrated using particle-level correction factors derived from simulation [147]. Only jets with $p_{\mathrm{T}} > 250$ GeV, $|\eta| < 2.0$ and mass (after calibration) above 50 GeV are considered. The distribution of large-R jet p_{T} can be found in the left plot of Figure 6.5. As expected, the p_{T} distribution for jets in higher mass RSG samples tend to be harder than the background samples, suggesting a better S/B in the boosted phase space as mentioned earlier.

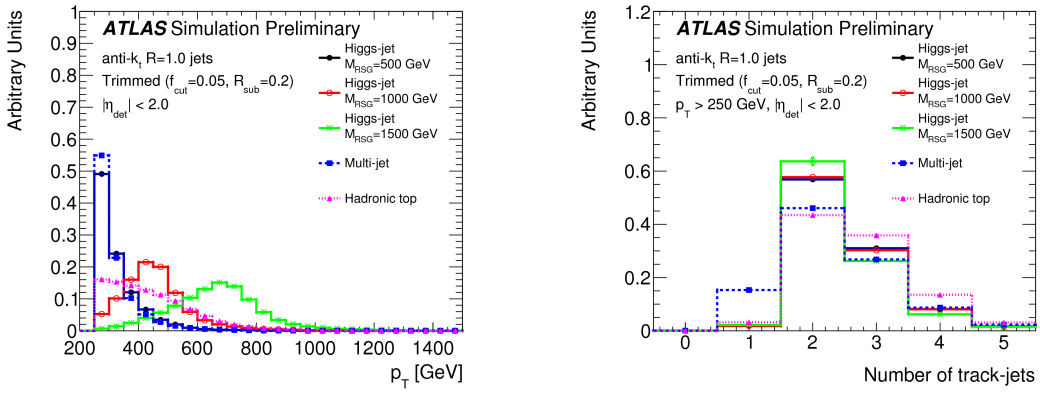


Figure 6.5: Distribution of p_{T} (left) and number of associated $R = 0.2$ track jets (right) of large-R jet passing basic kinematic cuts in multijet, hadronic top and RSG Higgs-jet signal samples for three resonance masses of 500, 1000 and 1500 GeV. [123]

6.3.2 Small Radius Track Jet b-Tagging

The next thing would be b-tagging. Different from the usual case as discussed in Section 5.4, we are having two close-by b-hadrons inside a single large-R jet. Therefore, a direct application of b-tagging as described in Section 5.4 is not feasible here, mainly because most (2 out of 3) underlying displaced vertex pattern recognition algorithms in b-tagging make an explicit assumption that there is only

one b-hadron inside each jet; Furthermore, most of these algorithms assume the flight direction of b-hadron can be well estimated by jet axis. Apparently, in boosted $H \to b\bar{b}$ case, both assumptions break. Instead, one should try to reconstruct each b-hadron first and then apply b-tagging on each of them.

This motivates the use of small radius track jet b-tagging as introduced in Section 5.5. As shown in Figure 6.6, in the RSG of mass 1500 GeV samples, only about 40% of the events have two b-labeled $R = 0.4$ track jets associated to the leading large-R jet, indicating that both b-hadrons are contained inside one $R = 0.4$ jet for a majority of the events. Decreasing the track jet distance parameter from $R = 0.4$ to $R = 0.3$ drastically increases the number of resolvable truth b-labeled jets to around 80%. Similarly, in the RSG of mass 2000 GeV samples, the effects of merging can be seen in both the $R = 0.4$ and $R = 0.3$ jets, while the $R = 0.2$ track jets are still able to resolve two truth b-labeled jets for around 80% of events. Figure 6.6 and studies in Section 5.5 also suggests the advantage of using small radius track jets over calorimeter subjets of same radius. Therefore, $R = 0.2$ track jet is adopted in Run 2 to resolve close-by b-hadron inside large-R jet[1]. The number of $R = 0.2$ track jets ghost associated to large-R jet in multijet, hadronic top and RSG signal samples can be found in the right plot of Figure 6.5: In signal (and hadronic top), at least 2 track jets are found in most cases due to the heavy particle decay; In the multijet background, on the other hand, a non-negligible fraction of events has only 1 track jets. This suggests small radius track jets are also able to probe the substructure properties of heavy particle decay.

$R = 0.2$ track jets are first built by running anti-k_t algorithms on reconstructed tracks passing certain criteria as discussed in Section 5.5.2. Only track jets with $p_{\mathrm{T}} > 10$ GeV and $|\eta| < 2.5$ are used, as discussed in Section 5.5.4. Track jets are also required to have at least 2 tracks in order to avoid standalone leptons. The b-tagging for large-R jets are therefore performed by b-tagging of track jets which would be ghost associated to the large-R jets. Several different ways to impose b-tagging requirements are examined:

- **Double *b*-tagging**: both two leading p_{T} track jets must pass the same b-tagging working point.
- **Single *b*-tagging**: only the leading p_{T} track jet must pass the b-tagging working point.
- **Asymmetric (Asymm.) *b*-tagging**: Of the two leading p_{T} track jets, the track jet with largest b-tagging weight must pass some fixed tight b-tagging working point, while the b-tagging requirement on sub-leading track jets is varied.

One might notice that only leading and sub-leading track jets are considered in the b-tagging here. Alternatively, one could also sort track jets by b-tagging weights, which would also provide good b-tagging performance, depending on kinematics. However, sorting by b-tagging weights means

[1] At the end of Run 1, $R = 0.3$ was adopted mainly because the calibration for $R = 0.2$ track jets was not ready then

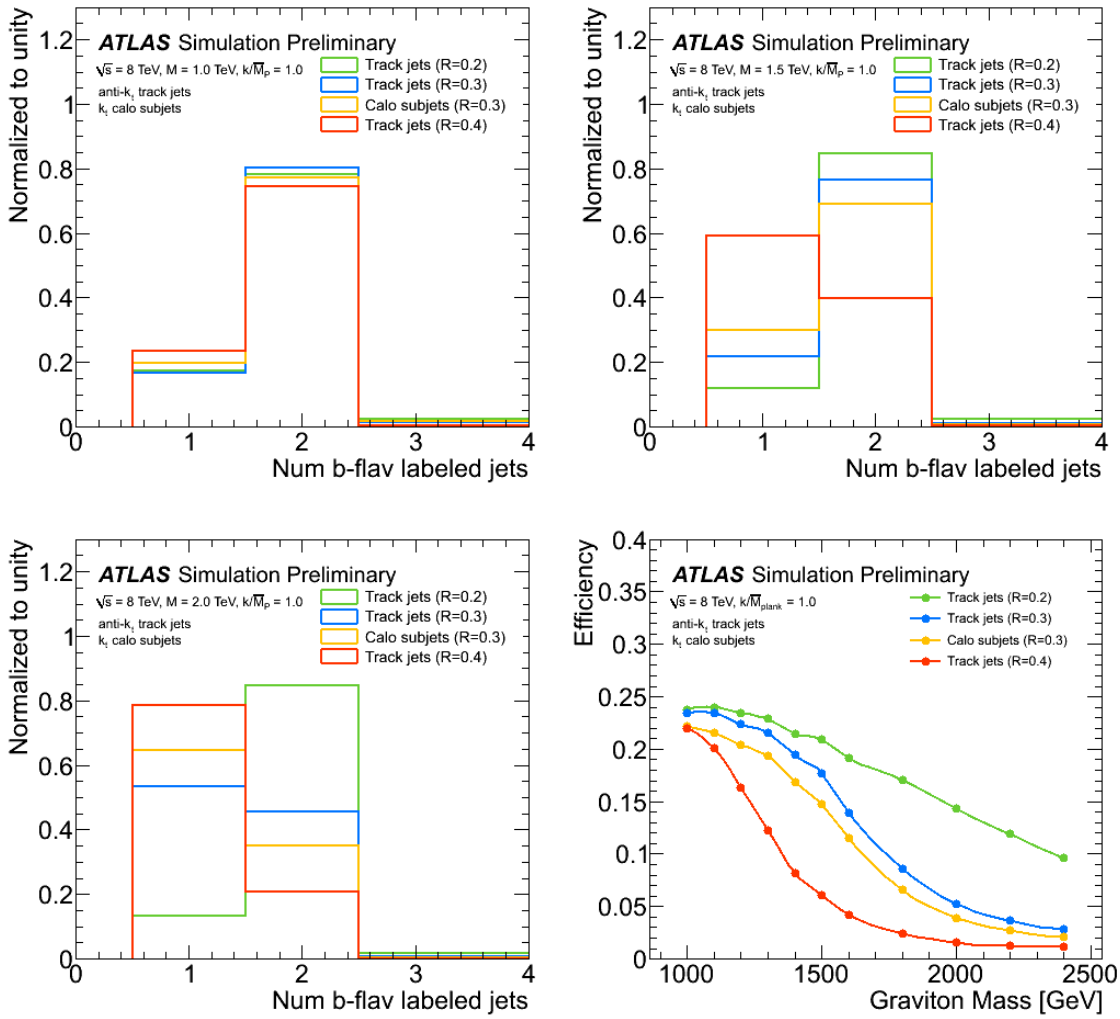


Figure 6.6: Number of truth b-flavor labeled subjets associated to the leading large-R jet in an RSG sample with mass of 1000 GeV (top left), 1500 GeV (top right) and 2000 GeV (bottom left). Efficiency to find two b-tagged track jets / subjets in both large-R jets for RSG mass points are also shown in the bottom right. [121]

one needs to check *all* the associated track jets, and thus taking their b-tagging scale factor (and uncertainties) into account. On the other hand, only tagging the two leading track jets can simplify the picture a lot since only those being considered needs to be applied scale factors. Therefore, once scale factor and its systematics are taken into account, the difference between these two schemes would be more smeared out.

The Higgs-jet efficiency versus the inclusive multijet rejection can be found in left plot of Figure 6.7, where the performance of double b-tagging, single b-tagging, and asymmetric b-tagging is shown. None of the curves reach a Higgs-jet efficiency of 100% due to the imperfect efficiency to reconstruct the track jets needed for b-tagging and, in the case of asymmetric b-tagging, due also to the 70% b-tagging working point requirement on one of the track jets.

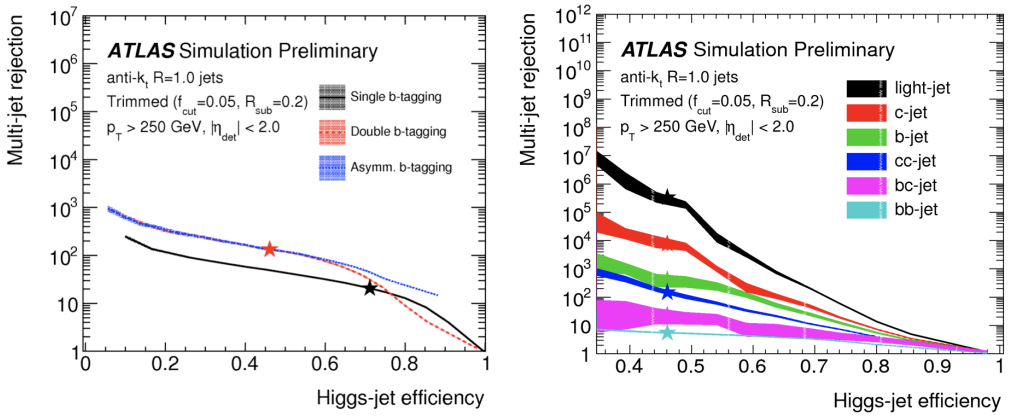


Figure 6.7: (left) The rejection of inclusive multijets versus Higgs-jet efficiency using all large-R jets with $p_{\mathrm{T}} > 250$ GeV for (single / double / asymmetric) b-tagging requirements. (Right) Multijet rejection versus Higgs-jet efficiency using all large-R jets with $p_{\mathrm{T}} > 250$ GeV, broken down by multijet flavor composition, using double b-tagging. The stars correspond to a 70% b-tagging WP. The bands represent the statistical uncertainties. None of the curves reach a Higgs-jet efficiency of 100% due to the imperfect efficiency to reconstruct the track jets needed for b-tagging and in the case of asymmetric b-tagging the 70% b-tagging working point requirement on one of the track jets. [123]

For high Higgs-jet efficiencies, above $\sim 80\%$, the single b-tagging approach tends to have a better multijet rejection than the double b-tagging, while for lower Higgs-jet efficiency the double b-tagging approach provides a significantly higher multijet rejection. Finally, the asymmetric b-tagging option is seen to capture much of the benefits of double b-tagging in the low Higgs-jet efficiency regime, while being significantly better than both single and double b-tagging in the high Higgs-jet efficiency regime. Furthermore, this performance features are similar across various p_{T} bins.

The multijet sample can be broken down by the number of b- and c- hadrons within the large-R jet in order to understand the performance for the different categories. Right plot of Figure 6.7 shows the multijet rejection versus Higgs-jet efficiency for each flavor composition of light-flavor, single-c,

single-b, double-b, double-c, and bc large-R jets from multi-jet production when using double b-tagging. One can see that the rejection of light-flavor large-R jets is largest, followed by single-c, and single-b large-R jets, due to the fact that two b-tagged track jets are required. The lowest background rejection is against double-b large-R jets, which is not surprising as the two b-hadrons within these large-R jets should have high b-tagging efficiencies. The rejection of double-b large-R jets derives from: (1) difficulties in identifying multiple b-jets in low mass large-R jets with small angular separation between the b-hadrons, and (2) inefficiencies in b-tagging at low p_{T} in the case of a large p_{T} asymmetry between well separated b-jets.

Another common background to boosted Higgs boson searches are boosted hadronic top-quark decays. The inclusive hadronic top jet rejection versus the Higgs-jet efficiency can be found in left plot of Figure 6.8, where the performance of double b-tagging, single b-tagging and asymmetric b-tagging is shown. Double and asymmetric b-tagging perform similarly and both provide significantly better rejection than single b-tagging with no significant loss in Higgs-jet efficiency. Such performance features of each of the possible b-tagging requirements is similar when examining the Higgs-jet efficiency versus the hadronic top rejection in different regions of large-R jet p_{T}. The hadronic top jet rejection versus the Higgs-jet efficiency for double b-tagging with the hadronic top jets broken down by the number of b- and c- hadrons found in the large-R top jet can be seen in right plot of Figure 6.8. A large fraction of top jets is rejected by the double-b-tagging requirement, however the hadronic top jets containing both a b- and c- hadron are rejected at a significantly lower rate than other flavors of hadronic top jets.

An important thing to remark here is that use of track jet b-tagging for large-R jet is actually very flexible, and should not be limited to the three variations as discussed here, which are simply used as benchmarks. In most physics analysis, people usually choose some fixed working point first (depending on optimization studies for each analysis) and then categorize events based on the counting of b-tagged track jets, which is exactly what is done in the searches of this thesis as we will see. Furthermore, one could also take advantage of sensitivity of different working points, and thus design an event categorization with various b-tagging working point as well, or even asymmetric b-tagging working point for different track jets. This would in general improve the analysis sensitivity by non-negligible amount, although a continuous b-tagging calibration is needed since more than one working points are used at the same time.

Furthermore, there are two potential issues related to $R = 0.2$ track jets as one starts to explore extremely boosted Higgs, which we already start to encounter in both searches presented in this thesis: 1) When p_{T} is high enough, the double close-by b-hadron would even merge inside one $R = 0.2$ track jets; 2) The b-tagging performance degrades a lot in such boosted environment. There are also in general two approaches to address this such issue. The first way, which is what would be adopted in both searches in this thesis, is to increase event b-tag multiplicity categorization. For example, when two b-hadrons merge into one track jet, one could require only one b-tagged track jets instead

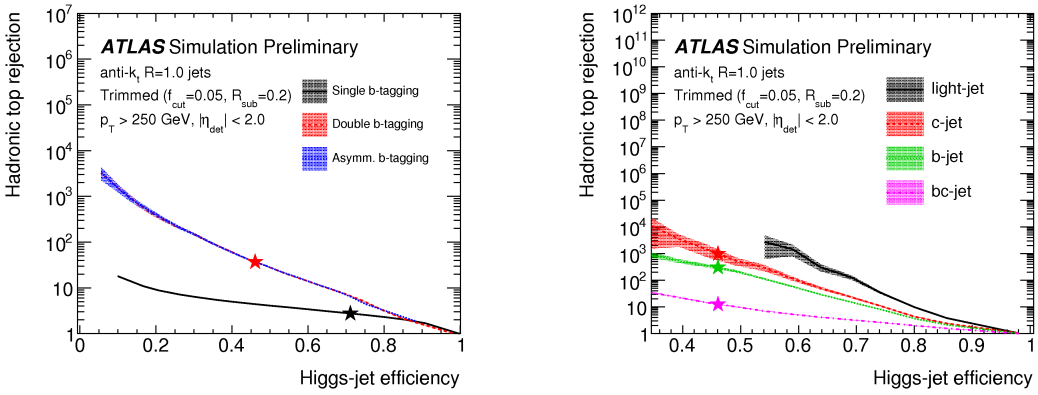


Figure 6.8: (left) The rejection of inclusive hadronic top jets versus Higgs-jet efficiency using all large-R jets with $p_{\mathrm{T}} > 250$ GeV, for (single / double / asymmetric) b-tagging requirements. (right) Hadronic top jet rejection versus Higgs-jet efficiency using all large-R jets with $p_{\mathrm{T}} > 250$ GeV, broken down by hadronic top jet flavor composition, using double b-tagging. The stars correspond to a 70% b-tagging WP. The bands represent the statistical uncertainties. No star is seen for the light-flavor curve as the statistics of the sample were not sufficient to reach this point. Note that none of the curves reach a Higgs-jet efficiency of 100% due to the imperfect efficiency to reconstruct the track jets needed for b-tagging and in the case of asymmetric b-tagging the 70% b-tagging working point requirement on one of the track jets. [123]

of two to make sure acceptance would not drop significantly. While this is easy to implement, its disadvantage would be also clear since the background could increase significantly as requirement on b-tag multiplicity is relaxed. Therefore, this method would typically work only in the phase space where multijet can be suppressed by other factors, such as extremely high p_{T} etc. Another approach is to develop new algorithms to further resolve these extremely close-by b-hadrons in such high p_{T}. Various algorithms are being developed inside ATLAS[2] in this direction. Similar effort in tagging very close-by b-hadrons, but under the context of $g \to b\bar{b}$ can be found in Appendix B.

6.3.3 Mass Window

Similar to W/Z-tagging, $H \to b\bar{b}$ large-R jets are first groomed. A mass window compatible with Higgs mass which is 125 GeV is then applied. However, different mass window can be chosen depending on the mass resolution, as well as sensitivity requirement in the physics analysis. In this section, two benchmarks, which are 68% and 90% mass window, are discussed. However, one should absolutely not be restricted by these benchmarks. As a matter of fact, one could even adopt cuts beyond a simple mass window cut: For example, in the $pp \to hh \to b\bar{b}b\bar{b}$ search as will be presented in Chapter 7, a χ^2-like selection is adopted.

Before choosing the mass window, one can notice that in addition to detector smearing, the mass

[2]As a matter of fact, they are very close to be published at the time when this thesis is being written

resolution of Higgs-jets is degraded due to the semi-leptonic decays of the b-hadrons produced in Higgs boson decays. The semi-leptonic decays lead to the production of neutrinos, which are not directly measured in ATLAS, electrons, which are measured in the calorimeter and inner detector, and muons, which are not measured in the calorimeter but are measured in the inner detector and muon spectrometer. As it is difficult to identify the calorimeter depositions of electrons within jets, and neutrinos are not measured directly by the detector, only the muon from the semi-leptonic decays of b-hadrons are considered. The effect of the semi-leptonic decays to muons is corrected by finding muons within $\Delta R < 0.2$ of the b-tagged track jets and adding the four vector of these muons to that of the large-R jet. If more than one muon is found within a track jet, only the muon closest to the track jet axis is considered. The mass distributions of the large-R jets are shown in Figure 6.9 before and after the muon correction in two large-R jet p_{T} ranges. A clear improvement in mass resolution for the Higgs-jets is observed at low Higgs-jet p_{T}, while the improvement is not as significant at higher Higgs-jet p_{T}.

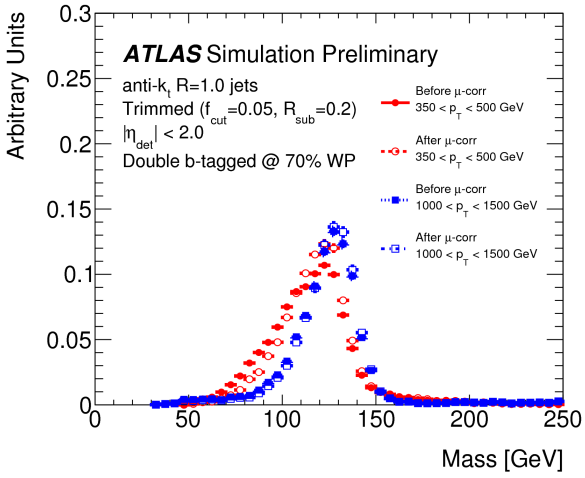


Figure 6.9: The calibrated mass distribution for large-R trimmed double b-tagged jets before and after the muon correction for Higgs-jets is shown in the large-R jet transverse momentum ranges $350 < p_{\mathrm{T}} < 500$ GeV and $1000 < p_{\mathrm{T}} < 1500$ GeV. Higgs bosons are simulated with a mass of 125 GeV. All jets, whether they have a close-by muon or not, are used. [123]

The mass distribution after the muon correction for Higgs-jets, multijet production, and hadronic top jets, is shown in Figure 6.10 in two large-R jet p_{T} bins. There is not a significant peak at the W boson mass of 80 GeV in the hadronic top jet mass distributions because of the double b-tagging requirement. In terms of p_{T}-dependence, the peak of the mass distribution is quite stable within 4% as a function of p_{T}, after jet mass calibration. In addition, the width of the core of the mass distribution decreases with p_{T}, but high mass tails are observed at high $p_{\mathrm{T}} > 1000$ GeV.

Based on jet mass distribution, benchmark mass windows can be determined. The exact value

of mass windows can be found in Figure 6.14.

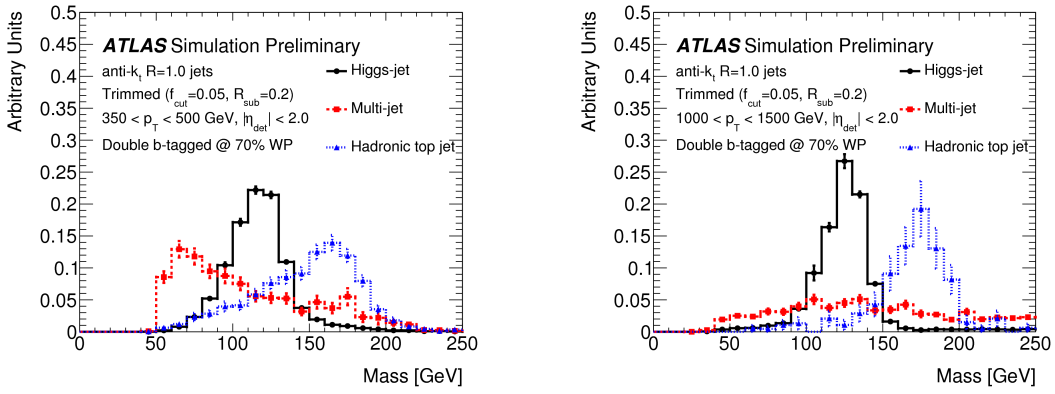


Figure 6.10: Mass distribution, after the muon correction, in the large-R jet transverse momentum ranges $350 < p_{\mathrm{T}} < 500$ GeV (left) and $1000 < p_{\mathrm{T}} < 1500$ GeV (right) for Higgs-jets and multijet and hadronic top backgrounds. Higgs bosons are simulated with a mass of 125 GeV. [123]

6.3.4 Jet Substructure Variables for $H \to b\bar{b}$

In addition to the heavy flavor content of the large-R jet, and the jet mass, the internal structure of the jet can be used to discriminate Higgs-jets from multijet production and hadronic top decays. There are a large number of substructure variables that capture features of a jets internal structure. A subset of variables defined in Section 6.1 is used here: $D_2^{(\beta=1)}$, $C_2^{(\beta=1)}$ and τ_{21}^{wta}. Their distribution for Higgs-jets, multijet production, and hadronic top jets can be seen in Figure 6.11. In the distributions for all three variables, there are larger difference between the Higgs-jets and the multijet distributions than between the Higgs-jets and the hadronic top jet distributions. This is not only observed inclusively in large-R jet p_{T}, but also when examining these distributions in different ranges of large-R jet p_{T}.

Several substructure variables are compared in Figures 6.12 and 6.13 in terms of their rejection power against multijet production and hadronic top jets, respectively, in two different ranges of large-R jet p_{T}. The curve labeled "Double b-tagging" shows the performance of varying only the double b-tagging requirement after the 68% mass window requirement. The stars in the figures indicate the performance after a 68% mass window requirement and a fixed b-tagging requirement of 70% or 85%. The curves for the different substructure variables are produced by varying only the substructure requirements after the mass and fixed b-tagging requirements are applied. The addition of substructure variable requirements to the tagger improves rejection power against multijet production, especially in the lower Higgs-jet efficiency region below 30%. At higher Higgs-jet efficiencies, which can be achieved when using looser b-tagging working points such as the 85% WP, the gains from adding substructure variables to the tagger are not as large. It can also be seen that

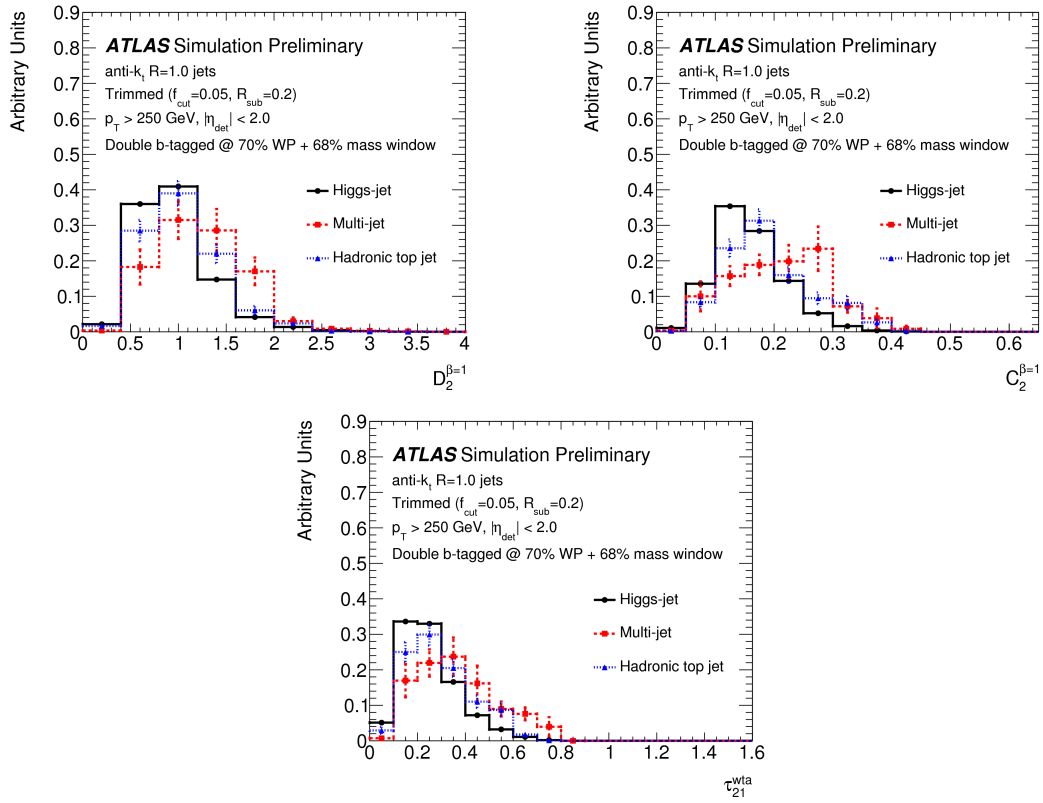


Figure 6.11: Distributions of $D_2^{(\beta=1)}$ (top left), $C_2^{(\beta=1)}$ (top right) and τ_{21}^{wta} (bottom) for Higgs-jets (black), multijet (red) and hadronic top (blue) in Monte Carlo after the 68% mass window selection and after applying double b-tagging at the 70% efficiency WP. [123]

the performance gains from the different substructure variables are quite similar.

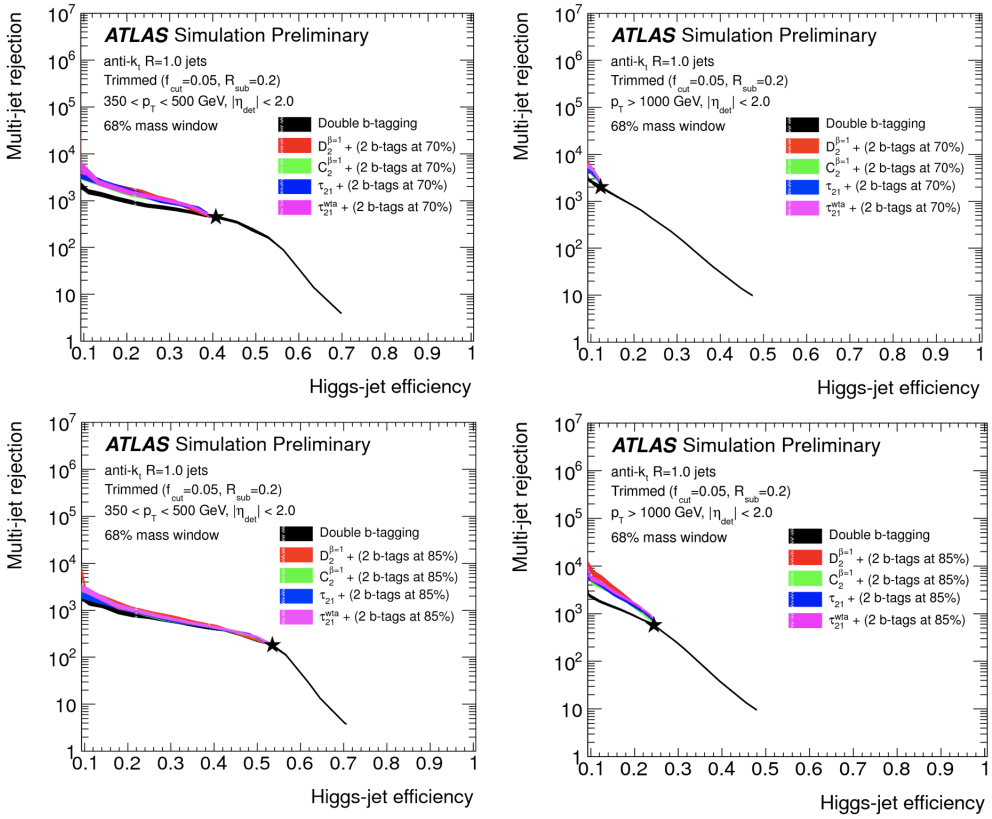


Figure 6.12: The Higgs-jet efficiency versus multijet background rejection power, in large-R jet transverse momentum ranges of $350 < p_{\mathrm{T}} < 500$ GeV (left) and $1000 < p_{\mathrm{T}} < 1500$ GeV (right), for selected tagging variables (combined with the calibrated groomed 68% mass window and double b-tagging using 70% in (top) and 85% WP in (bottom)). The high end point of the Higgs-jet efficiency curves are a result of the 68% mass window requirement. The stars correspond to the nominal 70% (top) and the 85% (bottom) b-tagging working points. The bands represent the statistical uncertainties. [123]

A better hadronic top jet rejection for a fixed Higgs-jet efficiency can be achieved by requiring more stringent b-tagging requirements than can be achieved by adding substructure requirements in addition to a fixed b-tagging requirement. While only two p_{T} ranges are shown in Figure 6.13, this behavior was observed in all p_{T} ranges considered in this analysis and also when combining substructure discrimination with several different b-tagging working points.

The performance of single b-tagging combined with substructure information is not shown because the background rejection was observed to be significantly lower than that of the double b-tagging combined with substructure. However, at high track jet $p_{\mathrm{T}} >\sim 300$ GeV, the uncertainties

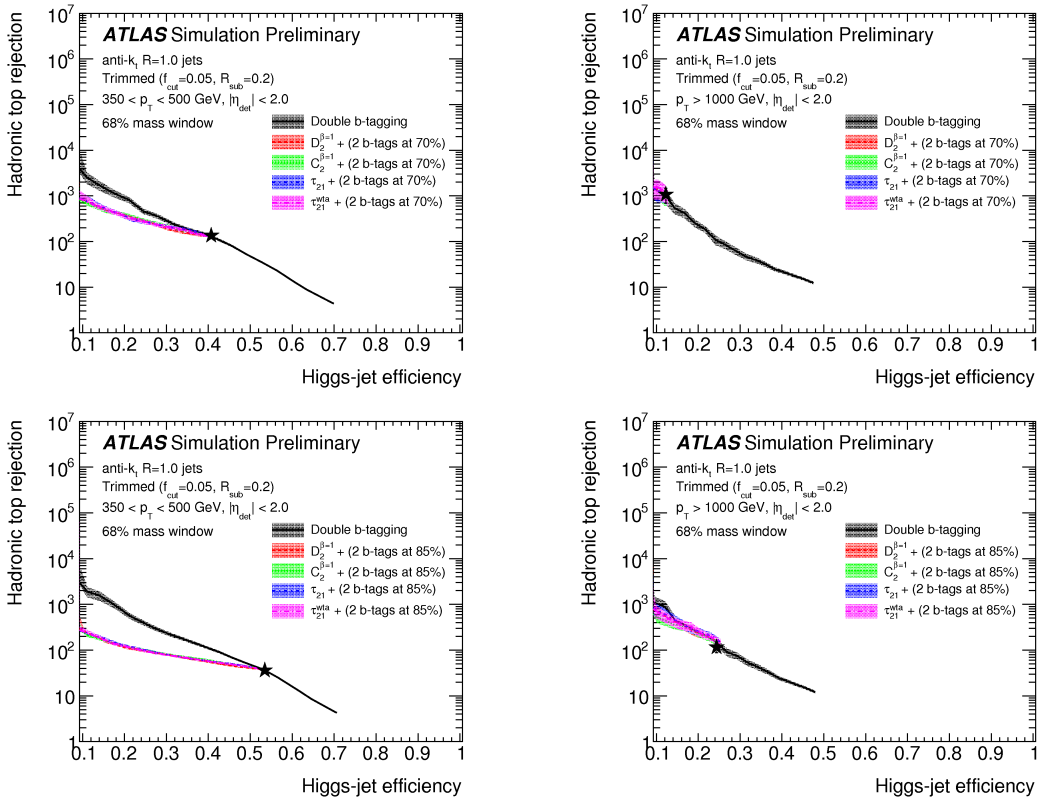


Figure 6.13: The Higgs-jet efficiency versus hadronic top rejection power, in large-R jet transverse momentum ranges of $350 < p_{\mathrm{T}} < 500$ GeV (left) and $1000 < p_{\mathrm{T}} < 1500$ GeV (right), for selected tagging variables (combined with the calibrated groomed 68% mass window and double b-tagging using 70% in (top) and 85% WP in (bottom)). The high end point of the Higgs-jet efficiency curves are a result of the 68% mass window requirement. The stars correspond to the nominal 70% (top) and the 85% (bottom) b-tagging working points. The bands represent the statistical uncertainties. [123]

on the calibration of the b-tagging efficiency can be large, and thus the usage of only single b-tagging may reduce uncertainties on a Higgs-jet tagger at high p_{T}, making this an interesting option for certain analyses.

Since all substructure variables examined show similar performance, $D_2^{(\beta=1)}$ is chosen to be aligned with the W/Z-tagging. It should also be noticed that, the usage of substructure is optional, for two reasons: 1) Use of small radius track jet can already reveal some substructure difference between signal and background as shown in Figure 6.5; 2) Use of substructure may harm the sensitivity since it would lower down signal efficiency while rejection is already very high by b-tagging and mass cut alone. Therefore, it is always recommended for each analysis to check if substructure is necessary case-by-case. So far, all boost analysis in ATLAS does not use substructure information since it is found to harm sensitivity in the very high resonance mass end. Nevertheless, a categorization on substructure variables into "high-purity" and "low-purity" regions, which is a common approach adopted by CMS, is worth investigation for future studies.

6.3.5 Benchmark Tagging Performance

In order to have a Higgs-jet tagging efficiency that does not vary with p_{T}, as many analyses find helpful, the double b-tagging and mass window requirement can be combined with p_{T}-dependent selections on the variable $D_2^{(\beta=1)}$ in order to maintain a flat efficiency at, in this case, 25%. The p_{T}-dependent requirement is smoothed using a polynomial fit in order to reduce bin-edge effect. A 25% efficiency can only be achieved up to $p_{\mathrm{T}} \sim 800$ GeV, while above $p_{\mathrm{T}} \sim 800$ GeV it is not possible to reach 25% efficiency because the b-tagging efficiency is strongly dependent on p_{T}. Therefore, the requirement on $D_2^{(\beta=1)}$ is not applied for jets with $p_{\mathrm{T}} > 800$ GeV for a 70% b-tagging WP and 68% mass window.

Figure 6.14 shows the three benchmark working mode that a $H \to b\bar{b}$ tagger can choose. Again, it should be emphasized that the $H \to b\bar{b}$ tagging itself is very flexible at all stages from b-tagging, mass cut and use of substructure, which is exactly what we do in practice in physics analysis. Performance shown here are only for certain representative benchmarks.

Selection	double b-tagging	jet Mass	
`Loose`	70% WP	90% window, $m \in [76, 146]$ GeV	-
`Medium`	70% WP	68% window, $m \in [93, 134]$ GeV	-
`Tight`	70% WP	68% window, $m \in [93, 134]$ GeV	p_{T}-dependent cut

Figure 6.14: Criteria used for the different Higgs-jet tagging selections. [123]

Figure 6.15 shows the Higgs-jet efficiency and background rejection for multijet and hadronic top events as a function of p_{T} at various stages after applying the 70% b-tagging WP. After b-tagging, mass window and $D_2^{(\beta=1)}$ cut, the Higgs-jet efficiency drops to below the target 25% efficiency above $p_{\mathrm{T}} = 800$ GeV. This could be compensated by using a looser b-tagging WP in order to obtain a

fixed Higgs-jet efficiency up to higher jet p_{T}. The lower Higgs-jet efficiency observed at low p_{T}, after requiring two b-tagged track jets, is related with the p_{T} distribution of track jets within the large-R jet and the lower b-tagging efficiency for low p_{T} track jets.

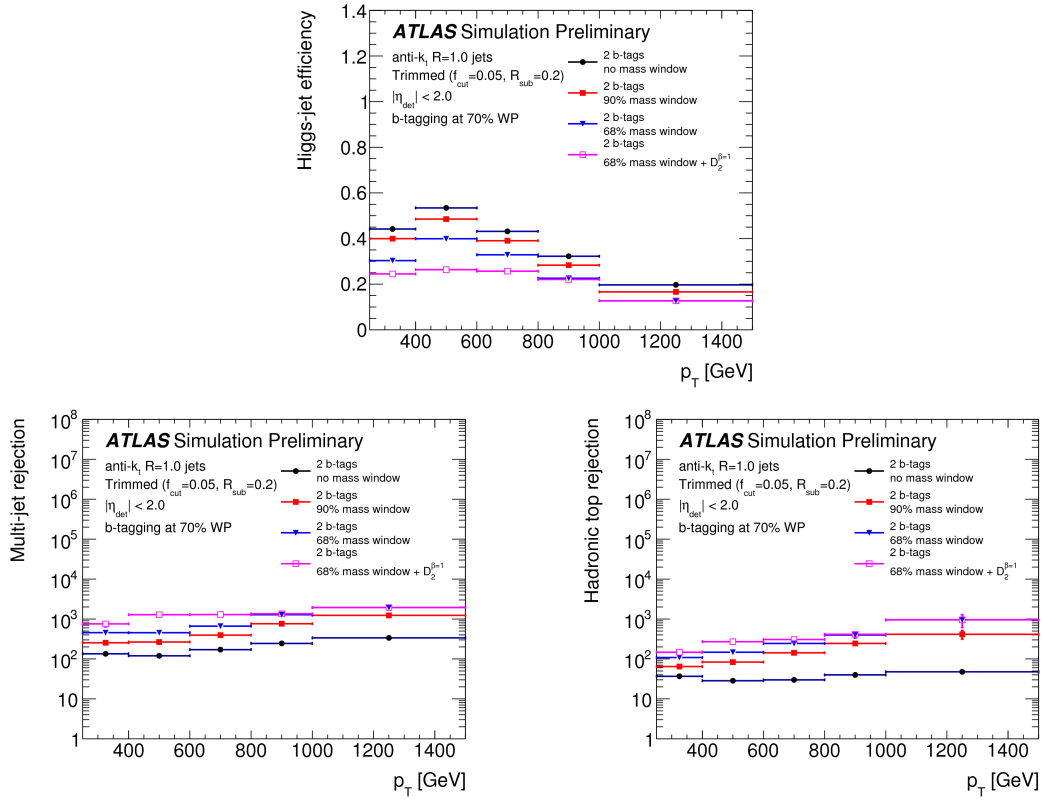


Figure 6.15: Higgs-jet efficiency versus large-R jet p_{T} (top) and multijet (bottom left) and hadronic top (bottom right) background rejection for different benchmark Higgs-jet taggers. The plots correspond to a nominal b-tagging working point of 70%. [123]

Chapter 7

Search of Pair Production of Higgs Bosons in $b\bar{b}b\bar{b}$ Final States

7.1 Introduction

The discovery of a Higgs boson (h) [1, 2] at the Large Hadron Collider (LHC) consistent with the predictions of the Standard Model (SM) [150, 151] motivates an enhanced effort to search for new physics via the Higgs sector. Many new physics models predict rates of Higgs boson pair production significantly higher than the SM rate [152, 153, 154]. For example, TeV-scale resonances such as the first Kaluza-Klein (KK) excitation of the graviton, G^*_{KK}, predicted in the bulk Randall-Sundrum (RS) model [29, 155] or the heavy neutral scalar, H, of two-Higgs-doublet models (2HDM) [156] can decay into pairs of Higgs bosons, hh. Enhanced non-resonant $pp \to hh$ production can arise in models such as those with new, light, coloured scalars [157], or direct $t\bar{t}hh$ vertexes [158, 159].

This analysis is based on the Run 1 ATLAS search in the $b\bar{b}b\bar{b}$ final state [122], which set limits on both resonant and non-resonant Higgs boson pair production. For resonant KK Gravitons, the Run 1 analysis excluded resonance masses between 500 GeV up to 720 - 990 GeV, depending on the model parameters, and set cross section limits of $\sim 5 - 10$ fb depending on resonance mass. For non-resonant production, the analysis set a cross section upper limit of 0.62 pb [160]. ATLAS has carried out searches using other final states – $b\bar{b}\gamma\gamma$, $b\bar{b}\tau^+\tau^-$ and $W^+W^-\gamma\gamma$ – which were combined with the $b\bar{b}b\bar{b}$ results in [160].

Our results from Run 1, along with phenomenlogical studies, demonstrate that despite the fully hadronic final state being subject to a large multijet background, searches for new physics in the $pp \to hh \to b\bar{b}b\bar{b}$ process have good sensitivity for both resonant [161, 162] and non-resonant signals [163, 164]. As a matter of fact, $pp \to hh \to b\bar{b}b\bar{b}$ channel has the highest sensitivity across all final states in Higgs pair production for both resonance and non-resonance case [160]. One contributing factor to

this sensitivity is the high expected branching ratio for $h \to b\bar{b}$. Furthermore, the analysis presented here is designed to search for two high-momentum $b\bar{b}$ systems with masses consistent with m_h. Compared to a more inclusive $b\bar{b}b\bar{b}$ final-state analysis, this topology has many benefits due to the large required momentum and angular separation between the two $b\bar{b}$ systems: Excellent rejection of all backgrounds; Highly efficient triggering using b-tagged multijet and high-p_{T} large radius jet triggers; Negligible combinatorial ambiguity in forming Higgs boson candidates.

The boosted Higgs boson identification technique as presented in Chapter 6 is therefore adopted, with optimization suited for this analysis, in order to maintain good acceptance for resonances of mass above 1 TeV, as well as high rejection of backgrounds. The Higgs boson candidate is reconstructed as a single, trimmed anti-k_t $R = 1.0$ jet which with two associated b-tagged anti-k_t $R = 0.2$ track-jets [121, 123]. The use of jet grooming algorithm helps to mitigate the effects of pileup and improve the jet mass and energy resolution, whilst fully capturing the Higgs boson decay products. The use of track jets with a smaller R parameter allows for the identification of close-by b-jet and thus allows the Higgs bosons with higher p_{T} to be reconstructed.

For this analysis, the dominant background is multijet process, which is hard to model in MC simulation in particular with high heavy flavor multiplicity. Therefore, a data-driven background estimation technique is developed to estimate both the normalization and shape of multijet background. This method relies on (a) reducing the number of required b-tagged track jets and (b) using alternative selection of the leading and sub-leading Higgs candidate masses which are orthogonal to the signal region. Systematic uncertainty estimation for this procedure is also developed through dedicated control / validation regions.

This chapter presents the searches for pair production of Higgs bosons in the $b\bar{b}b\bar{b}$ final states using proton-proton collisions at $\sqrt{s} = 13$ TeV with ATLAS detector in Run 2. Following the searches done in Run 1 with 19.5 fb^{-1} data at $\sqrt{s} = 8$ TeV [122], the analysis in Run 2 has been progressively done in two stages: First a search fully taking advantage of higher signal cross section brought by increased collision energy at LHC is published with 3.2 fb^{-1} data collected in 2015 [165]; Then a second-stage analysis is done using more abundant data collected in 2015 and part of 2016 of in total 13.3 fb^{-1} with various key optimizations for boosted regions [166]. Since the first stage of analysis defines the basic strategy in terms of both event selection, background estimation and systematic uncertainties, it would be described with great details in this chapter. However, due to the significant improvement in search sensitivity, second stage of analysis would be summarized in Section 7.7 with focus on the improvements and latest results.

Inside ATLAS, the search of pair production of Higgs boson in $b\bar{b}b\bar{b}$ consists of two parts: the resolved part focusing on resonance of masses less than 1 TeV and non-resonance hh production, and the boosted part focusing on heavy resonance of masses larger than 1 TeV. Only the boosted part would be presented here, as the resolved part is a fairly different analysis due to its non-boost nature (although two analysis are usually reported together). Readers with interest in resolved analysis can

find more information in [122, 165, 166].

This chapter is organized as following: Sample used are summarized in Section 7.2; Objects and event selections are defined in Section 7.3; Strategies for background estimation can be found in Section 7.4; Details of systematic uncertainties are in Section 7.5; Unblinded results along with statistical analysis are in Section 7.6; The optimization and improvement of this search, as well as latest results, in second stage are summarized in Section 7.7.

7.2 Data and Simulation Samples

7.2.1 Data

The studies presented here are based on the 2015 dataset at $\sqrt{s} = 13$ TeV recorded by the ATLAS experiment. After requiring that the data be collected during stable beam conditions and the relevant detector systems be functional, the total integrated luminosity is estimated to be 3.2 fb^{-1}. Jet triggers are used to select the data (details below).

7.2.2 Simulated Signal and Background Samples

All MC samples used in this analysis are produced with full simulation, with additional pile-up interactions in each simulated event modeled by adding multiple soft pp collisions generated by Pythia 8 [167] with the MSTW2008 LO PDF and AU2 tune [168]. Charm-hadron and bottom-hadron decays are handled by EvtGen 1.2.0 [169] for all MC samples described below. After event generation and the addition of pile-up, the response of the ATLAS detector to particles passing through the detector elements is simulated with the GEANT4 toolkit [170, 171] and events are reconstructed using the same software used to reconstruct events in data.

Signal MC production

Two benchmark resonant signal models are considered: a spin-2 graviton within a Bulk Randall-Sundrum Kaluza-Klein model (RSG for short below) and a spin-0 heavy neutral Higgs boson within a 2HDM model (2HDM for short below).

Signal G^*_{KK} events are generated at leading order (LO) with MG5_aMC@NLO v2.2.2 [172] using the NNPDF2.3 LO parton distribution function (PDF) set [173], and Pythia 8.186 [167] to model the parton shower and hadronization process using the A14 set of tuned underlying-event parameters [174]. The Higgs-boson mass is set to 125.0 GeV. Values of the signal cross section times branching ratio for $G^*_{\mathrm{KK}} \to hh \to b\bar{b}b\bar{b}$ with the coupling constant $k/\bar{M}_{\mathrm{Pl}} = 1$ are 11.2 fb and 0.185 fb for G^*_{KK} masses of 1 TeV and 2 TeV, respectively. The parameter k corresponds to the curvature of the warped extra dimension and the effective four-dimensional Planck scale $\bar{M}_{\mathrm{Pl}} = 2.4 \times 10^{18}$ GeV.

Signal samples are also generated with $k/\bar{M}_{\mathrm{Pl}} = 2$ to study broader resonances. Both the cross section and natural width depend on $(k/\bar{M}_{\mathrm{Pl}})^2$.

Generation of the heavy H scalar in a simplified model with a fixed narrow width $\Gamma_H = 1$ GeV is performed with MG5_aMC@NLO and the CT10 PDF set [175]. With this Γ_H choice, the width of the reconstructed hh resonance is dominated by the experimental resolution. For this model, parton showering and hadronization are handled by Herwig++ [176] with the CTEQ6L1 PDF set [177] and the UEEE5 underlying-event tune [178]. The scalar interpretation for this search only makes use of the acceptance times efficiency from this model and no interpretation in terms of 2HDM parameters is presented.

Background MC Samples

While multijet process will be estimated from data, a Pythia [167] dijet sample is used to assess the initial process creating multijet events after final selection. Not enough events pass the full events selection.

The second largest background, but with a much smaller contribution, arises from $t\bar{t}$. The $t\bar{t}$ background is modeled using large all-hadronic and non-all-hadronic decay mode samples. In order to populate events of large mass of $t\bar{t}$ system, additional events are generated in slices of $m_{t\bar{t}}$. Generation of $t\bar{t}$ events is performed with Powheg-box v1 using the CT10 PDF set. The parton shower, hadronization, and the underlying event are simulated using Pythia 6.428 [179] with the CTEQ6L1 PDF set and the corresponding Perugia 2012 tune [180]. The top-quark mass is set to 172.5 GeV. Higher-order corrections to $t\bar{t}$ cross sections are computed with Top++ 2.0 [181]. These incorporate NNLO corrections in QCD, including resummation of next-to-next-to-leading logarithmic soft gluon terms. The overall $t\bar{t}$ normalization is extracted from the data while the shape of kinematic distributions is taken from MC simulation.

$Z+$jets only contributes around at most 1% of the total background in this analysis. The $Z+$jets sample is generated using Pythia 8.186 with the NNPDF2.3 LO PDF set.

7.3 Selections

7.3.1 Event Reconstruction

Event reconstruction of the whole analysis relies on reconstruction of jets using anti-k_t algorithm of radius $R = 1.0$ with locally calibrated clusters as inputs, as described in Section 5.3 and Chapter 6. These jets are then trimmed to remove energy deposition from pile-up and the underlying event, by reclustering the $R = 1.0$ jet with the k_t algorithm into smaller $R = 0.2$ subjets and removing those subjets with $p_{\mathrm{T}}^{\mathrm{subjet}}/p_{\mathrm{T}}^{jet} < 0.05$, where $p_{\mathrm{T}}^{\mathrm{subjet}}$ is the transverse momentum of the subjet and p_{T}^{jet} that of the original jet. The resulting trimmed $R = 1.0$ jet is then calibrated to correct the four momentum for detector response.

Jets containing b-hadrons are identified using the track jet b-tagging as described in Section 5.4, 5.5 and Chapter 6. Track jets are chosen to originate from the primary vertex, and calibrated down to a smaller distance parameter and lower p_{T} than calorimeter jets without suffering from a large fake rate due to pileup interactions in the event or resolution effects (as in the calorimeter based jets). The b-tagging algorithm is applied to tracks with loose impact parameter (IP) constraints in a region of interest around each track jet axis, enabling the secondary vertex from the b-hadron decay to be reconstructed. The 77% b-tagging working point is used. These track-jets are then matched to the $R = 1.0$ jet used to reconstruct the Higgs boson candidates by the ghost association algorithm. In this method, large-R jet algorithm is rerun with both four momentum of track jets modified to have infinitesimally small momentum ("ghosts") and all topological energy clusters in the event as potential constituents of jets. Due to IRC safety of jet clustering algorithm, presence of "ghost" track jets would not affect clustering results as if they were not there, while the association is determined unambiguously from clustering procedure.

Muons are reconstructed by combining measurements from the inner tracking and muon spectrometer systems, and are required to satisfy *tight* muon identification quality criteria. In this analysis, muons are only used to correct the jet four momentum for the energy lost in semi-leptonic b-decay. If a muon with $p_{\mathrm{T}} > 4\,\mathrm{GeV}$ and $|\eta| < 2.5$ can be ΔR-matched to a b-tagged jet, then the four momentum of the muon is added to that of the jet. The ΔR match requirements correspond to the track jet radius parameter, i.e. $\Delta R < 0.2$. The jet four momentum is further corrected for the expected energy deposited by the muon in the calorimeter. It should be noted that these muons are only used for corrected the jet energy after b-tagged has been performed, and are not used for b-hadron identification.

7.3.2 Trigger

Events in data and simulation are required to pass the lowest unprescaled large-R jet trigger, `HLT_j360_a10r`, which is seeded by the lowest unprescaled L1 jet trigger, `L1_J100`. This is different from the Run 1 boosted analysis, which used an `OR` of five triggers to get high signal efficiency, because large-R jet trigger now provides excellent signal efficiency across the range of signal masses considered. Further advantage comes from the fact that it does not rely on online b-tagging.

HLT trigger	L1 seed
`HLT_j360_a10r`	`L1_J100`
`HLT_ht850`	`L1_J100`
`HLT_j225_bloose`	`L1_J100`
`HLT_4j85`	`L1_3J40`
`HLT_3j175`	`L1_J100`

Table 7.1: HLT triggers, and their L1 seeds, considered for use in the boosted regime.

The triggers considered are listed in Table 7.1. The efficiencies of various L1 items is shown in Figure 7.1 for the inclusive signal samples, and the `L1_J100` provides good efficiency across the entire mass range. The efficiencies of the HLT items considered is shown in Figure 7.2 and Figure 7.3, both for the inclusive signal samples and for the signal samples after passing the signal region requirements inherited from the Run 1 analysis. The `HLT_j360_a10r` provides good efficiency across the entire mass range, especially after selecting the signal region at high mass. Also seen in Figure 7.3, the efficiencies of triggers requiring multiple jets drop at high p_T because the decays of each Higgs are merged into one jet, thus making it difficult to identify and trigger on multiple jets. The large-R jet trigger avoids this complication as it only requires a single jet which is large enough to capture the energy from the merging decay products.

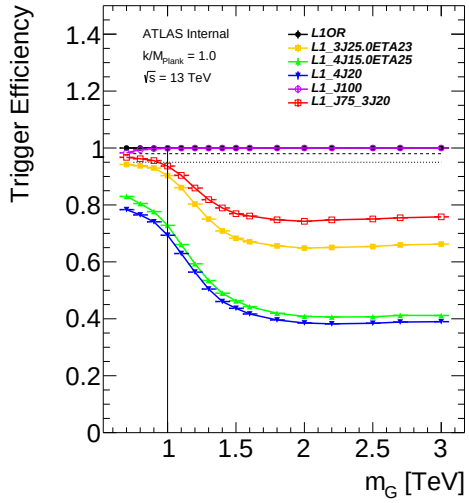


Figure 7.1: L1 trigger efficiencies as a function of the signal resonance mass with no selection applied. The lowest unprescaled single jet trigger (`L1_J100`) has good efficiency across the entire mass range.

Since the large-R jet trigger is efficient by itself, it is chosen as the only trigger requirement for the boosted analysis. This avoids the complication of `OR`-ing multiple triggers as is needed at lower mass.

The large-R jet trigger efficiency has been measured in data and a good agreement is observed with the prediction from the MC simulation, also on the turn-on curve, as shown in Figure 7.4.

7.3.3 Preselection

Data events are required to be contained in the standard Good Runs List (GRL), which defines a set of lumi blocks passing data quality requirements for the ATLAS detector, as mentioned in Section 7.2.1. Furthermore, various event cleaning criteria are required to pass:

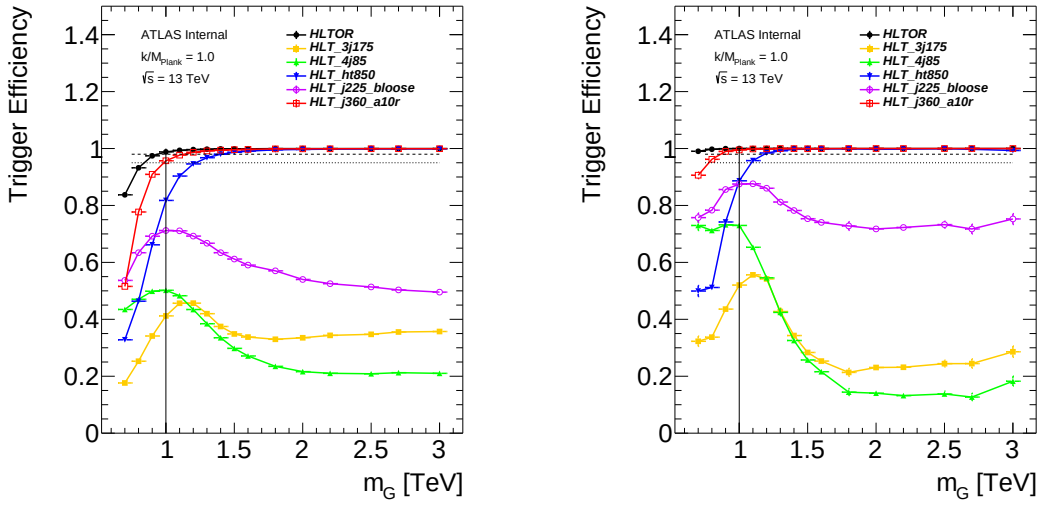


Figure 7.2: HLT trigger efficiencies as a function of the signal resonance mass with no selection (left) and after leading jet p_T requirement (right).

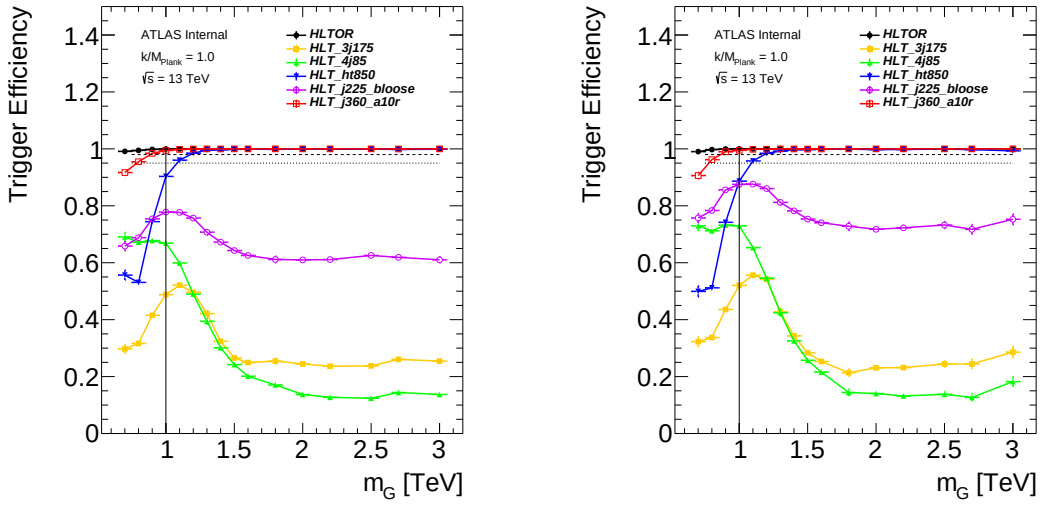


Figure 7.3: HLT trigger efficiencies as a function of the signal resonance mass for events in 3b (left) and 4b (right) signal regions. The lowest unprescaled large-R jet trigger (`HLT_j360_a10r`) has good efficiency across the entire mass range and is fully efficient above $\sim$ 1 TeV in the signal region selection.

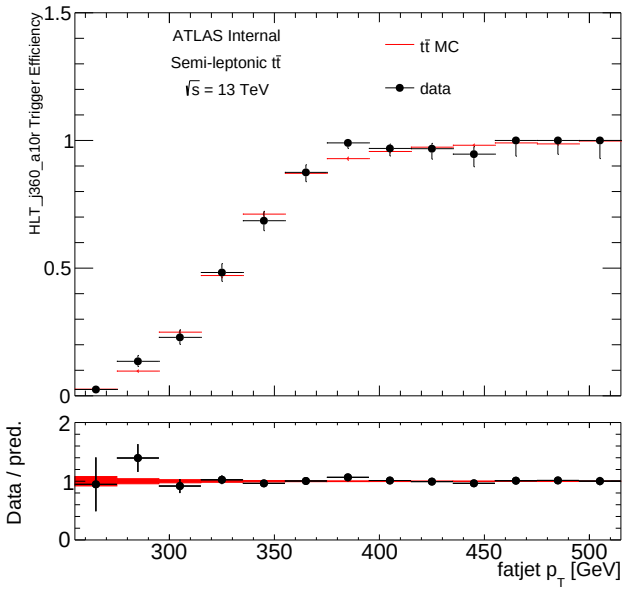


Figure 7.4: `HLT_j360_a10r` trigger efficiency measured as function of large-R jet p_{T}. Data and MC show good agreement.

- Bad events due to problems in TileCal are removed
- Bad events due to problems in LAr are removed
- Events affected by the recovery procedure for signal event upsets in the SCT are removed
- Incomplete events are removed

In addition to cleaning and trigger requirements (Section 7.3.2), events are pre-selected with kinematic criteria shown in Table 7.2 to be consistent with the signal hypotheses.

kinematic pre-selection
• at least two large-R jets with $250 < p_{\mathrm{T}} < 1500$ GeV, $\lvert\eta\rvert < 2$, $m > 50$ GeV
• leading large-R jet must have $p_{\mathrm{T}} > 350$ GeV
• the leading and sub-leading large-R jets are considered the Higgs candidates
• the Higgs candidates must have $\Delta\eta < 1.7$
• each Higgs candidate must have ≥ 2 associated track jets with $p_{\mathrm{T}} > 10$ GeV and $\lvert\eta\rvert < 2.5$

Table 7.2: List of kinematic pre-selection used in the boosted analysis. These cuts are generally efficient for signal.

Events are required to have at least two large-R jets, each of which is required to have $250 < p_{\mathrm{T}} < 1500$ GeV, $|\eta| < 2$, and $m > 50$ GeV. The upper bound on the p_{T} is due to the fact that jet

calibration uncertainties above this value were not available at the time of this analysis. The lower bound of p_{T} threshold corresponds to the minimum p_{T} required to contain all decay products from boosted Higgs boson inside a jet of radius $R = 1.0$, following the relation $\Delta R \sim 2m/p_{\mathrm{T}}$. $|\eta|$ and mass threshold corresponds to the region where detector response for large-R jet was well understood.

Only two large-R jets with highest p_{T} are retained for further selection – they would also be called Higgs candidate sometimes below. In order to reduce the contamination from $t\bar{t}$ events, leading jet is additionally required to have $p_{\mathrm{T}} > 350$ GeV, ensuring that all top-quark decay products are contained in a single large-R jet with mass close to that of the top quark.

Since high-mass resonances tend to produce jets that are more central than multijet background process, the two large-R jets are required to have a separation $|\Delta\eta| < 1.7$. For RSG resonances of mass higher than 2.5 TeV, $\Delta\eta$ cut would be less efficient due to the wider distribution as shown in Figure 7.5. Furthermore, $\Delta\eta$ cut is expected to be more efficient for spin-2 RSG signals than spin-0 heavy neutral Higgs in 2HDM model due to spin difference as found in Figure 7.5: Sensitivity, as simply quoted as $S/\sqrt{B}$, improvement for $\Delta\eta$ cut alone is about 8% for RSG signal with $c = 1.0$, while improvement for heavy neutral Higgs in 2HDM model is much smaller.

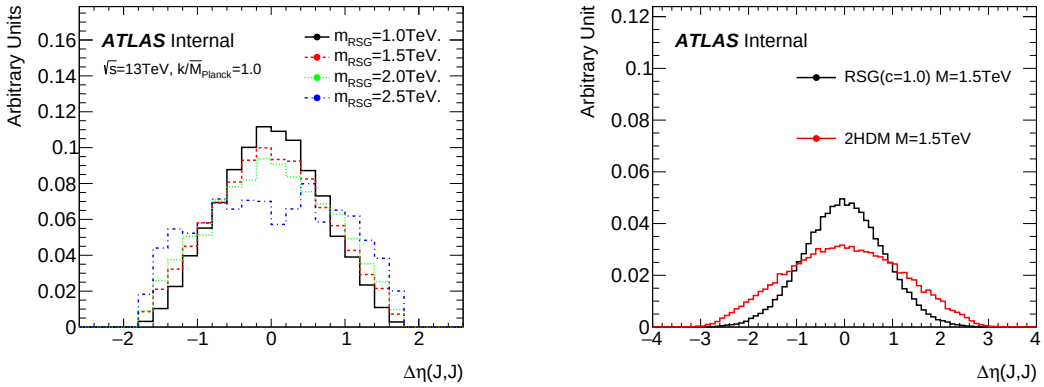


Figure 7.5: Distribution of $\Delta\eta$ for RSG signal samples of various mass with $c = 1.0$ (left) and heavy neutral Higgs in 2HDM model (right)

Selected kinematic distributions of RSG signal samples of various resonance masses can be found in Figure 7.6. As expected, the large-R jet p_{T} increases significantly as function of resonance mass. The mass of Higgs candidate jet is peaked around 125 GeV, whose resolution does not degrade significantly at higher resonance mass. The whole dijet system is produced centrally and back-to-back. Invariant mass of dijet system is consistent with the resonance mass, but gets smeared out due to detector resolution effect. In particular, resolution of dijet invariant mass gets worse as resonance mass gets higher. This is mainly due to degraded p_{T} resolution in very boosted region, while Higgs candidate mass resolution effect has little contribution to it (invariant mass of boosted dijet system is mainly determined by splitting angle between two jets and their momentum while individual jet

mass is largely irrelevant).

7.3.4 Signal Regions

b-Tagging Categorization

After basic selection on track jets as shown in Table 7.2 and ghost association to large-R jets, event is categorized based on the number of b-tagged leading and subleading track jets associated with each Higgs candidate jet: "3-tag" and "4-tag" category. The presence of two $h \to b\bar{b}$ decays in the final state naturally suggests requiring 4 track jets passing b-tagging requirements (two for each Higgs candidate jet), and this is defined as the "4-tag" selection. However, since this requirement has an overall efficiency of roughly ϵ^4, where ϵ is the efficiency of the tagger. Furthermore, ϵ will be less than the nominal efficiency where working point is defined on across whole p_{T} spectrum, since b-tagging efficiency typically drops heavily at high p_{T} region, as shown in Section 5.4 and 5.5.

To recover signal efficiency at high mass, the exclusive "3-tag" region, where three track jets need to pass b-tagging requirement and the other one must not pass b-tagging requirement, is considered. In the "3-tag" region, four track jets (two in each large-R jet) are still required, to ensure that the jets have the same internal structure as is expected by the signal. This ensures that the jet mass is generated by the splitting of the jet into two subjets. Without this requirement, the multijet background would be much larger and have a different structure to the "4-tag" events, making the background estimation more difficult. Therefore, the "3-tag" region used here is primarily targeting the recovery of efficiency loss of the b-tagging, while it cannot solve the issue for resonances of very high mass (typically > 2.5 TeV) that decay products are so collimated that even track jets of radius 0.2 cannot resolve two b-hadrons. This issue are later addressed in the second stage of this analysis as summarized in Section 7.7. 77% track jet b-tagging working point is used in this analysis since it is found to provide best sensitivity in "4-tag" region where resonance masses are less than 2 TeV and better sensitivity in "3-tag" region where resonance masses are larger than 2 TeV.

Muon-in-jet Correction

After categorization based on b-tagging, the last step toward signal region is requiring both Higgs candidate jets mass to be consistent with Higgs at 125 GeV. Before defining cuts on mass, Higgs candidate jet masses need to go through a further correction called *muon-in-jet* correction, as introduced in Chapter 6. This correction on large-R jet aims to account for energy loss due to leptonic b-hadron decays with a muon in the final state. Muons selected through cuts described in Section 7.3.1 are ΔR matched to the track jets associated to the large-R jets. The muons are required to be matched to the b-tagged track jets in order to focus only on semi-leptonic b-hadron decays. In case more than one muon is found within a track jet, only the muon closest in ΔR is considered. The four momentum of the muons is then added to the large-R jet four momentum to better reconstruct

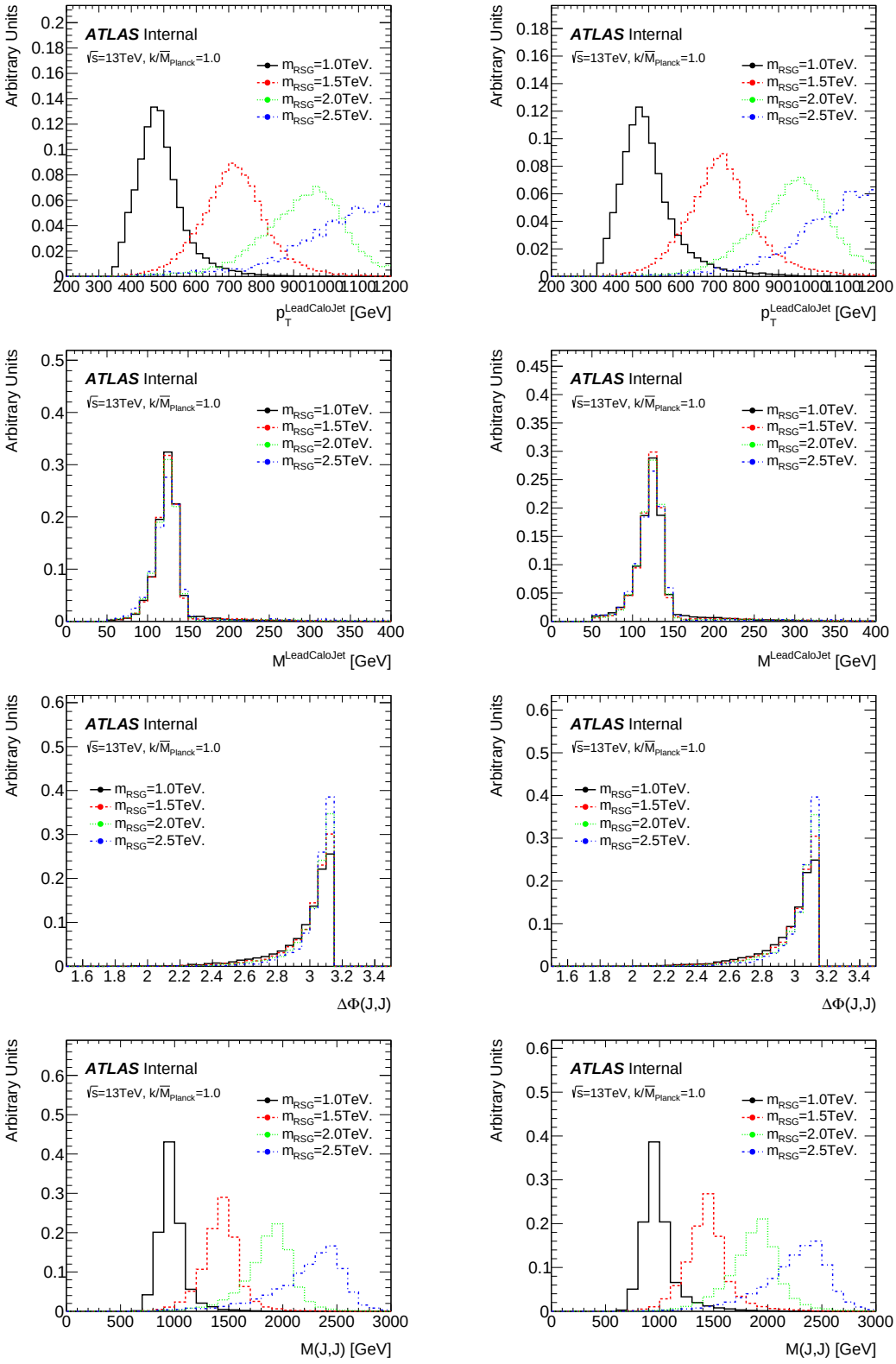


Figure 7.6: Distribution of selected signal kinematics for RSG signal resonance masses with $c = 1.0$ in "4-tag" (left) and "3-tag" (right) category. Definition of "4-tag" and "3-tag" can be found in Section 7.3.4. First row is the leading large-R jet p_{T}. Second row is the leading large-R jet mass. Third row is the angular separation between two leading large-R jets in ϕ direction. Last row is the invariant mass of dijet system.

the Higgs candidate. Figure 7.7 show the impact of the correction on the 1 TeV signal sample. The sub-leading large-R jet is especially improved after the correction.

It should be noticed that muon-in-jet corrections are applied only after preselection as described in Section 7.3.3. This is mainly because the uncorrected jet four-momentum is used in the derivation and ntuple-making steps of the analysis. The muon-in-jet corrections therefore affect the large-R jet mass plane cuts to define the signal region and the final discriminating variable, $m(JJ)$.

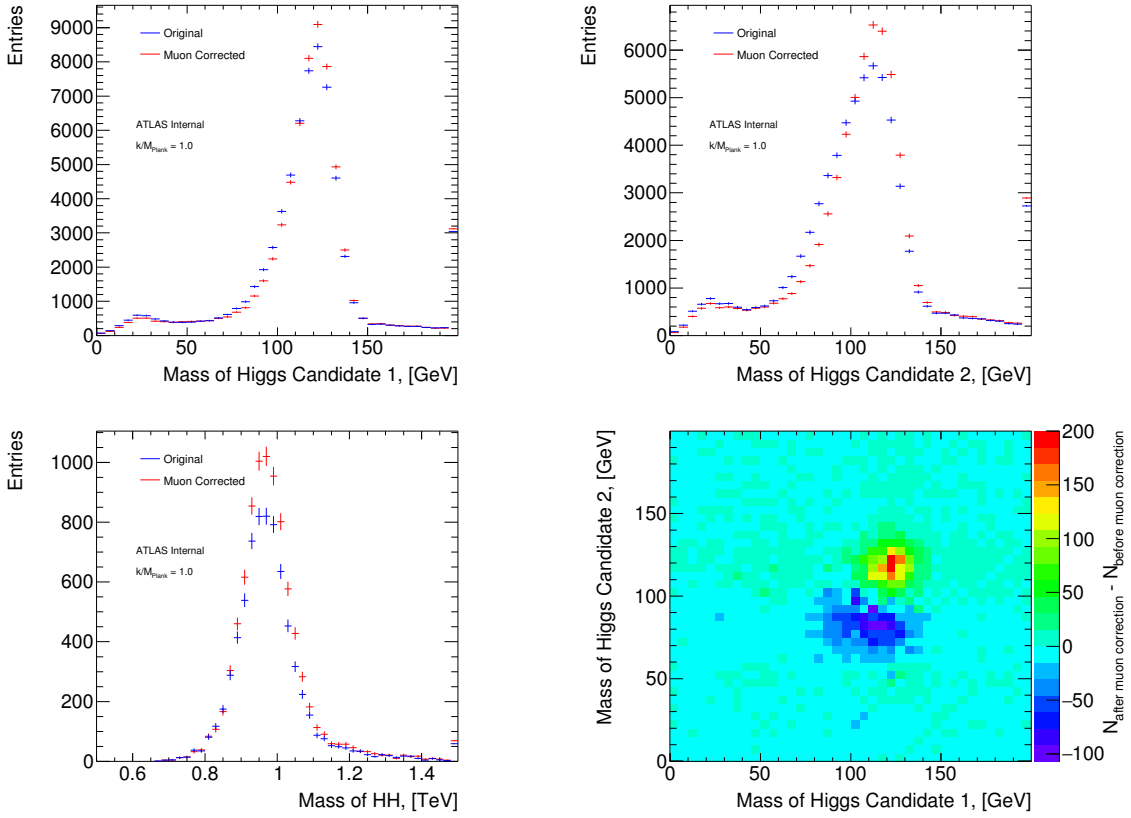


Figure 7.7: Kinematics of 1 TeV signal before and after muon-in-jet corrections. Both leading (top left) and subleading (top right) large-R jet mass, as well as invariant mass of dijet system (bottom left) gets improved mass resolution after the muon-in-jet correction. Events are therefore able to migrate from sideband / control region to the signal region, improving signal efficiency.

X_{hh} Cut

Following the muon-in-jet correction, signal region is defined using the expression:

$$X_{hh} = \sqrt{\left(\frac{m_{\mathrm{J}}^{\mathrm{lead}} - 124\ \mathrm{GeV}}{\sigma\left(m_{\mathrm{J}}^{\mathrm{lead}}\right)}\right)^2 + \left(\frac{m_{\mathrm{J}}^{\mathrm{subl}} - 115\ \mathrm{GeV}}{\sigma\left(m_{\mathrm{J}}^{\mathrm{subl}}\right)}\right)^2} \tag{7.1}$$

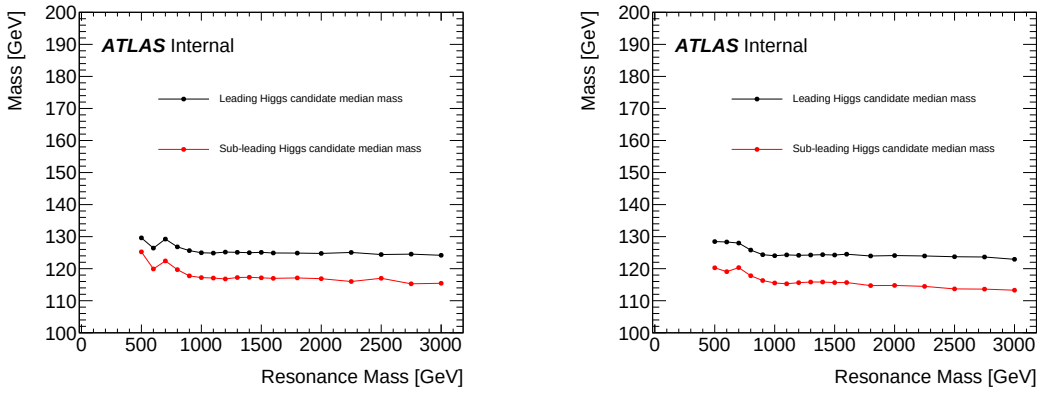


Figure 7.8: Median mass of leading (black) and sub-leading (red) large-R jet mass distribution for signal samples of different resonance masses, after 4 b-tag (left) and 3 b-tag (right) selection

The denominator of each term in the definition can be interpreted as a resolution on the reconstructed mass of 10%, hence X_{hh} can be interpreted as a χ^2 compatibility with the hh hypothesis. These $\sigma\left(m_{\mathrm{J}}\right)$ are only a rough approximation to the true resolution, but the X_{hh} requirement gives nearly optimal performance from experience in Run 1. The value of 124 and 115 GeV is taken from the median of mass distribution for leading and subleading large-R respectively, as shown in Figure 7.8. It is noticed that subleading large-R jet typically has a reconstructed mass biased downward due to the ordering of jet p_{T}. The energy losses result from neutrinos in leptonic b decays, cracks in the calorimeter, and other effects. Then the signal region is defined as $X_{hh} < 1.6$. The cut value inherits from Run 1, and is further validated by optimization studies in Run 2. An illustration of the shape of X_{hh} contours can be found in Figure 7.9.

Signal efficiency

This analysis covers multiple TeV of signal resonance masses, and the backgrounds fall steeply as a function of the reconstructed di-Higgs mass. Understanding how the signal efficiency trends with resonance mass can be helpful in gauging the natural limitations of this analysis coming from very boosted objects.

The acceptance times efficiency for each step of the event selection as outlined in this section is

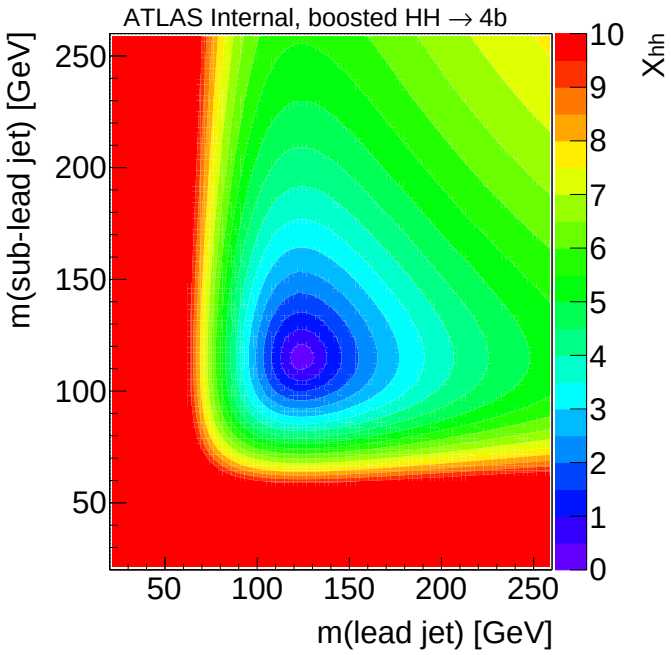


Figure 7.9: Values of the X_{hh} variables, which are shapes in the two-dimensional plane of the large-R jet masses used to defined signal region. A smaller value of X_{hh} indicates the jets are closer to the Higgs mass.

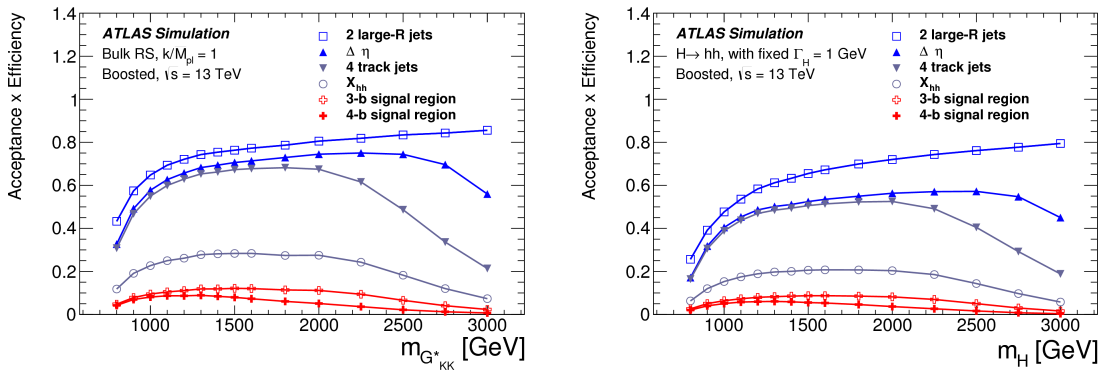


Figure 7.10: The selection efficiency as a function of resonance mass at each stage of the event selection for (left) $G^*_{\mathrm{KK}} \to hh \to b\bar{b}b\bar{b}$ and (right) $H \to hh \to b\bar{b}b\bar{b}$ decays in the boosted analysis. The "2 large-R Jets" curve includes the requirements that the leading jet has $p_{\mathrm{T}} > 350$GeV and that the large-R jets have a mass greater than 50 GeV. [165]

shown in Figure 7.10. An enlarged version of this plot focusing only in final signal region efficiency can be found in Figure 7.11. Above mass of $\sim$ 1 TeV, the reconstruction of high momentum large-R jets with small $\Delta\eta$ is efficient. Above mass of $\sim$2 TeV, the requirement of two track jets per large-R jet starts becoming inefficient due to merging of the track jets

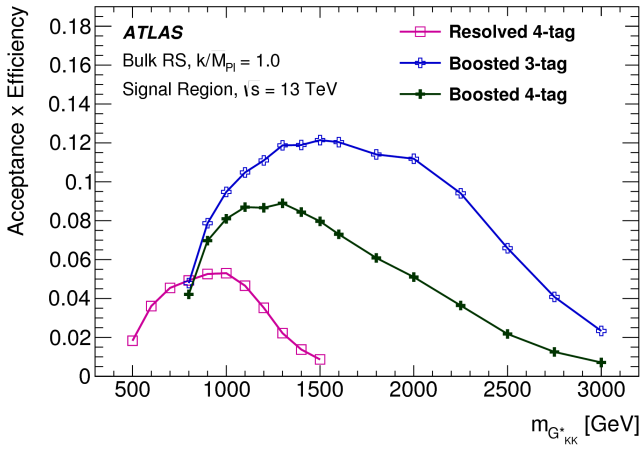


Figure 7.11: The selection efficiency as a function of resonance mass after the full event selection for G*KKhhbanti-bbanti-b decays in the resolved analysis as well as in the boosted analysis for the 3-tag and 4-tag selections. [182]

7.3.5 Cut Flow

Table 7.3 shows the cutflow numbers in data, two different graviton signal MC mass points, $t\bar{t}$ MC samples and $Z+$jets MC samples. The selection efficiency at various stages for RSG graviton $c = 1.0$ (narrow width scalar resonance) signal samples of all mass points can be found in Table 7.4 (Table 7.5). Cutflow numbers presented here are already the unblinded numbers. Numbers in efficiency table is provided as complementary to the efficiency plot shown in Figure 7.10.

Cut	Data	$m_G = 1$TeV	$m_G = 2$TeV	$t\bar{t}$	$Z + jets$
Initial	4017900	25.5	0.48	107087.3	7763.9
Pass trigger	2579869	24.4	0.48	39910.9	4336.1
Pass GRL	2233547	24.4	0.48	39910.9	4336.1
Pass Jet Cleaning	2233109	24.4	0.48	39903.1	4335.3
N(fiducial large-R jets)≥ 2	2202396	23.3	0.48	32345.2	4255.7
leading large-R jet $p_T > 350$ GeV	1873741	22.9	0.48	26511.7	3649.9
Both large-R jet $m > 50$ GeV	1854625	21.2	0.47	24369.8	3575.8
Both large-R jet $p_T < 1500$ GeV	1853601	21.2	0.46	24346.5	3572.9
$\lvert\Delta\eta(JJ)\rvert < 1.7$	1435273	20.8	0.44	20751.0	3265.8
≥ 2 track-jets per large-R jet	1224727	19.8	0.40	18234.5	2692.6
2 b-tags, $X_{hh} < 1.6$	1520	0.53	0.013	36.1	10.9
2 b-tags, $X_{hh} > 1.6$ and $R_{hh} < 35.8$	3956	0.46	0.0096	94.0	61.5
2 b-tags, $R_{hh} > 35.8$	28105	0.85	0.015	794.7	226.9
3 b-tags, $X_{hh} < 1.6$	316	3.4	0.067	46.7	2.0
3 b-tags, $X_{hh} > 1.6$ and $R_{hh} < 35.8$	724	2.2	0.042	98.0	7.7
3 b-tags, $R_{hh} > 35.8$	5043	2.4	0.040	672.5	31.8
4 b-tags, $X_{hh} < 1.6$	20	2.9	0.030	1.4	0.0
4 b-tags, $X_{hh} > 1.6$ and $R_{hh} < 35.8$	45	1.5	0.016	6.2	0.55
4 b-tags, $R_{hh} > 35.8$	279	0.90	0.012	34.8	3.4

Table 7.3: Cutflow of data, signal samples of two particular mass points, $t\bar{t}$ and $Z + jets$

Resonance Mass [GeV]	Mini-ntuple Skimming	2 large-R jets	$\Delta\eta$	4 Track-jet	Xhh	3-b Signal Region	4-b Signal Region
500	0.29	0.045	0.027	0.024	0.0034	0.00094	0.00020
600	0.44	0.090	0.055	0.051	0.010	0.0035	0.0021
700	0.55	0.22	0.13	0.12	0.035	0.014	0.011
800	0.63	0.43	0.33	0.31	0.12	0.048	0.042
900	0.68	0.57	0.49	0.47	0.19	0.079	0.070
1000	0.71	0.65	0.58	0.55	0.23	0.095	0.081
1100	0.73	0.69	0.63	0.60	0.25	0.10	0.087
1200	0.75	0.72	0.66	0.63	0.26	0.11	0.087
1300	0.76	0.74	0.68	0.65	0.28	0.12	0.089
1400	0.77	0.75	0.69	0.66	0.28	0.12	0.084
1500	0.77	0.76	0.71	0.67	0.28	0.12	0.080
1600	0.78	0.77	0.71	0.68	0.28	0.12	0.073
1800	0.79	0.79	0.73	0.68	0.27	0.11	0.061
2000	0.81	0.81	0.74	0.67	0.28	0.11	0.051
2250	0.82	0.82	0.75	0.62	0.24	0.094	0.036
2500	0.84	0.83	0.74	0.49	0.18	0.066	0.022
2750	0.84	0.84	0.70	0.34	0.12	0.041	0.013
3000	0.86	0.86	0.56	0.21	0.073	0.023	0.0071

Table 7.4: The selection efficiency for $G^*_{KK} \to hh \to b\bar{b}b\bar{b}$ events ($c = 1.0$) at each stage of the event selection.

Resonance Mass [GeV]	Mini-ntuple Skimming	2 large-R jets	$\Delta\eta$	4 Track-jet	Xhh	3-b Signal Region	4-b Signal Region
500	0.16	0.0036	0.00078	0.00072	0.00014	0.000030	0.0000100
600	0.29	0.017	0.0065	0.0062	0.0010	0.00034	0.000040
700	0.40	0.087	0.035	0.034	0.0083	0.0031	0.0019
800	0.49	0.26	0.17	0.16	0.063	0.026	0.021
900	0.55	0.39	0.32	0.31	0.12	0.051	0.040
1000	0.59	0.48	0.40	0.39	0.15	0.064	0.051
1100	0.63	0.54	0.45	0.44	0.17	0.073	0.058
1200	0.66	0.58	0.49	0.47	0.19	0.080	0.060
1300	0.67	0.61	0.50	0.48	0.20	0.083	0.061
1400	0.69	0.63	0.51	0.49	0.20	0.085	0.059
1500	0.70	0.65	0.52	0.51	0.21	0.087	0.055
1600	0.71	0.67	0.54	0.51	0.21	0.087	0.053
1800	0.73	0.70	0.55	0.52	0.21	0.085	0.046
2000	0.74	0.72	0.56	0.53	0.20	0.082	0.037
2250	0.76	0.74	0.57	0.49	0.19	0.070	0.026
2500	0.78	0.76	0.57	0.40	0.14	0.050	0.016
2750	0.79	0.78	0.55	0.29	0.097	0.030	0.0081
3000	0.81	0.79	0.45	0.19	0.058	0.016	0.0037

Table 7.5: The selection efficiency for $H \to hh \to b\bar{b}b\bar{b}$ events at each stage of the event selection.

7.4 Background Estimations

The primary backgrounds to this analysis in the "4-tag" signal region, in order of size, are multijet production ($\sim$ 93%), $t\bar{t}$ ($\sim$ 7%), and $Z+$jets ($<$ 1%), where the percentages are the expected fraction of the background coming from each source. In the "3-tag" signal region, the fractions are mutlijet $\sim$ 85%, $t\bar{t} \sim$ 15%, and $Z+$jets $<$ 1%. Multijet is by far the dominant background. However, there is no reliable high statistics Monte Carlo simulation sample in the specific phase space where this analysis focuses on and thus a data-driven background estimation is needed. For the $t\bar{t}$ background, Monte Carlo simulation samples of reasonable size are available, and thus can be used to guide an estimation of this background. $Z+$jets is small enough that we will rely on the Monte Carlo simulation of Z+heavy flavor jets. $ZZ \to b\bar{b}b\bar{b}$ has been estimated to be completely negligible using a particle-level analysis, with less than 0.5 events expected after three b-tags are required, which will be further heavily suppressed by the X_{hh} requirement.

The multijet background prediction relies on finding a dedicated sample orthogonal to signal region but with similar kinematics (at least in terms of variables of interest) to the shape of expected multijet background in signal region. This sample is identical to the signal region defined by the full selection, with the exception that the events must have two b-tagged track jets, instead of four or three. However, this "2-tag" region only supplies the shapes of the expected background while normalization is determined through a second dedicated sample, called *sideband* region. The sideband is obtained by doing the full analysis selection, with the exception that a different large-R jet mass cut is applied instead of $X_{hh} < 1.6$. To validate this data-driven approach, a third region orthogonal to regions defined above, which we call *control* region, is defined on the two-dimensional plane of leading and subleading large-R jet mass. The purpose of control region is to validate our background estimation strategy before unblinding, as well as provide estimation of systematic uncertainty related to background modeling.

A data-based estimation of the $t\bar{t}$ background normalization is also performed simultaneously with the mutlijet background normalization through a binned likelihood fit on carefully chosen kinematic variable in the sideband. Such fitting procedure is done independently for "3-tag" and "4-tag" regions. Shape of $t\bar{t}$ background in signal region would be estimated from MC simulation directly.

In the last, a smoothing procedure on background estimation in signal region is performed to overcome the fluctuation due to lack of statistics.

Details on determination of multijet ($t\bar{t}$) background shape and normalization can be found in Section 7.4.1 (Section 7.4.2). The fitting procedure for normalization determination would be detailed in Section 7.4.3. Validation of this data-driven background estimation strategy is shown in Section 7.4.4. Smoothing procedure is described in Section 7.4.5. Summary of event yields in each region can be found in Section 7.4.6.

7.4.1 Multijet Background

As mentioned above, the first step for multijet prediction is to find a region orthogonal to signal region but shares similar kinematics as multijet background in the signal region. This is done through the "2-tag" region, which is identical to "4-tag" or "3-tag" signal region, except exactly two track jets should be b-tagged.

It should be noted that the "2-tag" region is orthogonal to the signal regions. Similar to signal regions, four track jets are also required with two track jets on each side of Higgs candidate jet. Only two track jets are allowed to be b-tagged while the other two must not be b-tagged. In addition, the 2 b-tagged track jets are required to be associated to the same large-R jet to keep a high purity of multijet events. The unused $2b$ region where the 2 b-tagged track jets are associated to different large-R jets would be significantly contaminated by $t\bar{t}$ events. To further decouple $t\bar{t}$ component from multijet part, $t\bar{t}$ events in the "2-tag" region are subtracted from data using $t\bar{t}$ MC estimation.

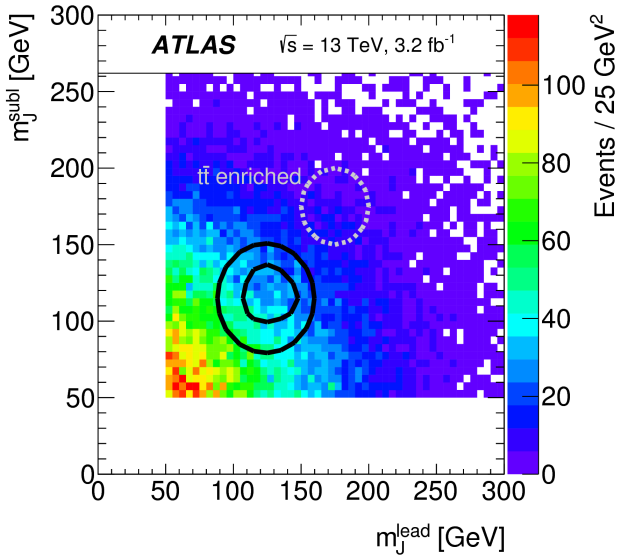


Figure 7.12: The m_J^{subl} vs. m_J^{lead} distribution for the 2-tag data sample used to model the multijet background in the boosted analysis. The signal region is the area surrounded by the inner black contour line, centered on $m_J^{subl} = 124$ GeV, $m_J^{lead} = 115$ GeV. The control region is the area inside the outer black contour line, excluding the signal region. The sideband region is the area outside the outer contour line. The kinematic region enriched in $t\bar{t}$ events is indicated by the dashed white contour line. [165]

Besides "2-tag" region, two additional regions, *sideband* (SB) and *control region* (CR), are defined for normalization estimation/correction and validation purpose. Both the SB and CR are chosen by requiring events to fail the X_{hh}, and are defined as regions in the 2D plane of the leading and sub-leading large-R jet mass plane as seen in Table 7.6, where $R_{hh} = \sqrt{(m_{J_1} - 124)^2 + (m_{J_2} - 115)^2}$.

The relation between SR, CR and SB is further illustrated in Figure 7.12. Both CR and SB are defined by a set of circle around $(124, 115)$ GeV, making sure SR, CR and SB are mutually exclusive to each other.

Region	Definition
Signal Region (SR)	$X_{hh} < 1.6$
Control Region (CR)	$R_{hh} < 35.8$ GeV and $X_{hh} > 1.6$
Sideband Region (SB)	$R_{hh} > 35.8$ GeV

Table 7.6: Definitions of the Signal (SR), Sideband (SB) and Control (CR) regions. X_{hh} is defined in Section 7.3.4 and R_{hh} is defined as $R_{hh} = \sqrt{(m_{J_1} - 124)^2 + (m_{J_2} - 115)^2}$.

With definition of all regions mentioned above, the multijet background estimation strategy is straightforward: Shape of the multijet background in data "4-tag" and "3-tag" of SR/CR/SB is extracted from the distribution in data "2-tag" of SR/CR/SB respectively (with $t\bar{t}$ subtracted). Since the normalization between "2-tag" and "4-tag" (or "3-tag") is different, a normalization transfer factor (called μ_{Multijet} sometimes below) needs to be applied, which is obtained in SB. More details on normalization transfer factor determination can be found in Section 7.4.3. In principle, such method can be applied on any kinematic variable, as long as the assumption that such kinematic variable is invariant under extrapolation holds, which is exactly the purpose of CR: After transfer factor is obtained from SB, one can test agreement between data and prediction from extrapolation in CR before applying this technique in the SR where we really care about. One implication of this strategy is that the shapes of multijet background estimation in "4-tag" and "3-tag" are the same since they are both derived from the same "2-tag" region, although the normalization transfer factors are independently estimated.

Since CR is used as a "proxy" of SR before unblinding, it should be as close to SR as possible in order to mimic SR kinematics as much as possible. Therefore, CR is arranged right next to SR. SB is defined as all regions beyond CR so that it is able to fully exploit a $t\bar{t}$ enriched region as illustrated as the grey dotted circle in Figure 7.12, as will be described in Section 7.4.3.

Determination of CR/SB Boundary

The determination of boundary between CR and SB is re-optimized with respect to Run 1. In the Run 1 analysis, this boundary was a box in the mass plane with $95 < m(J_1) < 160$ GeV and $85 < m(J_1) < 155$ GeV. Here a shape of boundary is chosen as a circle (R_{hh}) in order to avoid producing sharp kinematic edges in the jet mass distributions in the SB.

Next one needs to determine the center and radius of boundary between CR and SB. The general rule is that 1) normalization transfer factor determined in SB should be applicable on both CR and SR 2) CR is a good "proxy" of SR so that the results in CR is reliable in determining the validity of our strategy estimation method (and kinematic variable applicable for this method). The center is

naturally chosen to be same as SR to avoid any bias. To determine the radius, a handful of factors are considered when optimizing the CR/SB boundary:

- The leading large-R jet in the CR should have mass less than 160 GeV. This is to ensure minimal contamination of $t\bar{t}$ since not many $t\bar{t}$ events are expected in the SR.
- The leading and sub-leading large-R jets in the control region should have average masses as close as possible the expected Higgs masses in the SR. For the leading (sub-leading) jet, this means an average mass near 124 (115) GeV. This ensures a symmetric sampling of topology where the jets have higher and lower masses than the Higgs, so that the average topology of the CR is similar to the SR.
- The statistics of the CR should be sufficient for validating that the predicted shapes of the multijet background agree with the data. We choose that the CR statistics be twice the SR statistics.

In addition to these criteria, it is important that both the leading and subleading jets have a similar mass profile in the sideband region, and the event kinematics in the sideband must be as representative as possible of the events in the control region. If the event kinematics in the sideband are not representative, then the normalization transfer factor derived in the sideband may not accurately estimate the actual $2b$ to $4b$ or $3b$ ratio in the control region and signal regions. Following the Run 1 study, we define the "medium mass region" as $m \in \{60,\ 150\}$ GeV. We study the ratio of the number of sideband to control region events in the $2b$ sample in the medium mass region comparing the leading and subleading jet. The exact definition of this ratio is shown below where the region definition can be found in the left of Figure 7.13:

$$\frac{(B+H)-(D+F)}{E_{CR}} = \text{medium mass ratio difference} \tag{7.2}$$

where B, H, D and F are the number of $2b$ events in those regions and E_{CR} is the number of $2b$ events in the portion of the control region contained within region E minus the number of events in the signal ellipse (represented by a red area in the figure).

Thus, for each control region examined, E_{CR} is the number of events in the control region and inside of the box E. The right plot of Figure 7.13 shows the fractional difference in μ_{Multijet} derived in the sideband and the value of μ_{Multijet} had it been derived directly in the control region versus the medium mass ratio difference. Each point in this figure corresponds to a possible choice of control region radius (the central position could in principle also be varied, but is kept fixed here). As we can see from this figure, as the medium mass difference decreases, so does the fractional difference in μ_{Multijet}. Therefore, choices with smaller medium mass difference also minimize μ_{Multijet} differences between SB and CR/SR.

The boundary which was found to best satisfy the above criteria is $R_{hh} < 35.8$ GeV.

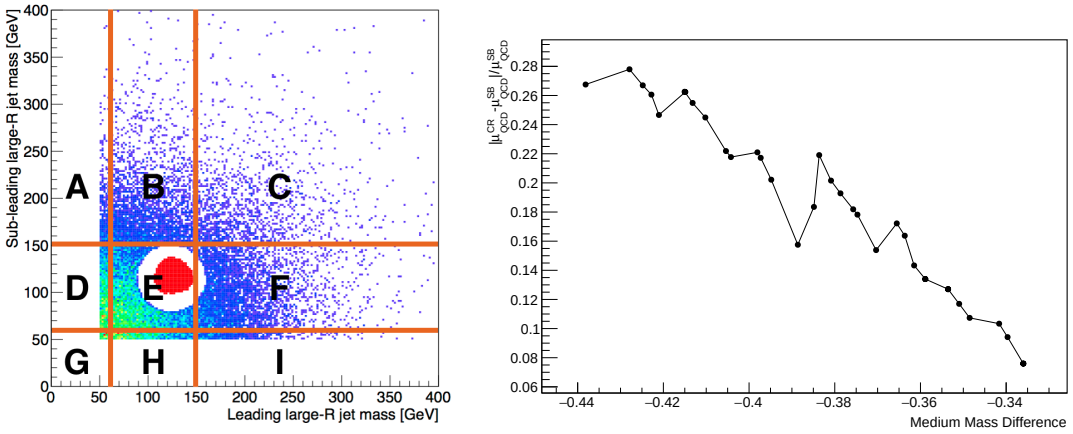


Figure 7.13: (Left) Regions defining different areas of the sideband. The white box is the control region, while the red area is the signal region. The regions used for the middle mass region method are shown with orange lines and labels. E_{CR} used in Equation 7.2 corresponds to the number of $2b$ events in the portion of the white control region contained within region E. (Right) Fractional difference between normalization transfer factor derived in the sideband and $2b$ to $4b$ ratio in the control region, versus the difference in medium mass events in the sideband and medium mass events in the control region.

As a final note, we want to avoid possible signal contamination in the $2b$ regions used in our multijet predictions. The primary concern for this contamination is in the SR prediction at high mass, where the expected backgrounds are small. As such, in the $2b$ sample in the SR, we do not use (or look at) events above 2 TeV. For background predictions above 2 TeV, we will perform a background smoothing up to 2 TeV, and extrapolate above 2 TeV (see Section 7.4.5). The choice of 2 TeV as a transition point is determined by ensuring that the signal contamination in dijet mass regions is at the few percent level or less, even when scaling by expected signal strength limits as determined from Run 1.

7.4.2 $t\bar{t}$ Background

The number of $t\bar{t}$ events in the signal region coming mainly from the all-hadronic decay mode (with a smaller contribution from the leptonic decay mode) comprising of around 7% (15%) of the inclusive total background in the $4b$ ($3b$) regions due to the high p_{T} threshold imposed on the leading large-R calorimeter jet. In the sideband region, roughly 13% of the data are $t\bar{t}$ events in each the $4b$ and $3b$ sidebands. A good estimation on both normalization and shape of $t\bar{t}$ events is important, not only in the SR but in CR/SB as well, since the normalization and the shape of $t\bar{t}$ events in the sideband region can affect the multijet estimation in SR based on our strategy.

For the normalization of the $t\bar{t}$ background, we start with the MC prediction estimated by scaling

the MC sample by the cross section and luminosity, and then applying the boosted event selection as described above. To account for possible differences between data and MC, a normalization scaling factor (some times called $\alpha_{t\bar{t}}$ below) is derived from a fit to data in the sideband region. Different from μ_{Multijet}, which is the transfer factor from "2-tag" to "4-tag" (or "3-tag"), $\alpha_{t\bar{t}}$ is a normalization correction factor to be applied on the $t\bar{t}$ MC in "4-tag" or "3-tag" directly. Although estimated in the SB, $\alpha_{t\bar{t}}$ is to be applied also in the CR and SR. Separate fits are done in the $4b$ and $3b$ SB.

For the shape of the $t\bar{t}$ background, MC estimation is used directly. However, there are not sufficient MC statistics in the $4b$ SR to get a reasonable shape estimate. As a result, the shape of $t\bar{t}$ distribution in $4b$ signal region is taken from MC $t\bar{t}$ shape in $3b$ signal region, while normalization is still determined in $4b$ as described above. It should be noticed that such trick is applied in the shape of $4b$ signal region only , while $4b$ CR/SB uses $t\bar{t}$ MC directly since statistics is enough in CR/SB. A comparison between the $3b$ and $4b$ shapes for the dijet invariant mass distributions in SR can be found in Figure 7.14. The shapes are compatible within given statistical uncertainty. Any differences between these distributions will be used as one of systematic uncertainties.

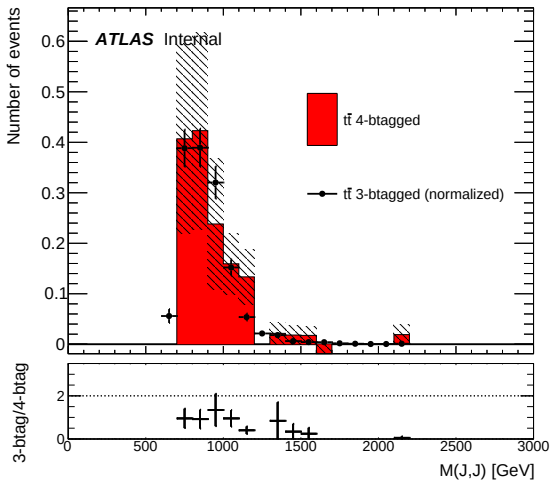


Figure 7.14: comparison between the $3b$ and $4b$ shapes for the dijet invariant mass distributions (the final discriminant) in the SR

7.4.3 Fitting Procedure for Multijet and $t\bar{t}$ Normalization

This section describes the fitting procedure to derive normalization transfer factor for multijet (μ_{Multijet}) and $t\bar{t}$ ($\alpha_{t\bar{t}}$) simultaneously from SB.

The expected yields from all backgrounds in a given region (SB / CR / SR) can be described as:

$$N_{\text{bkg}}^{3(4)\text{-tag}} = \mu_{\text{Multijet}}^{3(4)\text{-tag}} N_{\text{Multijet}}^{2\text{-tag}} + \alpha_{t\bar{t}}^{3(4)\text{-tag}} N_{t\bar{t}}^{3(4)\text{-tag}} + N_{Z+\text{jets}}^{3(4)\text{-tag}} , \tag{7.3}$$

where $N^{\text{2-tag}}_{\text{Multijet}}$ is the number of multijet events in the 2-tag sample, $N^{\text{3(4)-tag}}_{t\bar{t}}$ and $N^{\text{3(4)-tag}}_{Z+\text{jets}}$ are the numbers of events predicted by the 3(4)-tag $t\bar{t}$ and Z+jets MC samples. $N^{\text{2-tag}}_{\text{Multijet}}$ is further obtained by subtracting $t\bar{t}$ and $Z+$jets contribution in "2-tag" region, as estimated from MC, from total yields in "2-tag" sample in data. Parameter μ_{Multijet} corresponds to the ratio of multijet event yields in the 3(4)-tag and 2-tag samples. Parameter $\alpha_{t\bar{t}}$ is a scale factor designed to correct the $t\bar{t}$ event yield estimated from the MC simulation.

Equation 7.3 can be applied in SB/CR/SR, but with different purpose: When applied in SB, $N^{\text{3(4)-tag}}_{\text{bkg}}$ is set to be the total yields of data (since we do not expect any signal here) so that μ_{Multijet} and $\alpha_{t\bar{t}}$ can be fit; When applied in CR, $N^{\text{3(4)-tag}}_{\text{bkg}}$ is also set to be the total yields of data (again since we do not expect any signal here) while μ_{Multijet} and $\alpha_{t\bar{t}}$ derived in SB is used so that one can do the validation by comparing left side and right side of Equation 7.3; When applied in SR, $N^{\text{3(4)-tag}}_{\text{bkg}}$ is the estimated background so that one can compare with actual data after SR is ublinded.

When applied in SB, there are two unknown parameter according to Equation 7.3. Therefore, a binned maximum likelihood fit is employed to find the values of μ_{Multijet} and $\alpha_{t\bar{t}}$ simultaneously. The correlation matrix between these two parameters can also be extracted during the fitting. The Maximum likelihood fit is performed in $3b$ and $4b$ independently since these are two statistically independent sample.

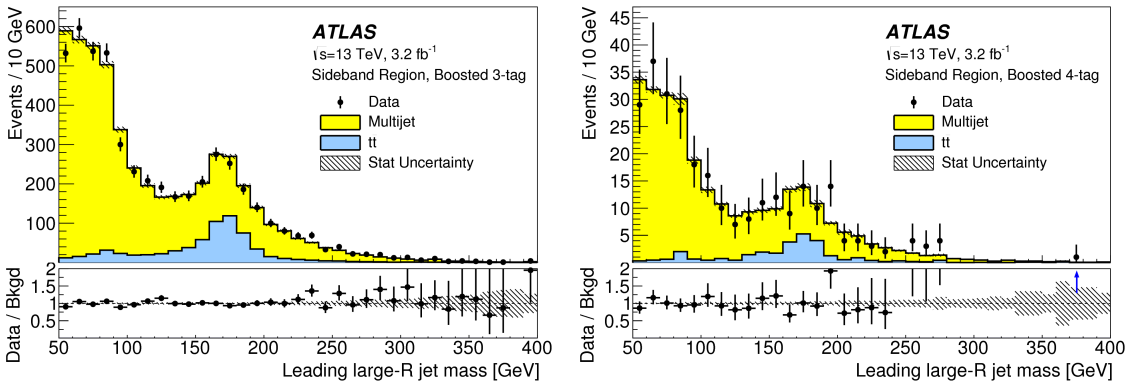


Figure 7.15: The leading large-R jet mass distribution in the hh sideband region for data (points) and background estimate (histograms) in the boosted analysis for events in the (left) 3-tag and (right) 4-tag categories. The shape of the multijet distributions is taken from the 2-tag region and is fitted to the data. The hatched bands represent the statistical uncertainty in the total background estimate. [165]

The fit is performed on the leading p_{T} jet mass spectrum in the sideband region, as it has the best separation between multijet and $t\bar{t}$ shapes. Due to the $p_{\text{T}} > 350$ GeV cut imposed on the leading large-R jet, the hadronic top quark is likely to be fully reconstructed inside the large-R jet. Therefore the leading jet mass in the $t\bar{t}$ sample should have a clean peak around top quark mass in the sideband region. Figure 7.15 shows the post-fit spectrum of the leading large-R calorimeter

jet mass in the "4-tag" and "3-tag" sideband regions. The normalization of $t\bar{t}$ is constrained by the top quark mass peak around 170 GeV. The shapes of the data is also well modeled by the predicted background. Fitted value of μ_{Multijet} and $\alpha_{t\bar{t}}$ along with their errors and correlations can be found in Table 7.7. The fitting errors on μ_{Multijet} and $\alpha_{t\bar{t}}$ will be applied as uncertainties with correlation matrix taken into account.

Sample	μ_{qcd}	$\alpha_{t\bar{t}}$	$\rho(\mu_{qcd},\ \alpha_{t\bar{t}}) = \frac{Cov(\mu_{qcd},\ \alpha_{t\bar{t}})}{\sigma_{\mu_{qcd}}\sigma_{\alpha_{t\bar{t}}}}$
$4b$ SB	0.00913±0.00073	0.82±0.39	-0.58
$3b$ SB	0.1598±0.0032	1.016±0.093	-0.60

Table 7.7: Background normalization transfer parameters (μ_{Multijet} and $\alpha_{t\bar{t}}$) estimated from fits in the leading jet mass distributions in $4b$ and $3b$ sideband regions.

The robustness of fitting procedure is checked by repeating with different binning on large-R jet mass spectrum. By default, the fit is done on leading large-R jet mass with a binning of 10 GeV. This is compared with two variations where the large-R jet mass spectrum is binned with 20 GeV and 50 GeV. The fitting result for both default binning and varied binning can be found in Table 7.8 (Table 7.9) for "4-tag" ("3-btag") region. The result shows that all fitted μ_{Multijet} and $\alpha_{t\bar{t}}$ between different binnings are consistent with each other within statistical uncertainty.

Bin Width	μ_{qcd}^{4b}	$\alpha_{t\bar{t}}^{4b}$	$Correlation^{4b}$
10 GeV (Nominal)	0.00913±0.00073	0.82±0.39	-0.58
20 GeV	0.00877±0.00075	1.10±0.42	-0.59
50 GeV	0.00881±0.00078	1.07±0.45	-0.63

Table 7.8: Fited μ_{Multijet} and $\alpha_{t\bar{t}}$ for different binning of leading large-R jet mass spectrum for boosted "4-tag" region

Bin Width	μ_{qcd}^{3b}	$\alpha_{t\bar{t}}^{3b}$	$Correlation^{3b}$
10 GeV (Nominal)	0.1598±0.0032	1.016±0.093	-0.60
20 GeV	0.1601±0.0033	1.004±0.098	-0.62
50 GeV	0.1601±0.0034	1.00±0.10	-0.64

Table 7.9: Fited μ_{Multijet} and $\alpha_{t\bar{t}}$ for different binning of leading large-R jet mass spectrum for boosted "3-tag" region

Comparison between Data and Background Prediction in Sideband

While the fitting procedure is done on leading large-R jet mass spectrum in SB explicitly, this background estimation approach can be applied on any kinematic variable. Since the normalization

between data and prediction in SB agrees by construction (due to the fitting), shapes are the feature of prediction here.

Comparison between data and prediction in sideband for selected kinematic variables can be found in Figure 7.16 and 7.17. The quality of prediction is good without systematic deviation observed. Hence no further correction is needed.

7.4.4 Validation in Control Region

This section shows comparisons of data with the prediction of multijets and $t\bar{t}$ in the control region (CR). As mentioned above, one of the purposes for CR is the validation of our background estimation strategy in a region that is 1) orthogonal to SB where the fit is performed so that we are not biased (in particular on normalization) and 2) orthogonal but kinematically similar to SR so that such validation is meaningful.

Comparison between data and prediction in CR for selected kinematic variables can be found in Figure 7.18 and 7.19. In CR, both normalization and shape are the features of prediction. One can see that quality of the prediction is generally good, and no clear systematic biases are observed.

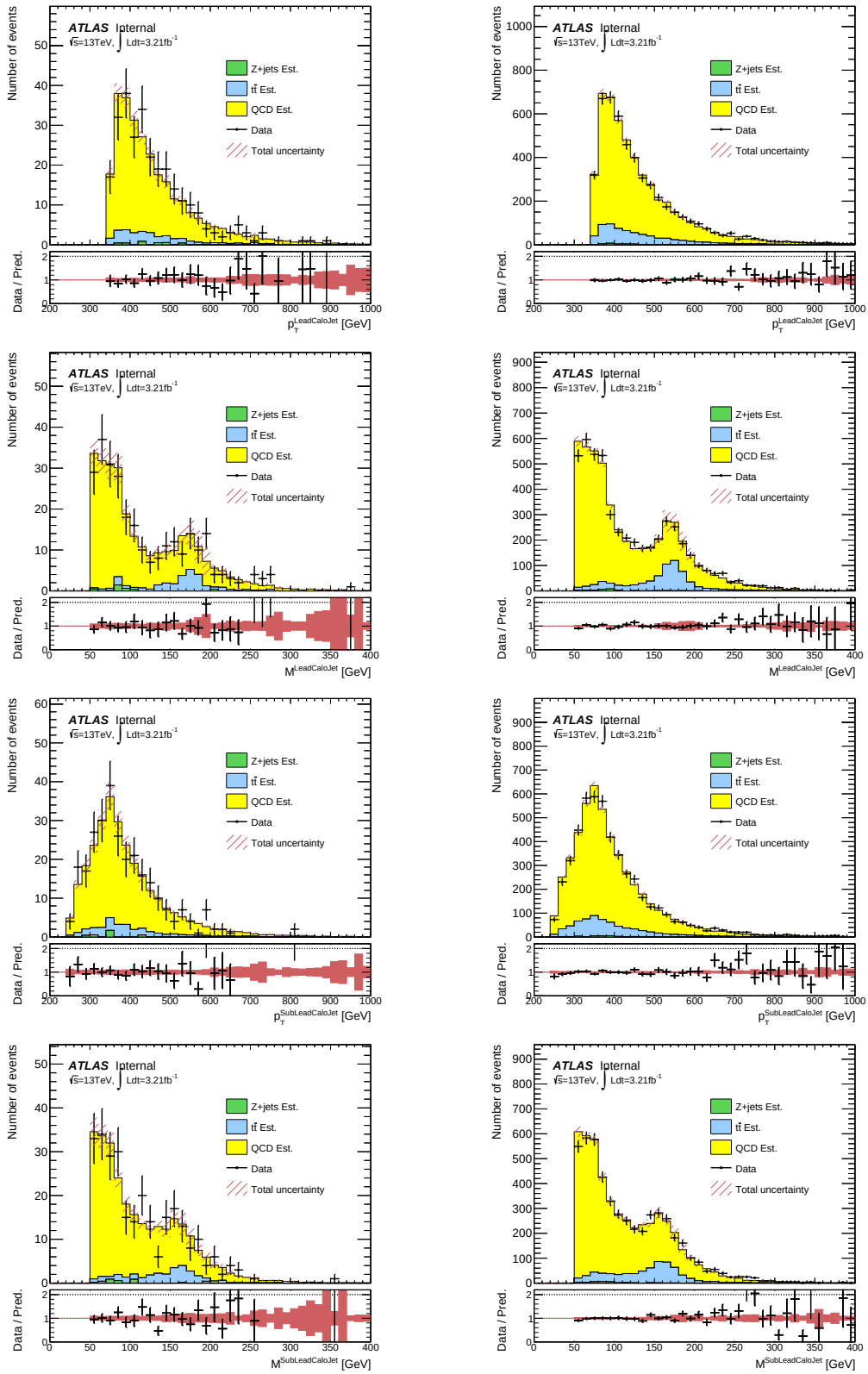


Figure 7.16: Distribution of leading large-R jet p_{T} (first row), leading large-R jet mass (second row), subleading large-R jet p_{T} (third row) and subleading large-R jet mass (fourth row) between data and prediction in "4-tag" (left) and "3-tag" (right) sideband.

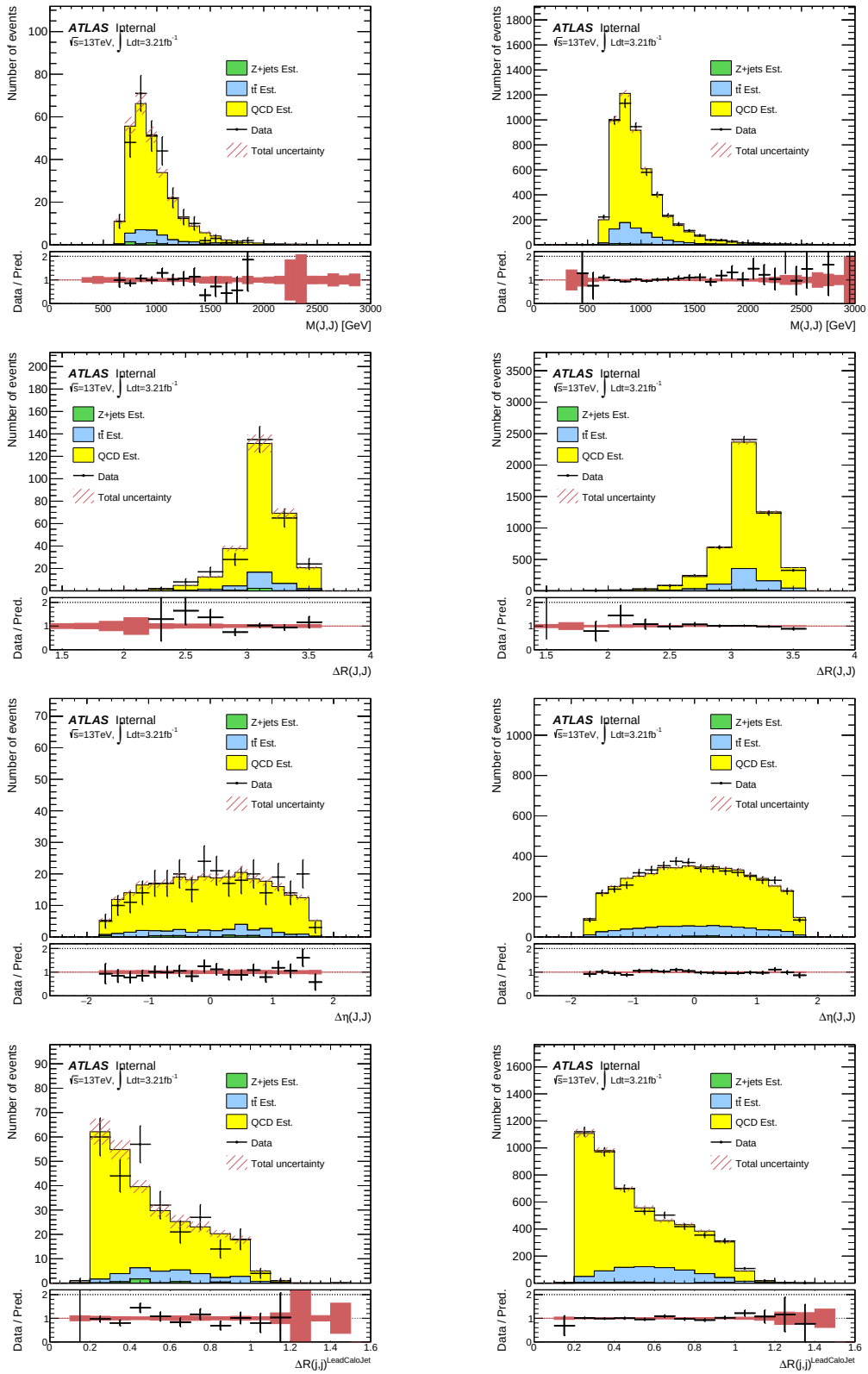


Figure 7.17: Distribution of dijet invariant mass (first row), ΔR between dijet (second row), $\Delta\eta$ between dijet (third row) and ΔR between two leading track jets associated with leading large-R jet (fourth row) between data and prediction in "4-tag" (left) and "3-tag" (right) sideband.

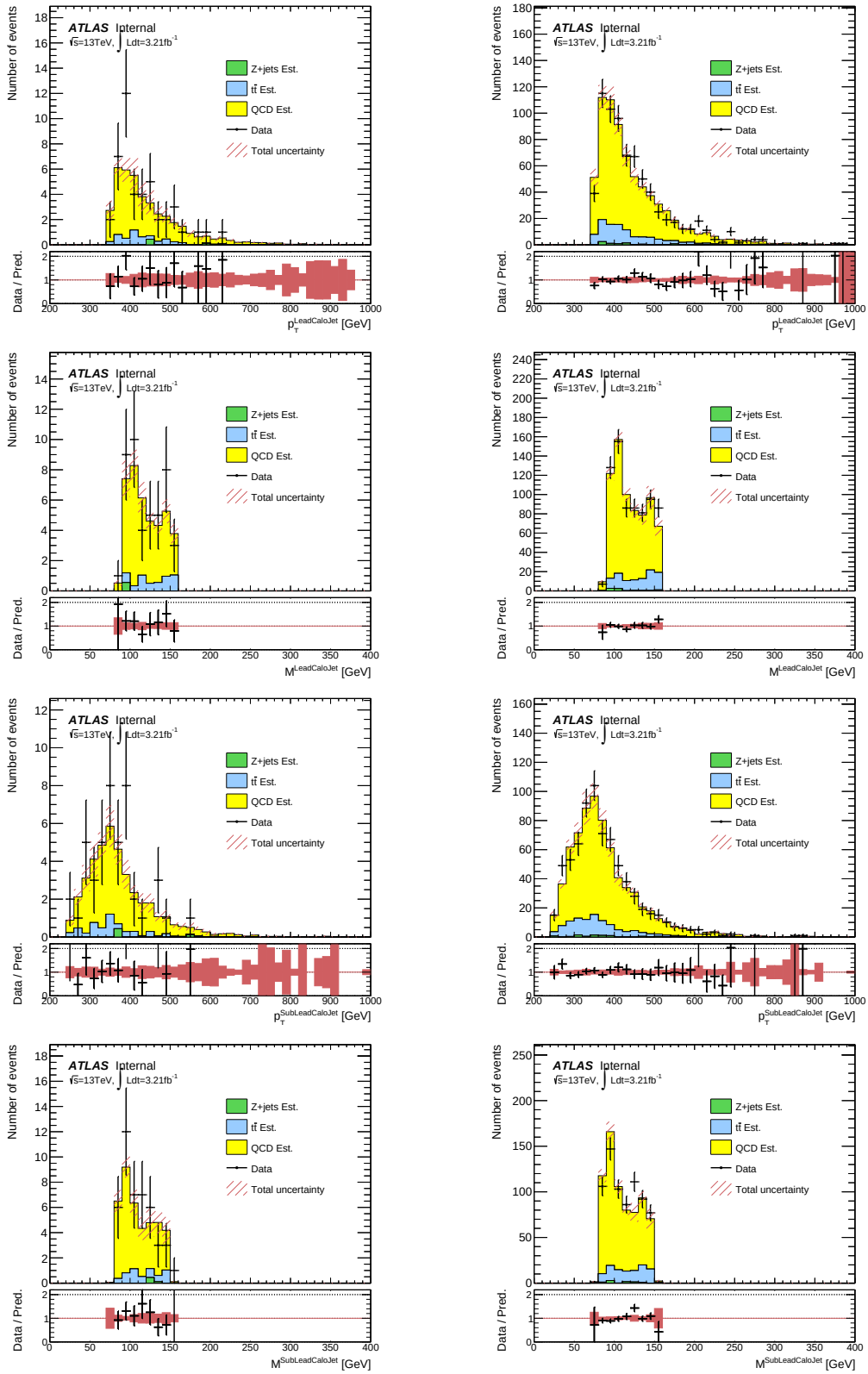


Figure 7.18: Distribution of leading large-R jet p_{T} (first row), leading large-R jet mass (second row), subleading large-R jet p_{T} (third row) and subleading large-R jet mass (fourth row) between data and prediction in "4-tag" (left) and "3-tag" (right) control region.

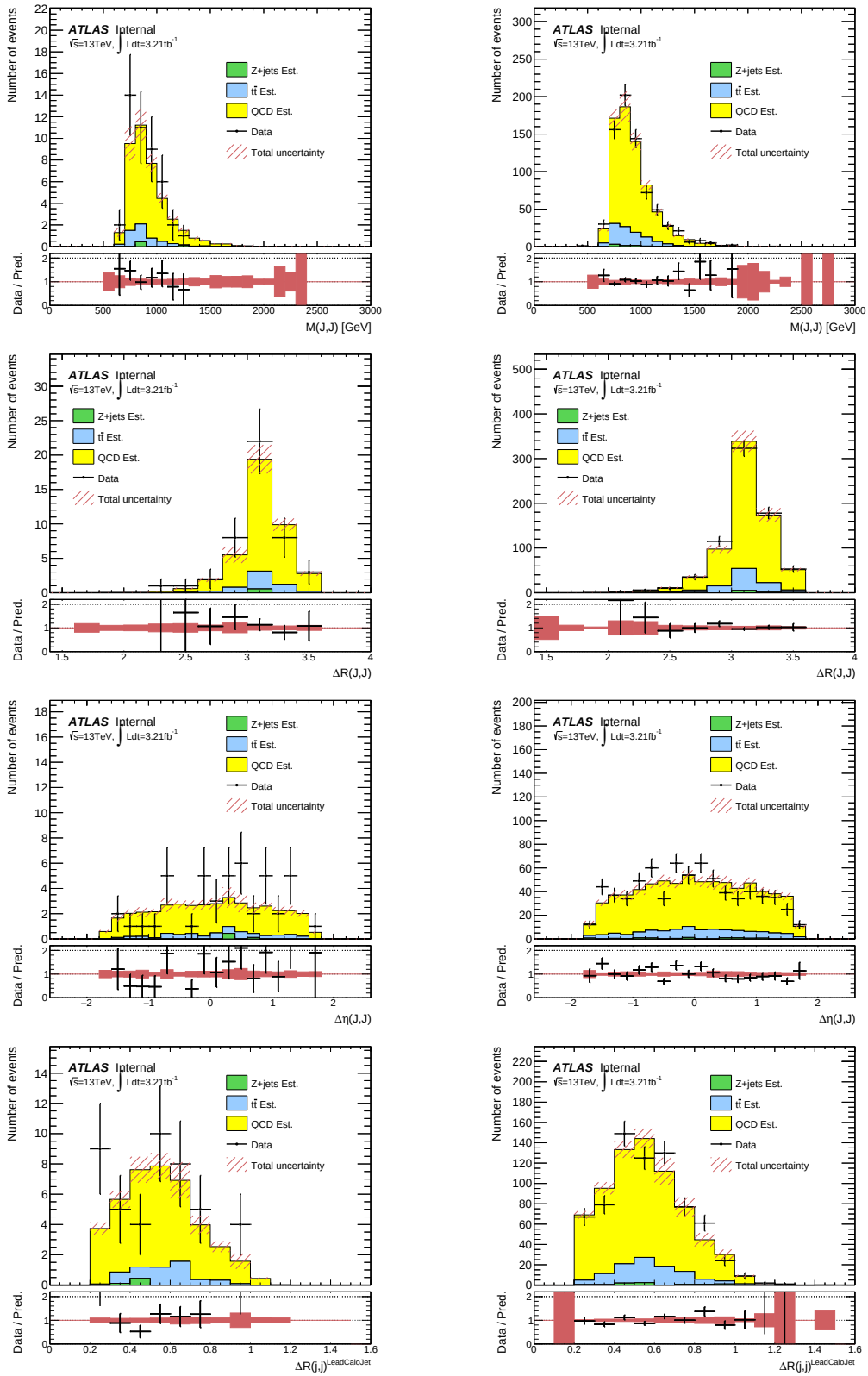


Figure 7.19: Distribution of dijet invariant mass (first row), ΔR between dijet (second row), $\Delta\eta$ between dijet (third row) and ΔR between two leading track jets associated with leading large-R jet (fourth row) between data and prediction in "4-tag" (left) and "3-tag" (right) control region.

7.4.5 Prediction in Signal Region

Final Discriminant Variable

In a search-type analysis, one needs to define a final discriminant variable in the signal region as the major features to separate background and potential signals. In particular, such variable would be used as the only input to further statistical analysis as presented in Section 7.6.

As a hadronic resonance search, invariant mass of dijet system (M_{JJ}) is a nature choice as such final discriminant variable coming from resonances would appears as a local "bump" on the falling background distribution, as long as the intrinsic mass resolution is small and smearing effect from detector resolution effect is not severe. Furthermore, a scaled M_{JJ} is introduced for signal region: Both Higgs candidate jets four momentum are scaled by m_h/m_J where $m_h = 125$ GeV and m_J is the Higgs candidate jet mass. Then invariant mass is re-calculated using this scaled four momentum. It should be noticed that such scaling is done after SR/CR/SB has been defined with the un-scaled four momentum, and it is done only in signal region. Therefore, the scaled invariant mass is simply another different kinematic feature of the event that is not involved in any part of the event selection. Unless explicitly mentioned, term "invariant mass" in the signal region refers to the scaled version in the rest of this chapter.

The distribution of invariant mass in SR can be found in Figure 7.20. Expected limits by using the unscaled and scaled dijet mass distribution are computed and no significant difference is found between two variables. Since the scaled one is chosen by several other di-Higgs analysis (with different final states), we decide to use the same variable in order to ease the process of any potential statistical combination in the future.

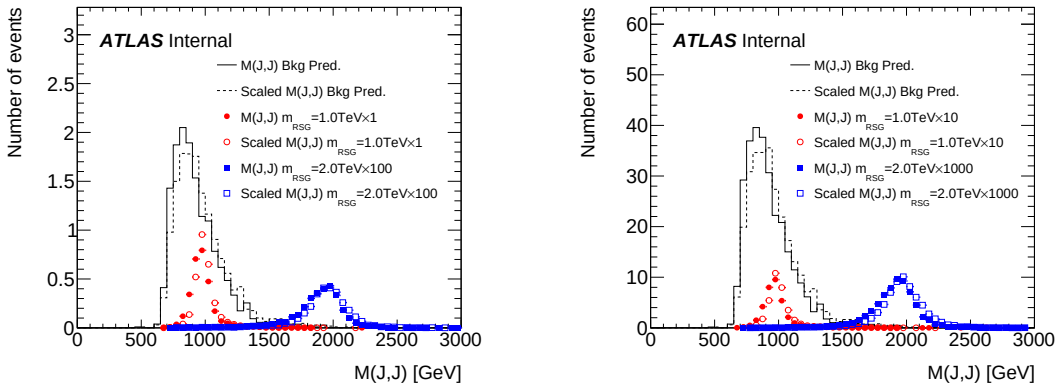


Figure 7.20: Scaled invariant mass of dijet system for the $4b$ (left) and $3b$ (right) signal regions. For comparison, the unscaled distributions are shown on the same plot

Smoothing in Signal Region

Due to the limited $2b$ statistics at high dijet invariant mass above 1500 GeV and the limited $t\bar{t}$ statistics above 1100 GeV, an exponential fit is performed to smooth the tail of dijet invariant mass in the signal region. The $t\bar{t}$ component of total background in signal region is fit with $y = \exp(a_{t\bar{t}}x + b_{t\bar{t}})$ functional form in the range $900 < M_{JJ} < 2000$ GeV, without parameter constraints. The multijet component of total background in signal region is fit with $y = \exp(a_{\text{Multijet}}x + b_{\text{Multijet}})$ in the range $950 < M_{JJ} < 2000$ GeV.

As mentioned earlier, the choice of smoothing upper bound of 2 TeV to avoid possible signal leakage in the region where expected background is very small (less than 1). The lower bound of smoothing fit is chosen such that only falling part of background is smoothed. Smoothing result can be found in Figure 7.21. While the fitting quality is good for multijet component, tail of $t\bar{t}$ component is underestimated by the smoothing procedure. This would be taken into account through the systematic uncertainties related to choice of smoothing function and range as would be discussed in Section 7.5.

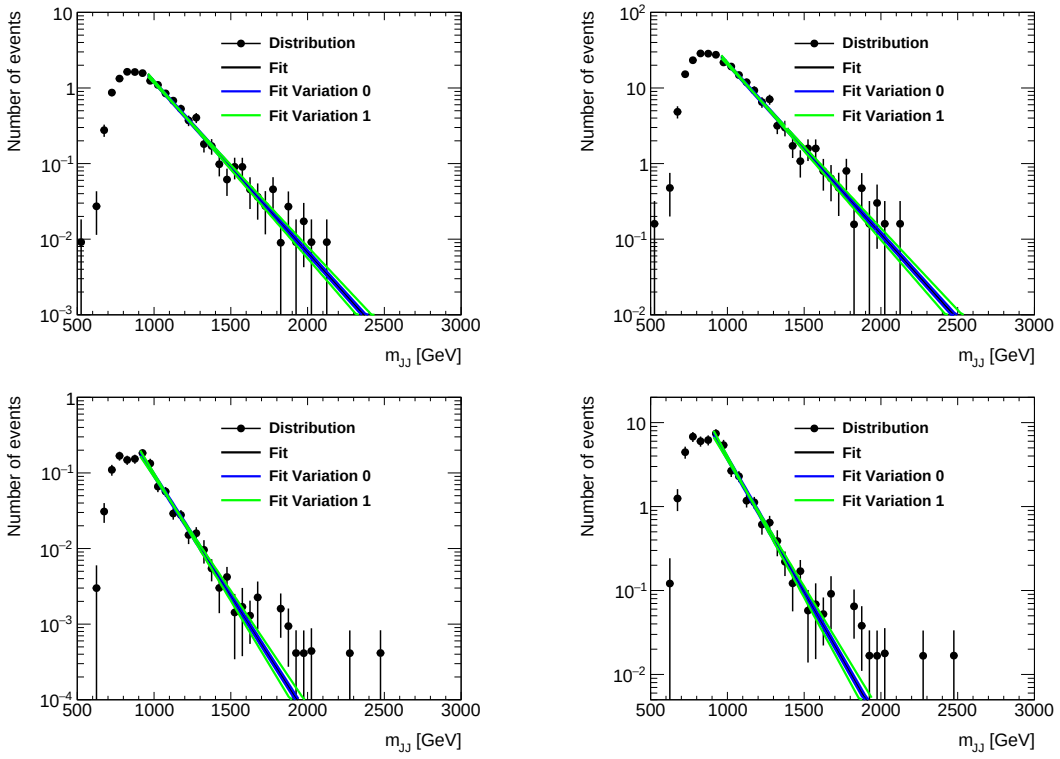


Figure 7.21: Smoothed background estimations for the $4b$ (left) and $3b$ (right) signal regions. Multijet is shown on top, and $t\bar{t}$ is on bottom. Only smoothing statistical uncertainties are shown here.

Predictions

The final signal region prediction, using scaled di-jet mass distribution, with all statistical and systematic uncertainties, are shown in Figure 7.22 (Figure 7.23) before (after) smoothing.

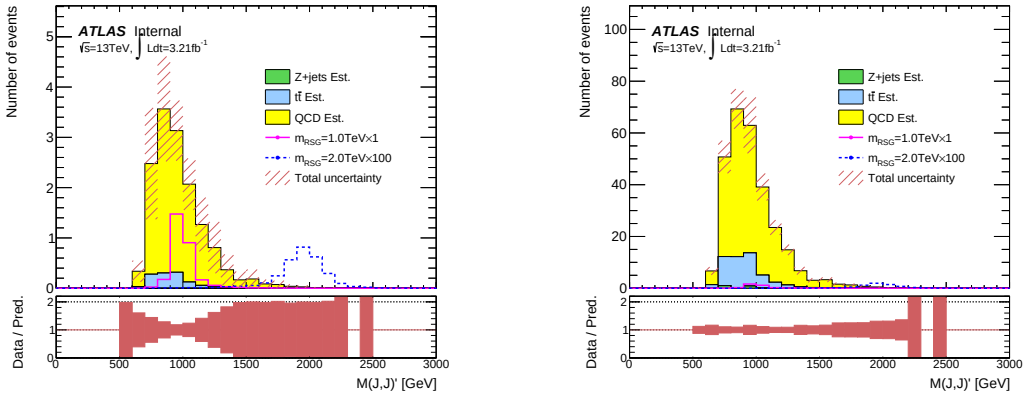


Figure 7.22: Background prediction for $4b$ (left) and $3b$ (right) signal region using scaled dijet invariant mass before smoothing. The uncertainty band includes all statistical and systematic uncertainties.

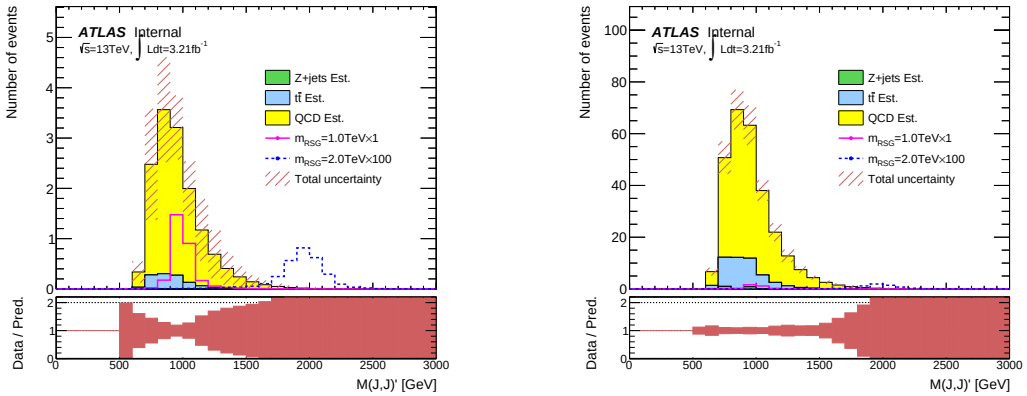


Figure 7.23: Background prediction for $4b$ (left) and $3b$ (right) signal region using scaled dijet invariant mass after smoothing. The uncertainty band includes all statistical and systematic uncertainties.

7.4.6 Event Yields

The event yield results showing the estimated backgrounds, the signal predictions, and the data observations in the $4b$ and $3b$ signal regions, control regions, and sideband regions can be found

in Table 7.10 and Table 7.11 respectively for reference. A succinct version of yield tables in signal region only can be found in Table 7.35.

	SR	SB	CR
QCD Est.	13.45±0.36±2.40	247.4±1.5±25.0	34.71±0.58±3.49
$t\bar{t}$ Est.	1.159±0.054±0.977	28.4±1.5±21.0	5.08±0.67±2.99
$Z + jets$	0.0±0.0±0.0	3.4±1.2±1.2	0.55±0.45±0.58
Total Bkg Est.	14.61±0.36±2.38	279.2±2.5±16.2	40.34±1.00±3.15
Data	20±4.5±0.0	279±16.7±0.0	45±6.7±0.0
$c = 1.0$,$m = 1.0TeV$	2.869±0.032±1.057	0.904±0.018±0.320	1.458±0.023±0.612
$c = 1.0$,$m = 1.5TeV$	0.2902±0.0033±0.1167	0.1034±0.0020±0.0395	0.1403±0.0023±0.0649
$c = 1.0$,$m = 2.0TeV$	0.02995±0.00045±0.01276	0.01207±0.00028±0.00490	0.01606±0.00033±0.00777
$c = 2.0$,$m = 1.0TeV$	10.08±0.12±3.71	3.294±0.066±1.152	5.184±0.083±2.135
$c = 2.0$,$m = 1.5TeV$	0.963±0.011±0.388	0.3399±0.0067±0.1328	0.4898±0.0080±0.2246
$c = 2.0$,$m = 2.0TeV$	0.1014±0.0019±0.0415	0.0410±0.0012±0.0165	0.0562±0.0014±0.0238
2HDM,$m = 1.0TeV$	83.3±1.2±31.1	28.61±0.69±9.99	45.27±0.87±18.36
2HDM,$m = 1.5TeV$	4.506±0.061±1.849	1.735±0.038±0.659	2.241±0.043±1.007
2HDM,$m = 2.0TeV$	0.2761±0.0046±0.1159	0.1195±0.0030±0.0476	0.1512±0.0034±0.0656

Table 7.10: Expected yields for backgrounds in the $4b$ signal region, control region, and sideband region, along with the observed number of data events. The signal predictions for RS $m = 1.0, 1.5, 2.0$ TeV of both $c = 1.0$ and $c = 2.0$, and for narrow width heavy Higgs of $m = 1.0, 1.5, 2.0$ TeV are also listed. For each predicted value, the first uncertainty listed is statistical, and the second is the sum in quadrature of all systematic uncertainties.

	SR	SB	CR
QCD Est.	235.4±6.2±12.5	4327.9±26.9±157.1	607.3±10.1±22.9
$t\bar{t}$ Est.	47.5±2.2±21.7	683.5±8.1±142.7	99.6±3.1±49.4
$Z + jets$	2.0±1.1±1.9	31.8±3.7±10.4	7.7±1.8±5.0
Total Bkg Est.	284.8±6.7±18.2	5043.2±28.3±70.8	714.6±10.7±50.7
Data	316±17.8±0.0	5043±71.0±0.0	724±26.9±0.0
$c = 1.0$,$m = 1.0TeV$	3.437±0.035±0.874	2.406±0.030±0.288	2.195±0.028±0.497
$c = 1.0$,$m = 1.5TeV$	0.4501±0.0041±0.1303	0.2771±0.0032±0.0351	0.2612±0.0031±0.0771
$c = 1.0$,$m = 2.0TeV$	0.06679±0.00067±0.01854	0.04004±0.00052±0.00718	0.04211±0.00053±0.01175
$c = 2.0$,$m = 1.0TeV$	12.68±0.13±3.09	8.92±0.11±1.00	7.96±0.10±1.68
$c = 2.0$,$m = 1.5TeV$	1.511±0.014±0.417	0.915±0.011±0.135	0.923±0.011±0.257
$c = 2.0$,$m = 2.0TeV$	0.2200±0.0028±0.0578	0.1334±0.0022±0.0220	0.1382±0.0022±0.0401
2HDM,$m = 1.0TeV$	107.4±1.4±27.7	80.5±1.2±9.8	76.8±1.1±17.2
2HDM,$m = 1.5TeV$	7.230±0.078±2.258	4.705±0.063±0.579	4.423±0.061±1.272
2HDM,$m = 2.0TeV$	0.6245±0.0069±0.1808	0.4136±0.0056±0.0655	0.3967±0.0055±0.1037

Table 7.11: Expected yields for backgrounds in the $3b$ signal region, control region, and sideband region, along with the observed number of data events. The signal predictions for $m = 1.0, 1.5, 2.0$ TeV of both $c = 1.0$ and $c = 2.0$, and for narrow width heavy Higgs of $m = 1.0, 1.5, 2.0$ TeV are also listed. For each predicted value, the first uncertainty listed is statistical, and the second is the sum in quadrature of all systematic uncertainties.

7.5 Systematic Uncertainties

Systematic Uncertainties consists of three major parts: MC uncertainties, theoretical uncertainties and background prediction uncertainties. MC uncertainties are related to the uncertainties coming from detector and reconstruction effect and only supposed to be applied on MC simulation only. Therefore, MC uncertainties would only be applied to $t\bar{t}$ and $Z+$jets. However, the whole background estimation procedure as described in Section 7.4 is repeated for each MC uncertainty variation so that it can be properly propagated to the multijet backgrounds. Details of MC uncertainties can be found in Section 7.5.1. Theoretical uncertainties are more on the signal acceptance and hence would be applied on signal sample only, as discussed in Section 7.5.2. Background estimation uncertainties are used to estimate any potential uncertainty due to our prediction procedure, as detailed in Section 7.5.3. A summary of all systematics is presented in Section 7.5.4.

7.5.1 MC Uncertainties

MC based uncertainties are propagated in the analysis using standard combined performance group recommendations at the time of this analysis. These uncertainties can change both the shape and normalization of the signal and of the MC-based background prediction ($t\bar{t}$ and $Z+$jets). For each MC variation, background estimation procedure is redone so that this MC variation can be propagated to multijet (and normalization of $t\bar{t}$) in a correlated way.

Luminosity Uncertainty

The uncertainty on the integrated luminosity is 5.0%. It is derived from a preliminary calibration of the luminosity scale derived from beam-separation scans performed in August 2015, following the methodology detailed in [74]. This uncertainty is only applied to the signal samples and $Z+$jets.

Large-R jet resolution and scale uncertainties

Trimmed jets with $R = 1.0$ are fully supported in the jet substructure performance group [183] in terms of both calibration of jet energy and mass scale (JES and JMS respectively). Systematic Uncertainties for JES and JMS is also provided which includes uncertainties handling the heavy flavor differences between multijet (where the uncertainties are derived) and the signal Higgs jets [147, 123].

The uncertainties in our kinematic regime for signal yield predictions are below 4% for JES, and between ∼10-15% for JMS. For $t\bar{t}$ yield predictions the uncertainties are ∼14-16% for JES, and between ∼13-37% for JMS.

Systematic uncertainties for energy and mass resolution (JER and JMR respectively) are currently not well constrained. MC-based studies in 2010 implied that variations of the order of 20% were possible. For large-R jets used in this analysis, this is also validated with boosted W bosons in 2012 data [184]. For each signal mass point, we smear the energy and mass resolution of the large-R

trimmed jets by a Gaussian such that the intrinsic resolution is increased by 20%. The nominal MC mass or p_{T} resolution ($\sigma_{M,p_{\mathrm{T}}}$) for every signal mass point is determined by fitting the reco_M/truth_M or reco_p_{T}/truth_p_{T} distribution with a Gaussian, respectively. The reco_p_{T}/truth_p_{T} is found before the large-R jet p_{T} cut, and the reco_M/truth_M is found before the final X_{hh} cut. Here, a truth trimmed jet is matched to the reconstructed trimmed jet within $\Delta R < 0.7$.

In all cases, the intrinsic resolution is small, due to the fact that each large-R jet already has a more stable substructure after the two ghost-associated track jets requirement (it has been shown in the Jet Substructure group that large-R jets with 2 or 3 subjets have a much better resolution than large-R jets with only one subjet). The JMR is slightly larger than the JER for all mass points, and also slightly increases as a function of mass point while the JER slightly decreases as a function of mass point. To apply a 20% systematic on the resolution, the jet mass or p_{T} is then smeared with a Gaussian with width $0.66^{*}\sigma_{M,p_{\mathrm{T}}}$ (see [183]), also independently for every signal mass point.

This smearing tends to increase the width of the dijet mass distributions, but with very little impact. The uncertainties in our kinematic regime for signal yield predictions are $\sim$ 1% for JER, and between $\sim$12-14% for JMR. For $t\bar{t}$ yield predictions the uncertainties are $\sim$1-4% for JER, and between $\sim$17-65% for JMR. It is noticed that the JMR uncertainty on $t\bar{t}$ is larger in the $4b$ SR than the $3b$ SR, even though the same $3b$ shape is used in both signal regions. This is partially driven by the smaller statistics in the $4b$ region used in the background fit to constrain the background normalizations (which is done independently for the $3b$ and $4b$ SR).

Track Jet Scale Factor Uncertainties

Calibrations, or correction factors in the form of scale factors per p_{T} bin, for the b-tagging efficiency of $R = 0.2$ track jets passing an MV2c20 weight cut corresponding to 77% efficiency have been derived in [125, 126]. These calibrations are applied to the signal samples, $t\bar{t}$ and to the $Z+$jets simulation. The calibrations also include uncertainties which modify the b-tagging efficiency and thus modify the signal ($t\bar{t}$ and $Z+$jets) acceptance, and thus these uncertainties must be propagated through the analysis.

These calibrations are derived from Run 1 data for b-jets. Additional Run1-to-Run2 extrapolation uncertainties are included to account for possible differences. In addition, the charm and light jet calibrations are taken from calo-jets, with an appropriate jet p_{T} rescaling to account for the difference in calo and track jet p_{T}. Additional uncertainties are added to the charm and light calibrations to account for possible differences in track and calo jet calibrations. More information can be found in [123].

In order to check for any additional uncertainties or mismodeling of the b-tagging performance in dense environments, where two b-jets are close by, a cross check of the b-tagging calibration has been performed in a boosted gluon$\rightarrow b\bar{b}$ jet sample as found in [185, 124]. These studies show no major mismodeling of the Monte Carlo simulation inconsistent with the data within the b-tagging

uncertainties.

For track jets with $p_{\mathrm{T}} > 250$ GeV, not enough statistics are available in the data based analysis to provide an accurate calibration. As a result, an extrapolation is required. The extrapolation is performed only on the calibration uncertainty. The baseline scale factor for track jets with $p_{\mathrm{T}} > 250$ is taken to be the same as the 100-250 GeV bin, as is the baseline uncertainty. The extrapolation aims to include additional uncertainties that may affect the calibration uncertainties in the high p_{T} bins that can not be calibrated directly from data. The extrapolation is performed in Monte Carlo, and relies on varying the inputs to b-tagging and examining the b-tagging efficiency under all of these variations. The variations include tracking efficiency, tracking resolution, and variations in the number fake and shared tracks. The variations observed with respect to the 100-250 GeV track jet p_{T} bin are taken as the extrapolation uncertainty of the variation. The uncertainty from all variations are added in quadrature to estimate the full extrapolation uncertainty.

The b-tagging calibrations are applied to the leading two track jets in each of the leading large-R jets in each event. In order to properly handle the correlations of the b-tagging calibration uncertainty between jets in an event, and between events, the b-tagging uncertainties are applied using the eigenvector approach, which computes the total covariance matrix including correlations of all p_{T} bins in the calibration and decomposes them into a smaller number of eigenvector variations.

The impact of the b-tagging uncertainties is 10-20% on the $t\bar{t}$ background yield estimates. The variation is larger for the signal samples, due to the large b-tag uncertainties for high-p_{T} jets which are more common in the high mass samples. As a result, the uncertainties on the signal yield vary between 15-40%, depending on signal region ($3b$ or $4b$) and signal mass.

In particular, we notice a significant reduction of b-tagging systematic uncertainty in $3b$ signal region compared to $4b$ signal region. The reduced b-tagging uncertainty is due to the requirement that there must be one anti-tagged jet. For the signal, this is likely an anti-tagged b-jet. The uncertainty reduction occurs since when a b-tagged jet is calibrated with a scale factor w_{sf} with uncertainties Δw_{sf}, any change in tagging efficiency must be corrected in the opposite direction for the anti-tagged jets in order to ensure that the total number of tagged plus anti-tagged jets does not change once the calibration is applied. Thus the anti-tagging calibration scale factor would be $w_{sf}^{anti} = (1 - w_{sf}\epsilon_b)/(1 - \epsilon_b)$ where ϵ_b is the tagging efficiency. From this equation, it is clear that a shift in the scale factor for tagged jets causes an anti-correlated shift in the anti-tagging efficiency scale factor. This anti-correlation in turn reduces the overall impact of the b-tagging uncertainty on the $3b$ SR.

7.5.2 Theoretical Uncertainties

The effect of the following theoretical uncertainties on the signal acceptance and efficiency has been evaluated: uncertainties in the parton density functions; uncertainties due to missing higher order terms in the matrix element; uncertainties in the modeling of the underlying event (including

multi-parton interactions), of hadronic showers and of initial and final state radiation. All of the uncertainties are evaluated for the Bulk RS $c = 1.0$ benchmark model.

To evaluate the potential effect of missing higher order terms in the matrix element, the renormalization and factorization scales used in the signal generation were varied coherently by factors of 0.5× and 2×. While signal acceptance by doubling the scales is consistent with nominal value, it is shifted by -1% by halving the scales.

Uncertainties due to modelling of the parton shower and the underlying event (including multi-parton interactions) are evaluated by varying the parameters of the A14 Pythia 8 tune used in the simulation of the graviton signal samples. Ten "eigentune" variations are produced for each mass point. These variations, along the principal directions of the covariance matrix at the A14 tune minimum as described in [174], provide good coverage of the experimental and modeling uncertainties implicit in the tuning. Variation is resonance mass dependent, ranging between 2% to 8%.

The PDF uncertainty is evaluated using the 100 NNPDF 2.3 LO replicas. The uncertainty in acceptance due to PDF uncertainties is less than 1% when resonance mass is smaller than 2 TeV, but grows to 3% at the highest mass (3 TeV) considered for this analysis.

7.5.3 Background Prediction Uncertainties

An 8% (2%) statistical uncertainty on the value of μ_{Multijet} for the $4b$ ($3b$) SR was determined from the fitting procedure described in Section 7.4.3. The statistical uncertainty of the $t\bar{t}$ normalization is accounted for through the uncertainties on $\alpha_{t\bar{t}}$ from the fit in data as described in Section 7.4.3. The statistical uncertainty of 48% on $\alpha_{t\bar{t}}$ are 58% anti-correlated to the value of μ_{Multijet} found in the fitting procedure in the "4-tag" region, and the uncertainties of 9% on $\alpha_{t\bar{t}}$ are 60% anti-correlated to the value of μ_{Multijet} found in the fitting procedure in the "3-tag" region. Due to the presence of correlation, statistical uncertainties of μ_{Multijet} and $\alpha_{t\bar{t}}$ are evaluated by varying both parameters jointly along the eigen-direction of their covariant matrix by 1σ

In additional, other background systematic uncertainties in the signal region are divided into the following components:

- Non-closure uncertainty on μ_{Multijet} derived by comparing normalization difference between observation and prediction in control region.
- Effects on the multijet prediction from variations of the sideband and control region definitions.
- Shape uncertainty of $t\bar{t}$ distribution in $4b$ signal region.
- Shape uncertainty of multijet estimation derived from control region.
- Smoothing uncertainty for multijet estimation due to choice of smoothing function and fit range.

Non-closure uncertainty on μ_{Multijet}

This is derived by comparing the normalization difference between predicted and observed events in the control region. While the total $4b$ ($3b$) predicted background (showing stat error only) of 40.34 $\pm$ 1.00 events (714.6 $\pm$ 10.7 events) agrees with the total $4b$ ($3b$) data of 45 (724) events in the control region within statistical error, we consider an added systematics on the background prediction normalization, taken as the maximum between 1) total normalization difference between data and prediction in control region and 2) statistical uncertainty of observed yields in control region. For the first factor, we have 11.55% for $4b$ control region and 1.32% for $3b$ control region. For second factor, we have 14.9% for $4b$ control region and 3.7% for $3b$ control region. Therefore the statistical uncertainty is used. Although such normalization difference should be a mixed effect from both multijet and $t\bar{t}$ normalization, we attribute all of them to multijet (i.e. μ_{Multijet}) in order to simplify the process, and also serve as a conservative estimation.

Variation of Multijet Prediction from Redefined CR/SB

As discussed in Section 7.4.1, a dedicated CR and SB is chosen from several considerations for background estimation procedure. However, it would be dangerous if the whole analysis is sensitive to such choice. Therefore, the purpose of the test described in this section is to check if 1) multijet prediction in SR/CR/SB is stable for small modification of the definition of CR/SB and 2) the systematics is enough to cover any difference found.

Besides the nominal control region as described earlier, we design four additional alternative control regions, as illustrated in Figure 7.24:

- Low-mass CR: The central position of the circle that defines nominal CR is moved down by 5 GeV, in both leading and subleading large-R jet mass
- High-mass CR: The central position of the circle that defines nominal CR is moved up by 5 GeV, in both leading and sub-leading large-R jet mass
- Signal-depletion CR: The X_{hh} cut that defines signal region is increased to 2.0 from 1.6. This variation only affect CR, while SR remains unchanged (i.e. signal region is still defined by $X_{hh} < 1.6$, while CR is defined as $X_{hh} > 2.0$ and $R_{hh} < 35.8$).
- Sideband-restricted CR: The signal region and control region remains unchanged, but we remove all events with $R_{hh} > 135$ GeV. The μ_{Multijet} will need to be re-fit since SB has changed.

The High-mass and Low-mass CR is designed to test how background modeling is sensitive to the exact (central) position of CR. The Signal-depletion CR is designed to test whether there is significant signal contamination in the CR. The agreement between data and prediction in the CR

would be significantly different from the number calculated with nominal CR, if there is a large amount of signal contamination in CR. The Sideband-restricted CR is designed to test how sensitive the normalization fit is to the events at tail.

We redo the whole background estimation procedure as described above on each of these variations. The summary of estimated background yields for $4b$ ($3b$) region can be found in Table 7.12, 7.13, 7.14, 7.15, 7.16 (Table 7.17, 7.18, 7.19, 7.20, 7.21) for nominal CR, High-mass CR, Low-mass CR, Signal-depleted CR and Sideband-restricted CR respectively. This would be the raw table for our evaluation as presented next.

The first thing to check is the variation of predicted yields in SR. With tables obtained above, the variation of normalization prediction in SR is summarized in Table 7.22 (Table 7.23) for 4-tag (3-tag) SR. The variation in SR from Signal-depletion CR is not shown since that will be zero by definition. As we can see, the variation of background prediction in SR is very small and all are within statistical uncertainty. This is mainly due to the data-driven background estimation technique we are using.

Mass Region	Data	Total Bkg.	QCD	$t\bar{t}$	$Z+jets$	$m_G = 1.0$TeV	$m_G = 2.0$TeV
SR	20	14.6	13.5	1.2	0.0	2.87	0.0299
CR	45	40.3	34.7	5.1	0.55	1.46	0.0161
SB	279	279.2	247.4	28.4	3.4	0.904	0.0121

Table 7.12: Background prediction in SR/CR/SB for nominal CR definition in 4 b-tag region

Mass Region	Data	Total Bkg.	QCD	$t\bar{t}$	$Z+jets$	$m_G = 1.0$TeV	$m_G = 2.0$TeV
SR	20	14.6	13.4	1.1	0.0	2.87	0.0299
CR	41	35.5	29.2	5.7	0.55	1.33	0.0141
SB	283	283.1	252.8	26.9	3.4	1.04	0.014

Table 7.13: Background prediction in SR/CR/SB for high mass CR definition in 4 b-tag region

Mass Region	Data	Total Bkg.	QCD	$t\bar{t}$	$Z+jets$	$m_G = 1.0$TeV	$m_G = 2.0$TeV
SR	20	14.7	13.5	1.1	0.0	2.87	0.0299
CR	50	46.3	41.8	4.0	0.55	1.48	0.0167
SB	274	274.3	242.0	28.9	3.4	0.88	0.0114

Table 7.14: Background prediction in SR/CR/SB for low mass CR definition in 4 b-tag region

Next we also check the variation of multijet shape in SR, as shown in Figure 7.25. All variations observed are within the multijet shape uncertainty derived from nominal CR (see description on this later).

Besides SR, we also check the agreement between data and prediction in CR, based on raw tables obtained above. The results are summarized in Table 7.24 (Table 7.25) for $4b$ CR ($3b$ CR). One

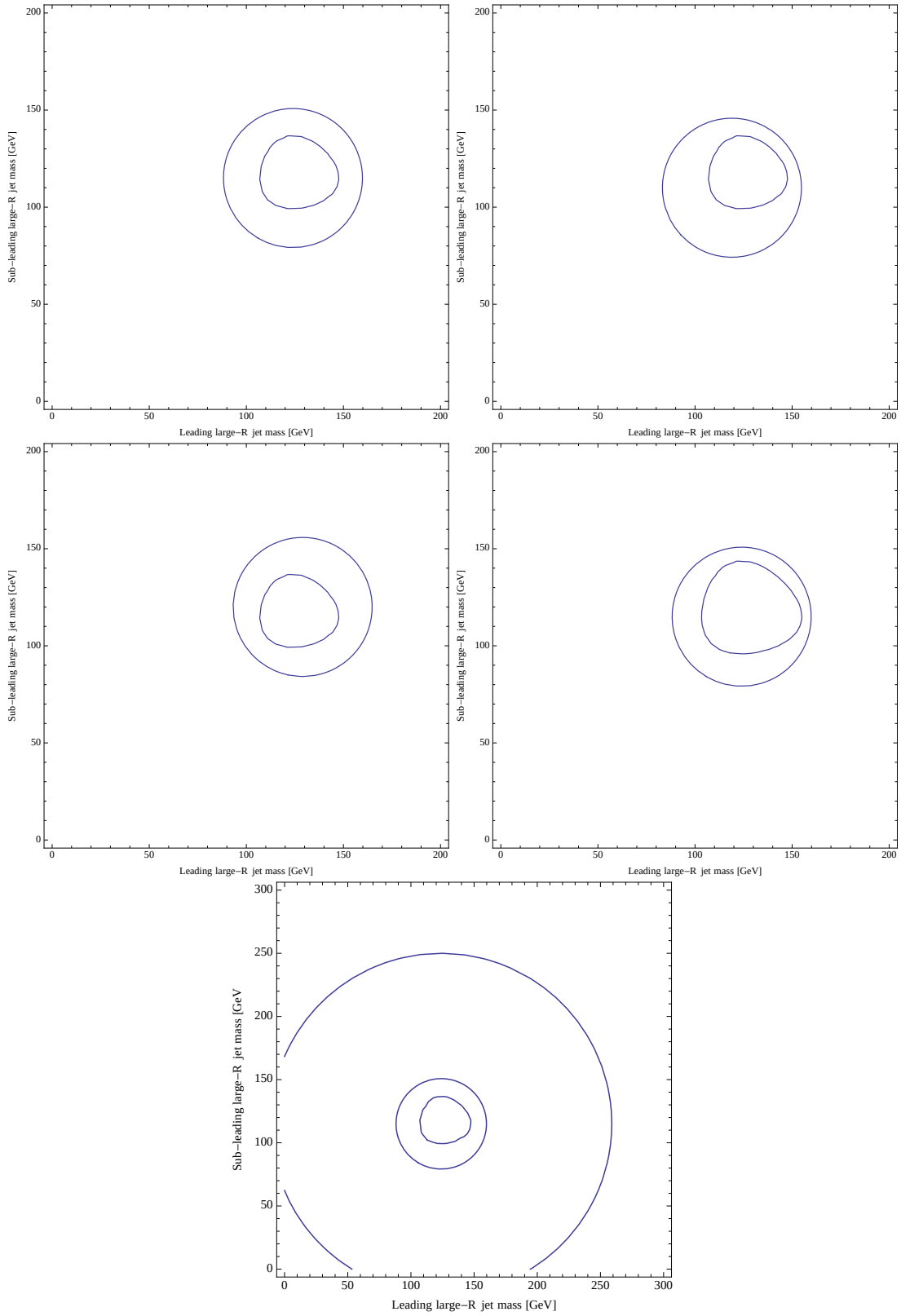


Figure 7.24: Illustration of all variation of control regions (CR) and sideband regions (SB) under consideration. Left top is the nominal CR. Right top is low-mass CR. Bottom left is High-mass CR. Bottom right is signal-depletion CR. Bottom is sideband-restricted region

Mass Region	Data	Total Bkg.	QCD	$t\bar{t}$	$Z + jets$	$m_G = 1.0$TeV	$m_G = 2.0$TeV
SR	20	14.6	13.5	1.2	0.0	2.87	0.0299
CR	35	31.6	27.3	3.8	0.55	0.898	0.00979
SB	279	279.2	247.4	28.4	3.4	0.904	0.0121

Table 7.15: Background prediction in SR/CR/SB for signal depleted CR definition in 4 b-tag region

Mass Region	Data	Total Bkg.	QCD	$t\bar{t}$	$Z + jets$	$m_G = 1.0$TeV	$m_G = 2.0$TeV
SR	20	14.6	13.4	1.1	0.0	2.87	0.0299
CR	45	40.2	34.7	4.9	0.55	1.46	0.0161
SB	264	264.2	235.1	25.6	3.4	0.846	0.00871

Table 7.16: Background prediction in SR/CR/SB for sideband restricted CR definition in 4 b-tag region

Mass Region	Data	Total Bkg.	QCD	$t\bar{t}$	$Z + jets$	$m_G = 1.0$TeV	$m_G = 2.0$TeV
SR	316	284.8	235.4	47.5	2.0	3.44	0.0668
CR	724	714.6	607.3	99.6	7.7	2.2	0.0421
SB	5043	5043.2	4327.9	683.5	31.8	2.41	0.04

Table 7.17: Background prediction in SR/CR/SB for nominal CR definition in 3 b-tag region

Mass Region	Data	Total Bkg.	QCD	$t\bar{t}$	$Z + jets$	$m_G = 1.0$TeV	$m_G = 2.0$TeV
SR	316	282.7	235.0	45.8	2.0	3.44	0.0668
CR	677	631.1	510.2	115.5	5.5	1.93	0.0362
SB	5090	5090.0	4416.0	639.9	34.0	2.67	0.0459

Table 7.18: Background prediction in SR/CR/SB for high mass CR definition in 3 b-tag region

Mass Region	Data	Total Bkg.	QCD	$t\bar{t}$	$Z + jets$	$m_G = 1.0$TeV	$m_G = 2.0$TeV
SR	316	286.3	235.9	48.5	2.0	3.44	0.0668
CR	811	829.1	727.9	90.6	10.6	2.31	0.045
SB	4956	4956.2	4217.6	709.7	28.9	2.3	0.0371

Table 7.19: Background prediction in SR/CR/SB for low mass CR definition in 3 b-tag region

Mass Region	Data	Total Bkg.	QCD	$t\bar{t}$	$Z + jets$	$m_G = 1.0$TeV	$m_G = 2.0$TeV
SR	316	284.8	235.4	47.5	2.0	3.44	0.0668
CR	542	554.8	477.1	69.9	7.7	1.47	0.0273
SB	5043	5043.2	4327.9	683.5	31.8	2.41	0.04

Table 7.20: Background prediction in SR/CR/SB for signal depleted CR definition in 3 b-tag region

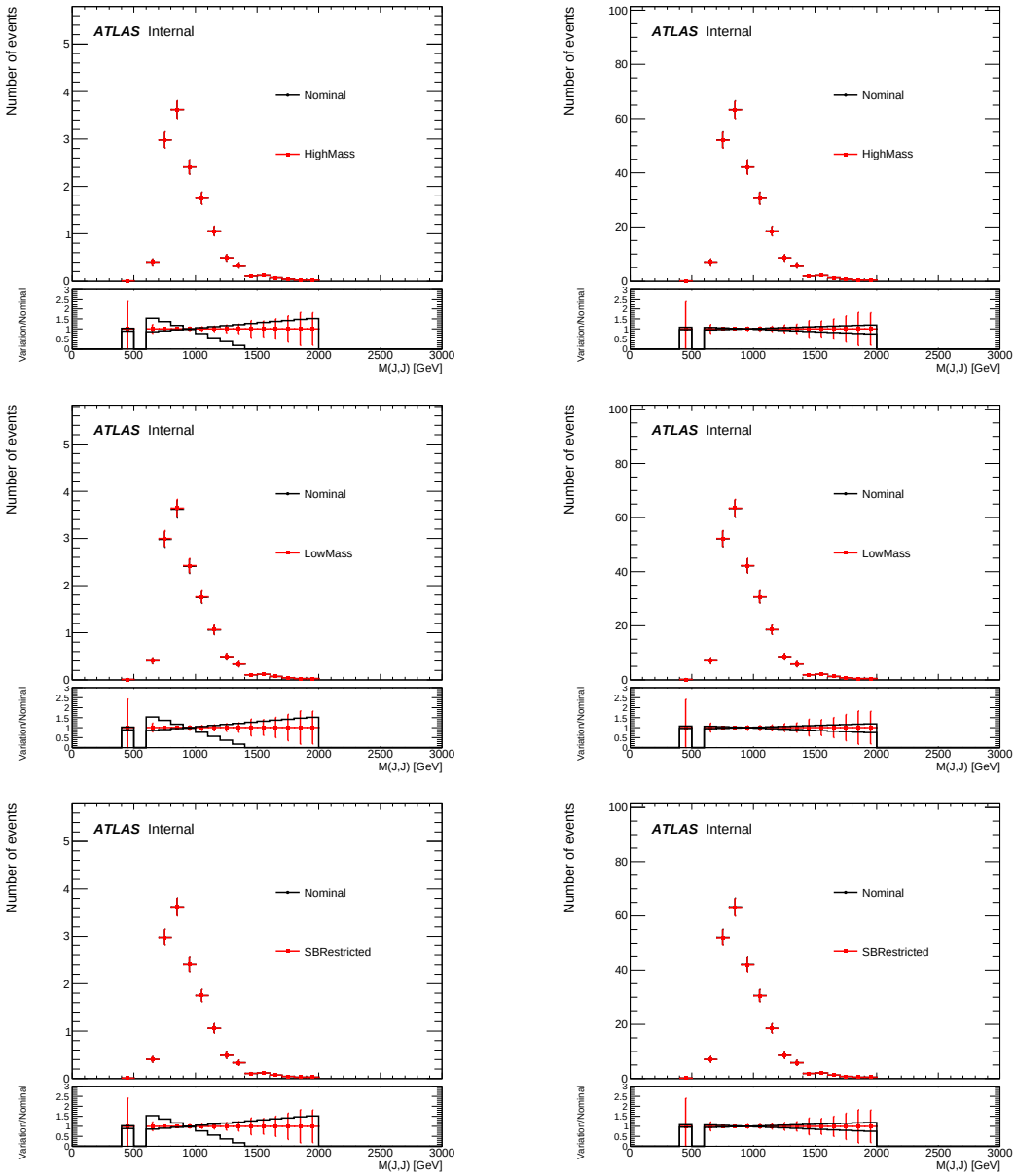


Figure 7.25: Comparisons of the nominal multijet shape prediction (black points) with the results of Control and Sideband Region definition variations (red points). The ratio of the shape from each variation to the nominal shape is shown in the lower panel, with the nominal shape uncertainty shown as the black-outlined band. The first row shows the high-mass CR variation; the second row shows the low-mass CR variation; and the third row shows the sideband restricted CR variation. The left column shows the relevant distributions for the 4 b-tag Signal Region and the right column is for the 3 b-tag Signal Region.

Mass Region	Data	Total Bkg.	QCD	$t\bar{t}$	$Z + jets$	$m_G = 1.0$TeV	$m_G = 2.0$TeV
SR	316	282.0	234.7	45.3	2.0	3.44	0.0668
CR	724	708.4	605.7	95.0	7.7	2.2	0.0421
SB	4759	4759.4	4105.4	623.5	30.5	2.12	0.0283

Table 7.21: Background prediction in SR/CR/SB for sideband restricted CR definition in 3 b-tag region

SR Variations	Total Bkg.	QCD	$t\bar{t}$	$Z + jets$
HighMass	-0.247%	-0.0381%	-2.67%	–
LowMass	0.423%	0.608%	-1.72%	–
SBRestricted	-0.315%	-0.0732%	-3.12%	–

Table 7.22: Variation of prediction in 4 b-tag SR

SR Variations	Total Bkg.	QCD	$t\bar{t}$	$Z + jets$
HighMass	-0.739%	-0.182%	-3.53%	0%
LowMass	0.538%	0.209%	2.19%	0%
SBRestricted	-0.993%	-0.274%	-4.6%	0%

Table 7.23: Variation of prediction in 3 b-tag SR

can see that for most CR variations, the disagreement between data and prediction is well covered by statistical uncertainty of data. The only exception is 3 b-tag high mass CR variation, where the prediction is $\sim 2\sigma$ away from the data.

We also notice that variation in Signal-depletion CR definition is not significantly deviated from the number derived from nominal CR definition, and the discrepancy is also within the statistical uncertainty of data as well. This shows no significant signal contamination in CR is found.

CR Variations	Stat. Uncertainty of Data	(Data-Pred)/Data	(Data-Pred)/Pred
Nominal	14.9%	10.3%	11.5%
High Mass	15.6%	13.5%	15.6%
Low Mass	14.1%	7.32%	7.9%
Signal Depleted	16.9%	9.78%	10.8%
SB Restricted	14.9%	10.8%	12.1%

Table 7.24: Agreement between data and prediction in 4 b-tag CR

Validation in ZZ Signal Region

Another check we make is the the so-called "ZZ signal region rehearsal". Instead of a signal region around di-Higgs mass region on leading-subleading large-R jet mass 2D plane, we redefine a separate

CR Variations	Stat. Uncertainty of Data	(Data-Pred)/Data	(Data-Pred)/Pred
Nominal	3.72%	1.29%	1.31%
High Mass	3.84%	6.77%	7.27%
Low Mass	3.51%	-2.23%	-2.18%
Signal Depleted	4.3%	-2.35%	-2.3%
SB Restricted	3.72%	2.16%	2.2%

Table 7.25: Agreement between data and prediction in 3 b-tag CR

signal region dedicated for ZZ searches:

$$X_{zz} = \sqrt{\left(\frac{m(J_1) - 93\text{ GeV}}{0.1m(J_1)}\right)^2 + \left(\frac{m(J_2) - 86\text{ GeV}}{0.1m(J_2)}\right)^2} < 2.1 \tag{7.4}$$

which is also illustrated in Figure 7.26. Then we redo the analysis, using the same definition of sideband and control region as nominal (but with events contained in ZZ signal region excluded) for normalization fit, and unblind the ZZ signal region. This is to validate our background estimation strategy, and see how stable it is for another similar analysis.

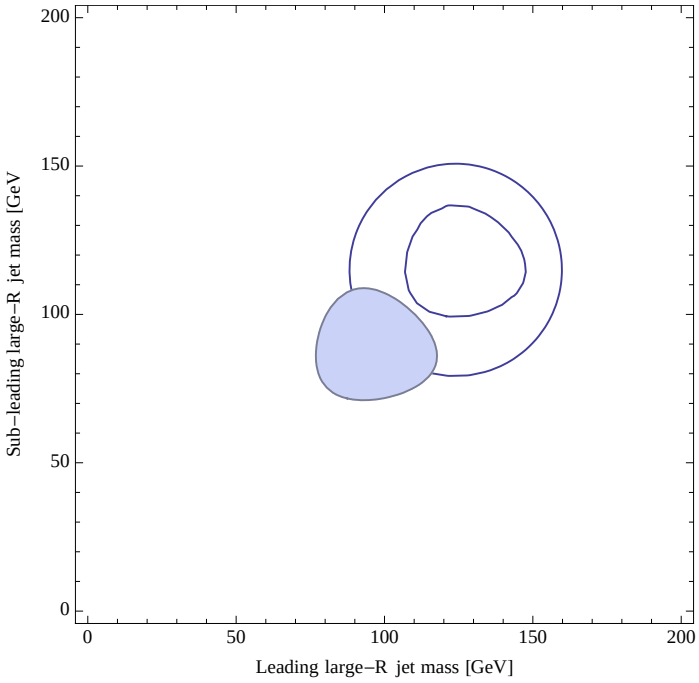


Figure 7.26: Illustration of ZZ signal region as shown in blue shaded region

The summary of background estimation for ZZ signal region can be found in Table 7.26 (Table 7.27) for 4 b-tag region (3 b-tag region). The difference between data and prediction in ZZ signal region is summarized in Table 7.28 and Table 7.29 for 4 b-tag and 3 b-tag regions respectively. The discrepancy between data and prediction is either covered by statistical uncertainty of data or compatible with data statistical uncertainty in 4 b-tag and 3 b-tag ZZ SR respectively. We further check the kinematic distribution between data and prediction in ZZ SR, as shown in Figure 7.27. The data agrees with prediction well in general, though a few bins might not agree perfectly.

Based on all the variation tests done above, we think there is no need to introduce extra uncertainty on non-closure systematics since most of the data/prediction disagreements are well covered by the data statistical uncertainty.

Mass Region	Data	Total Bkg.	QCD	$t\bar{t}$	$Z + jets$	$m_G = 1.0$TeV	$m_G = 2.0$TeV
SR	31	27.1	25.0	0.61	1.5	0.293	0.00354
CR	38	31.7	26.3	4.9	0.55	1.24	0.0136
SB	255	255.3	224.2	29.1	2.0	0.826	0.011

Table 7.26: Background prediction in SR/CR/SB for ZZ SR in 4 b-tag region

Mass Region	Data	Total Bkg.	QCD	$t\bar{t}$	$Z + jets$	$m_G = 1.0$TeV	$m_G = 2.0$TeV
SR	452	483.5	450.8	24.4	8.3	0.541	0.0113
CR	590	567.0	473.6	87.8	5.7	1.82	0.0344
SB	4725	4724.9	4035.9	663.5	25.6	2.24	0.0365

Table 7.27: Background prediction in SR/CR/SB for ZZ SR in 3 b-tag region

	Stat. Uncertainty of Data	(Data-Pred)/Data	(Data-Pred)/Pred
ZZ SR	18%	12.5%	14.4%

Table 7.28: Agreement between data and prediction in ZZ SR in 4 b-tag region

	Stat. Uncertainty of Data	(Data-Pred)/Data	(Data-Pred)/Pred
ZZ SR	4.7%	-6.96%	-6.51%

Table 7.29: Agreement between data and prediction in ZZ SR in 3 b-tag region

Shape Uncertainty of $t\bar{t}$

Because the $4b$ distribution is extremely statistically limited, the $3b$ shape is used to predict the final $t\bar{t}$ background shape in the $4b$ signal region. While such procedure is validated in Figure 7.14,

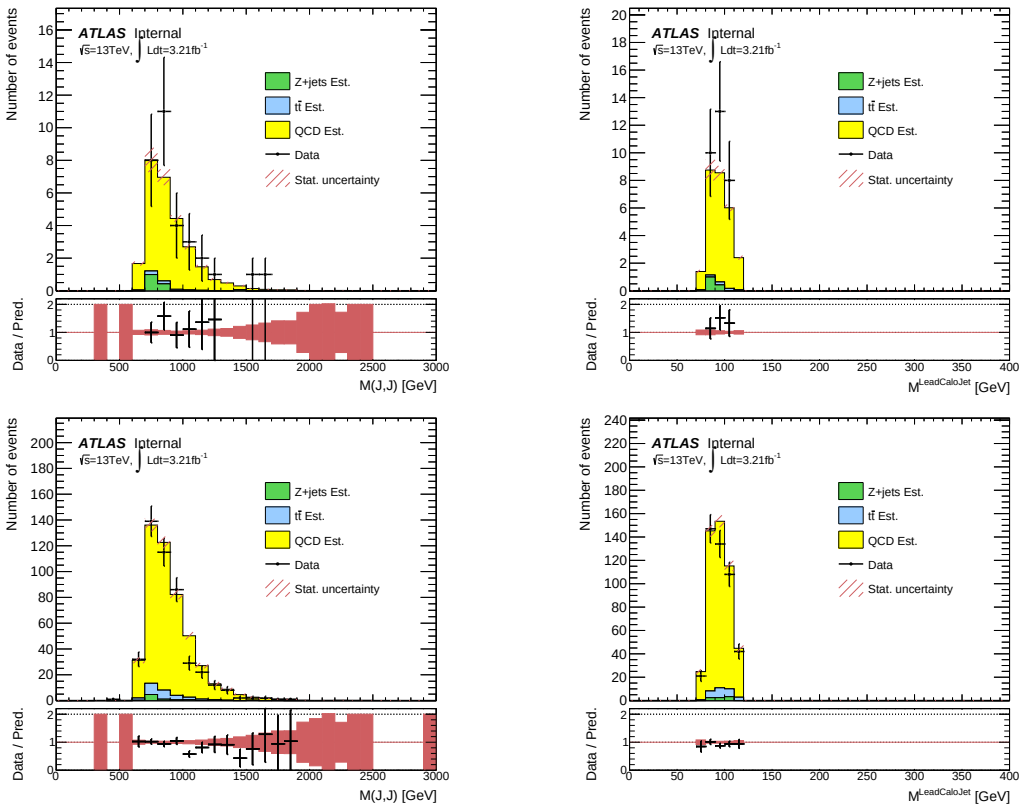


Figure 7.27: Distribution of di-jet mass (left column) and leading large-R jet mass (right column) in ZZ SR, for 4 b-tag (first row) and 3 b-tag (second row)

we still try to derive an uncertainty on the shape of $t\bar{t}$ distribution in $4b$ signal region, accounting for any difference while extrapolating from $3b$ to $4b$.

In order to estimate the possible shape uncertainty, the $4b$ and $3b$ shapes are compared in Figure 7.28. The distributions have been rebinned in order to reduce statistical fluctuations. At the right of Figure 7.28, we can find the ratio of the two distributions (after normalizing both to unity), as well as a linear fit to the ratio. The linear fit is found to have an offset of 0.82 ± 1.01 and slope of 0.0002 ± 0.0010. Due to lack of statistics, such fitting experiences large statistical uncertainty. Nevertheless, we vary the slop by 1σ (with offset parameter tuned to maintain same normalization) and take it as our estimation of the $t\bar{t}$ shape uncertainty in $4b$ signal region, as illustrated by the blue line on right plot of Figure 7.28.

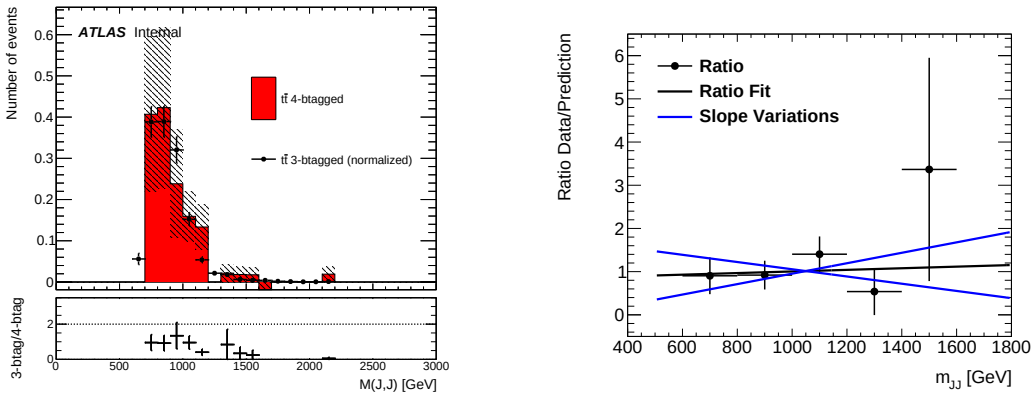


Figure 7.28: (left) Shape of the $t\bar{t}$ di-large-R-jet mass in the signal region, comparing various b-tag bins. (right) The ratio of $4b$ to $3b$ shapes, with a linear fit to the ratio. The same fit with negative slope is also shown on the figure. .

The same method is applied to for the $t\bar{t}$ shape uncertainty for the scaled dijet mass distribution. The ratio of the $4b$ to $3b$ shape, as well as the linear fits and variations used to determine the shape uncertainty can be found in Figure 7.29.

Shape Uncertainty of Multijet

As shown in Figures 7.19, the shape distribution of the total predicted background extrapolated from $2b$ sample is found to be in good agreement for both $4b$ and $3b$ data in the control region. However due to the low statistics in the data in the control region, a conservative shape uncertainty is determined using the ratio between $2b$ to $4b$ ($3b$) distributions, which will be propagated to the signal region multijet distribution. It should be noted that this uncertainty is used for both the dijet mass, and the scaled dijet mass distribution in signal region. The correction to to scaling is expected to be small relative to the dijet mass.

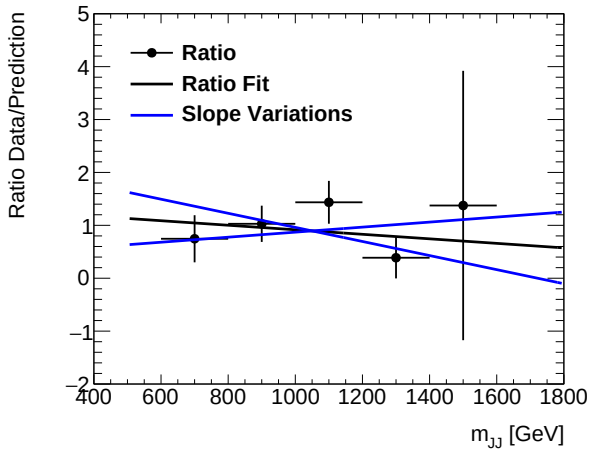


Figure 7.29: The ratio of $4b$ to $3b$ shapes of the $t\bar{t}$ scaled di-large-R-jet mass in the signal region, with a linear fit to the ratio. The same fit with negative slope is also shown on the figure.

A linear fit is performed on the dijet mass distribution in the control region, as shown in Figure 7.30. The $4b$ fit has a slope of $-7\times10^{-4}\pm1.3\times10^{-3}$, and $3b$ fit has a slope of $-4\times10^{-5}\pm2.2\times10^{-4}$. Both slopes are consistent with zero indicating a good agreement between the shape of the distributions. Since we only focus on the shape uncertainty here (normalization uncertainty is taken by the non-closure test), we vary the fitted slop by 1σ with offset tuned to maintain same normalization, as shown in the blue line in Figure 7.30.

Figure 7.31 shows the effect of this shape uncertainty on the predicted multijet dijet mass distribution in the signal region. The upwards and downwards variations in gray lines form the envelope of our background shape uncertainty in the signal region.

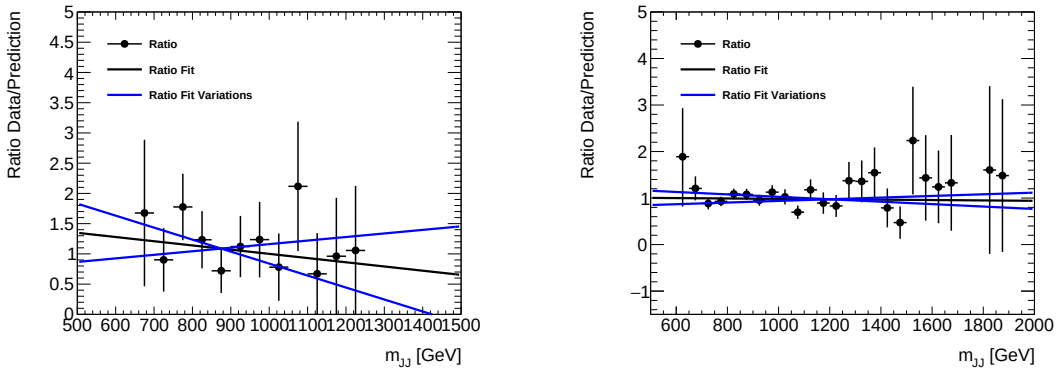


Figure 7.30: Dijet mass ratio of total background to 4b (left) and 3b (right) data in the control region, fit (red line), and $\pm1\sigma$ variation of the slope parameter (blue lines).

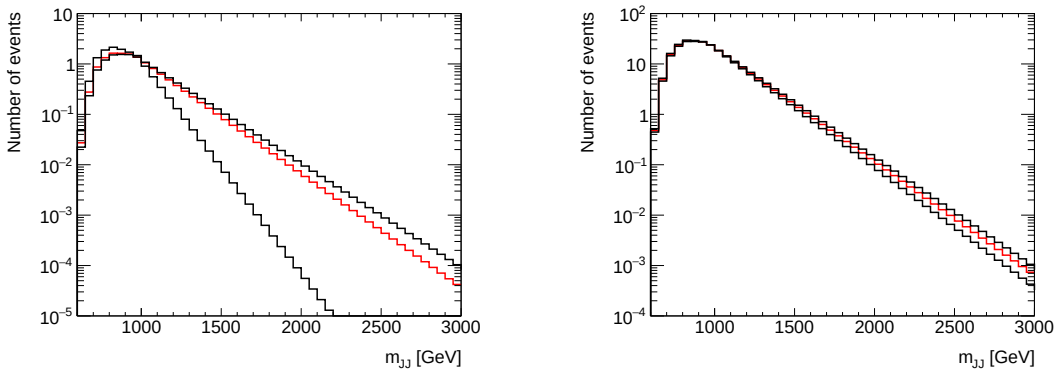


Figure 7.31: Effect of the up/down variation of the $2b$ multijet shape in the $4b$ (left) and $3b$ (right) signal regions. Gray lines show the upwards and downwards variations.

Smoothing Uncertainties

When dijet mass distributions for multijet and $t\bar{t}$ component are smoothed with exponential fit, the statistical uncertainties are obtained by varying smoothing parameters jointly in eigen direction defined by the covariant matrix.

Furthermore, two systematic uncertainties related to smoothing procedure is considered: 1) The choice of fit range 2) The choice of smoothing function. It should be noticed that these two systematics are only applicable for multijet background, since there is no enough MC statistics to derive reliable systematics for $t\bar{t}$.

First we vary the upper bound of fit range among the list $\{1500, 1750, 2000\}$. The ratio of fits for each option to that of nominal value can be found in Figure 7.32. Since all variations are well contained inside the data statistical uncertainties, no additional systematics is assigned for this aspect.

Next we vary smoothing function from a set of functional forms featuring in both power law behavior and longer tails, as listed in Table 7.30.

Name	Functional Form
MJ1	$f_1(x) = p_0(1-x)^{p_1}x^{p_2}$
MJ2	$f_2(x) = p_0(1-x)^{p_1}e^{p_2\ x^2}$
MJ3	$f_3(x) = p_0(1-x)^{p_1}x^{p_2\ x}$
MJ4	$f_4(x) = p_0(1-x)^{p_1}x^{p_2\ ln\ x}$
MJ5	$f_5(x) = p_0(1-x)^{p_1}(1+x)^{p_2\ x}$
MJ6	$f_6(x) = p_0(1-x)^{p_1}(1+x)^{p_2\ ln\ x}$
MJ7	$f_7(x) = \frac{p_0}{x}(1-x)^{p_1-p_2\ ln\ x}$
MJ8	$f_8(x) = \frac{p_0}{x^2}(1-x)^{p_1-p_2\ ln\ x}$

Table 7.30: Functions used to fit the multijet dijet mass distributions, where $x = m_{JJ}/\sqrt{s}$.

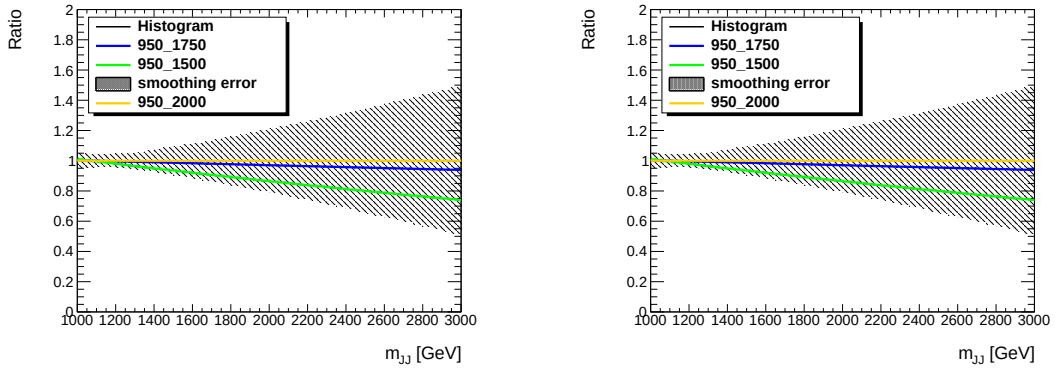


Figure 7.32: The ratio of the nominal exponential multijet prediction of the scaled dijet mass distribution (with hashed band statistical uncertainties) to the predictions when fit with different upper bounds, in the $4b$ (left) and $3b$ (right) signal regions.

The smoothing fit on multijet (scaled) M_{JJ} distribution can be found collectively in Figure 7.33. Each variation of smoothing fit is compared with the nominal fit using exponential function, as seen in Figure 7.34. Functional forms (MJ1) with poor fit quality is removed from the list of ratios. It is interesting to notice that all alternative functional forms gives a even steeper falling tails than the exponential fit. All deviations from alternative functional forms are larger than the statistical uncertainty given by nominal fit. Therefore, the curve with largest deviation is quoted as systematics.

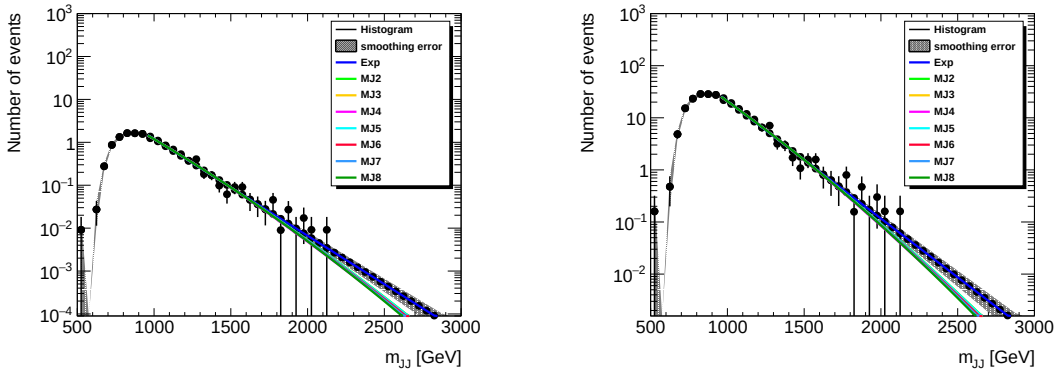


Figure 7.33: The multijet prediction of the scaled dijet mass distribution in the $4b$ (left) and $3b$ (right) signal regions, showing the nominal exponential fit (with has band statistical uncertainties) and the additional fits from Table 7.30.

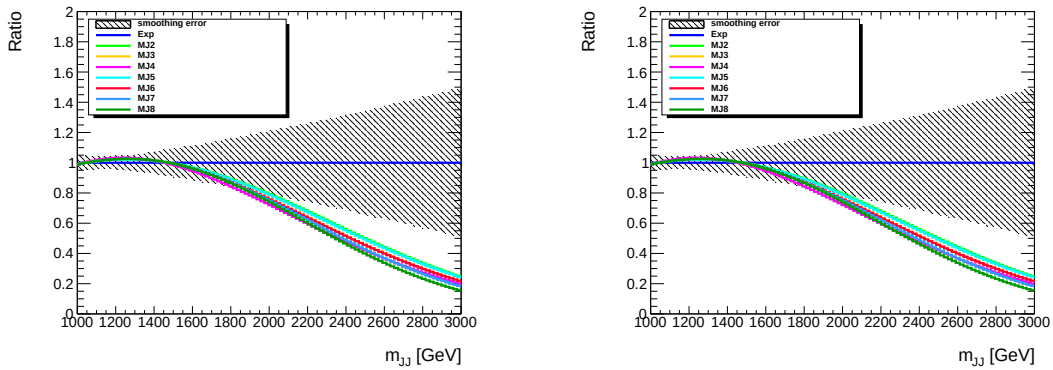


Figure 7.34: The ratio of the nominal exponential QCD prediction of the scaled dijet mass distribution (with hashed band statistical uncertainties) to the predictions of the additional fit functions of Table 7.30 in the $4b$ (left) and $3b$ (right) signal regions.

7.5.4 Summary of Systematics

This section serves as the reference point as a summary of all systematics considered for this analysis (if readers do not wish to go through detailed derivation above).

Table 7.31 and 7.32 shows a summary of systematic uncertainties on backgrounds and selected signal samples in $4b$ signal region. Similar table for $3b$ signal region can be found in Table 7.33 and 7.34. Shape uncertainties defined earlier are not shown on this table since they do not affect the yields.

A summary of MC systematic uncertainty on signal acceptance can be found in Figure 7.35. The largest uncertainty in the $4b$ signal region is from b-tagging, followed by the jet mass scale and resolution. In the $3b$ signal region, although b-tagging systematics is still one of the largest uncertainty, it has been much reduced compared to $4b$ region due to anti-correlation between efficiency scale factor and inefficiency scale factor. Jet mass scale and resolution are the largest uncertainties after b-tagging in $3b$.

The background estimation related uncertainties on the dominant multijet component, with both shape uncertainty and smoothing uncertainty, can be found in Figure 7.36. While mutlijet shape uncertainty is dominant below 1500 (1000) GeV in $4b$ ($3b$) signal region, smoothing uncertainty becomes dominant in high dijet mass end. The total background prediction along with total uncertainties can be found in Figure 7.37.

For the background prediction, we find that smoothing and multijet shape uncertainty could vary the shape of background prediction a lot, though they are covering different dijet mass regions. A direct comparison of these two systematics can be found in Figure 7.36. While multijet shape uncertainty is dominant below 1500 (1000) GeV in $4b$ ($3b$) signal region, smoothing uncertainty becomes dominant in high dijet mass end. The total background prediction along with total uncertainties

Systematics	Total Bkg	QCD	$t\bar{t}$	$Z + jets$	RSG $c = 1.0$ $m = 1.0$TeV	RSG $c = 1.0$ $m = 1.5$TeV	RSG $c = 1.0$ $m = 2.0$TeV
JES	0.63%	1.1%	16.0%	–	3.3%	0.26%	0.20%
JMS	4.7%	5.3%	13.7%	–	10.9%	12.9%	15.2%
JER	0.48%	0.48%	0.46%	–	0.90%	0.054%	0.18%
JMR	3.8%	1.2%	62.3%	–	13.9%	11.5%	12.2%
b-tag SF	1.6%	0.98%	20.8%	–	32.2%	36.3%	37.9%
Bkg. Norm. Fit	6.0%	8.0%	48.3%	–	–	–	–
QCD Non-Closure	13.7%	14.9%	0.0%	–	–	–	–
Total Sys.	16.3%	17.8%	84.3%	–	36.9%	40.2%	42.6%
Stat.	2.5%	2.7%	4.7%	–	1.1%	1.1%	1.5%
Event Number	14.6	13.5	1.2	0.0	2.9	0.29	0.030

Table 7.31: Percent impact of the dominant systematics on the background acceptance and on the signal acceptance of RS $c = 1.0$ graviton predictions in the $4b$ signal region.

Systematics	RSG $c = 2.0$ $m = 1.0$TeV	RSG $c = 2.0$ $m = 1.5$TeV	RSG $c = 2.0$ $m = 2.0$TeV	2HDM $m = 1.0$TeV	2HDM $m = 1.5$TeV	2HDM $m = 2.0$TeV
JES	3.7%	0.52%	0.27%	4.2%	0.20%	0.29%
JMS	10.4%	12.5%	12.4%	13.0%	14.0%	13.1%
JER	0.95%	0.63%	0.73%	1.1%	0.31%	0.78%
JMR	12.6%	13.0%	11.1%	13.8%	12.8%	11.7%
b-tag SF	32.8%	36.0%	37.4%	31.8%	36.4%	38.1%
Total Sys.	36.9%	40.3%	40.9%	37.3%	41.0%	42.0%
Stat.	1.1%	1.2%	1.8%	1.4%	1.4%	1.7%
Event Number	10.1	0.96	0.10	83.3	4.5	0.28

Table 7.32: Percent impact of the dominant systematics on the signal acceptance of RS $c = 2.0$ graviton and 2HDM predictions in the $4b$ signal region.

Systematics	Total Bkg	QCD	$t\bar{t}$	$Z + jets$	RSG $c = 1.0$ $m = 1.0$TeV	RSG $c = 1.0$ $m = 1.5$TeV	RSG $c = 1.0$ $m = 2.0$TeV
JES	2.2%	0.59%	14.8%	55.5%	2.7%	0.20%	0.13%
JMS	4.7%	1.9%	37.1%	54.8%	14.8%	13.8%	15.4%
JER	0.44%	0.41%	3.7%	22.5%	0.81%	0.57%	0.39%
JMR	1.1%	2.1%	17.2%	4.0%	12.9%	12.0%	12.7%
b-tag SF	0.90%	1.4%	10.2%	49.8%	15.9%	22.5%	19.3%
Bkg. Norm. Fit	1.4%	2.0%	9.2%	0.0%	–	–	–
QCD Non-Closure	3.1%	3.7%	0.0%	0.0%	–	–	–
Total Sys.	6.4%	5.3%	45.8%	95.3%	25.4%	29.0%	27.8%
Stat.	2.4%	2.7%	4.7%	54.0%	1.0%	0.91%	1.0%
Event Number	284.8	235.4	47.5	2.0	3.4	0.45	0.067

Table 7.33: Percent impact of the dominant systematics on the background acceptance and on the signal acceptance of RS $c = 1.0$ graviton predictions in the $3b$ signal region.

Systematics	RSG $c = 2.0$ $m = 1.0$TeV	RSG $c = 2.0$ $m = 1.5$TeV	RSG $c = 2.0$ $m = 2.0$TeV	2HDM $m = 1.0$TeV	2HDM $m = 1.5$TeV	2HDM $m = 2.0$TeV
JES	2.8%	0.47%	0.34%	4.2%	0.28%	0.23%
JMS	13.0%	12.6%	12.7%	17.8%	17.4%	17.1%
JER	0.79%	0.44%	0.22%	0.86%	0.96%	0.54%
JMR	11.6%	11.6%	12.9%	11.1%	11.6%	11.1%
b-tag SF	16.8%	21.6%	19.1%	14.3%	23.2%	20.5%
Total Sys.	24.4%	27.6%	26.3%	25.8%	31.2%	28.9%
Stat.	1.0%	0.94%	1.3%	1.3%	1.1%	1.1%
Event Number	12.7	1.5	0.22	107.4	7.2	0.62

Table 7.34: Percent impact of the dominant systematics on the signal acceptance of RS $c = 2.0$ graviton and 2HDM predictions in the $3b$ signal region.

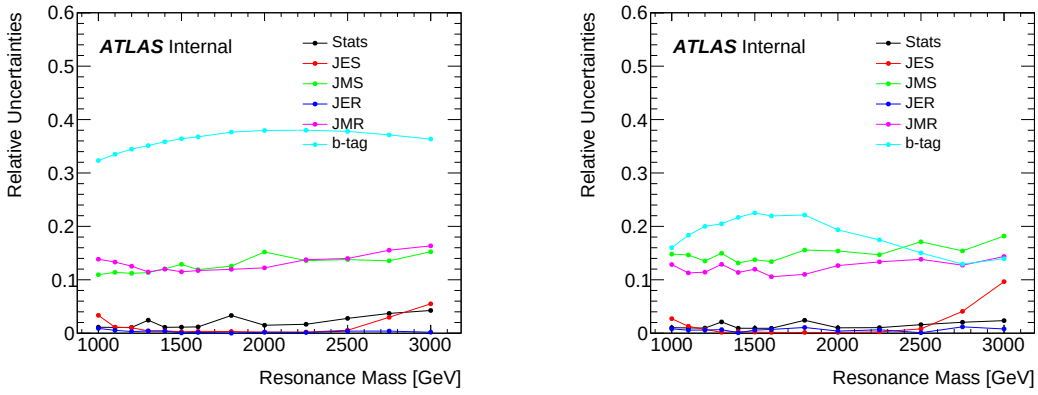


Figure 7.35: Impact of each systematic on the signal prediction as a function of the signal mass, in the $4b$ (left) and $3b$ (right) signal regions.

can be found in Figure 7.37.

7.6 Results

7.6.1 Unblinded Results in Signal Region

After unblinding, we observe 20 events, with $14.61 \pm 0.36 \pm 2.38$ events predicted in 4 b-tag signal region. In 3 b-tag signal region, we observe 316 events, with $284.8 \pm 6.7 \pm 18.2$ events predicted (the uncertainties given here represent the statistical and the total systematic uncertainties). The yields in signal region are summarized in Table 7.35, while a more detailed version can be found in Section 7.4.6. The distribution of (scaled) dijet invariant mass in signal region can be found in Figure 7.38. An excess of data is observed in the 3-tag region for $m_{2J} \sim 900$ GeV and in the range between 1600 and 2000 GeV. Distribution of selected kinematic variables in signal region can be found in Figure 7.39 and 7.40.

7.6.2 Statistical Analysis

The results are interpreted using the statistical procedure described in [1] and references therein. A test statistic based on the profile likelihood ratio [186] is used to test hypothesized values of μ, the global signal strength factor, separately for each model tested. A more general introduction to the common procedure for statistical analysis in ATLAS can be found in [187].

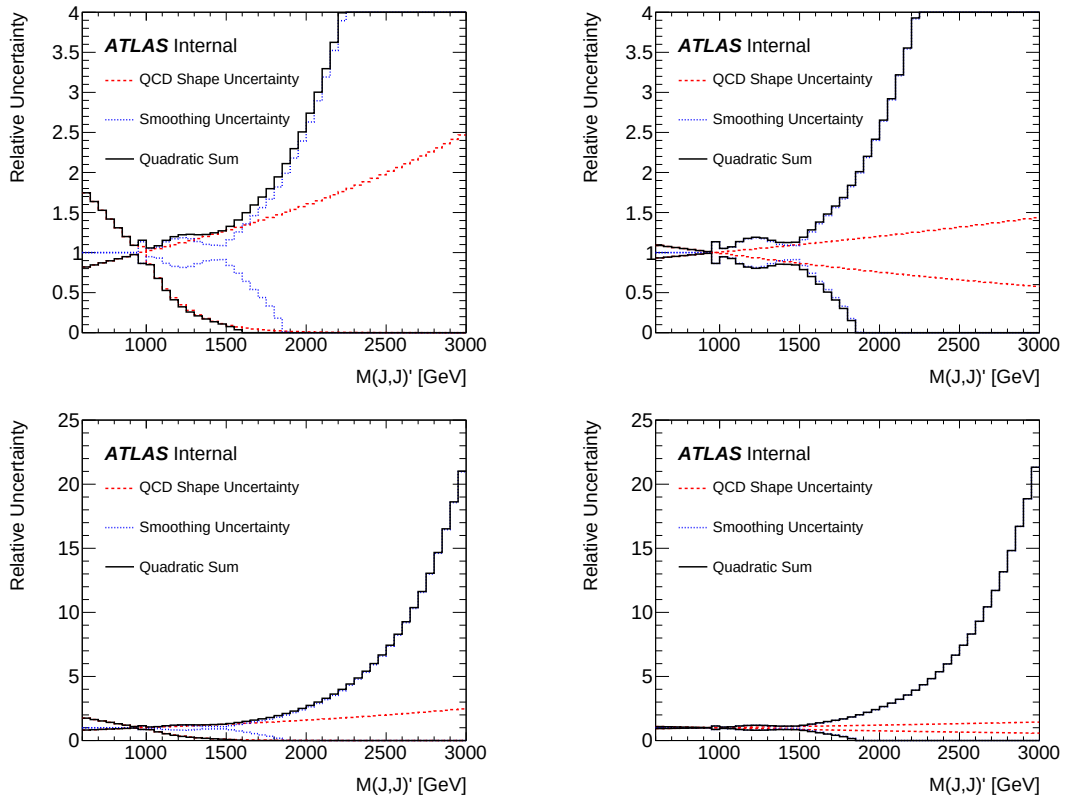


Figure 7.36: The systematic uncertainty from QCD shape variation as well as smoothing procedure for scaled dijet mass, in $4b$ (left) and $3b$ (right) signal region. The only difference between top and bottom is the range of y-axis.

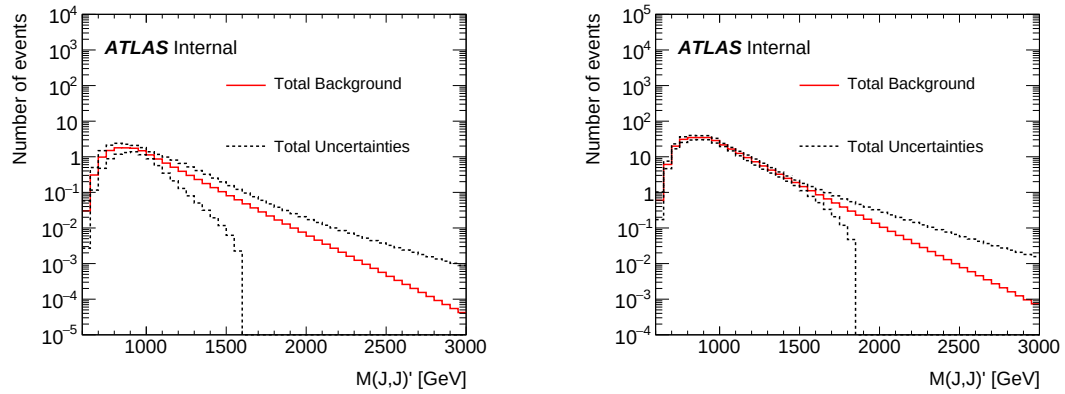


Figure 7.37: The total background estimation in $4b$ (left) and $3b$ (right) signal region, along with total uncertainties (stats.+systematic) variation up and down

Sample	Signal Region (3-tag)	Signal Region (4-tag)
Multijet	235 ± 14	13.5 ± 2.4
$t\bar{t}$	48 ± 22	1.2 ± 1.0
Z+jets	2.0 ± 2.2	–
Total	285 ± 19	14.6 ± 2.4
Data	316	20
$G^*_{\mathrm{KK}}(1000\,\mathrm{GeV})$, $k/\bar{M}_{\mathrm{Pl}}$= 1	3.4 ± 0.9	2.9 ± 1.1

Table 7.35: The number of predicted background events in the hh 3-tag and 4-tag signal regions, compared to the data for the boosted analysis. Errors correspond to the total uncertainties in the predicted event yields. The yields for a 1000 GeV G^*_{KK}in the bulk RS model with $k/\bar{M}_{\mathrm{Pl}}$= 1 is also given. [165]

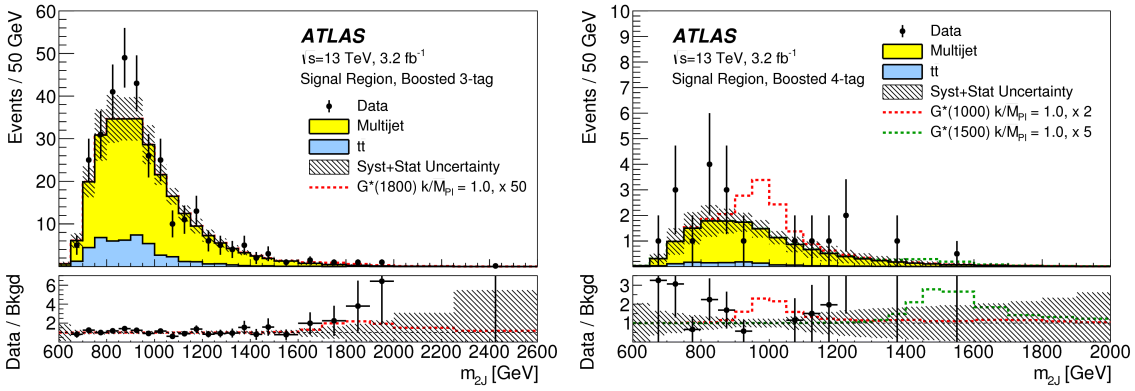


Figure 7.38: Dijet mass distribution in signal region for 3-tag (left) and 4-tag (right) category. The uncertainty band includes both the statistical and systematic uncertainties in the background estimate. [165]

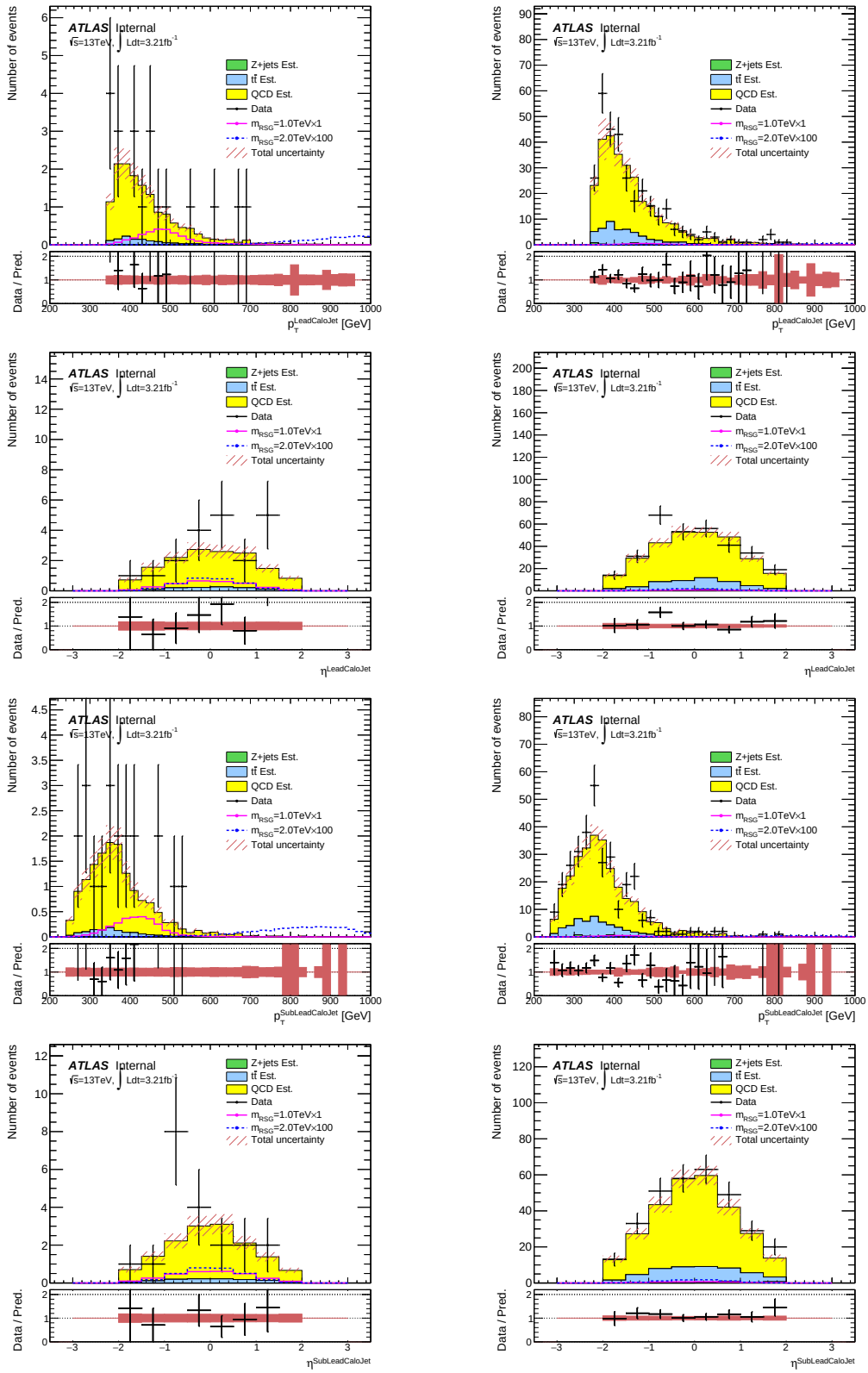


Figure 7.39: Distribution of leading large-R jet p_{T} (first row), leading large-R jet mass (second row), subleading large-R jet p_{T} (third row) and subleading large-R jet mass (fourth row) between data and prediction in "4-tag" (left) and "3-tag" (right) signal region.

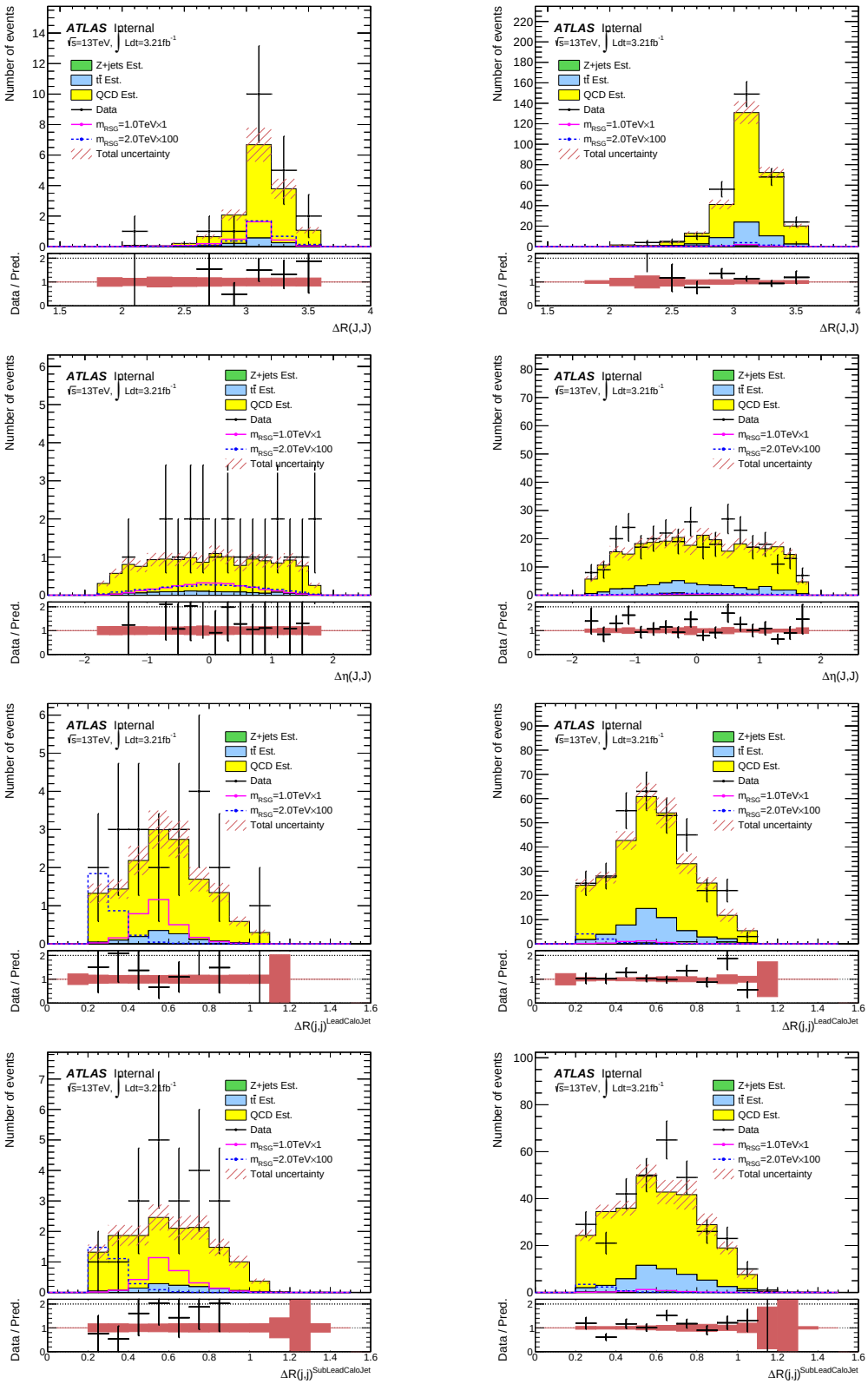


Figure 7.40: Distribution of ΔR between dijet (first row), $\Delta\eta$ between dijet (second row), ΔR between two leading track jets associated with leading large-R jet (third row) and ΔR between two leading track jets associated with subleading large-R jet (fourth row) between data and prediction in "4-tag" (left) and "3-tag" (right) signal region.

Treatment of Systematic Uncertainties

The statistical analysis described below is performed using the data observed in the signal regions. As discussed in [187], systematic uncertainties are treated as independent nuisance parameter within each signal region using Gaussian (for shape systematics) or log-normal (for normalization systematics) *priori* constraint terms in the definition of likelihood function. The exact varied histogram for each source of systematics is obtained through linear interpolation between $\pm 1\sigma$ histograms which are obtained when deriving systematics. Uncertainties that can change both shape and normalization is treated with different constraints as mentioned above, keeping their variation fully correlated with a single nuisance parameter (*prior* factorized into a Gaussian term and log-norm term as function of a single nuisance parameter).

In the combination of $3b$ and $4b$ signal regions, data from the 3-tag and 4-tag signal regions are fitted simultaneously treating systematic uncertainties related to the luminosity and the MC modeling as fully correlated while other uncertainties are treated as uncorrelated. Whole distribution of m_{JJ} is used during the likelihood fit to fully exploit discrimination between signal and backgrounds on shape.

The impact of each source of uncertainties on the expected 95% confidence level exclusion limit can be found in Figure 7.41. This can be regarded as the summary of *post-fit* systematic uncertainties.

Pull, Correlation and Post-fit Distributions

Pull, correlation and post-fit distribution is useful in checking if there is any problem either from statistical fit itself or nuisance parameters. Since the post-fit depends on signal model (mass) as well as hypothesis (μ), it is impractical to include all possible plots here. Therefore only unconditional fit results on mass of 1500 GeV is shown in Figure 7.42, for Bulk RS $c = 1.0$ $3b$ and $4b$ channel (simultaneous fit combining $3b$ and $4b$ is done). Largest pull is less than 2σ coming from JMR systematics with all other nuisance parameters well below 1σ. More tests suggest the statistical fit is robust.

Background-only Hypothesis Test

In order to determine if there are any statistically significant local excesses in the data, a test of the background-only hypothesis ($\mu = 0$) is performed following procedure outlined in [187]. The significance of an excess is quantified using the local p_0, the probability that the background could produce a fluctuation greater than or equal to the excess observed in data. A global p_0 is also calculated for the most significant discrepancy, using background-only pseudoexperiments to derive a correction for the look-elsewhere effect across the mass range tested [188]. Toy MC technique is used for the significance test here.

The results of local p_0 value scan can be found in Figure 7.43 for individual $3b$ or $4b$ channel.

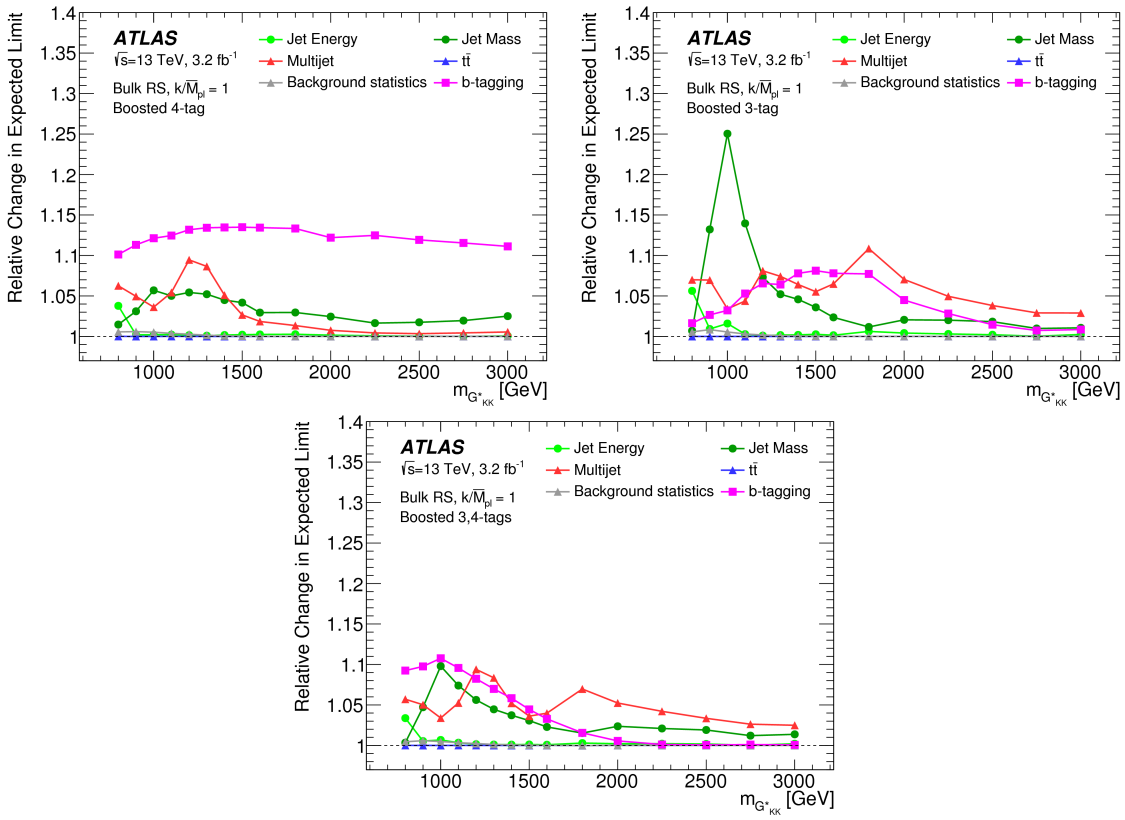


Figure 7.41: The individual relative impact of the systematic uncertainties considered in the $4b$ (top left), $3b$ (top right) and combined boosted analysis on the G^*_{KK} $k/\bar{M}_{\mathrm{Pl}} = 1.0$ expected 95% confidence level exclusion limit, as a function of KK graviton mass. The impact is the ratio of the limit calculated using all systematic uncertainties sources to the limit calculated using all systematic uncertainty sources excluding those under investigation. [182]

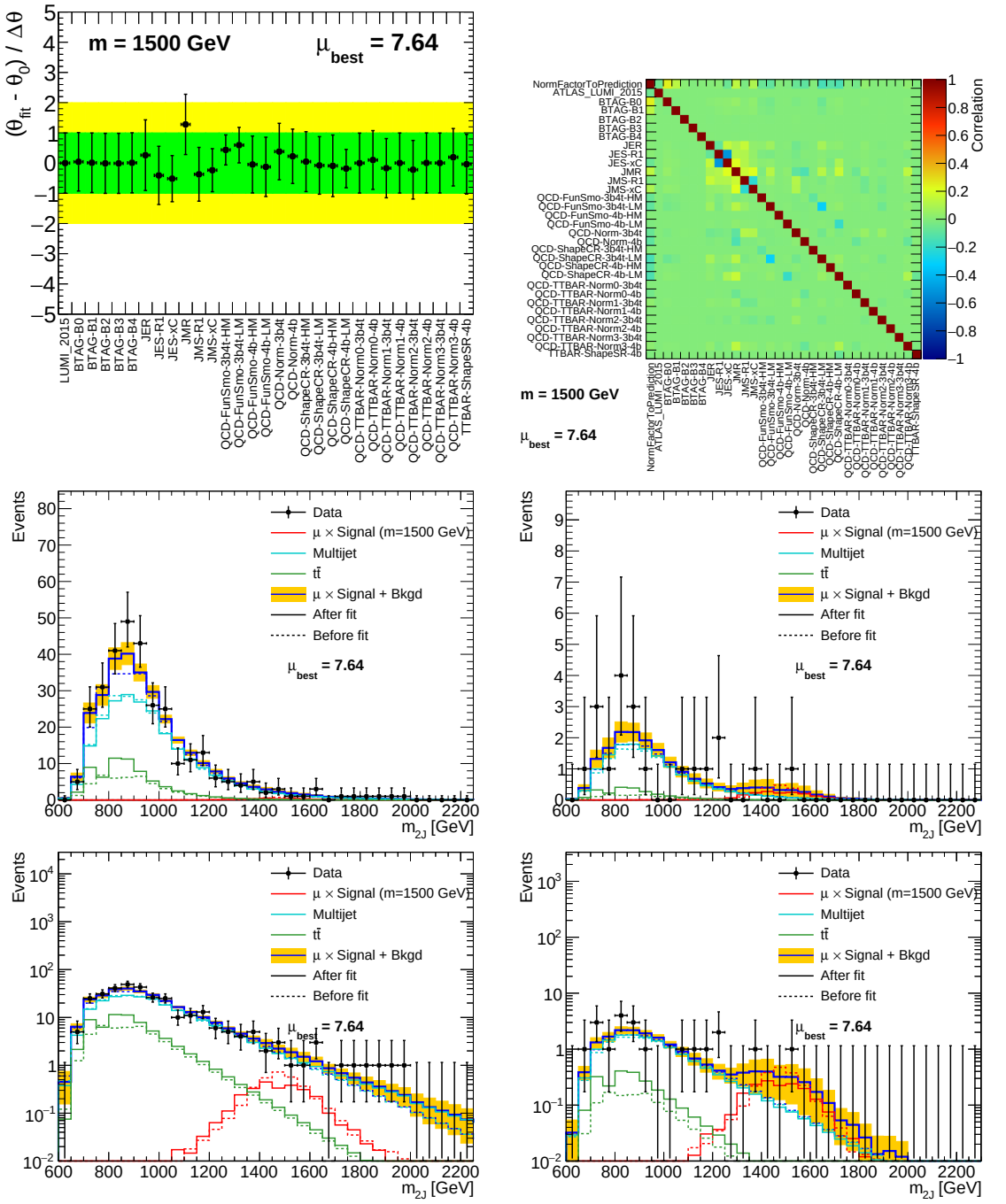


Figure 7.42: Pulls (top left) and correlation (top right) of nuisance parameters and post-fit distributions in linear (second row) and log (third row) scale obtained from the unconditional likelihood fits combining $3b$ and $4b$ channels. The signal is the KK graviton model with $c \equiv k/\bar{M}_P = 1.0$ and mass set to 1500 GeV. In second and third rows, left column is the post-fit distribution in $3b$ channel and right column is the post-fit distribution in $4b$ channel

The local significance with two channels combined can be found in Figure 7.44. A summary of most significant local and global excess can be found in Table 7.36, 7.37 and 7.38. No significant excess is observed in all cases. The largest deviation from background-only hypothesis corresponds to a broad data excess in the 3-tag signal region starting from $\sim$ 1700 GeV. The maximum local significance here is 2σ.

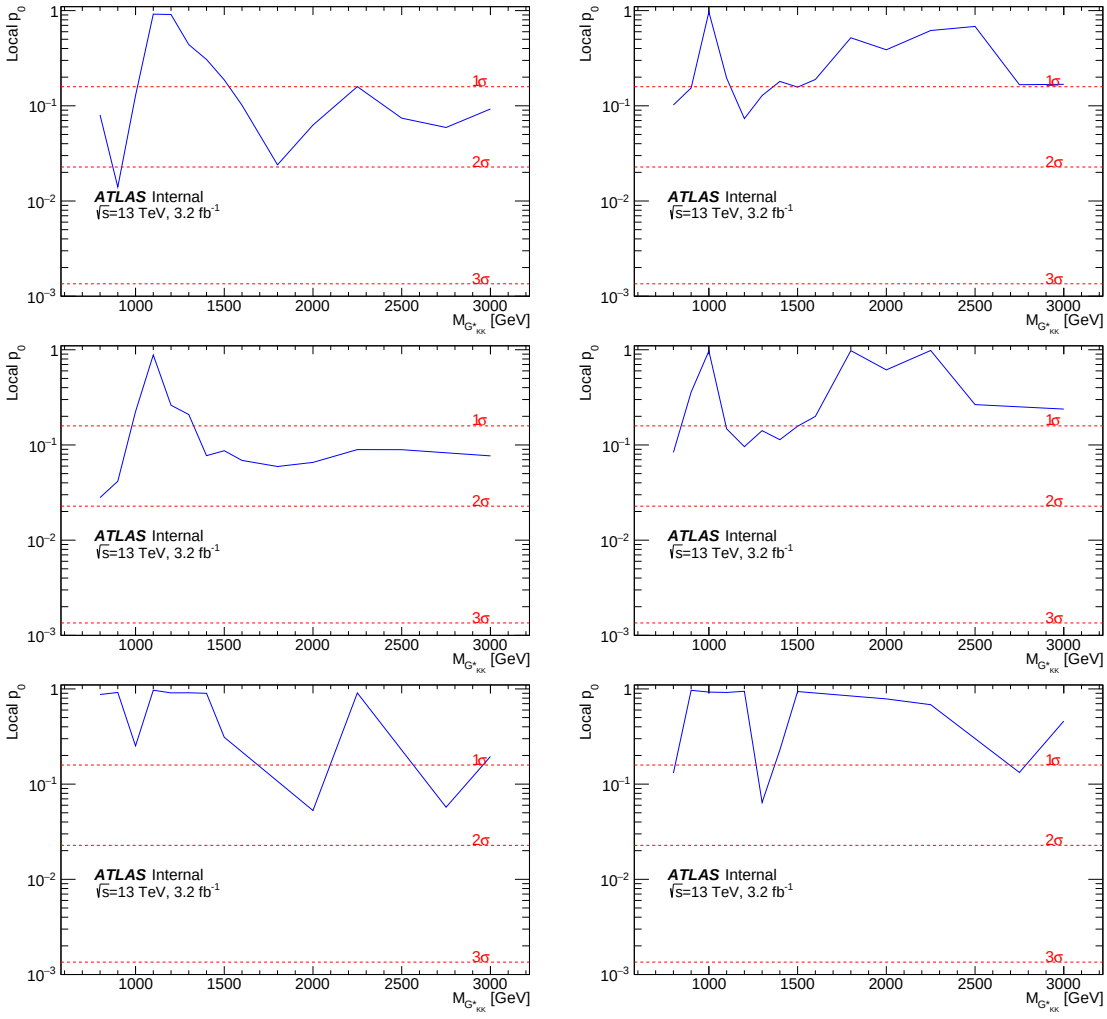


Figure 7.43: Local p_0 value for the $3b$ (left) and $4b$ (right) boosted analysis as a function of the resonance mass for G^*_{KK} with $k/\bar{M}_{\mathrm{Pl}} = 1.0$ (first row), $k/\bar{M}_{\mathrm{Pl}} = 2.0$ (second row) and heavy neutral Higgs from 2HDM model (third row)

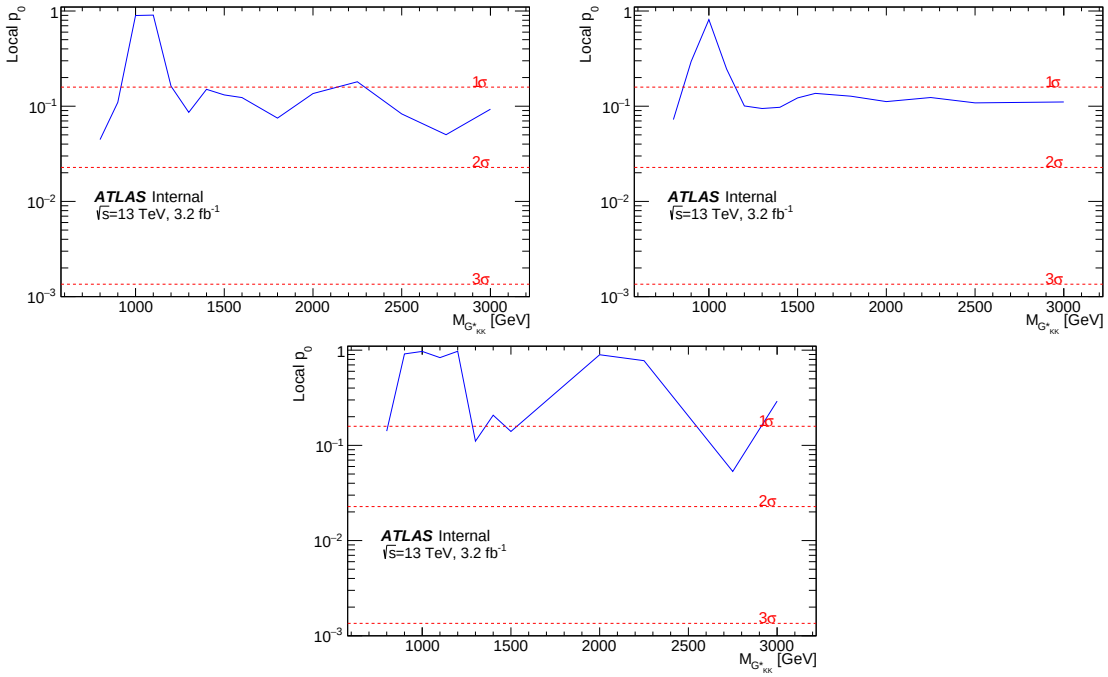


Figure 7.44: Local p_0 value for boosted $3b$+$4b$ analysis as a function of resonance mass for G^*_{KK} with $k/\bar{M}_{\mathrm{Pl}} = 1.0$ (top left), $k/\bar{M}_{\mathrm{Pl}} = 2.0$ (top right) and heavy neutral Higgs from 2HDM model (bottom)

	Local p_0 (mass [GeV])	Local sign.	Trial factor	Global p_0	Global sign.
Resolved	0.1 (900)	1.2	-	-	-
Boosted (4b)	0.073 (1200)	1.5	-	-	-
Boosted (3b)	0.014 (900)	2.2	29.9	0.42	0.2
Boosted (3b+4b)	0.045 (800)	1.7	-	-	-

Table 7.36: Minimum local and global p_0 values along with the corresponding significances and the trial factors for the different analyses and for the KK graviton model with $c \equiv k/\bar{M}_P = 1.0$. The trial factor is computed only when a local significance greater then 2 *sigma* is observed.

	Local p_0 (mass [GeV])	Local sign.	Trial factor	Global p_0	Global sign.
Resolved	0.2 (900)	0.8	-	-	-
Boosted (4b)	0.085 (800)	1.4	-	-	-
Boosted (3b)	0.028 (800)	1.9	-	-	-
Boosted (3b+4b)	0.072 (800)	1.5	-	-	-

Table 7.37: Minimum local and global p_0 values along with the corresponding significances and the trial factors for the different analyses and for the KK graviton model with $c \equiv k/\bar{M}_P = 2.0$. The trial factor is computed only when a local significance greater then 2 *sigma* is observed.

	Local p_0 (mass [GeV])	Local sign.	Trial factor	Global p_0	Global sign.
Resolved	0.059 (900)	1.6	-	-	-
Boosted (4b)	0.064 (1300)	1.5	-	-	-
Boosted (3b)	0.053 (2000)	1.6	-	-	-
Boosted (3b+4b)	0.053 (2750)	1.6	-	-	-

Table 7.38: Minimum local and global p_0 values along with the corresponding significances and the trial factors for the different analyses and for the 2HDM model. The trial factor is computed only when a local significance greater then 2 *sigma* is observed.

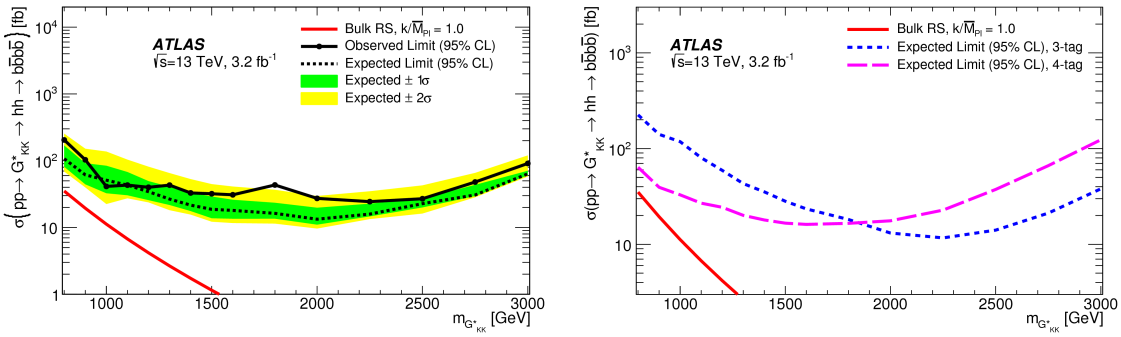


Figure 7.45: The expected and observed limits for $G^*_{\mathrm{KK}} \rightarrow hh \rightarrow b\bar{b}b\bar{b}$ in the bulk RS model with $k/\bar{M}_{\mathrm{Pl}} = 1.0$ for combined 3b and 4b boosted analysis (left) and individual component from 3b and 4b alone (right). [182]

Exclusion Limits

As no significant excess is found, data is further used to set upper bound on cross sections for different benchmark signal processes at 95% confidence level (where $CL_s < 5\%$), following the procedure described in [187]. Toy MC technique is used for exclusion limits here.

The exclusion limit on G^*_{KK} of $k/\bar{M}_{\mathrm{Pl}} = 1.0$ can be found in Figure 7.45, along with a decomposition of the contributions from individual channels. As expected, $4b$ channel is more sensitive for resonance masses less than $\sim$ 1800 GeV, while $3b$ is more sensitive for masses above. Furthermore, we notice the sensitivity of boosted analysis gets worse for $m_{G^*_{\mathrm{KK}}} <\sim$ 1000 GeV. This degradation comes from the 1) threshold effect from single large-R jet trigger, 2) worse reconstruction efficiency since decay products from Higgs boson can no longer be contained inside a single large-R jet. This is complemented by another separate dedicated "resolved analysis", which is also included in [165].

The final results combining both resolved and boosted analysis can be found in Figure 7.46. Instead of a statistical combination, simple combination, that limits from resolved analysis is used for resonance mass below 1100 GeV. and limits from boosted analysis is used for resonance mass above 1100 GeV, is adopted. The choice of splitting point is determined such that the most stringent limit can be imposed on each mass point.

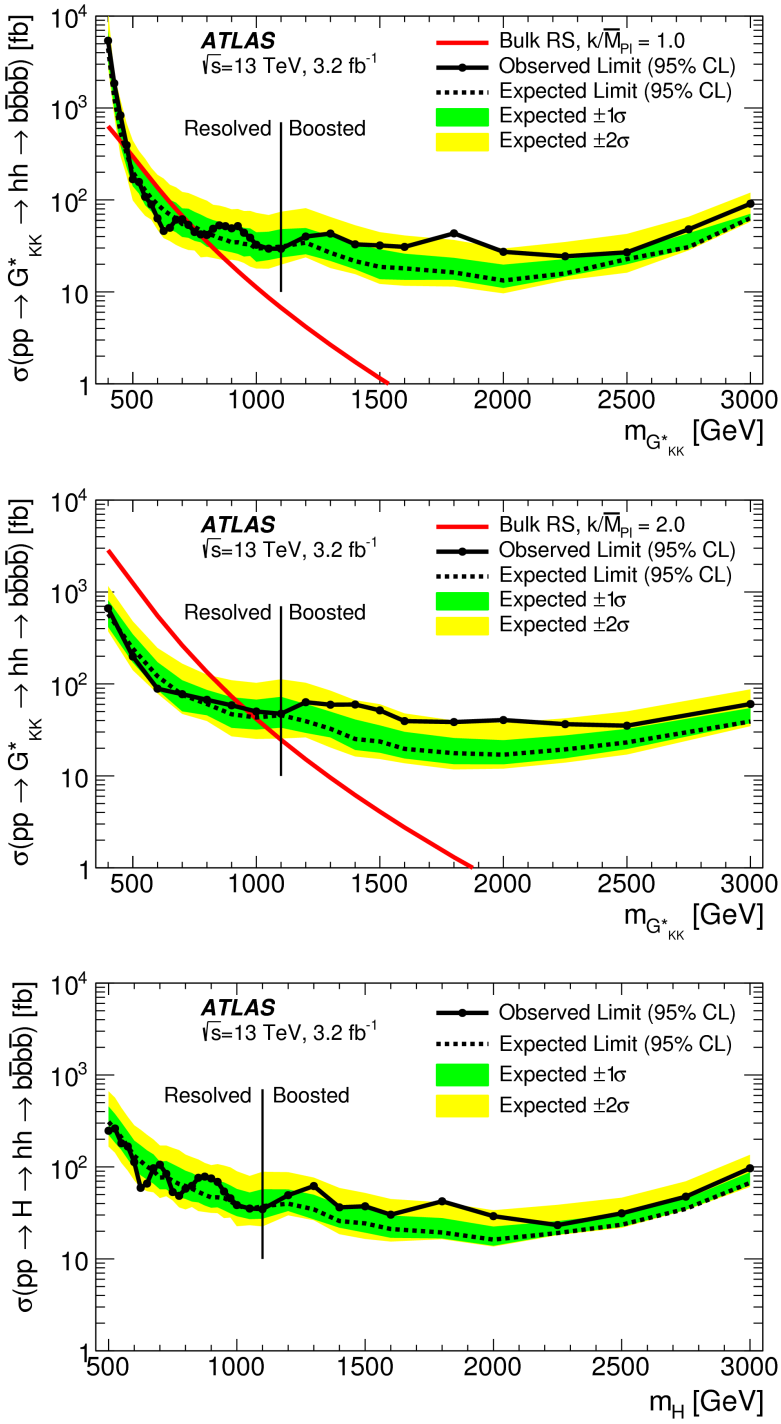


Figure 7.46: The expected and observed upper limit on $G^*_{\mathrm{KK}} \to hh \to b\bar{b}b\bar{b}$ in the bulk RS model with $k/\bar{M}_{\mathrm{Pl}} = 1.0$ (first row) and $k/\bar{M}_{\mathrm{Pl}} = 2.0$ (second row) as well as $H \to hh \to b\bar{b}b\bar{b}$ with fixed $\Gamma_H = 1$ GeV (third row), at 95% confidence level. The results of the resolved analysis are used up to a mass of 1100 GeV and those of the boosted analysis are used at higher mass where its expected sensitivity is higher. The red curves show the predicted cross sections as a function of resonance mass for the models considered. [165]

For spin-2 G^*_{KK} with $k/\bar{M}_{\mathrm{Pl}} = 1.0$, limits on $\sigma(G^*_{\mathrm{KK}} \to hh \to b\bar{b}b\bar{b})$ are set in range between 21 and 73 fb for masses between 600 and 3000 GeV. For $k/\bar{M}_{\mathrm{Pl}} = 2.0$, this becomes 34 to 86 fb. For spin-0 narrow-width H boson, this is between 30 to 300 fb (30 to 100 fb for boosted analysis only). Although no events are observed around 3000 GeV or above, observed limit is above 1σ weaker than expected limit due to 1) substantial tail at low mass region from high-mass signals due to degraded resolution and 2) slight data excess at high mass. For boosted analysis, no signal model is able to be excluded yet. Mass range of 480-770 (< 965) GeV is observed to be excluded for $k/\bar{M}_{\mathrm{Pl}} = 1.0$ ($k/\bar{M}_{\mathrm{Pl}} = 2.0$)

The search sensitivity of Run 2 analysis as presented here exceeds that of Run 1 [122] for resonance masses above 1350 GeV, despite of less luminosity accumulated (3.2 fb^{-1} for Run 2 at the time of analysis compared to 19.5 fb^{-1} for Run 1), as illustrated in Figure 7.47. The improvement mainly comes from 1) a higher signal cross section due to increase in center of mass energy and 2) introduction of $3b$ channel that is able to extend the sensitivity significantly above $\sim$ 1700 GeV.

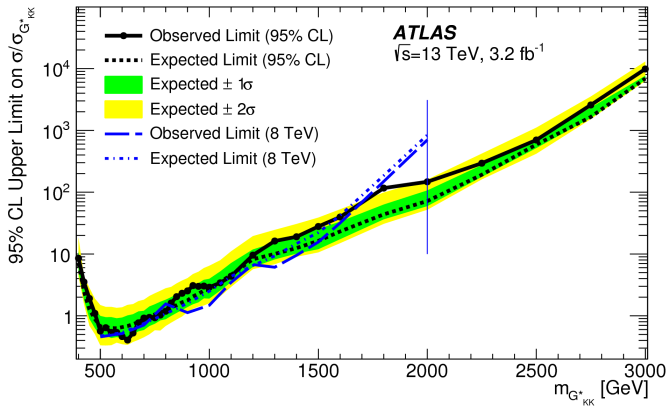


Figure 7.47: The expected and observed 95% CL upper limits on the $G^*_{\mathrm{KK}} \to hh \to b\bar{b}b\bar{b}$ cross section strength modifier μ ($\sigma = \mu\sigma(G^*_{\mathrm{KK}})$) in the bulk RS model with $k/\bar{M}_{\mathrm{Pl}} = 1.0$ for the combination of resolved and boosted analyses at $\sqrt{s} = 8$ and 13 TeV. The search sensitivity of the analysis at $\sqrt{s} = 13$ TeV is similar to that achieved at $\sqrt{s} = 8$ TeV with 19.5 fb^{-1} for resonance masses below 1350 GeV but exceeds it above that mass by factors of 1.4 at 1500 GeV and 12 at 2000 GeV. The vertical blue line at a mass of 2000 GeV indicates the upper end of the search region for the 8 TeV analysis. [182]

7.6.3 Conclusion

No significant data excess is observed above the estimated background consisting mainly of multijet and $t\bar{t}$ events. Upper limits on production cross section times branching ratio to $b\bar{b}b\bar{b}$ final state are set for spin-0 and spin-2 resonances with values between 24 to 113 fb for resonance masses between 600 and 3000 GeV, at 95% confidence level. The search sensitivity of this analysis exceeds that achieved at $\sqrt{s} = 8$ TeV with 19.5 fb^{-1} for resonance masses above 1350 GeV. Furthermore, search

has been extended to cover mass range 2000 to 3000 GeV.

7.7 Improved Search and Results

After the result shown above was published using data collected in 2015, work continues as much more abundant data flushes in during 2016. Therefore, a second stage of the analysis is conducted, using data collected during 2015 and March-July 2016, and became public since 2016 summer. Since the second stage of analysis is based on the work of first stage, basic strategies as well as techniques are shared. Therefore, instead of a detailed description, the second stage of analysis will be reviewed in this section with emphasis on the differences and improvements with respect to the earlier one. In the descriptions below, "this analysis" always refers to second stage of this search, unless otherwise mentioned explicitly.

The improvement mainly comes from two aspects: a factor of four increase in integrated luminosity and improved sensitivity for resonances with masses above 2500 GeV due to the removal of track jet multiplicity. The multijet background estimation strategy is also adjusted accordingly since signal region categorization is changed due to our optimizations. Readers with interest in second stage of the analysis, as well as the resolved part of analysis, can find more details in [166].

7.7.1 Data and Trigger

Though 2015 data is reused in this analysis, dataset is re-processed due to improvement in reconstruction software and algorithms (e.g. b-tagging optimization, improved tracking alignment, improved track reconstruction). While integrated luminosity for 2015 data is still 3.2 fb^{-1}, luminosity uncertainty on gets reduced to $\pm 2.1\%$ from 5% through improved luminosity measurement by following methodology as detailed in [74, 75]. Data collected during March-July 2016 corresponds to an integrated luminosity of 10.1 fb^{-1}, with a preliminary uncertainty of $\pm 3.7\%$ from measurements performed in May 2016. The total integrated luminosity is then 13.3 fb^{-1}.

Triggers used in 2015 data and 2016 are also different. For 2015 dataset, same trigger as first stage of analysis as presented above is used, requiring a single anti-k_t jet with $R = 1.0$ and $p_{\mathrm{T}} > 360$ GeV. For 2016 dataset, similar trigger is used but with higher threshold of $p_{\mathrm{T}} > 420$ GeV. The increase in threshold in 2016 is to make sure trigger can still remain un-prescaled in the presence of increased instantaneous luminosity from LHC.

7.7.2 Selections

Event reconstruction and selections are almost identical to the previous analysis as shown in Section 7.3, except for the categorizations in number of b-tags. While "4-tag" region is still used, "3-tag" has been modified such that requirement of four track jets (two on each Higgs candidate

jet) are dropped. However, due to the requirement of exactly 3 b-tagged track jets, requirement of at least three track jets is still implicitly imposed. One thing important to clarify is that, only leading and subleading track jets, if exist, are considered when counting number of b-tags. This is to ease the procedure of assignment b-tagging scale factors and their uncertainties without hurt on sensitivity. Therefore "4-tag" means two b-tagged track jets on each Higgs candidate, and "3-tag" means two b-tagged track jets on one Higgs candidate while one b-tagged track jet on another Higgs candidate jet.

Besides "4-tag" and modified "3-tag" ("3-tag" for short below), an additional "2-tag-split" signal region is also considered. "2-tag-split" samples are required to have exactly one b-tagged track jet for each Higgs candidate jet, without any requirement on track jet multiplicity except for the requirement imposed by b-tags implicitly.

The cutflow and signal efficiencies can be found in Figure 7.48. Comparing with Figure 7.10, efficiency of "3-tag" category is improved in general due to the looser requirement on track jet multiplicity, in particular for resonance mass above 2000 GeV, while "4-tag" efficiency is almost identical. The gain in "3-tag" efficiency reflects the recovered cases where one Higgs candidate is so boosted that two close-by b-hadrons merge into a single track jet. As resonance masses get even higher, both Higgs candidate would get so boosted that double b-hadrons on each side get merged into a single track jet. This topology motivates the "2-tag-split" region, which can significantly recover signal acceptance at high resonance masses as shown here. Three orthogonal signal regions are complementary to each other: "4-tag" is most sensitive for resonance masses roughly from 1000 to 1600 GeV; "3-tag" is most sensitive for resonance masses roughly from 1600 to 2300 GeV; "2-tag-split" is most sensitive for resonance masses roughly from 2300 GeV above.

7.7.3 Background Estimation

The background estimation strategy also inherits from first stage of the analysis. Several changes, however, are introduced in accordance with the change in signal selections.

As described in Section 7.4, shape of dominant multijet background in signal region is extrapolated from the multijet distribution in a region same as signal region except looser b-tagging requirement. In the past, "2-tag" region is used as this "template region". While this is still good for "4-tag" and "3-tag" SR here, it is no longer appropriate for "2-tag-split" region newly introduced. Therefore, a "0-tag" region is instead introduced as the "template region". In "0-tag" region, no track jets, if any exist, should be b-tagged. However, when extrapolating from "0-tag" to any of three SR, same track jet multiplicity requirement as implicitly imposed on target SR should be applied on the template "0-tag" regions as well in order to mimic the kinematics of target SR.

When extrapolating from "0-tag" to signal regions, it is observed that the good shape agreement as found in first stage of analysis is no longer the case. Therefore, a kinematic re-weighting is introduced during the extrapolation to correct the shape difference. The same technique is also used

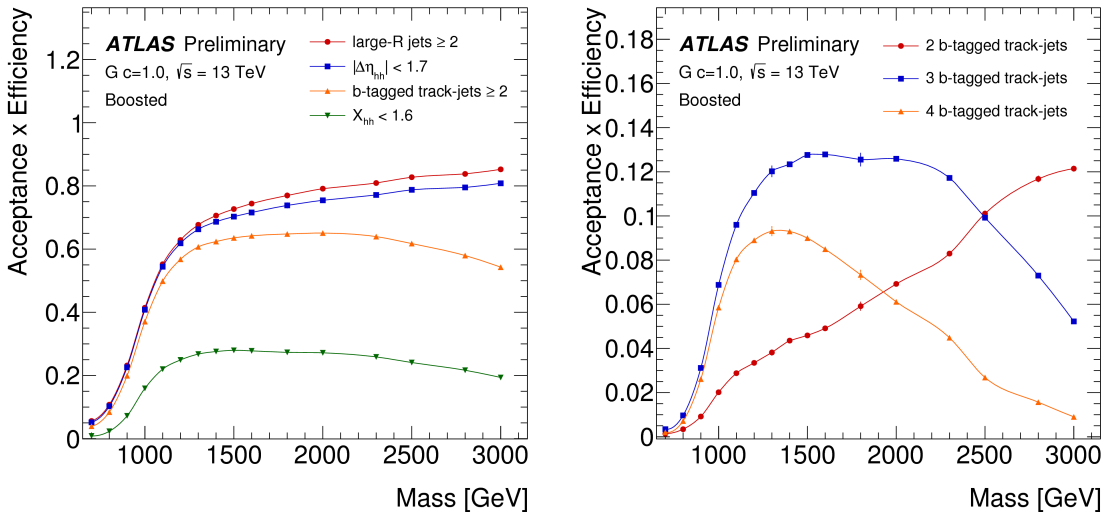


Figure 7.48: (Left) The absolute selection efficiency as function of G^*_{KK} mass at eacg stage of the event selection. Trigger efficiency is 100% after requiring two large-R jets, hence now shown on the plot. (Right) The selection efficiency of in each b-tag categorization after requiring $X_{hh} < 1.6$ as function of G^*_{KK} mass. [166]

in the resolved part of this search, as well as the other search that will be presented in this thesis. Therefore, more details on kinematic re-weighting can be found in Chapter 8.

Furthermore, definition of control region and sideband is also modified slightly. While boundary between signal region and control region is the same as earlier, sideband is now defined as $36 < R_{hh} < 63$ GeV. The upper bound on sideband is to limit the sideband so that it can be kinematically closer to SR and CR.

$t\bar{t}$ distribution in "4-tag" is now taken from MC simulation direction, instead of extrapolating from "3-tag" as before. This is mainly due to the availability of inclusive $t\bar{t}$ sample with significantly more statistics in ATLAS.

In the last, when smoothing multijet invariant mass distribution as predicted in the signal region, a "dijet" functional form is now used as nominal instead of exponential fit:

$$f(m_{JJ}) = p_1(1 - \frac{m_{2J}}{\sqrt{s}})^{p_2}(\frac{m_{2J}}{\sqrt{s}})^{p_3} \tag{7.5}$$

This is motivated by the observation from first stage of analysis that exponential fit might underestimate background prediction in the tail. Such underestimation becomes even more evident when we have substantially more data enriching the tail part due to more data being collected. Therefore, the "dijet" functional form which can better describe the tail of distribution is introduced.

7.7.4 Results

The results for this second stage of analysis can be found in Table 7.39 and Figure 7.49, showing the comparison between data and prediction in signal region in terms of yields and shapes respectively.

Sample	2-tag-split	3-tag	4-tag
Multijet	2310±240	515±41	32.6±7.6
$t\bar{t}$	460±170	81±37	5.7±5.2
Total	2770±130	596±39	38.3±9.0
Data	2813	671	32
G^*_{KK} (2 TeV), $kMPl = 1.0$	0.17±0.10	0.31±0.06	0.15±0.06

Table 7.39: Number of predicted background events in signal region compared to data. Quoted errors include both statistical and systematic uncertainties. Anti-correlation between multijet and $t\bar{t}$ yield is accounted for. [166]

No excess is found in the data, and exclusion limit on $\sigma(G^*_{\mathrm{KK}} \to hh \to b\bar{b}b\bar{b})$ from Bulk RS G^*_{KK} with $k/\bar{M}_{\mathrm{Pl}} = 1.0$ is setup with 95% confidence level, as shown in Figure 7.50. A significant improvement with respect to first stage analysis can be found. The improvement for resonance masses below 2000 GeVmainly comes from a factor of four increase in integrated luminosity, while improvement for high resonance masses mainly comes from the looser requirement on track jet multiplicity and introduction of "2-tag-split" signal region.

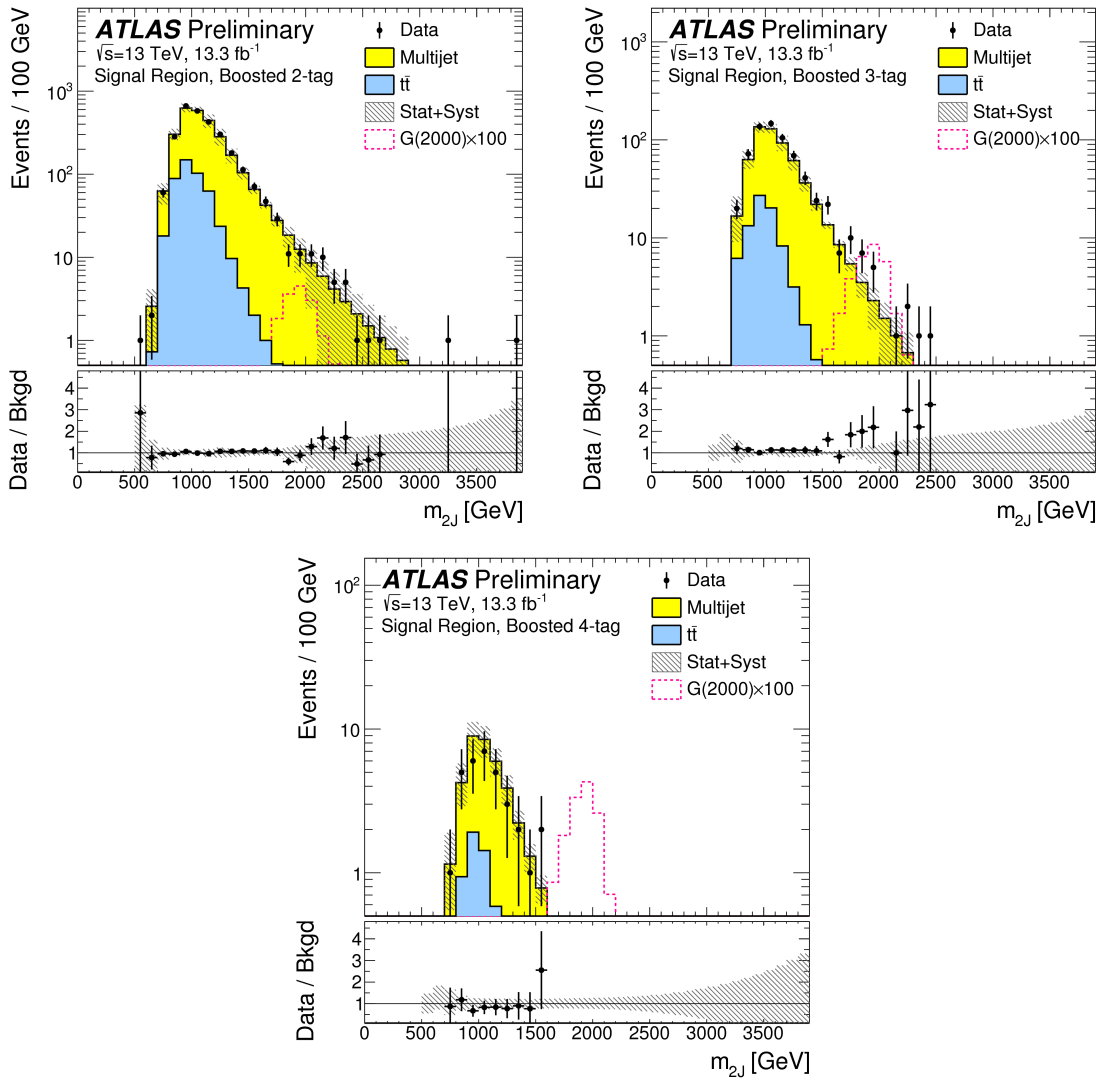


Figure 7.49: Distribution of m_{2J} in the signal region for "2-tag-split" (top left), "3-tag" (top right) and "4-tag" (bottom) [166]

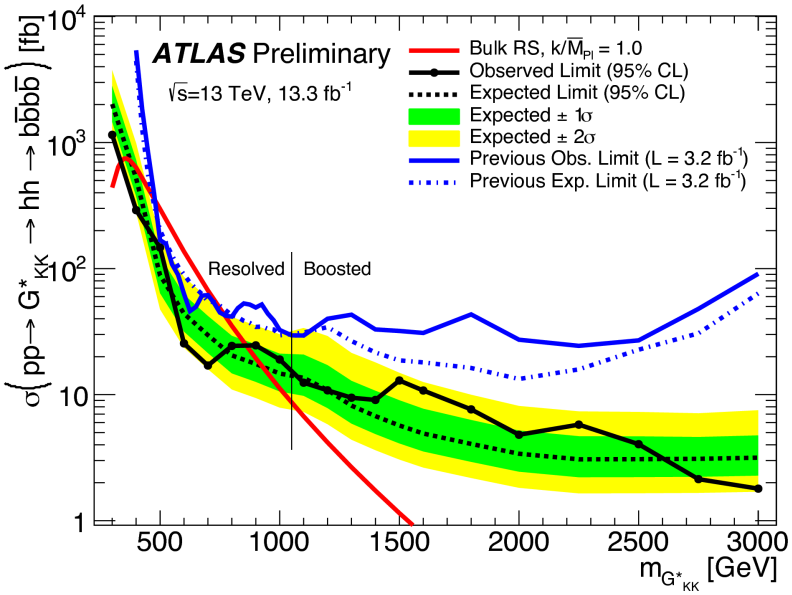


Figure 7.50: The expected and observed uppser limit for $G^*_{\mathrm{KK}} \rightarrow hh \rightarrow b\bar{b}b\bar{b}$ in the bulk RS model with $kMPl = 1.0$ at 95% confidence level. Transition point from resolved analysis to boosted analysis is at 1000 GeVsuch that maximal sensitivity is used for each mass point. Blue curve corresponds to the results from first stage of analysis. [166]

Chapter 8

Search for Heavy Resonance Decaying to W/Z Boson and Higgs Boson in qqbb Final States

8.1 Introduction

Besides the spin-2 and spin-0 heavy resonance as discussed in Chapter 7, many new physics beyond Standard Model also predicts spin-1 heavy resonances at TeV scale. Typically, these spin-1 resonance has non-negligible coupling with the Standard Model gauge bosons and Higgs boson, depending on the exact models behind. Such resonances are predicted in multiple models, such as composite Higgs [189, 190] and Little Higgs model [191].

In this chapter, we will focus on search of such spin-1 resonances at TeV scale decaying to a W or Z boson and Higgs boson in fully hadronic $q\bar{q}^{(\prime)}b\bar{b}$ final states, using proton-proton collision data of 36.1 fb^{-1} at $\sqrt{s} = 13$ TeV. In particular, the search and its results are expressed in the context of a simplified model which incorporates a Heavy Vector Triplet (HVT) [31] of bosons, allowing for the interpretation of the results in a large class of models. The new heavy vector bosons, W' and Z', couple to the Higgs boson and SM gauge bosons with coupling strength $c_H g_V$ and to the fermions with coupling strength $(g^2/g_V)c_F$, where g is the SM SU(2)$_L$ coupling constant. The parameter g_V represents the typical strength of the new vector bosons' interaction, while the dimensionless coefficients c_H and c_F parameterize departures of this typical strength for interactions with the Higgs boson and with fermions, respectively, and are expected to be of order unity in most models. Two benchmark models are used: in the first, referred to as *Model A*, the branching fractions of the new heavy vector to fermions and gauge bosons are comparable, as in some extensions of the SM gauge group [32]. In *Model B*, fermionic couplings to the new heavy vector are much suppressed,

as for example in a composite Higgs model [33]. The regions of HVT parameter space studied correspond to the production of resonances with an intrinsic width that is narrow relative to the experimental resolution in order to have simplified model validated. The experimental resolution is roughly 8% of the resonance mass. The sensitivity of the analysis to wider resonances is not tested.

This search is part of a very large family of di-boson searches in LHC physics, conducted by both ATLAS and CMS experiments. Two other final states that are closely related to this search are leptonic VH searches and VV searches. For leptonic VH searches, ATLAS set a lower limit at 95% confidence level (CL) on W' (Z') mass at 1.47 (1.36) TeV in HVT Model A with $g_V = 1$ [192] based on data collected at $\sqrt{s} = 8$ TeV. This limit has been extended to 1.75 (1.49) TeV based on same search in ATLAS using 3.2 fb^{-1} data collected at $\sqrt{s} = 13$ TeV [149] in the context of W' (Z') in HVT Model A. For HVT Model B, the limits are 2.22 (1.58) TeV. In the CMS, VH searches exploiting both hadronic and leptonic final states already exist in Run 1. Searches by CMS at $\sqrt{s} = 8$ TeV in hadronic channels based on HVT Model B with $g_V = 3$ exclude heavy resonance masses below 1.6 TeV ($W' \to WH$), below 1.1 TeV and between 1.3 TeV and 1.5 TeV ($Z' \to ZH$) and below 1.7 TeV (combined $V' \to VH$) at 95% CL [193]. Leptonic channel $W' \to WH \to l\nu b\bar{b}$ carried by CMS excludes masses up to 1.5 TeV in the same context [194]. There is also a $Z' \to ZH \to q\bar{q}\tau^+\tau^-$ channel by CMS in Run 1 setting limits on Z' production cross-section [195]. For VV final states (WW/WZ/ZZ), a new gauge boson with mass below 2.6 TeV is excluded at 95% CL by ATLAS using 3.2 fb^{-1} of data at $\sqrt{s} = 13$ TeV [196]. In addition to these publications, readers can find more recent public results on ATLAS exotics public result page [197].

Since there is no search by ATLAS in full hadronic channel during Run 1, this is the first time this channel is explored inside ATLAS using Run 2 data collected so far. Results using 2015 data and part of 2016 data have been made public during 2016 summer [198]. A more complete result using 2015 and 2016 full year data are also made public during 2017 spring [199], and will be the main content to be presented in this chapter.

Search strategy used in this search is very similar to the ones explored in Chapter 7 due to similar boost event topology. This search will focus on new resonances with mass above 1 TeV. As a result, the V and H bosons produced are highly boosted, with resulting decay products of each boson likely to be collimated and merged into single large radius jets. Booosted boson identification techniques as discussed in Chapter 6 is therefore used. The dijet invariant mass spectrum of two large radius jet is used as discriminant variable, where the signature of new heavy resonance decay yields a resonant structure on top of the smoothly falling background. The dominant background corresponds to multijet processes, with much smaller contributions from other non-resonant backgrounds including $t\bar{t}$ and V+jets. The dominant multijet background can be heavily suppressed by employing jet substructure techniques and b-tagging requirements. Similar to the searches presented in Chapter 7, a similar data-driven method is used for multijet background estimation while remaining backgrounds are modelled with Monte Carlo (MC) samples.

As mentioned above, many methods and procedures adopted in this analysis, including search strategy, background estimation, systematic uncertainties as well as systematic analysis are similar to the search presented in Chapter 7. Therefore, we will not describe these in great details as last chapter, but instead only highlights studies specific to this search. This chapter will be organized as following: Section 8.2 provides a quick overview of samples being used; Event selections can be found in Section 8.3; Background estimation is in Section 8.4; Studies of systematic uncertainties can be found in Section 8.5; Results are discussed in Section 8.6.

8.2 Data and Simulation Samples

This section describes the pp collision data collected by the ATLAS detector that is used in this analysis as well as the MC samples used to model the signal and background processes, generated at the same centre-of-mass energy. The MC events are passed through the ATLAS detector simulation [171], based on GEANT4 [170]. Both the collected and simulated data are reconstructed using the standard ATLAS reconstruction algorithms.

8.2.1 Data

This search is performed with a combination of $\sqrt{s} = 13$ TeV data collected by the ATLAS experiment during the 2015 and 2016 LHC pp runs, in the 25 ns running configuration. Only data selected in the standard good runs list (GRL) are used, ensuring that all the relevant elements of the ATLAS detector were fully operational and efficient while the data were collected.

The integrated luminosity of the runs is estimated following the methodology described in [74]. The 2015 dataset corresponds to an integrated luminosity of 3.2 fb^{-1}, with runs of 50 ns configurations excluded. The preliminary uncertainty on the combined 2015+2016 integrated luminosity is 3.2%. It is derived, following a methodology similar to that detailed in [75], from a preliminary calibration of the luminosity scale using $x - y$ beam-separation scans performed in August 2015 and May 2016.

Additional quality conditions are applied, as recommended by the Data Preparation group. These include the rejection of incomplete events, as well as events with LAr noise bursts and LAr or Tile data corruption. No pile-up re-weighting procedure is applied since the dominant background in this analysis is data-driven.

8.2.2 Simulated Signal and Background Samples

Signal Samples

The Heavy Vector Triplet (HVT) Model A with $g_V = 1$ samples are used as a benchmark model to set limits in this analysis. Under the assumption that there are no differences between Model A

and Model B in terms of shapes, the results interpreted with the Model A samples can be directly translated to Model B by scaling the relevant branching ratios. Therefore only MC simulation for Model A is performed.

The MC samples are generated with MG5_aMC@NLO v2.2.2 [172] interfaced to Pythia 8.186 [167] for shower and hadronization, with the NNPDF23 PDF set [173] and the ATLAS A14 tune [174]. The Higgs decays to all quarks are included, with $H \to b\bar{b}$ and $H \to c\bar{c}$ contributions, corresponding to a branching ratio of 0.569 + 0.0287 for $m_H = 125.5$ GeV.

Background Samples

The dominant background to this search originates from multijet processes. Since the multijet MC samples do not have enough statistics in the high mass region of interest, where are highly suppressed by the V/H-tagging techniques, data-driven technique is used in the analysis for multijet background. The MC simulation are only used to validate data-driven method, as well as to optimize the event selection strategy.

Other contributions to the background composition come from $t\bar{t}$, V+jets and diboson processes, totaling from 2 to 10% of the background, depending on the region. The modeling of these processes relies on MC simulation.

For studies with simulated multijet events, the nominal MC samples used are generated with Pythia 8.186, with the NNPDF23LO PDF and the ATLAS A14 tune for the underlying event. Events are generated in bins of p_{T} of anti-k_t R=0.6 truth jets in order to populate statistics in each p_{T} range.

The $t\bar{t}$ samples are generated with Powheg-box v2 [200] with the CT10 PDF, interfaced with Pythia 6.428 [179] with CTEQ6L1 PDF [201] and Perugia 2012 tune for parton shower [180]. EvtGen v1.2.0 [169] is used for properties of bottom and charm hadron decays. The samples are divided in terms of final state: the dominant contribution comes from $t\bar{t}$ events where both top quarks decay hadronically, but an additional sample is also considered which includes leptonic and semi-leptonic decays[1]. In order to keep statistical fluctuations small across the dijet mass spectrum, additional $t\bar{t}$ samples are used which are generated in slices of $t\bar{t}$ invariant mass, starting from 1.1 TeV. Double-counting is avoided by explicitly cutting out events in the inclusive sample that have a $t\bar{t}$ mass greater than 1.1 TeV. The cross-section of the $t\bar{t}$ process is normalized to NNLO+NNLL in QCD, as calculated by Top++ 2.0 [181]. The Powheg hdamp parameter [202] is set to the top mass, taken as $m_t = 172.5$ GeV.

The $W+$jets and $Z+$jets events are generated with Sherpa 2.1[2] [203] interfaced with the CT10 PDF set. Matrix elements of up to 4 extra partons are calculated at leading order in QCD. Only

[1]The leptonic and semi-leptonic final states contribute to 18% of the $t\bar{t}$ component in the signal regions of this analysis.

[2]These are the newest available samples for this final state.

the hadronic decays of the W and Z are included. The samples are split by boson p_{T} in order to populate statistics in each p_{T} slice.

8.3 Selections

8.3.1 Event Reconstruction

Collision vertices are reconstructed requiring a minimum of two tracks each with transverse momentum $p_{\mathrm{T}} > 0.4$ GeV. The primary vertex is chosen to be the vertex with the largest $\sum p_{\mathrm{T}}^2$, where the sum extends over all tracks associated with the vertex.

The identification and reconstruction of hadronically decaying gauge boson and Higgs boson candidates is performed with the anti-k_t jet clustering algorithm with R parameter equal to 1.0. These large-R jets are reconstructed from locally calibrated topological clusters of calorimeter energy deposits. To mitigate the effects of pileup, the large-R jets are trimmed: the jet constituents are reclustered into subjets using the k_t algorithm with $R = 0.2$, removing those with $p_{\mathrm{T}}^{\mathrm{subjet}}/p_{\mathrm{T}}^{\mathrm{jet}} < 0.05$, where $p_{\mathrm{T}}^{\mathrm{subjet}}$ is the transverse momentum of the subjet and $p_{\mathrm{T}}^{\mathrm{jet}}$ is the transverse momentum of the original large-R jet. In order to improve over the limited angular resolution of the calorimeter, the combined mass of a large-R jet is computed using a combination of calorimeter and tracking information [204]. The mass is defined as

$$m_J \equiv w_{\mathrm{calo}} \times m_{\mathrm{J}}^{\mathrm{calo}} + w_{\mathrm{track}} \times \left(m_{\mathrm{J}}^{\mathrm{track}} \frac{p_{\mathrm{T}}^{\mathrm{calo}}}{p_{\mathrm{T}}^{\mathrm{track}}} \right)$$

where $m_{\mathrm{J}}^{\mathrm{calo}}$ is the calorimeter-only estimate of the jet mass, $m_{\mathrm{J}}^{\mathrm{track}}$ is the jet mass estimated via tracks with $p_{\mathrm{T}} > 0.4$ GeV associated with the large-R jet using ghost association. To corrected for the missing neutral component of the jet, $m_{\mathrm{J}}^{\mathrm{track}}$ is scaled by the ratio of calorimeter to track p_{T} estimates. The weighting factors w_{calo} and w_{track} are $p_{\mathrm{T}}^{\mathrm{calo}}$ dependent functions of the calorimeter and track based jet mass resolutions used to optimize the combined mass resolution.

Track jets clustered using the anti-k_t algorithm with $R = 0.2$ are used to aid the identification of b-hadron candidates from the Higgs boson decay. Track jets are built from charged particle tracks with $p_{\mathrm{T}} > 0.4$ GeV and $|\eta| < 2.5$ that pass a set of hit and impact parameter criteria to minimize the impact of tracks from pileup interactions, and are required to have track jet $p_{\mathrm{T}} > 10$ GeV, $|\eta| < 2.5$, at least two tracks clustered in the track jet. Track jets are associated with large-R jets using ghost association. The identification of b-hadrons relies on a multivariate tagging algorithm which combines information from several vertexing and impact parameter tagging algorithms. The vertexing and impact parameter tagging algorithms are applied to a set of tracks in a region of interest around each track jet axis to enable the reconstruction of the b-hadron decay vertex. The b-tagging requirements result in an efficiency of 77% for track jets containing b-hadrons, and a misidentification rate of $\sim 2\%$ ($\sim 24\%$) for light-flavored (charm) jets, as determined in a sample of

simulated $t\bar{t}$ events.

Muons are reconstructed by combining tracks in the inner detector and the muon system, and are required to satisfy "Tight" muon identification criteria. The four-momentum of the closest muon with $p_{\mathrm{T}} > 4$ GeV and $|\eta| < 2.5$ that is within $\Delta R = \sqrt{\Delta\eta^2 + \Delta\phi^2} < 0.2$ of a track jet is added to the calorimeter jet four-momentum to partially account for the energy carried by muons from semileptonic b-hadron decays.

Electrons and muons (leptons) are also used in a "veto" to ensure the orthogonality of the analysis selection with respect to other heavy VH resonance searches in non-fully hadronic final states. Electrons are reconstructed with the "Loose" likelihood selection. The considered leptons have $p_{\mathrm{T}} > 7$ GeV, $|\eta| < 2.5$ (2.47) for muons (electrons), and their associated tracks must have $|d_0/\sigma_{d_0}| < 3$ (5) and $|z_0 \sin\theta| < 0.5$ mm, where d_0 is transverse impact parameters with respect to the beam line, σ_{d_0} is the uncertainty on d_0, z_0 is the difference between the longitudinal position of the track along the beam line at the point where d_0 is measured and the longitudinal position of the primary vertex, and θ is the polar angle of the track. Leptons are also required to pass an isolation criterion, whereby the ratio of the p_{T} sum of all tracks with $p_{\mathrm{T}} > 0.5$ GeV (excluding the lepton's) within a cone around the lepton (with radius dependent on the lepton p_{T}) to the lepton momentum must be less than a p_{T}- and $|\eta|$-dependent threshold I_0. I_0 is defined such that a flat efficiency of 99% as a function of p_{T} and $|\eta|$ is obtained for leptons in events with identified $Z \to \ell\ell$ candidates, where ℓ denotes an electron or muon.

The missing transverse momentum ($\vec{E}_{\mathrm{T}}^{\mathrm{miss}}$) is calculated as the negative vector sum of the transverse momenta of all the muons, electrons, calorimeter jets with $R = 0.4$, and any inner-detector tracks from the primary vertex not matched to any of these objects. The magnitude of the $\vec{E}_{\mathrm{T}}^{\mathrm{miss}}$ is denoted by $E_{\mathrm{T}}^{\mathrm{miss}}$.

8.3.2 Trigger and Preselection

For analysis of 2015 and 2016 dataset, single large-R jet trigger is used since it can provide full efficiency without complication of an `OR` of multiple HLT triggers. Trigger threshold is different between 2015 and 2016 due to the increase of instantaneous luminosity in 2016. In 2015, trigger `HLT_j360_a10_lcw_sub_L1J100` is used[3]. In 2016, trigger `HLT_j420_a10_lcw_L1J100` is used. These are similar to the ones used in Chapter 7.

A key part of trigger studies is to make sure our signal samples are fully efficient with respect to the choice of trigger. For 2015 this is less an issue as illustrated in Section 7.3.2 since the threshold is not very high. However, for 2016, the threshold increases to 420 GeV, meaning threshold effect can start to affect the analysis. Therefore, a dedicated "protection" is needed in the analysis to make sure after these "protection" cuts, events are fully efficient with respect to the chosen trigger.

[3]Reader might notice that this is slightly different from the one used in Chapter 7. This is mainly due to the change in ATLAS reconstruction release from 20.1 to 20.7

Therefore, a trigger efficiency measurement in data is performed in order to determine the best offline cut to be used. Instead of reading from trigger name directly, the offline cut is determined from a measurement since turn on curve might be smeared out by the difference between trigger and offline, and difference between data and MC.

The efficiency of trigger is measured relative to an equivalent pre-scaled trigger with lower p_{T} threshold, `HLT_j240_a10_lcw_L1J75`. The (relative) trigger efficiency as function of p_{T} and m_{JJ} can be found in Figure 8.1. From left of Figure 8.1, one can see that trigger is not fully efficient until $\sim$ 450 GeV. Therefore, an offline cut on leading large-R jet of 450 GeV is applied to make sure one is on the trigger plateau. Furthermore, we restrict our search range to $m_{JJ} > 1000$ GeV to as another safe-guard that one is on the trigger plateau in both signal regions and sidebands.

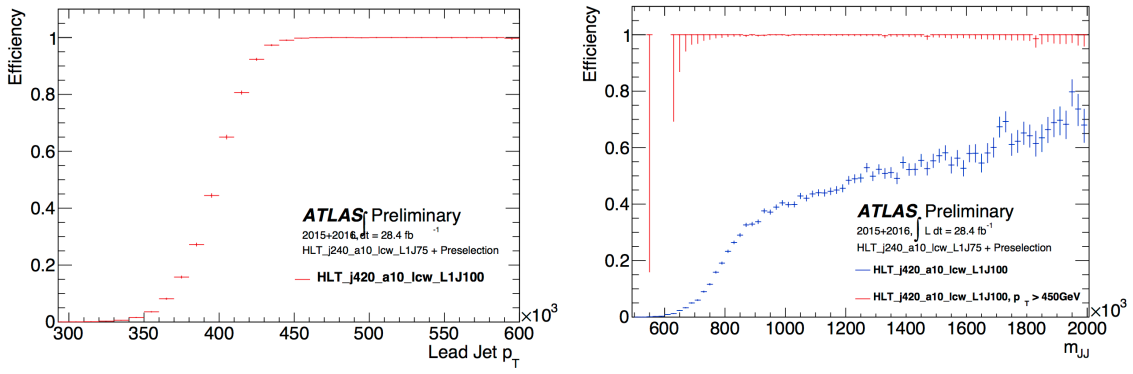


Figure 8.1: Trigger efficiency of `HLT_j420_a10_lcw_L1J100` with respect to `HLT_j240_a10_lcw_L1J75` as function of leading large-R jet p_{T} (left) and dijet mass of two leading large-R jet. [205]

Non-collision backgrounds originating from calorimeter noise, beam halo interactions or cosmic rays can lead to spurious calorimeter signals and the reconstruction of "bad" jets. This effect can be suppressed by applying a standard jet cleaning procedure, which has been developed for 2015 data to reject jets based on their shape and timing information [206]. Following these criteria, events are rejected if they contain at least one small radius jet (anti-k_t, with $R = 0.4$) classified as *bad-loose*.

Vetos are applied to reject events where Tile or LAr errors occur, as well as single event upsets in the SCT. These cuts are applied by accessing information via the `xAOD::EventInfo::Error` flag associated to each subdetector. Incomplete events are also flagged and rejected via the coreFlags variable.

Events are required to have at least one primary vertex with at least two tracks, selected as the vertex with the highest sum of transverse momentum of tracks associated to it.

8.3.3 Event Selection

Basic Jet Kinematics

At least two groomed large-R jets are required to be present in the event, passing a basic kinematic requirement of $p_{\mathrm{T}} > 250$ GeV and $|\eta| < 2.0$. Jets are further required to pass $m_J > 50$ GeV where the mass responses are well understood. Leading large-R jets are required to pass $p_{\mathrm{T}} > 450$ GeV for trigger considerations as discussed above. Furthermore, events are required to have $m_{JJ} > 1.0$ TeV also making sure events after these basic kinematic cuts are fully efficient with respect to the trigger chosen in this analysis.

Orthogonality Vetos

Several event vetos are applied to make sure phase space being explored in this analysis is orthogonal to the other (semi-)leptonic channels inside ATLAS VH searches. In particular, these vetos are applied before splitting into SR/VR/SB (which we will define later) such that we do not accidentally "unblind" SR events in the other analysis. These vetos include:

- Events with at least one loose lepton, as defined above, are rejected.
- $E_{\mathrm{T}}^{\mathrm{miss}}$-based veto: Events with $E_{\mathrm{T}}^{\mathrm{miss}} > 150$ GeV are accepted only if direction of total missing transverse energy is approximately aligned to that of Higgs candidate, i.e. $\Delta\phi(E_{\mathrm{T}}^{\mathrm{miss}}, H) < 120°$. This cut is applied to ensure orthogonality between full-hadronic and $ZH \to \nu\nu b\bar{b}$ analysis. A simple cut of $E_{\mathrm{T}}^{\mathrm{miss}} > 150$ GeV was attempted at the beginning, but later found to have significant impact on signal efficiency, since there could be real $E_{\mathrm{T}}^{\mathrm{miss}}$ from signal final states when neutrino can be produced from b-hadron semi-leptonic decay, as illustrated at left plot of Figure 8.2. An additional angular requirement in case of high $E_{\mathrm{T}}^{\mathrm{miss}}$ ensures almost 100% efficiency for our signal as shown in right plot of Figure 8.2. Such angular requirement can still keep orthogonality with $ZH \to \nu\nu b\bar{b}$ signal region since $E_{\mathrm{T}}^{\mathrm{miss}}$ direction should instead be opposite to the Higgs jet.

V/H Assignment

The two leading jets in the event will correspond to a vector boson and a Higgs boson candidate, through an assignment which is made based on large-R jet mass: the heaviest jet is chosen as the Higgs candidate and the lightest as the W/Z candidate. Figure 8.3, which is made only after basic kinematic selections described above, shows the fraction of events that are correctly matched with this V/H assignment, by checking that the jets chosen for vector and Higgs boson candidates match the truth-level bosons in the signal samples, as a function of the resonance mass. In signal MC simulation, this procedure results in 99% correct assignment after the full signal region selections described below.

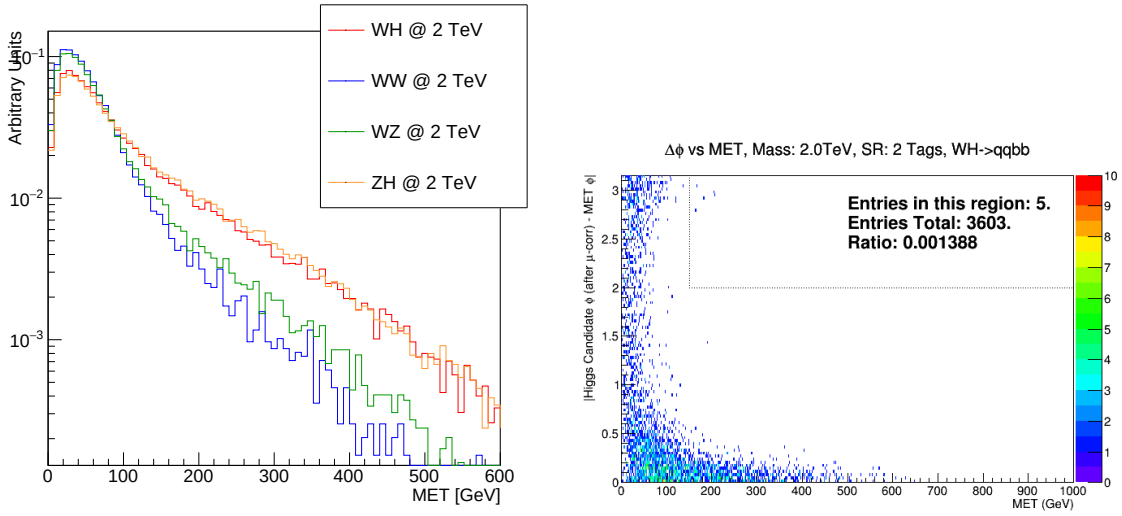


Figure 8.2: (Left) $E_{\mathrm{T}}^{\mathrm{miss}}$ distribution for various VH signal samples; (Right) Correlation between $E_{\mathrm{T}}^{\mathrm{miss}}$ and $\Delta\phi$ between $E_{\mathrm{T}}^{\mathrm{miss}}$ direction and Higgs candidate jet direction for a WH resonance mass of 2 TeVin 2-tag signal region.

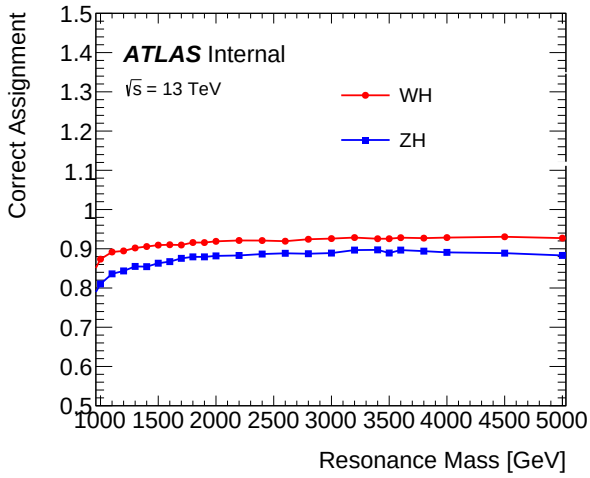


Figure 8.3: Fraction of events that are correctly matched with V/H assignment by checking if jets chosen for V/H candidates are consistent with the truth-level boson in signal samples. Only basic jet kinematic cuts are applied here.

Alternative ways of making such V/H assignment are studied, as listed below:

- "V-preferred". This is the one used in baseline. One apply the V-tagging on both large-R jets and require there should be exactly one passing the V-tagging. As a result, the remaining one is automatically Higgs candidate.
- "VH-or-HV". One can also test two different hypothesis that the leading large-R jet is either V-candidate or H-candidate (and consequently sub-leading large-R jet is either H-candidate or V-candidate). Then in each scenario, V/H-tagging is applied correspondingly, and one can check which scenario is correct. By requiring one and only one scenario to be true, one can then get V/H assignment.
- "Who-is-heavier". In this scheme, one simply compare the jet mass of two leading large-R jet, and assign the heavier one to be Higgs candidate, the lighter one to be V-candidate.

Table 8.1 shows the number of events in signal regions for a specific signal sample. One can see that both "VH-or-HV" and "Who-is-heavier" scheme would give more signal yields in signal regions than the baseline "V-preferred". This is mainly because "V-preferred" scheme explicitly veto the case where "VV" hypothesis is true, while the other two ways still take them into account. Furthermore, impact on sensitivity is also examined for these three assignment methods, as shown in Figure 8.4. Results show that an assignment simply based on large-R jet mass can achieve best sensitivity.

V/H assignment scheme	1-btag SR	2-btag SR
"V-preferred"	5.526	4.235
"VH-or-HV"	6.436	5.055
"Who-is-heavier"	6.017	4.792

Table 8.1: Number of events in signal region for WH signal sample with resonance mass being 2 TeV.

Rapidity Difference

Similar to the case in $pp \to hh \to b\bar{b}b\bar{b}$, Signal $W' \to WH$ and $Z' \to ZH$ events are expected to be more central than multijet events, resulting in a rapidity difference (Δy_{12}) between the two leading large-R jets which peaks near 0. A fixed cut of $|\Delta y_{12}| < 1.6$ is applied.

V/H-tagging

After vector boson jet candidate and Higgs jet candidate are identified, the V/H-tagging techniques as discussed in Chapter 6 are applied on them respectively.

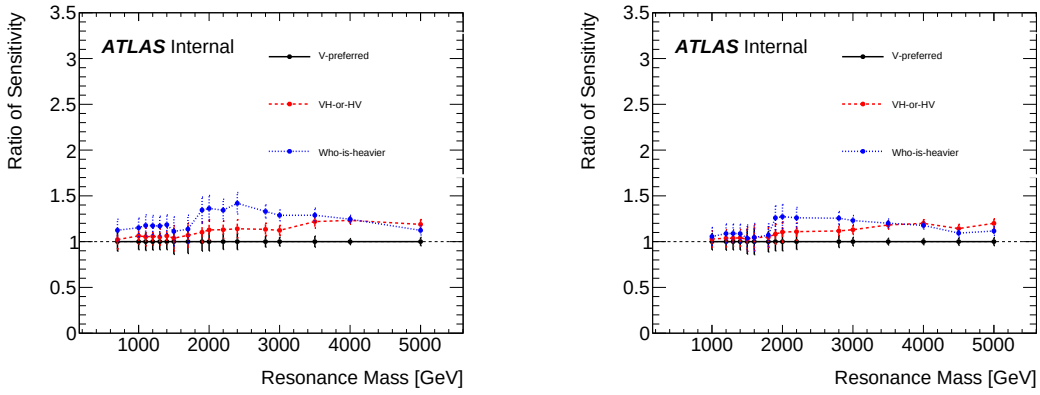


Figure 8.4: Ratio of sensitivity of various V/H assignment scheme over the reference scheme "V-preferred", as function of resonance mass points, for both WH(left) and ZH(right) signal samples. Sensitivity here is the combined sensitivity from 1-tag and 2-tag signal regions which will be defined below.

In particular, the identification of $h \to b\bar{b}$ decay mode relies on the groomed jet mass and $R = 0.2$ small radius track jet b-tagging. A 90% efficient mass window is considered, corresponding to mass range $75 < m_J < 145$ GeV. The number of b-tagged track jets are used to categorize events as will be discussed later. 77% track jet b-tagging working point is used. The Higgs jet with at least one b-tagged track jet among two leading track jets (if any) are used in this analysis. The Higgs tagging efficiency for double-(single-) b-tagged Higgs jet is about 40% (75%) for Higgs jet with $p_{\mathrm{T}} \sim 500$ GeV and about 25% (65%) for Higgs jet with $p_{\mathrm{T}} \sim 900$ GeV. As usual, muon-in-jet correction is applied for Higgs jet to take the semi-leptonic decaying b-hadrons into account. However, the muon correction procedure is slightly different here due to the use of track-assisted mass: While m_{calo} is still corrected in exactly same way as Chapter 7, only calorimeter jet p_{T} is corrected in case of m_{TA} since muon can leave a clear tracking trajectory in the ID system [124]. Since we are using combined mass, then corrected combined mass is re-computed using corrected m_{calo} and corrected m_{TA}.

The identification of hadronically-decaying W and Z bosons has been extensively studied in ATLAS and a tagger has been developed that relies on the invariant mass and on the D_2 variables associated to the groomed jet [147], providing additional discrimination power with respect to multijet events. The medium efficiency working point, corresponding to 50% signal efficiency, of the vector boson tagger is applied. Both jet mass cut and D_2 cut are parameterized as a smoothed function of p_{T} to avoid awkward jumping in spectrum due to the binning. The parameterization of both jet mass and D_2 cut can be found in Figure 8.5 for the chosen working point.

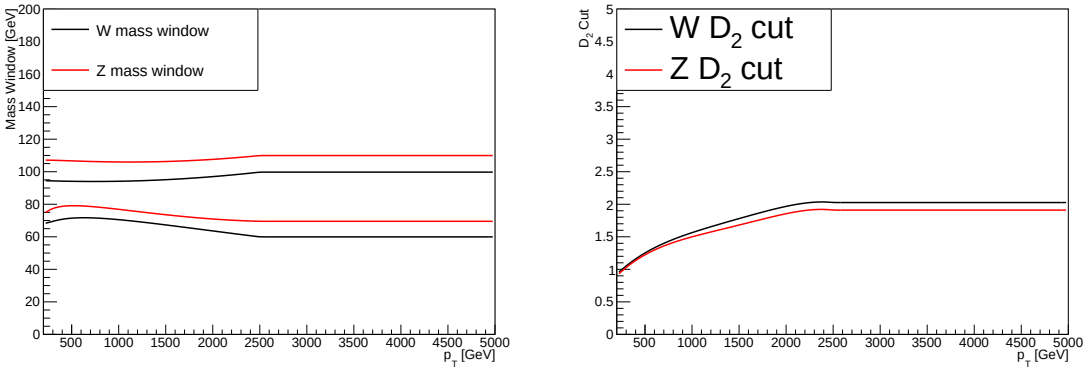


Figure 8.5: Parameterization of vector boson mass cut and D_2 cut as function of jet p_{T} in the 50% medium working point.

8.3.4 Signal Regions

Four signal regions (SR) are used in this analysis, which differ by the number of b-tagged track jets associated to the H-jet and by whether the V-jet passes a Z-tag or W-tag selection. The *1-tag* and *2-tag* SR require exactly one and at least two b-tagged track jets associated to the H-jet, respectively. A full list of event selections can be found in Table 8.2, where the final signal region efficiencies can be found in Figure 8.6.

Selection	Description
Lepton veto	Remove events with leptons
> 1 large-R jets	$p_{\mathrm{T}} > 250$ GeV, $\lvert\eta\rvert < 2.0$
Leading large-R jet p_{T}	> 450 GeV
V/H assignment	larger mass jet is H-jet, smaller mass jet is V-jet
Rapidity difference	$\lvert\Delta y_{12}\rvert < 1.6$
$E_{\mathrm{T}}^{\mathrm{miss}}$ veto	Remove events with $E_{\mathrm{T}}^{\mathrm{miss}} > 150$ GeV and $\Delta\phi(\vec{E}_{\mathrm{T}}^{\mathrm{miss}},\ H-\mathrm{jet}) > 120$ degrees
Higgs tagging	90% mass window, 77% track-jet b-tagging working point
W/Z-tagging	mass window + $D_2^{\beta=1}$ Medium working point
Dijet mass	$m_{\mathrm{JJ}} > 1$ TeV

Table 8.2: Summary of event selection criteria. [199]

As one can see, the 2-tag signal regions provide the larger efficiency for resonances with masses below ∼2.5 TeV. Above 2.5 TeV the 1-tag regions provide higher sensitivity because the Lorentz boost of the Higgs boson is large enough to merge the fragmentation products of both b-quarks into a single track jet. Events in which the V-jet passes a Z-tag are denoted as the ZH signal regions, while events in which the V-jet passes a W-tag are denoted as the WH signal regions. While the 1-tag and 2-tag signal regions are orthogonal regardless of the V-jet tag, the WH and ZH selections are not orthogonal within a given b-tag category. The overlap between the WH and ZH selections in the signal regions is approximately 60%.

One can notice there is a ∼5% difference in terms of efficiency between WH and ZH cases, which seems surprising at the beginning since same efficiency working point is chosen for both W

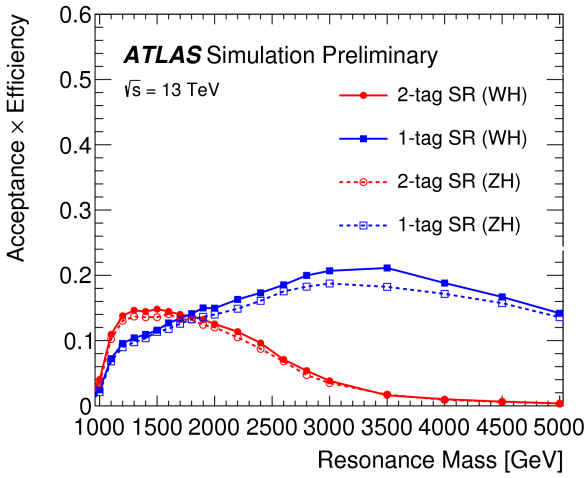


Figure 8.6: Signal acceptance×efficiency as a function of resonance mass [199]

and Z tagging. Further investigation, as shown in Figure 8.7, shows that such difference comes from angular component of $E_{\mathrm{T}}^{\mathrm{miss}}$ veto as discussed above. Due to the contribution of $Z \to b\bar{b}$ decays where b-hadrons can decay semi-leptonically, this $E_{\mathrm{T}}^{\mathrm{miss}}$ veto is slightly less efficient for ZH case.

A cutflow of our full event selections on signal samples (data) can be found in Figure 8.8 (Table 8.3). Figure 8.9 shows the efficiency as measured in the MC simulation for each of background process. It can be seen that backgrounds are highly suppressed by the V/H-tagging techniques.

Cut	2015 dataset	2016 dataset
Initial	2002070	18445225
Trigger	1807683	15768928
GRL	1592138	15104715
Jet cleaning	1586802	15013297
Muon veto	1580745	14966122
Electron veto	1560259	14791870
# large-R jets ≥ 2	1487818	14442155
Large-R jet kinematic cuts	921132	9598191
$\lvert\Delta y\rvert < 1.6$	640765	6680797
Missing E_T veto	636224	6628612
Pass V-tagging	40985	402204
$M_{VH} \geq 1000$ GeV	28404	278313
Signal region 1-tag (WH)	1457	13756
Signal region 2-tag (WH)	193	1453
Signal region 1-tag (ZH)	1391	13721
Signal region 2-tag (ZH)	176	1398

Table 8.3: Cutflow of events for the 2015 and 2016 datasets.

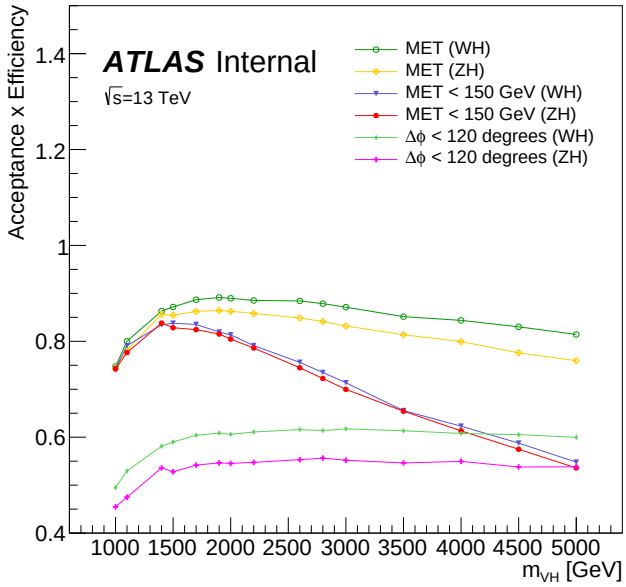


Figure 8.7: Signal efficiency of the total MET cut and of each of its sub-cuts (on the magnitude and azimuthal angle) as a function of the resonance mass, measured in WH and ZH signal samples. The "ME" line corresponds to an OR of the other cuts, i.e., an event is only kept if it has low MET or small $\Delta\phi$.

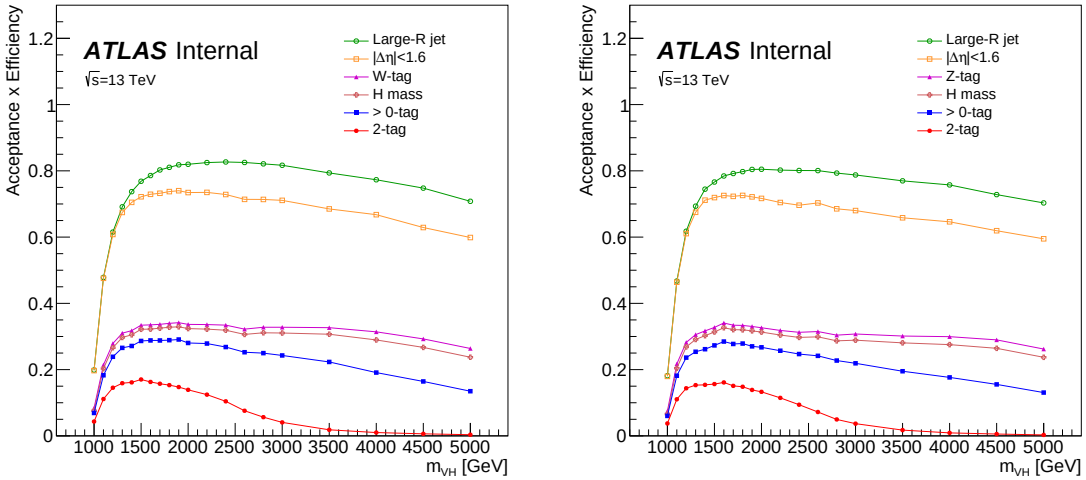


Figure 8.8: Signal efficiency at various stages of the event selection as a function of resonance mass for the WH (left) and ZH (right) selections (applied to the corresponding sample). The "large-R jet" curve includes the preselection cuts, such as lepton and MET vetoes.

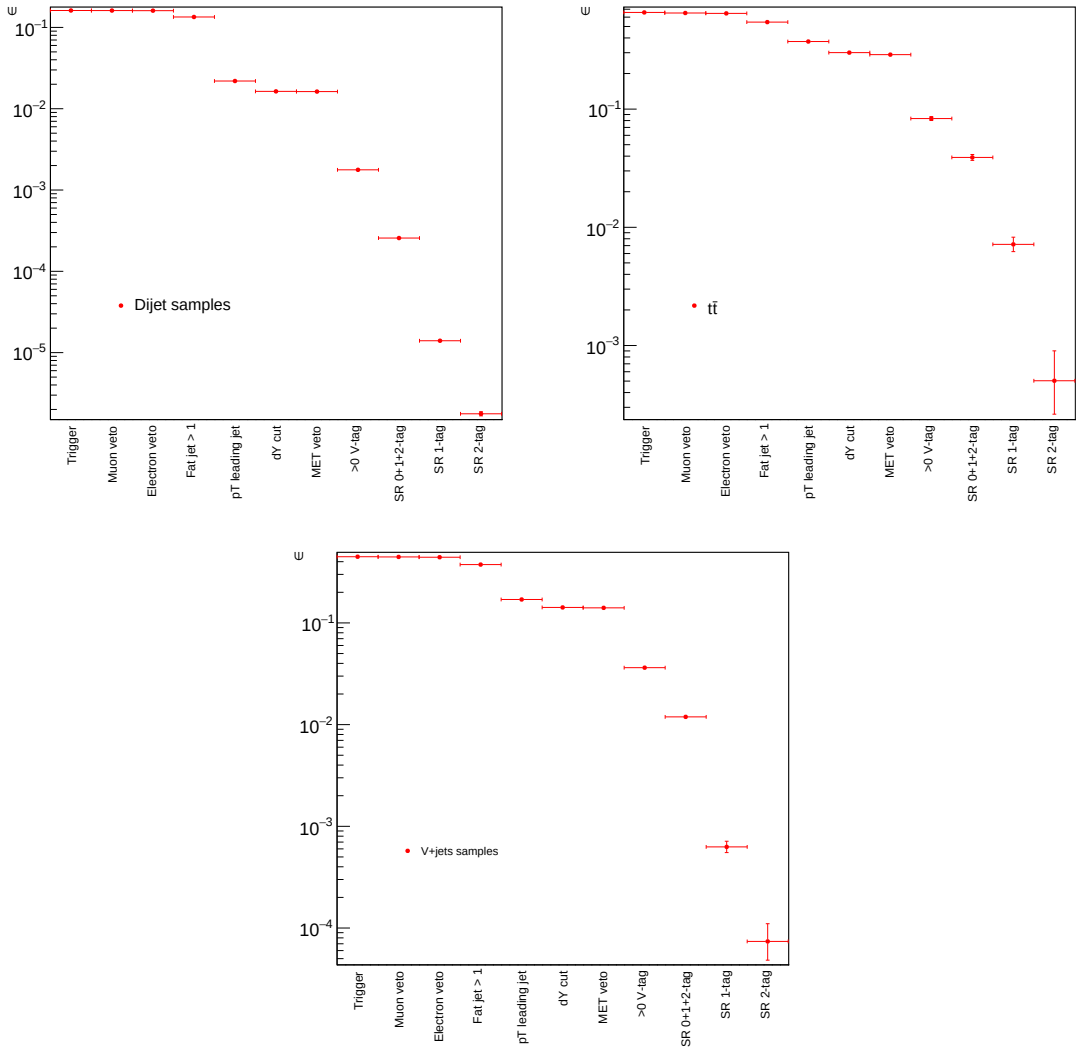


Figure 8.9: Background efficiencies at various stages of the event selection for the dijet, top and V+jets MC. The 1-tag and 2-tag regions correspond to the combined $V = W, Z$ signal regions.

8.4 Background Estimations

After the signal selections discussed in Section 8.3, ∼90% of the background in signal regions originates from multijet events. The remaining ∼10% is predominantly $t\bar{t}$ event with an additional small contribution from V+jets ($\leq 1\%$). SM diboson processes WW / WZ / ZZ are checked in MC and turns out to be negligible. Such background composition is similar to the search of $pp \to hh \to b\bar{b}b\bar{b}$ process in Chapter 7.

Since the dominant multijet background is hard to be estimated from MC simulation in the boosted phase space as our SR, a data-driven technique similar to the one used in Chapter 7 is used for multijet background estimation. The $t\bar{t}$ and V+jets components are estimated directly from MC simulation though. In this analysis, the invarinat mass of dijet system is used as the final discriminant variable. Therefore, we would be more focused on the modeling of this variable throughout this section.

Description of our data-driven method would be discussed in Section 8.4.1; Definition of various regions can be found in Section 8.4.2; Multijet normalization estimation before re-weighting can be found in Section 8.4.3; Kinematic re-weighting, a correction process found necessary in this analysis, would be discussed in details in Section 8.4.4; The cross-check of background estimation strategy in validation region, as well as how we make prediction in signal regions can be found in Section 8.4.5, 8.4.6 and 8.4.7.

8.4.1 0-Tag Extrapolation Method

The 0-tag multijet estimation uses events that pass the full event selection, except instead of requiring the Higgs candidate to have 1 or 2 b-tags, the Higgs candidate must have exactly 0 b-tags. This corresponds to the 0-tag SR, and is $\sim 99\%$ pure in multijet events, as predicted by MC. It should be noted that the 0-tag sample has one additional requirement that the Higgs candidate must have at least as many matched track jets as the number of b-tags in the SR being modeled. So when modeling the 1(2)-tag sample, the 0-tag Higgs candidate must have at least 1 (2) matched track jet(s). This requirement helps to ensure that the kinematics of the 0-tag sample is as close as possible to the tagged SR being modeled. An illustration of such 0-tag extrapolation strategy can be found in Figure 8.10. The 0-tag SR is used to estimate the shape of multijet events in the 1-tag and 2-tag SR. The sideband, which will be defined in Section 8.4.2, is used to estimate multijet background normalization in 1-tag and 2-tag (see Section 8.4.3).

Figure 8.11 shows the comparison of normalized shapes for the 0-tag SR to the 1-tag SR and the 2-tag SR, on the left and right respectively, in multijet MC. Using the MC allows us to test the validity of this shape extrapolation. We can see that the 0-tag shapes models the 1-tag shape extremely well, while the 2-tag shape modeling is not as good. However, the 2-tag sample is limited in statistics, making the comparison difficult. Nonetheless, the 0-tag sample without any adjustments

does provide a reasonable estimation in both 1 and 2 tag SRs within $\sim 50\%$.

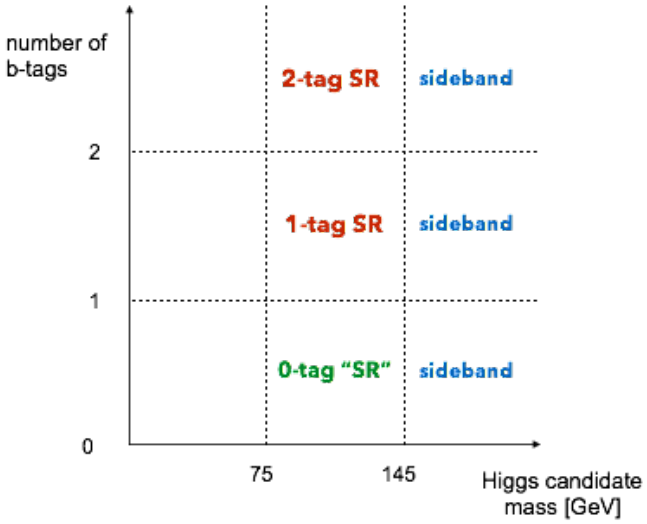


Figure 8.10: Illustration of 0-tag extrapolation method for multijet backgrounds. Such extrapolation is not only limited in SR, but can be applied on all mass regions such as sidebands and validation regions. The sideband illustrated here is for normalization estimation purpose as will be discussed in Section 8.4.3

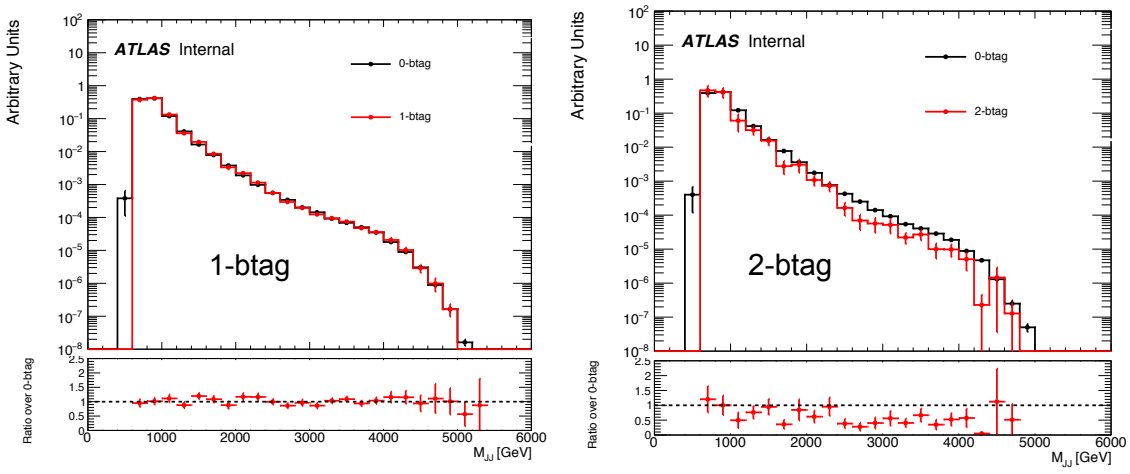


Figure 8.11: Comparison of 0-tag SR shape to the 1-tag (left) and 2-tag (right) SR shapes in multijet MC simulation.

As certain biases can be present in the 0-tag samples relative to the 1/2-tag sample, the 0-tag sample can be corrected to account for the reduced number of b-tags. Such correction is done

through a kinematic re-weighting in the 0-tag data sample, which will be discussed in details in Section 8.4.4.

It should be noted that this 0-tag SR only provides a model of the shape of 1/2-tag distributions of multijet, and not a normalization. The determination of normalization would be discussed in Section 8.4.3. Furthermore, several dedicated validation regions are designed to provide independent test of this method beyond sideband and SR, which will be covered in Section 8.4.5.

8.4.2 Definition of Various Regions

In the 0-tag extrapolation approach, several orthogonal regions are defined, for various purposes. These regions are shown in Figure 8.12, with definitions summarized in Table 8.4.

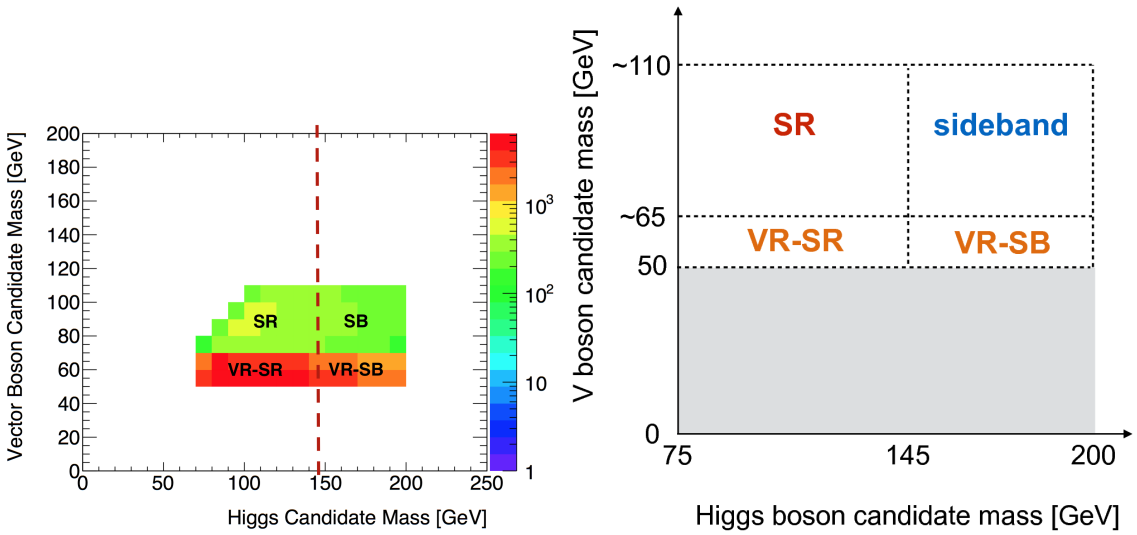


Figure 8.12: Illustration of orthogonal mass regions on the 2D H-jet / V-jet mass plane. Left is the illustration using 0-tag data sample and right is a schematic illustration of the divisions. Exact definition of regions in Table 8.4.

Here, "anti-V-tag" means failing the mass window cut imposed by V-tagging tool. Due to the method used for the V/H assignment, only the low mass sideband of the V-boson candidate is considered.

Higgs High-mass Sideband is mainly used to derive normalization scale factor and kinematic re-weighting. Validation Regions, which are further divided into two orthogonal "VR-SR" and "VR-SB" regions, will mainly be used to validate our background estimation strategy, as well as to derive background estimation systematics.

Another important thing to mention is, all validation regions (VR-SR and VR-SB) come with two versions: the inclusive one as defined above, and a one with D_2 applied. The latter one is defined for each VR by further requiring the V-candidate jet should still pass D_2 cut of both W and

Region	Definition	Comments
Signal Region (SR)	V-candidate jet pass V-tagging, H-candidate jet pass both mass window and b-tagging cuts	Used in the final likelihood fit
Higgs High-mass Sideband (SB)	V-candidate jet pass V-tagging, H-candidate jet pass b-tagging cuts, but with $145 \leq m_H < 200$ GeV	Used to extract normalization and weights used in the kinematic reweighting
Anti-V-tagged Higgs-mass Validation Region (VR-SR)	V-candidate jet is anti-V-tagged, H-candidate jet pass both mass window and b-tagging cuts	Used to optimize kinematic reweighting procedure, validate background estimation and derive associated modeling uncertainties
Anti-V-tagged Higgs High-mass Validation Region (VR-SB)	V-candidate jet is anti-V-tagged, H-candidate jet pass b-tagging cuts, but with $145 \leq m_H < 200$ GeV	Used to optimize kinematic reweighting procedure, validate background estimation and derive associated modeling uncertainties

Table 8.4: Definition of signal region, sidebands and validation regions.

Z tagging. Although these two new VRs are not orthogonal to the two VRs defined above, they are important in checking if there is any additional bias introduced by cutting on the jet substructure variable. Therefore, these two new VRs would be used in both background estimation cross-check as shown in this section and determining systematic uncertainties related to background estimation as will be discussed in Section 8.5.

8.4.3 Normalization Estimation

Following the 0-tag extrapolation method, number of events in any region of interest for a fixed number of b-tags can be calculated by:

$$N^{(i)}_{data} = \mu^{(i)}_{\text{Multijet}}(N^{(0)}_{data} - N^{(0)}_{t\bar{t}-MC} - N^{(0)}_{V+jets-MC}) + N^{(i)}_{t\bar{t}-MC} + N^{(i)}_{V+jets-MC} \tag{8.1}$$

where $N^{(i)}$ is the number of events in i-tag region. μ_{Multijet} is an estimate of the ratio of number of multijet events with 1 or 2 b-tags over 0 b-tag. $t\bar{t}$ and V+jets are the other major backgrounds, which are simply modeled with MC predictions due to their small contribution to total background. All other backgrounds, both from experimental (e.g. misidentification of electrons or calorimeter fluctuations) and SM sources, are not considered explicitly but absorbed into the multijet component, since their fraction is negligible.

To obtain $\mu^{(i)}_{\text{Multijet}}$ for each number of b-tags ($i = 1, 2$), we further assume that $\mu^{(i)}_{\text{Multijet}}$ is uniform across the phase space for a fixed number of b-tags. Therefore, we move to the SB and unblinded the data there in order to get an estimation of μ_{Multijet}. Since there is only one undetermined parameter, μ_{Multijet} can be obtained by solving the Equation 8.1 directly for a fixed number of b-tags.

Here we choose the invariant mass of the VH di-jet system in the fitting, and the fit results can be found in Figure 8.13. The shape of the data is well modeled by the predicted background. The fitting errors on μ_{Multijet} are applied as systematic uncertainties, which will be discussed further in systematics sections.

One thing to notice here is that, the region where we derive this fit result is inclusive for WH and

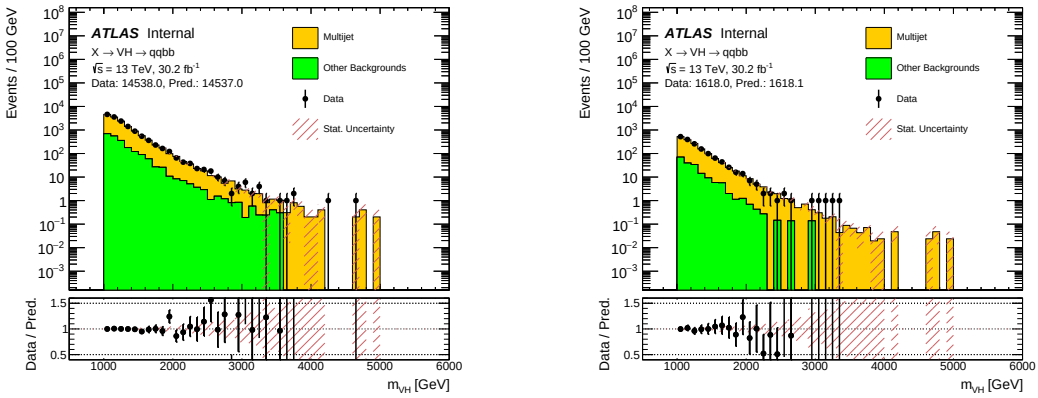


Figure 8.13: Post-fit distribution of m_{JJ} of VH di-jet system in 1-tag (left) and 2-tag (right) SB. No kinematic re-weighting applied here yet.

ZH signals, since definition of V-tagging in SB, as defined in Table 8.4, is "either W or Z tagged". As a result, when eventually applied in signal region, a uniform μ_{Multijet} is used regardless "WH" or "ZH" signal region. We derive the fitting (as well as the kinematic re-weighting in next part) in such inclusive way because the difference on μ_{Multijet}, if derived separately for "WH" and "ZH" signals, is expected to be very small, due to the overlap between current W/Z-tagging. This is shown in Table 8.5, where the values of μ_{Multijet} drived from the WH and ZH regions agree within approximately 1 σ.

Higgs High-mass Region	$\mu_{qcd}^{(1)}$	$\mu_{qcd}^{(2)}$
WH/ZH Inclusive (WH or ZH)	0.1762 ± 0.0017	0.0204 ± 0.0006
WH Only	0.1784 ± 0.0022	0.0197 ± 0.0007
ZH Only	0.1749 ± 0.0020	0.0208 ± 0.0007

Table 8.5: μ_{qcd} of both 1-tag and 2-tag derived for inclusive, "WH"-only and "ZH"-only signals. Only statistical uncertainties are shown.

8.4.4 Kinematic Re-weighting

The 0-tag extrapolation method is based on the assumption that most kinematic variables in 1 or 2 b-tag regions can be well modeled by 0-tag samples. However, kinematic distribution can be easily biased when transferring from 0-tag sample to 1/2-tag sample for two main reasons:

- Non-trivial kinematic dependency of track jets b-tagging efficiency. Since track jet b-tagging efficiency strongly depends on track jet p_{T} (and also some dependency on η), the kinematic distribution of event can be sculpted after b-tagging requirement.

- Change of heavy flavor composition. The 0-tag sample is dominated by q/g-initiated jets; The 1-tag sample is dominated by single b-jet; The 2-tag sample is dominated by $g \to b\bar{b}$ components. Kinematic distribution can change a lot depending on the heavy flavor composition in the multijet samples.

Since data-driven multijet background is the dominant background in this analysis, it would be important to model this background as best as possible in all regions of the analysis. Therefore, a re-weighting procedure is applied to the 0-tag sample in order to correct for any shape differences that may exist. On the other hand, since a kinematic re-weighting can balance the event in different mass regions on 2D mass plane as shown in Figure 8.12, one can essentially obtain a "kinematic-dependent μ_{Multijet}" through such re-weighting, which is another important correction on our assumption of uniform μ_{Multijet} across all mass regions.

Since the correction is mainly due to the b-quark composition in H-jet side, two leading track jets associated with the H-jet is used as the proxy of partons. In particular, the choice of kinematic variables to be re-weighted are[4]:

- A track jet p_{T} ratio, defined as the leading track jet p_{T} divided by the sum of leading and sub-leading track jet p_{T}, associated to Higgs candidate jet.
- Sub-leading track jet p_{T} associated to Higgs candidate jet

Indeed, the bias on these two variables can be illustrated in Figure 8.14. In the 2-tag region, a strong bias is found reflecting the mis-modeling when extrapolating from 0-tag to 2-tag. In 1-tag, such mis-modelling is much smaller though. Further studies on dijet system invariant mass distribution show that a correction for 2-tag is necessary, while modeling in 1-tag is adequate without re-weighting (see Section 8.4.5). Therefore, we decide to apply such kinematic re-weighting on 2-tag only throughout this analysis.

The re-weighting is performed using the 1-D distribution that are sensitive to the mis-modeling effect here, but is iterated so that correlation between two variables are taken into account. The exact procedure of deriving and applying kinematic re-weighting is described as below.

We first need to check the distributions of the re-weighting input variables in SB before re-weighting, which is exactly Figure 8.14 (Distribution of 1-tag is also there for completeness although 1-tag does not participate in the re-weighting here). Then we take the ratio of 1(2)-tag data sample after subtracting the $t\bar{t}$ and V+jets MC over the mutlijet estimate in the 1(2)-tag region. Figure 8.15 shows the fit to the weights as a function of each variable in the first iteration of the re-weighting.

Then the total weight applied to the 0-tag sample (both data, $t\bar{t}$ MC and V+jets MC) for 1(2)-tag multijet modeling purpose is the product of two weights, one from each variable. These weights

[4]In the early study as in conference note [198], leading and sub-leading track jet p_{T} is used as re-weighting variables. However, later internal studies reveal that a different combination as presented here using a p_{T} ratio is better since it is scale-invariant

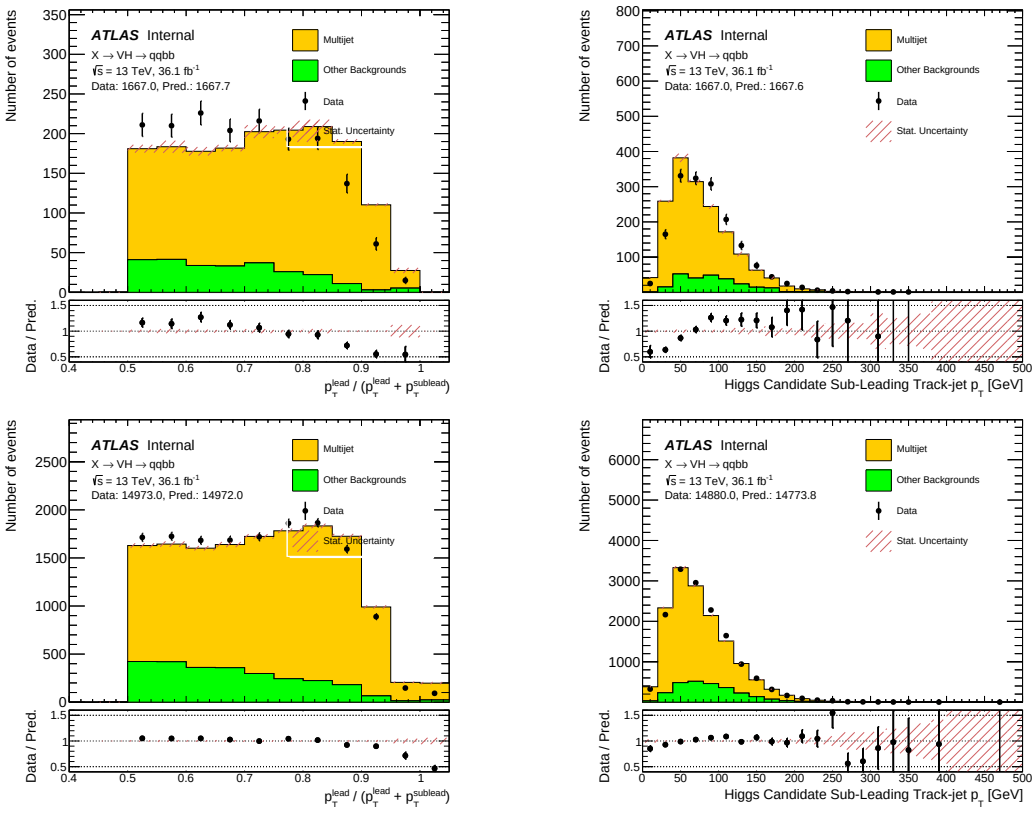


Figure 8.14: Distribution of track jet p_{T} ratio (left) and subleading track jet p_{T} associated to H-jet in 2-tag (first row) and 1-tag (second row) before kinematic re-weighting

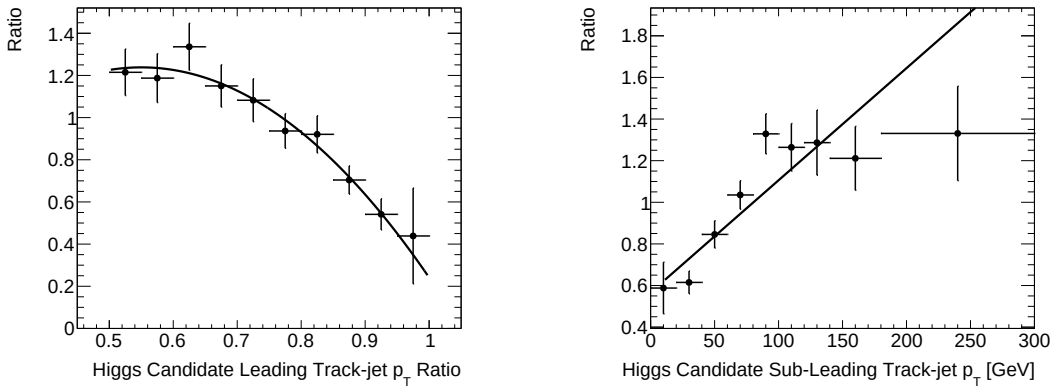


Figure 8.15: The weights applied for the track jet p_{T} ratio distribution (left) and sub-leading track jet p_{T} (right) in the 2-tag region at first iteration. Weights are smoothed with polynomial function in certain range with enough statistics. If kinematic variable is above (below) the fit range, then value evaluated at upper bound (lower bound) of fit range is used. Weight is also not allowed to fall below 0.1 to prevent events from receiving negative or zero weight due to the kinematic re-weighting.

are calculated for each event by taking the value of the fit at the value for the re-weighted variable. Then we repeat the procedure described in Section 8.4.3 to re-fit μ_{Multijet} for both 1(2)-tag region and obtain the updated multijet estimation in 1(2)-tag region, which will be followed up by next round of re-weighting as described here.

We find that the weights of first iteration are by far the largest, the subsequent weights being much smaller and just correcting for residual differences due to the correlations between the variables. After eight iterations, we find that the re-weighting procedure is already more or less converged in that the ratio is almost flat as shown in Figure 8.16.

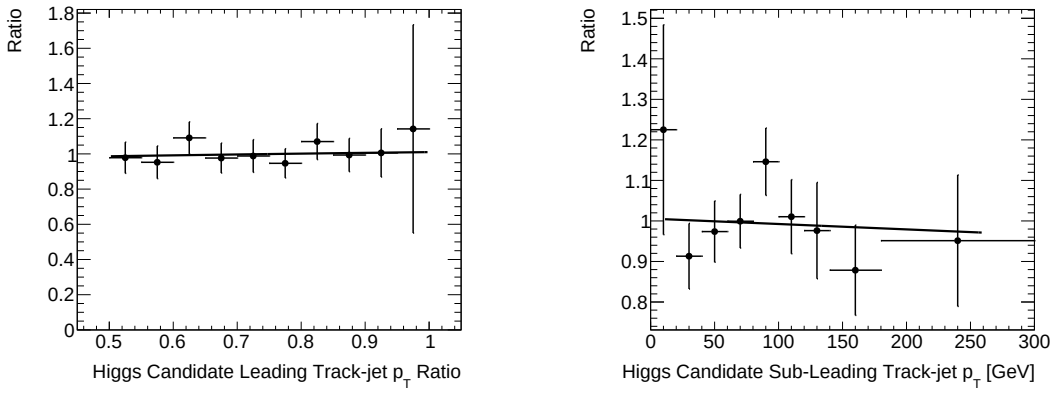


Figure 8.16: The weights applied for the track jet p_{T} ratio distribution (left) and sub-leading track jet p_{T} (right) in the 2-tag region at last (8th) iteration. Weights are smoothed with polynomial function in certain range with enough statistics. If kinematic variable is above (below) the fit range, then value evaluated at upper bound (lower bound) of fit range is used. Weight is also not allowed to fall below 0.1 to prevent events from receiving negative or zero weight due to the kinematic re-weighting.

By construction, the final weights applied on events are the products of all weights derived during each iteration as described above. The total weights applied for two chosen kinematic variables to be re-weighted on can be found in Figure 8.17.

After re-weighting is derived and applied, the μ_{Multijet} needs to be re-calculated following procedure in Section 8.4.3. The distribution of m_{JJ} in SB after this can be found in Figure 8.18 and the updated μ_{Multijet} is:

$$\begin{aligned} \mu_{qcd}^{(1)} &= 0.2026 \pm 0.0020 \\ \mu_{qcd}^{(2)} &= 0.0243 \pm 0.0007 \end{aligned} \tag{8.2}$$

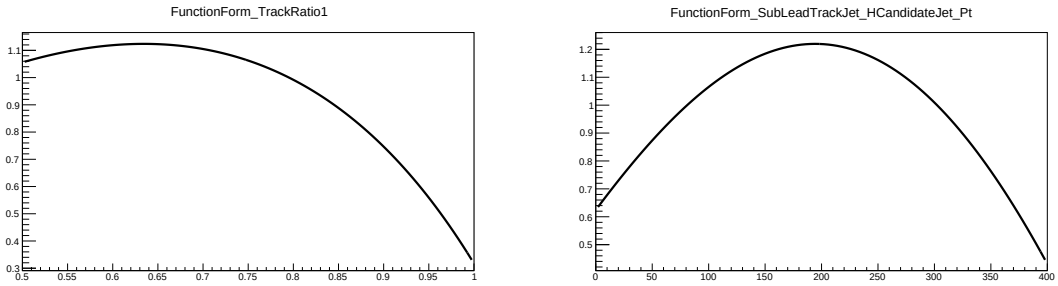


Figure 8.17: The total weights applied for the track jet p_{T} ratio distribution (left) and sub-leading track jet p_{T} (right) in the 2-tag region after all iteration.

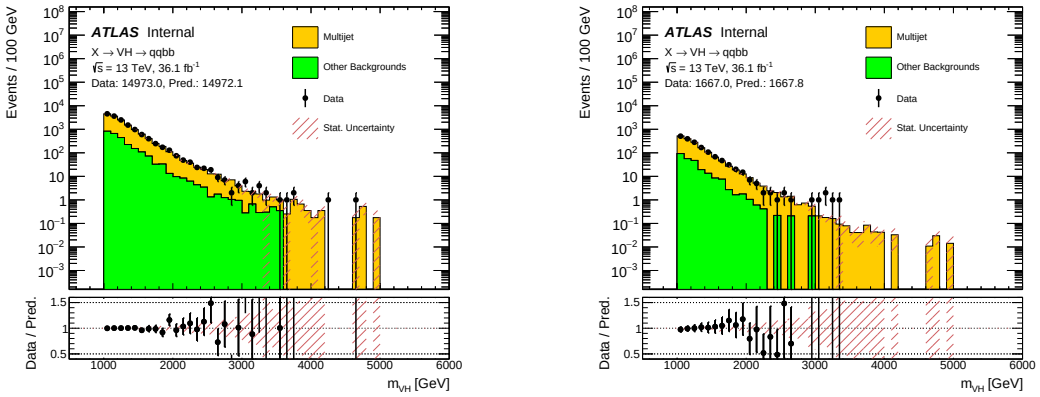


Figure 8.18: Distribution of invariant mass of VH di-jet system m_{JJ} in 1-tag (left) and 2-tag (right) SB. Kinematic re-weighting has been applied to the 2-tag region only.

8.4.5 Cross-check in Validation Region

This section shows the comparison of data and prediction in our validation regions, to test validity of our background estimation method. The prediction and observed yields are summarized in Section 8.4.7.

Figure 8.19 and 8.20 (Figure 8.21 and 8.22) shows selected kinematic distribution in VR-SR (VR-SB) region. A good agreement between data and prediction is observed in general. In particular, in the invariant mass of dijet system, which is the final discriminant variable, good agreement is found consistently in all validation regions. Nevertheless, any difference found in all validation regions will be treated as systematic uncertainty related to multijet modeling, which will be discussed in details in Section 8.5.

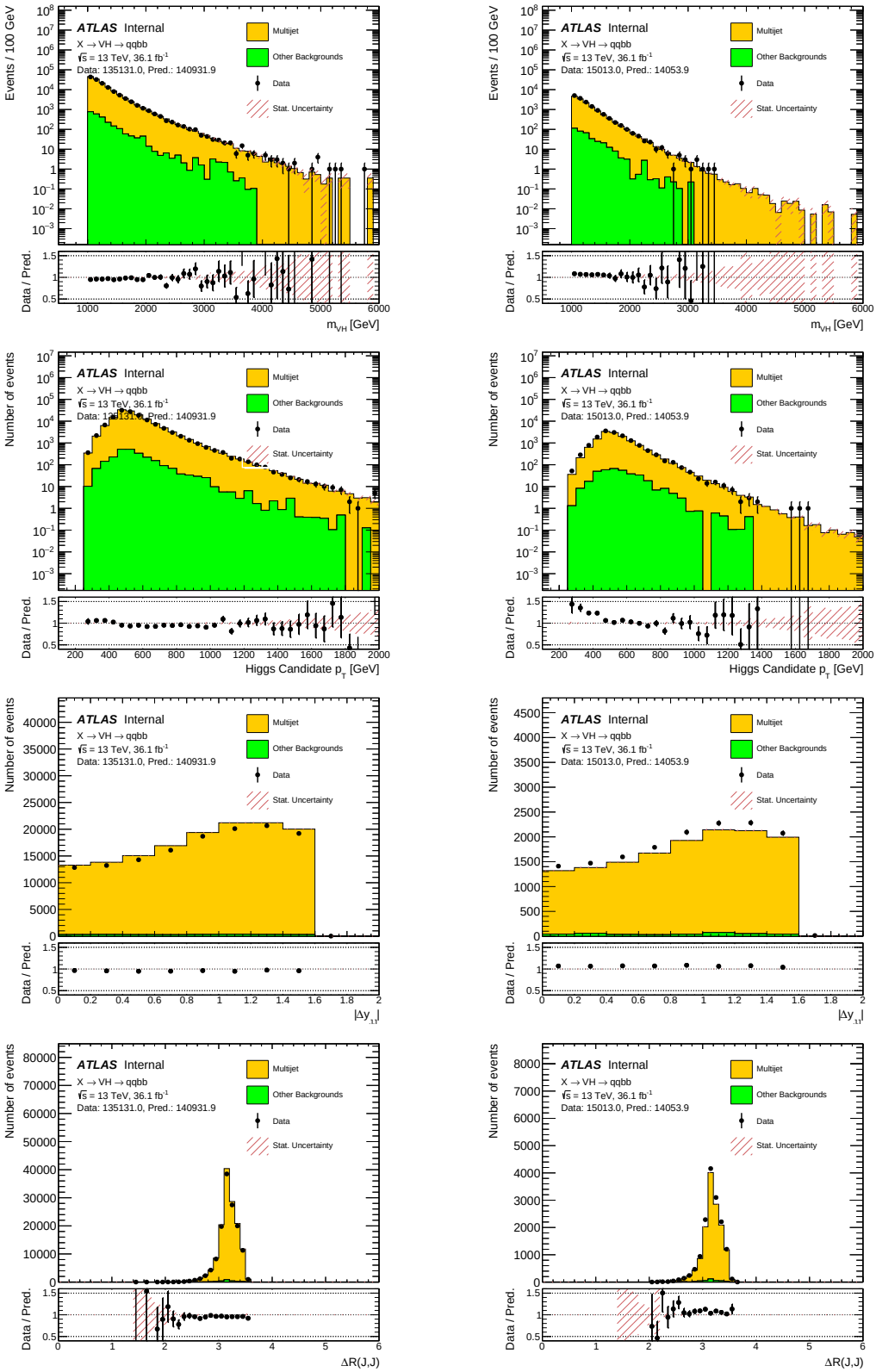


Figure 8.19: Distribution of dijet system invariant mass (first row), H-jet p_{T} (second row), Δy_{12} of dijet system (third row) and ΔR between dijet (last row) in 1-tag (left) and 2-tag (right) VR-SR. Kinematic re-weighting is applied for 2-tag only.

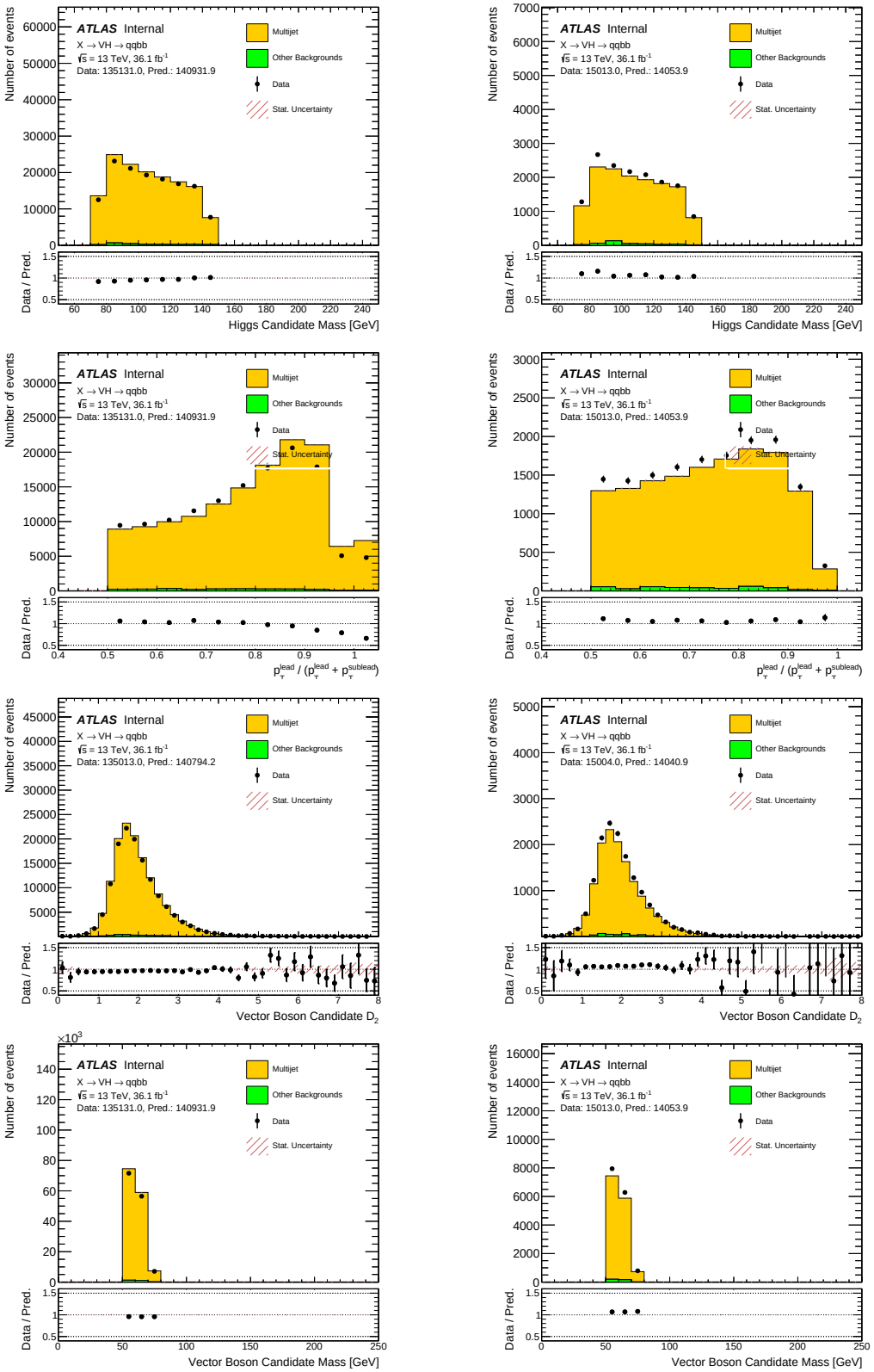


Figure 8.20: Distribution of H-jet mass (first row), track jet p_{T} ratio associated to H-jet (second row), V-jet D_2 (third row) and V-jet mass (last row) in 1-tag (left) and 2-tag (right) VR-SR. Kinematic re-weighting is applied for 2-tag only.

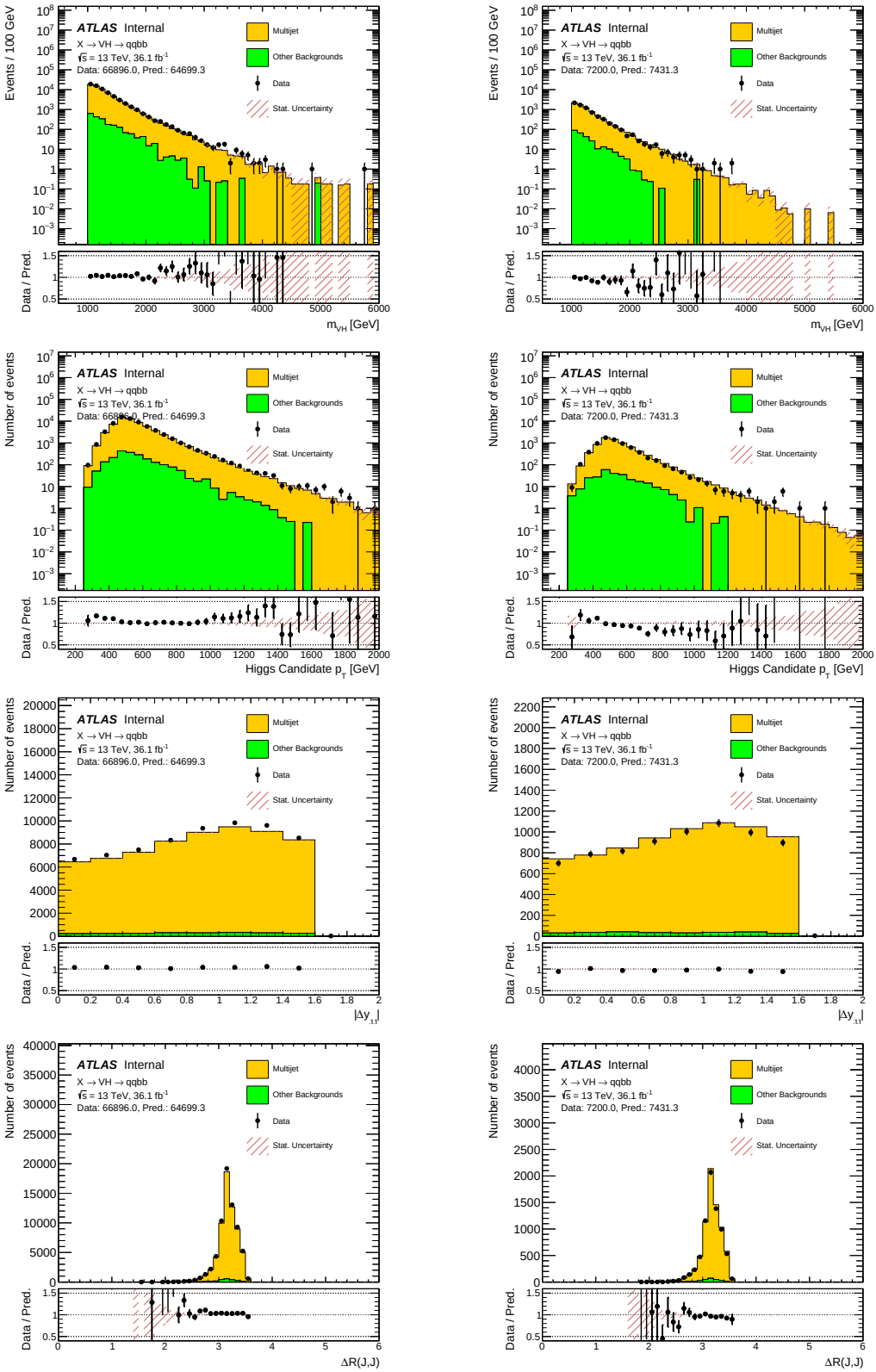


Figure 8.21: Distribution of dijet system invariant mass (first row), H-jet p_{T} (second row), Δy_{12} of dijet system (third row) and ΔR between dijet (last row) in 1-tag (left) and 2-tag (right) VR-SB. Kinematic re-weighting is applied for 2-tag only.

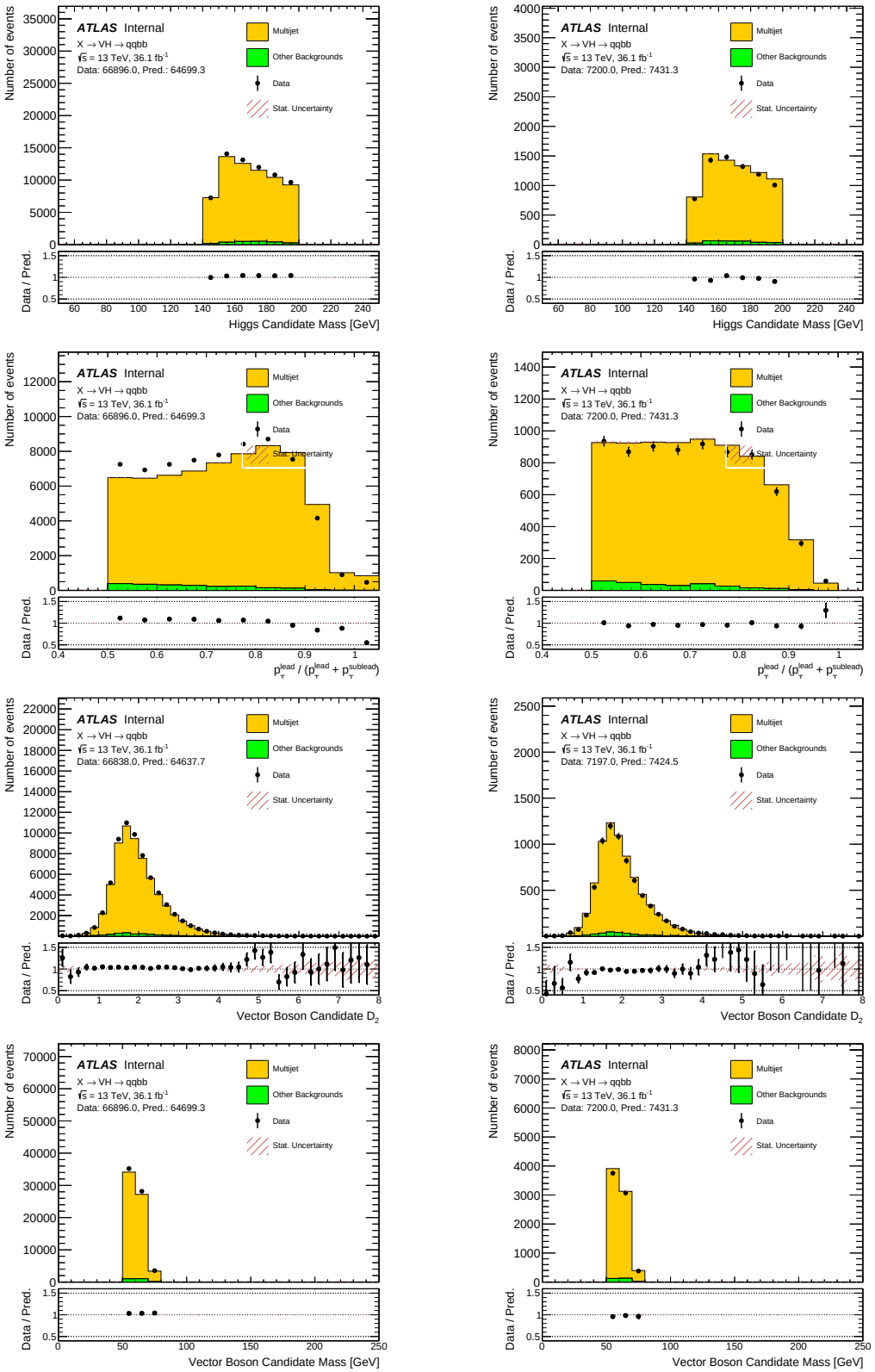


Figure 8.22: Distribution of H-jet mass (first row), track jet p_{T} ratio associated to H-jet (second row), V-jet D_2 (third row) and V-jet mass (last row) in 1-tag (left) and 2-tag (right) VR-SB. Kinematic re-weighting is applied for 2-tag only.

8.4.6 Prediction in Signal Region

Kinematic Distribution in Signal Region

Similar to validation regions, one can also make signal region predictions through 0-tag extrapolation with re-weighting applied. Selected kinematic distribution in WH (ZH) signal regions after unblinding can be found in Figure 8.23 and 8.24 (Figure 8.25 and 8.26). The unblinded yields can be found in Section 8.4.7.

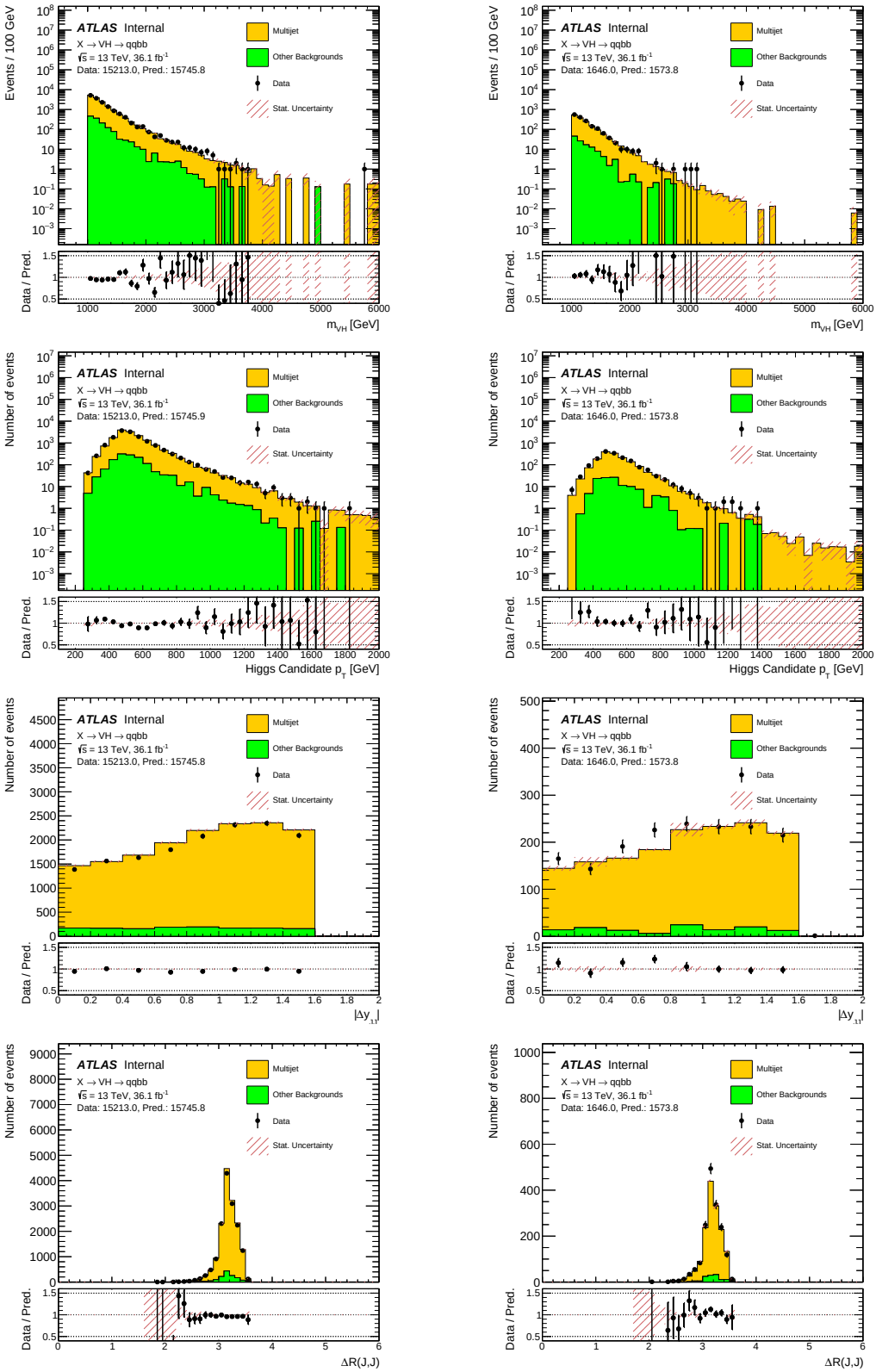


Figure 8.23: Distribution of dijet system invariant mass (first row), H-jet p_{T} (second row), Δy_{12} of dijet system (third row) and ΔR between dijet (last row) in 1-tag (left) and 2-tag (right) WH signal region. Kinematic re-weighting is applied for 2-tag only.

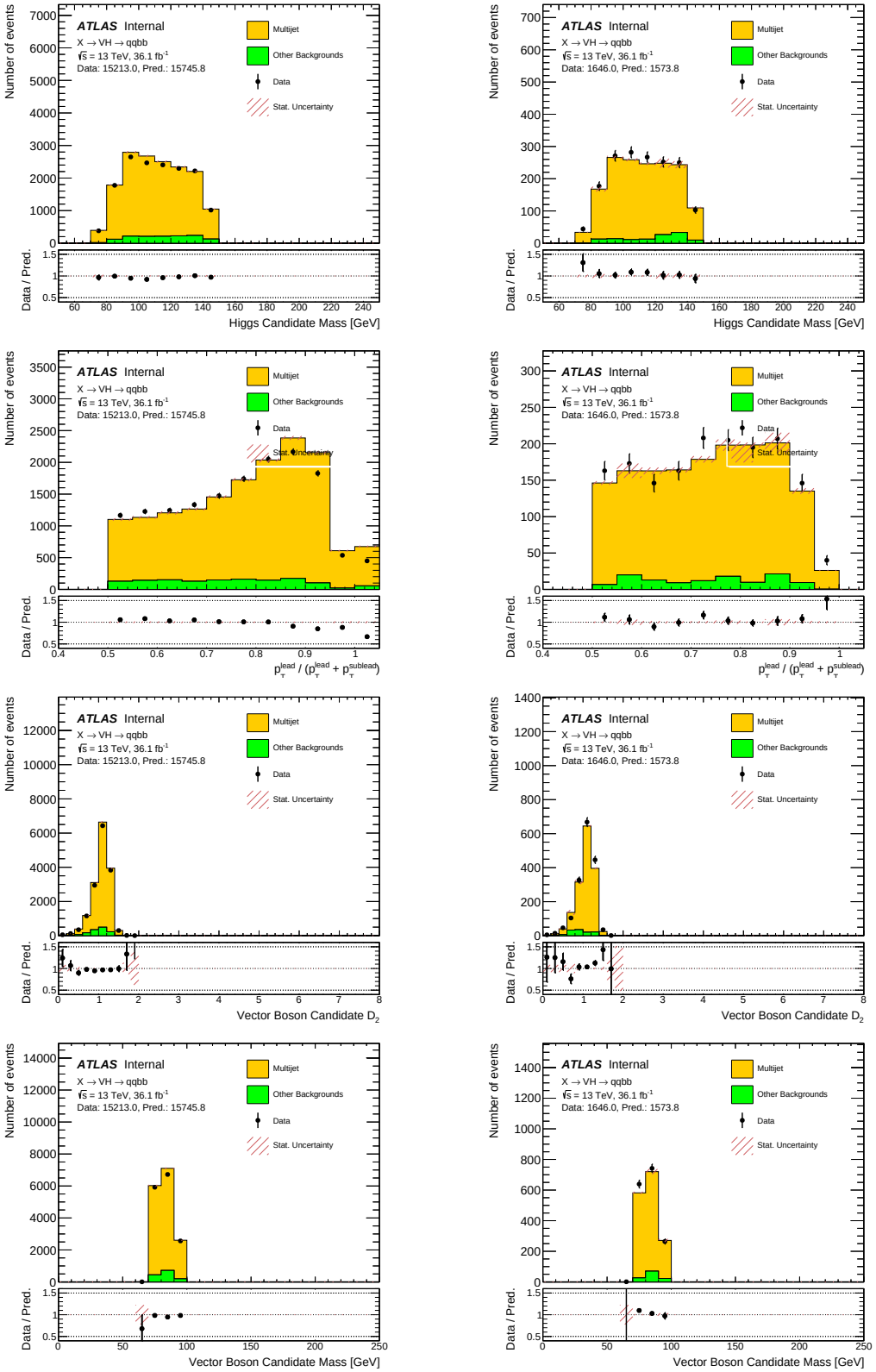


Figure 8.24: Distribution of H-jet mass (first row), track jet p_{T} ratio associated to H-jet (second row), V-jet D_2 (third row) and V-jet mass (last row) in 1-tag (left) and 2-tag (right) WH signal region. Kinematic re-weighting is applied for 2-tag only.

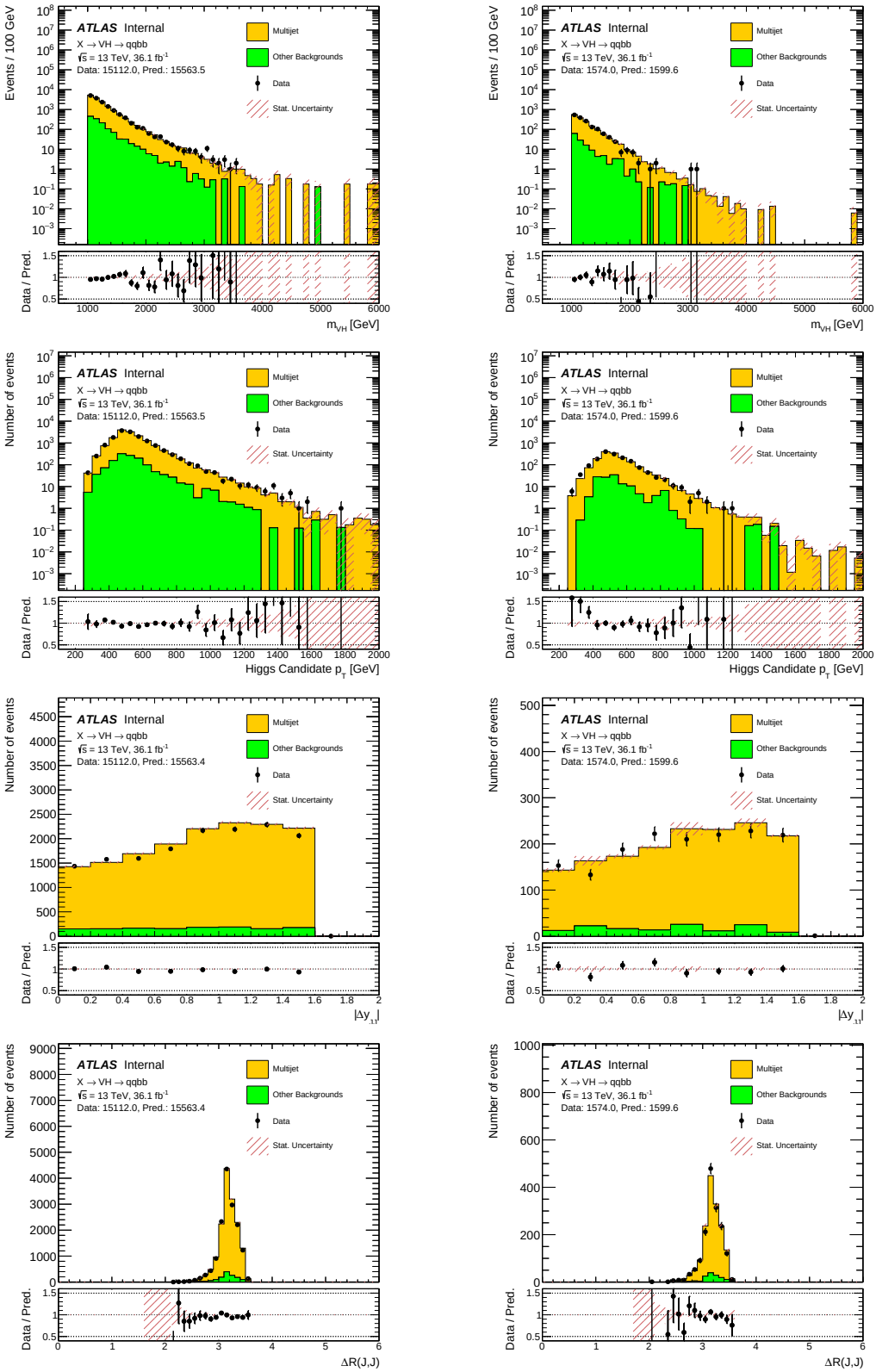


Figure 8.25: Distribution of dijet system invariant mass (first row), H-jet p_{T} (second row), Δy_{12} of dijet system (third row) and ΔR between dijet (last row) in 1-tag (left) and 2-tag (right) ZH signal region. Kinematic re-weighting is applied for 2-tag only.

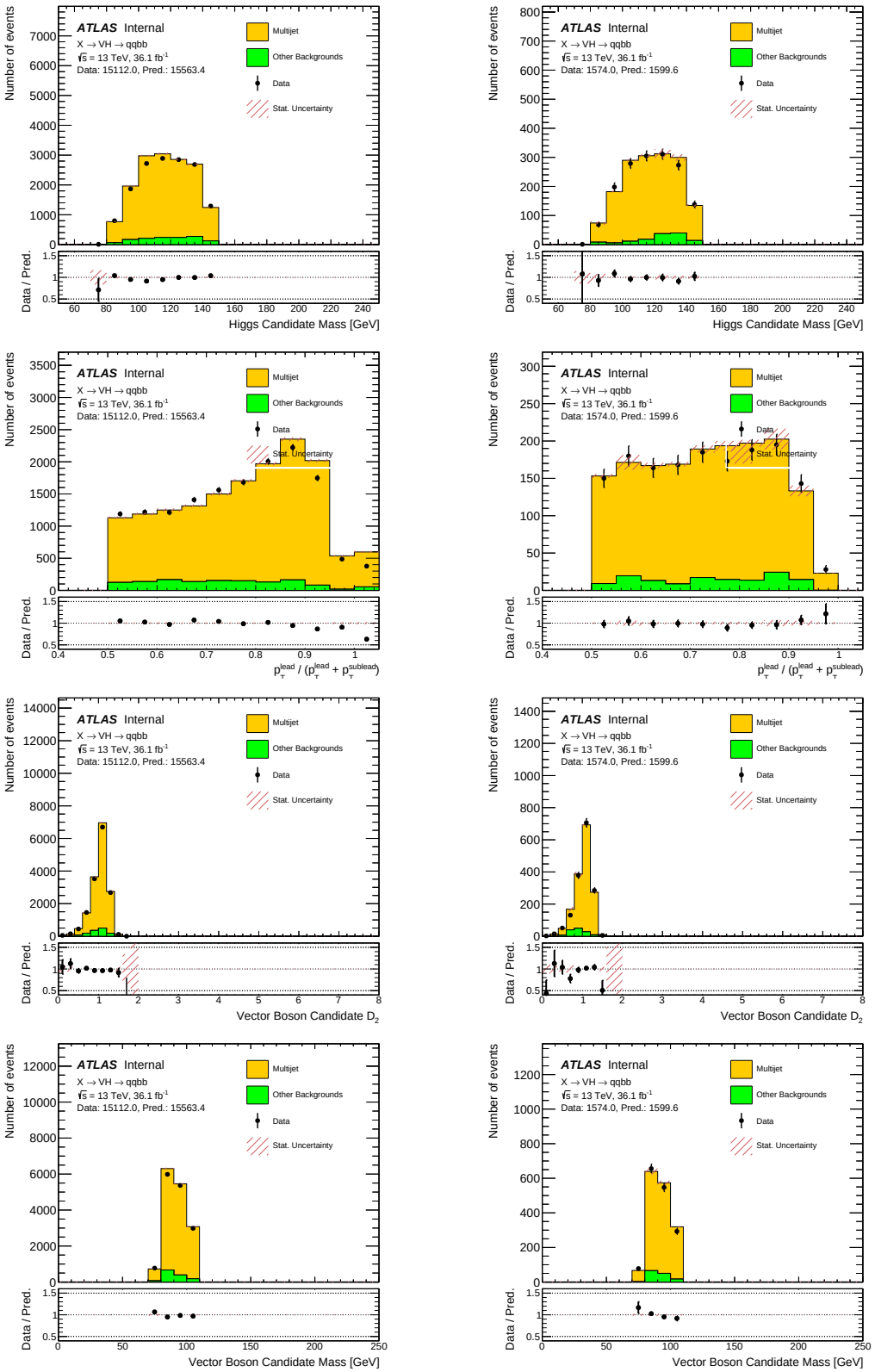


Figure 8.26: Distribution of H-jet mass (first row), track jet p_{T} ratio associated to H-jet (second row), V-jet D_2 (third row) and V-jet mass (last row) in 1-tag (left) and 2-tag (right) ZH signal region. Kinematic re-weighting is applied for 2-tag only.

Smoothing in Signal Region

Due to the limited multijet and $t\bar{t}$ statistics at high VH dijet invariant mass above 2000 GeV, it is necessary to smooth the tail of distribution of multijet and other background predictions in the signal regions. The MJ5 function [207] is used to fit the multijet distributions, whereas the other components (combining $t\bar{t}$ and V+jets) are fit with a dijet function [208] in the 1-tag region and an exponential function in the 2-tag region. The analytic forms of the MJ5 and dijet functions are shown in Equations 8.3 and 8.4, respectively:

$$f(x) = p_0(1-x)^{p_1}(1+x)^{p_2 \ln x} \tag{8.3}$$

$$f(x) = e^{a+b\times ln(1-x)+c\times ln(x)} = p_0(1-x)^{p_1}x^{p2} \tag{8.4}$$

where $x = m_{JJ}/\sqrt{s}$.

Figure 8.27 shows the smoothing fits for the multijet background in signal regions. The choice of function was not tested on multijet MC, but a fit with various alternative functions are performed to test the robustness of choice of function (see Section 8.5). Figure 8.28 shows the smoothing fits for the other background, which is the sum of $t\bar{t}$ and V+jets prediction from MC, in signal regions. The smoothing statistical uncertainties are also shown on the plot. More details on systematic uncertainties related to the smoothing procedure can be found in Section 8.5.

Statistical uncertainties on the fit parameters are propagated as systematic uncertainties in such a correlated way that all fit parameters are varied simultaneously along eigenvector directions of the fit parameters covariant matrix by 1σ.

Note that while the functional form is only fit within a certain fit range for both multijet and other background prediction, the function is used to smooth over the entire range above lower bound of fit range (i.e. covering the whole tail without any upper bound).

After smoothing, the m_{JJ} distribution in the signal regions for both pre-fit estimated background and observed data can be found in Figure 8.29. Along with the systematic uncertainties, which will be discussed in details in next section, this is the input for further statistical interpretation.

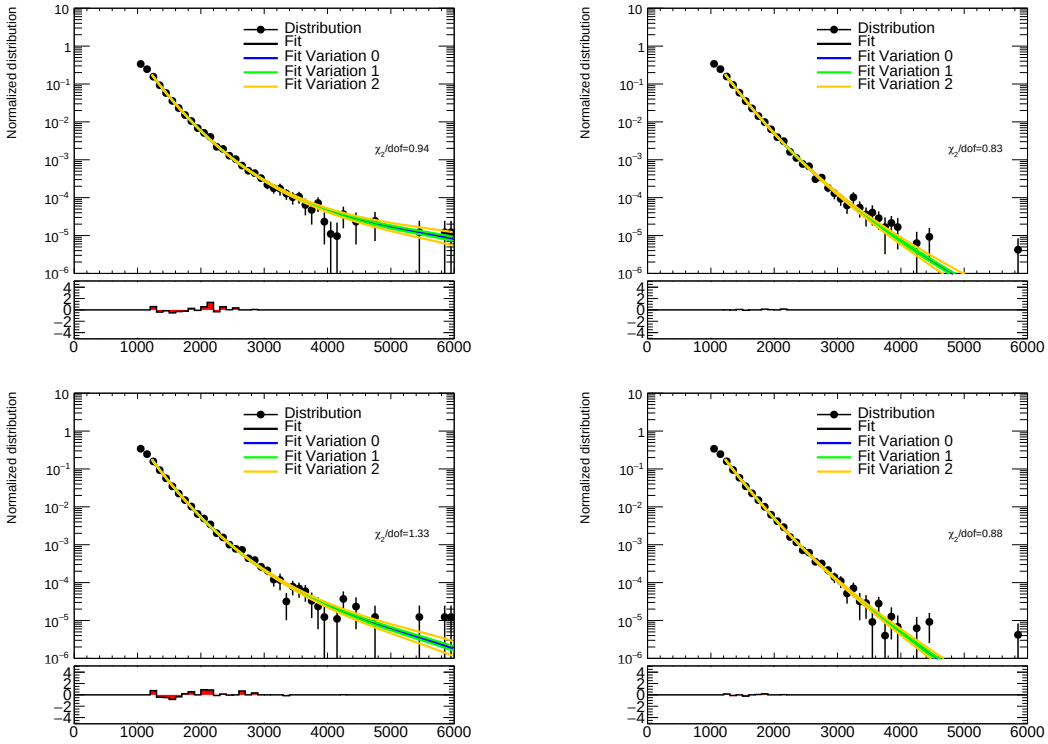


Figure 8.27: Smoothing fit using MJ5 function for multijet background prediction in WH (first row) and ZH (second row) signal regions of 1-tag (left) and 2-tag (right). Statistical smoothing uncertainties ("Fit Variations") are determined by varying fit parameters within uncertainties in a correlated way. The ratio panel shows the significance of the points with respect to the fit result.

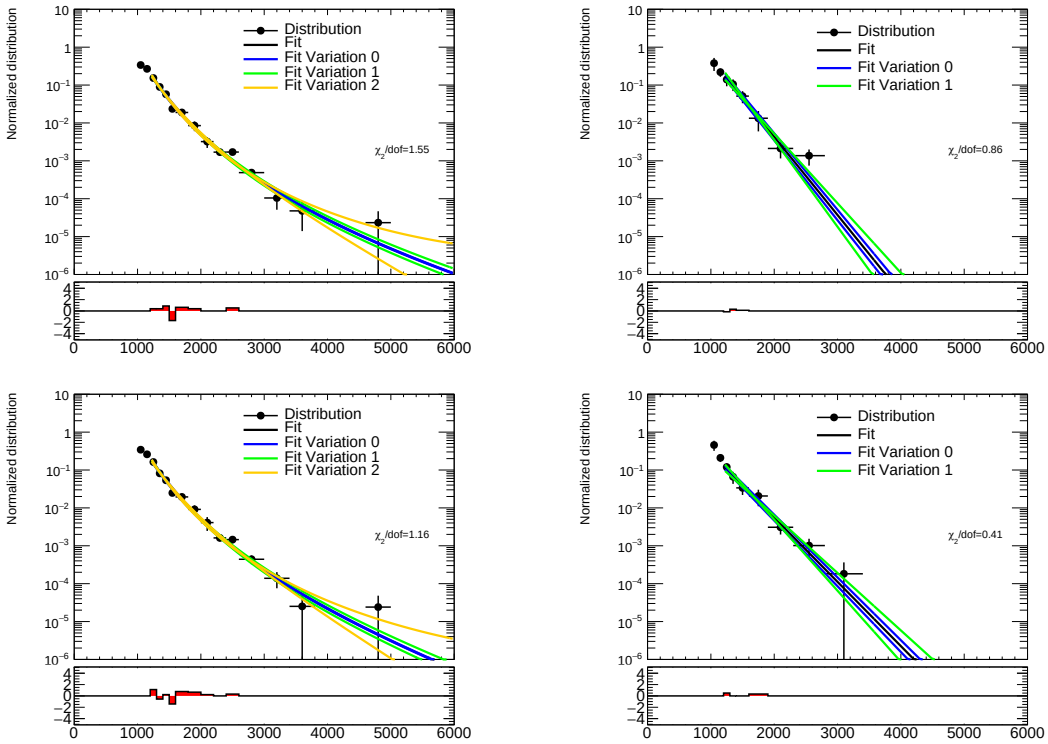


Figure 8.28: Smoothing fit using dijet/exponential functions for non-multijet background prediction in WH (first row) and ZH (second row) signal regions of 1-tag (left) and 2-tag (right). Statistical smoothing uncertainties ("Fit Variations") are determined by varying fit parameters within uncertainties in a correlated way. The ratio panel shows the significance of the points with respect to the fit result.

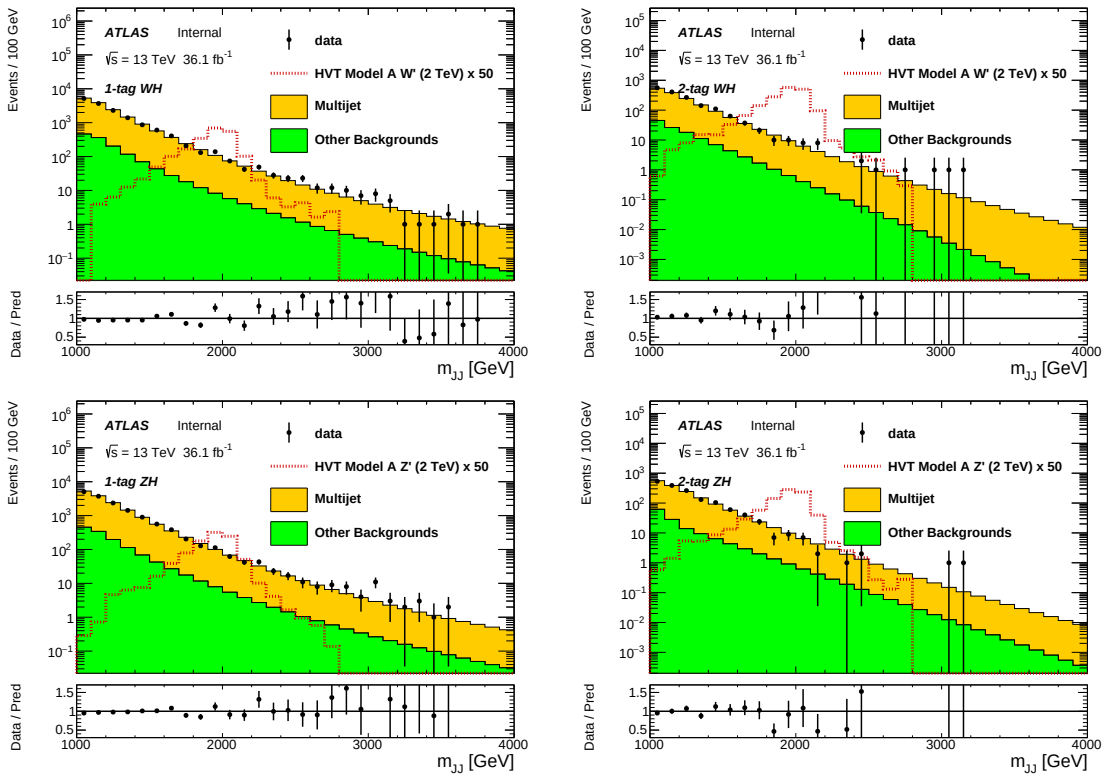


Figure 8.29: Pre-fit m_{VH} distributions in WH (top) and ZH (bottom), 1-tag (left) and 2-tag (right) signal regions.

8.4.7 Yields

Table 8.6 shows the yields obtained in SB and various VRs, with statistical uncertainties shown only.

Table 8.7 shows the pre-fit yields obtained for signal and background process in the signal regions, with both statistical and systematic uncertainties shown. It should be noticed that this table is the so-called *pre-fit* version, in that both yields and systematics are evaluated before fitting signal strength and nuisance parameters to the observed data in signal region.

Sample (1-tag)	SB	VR-SR	VR-SR(D_2)	VR-SB	VR-SB(D_2)
Multijet	12363.0 ± 51.1	138427.4 ± 160.6	8824.5 ± 40.9	62581.8 ± 107.0	3971.1 ± 27.4
$t\bar{t}$	2203.0 ± 31.3	1028.6 ± 27.0	114.9 ± 6.8	1702.4 ± 35.0	208.2 ± 9.9
V+jets	406.1 ± 43.0	1475.9 ± 89.2	116.0 ± 24.0	415.0 ± 51.8	34.9 ± 12.8
Total	14972.1 ± 73.8	140931.9 ± 185.6	9055.5 ± 47.9	64699.3 ± 123.9	4214.2 ± 31.8
Data	14973	135131	8685	66896	4418

Sample (2-tag)	SB	VR-SR	VR-SR(D_2)	VR-SB	VR-SB(D_2)
Multijet	1414.0 ± 6.1	13681.8 ± 17.2	875.1 ± 4.4	7157.1 ± 12.7	455.8 ± 3.3
$t\bar{t}$	221.0 ± 10.6	115.5 ± 9.6	12.3 ± 3.2	247.2 ± 14.9	25.9 ± 4.2
V+jets	32.8 ± 13.1	256.6 ± 27.8	14.0 ± 5.7	27.0 ± 9.5	2.8 ± 2.7
Total	1667.8 ± 17.9	14053.9 ± 34.0	901.4 ± 7.9	7431.3 ± 21.8	484.5 ± 6.0
Data	1667	15013	934	7200	426

Table 8.6: Yields in the SB and various validation regions for both 1-tag and 2-tag cases. Only statistical uncertainties are shown on this table.

8.5 Systematic Uncertainties

In this section we will have an overview of the systematics being considered in this analysis. Both the sources of systematic uncertainties and the methods to determine these uncertainties are very similar to that as presented in Chapter 7. Here we will still go through each systematic uncertainty, but with more focus on those that are important for the analysis being considered here. As usual, readers with no patience in all the details can find an executive summary in Section 8.5.3.

8.5.1 Theoretical and Experimental Uncertainties

Systematic uncertainties in the signal and background predictions arising from experimental and theoretical sources are considered. These uncertainties include: theoretical uncertainties on the acceptance, uncertainties in the jet energy scale (JES) and resolution (JER), uncertainties on the jet

	WH 1-tag	ZH 1-tag
Multijet	14390.81 ± 1120.42	14251.42 ± 1104.81
Other Backgrounds	1355.01 ± 357.19	1312.03 ± 346.34
Total Backgrounds	15745.82 ± 924.63	15563.45 ± 904.91
Data	15213	15112
Model A, M=2TeV	41.98 ± 9.58	19.33 ± 4.33

	WH 2-tag	ZH 2-tag
Multijet	1454.61 ± 217.03	1464.86 ± 219.77
Other Backgrounds	119.18 ± 65.35	134.73 ± 62.35
Total Backgrounds	1573.79 ± 206.50	1599.59 ± 203.12
Data	1646	1574
Model A, M=2TeV	35.19 ± 6.81	16.59 ± 3.13

Table 8.7: Yields in both 1-tag and 2-tag SR, for both WH and ZH signal samples. Yields for signal sample with $M = 2000$ GeV are also shown. Uncertainties shown on this table is the combination of statistical and systematic uncertainties.

mass scale (JMS) and resolution (JMR), uncertainties in the b-tagging efficiency, and the luminosity uncertainty.

Theoretical Uncertainties

The theoretical uncertainties in the signal acceptance take into account factorization and renormalization scale uncertainties, PDF uncertainties, and modeling of the underlying event, hadronic showers, initial and final state radiation. Two sources of PDF uncertainties on the signal acceptance are estimated: difference between recommended PDF sets and internal PDF uncertainties associated to the nominal PDF.

The impact on the acceptance from each alternative PDF set is observed to be generally below 1%. The internal PDF errors, on the other hand, are also found to be well below 1% as well. Additionally, the impact on the m_{JJ} shapes was determined to be negligible. Therefore, no theoretical uncertainty due to the PDF is set on signal samples.

To determine the impact of scale uncertainties on signal acceptance, new Madgraph samples are generated with factorization and renormalization scales varied by factors of 0.5 and 2.0. Samples with 15k events are generated for nominal, 0.5 and 2.0, and passed through a Rivet routine requiring basic kinematic cuts: at least two large-R trimmed jets with same fiducial cuts as this analysis, leading large-R jet $p_{\mathrm{T}} > 450$ GeV, mass window cut for V and H candidates and $m_{JJ} > 1$ TeV. The resulting acceptances are observed to be varied by less than 1%. No significant impact on m_{JJ} distribution shape is found. Therefore no theoretical uncertainty due to scale variations is set on

signal samples.

Theoretical uncertainties in the $t\bar{t}$ background estimate include uncertainties to account for missing higher order terms in the matrix elements and PDF sets, uncertainties in modeling the hadronic shower and initial and final state radiation, and the uncertainty in the top quark mass. A 30% normalization uncertainty is applied to the $t\bar{t}$ background based on ATLAS $t\bar{t}$ differential cross-section measurement [209].

Due to the small contribution of the V+jets backgrounds, their theoretical uncertainties are not considered.

Experimental Uncertainties

The preliminary uncertainty on the combined 2015+2016 integrated luminosity is 3.2%. It is derived, following a methodology similar to that detailed in [75], from a preliminary calibration of the luminosity scale using $x - y$ beam-separation scans performed in August 2015 and May 2016.

Experimental systematic uncertainties affect the signal as well as the $t\bar{t}$ and V+jets backgrounds estimated from MC simulation. The systematic uncertainties related to the scales of the large-R jet p_{T}, mass and $D_2^{\beta=1}$ are of the order of 2%, 5% and 3%, respectively. They are derived in-situ [210] and extracted following the technique described in [131]. The resolution of each of these large-R jet observables are evaluated by smearing the jet observable according to the systematic uncertainties of the resolution measurement [131, 147]. For the large-R jet p_{T} a 2% absolute uncertainty is assigned, while for the mass resolution and $D_2^{\beta=1}$ resolution a relative 20% and 15% uncertainty is assigned respectively. The uncertainty in the b-tagging efficiency for track jets is based on the uncertainty in the measured tagging efficiency for b-jets in data following the same methodology as used in [211]. This is measured as a function of b-jet p_{T} and ranges between 2% and 8% for track jets with $p_{\mathrm{T}} < 250$ GeV. For track jets with $p_{\mathrm{T}} > 250$ GeV the uncertainty in the tagging efficiencies is extrapolated using MC simulation [118] and is approximately 9% for track jets with $p_{\mathrm{T}} > 400$ GeV.

8.5.2 Background Estimation Uncertainties

The systematic uncertainties related to multijet background estimation method consists of three parts: normalization uncertainty (a.k.a non-closure uncertainty on μ_{Multijet}), shape uncertainty and smoothing uncertainty. The first two uncertainties are derived from validation regions, while the last uncertainty is derived from signal region directly.

Normalization Uncertainty

In addition to the 0.97% (2.8%) statistical uncertainty on μ_{Multijet} in the 1-tag (2-tag) region coming from the normalization fit discussed in Section 8.4, a further non-closure uncertainty is derived by comparing the data (with $t\bar{t}$ and V+jets subtracted) to the multijet prediction in several validation

regions. Since multijet is the dominant background in this analysis, we will attribute all the observed non-closure to the multijet normalization predictions, and thus to the systematic uncertainty on μ_{Multijet} itself. In particular, the systematic uncertainty is taken through following rules: 1) In validation regions without D_2 cut applied, take maximum between (subtracted) data statistical uncertainty and non-closure; 2) Validation regions with D_2 applied is considered only if non-closure is larger than the (subtracted) data statistical uncertainty; 3) Take maximum from all numbers quoted in each validation region.

A summary of multijet normalization agreement in various validation regions can be found in Table 8.8 and 8.9, for 1-tag and 2-tag regions, respectively.

Validation Regions	Data Stat. Uncert.	(Pred-Data)/Data	|Pred-Data|/Pred
VR-SR	0.27%	4.35%	4.17%
VR-SR (pass D_2)	1.09%	4.32%	4.14%
VR-SB	0.39%	-3.36%	3.48%
VR-SB (pass D_2)	1.55%	-4.76%	4.99%

Table 8.8: Agreement between data and prediction in various 1-tag validation regions. The "data" denoted in this table is the data after subtraction of $t\bar{t}$ and V+jets MC contributions. The "Pred" denoted in this table is the normalization prediction of multijet component.

Validation Regions	Data Stat. Uncert.	(Pred-Data)/Data	|Pred-Data|/Pred
VR-SR	0.83%	-4.62%	4.84%
VR-SR (pass D_2)	3.32%	-1.59%	1.61%
VR-SB	1.20%	5.40%	5.12%
VR-SB (pass D_2)	4.99%	16.38%	14.08%

Table 8.9: Agreement between data and prediction in various 2-tag validation regions. The "data" denoted in this table is the data with $t\bar{t}$ and V+jets MC subtracted. The "Pred" denoted in this table is the normalization prediction of multijet component.

In the 1-tag case, when no additional D_2 requirement is imposed, a deviation of $\sim 4\%$ from data is found. The largest deviation from data comes from the VR-SB (pass D_2) region, 5%, which is larger than data statistical uncertainty of 1.6%. Therefore, a non-closure uncertainty of 5% is quoted for $\mu^{(1)}_{\text{Multijet}}$. In the 2-tag case, the largest uncertainty comes from VR-SB with the D_2 requirement, and therefore the non-closure uncertainty assigned to $\mu^{(2)}_{\text{Multijet}}$ is 14%.

Shape Uncertainty

By looking at Figure 8.19 and 8.21, we find that the modeling of m_{JJ} shape agrees well with the data in validation regions, within statistical uncertainty. A systematic uncertainty on shape modeling is derived by taking the ratio of shape between data (with $t\bar{t}$ and V+jets MC subtracted) and

multijet prediction in validation regions, which will be further propagated to signal region multijet distribution. It should be noticed that, shape uncertainty is considered only on m_{JJ}, since this is the final discriminant variables for deriving final results (significance, exclusion limits etc.).

To be robust against the statistical uncertainty, we first perform a smoothing fit on both the (subtracted) data and multijet prediction m_{JJ} distribution. The smoothing function we use is the dijet functional form. The fit range is $1200 < m_{JJ} < 4500$ GeV in order to better model the tail of the distribution. The smoothing fit results for both subtracted data and multijet prediction can be found in Figures 8.30, 8.31, 8.32 and 8.33. Along with the nominal smoothing fit result, the fit variations due to the smoothing statistical uncertainty are also shown, by varying the free parameters along eigenvector directions by 1σ, in order to take the correlation between parameters into account.

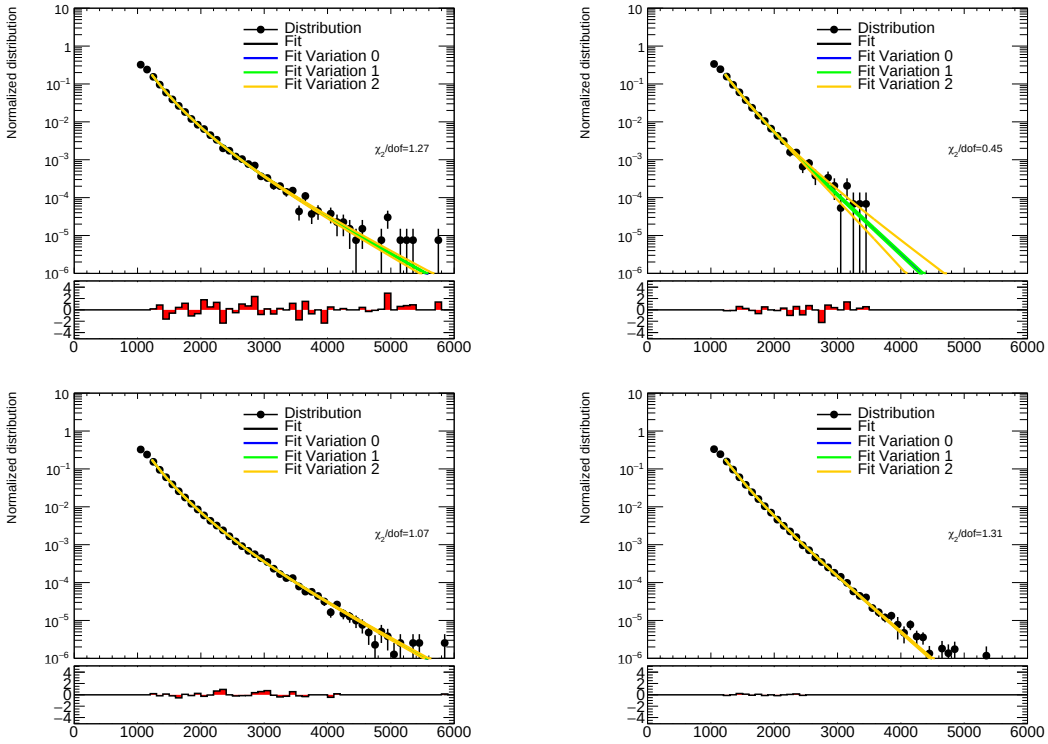


Figure 8.30: Smoothing fit on data with $t\bar{t}$ and V+jets MC subtracted (first row) and multijet prediction (second row) in 1-tag (left) and 2-tag (right) VRSR.

We then take the ratio of the smoothed multijet prediction over the smoothed (subtracted) data and compare it to the statistical uncertainty envelope from the smoothing fit itself. Systematic uncertainties related to the smoothing procedure will be treated separately as discussed later. The comparison of shape deviation and statistical uncertainty can be found in Figures 8.34, 8.35, 8.36 and 8.37.

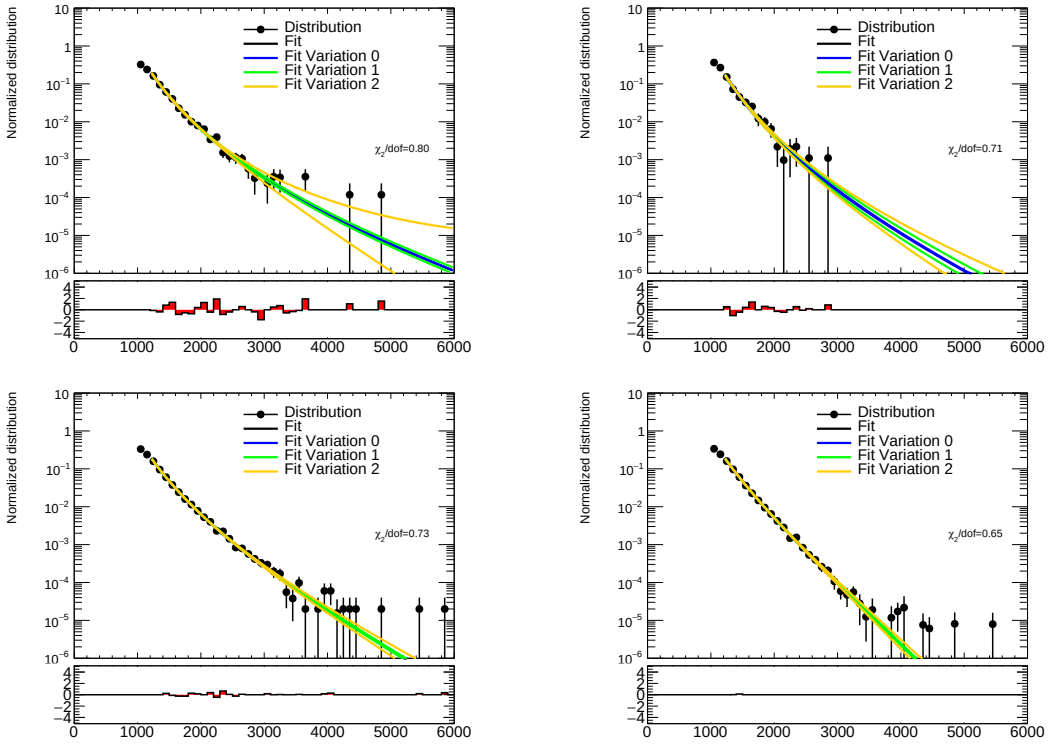


Figure 8.31: Smoothing fit on data with $t\bar{t}$ and V+jets MC subtracted (first row) and multijet prediction (second row) in 1-tag (left) and 2-tag (right) VRSR with the D_2 requirement.

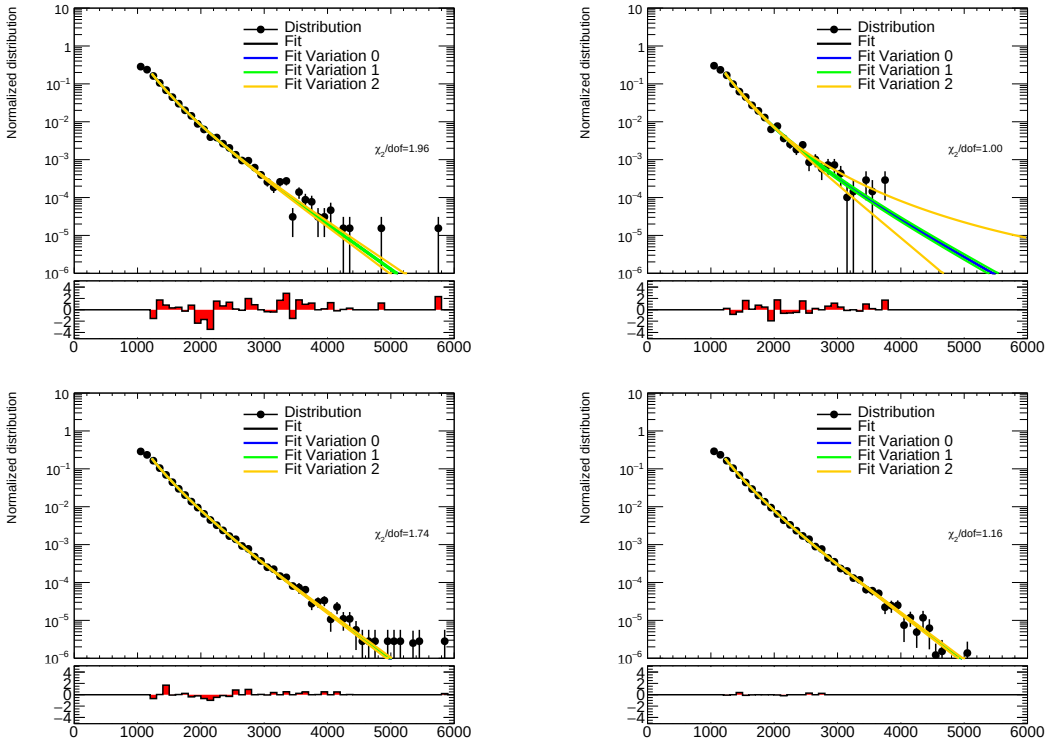


Figure 8.32: Smoothing fit on data with $t\bar{t}$ and V+jets MC subtracted (first row) and multijet prediction (second row) in 1-tag (left) and 2-tag (right) VRSB.

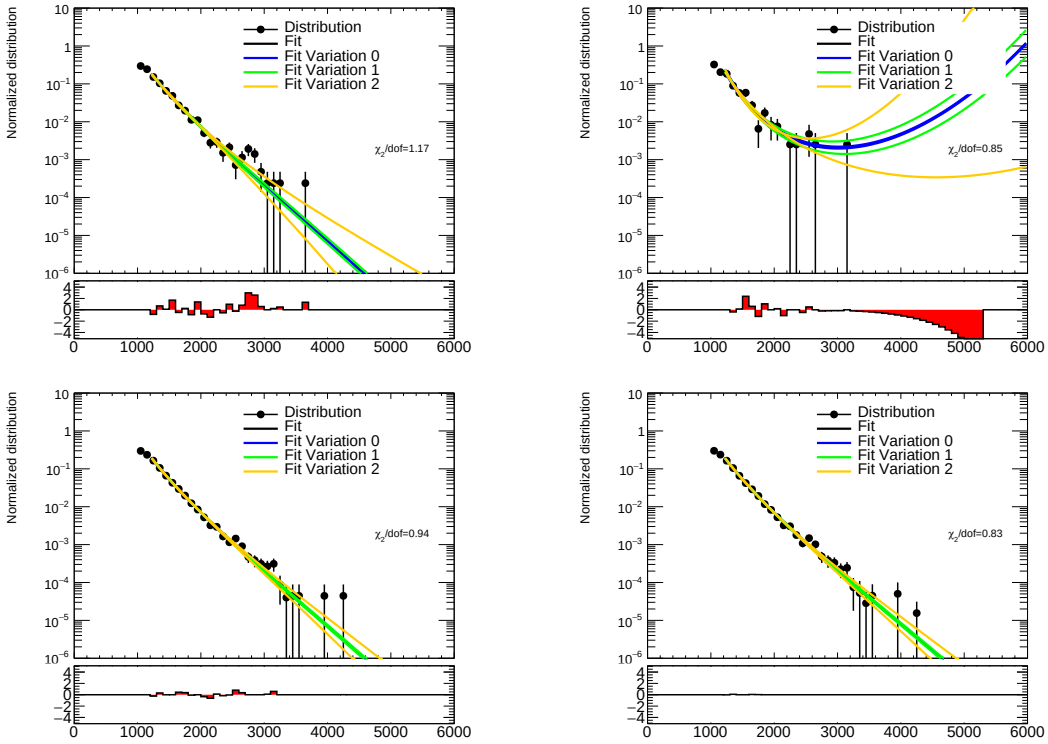


Figure 8.33: Smoothing fit on data with $t\bar{t}$ and V+jets MC subtracted (first row) and multijet prediction (second row) in 1-tag (left) and 2-tag (right) VRSB with the D_2 requirement.

Although VR-SR is closer to the final SR on the mass plane as shown in Figure 8.12, the validation regions with the largest deviation of prediction over data are used to derive the multijet shape uncertainty, in order to be conservative. The exception to this rule are the 2-tag validation regions with the D_2 requirement, where the statistics are insufficient to take conclusions on the shape at high masses. Furthermore, in order to avoid over-constraining the m_{JJ} high-mass tails from the fit to the m_{JJ} low-mass region, shape uncertainties are split into low-mass and high-mass region at the position of 2 TeVon m_{JJ} spectrum.

In summary, two shape uncertainties, one covering the low-mass region and one covering high-mass region independently, are assigned to the multijet background based on the (nominal) agreement observed in the validation regions. For the 2-tag, the low mass uncertainty is derived from the VR-SR (with D_2), while the high mass uncertainty comes from VR-SB. For the 1-tag case, both are derived from VR-SR (with D_2).

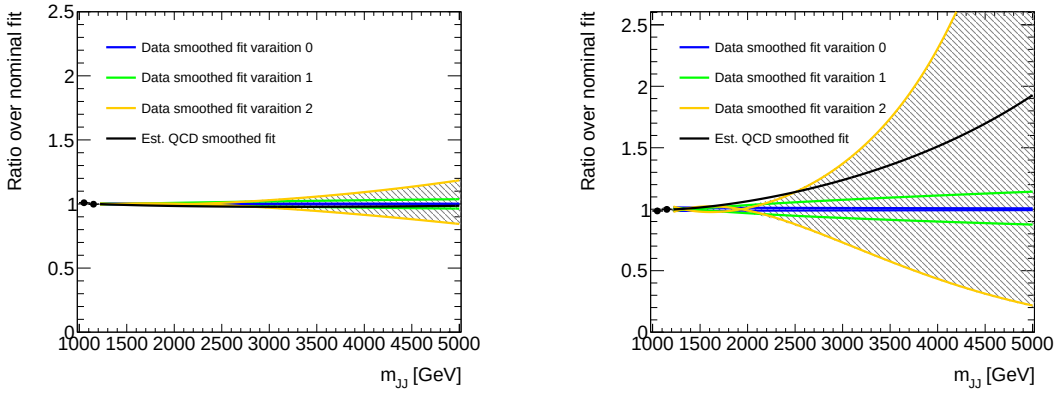


Figure 8.34: Fitted smoothing function ratio between multijet prediction over (subtracted) data as function of m_{JJ}, in 1-tag (left) and 2-tag (right) VRSR. The ratio of data eigenvariations from smoothing fit statistical fluctuation over data nominal fit is also shown for comparison.

Smoothing Uncertainty

Systematic uncertainties related to the smoothing fit itself are estimated by varying the choice of fit function used and the fit range to which the nominal function is applied. In general, the uncertainty is quoted as the largest deviation from nominal setup among all possible configurations resulting in a reasonable fit quality (χ^2/dof etc.).

Figure 8.38 shows the results of the fits performed with different function of the dijet and multijet family with respect to the nominal fit result, as a function of the dijet mass. In this case, the associated uncertainty has been estimated as the total band of the symmetrized MJ4 (yellow) function around the nominal (MJ5).

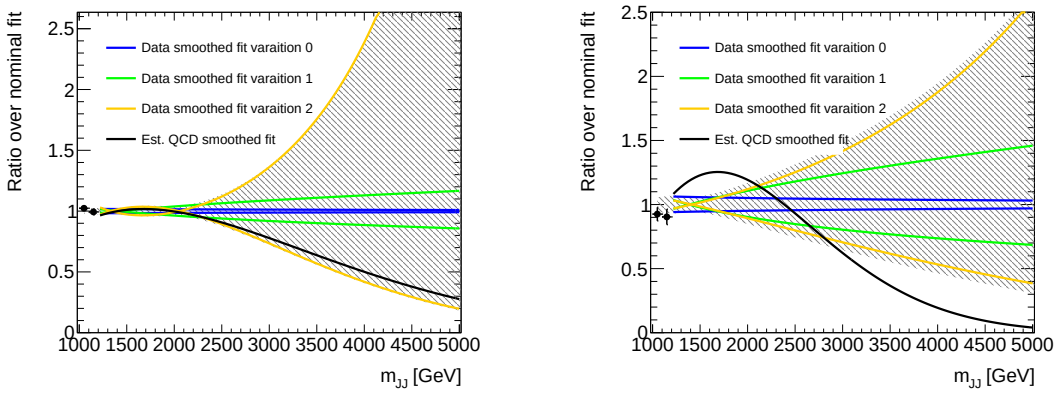


Figure 8.35: Fitted smoothing function ratio between multijet prediction over (subtracted) data as function of m_{JJ}, in 1-tag (left) and 2-tag (right) VRSR with the D_2 requirement. The ratio of data eigenvariations from smoothing fit statistical fluctuation over data nominal fit is also shown for comparison.

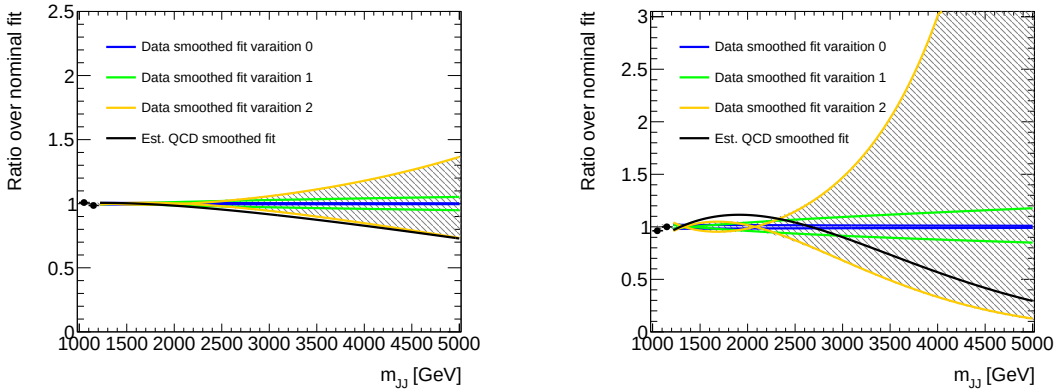


Figure 8.36: Fitted smoothing function ratio between multijet prediction over (subtracted) data as function of m_{JJ}, in 1-tag (left) and 2-tag (right) VRSB. The ratio of data eigenvariations from smoothing fit statistical fluctuation over data nominal fit is also shown for comparison.

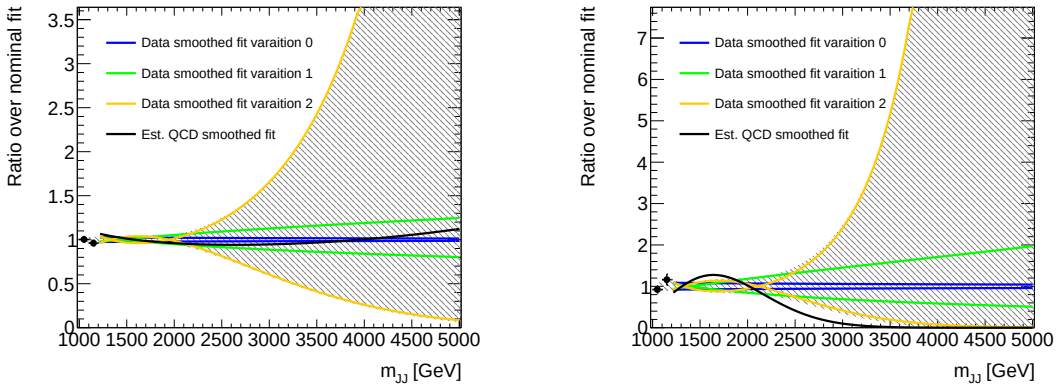


Figure 8.37: Fitted smoothing function ratio between multijet prediction over (subtracted) data as function of m_{JJ}, in 1-tag (left) and 2-tag (right) VRSB with the D_2 requirement. The ratio of data eigenvariations from smoothing fit statistical fluctuation over data nominal fit is also shown for comparison.

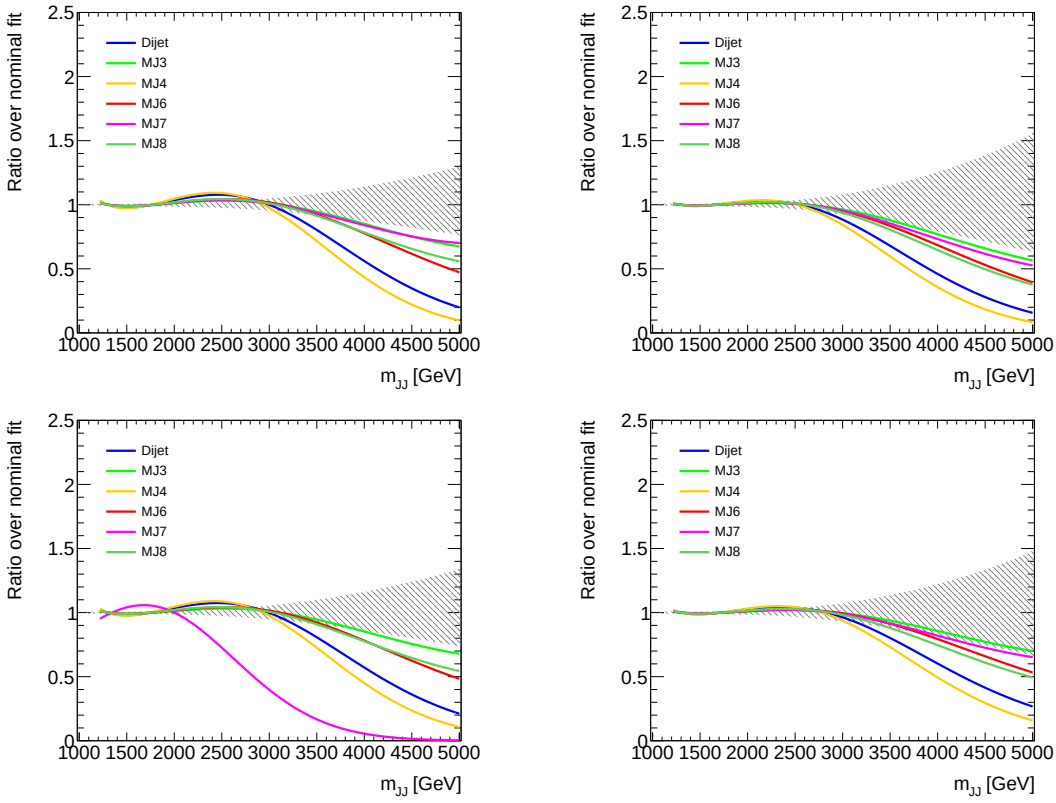


Figure 8.38: Ratio of fitted multijet predictions obtained with the dijet and MJ3-8 functions with respect to the nominal MJ5 function, in each signal region.

Figure 8.39 shows the impact of applying the smoothing fit to different ranges of the m_{JJ} distribution, where the nominal configuration fits the range from 1.2 TeV to 4 TeV. The uncertainty associated to the fit range is derived by symmetrizing the curve that produces the largest reasonable variation: 1.2 to 3 TeV (pink) for all regions except WH 2-tag, where the 1.1-4 TeV (green) curve is used.

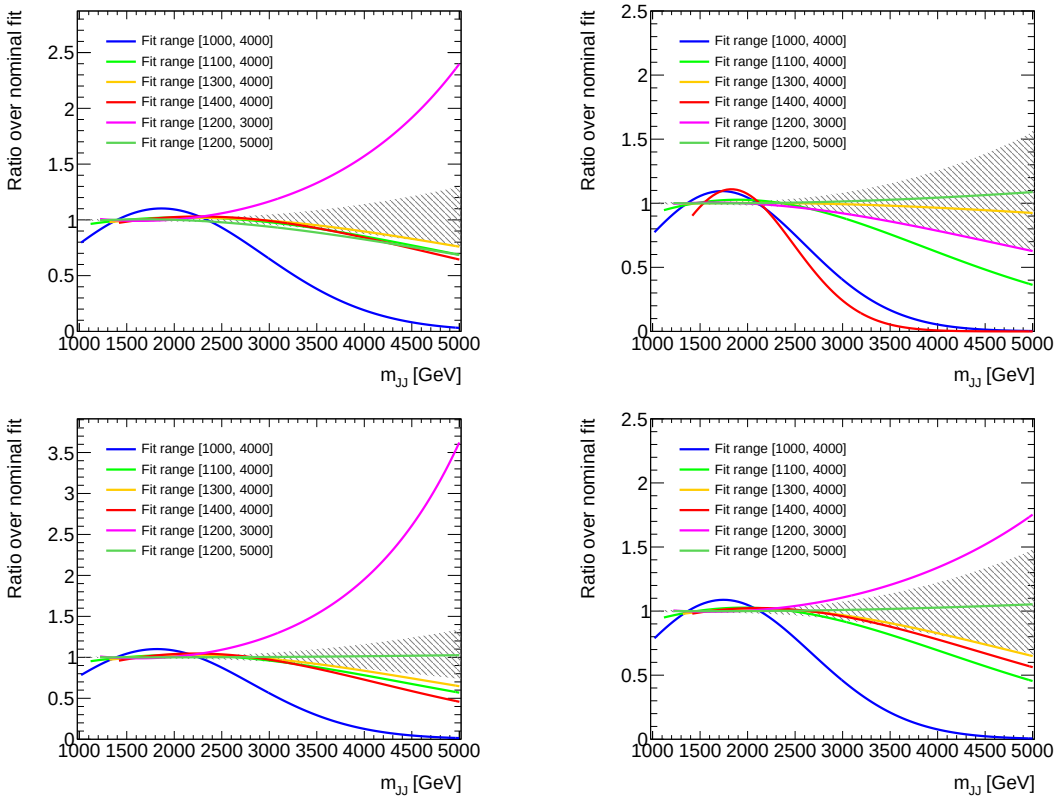


Figure 8.39: Ratio of multijet predictions obtained by fitting the dijet function to different ranges of the m_{JJ} distribution with respect to the nominal range, in each signal region.

8.5.3 Systematics Summary

This section aims to provide a summary of systematic uncertainties. All numbers provided here are *pre-fit* values.

The effect of the different experimental uncertainties on the signal yield is shown on Figure 8.40.

Tables 8.10, 8.11, 8.12, 8.13 show the impact of different sources of systematic uncertainties in percentage on the background and signal processes, for each of the signal regions. A complete summary of all systematics can also be found in Table 8.14. All modeling systematics on the multijet

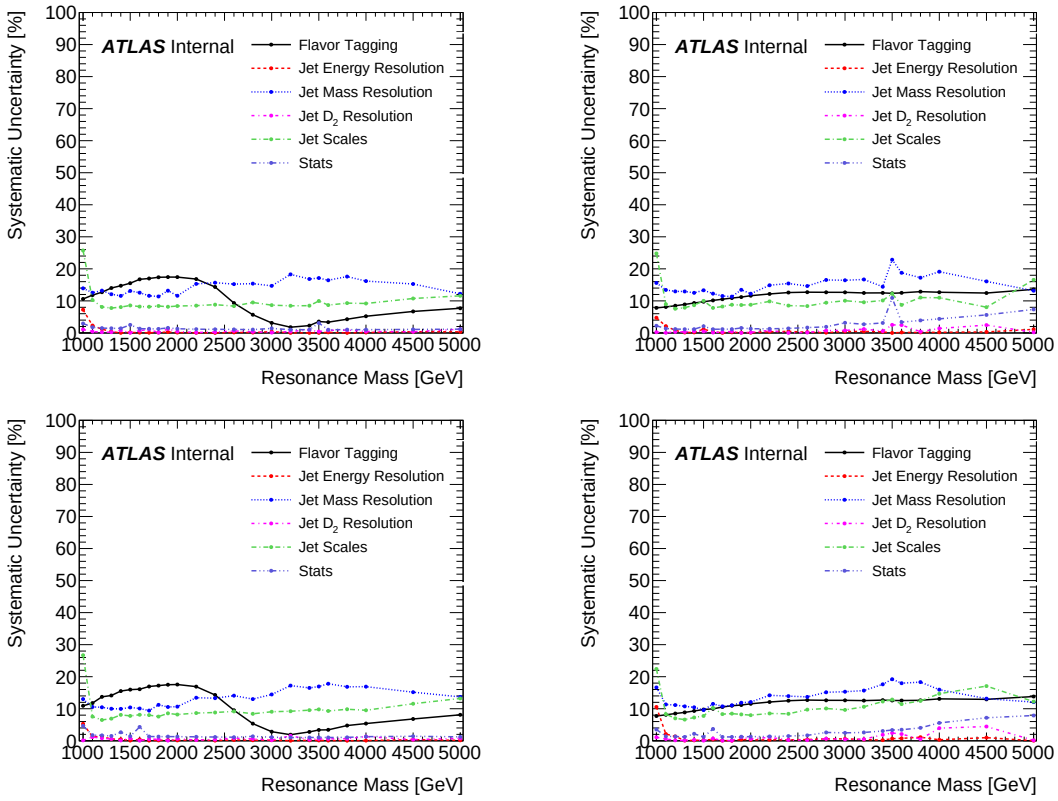


Figure 8.40: Impact of different experimental systematic uncertainties on the signal yields of the (top left) WH 1-tag, (top right) WH 2-tag, (bottom left) ZH 1-tag and (bottom right) ZH 2-tag signal regions, as a function of the resonance mass. Of the up and down variations, the one with the largest impact is plotted.

background are de-correlated between 1-tag and 2-tag regions, whereas all experimental uncertainties are correlated across regions.

Source	Background	Multijet	Other Bkg.	M=1500 GeV	M=2400 GeV
Lumi	0.36	0.69	3.20	3.20	3.20
JetScales	1.37	2.34	13.18	8.58	8.83
JER	0.21	0.37	1.41	0.16	0.00
JMR	0.30	0.98	6.85	13.10	15.68
JD2R	0.00	0.30	3.13	0.06	0.24
FT	0.55	0.82	9.62	15.52	14.35
QCDNorm	4.78	5.23	0.00	0.00	0.00
Ttbar	3.00	5.03	18.62	0.00	0.00
Stats	0.47	0.39	3.61	2.51	1.13
Total	5.87	7.79	26.36	22.42	23.26

Table 8.10: Impact of difference sources of systematic uncertainties in percentage on the background and signal process in 1-tag signal region of WH signal sample.

Source	Background	Multijet	Other Bkg.	M=1500 GeV	M=2400 GeV
Lumi	0.26	0.54	3.20	3.20	3.20
JetScales	2.97	2.84	26.98	10.01	8.53
JER	0.57	0.23	4.78	1.17	0.48
JMR	1.46	0.11	20.65	13.31	15.43
JD2R	0.55	0.16	5.29	0.48	0.01
FT	2.21	4.99	35.25	9.73	12.60
QCDNorm	12.15	13.15	0.00	0.00	0.00
Ttbar	2.49	4.02	16.27	0.00	0.00
Stats	1.33	0.42	16.87	2.08	1.40
Total	13.12	14.92	54.84	19.70	21.96

Table 8.11: Impact of difference sources of systematic uncertainties in percentage on the background and signal process in 2-tag signal region of WH signal sample.

8.6 Results

8.6.1 Statistical Analysis

With smoothed m_{JJ} prediction and data observation in signal region as seen in Figure 8.29, systematic uncertainties as determined in Section 8.5, one is able to perform statistical analysis using the framework as described in [187]. In particular, 1-tag and 2-tag signal regions are combined through a simultaneous binned maximum likelihood fit on the m_{JJ} distribution. Systematic uncertainties are

Source	Background	Multijet	Other Bkg.	M=1500 GeV	M=2400 GeV
Lumi	0.34	0.66	3.20	3.20	3.20
JetScales	1.14	2.26	13.69	7.77	8.82
JER	0.24	0.44	1.93	0.08	0.06
JMR	0.63	0.90	2.33	10.40	13.30
JD2R	0.31	0.32	0.15	0.77	0.38
FT	0.47	0.84	8.71	15.96	14.29
QCDNorm	4.79	5.23	0.00	0.00	0.00
Ttbar	2.91	5.03	20.01	0.00	0.00
Stats	0.47	0.39	3.66	1.41	1.17
Total	5.81	7.75	26.40	20.89	21.70

Table 8.12: Impact of difference sources of systematic uncertainties in percentage on the background and signal process in 1-tag signal region of ZH signal sample.

Source	Background	Multijet	Other Bkg.	M=1500 GeV	M=2400 GeV
Lumi	0.21	0.52	3.20	3.20	3.20
JetScales	2.15	3.07	15.34	7.75	8.42
JER	0.50	0.28	2.87	0.23	0.28
JMR	0.67	0.21	10.19	9.58	13.94
JD2R	0.61	0.11	6.06	0.05	0.23
FT	1.94	5.09	34.73	9.76	12.51
QCDNorm	12.04	13.15	0.00	0.00	0.00
Ttbar	2.23	4.04	17.48	0.00	0.00
Stats	1.35	0.41	15.36	1.20	1.47
Total	12.70	15.00	46.28	16.09	20.84

Table 8.13: Impact of difference sources of systematic uncertainties in percentage on the background and signal process in 2-tag signal region of ZH signal sample.

Source	ZH 2 tag Background	ZH 2 tag HVT *Model A* Z'(2 TeV)	ZH 1 tag Background	ZH 1 tag HVT *Model A* Z'(2 TeV)
Luminosity	0.21	3.20	0.34	3.20
Jet Scales	2.15	7.99	1.14	8.19
JER	0.50	0.28	0.24	0.12
JMR	0.67	12.09	0.63	10.66
JD2R	0.61	0.57	0.31	0.62
b-tagging	1.94	11.53	0.47	17.56
Theoretical	-	-	-	-
Multijet Normalization	12.04	-	4.79	-
$t\bar{t}$ Modeling	2.23	-	2.91	-
Statistical	1.35	1.28	0.47	1.29
Total	12.70	18.85	5.81	22.39

Source	WH 2 tag Background	WH 2 tag HVT *Model A* W'(2 TeV)	WH 1 tag Background	WH 1 tag HVT *Model A* W'(2 TeV)
Luminosity	0.26	3.20	0.36	3.20
Jet Scales	2.97	8.79	1.37	8.40
JER	0.57	0.08	0.21	0.11
JMR	1.46	12.24	0.30	11.60
JD2R	0.55	0.19	0.00	0.45
b-tagging	2.21	11.61	0.55	17.42
Theoretical	-	-	-	-
Multijet Normalization	12.15	-	4.78	-
$t\bar{t}$ Modeling	2.49	-	3.00	-
Statistical	1.33	1.31	0.47	1.30
Total	13.12	19.34	5.87	22.82

Table 8.14: Impact of difference sources of systematic uncertainties in percentage on the background and signal process in all signal regions.

parameterized using either Gaussian or log-norm constraint terms as *priori*. Experimental systematic uncertainties, including luminosity, jet scales, jet resolutions and b-tagging are considered fully correlated between two signal regions. Systematic uncertainties related to the background estimation, including both μ_{Multijet} non-closure and shape uncertainty, are treated as independent between two signal regions. In addition, the two shape uncertainties, one for high-mass region one for low-mass region, are treated as independent as well. Smoothing systematics are naturally independent between 1-tag and 2-tag.

The post-fit m_{JJ} distribution in signal regions can be found in Figure 8.41. Nuisance parameters are allowed to vary within their constraints to maximize the likelihood given the observed data. As a result, the post-fit distribution would be pulled to get closer to the data. The pulling of these nuisance parameters can be found in Figure 8.42 (Figure 8.43) for mass point of 2 TeV (3 TeV) as a cross check. As one can see, all nuisance parameters are well constrained within 1σ, indicating no strong bias from the fitting procedure itself.

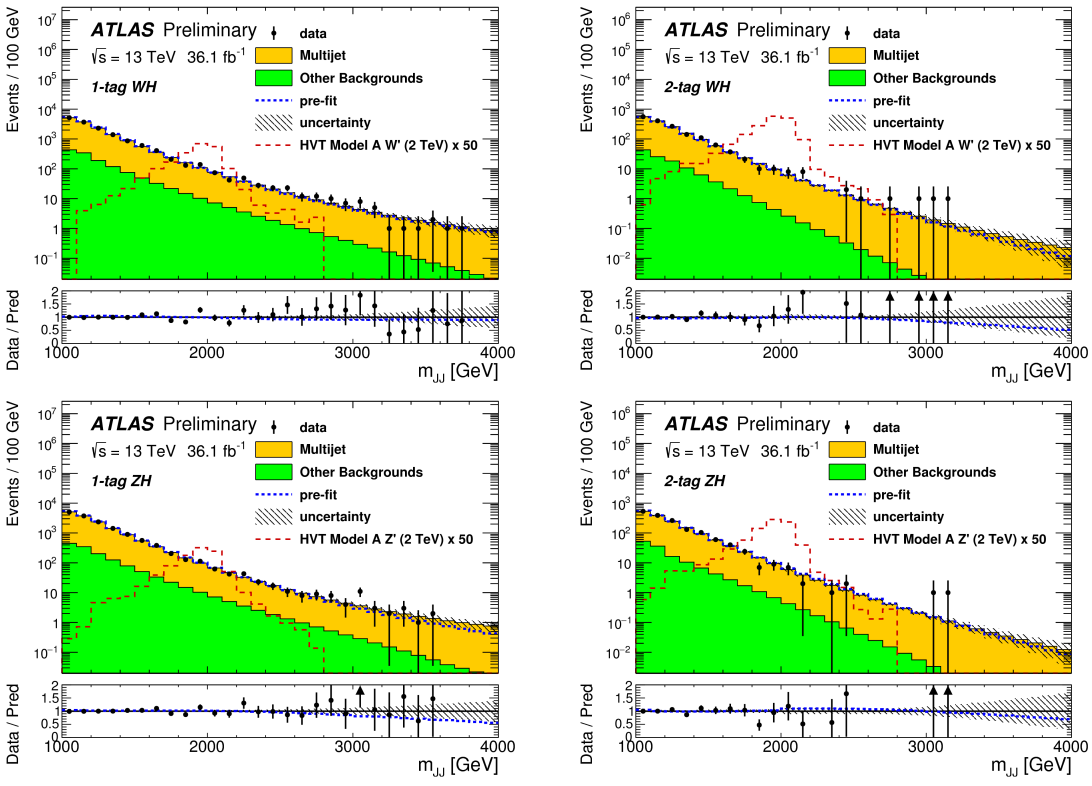


Figure 8.41: Post-fit m_{JJ} distribution in WH (top) and ZH (bottom) signal regions for 1-tag (left) and 2-tag (right) respectively. [199]

The impact of main systematic uncertainties on postfit event yields can be found in Table 8.15.

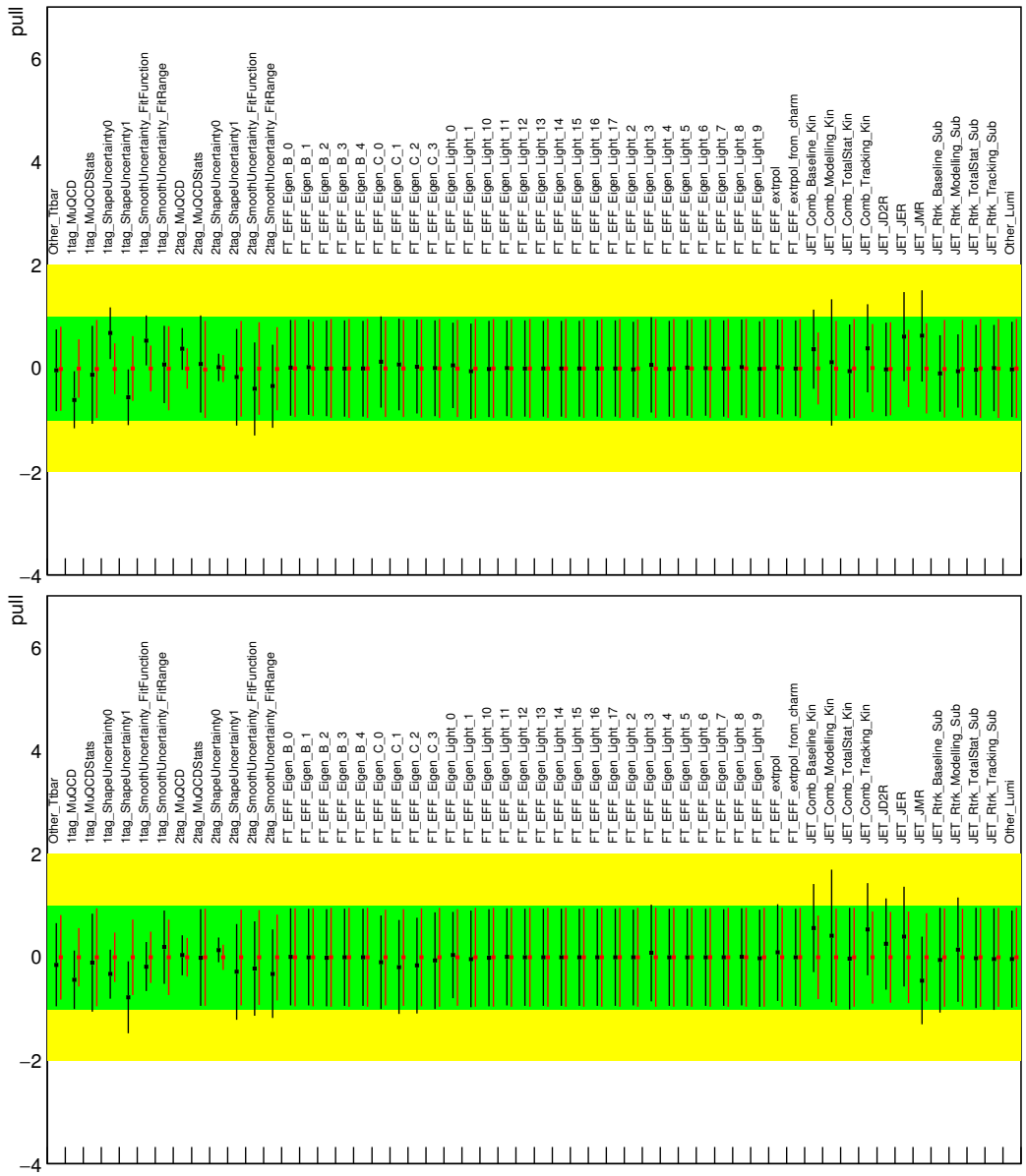


Figure 8.42: Pulls and constrains on nuisance parameters in the combined fit to the full dataset, in the 2 TeV mass point, shown for the WH (top) and ZH (bottom) channels, comparing observed (black) with the Asimov dataset (red).

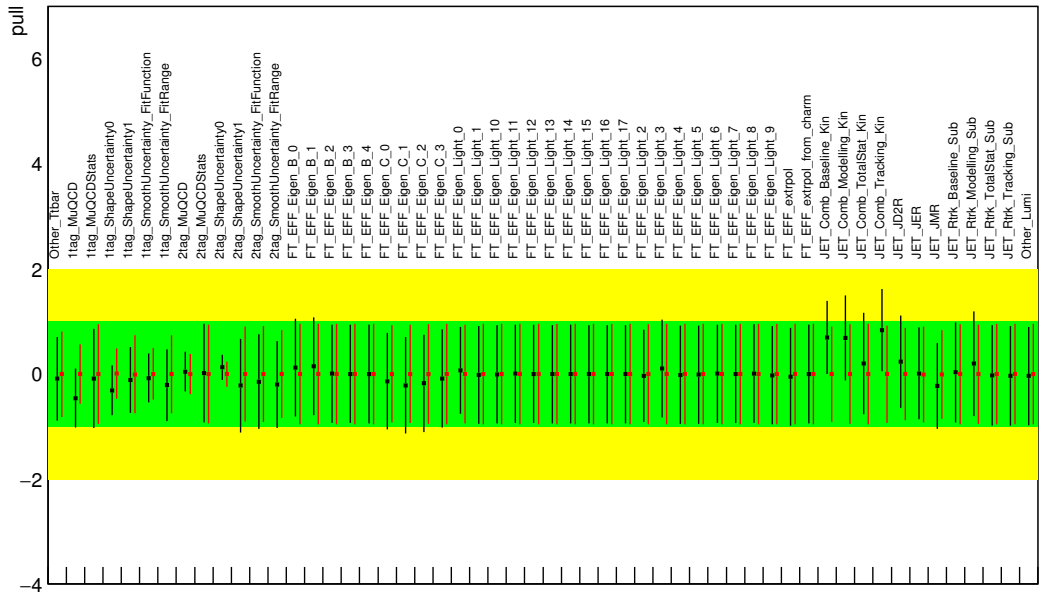


Figure 8.43: Pulls and constrains on nuisance parameters in the combined fit to the full dataset, in the 3 TeV mass point, shown for the WH channels, comparing observed (black) with the Asimov dataset (red).

Different from the prefit version as shown in Table 8.14, this is obtained by varying nuisance parameter around the *postfit* value according to its error bar which is also determined duing the likelihood fit. As a result, the postfit systematic uncertainties are smaller than prefit version. Another way to check the postfit systematic uncertainty is the ranking of nuisance parameter in terms of its impact on signal strength by re-fitting all nuiance parameters but the one being tested. This is shown in Figure 8.44 (Figure 8.45) for 2 TeV (3 TeV) signal mass point. This can reflect importance of both normalization and shape uncertainties.

The *postfit* yields in signal regions can be found in Figure 8.46. Due to the likelihood fit, total data and background yields in each region are constrained to agree. This suggests the data and background is consistent in terms of normalization within the uncertainties that we assigned.

However, for such kind of narrow width resonance searches, shape is more important than normalization. Furthermore, it is important to check if there is any disagreement in terms of shape even after nuisance parameters that could affect m_{JJ} spectrum shape are pull toward the data, in which case would indicate either a local excess beyond our understanding of background estimation, or some frustrating mis-modeling effect. From Figure 8.41 a small excess can be found around 3 TeV. Therefore, a local p-value scan (significance test) is performed as shown in Figure 8.47, and further broken down to the individual 1-tag and 2-tag regions as shown in Figure 8.48. The largest excess is found at 3 TeV in the ZH channel, with a local significance of approximately 3.3 σ and a

Source	ZH 2 tag yield variation [%] Background	HVT *Model A* Z'(2 TeV)	ZH 1 tag yield variation [%] Background	HVT *Model A* Z'(2 TeV)
Luminosity	0.2	3.2	0.3	3.2
JES	2.0	7.0	1.1	7.3
JMR	0.6	9.5	0.4	8.5
b-tagging	1.6	10	0.5	15
$t\bar{t}$ Normalization	1.8	-	2.5	-
Multijet Normalization	4.7	-	2.8	-

Source	WH 2 tag yield variation [%] Background	HVT *Model A* W'(2 TeV)	WH 1 tag yield variation [%] Background	HVT *Model A* W'(2 TeV)
Luminosity	0.2	3.2	0.3	3.2
JES	2.4	5.7	0.8	5.6
JMR	0.4	8.6	0.4	8.0
b-tagging	1.7	11	0.4	15
$t\bar{t}$ Normalization	1.9	-	2.5	-
Multijet Normalization	4.3	-	2.8	-

Table 8.15: Summary of systematic uncertainties (expressed in percentage yield) in the background and signal event yields in the 1-tag and 2-tag signal regions. The values for the JES and b-tagging efficiency uncertainties represent the sum in quadrature of the values from the dominant components. The JES, JMR, b-tagging efficiency, luminosity and MC statistics uncertainties do not apply to the multijet contribution, which is determined from data. Uncertainties are provided for a resonance mass of 2 TeV in the context of the HVT *Model A*, for both $V' \to WH$ and $V' \to ZH$ resonances. [199]

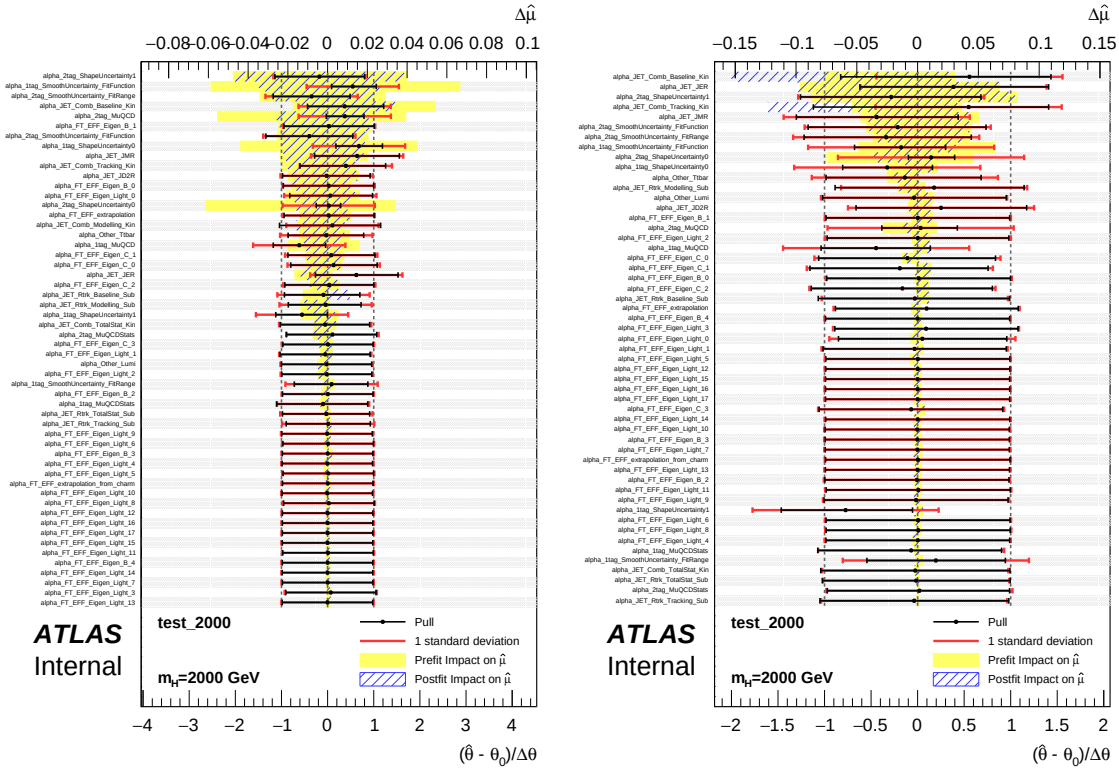


Figure 8.44: Ranking of nuisance parameters in terms of post-fit impact on $\hat{\mu}$ for the WH (left) and ZH (right) channels, for the 2 TeV S+B fit. The best-fit μ and associated statistical uncertainties are (left) $\mu = 0.145033 + 0.188445/ - 0.171449$ (stat.) and (right) $\mu = -0.143086 + 0.287485/ - 0.237264$ (stat.).

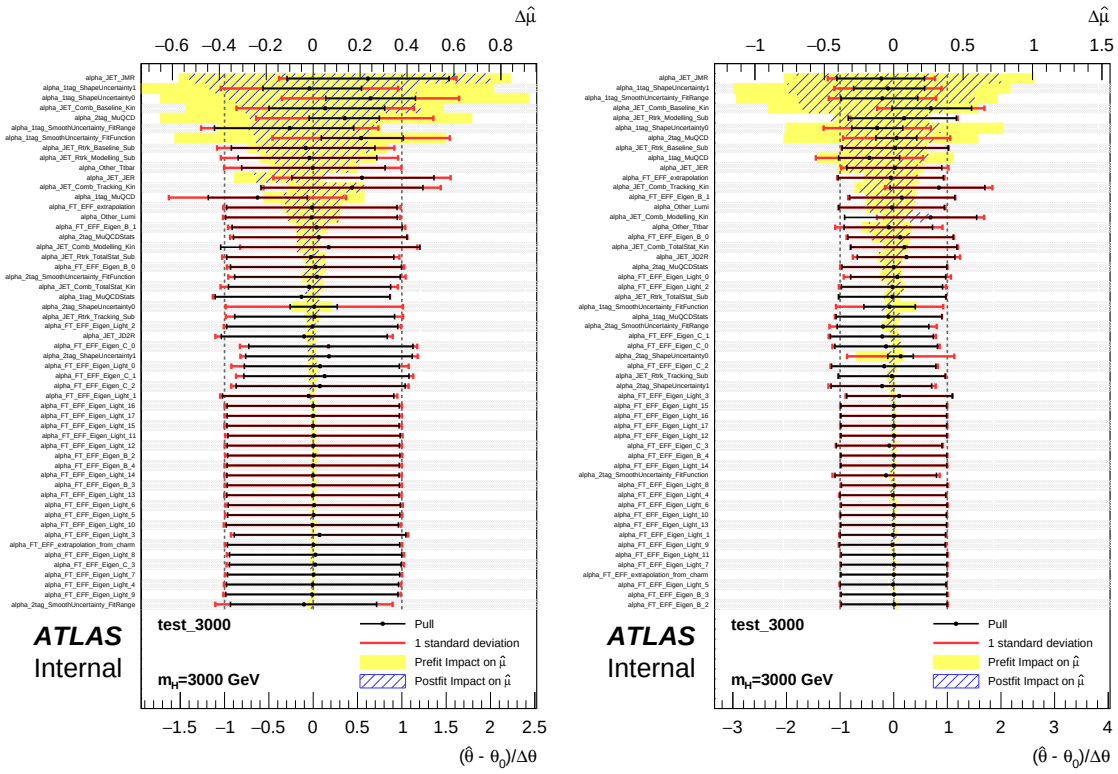


Figure 8.45: Ranking of nuisance parameters in terms of post-fit impact on $\hat{\mu}$ for the WH (left) and ZH (right) channels, for the 3 TeV S+B fit. The best-fit μ and associated statistical uncertainties are (left) $\mu = 3.77929 + 1.41278/-1.25674$ (stat.) and (right) $\mu = 6.89471 + 2.54038/-2.22707$ (stat.).

	ZH 2-tag	ZH 1-tag
Multijet	1440 $\pm$ 60	13770 $\pm$ 310
Other Backgrounds	135 $\pm$ 45	1350 $\pm$ 270
Total Backgrounds	1575 $\pm$ 40	15120 $\pm$ 130
Data	1574	15112
Model B, M=2 TeV	25 $\pm$ 7	29 $\pm$ 10
	WH 2-tag	WH 1-tag
Multijet	1525 $\pm$ 65	13900 $\pm$ 290
Other Backgrounds	110 $\pm$ 45	1310 $\pm$ 260
Total Backgrounds	1635 $\pm$ 40	15220 $\pm$ 120
Data	1646	15212
Model B, M=2 TeV	51 $\pm$ 10	62 $\pm$ 16

Figure 8.46: The number of predicted background events in the VH 1-tag and 2-tag signal regions after the fit, compared to the data. The "Other Backgrounds" entries include both $t\bar{t}$ and V+jets. Uncertainties correspond to the total uncertainties in the predicted event yields, and are smaller for the total than for the individual contributions because the latter are anti-correlated. The yields for m =2 TeV V' bosons decaying to VH in *Model A* are also given. Due to rounding the totals can differ from the sums of components. [199]

global significance of 2.2 σ.

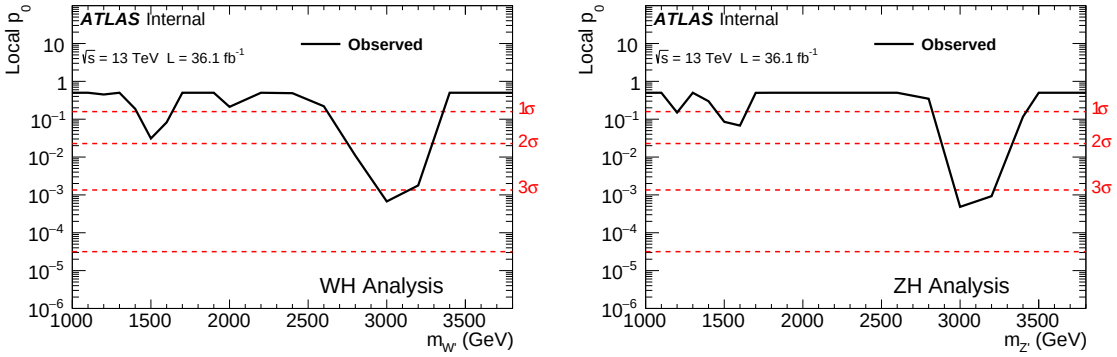


Figure 8.47: Observed p_0 values shown for the WH (left) and ZH (right) channels.

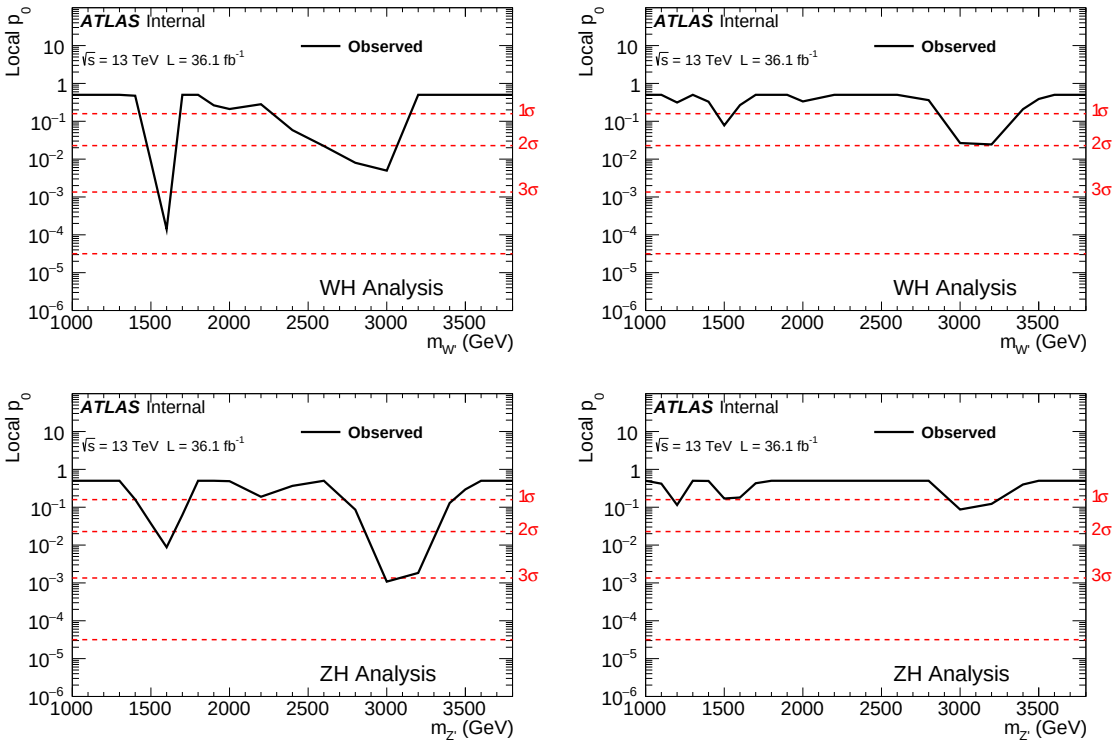


Figure 8.48: Observed p_0 values shown for the (top left) WH 1-tag, (top right) WH 2-tag, (bottom left) ZH 1-tag and (bottom right) ZH 2-tag regions.

In the absence of significant excess, an exclusion limit on the cross section times branching ratio

are derived, as shown in Figure 8.49, with a value of μ regarded as excluded at the 95% confidence level.

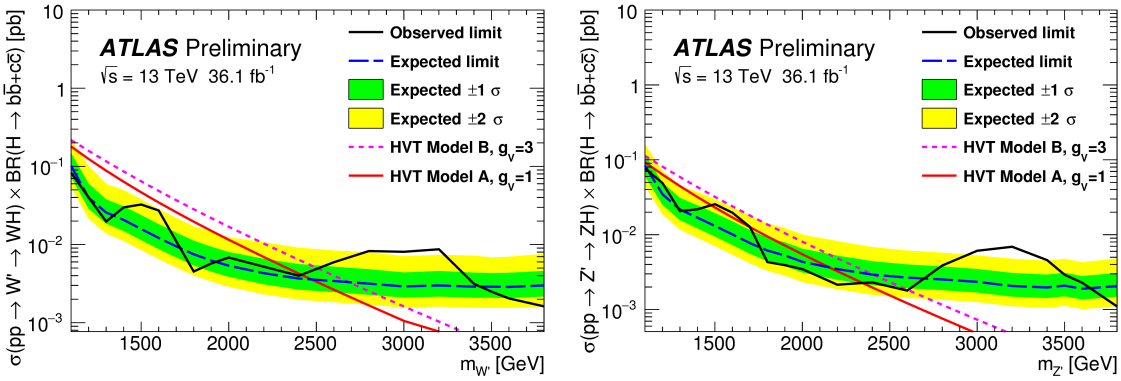


Figure 8.49: The observed and expected cross-section upper limits at the 95% confidence level for $pp \to V' \to VH \to q\bar{q}'(b\bar{b} + c\bar{c})$ in *Model A* and *Model B* in the (left) ZH and (right) WH signal regions. The red and magenta curves show the predicted cross-sections as a function of resonance mass for the models considered. [199]

8.6.2 Conclusion

A search for resonances decaying to a W or Z boson and a Higgs boson has been carried out in the $q\bar{q}^{(\prime)}b\bar{b}$ channel with 36.1 fb^{-1} of pp collision data collected by ATLAS during the 2015 and 2016 runs of the LHC at $\sqrt{s} = 13$ TeV. Both the vector boson and Higgs boson candidates are reconstructed using large radius jets. Jet mass and substructure observables are used to tag W, Z and Higgs boson candidates and suppress the dominant multijet background. In addition, small radius b-tagged track jets ghost-associated to the large-R jets are exploited to select the Higgs boson candidate jet. The data are in agreement with the Standard Model expectations, with the largest excess observed at $m_{\mathrm{JJ}} \sim 3.0$ TeV with a local significance of 3.3 σ. The global significance of this excess is 2.2 σ. Upper limits on the production cross-section times branching ratio to the $q\bar{q}^{(\prime)}b\bar{b}$ final state are set for resonance masses in the range between 1.1 and 3.8 TeV with values ranging from 83 fb to 1.6 fb and 77 fb to 1.1 fb (at 95% CL) for WH and ZH resonances, respectively. The corresponding excluded Heavy Vector Triplet *Model B* signal mass ranges are 1.10 - 2.50 TeV for WH resonances, and 1.10 - 2.60 TeV for ZH resonances.

Chapter 9

Summaries and Future Prospects

In both searches as presented in this thesis, no significant deviation from background estimation has been found yet. Therefore, exclusion limits on the heavy resonance production cross-section times branching ratios are imposed as function of resonance masses. The search sensitivities are significantly improved in two aspects: 1) Much more stringent exclusion limits for resonances being explored by previous searches; 2) Either open new search channel or extend the reach of existing searches.

For the search of heavy resonance decaying to pair of Higgs bosons, our $b\bar{b}b\bar{b}$ channel turns out to the most sensitive one across all different final states so far [212]. Nevertheless, we are still not able to exclude any resonance of mass above 1 TeV yet. While this is mainly due to the lack of data accumulated so far, several further optimization can be considered in the analysis: A kinematics-dependent cut can be imposed instead of fixed cut as it is now might help improve sensitivity at the low mass end; 0-tag signal region can be considered to extend sensitivity for masses above 3 TeV, although this may require some re-thinking of background estimation strategy; When enough data gets accumulated at some point in the future, a revisit of background estimation strategy using direct fit method can be considered since that may reduce systematic uncertainties on background modeling; We did not really explore the option of jet substructure variable in this analysis since studies showed that any simple cut on jet substructure variable would hurt sensitivity. However, a more complicated approach, such as categorization of "high-purity" and "low-purity" region based on jet substructure variable might bring some additional improvement.

For the search of heavy resonance decaying to a Higgs boson associated with W/Z boson, we open a new sensitive channel that was not explored in ATLAS before. A local significance of 3σ is observed at about 3 TeV, although this is not confirmed by the CMS [213]. A low hanging fruit for immediate future is the combination of our all-hadronic final state with the existing (semi-)leptonic VH searches effort in ATLAS, which should lead to a significant gain in sensitivity due to similar sensitivities across all channels. However, even on the $qqbb$ channel itself, large improvement on sensitivity is

expected by a more sophisticated search strategy, since the analysis so far is more or less a direct application of the W/Z tagging and $h \to b\bar{b}$ tagging: A dedicated discrimination between W/Z boson can not only improve sensitivity for low resonance mass, but also allow a statistical combination of WH and ZH searches which is not possible in the existing strategy. Such combination can bring more stringent exclusion limits on both the VH cross-section and HVT parameter spaces; Dedicated categorization into "high-purity" and "low-purity" based on jet substructure variable can bring improvement on sensitivity in general since S/B could be drastically different in these two categorizations; Mass window cut on W/Z and Higgs boson can be further optimized. Besides a re-optimization on each object independently, one can also consider a χ^2-like cut on the 2D mass plane, similar to the HH search; Optimization on b-tagging is also possible by using "asymmetric categorization", where different b-tagging working point can be used for different track jets.

Besides direct optimization on search strategy as discussed above, more fundamental impacts can be made by development of b-tagging in extremely boosted environments. It is well-known that b-tagging efficiency drops dramatically in very high-p_{T} region. This comes from various aspects: 1) b-hadrons of such high p_{T} might not decay until passing through the first or first few layers of pixel detector. In this case, missing hits are expected for first few pixel layers, which might be treated as pattern of poor quality in the existing tracking algorithm and b-tagging pattern recognition algorithm. Therefore, some low-level studies on both tracking and b-tagging is needed to address this issue appropriately; 2) For the purpose of double b-tagging, a fixed small radius track jet would break down in such boosted region since all decay products from double b-hadrons would be merged together. Dedicated algorithm development is therefore needed to resolved extremely closeby b-hadrons. There has already been efforts on this in ATLAS under the context of both $g \to b\bar{b}$ and $h \to b\bar{b}$. For $g \to b\bar{b}$, details can be found in Appendix B. For $h \to b\bar{b}$, details can be found in [214], a PUB note about to be released very soon; 3) Even for the more generic single b-tagging, performance would degrade in very high-p_{T}, due to worse tracking resolution (impact parameter, p_{T}, etc.). While efforts can be made on the tracking side, one could also try to make b-tagging more robust against degradation of tracking performance.

Jet substructure is another key variables in our analysis, which unfortunately also experiences degradation in extremely high p_{T}. This mainly comes from the merging of incoming particles into single calorimeter clusters. One way to address this is the use of tracks of very high granularity. As a matter of fact, the track-assisted mass is already used in ATLAS for large-R jet mass reconstruction, while the track-assisted substructure variables are ongoing. This is related, if not fully overlapped, with the concept of "particle flow" as developed in both ATLAS and CMS. Another way to tackle this is the splitting of calorimeter clusters, similar to the neural network splitting as applied on pixel cluster. However, situation is more complicated for calorimeter since calorimeter cluster is a 3D object instead of 2D in the case of pixel cluster. Furthermore, calorimeter granularity varies on the layers, making this more complicated. Image recognition techniques, especially those developed

in the realm of *deep learning* from computer science domain, can potentially be adapted for this problem.

The quest of new physics should never end. Exactly during the period when this thesis is being written, first stable beam from LHC with proton-proton collision at 13 TeV in 2017 is observed, signaling the start of data taking in 2017. With the excellent performance of both LHC and detectors, much more abundant physics results are expected in next few years, not to mention the upgrades following that. While there are always many uncertainties and doubts over whether we would ever discover anything beyond the Standard Model on LHC, I would like to encourage all of us with a phrase that we always use in presentations: *STAY TUNED*!

All human wisdom is contained in these two words – "Wait and Hope."

— Alexandre Dumas, *The Count of Monte Cristo*

Appendix A

Improved Simulation of Particles Interacting with Pixel Detectors

A.1 Introduction

Although events can be simulated from Monte Carlo following the theoretical calculations, they cannot be compared with experimental data before a realistic simulation of the response of generated particles with ATLAS detector. The key of this detector simulation, using Geant4 [171, 170] (G4), is a good understanding of the physics principle on how particles interact with materials: This does not only include the collision process between particles and atoms in materials, but also the process of charge being collected by diodes which is directly related on how electronic signals are formed. In ATLAS terminology, the first part is usually called *detector simulation* or simple *simulation*, while the second part is called *digitization*.

While the whole simulation chain is common for all particles and sub-system of the detector, the concrete implementation could be totally different depending on the technology being used behind the scene. In this appendix, we will focus on the simulation of pixel detectors, in particular, an improvement over the existing simulation.

The whole pipeline of pixel simulation (including digitization part) is illustrated in Figure A.1. When particle passes through a pixel layer, the G4 would determine its entry point and exit point which defines the path inside pixel layer – one should notice that the G4 is not aware of the pixel grids on that layer at all at this moment. Then it will sample the amount of energy being deposited in this layer due to interaction with silicon materials. While the total amount of deposited energy for ATLAS pixel detector can be determined from some underlying distribution that has been well tested against test beam data, it does not really tell us how these charges distribute along the path transversing the pixel layer. Therefore, certain assumption needs to be made to determine that.

Once the distribution of deposited charges along path is determined, they will be drifted to the surface of pixel layer due to the external electric field and magnetic field. Besides, the drift process can also be affected by many other random effects such as thermal diffusion and trapping effect from irradiation. After charges are drifted to the surface, the layout of pixel sensors would be taken into account so that one could determine if a pixel is fired or not based on time-over-threshold (ToT).

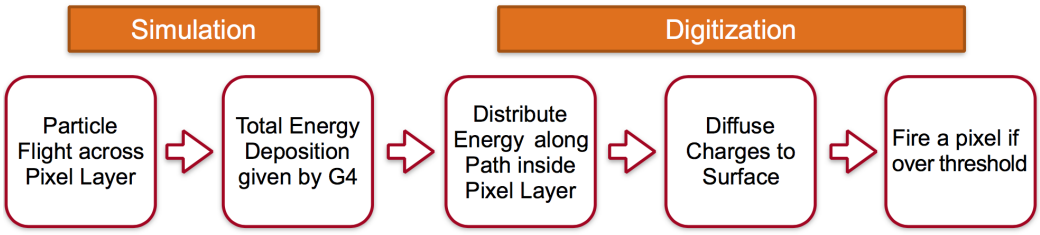


Figure A.1: Pipeline of pixel detector simulation and digitization chain

In this appendix, we would focus on how charge should be distributed along the path inside pixel layer. In the ATLAS simulation previous to this work, a uniform assumption has been made that charges are equally divided into tens of pieces and then distributed along the path. While this is a good guess to the leading order, it fails to describe the local fluctuation along path, which turns out to be larger than originally thought. Furthermore, as will be shown in this appendix, such local fluctuation can directly affect the charge distribution inside a pixel cluster, to which the determination of pixel cluster centroid is susceptible. As a result, it has essential influence on the tracking performance (in particular the residual performance) which is the inputs for many other physics objects. Therefore, a more realistic model, called *Bichsel Model* is adopted to describe local charge fluctuation inside pixel layer and its consequence on the ATLAS reconstruction performance is studied. The model has now replaced the old one since ATLAS offline software release 21, and used for MC16 campaign, which is the sample to be used for most physics analysis in ATLAS since 2017.

Due to the limit of pages, we are unable to present all details of the studies. Readers with interest can find complete records of the ATLAS internal presentations in [215, 216, 217, 218, 219, 220, 221, 222, 223, 224, 225, 226, 227].

A.2 The Bichsel Model

Since the current setup for Geant4 would only generate a single total deposited energy for a given entry and exit point (G4 *hit* object), there is no way to reconstruct the charge distribution along path with exiting information. One way to get around this would be chopping the pixel layer into many sub-layers, and re-doing the simulation for each sub-layer. Apparently, the finer we do segmentation, the better we are able to restore local charge fluctuation.

However, there are two potential issues for this approach, one being practical while another being more fundamental. The practical issue is that existing ATLAS reconstruction software architecture (Athena) does not allow re-simulation with G4 for each sub-layer in an easy way. If one wants to follow the "chopping down" procedure for a given G4 *hit*, there is no interface to load G4 program since this is already in the digitization step with G4 *HIT* file as input. The alternative is to reverse the order and do the chopping at the very beginning so that one can apply the G4 simulation on each sub-layer before G4 *HIT* file is generated. However, this requires some low-level changes either on the ATLAS G4 configuration, or even the G4 itself[1]. The second reason is much more fundamental. Roughly speaking, the deposited energy as returned by G4 simulation is sampled from a Landau-like distribution (e.g. Landau convoluted with Gaussian), with mean value determined by the dE/dx curve following Bethe equation [228, 229]. While this approach is valid for thick silicon sensors, it would break down when we turns to very thin sensors [230], which is our case for sub-layers here. Since we would like to capture the local charge fluctuation as precise as possible, one would inevitably run into such limit where the traditional "dEdx-Landau" model starts to fail.

Fortunately, this effect has already been discussed in great details in [230], where it calculates single particle-atom collision cross-section from basic atomic physics, as shown in Figure A.2. As one can see, the spectrum for energy loss at single collision level is highly discrete due to the underlying atomic shell structure. For silicon material, there are on average about four collisions per micro-meter and most of them are very low energy, corresponding to the first peak in differential spectrum ($\sim 17\ eV$). Occasionally, there is large energy loss corresponding to secondary, third or even higher energy peak (or simply the tail of distribution). It is these sporadic high energy loss that defines the local fluctuation, as well as the total energy loss, when particle is transpassing the silicon layer of certain thickness.

The total energy loss for silicon layer of any thickness can be obtained by convolution over energy loss spectrum of thinner layers in an iterative way, or simply addition over all single collisions [2] [3]. The folded energy loss spectrum per unit length can be found in Figure A.2. There are several important implications for this: 1) For very thin silicon layer at the order of O(1) micro-meter, the discrete effect from atomic shell structure is still significant, making the energy loss spectrum completely different from a smoothed Landau-like distribution; 2) For silicon layer at order of O(10) micro-meter, the exact shape of energy loss spectrum is better described from Bichsel Model than other models; 3) The concept of dE/dx itself is not quite scalable for thin silicon layers as the name suggests, since it might change drastically for different thickness.

[1] We decided not to follow this approach since it was unclear if these can be done in short terms. However, this would be probably the optimal approach since it can save many overheads from "re-simulation"

[2] The convolution method is used in the original paper in 1980s when the computing is not so powerful. Nowadays, straightforward addition is super fast even on personal laptops.

[3] The energy loss spectrum for single particle can be generated using Fortran codes in `http://www.slac.stanford.edu/~sudong/silicon/`, developed by Hans Bichsel and kindly distributed by Su Dong

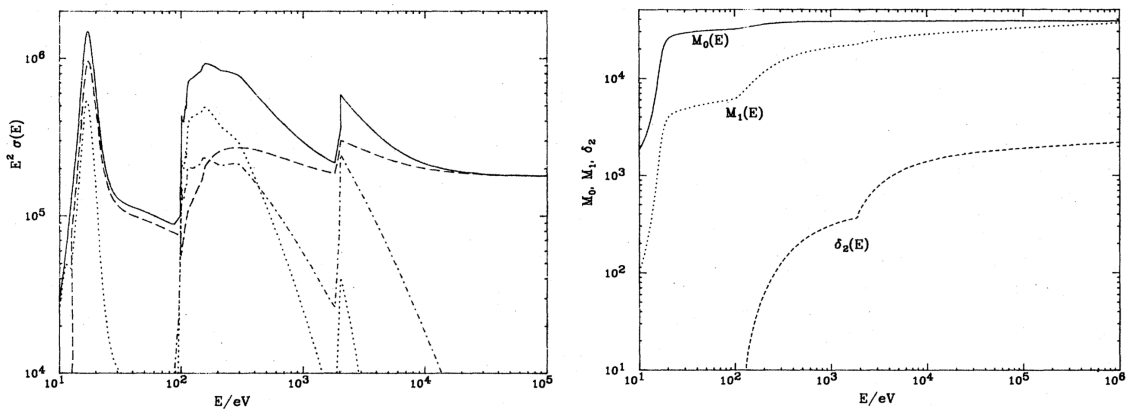


Figure A.2: Differential (left) and Integrated (right) cross section as function of energy loss for single collision between 45 GeV pion and silicon material. The differential cross section is expressed in the form of $E^2\sigma(E)$, while the integrated cross section is expressed in the form of moments defined as $M_v = N_a \int_0^\infty E^v \sigma(E) dE$. [230]

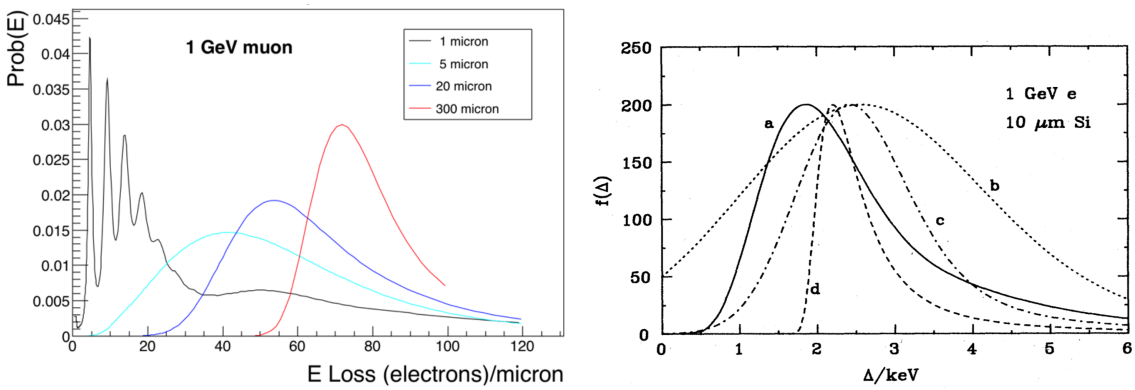


Figure A.3: (Left) Total energy loss per micro-meter for muon of 1 GeV transpassing silicon layers of different thickness, convoluted from single collisions cross-section [231]; (Right) Total lenergy loss spectrum for 1 GeV passing through a silicon detector of thickness 10 μm as calcualted under different models. Curve a is the one from Bichsel Model; Curves b,c and d are from Shulek function [230]

A.3 Implementations

Since the underlying energy loss spectrum could be very different depending on thickness, we decide to follow a "bottom-up" strategy in ATLAS implementation, that every single particle-atom collision is re-simulated along the particle flight path inside silicon layer based on the calculated cross-section. In this way, one does not need to figure which underlying spectrum model to be used based on the thickness. More importantly, the local fluctuation along path can be automatically captured in this process, which is the main goal of this work.

As discussed in Section A.2, it is impractical to implement the Bichsel Model in the simulation step before G4 *HIT* file is generated in short terms. Therefore, we decide to put this module in the *digitization* part, where the G4 *HIT* file serves as input file.

The implementation of this re-simulation procedure is essentially a MC sampling of two different physics process: the single collision energy deposition and free flight length before next collision. After each collision, we would sample the free flight length of incoming particle before next collision, assuming an exponential distribution with mean value being the mean-free path. At the same time, one would sample the amount of energy being deposited in next collision from the single collision cross-section as calculated in Bichsel Model. In particular, the cross-section table is prepared in the integrated form as shown in the right plot of Figure A.2. In this way, one simply needs to repeatedly generate random numbers between 0 and maximal integrated cross-section uniformly (the y-axis) in order to get sampled collision energies by finding corresponding value on x-axis through function inversion. Since the spectrum also depends on the beta-gamma of incoming particle, cross-section table contains three columns for beta-gamma, collision energy loss and the integrated cross-section respectively. Every row in the table corresponds to a point on the curve shown on right plot of Figure A.2 for the given beta-gamma. As a result, two interpolations are needed here, one for finding appropriate beta-gamma and one for determining collision energy during function inversion. Furthermore, one such table is prepared for each type of incoming particles. For now, only five types of particles are available: proton, pion, electron, kaon and muon. While this should cover most physics cases, incoming particles beyond these categories cannot be processed using Bichsel Model, and thus would be processed with uniform model as before.

One important implementation detail is the treatment of δ-ray. δ-ray refers to the cases when collision energy being transferred is so large that the kicked electrons can be essentially treated as a separate incoming particles. In the input G4 *HIT* file, these δ-ray has already been generated as a standalone *hit* object. Therefore a cut-off on the sampled collision energy is imposed to avoid double counting of the δ-ray: if the sampling for one collision generates collision energy higher than the cut-off, it would be simply set to 0 since that collision already exists in G4 *HIT* file. However, it is important to make sure the choice of cut-off is consistent with the configuration used in G4 simulation step. There is another thing special for the δ-ray. Since MC truth particle link does not exist for these δ-ray *hit* as other particles created from hard proton-proton interactions, one is

unable to obtain the beta-gamma of incoming particle, which is necessary for Bichsel Model. As a result, G4 *hit* from δ-ray would also be processed with uniform model as before.

A sketch of the workflow of Bichsel Model implementation in ATLAS can be found in Figure A.4.

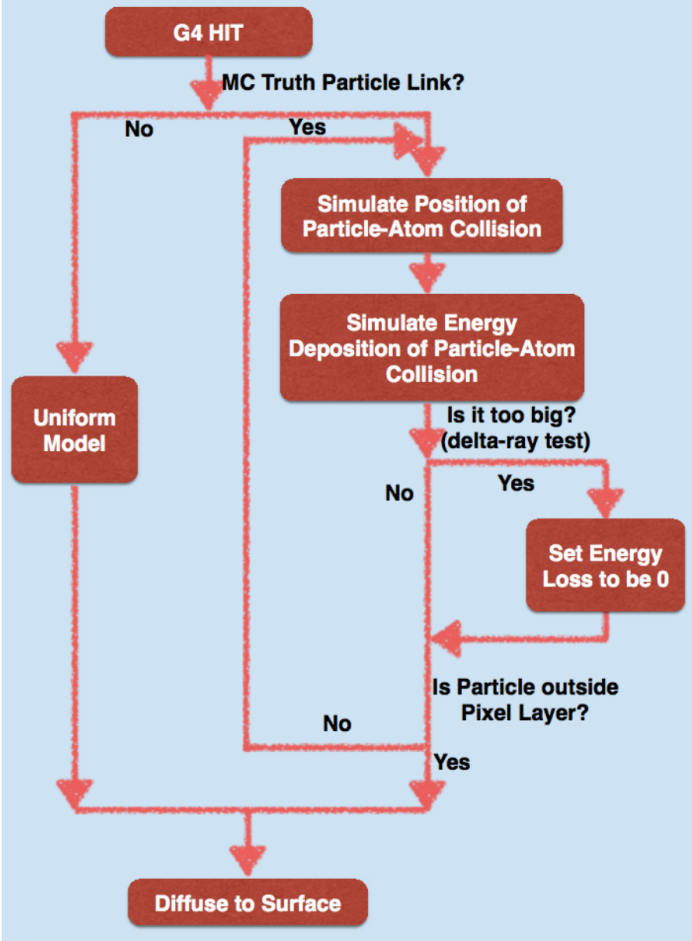


Figure A.4: Sketch of implementation workflow of the Bichsel Model in ATLAS

After all collision points are generated, ionized charges at each collision point would be drifted to the diodes as usual. Since we are having a very dense distribution of collision points, ionized charges are clustered into smaller number of groups before being drifted, in order to save computing time.

For a typical ATLAS pixel layer, the thickness is at the order of O(200) μm. This is no longer in the realm of "very thin layer" and therefore the existing G4 simulation can already describe total energy deposition very well. Since we are essentially re-simulating the energy deposition for every G4 *hit*, a closure test is needed for our simulation from Bichsel model, which is shown in Figure A.5. The total energy deposited by Bichsel Model and by original G4 simulation is consistent with each other across all different type of particles being considered and for beta-gamma larger than 0.5

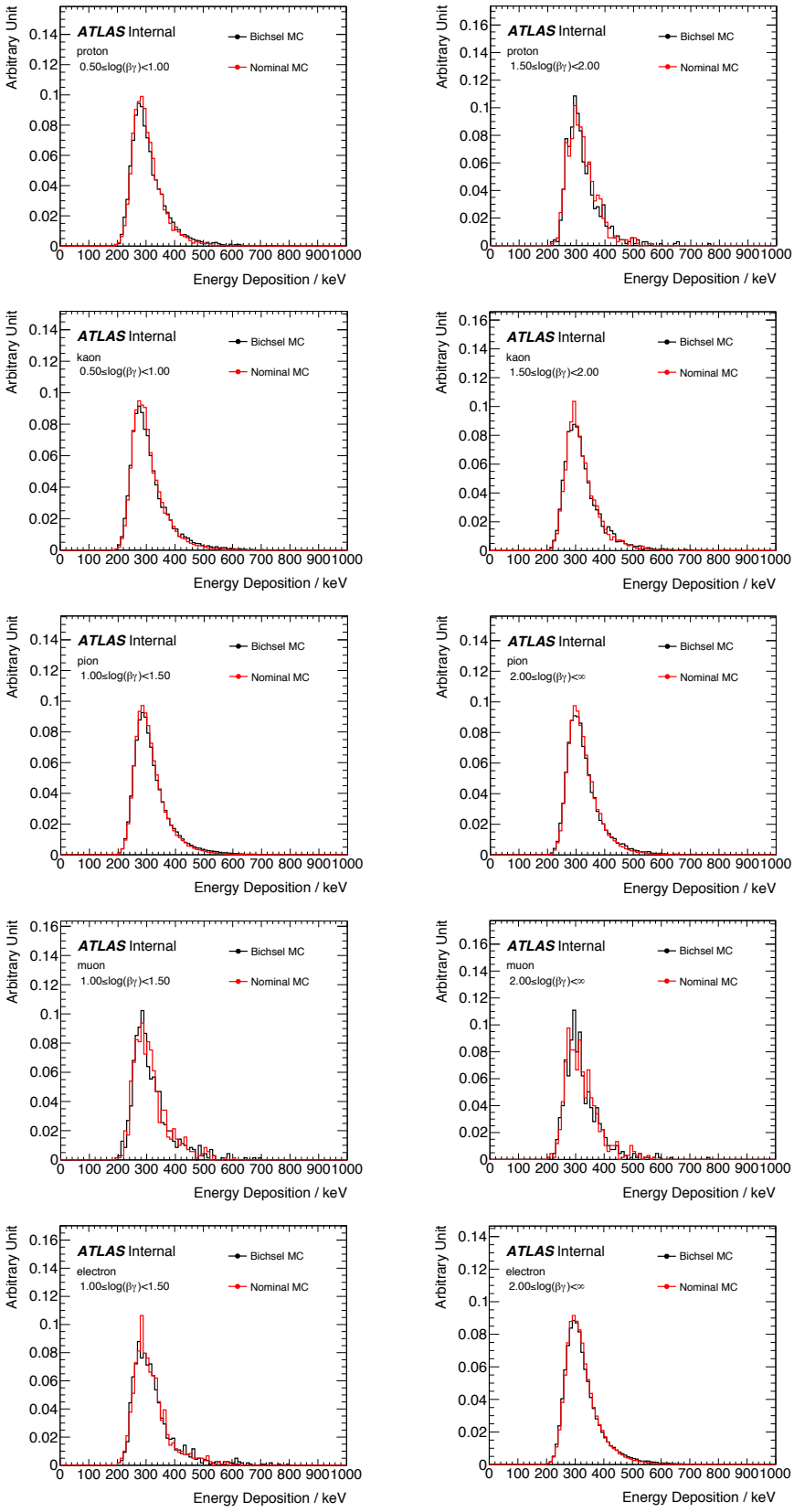


Figure A.5: Normalized distribution of deposited energy for different type of incoming particles of different selected beta-gamma ranges. From top to bottom it corresponds to proton, kaon, pion, muon and electron

($\log(\beta\gamma) > -0.3$). There are subtle differences though at the tail of distributions in general and it would be interesting to study reasons behind it as future studies. The effect of using Bichsel Model on local charge fluctuation is evident, as shown on right plot of Figure A.6. Instead of a fixed value of 5% and 10% as predicted by uniform model, Bichsel model shows a non-trivial distribution with peak located at slightly higher value than prediction from uniform model as well as a long tail toward high fractions. This suggests that Bichsel Model is essentially re-distributing the ionized charges with much more local fluctuation than the uniform model, despite of similar total energy deposition.

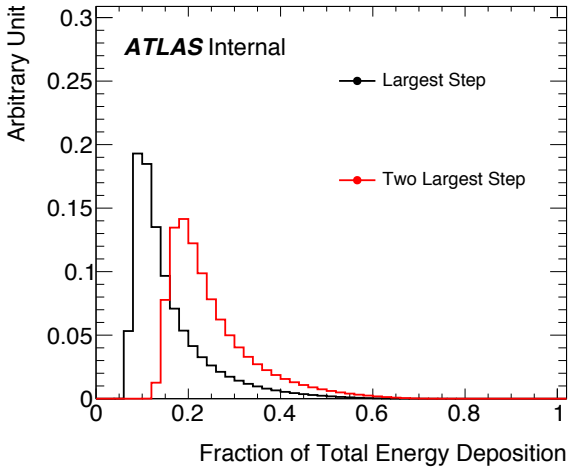


Figure A.6: Fraction of total energy deposited in the pixel layer. The flight path in pixel layer is divided into 20 segments evenly and sorted by the amount of energy deposited in each of them. Black curve corresponds to the fraction of deposited energy in first segment over total deposited energy and red curve corresponds to the fraction of deposited energy in first two segments over total deposited energy.

A.4 Effect on ATLAS Reconstruction Performance

A.4.1 Setup

To validate the Bichsel Model, the best way would be comparing our simulation with experiment data. While the most straightforward approach would be a test beam with very thin silicon layers, one can still do the validation using massive dataset produced by LHC proton-proton collisions. In particular, as we will see later, by checking observables in pixel cluster level and tracking level that are sensitive to the local charge fluctuation effect, one can determine whether Bichsel Model or uniform model is able to better describe the data.

The first thing to do is establishing a good event selection for comparison studies. $Z \to \mu\mu$ events are typically used for inner detector studies purpose since it is much "cleaner" with respect

to the dominant hadronic activities in LHC: The kinematics from $Z \to \mu\mu$ process is well modeled in the MC; It can provides unambiguously clear signature of a single muon through muon detector so that one is comparing apple to apple between data and MC; Lastly, the kinematics of muon from $Z \to \mu\mu$ decay is typically of tens of GeV, hence avoids many complications for low-p_{T} tracks such as multiple scattering etc.

The event selection for $Z \to \mu\mu$ candidates are summarized below:

- Basic event cleaning, including detector failure flag check and requiring at least two tracks from primary vertex
- Good-run list
- Trigger: `OR` between `HLT_mu20_iloose_L1MU15` and `HLT_mu50`
- Standard jet cleaning
- Selection on muon, including 1) $p_{\mathrm{T}} > 25$ GeV, $|\eta| < 2.4$; 2) Pass at lease *loose* quality cut; 3) Pass muon identification
- At least two muons survived in the event after cuts above
- Leading two muons should be in opposite charge signs
- Invariant mass of leading two muons should be in mass window consistent with Z boson: $76 < m_{ll} < 106$ GeV

In addition, great care must be taken on choosing the appropriate reconstruction software tags, geometry tags, calibration tags, as well as any necessary updates on offline reconstruction configurations so that the data and MC is consistent[4]. After event selection, two track collections are used for different purpose: Tracks from two leading muons, supposedly coming from $Z \to \mu\mu$ decay, are used as the benchmark track collection for most studies (called "$Z \to \mu\mu$ tracks" below); Tracks from jets on the other hand would be only used for comparison studies at low p_{T} (called "tracks in jets" below). The distribution of $Z \to \mu\mu$ track collection for both data and MC can be found in Figure A.7, showing a good agreement without any kinematic correction being applied.

A.4.2 Pixel Cluster Shapes

The first thing we check is pixel cluster shape, which is characterized by the number of pixels in each pixel cluster in transverse (X) and longitudinal (Y) direction, as shown in Figure A.8. The data and MC is in good general in agreement, although small systematic difference is observed as well. The difference between uniform model and Bichsel Model is very subtle. The pixel cluster

[4]It turns out this is critical for this studies since we will be checking many low-level observables in the reconstruction chain. One is strongly recommended to consult pixel offline and tracking experts for this.

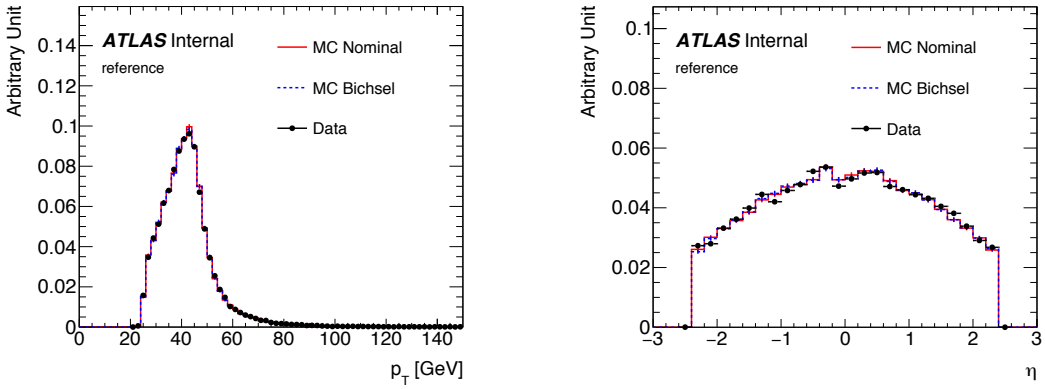


Figure A.7: Normalized distribution of p_{T} and η for tracks selected as candidates for $Z \to \mu\mu$ decay in both data and MC samples. The red curve represents the uniform model and blue dashed line represents the Bichsel Model.

shape was used to be expected as the benchmark showing difference between different simulation models. However, studies show that this is not a good candidate since pixel cluster size can be affected by so many factors beyond the choice of simulation model: High-voltage configuration, Lorentz angle modeling, cross-talk effects etc. Experiences show that any inconsistency in these factors (for example, inconsistent high-voltage setting between data and MC) can have significant effect on cluster shape.

Therefore, we turn to a different observable that was rarely considered before, the charge fraction, defined as ratio of maximal single-pixel charge among all pixels within a pixel cluster over sum of charges for that cluster. This observable is chosen since it may better reveal local charge fluctuation inside a pixel cluster. The distribution of this variable can be seen in Figure A.9. One can clearly see a strong mis-modeling in MC compared to data in the uniform model. After the Bichsel Model is used, data can be well described by the MC simulation. This clearly shows that Bichsel Model is able to appropriately describe the local charge fluctuation.

A.4.3 Tracking Performance

Since such correction effect already presents at the very early stage of reconstruction chain and does not depend on determination of pixel cluster centroid, its further consequence on tracking performance is evaluated. In particular, since the local charge fluctuation might jitter the centroid position, we would evaluate the effect on track-hit residual from choice of simulation model.

The result is shown in Figure A.10. In nominal uniform model, there is a systematic difference between data and MC, in that MC is always overestimating the track-hit resolution than data. After Bichsel Model is used, the track-hit residual distribution in MC gets much smeared out, in a direction consistent with the data. This is not too surprising, given we already see the increased

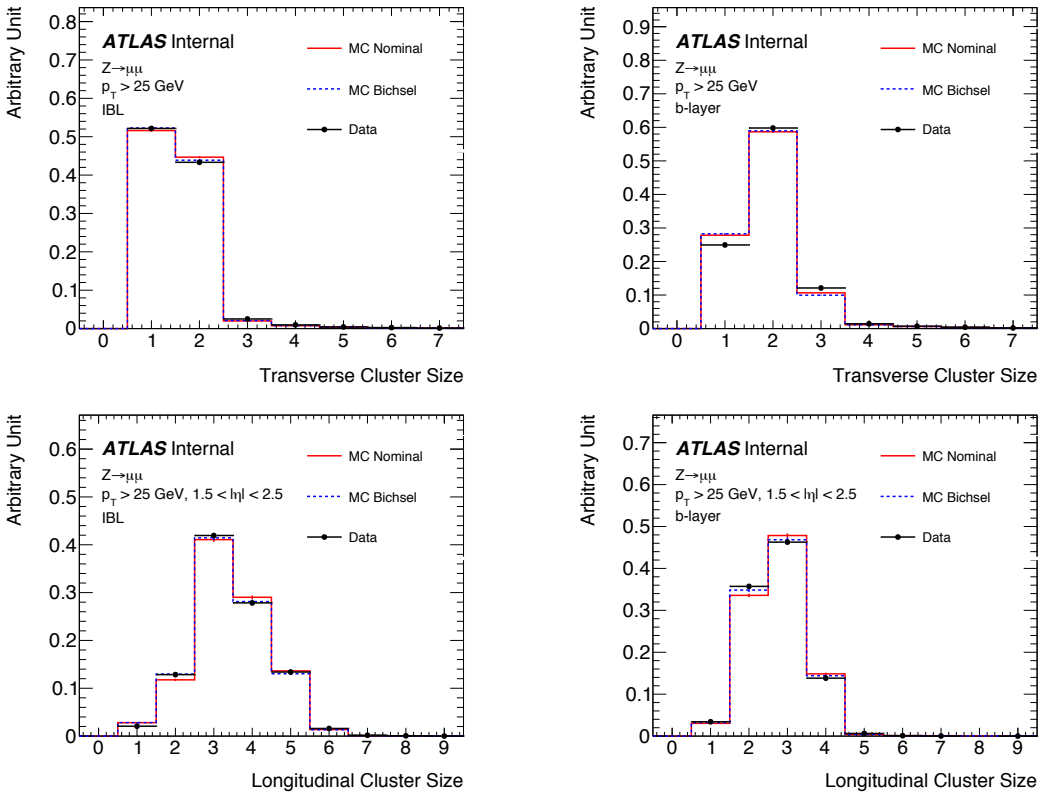


Figure A.8: Normalized distribution of pixel cluster size in transverse direction (first row) and longitudinal direction (second row) for IBL (left) and b-layer (right), measured on clusters associated to $Z \to \mu\mu$ tracks. The red curve represents the uniform model and blue dashed line represents the Bichsel Model.

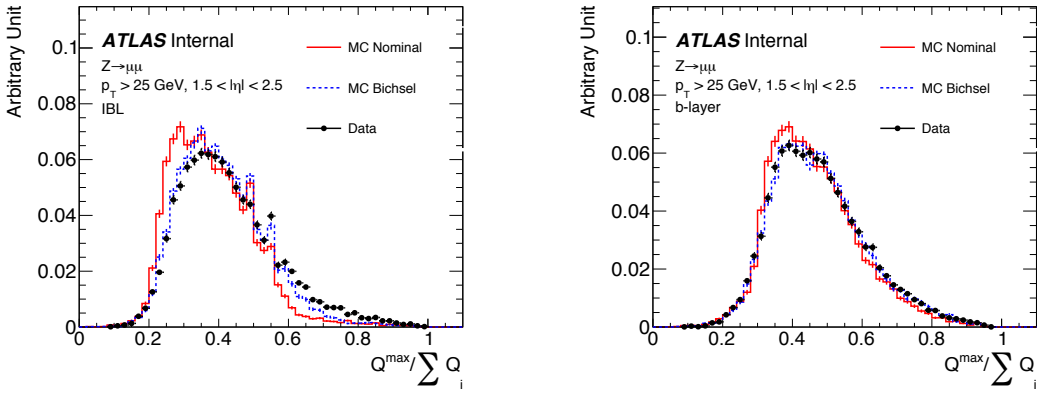


Figure A.9: Normalized distribution of pixel cluster maximal charge fraction in IBL (left) and b-layer (right) for $Z \to \mu\mu$ tracks. The red curve represents the uniform model and blue dashed line represents the Bichsel Model.

local charge fluctuation as shown in Figure A.9. The improvement, defined as the percentage of discrepancy when uniform model is used being corrected by Bichsel Model, in transverse direction is about 66% for all layers. In longitudinal direction, the improvement ranges from 60% in IBL, 66% in b-layer to 83% in other pixel layers. Similar effects are also confirmed across all p_{T} and η regions, as shown in Figure A.11. It is clear that using Bichsel Model can bring the MC simulation much closer to data. Similar conclusion applies to other types of particles as well.

While the effect from Bichsel Model is evident on all barrel layers as shown above, there is little effect in the end-cap region, as shown in Figure A.12. This is because incoming particles are almost perpendicular to the disk in the end-caps. As a result, even the ionized charges are re-distributed in correct way, the would still be drifted to almost the same place, leading to similar track-hit residuals in the end-cap.

Following the track-hit residuals, one can naturally expect similar effect in the tracking impact parameters. Indeed, we are also able to see this effect propagated to the impact parameter, as shown in Figure A.13. In the transverse direction, there is little effect. However, one should notice that data and MC already have good agreement even using the nominal uniform model. On the other hand, the resolution smearing effect happens in the longitudinal direction, making MC closer to the data. Similar conclusion also applies for all p_{T} and η regions, as shown in Figure A.14.

One major concern over this physics performance improvement (in the sense MC is closer to data) is if this is an artificial effect due to lack of pixel cluster NN re-training. However, since the better modeling has already been observed before pixel cluster NN as shown in Figure A.9, effect from NN re-training should be minor. Indeed, the track-hit / impact parameter resolution smearing effect is validated after dedicated NN re-training has been done [222, 225].

A.5 Computation Optimization

Despite of its strong motivation from physics performance as shown above, one practical issue used to be the major road-blocker for its deployment into official ATLAS offline software release, which is the CPU time increase. As one might expect, implementation of the Bichsel Model would inevitably increase CPU time since it is doing a very fine-granularity computation with every single collision being simulated. As a matter of fact, CPU time spent on the digitization step (from *HIT* file to *RDO* file) would increase by 20% per event on average if vanilla version of the Bichsel Model is implemented. Unfortunately this is simply too much, and significantly exceeds the budget left for digitization module, which is at most 5%. To make it even more challenging, there is additional requirement that CPU time increase should be robust against reasonable pile-up. This is really a stringent requirement because our CPU time simply increase linearly with the pile-up.

From studies in Section A.4 we learn that there is little effect in the end-cap regions with Bichsel Model applied. Therefore, we can simply replace Bichsel Model with the old uniform model in

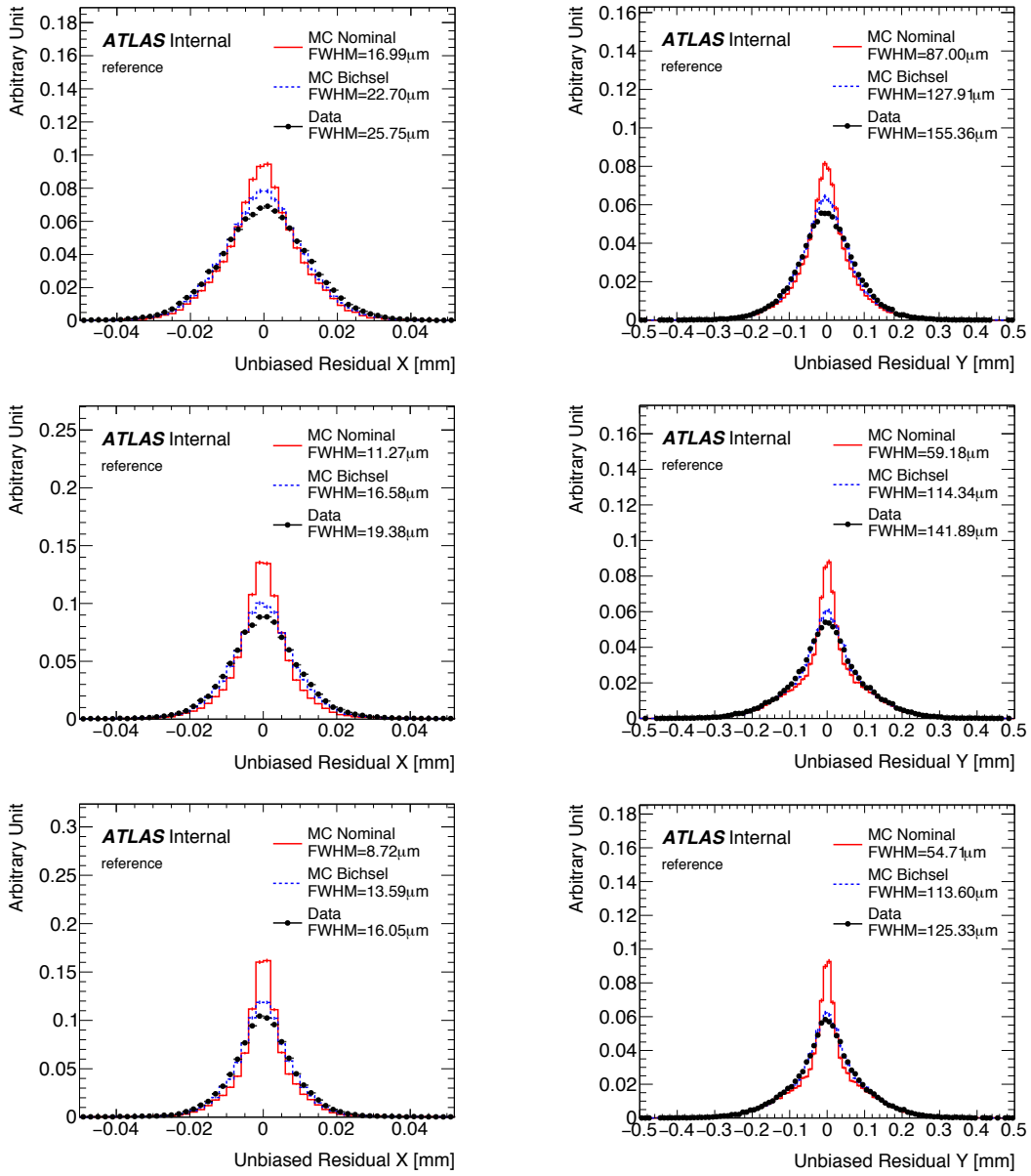


Figure A.10: Normalized distribution of track-hit residuals in transverse (left) and longitudinal (right) direction in IBL (first row), b-layer (second row), and other pixel layers (third row) for $Z \to \mu\mu$ tracks of $p_{\mathrm{T}} > 25$ GeV and $|\eta| < 1.5$. The red curve represents the uniform model and blue dashed line represents the Bichsel Model.

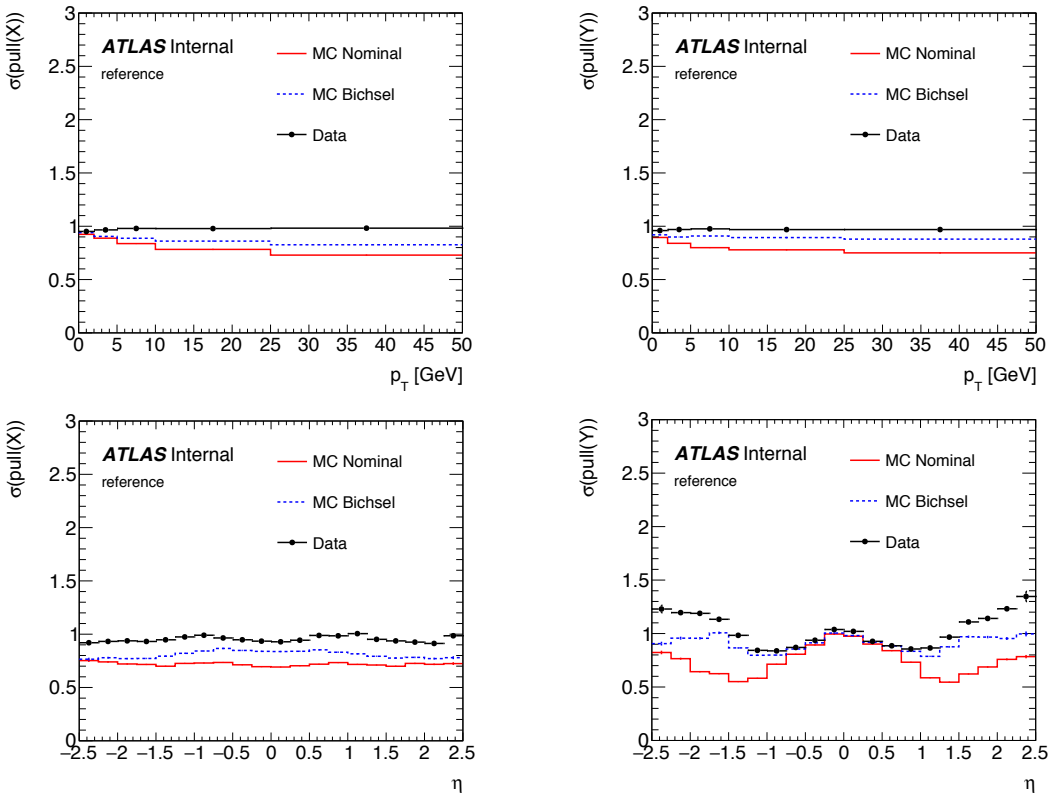


Figure A.11: Pull of track-hit residuals in transverse (left) and longitudinal (right) direction as function of track p_{T} (up) and η (down). Hits from all tracks in $Z \to \mu\mu$ track collection with $p_{\mathrm{T}} > 1$ GeV on all pixel layers are used. The red curve represents the uniform model and blue dashed line represents the Bichsel Model.

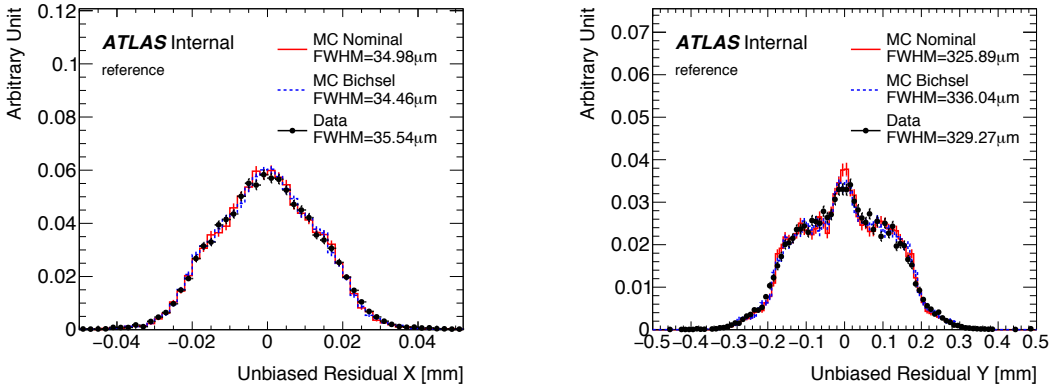


Figure A.12: Normalized distribution of track-hit residuals in transverse (left) and longitudinal (right) direction in end-caps for $Z \to \mu\mu$ tracks of $p_{\mathrm{T}} > 25$ GeV. The red curve represents the uniform model and blue dashed line represents the Bichsel Model.

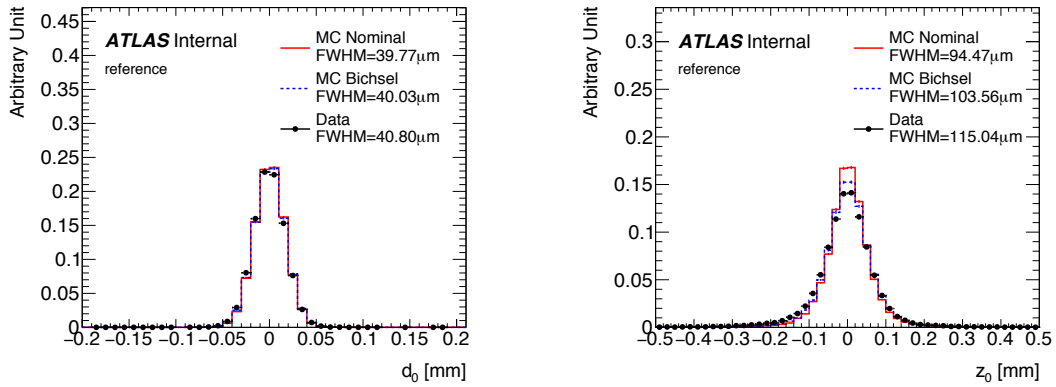


Figure A.13: Normalized distribution of track impact parameter in transverse (d_0, left) and longitudinal (z_0, right) direction for $Z \to \mu\mu$ tracks of $p_{\mathrm{T}} > 25$ GeV. The red curve represents the uniform model and blue dashed line represents the Bichsel Model.

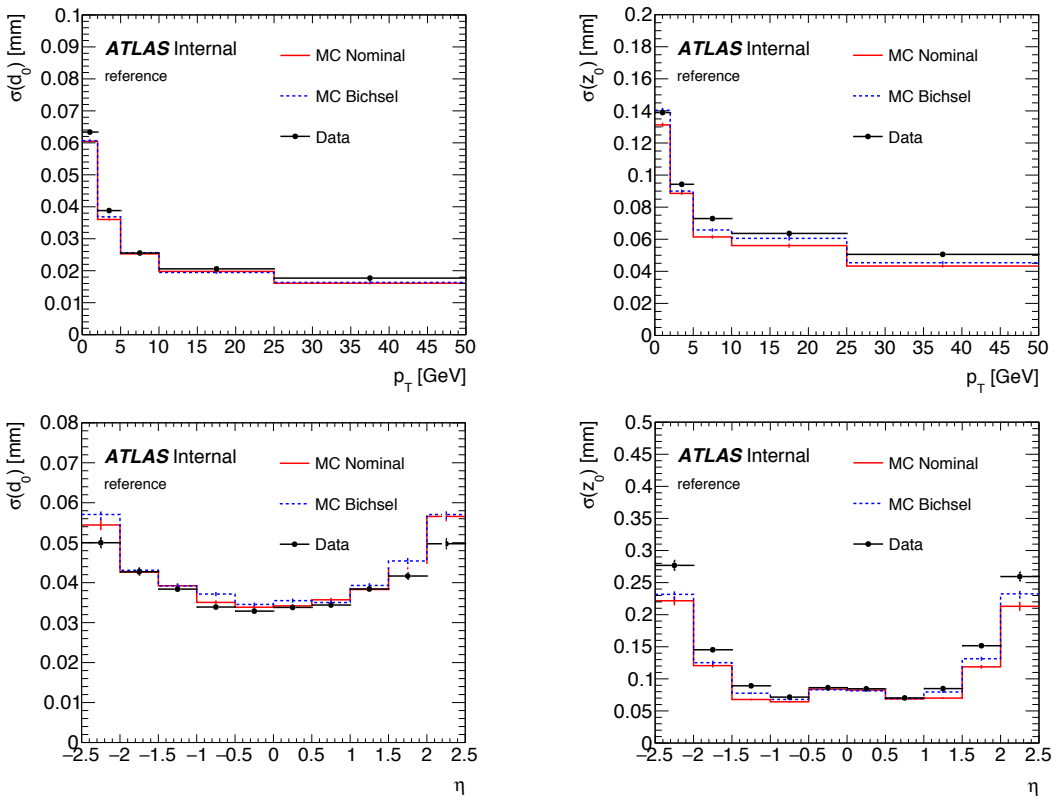


Figure A.14: Resolution of impact parameter in transverse (d_0, left) and longitudinal (z_0, right) direction as function of track p_{T} (up) and η (down). Hits from all tracks in $Z \to \mu\mu$ track collection with $p_{\mathrm{T}} > 1$ GeV on all pixel layers are used. The red curve represents the uniform model and blue dashed line represents the Bichsel Model.

end-caps regions. While this is able to bring down the CPU time increase to 18% from 20%, more efforts are needed to reduce it to acceptable level.

From the sketch of implementation workflow as shown in Figure A.4, the bulk of computation time is spent on the "Simulate Energy Deposition of Particle-Atom Collision" step. Instead of a collision-by-collision simulation, one could try n ($n > 1$) collisions for each sampling. Naturally the CPU reduction would decrease by a factor of n. As a matter of fact, this is very similar to the "convolution calculation" idea as adopted in [230]. Once the reduction factor n has been determined, one simply needs to prepare the same cross-section table as described in Section A.4, but now representing n consecutive collisions instead of single collision. While a larger n can save CPU time by factor of n, value of n cannot be too big since otherwise the local charge fluctuation would be lost. Considering that mean-free path for MIP is about 0.25 μm in the silicon, there would be little impact on physics performance as long as $0.25n$ is within the pixel resolution. Eventually, $n = 5$ is used in ATLAS implementation.

Another place to save CPU time is the reduction of cross-section table. As mentioned earlier, there are two interpolation inside the cross-section table for an incoming particle, one for finding beta-gamma, one for function inversion. In the vanilla version of algorithm, 1000 bins were used along the collision energy dimension. Since the distribution is mostly flat when collision energy is high enough as shown in Figure A.2, 1000 bins turns out to be unnecessary. By reducing this to 100 bins, CPU time increases by a factor of 3 without much loss of function inversion accuracy. Furthermore, the cross-section table file size gets reduced significantly from 25 Megabytes to 1.5 Megabytes, which is beneficial for the migration of cross-section table from *cvmfs* shared space to ATLAS offline database.

The effect of all these measures on CPU time reduction can be found in the left plot of Figure A.15. Each measure introduced above is able to bring down the computing time significantly at hit-by-hit level, leading to a factor of about 10 reduction in total. Eventually, the time needed to spend on simulating ionized charge distribution along flight path is at the order of O(100) micro-seconds. This already matches the time needed to drift ionized charges to the diodes, as shown on right plot of Figure A.15 which is another O(100) micro-seconds per *HIT*. This is very important, since it tells us the total time for Bichsel Model can now be contained at the order of O(100) micro-seconds, which is the same as uniform model (although there is a factor of 2 difference). By putting all components together, we measure the CPU time needed for whole digitization module (*HIT* to *RDO* step), as shown in Figure A.16. Compared to the nominal uniform model, at most 5% increase in CPU time is expected for foreseen pile-up level. With such robustness against the pile-up in CPU time, the last road-blocker for Bichsel Model deployment in ATLAS software is eliminated.

Since the reduction of CPU time comes at the cost of a less accurate simulation, it is important to check if approximations introduced during this process have any impact on the observables we care about. In particular, one should check if any difference brought by the Bichsel Model over

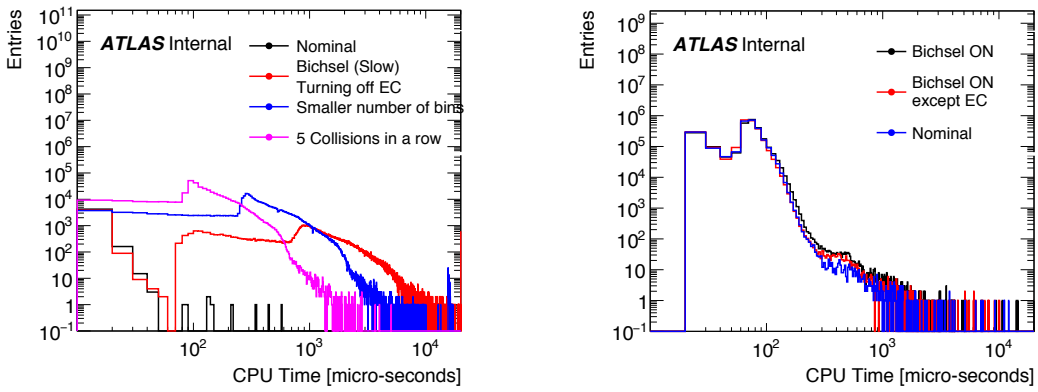


Figure A.15: CPU time per *HIT* spent on simulating charge distribution along flight path (left) and on simulating drift of ionized charges to diodes (right). In the left plot, the reduction sequence is red, blue and purple.

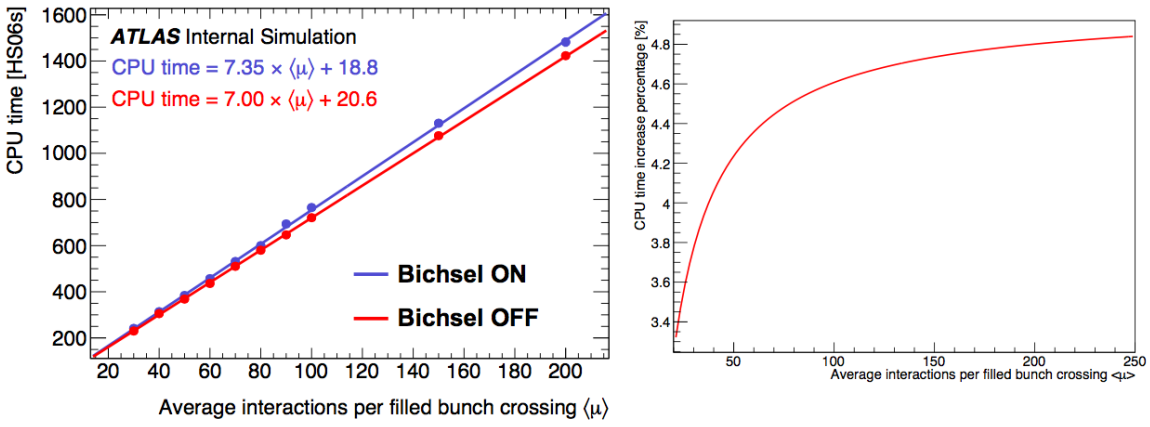


Figure A.16: (Left) CPU time as function of pile-up with Bichsel Model turned on and off; (Right) the percentage of CPU time increase as function of pile-up

uniform model is washed out by these approximations. This has been checked in Figure A.17 for selected variables, showing that these approximations have little effect on pixel cluster and tracking observables within detector resolution.

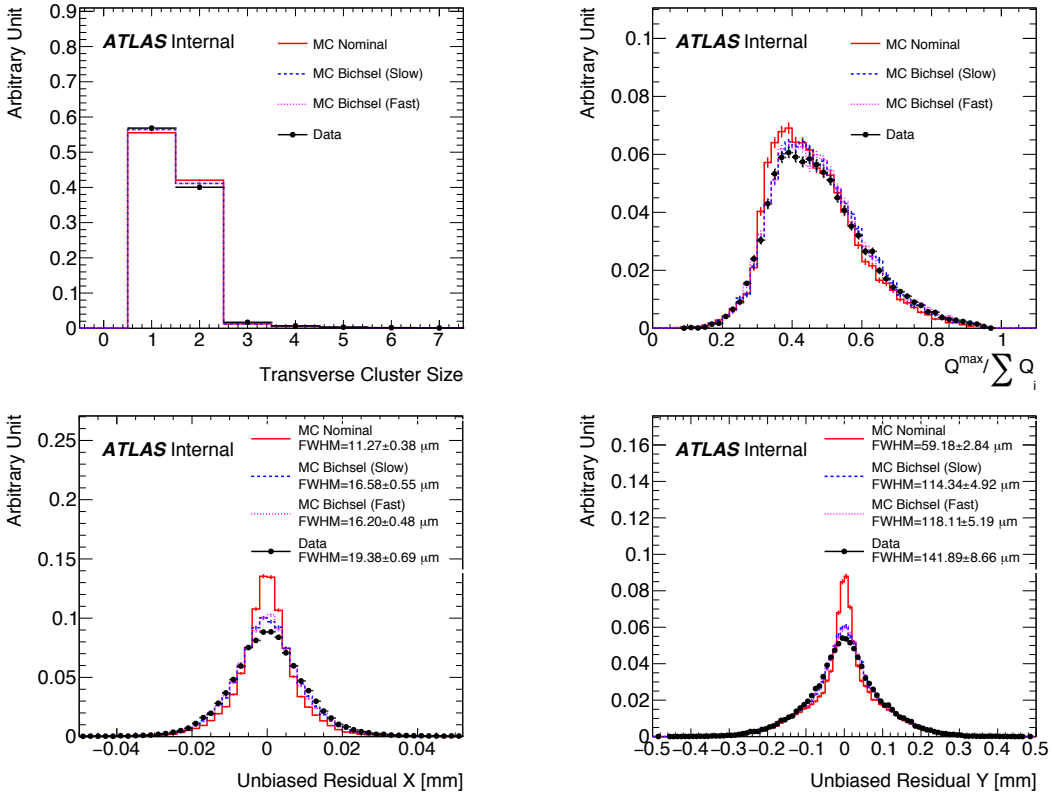


Figure A.17: Effect of approximations introduced during computing time optimization on selected pixel cluster and tracking observables: Pixel cluster size in transverse direction (top left), charge fraction (top right), track-hit residual in transverse direction (bottom left), track-hit residual in longitudinal direction (bottom right). Red curve represents the nominal uniform model; Dashed blue line represents the Bichsel Model before approximations; Dashed purple line represents the Bichsel Model after approximations.

Appendix B

Double b-Tagging for Small Angular Separation

B.1 Introduction

While small radius track jet b-tagging can greatly extend the capability of $h \to b\bar{b}$ tagging as shown in this thesis, its limit also emerges as we are searching for heavy resonances of higher and higher mass in physics analysis. As shown in Chapter 7 and 8, double b-hadrons would start to merge inside a single $R = 0.2$ track jets for resonance mass higher than about 2500 GeV. In the analysis, we address this issue by introducing additional signal regions with relaxed requirement on b-tag multiplicity. Although coming at the cost of lower background rejection, this strategy can still greatly extend search sensitivity to higher resonance mass by taking advantage of the steeply falling background of multijet events. Nevertheless, the incapability of resolving extremely close-by b-hadrons in very boosted environment is constraining any further sensitivity improvement.

However, there is another case which is not as lucky as the $h \to b\bar{b}$ tagging, being $g \to b\bar{b}$ tagging. Different from $h \to b\bar{b}$ decay, the gluon splitting process is not a two-body decay from on-shell heavy particles. As a result, ΔR between two b-hadrons in $g \to b\bar{b}$ is significantly different from $h \to b\bar{b}$ in that distribution in $g \to b\bar{b}$ is a falling spectrum with peak located at very small angular seapration, as shown in Figure B.1. As one can see, the ΔR from $h \to b\bar{b}$ has a nice peak structure located at the place roughly corresponding to $\Delta R \sim 2m/p_{\mathrm{T}}$. However, peak of ΔR distribution from $g \to b\bar{b}$ is always at very small value (< 0.1), with a very long falling tail. Furthermore, such dominance at small angular separation is a common feature independent of kinematics in $g \to b\bar{b}$, even in very low p_{T} as we will see later. As a result, the capability of resolving very small angular separation between double b-hadrons, which is defined as $\Delta R < 0.2$ throughout this appendix, becomes essential for $g \to b\bar{b}$ tagging.

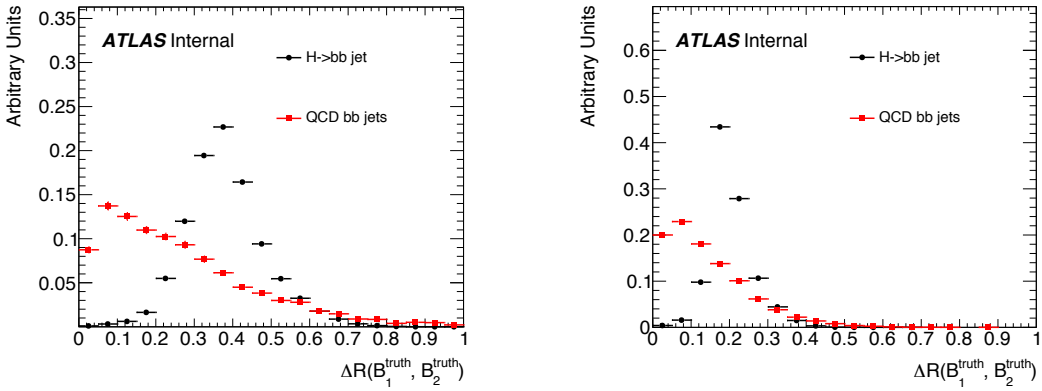
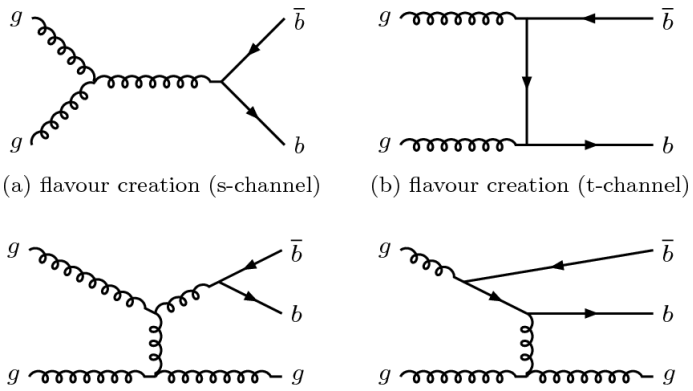


Figure B.1: ΔR between two b-hadrons in truth records for $h \to b\bar{b}$ jets and $g \to b\bar{b}$ jets in $600 < p_{\mathrm{T}} < 1000$ GeV (left) and $1250 < p_{\mathrm{T}} < 2000$ GeV (right)

Furthermore, a precise measurement of closeby double b-hadrons angular distribution can provide deep insights in understanding $b\bar{b}$ production in the Standard Model. A summary of the production mechanisms for $b\bar{b}$ can be found in Figure B.2. While the flavor creation and flavor excitation channels mainly produce $b\bar{b}$ in wide separation angle, gluon splitting channel is dominant with small angular separation. Therefore, a precise measurement of $b\bar{b}$ angular correlation down to small angular separation will allow a sensitive test of QCD physics in NLO. So far, the measurement of $b\bar{b}$ in di-jet environment is only able to probe down to $\Delta R \sim 0.4$ level [232]. Work being explored in this appendix can potentially be used for such measurement to break through existing limitations.



(a) flavour creation (s-channel) (b) flavour creation (t-channel)

(c) gluon splitting (d) flavour excitation

Figure B.2: LO and NLO Feynman diagram for $b\bar{b}$ production [232]

Related previous work can be found in [233] where jet substructure is exploited for double b-hadron identification. However, it is more focused on accepting single b-jets with double b-jets rejected. In the work presented in this appendix, we would reverse the goal, with our signal being the

double b-jets and background being single b-jets. Furthermore, in order to provide precise angular measurement, we require explicit reconstruction of double secondary vertices from $g \to b\bar{b}$ jet. Such change of goal has significant impact on our technique development as well as final performance. It should be noted that, although developed under $g \to b\bar{b}$ measurement context, many techniques as developed here can be applied in other physics scenario, such as high-p_{T} $h \to b\bar{b}$ tagging, as long as the topology of closeby b-hadrons is same. However, certain adaption is needed since in other cases people might just want to do *tagging* where the explicit reconstruction of secondary vertex is not necessary. An example of such adaption can be found in [214][1].

B.2 Exclusive-k_t Algorithm

An alternative to small radius track jets is the exclusive-k_t algorithm, which is a variation of the k_t jet algorithm. While exclusive-k_t uses exactly the same distance metric as the ordinary inclusive k_t jet algorithm, it will not stop clustering constituents until either all d_{ij} are above a certain threshold, or a certain fixed number of jets are obtained. A significant feature of the exclusive-k_t algorithm is that, unlike an inclusive algorithm, it does not have a distance parameter. This suggests that there is no intrinsic angular lower bound on the distance between subjets. Furthermore, since exclusive-k_t with exactly two subjets is equivalent to reversing the jet clustering with the k_t algorithm for the last clustering step, exclusive-k_t effectively splits the original jet into two parts, each of which is used to define a region of interest that is expected to contain one b-hadron from the $g \to b\bar{b}$ decay.

Specifically, the whole tagging procedure is consist of four steps:

1. Run exclusive-k_t algorithm with $N = 2$
2. Obtain two subjets representing two b-hadrons
3. Run standard b-tagging algorithm on each subjet and obtain secondary vertices
4. Apply topological selection

This workflow is illustrated in Figure B.3. As mentioned above, running jet clustering in exclusive mode is able to get rid of the limitation imposed by fixed radius parameter. As shown in Figure B.4, exclusive-k_t is able to reconstruct close-by b-hadrons with $\Delta R < 0.2$, while the small radius track jet is heavily limited by radius parameter.

However, one needs to take special care on the single b-jet background, since a single b-jet can also be split by exclusive-k_t algorithms in the middle. In particular, tracks coming from displaced vertex in single b-jet background might be assigned to two different subjets and get reconstructed into two secondary vertices. Apparently, these are the fake double secondary vertices compared to

[1] Public version of this note is close to be finalized at the time when this thesis is written. Therefore only internal link is available here.

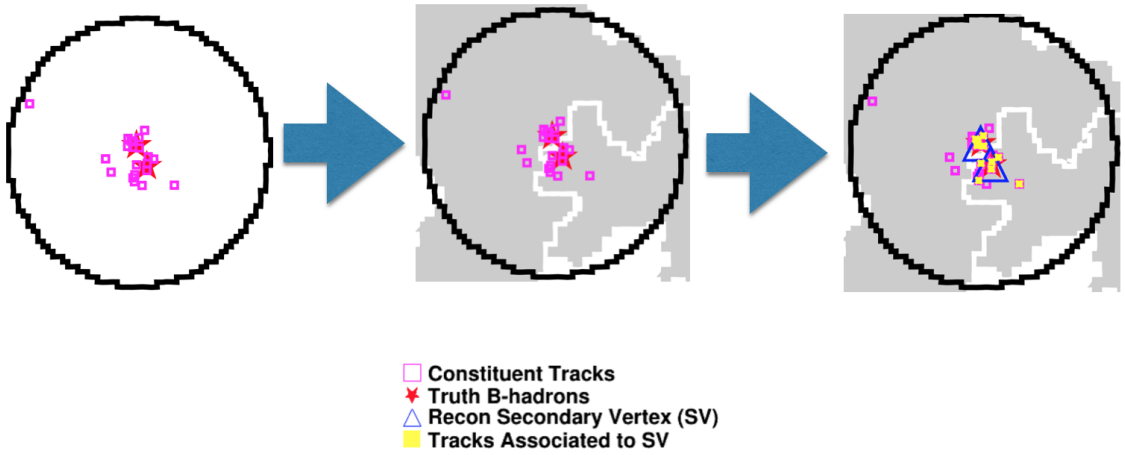


Figure B.3: Illustration of exclusive-k_t algorithm

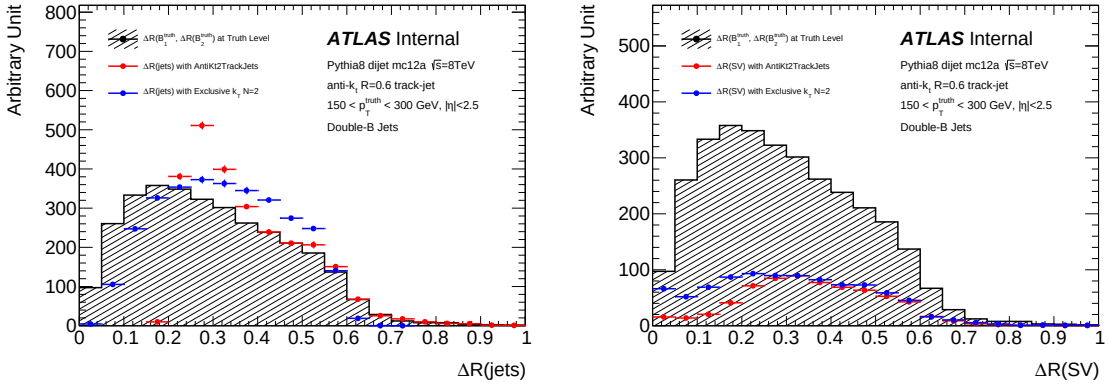


Figure B.4: Normalized distribution of ΔR between subjets (left) and reconstructed secondary vertices (right) for $g \to b\bar{b}$ jet with $150 < p_{\mathrm{T}} < 300$ GeV and $|\eta| < 2.5$

those from $g \to b\bar{b}$ splitting, due to the essential difference in origin. Therefore, dedicated topological selections are developed to distinguish these fake double secondary vertices. The key observation here is that the fake double secondary vertices are correlated to each other in the sense that they can be merged into a single secondary vertex representing one b-hadron; On the other hand, double secondary vertices from real $g \to b\bar{b}$ decay are independent to each other. Such intuition leads to following three variables to discriminate signal and background:

- "Second-MV1"
  This is defined as the second largest b-tagging weights among subjets being found. This is equivalently requiring both subjets should pass certain b-tagging cut. Apparently, if the background single secondary vertex is split in halves, one for each subjet, this variable would not be discriminative at all. However, there is certain probably that the single secondary vertex in background jet is assigned completely to one subjet while another subjet gets nothing, which is the scenario where this variable would be useful.

- "NtrksDiff"
  Besides the secondary vertex reconstructed in each subjet, one can also attempt to reconstruct an inclusive secondary vertex in the original jet before splitting. Then "NtrksDiff" is defined as the sum of number of tracks associated to each secondary vertex reconstructed in each subjet, subtracted by the number of tracks associated to inclusive secondary vertex as reconstructed in original jet. This is a variable specifically designed for the case of fake double secondary vertices as discussed above. For background single b-jet, this variable is expected to be around zero. However, for signal $g \to b\bar{b}$ jet, the secondary vertex reconstructed from original jet would either coincide with one of the double secondary vertices as reconstructed in subjets, or fails reconstruction quality cut at all, since tracks taken from double b-hadrons are not compatible with the assumption of single secondary vertex. In the latter case, the number of tracks associated with secondary vertex reconstructed from original jet is assigned to be zero. As a result, "NtrksDiff" would be some positive number for the signal $g \to b\bar{b}$ jet, providing discrimination power against the background.

- "Combined SV Mass" Another way to reject fake double secondary vertices is checking the invariant mass using all tracks associated to them. For background single b-jet, this should lead to a resonance mass spectrum corresponding to mass of b-hadron, while mass spectrum of signal double b-jet should be much broader since the gluon could be off-shell.

The distribution of these three variables between signal and background can be found in Figure B.5. All three variables provide clear discrimination power between signal and background as discussed above. Better discrimination power can be obtained by fully exploiting the correlation between these variables, which is done through a combination using *k-nearest neighborhood* (kNN) algorithm. The background rejection as function of signal efficiency can be found in Figure B.6.

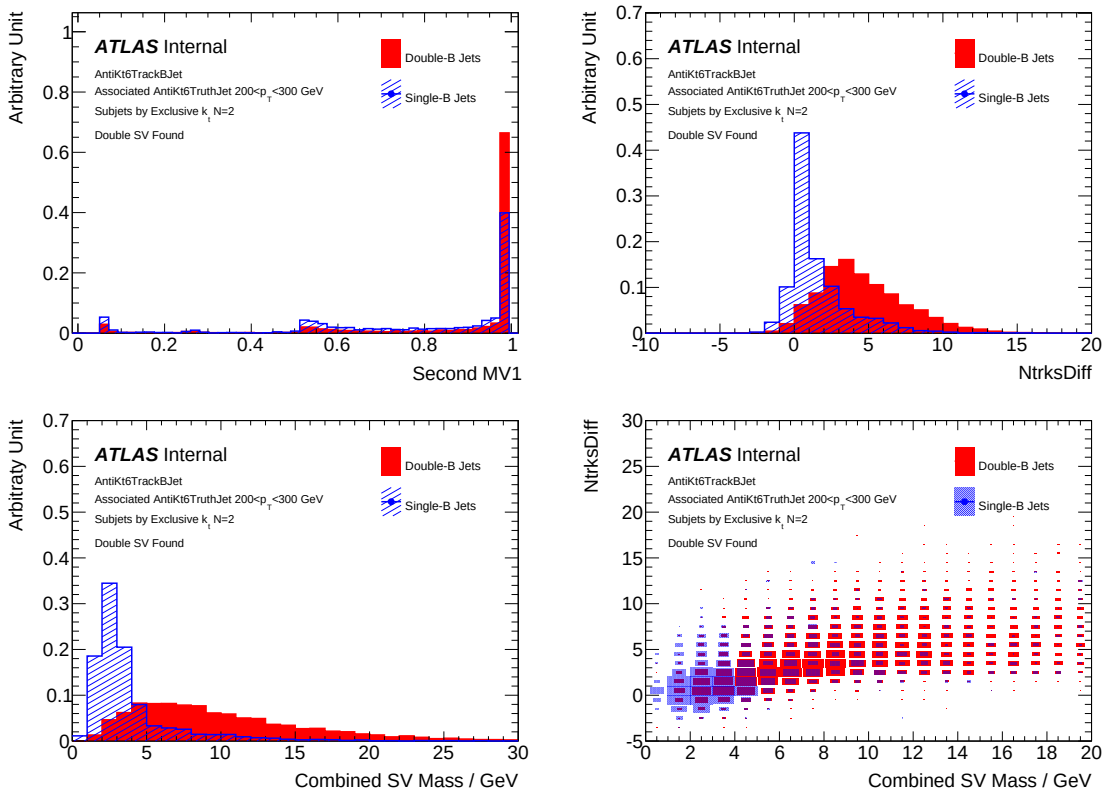


Figure B.5: Normalized distribution of "Second-MV1" (top left), "NtrksDiff" (top right), "Combined SV Mass" (bottom left) and correlation between "NtrksDiff" and "Combined SV Mass" (bottom right)

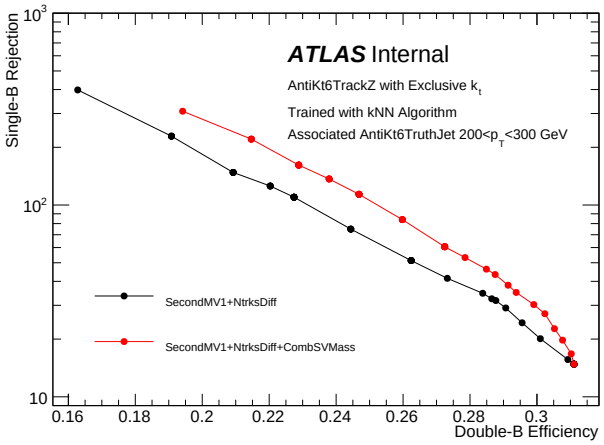


Figure B.6: Background single b-jet rejection as function of signal double b-jet efficiency using different combination schemes. The efficiency of having two secondary vertices passing quality cut is already included here.

To understand our performance, the probably of finding double secondary vertices in signal sample as function of ΔR is examined under various conditions, as shown in Figure B.7. There are several interesting observations from this plot:

- Ideally exclusive-k_t should split in-between the two b-hadrons, although this is not always the case. In reality, there is certain probability of assigning both b-hadrons to the same subjet, called "merging effect". In particular, such probability is larger when ΔR between two b-hadrons are closer, which is the gap observed between red and dashed blue line. This suggests that there would still be some angular limitation for exclusive-k_t, below which the probability of getting "merged" case is too big.

- Even each b-hadron is assigned to separate subjet, there is an efficiency drop at the large ΔR. Such drop can be recovered once requiring the distance between b-hadron and subjet to be less than 0.2. This is consistent with general property of b-tagging as shown in Figure 5.9 that b-tagging efficiency would drop drastically when subjet axis is too deviated from b-hadron flight direction.

- There is an upper bound on the efficiency at around 40%, even after all situations are considered. This is due to the intrinsic probability of reconstructing two secondary vertices with good enough quality from the pattern recognition algorithm itself. As a matter of fact, this is the main constrain on the tagging performance.

As discussed above, one reason accounting for efficiency loss is the merging of two b-hadrons in one subjet. Therefore, one could apply a further splitting with exclusive-k_t $N = 3$ setting to partially

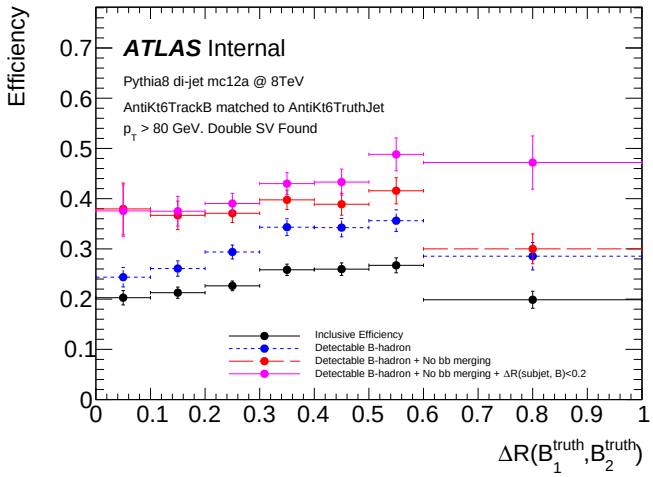


Figure B.7: Probability of finding double secondary vertices in signal sample as function of ΔR under different conditions. Black curve is the inclusive efficiency; Blue dashed line is the same efficiency but requiring both b-hadrons to be $p_{\mathrm{T}} > 5$ GeV, $|\eta| < 2.5$; Red line represents the efficiency under same condition as dashed blue line, but additionally requiring each b-hadron should be assigned to separate subjet; Purple line represents the efficiency under same condition as red line, but additionally requiring distance between b-hadron to corresponding subjet less than 0.2

recove this case, as illustrated in Figure B.8. In this event display, a third splitting provides another opportunity in splitting two b-hadrons into separate subjets, allowing further tagging. For $N = 3$ splitting, we focus on the two subjets with highest b-tagging weights as b-jet candidate, and then apply the same topological variables same as case of $N = 2$ splitting.

While a further splitting can bring some efficiency recovery, it can also potentially increase the fake rate since it also provides an additional opportunity of fake splitting of background single b-jet. Therefore, a proper combination between $N = 2$ and $N = 3$ splitting is needed. Specifically, exclusive-k_t algorithm with both $N = 2$ and $N = 3$ are run, and three topological variables under each configuration are computed separately. Additionally, we add an indicator variable, representing the whether one is able to reconstruct double secondary vertices with $N = 2$ configuration. The purpose of this indicator variable is to give preference on $N = 2$ splitting since $N = 3$ splitting is actually unnecessary if double secondary vertices are found successfully with $N = 2$ configuration. Then these seven variables are combined using *boosted decision tree* (BDT) algorithm. The background rejection as function of signal efficiency can be found in Figure B.9. As one can see, the tagging performance increases by a large amount after $N = 3$ splitting is introduced. Furthermore, a strong p_{T}-dependency of performance is found. In particular, the tagging performance is found to be poor in lowest p_{T} bin.

As introduced in Section B.1, one of physics motivations for $g \to b\bar{b}$ tagging is the precise measurement of angular correlation between double b-hadrons, which can be done by measuring the

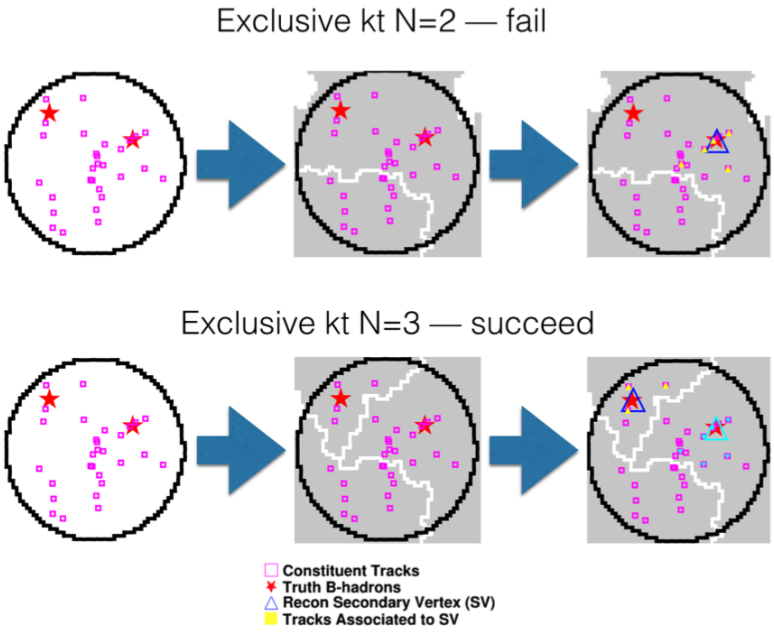


Figure B.8: Illustration of $N = 3$ splitting in exclusive-k_t when $N = 2$ splitting fails.

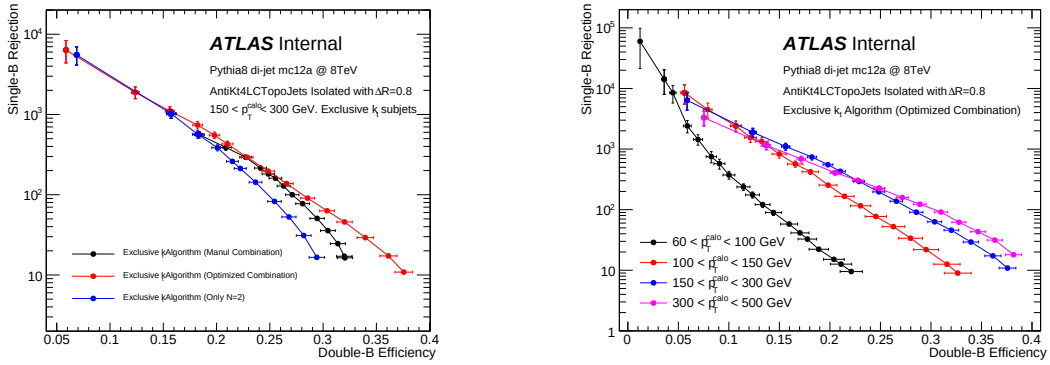


Figure B.9: Background single b-jet rejection as function of signal double b-jet efficiency after combining $N = 3$ and $N = 2$ configuration when 1) (left) compared to $N = 2$ only configuration 2) (right) compared across different p_{T} bins

ΔR between reconstructed double secondary vertices. In particular, the correlation between reconstructed and truth ΔR between secondary vertices can be found in Figure B.10 across all p_{T} bins. A strong angular correlation between reconstruction and truth level is found across all p_{T} bins, indicating great potential for ΔR measurement with this technique. Furthermore, the angular limitation of measurement can be clearly seen in each plot, below which the efficiency of identifying double secondary vertices is too low to see any angular correlation. The results show a strong p_{T}-dependency of such angular limitation, varying from 0.2 at lowest p_{T} bin to as small as 0.05 in highest p_{T} bin. This has already extended the hard limit imposed by $R = 0.2$ track jets significantly.

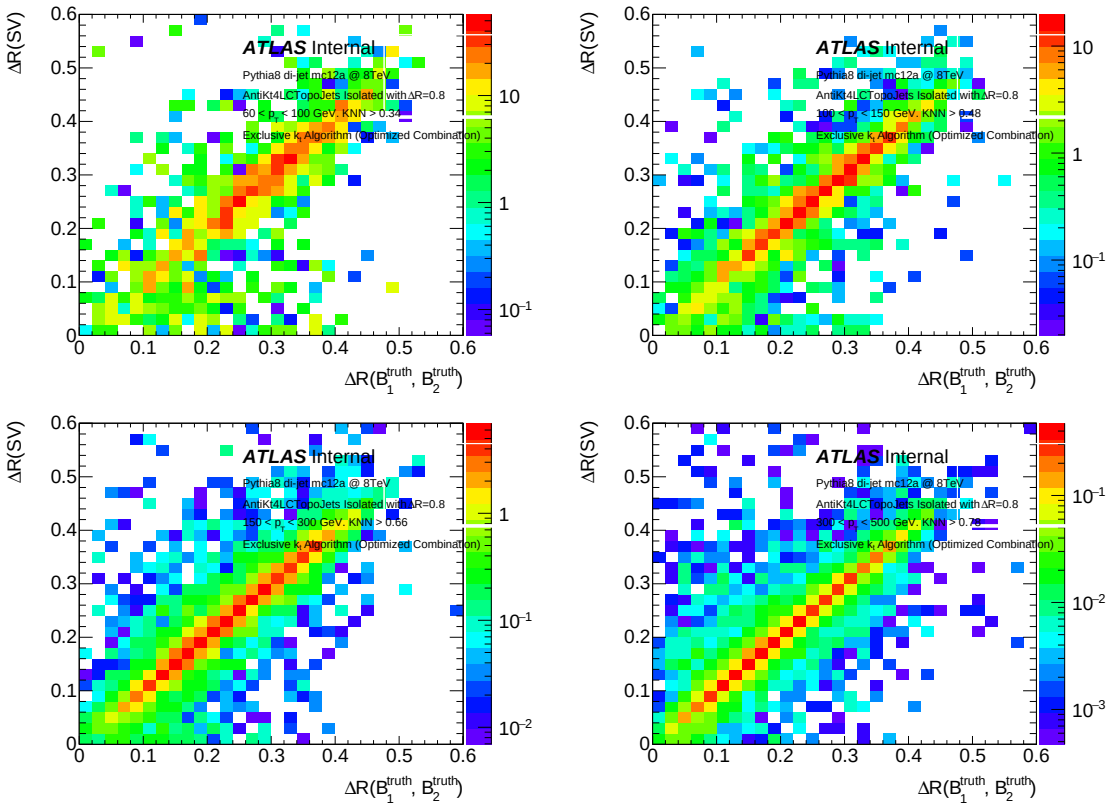


Figure B.10: Correlation between reconstructed and truth ΔR between secondary vertices in signal double b-jets using exclusive-k_t algorithm for $60 < p_{\mathrm{T}} < 100$ GeV (top left), $100 < p_{\mathrm{T}} < 150$ GeV (top right), $150 < p_{\mathrm{T}} < 300$ GeV (bottom left) and $300 < p_{\mathrm{T}} < 500$ GeV (bottom right). The z-axis is in log-scale.

B.3 *k-means* Clustering Algorithm

In addition to the exclusive-k_t algorithm, a different algorithm is also developed to resolve close-by b-hadrons, called *k-means*. An illustration of the algorithm workflow is shown in Figure B.11. The

algorithm is composed of following steps:

1. Identify input primitive vertices within the original jet. There are two options so far, one being the two-track vertices, one being the vertices found by *multi-secondary-vertex* (MSV) algorithm

2. Basic quality cut on primitive vertices by requiring them to be at least 3-σ away from primary vertex in the event.

3. Run *k-means* clustering on these primitive vertices, using 2-dimensional ATLAS coordinate system (θ, ϕ). Instead of a vanilla *k-means* clustering, the covariant matrix of primitive vertices are taken into account[2]. The number of clusters is fixed to be two, corresponding to our double secondary vertices assumption.

4. After clustering, the primitive vertex with largest χ^2 is identified. In particular, the one larger than a tunable parameter would be treated as outliers and removed. Then same clustering procedure as last step would be repeated with rest of primitive vertices. Such iteration is repeated until all outliers are removed.

5. After two clusters of primitive vertices are identified, tracks from all primitive vertices in each cluster would be used to fit an inclusive vertex, representing the secondary vertex from one of the b-hadrons in $g \to b\bar{b}$.

For the same reason as exclusive-k_t, additional topological selection is necessary to reject the fake double secondary vertices from background single b-jets. Similar to exclusive-k_t, "NtrksDiff" and "Combined SV Mass" are also used here. However, the "Second-MV1" is not longer applicable since there is no concept of "subjet" in *k-means* algorithm any more. Instead, a new variable called "ΔR Significance", defined as the ratio of ΔR between double secondary vertices over uncertainty of such ΔR measurement, is introduced for *k-means* algorithm. The distribution of three discriminative variables can be found in Figure B.12. The background jet rejection as function of signal jet efficiency with different algorithm configurations are also shown in this plot. The result suggests that using MSV as input primitive vertices can be significantly better than using two-track vertices. Furthermore, performance can increase slightly by removing outliers in an iterative way.

A comparison of tagging performance across different p_{T} bins, as well as with the exclusive-k_t algorithm, is shown in Figure B.13. Two algorithms show similar performance in general. In particular, *k-means* algorithm is slightly better in the low-p_{T} region, while exclusive-k_t is better in the high-p_{T} region.

Similarly, angular correlation for *k-means* algorithm is checked as shown in Figure B.14. Compared to the case of exclusive-k_t in Figure B.10, *k-means* algorithm has a very clear advantage in

[2]Therefore this is probably more like a multi-Gaussian clustering

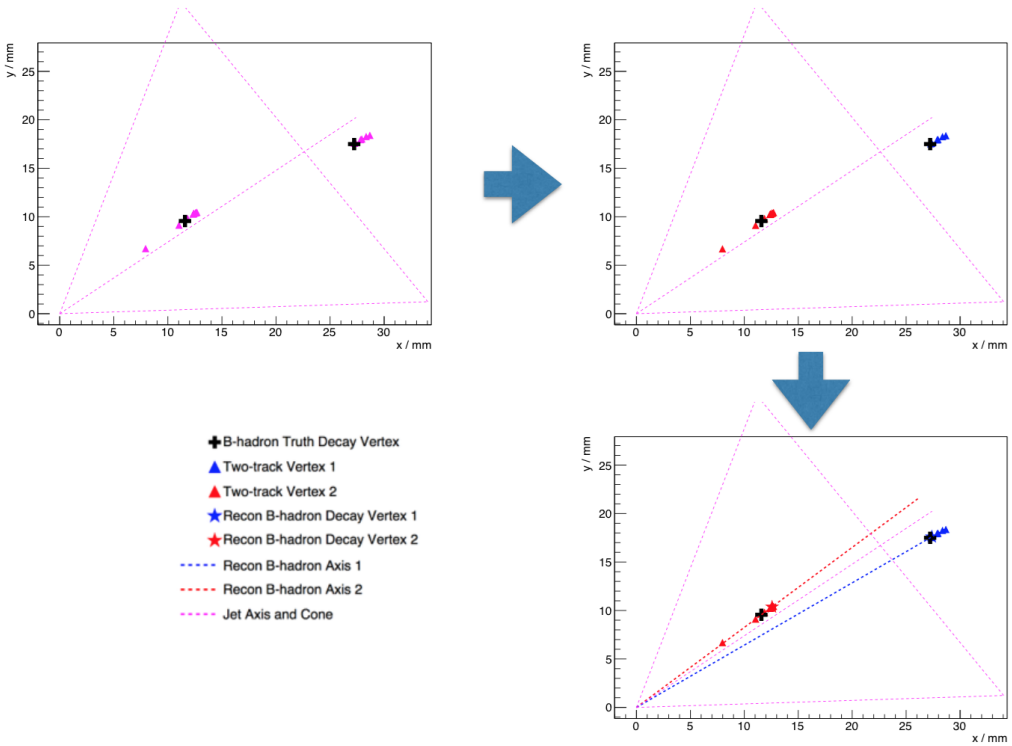


Figure B.11: Illustration of workflow of *k-means* clustering algorithm for $g \to b\bar{b}$ tagging

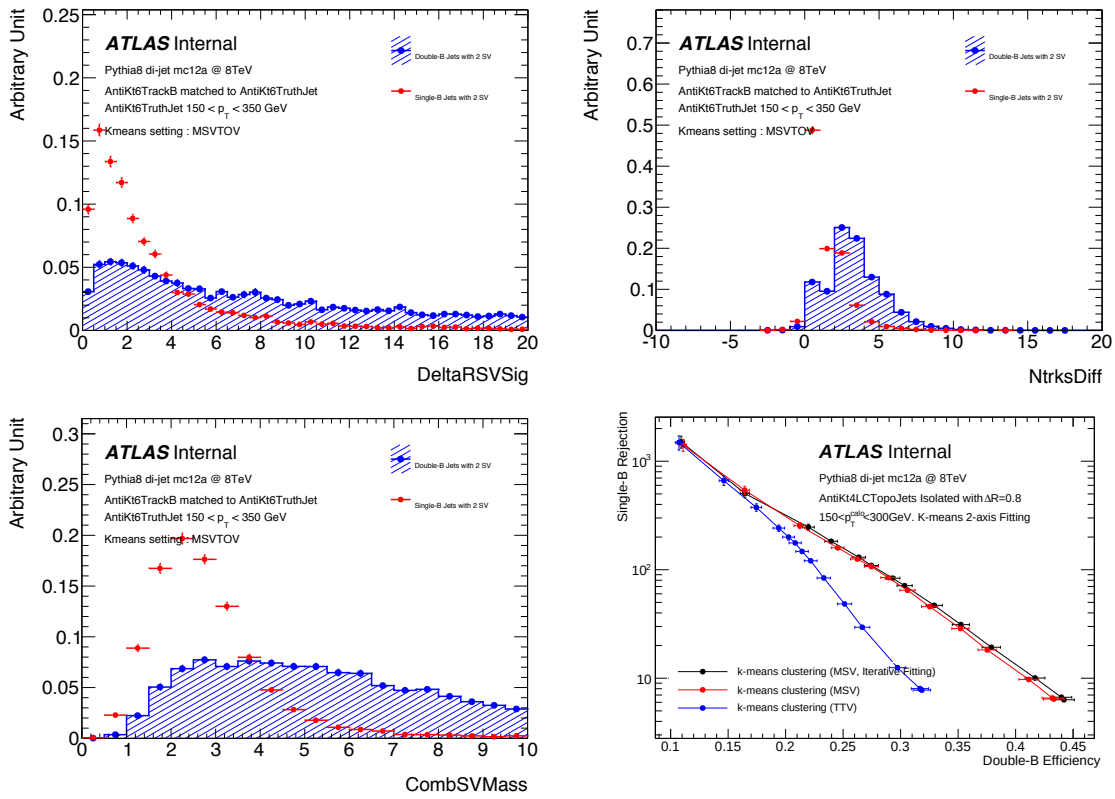


Figure B.12: Normalized distribution of "ΔR Significance" (top left), "NtrksDiff" (top right) and "Combined SV Mass" (bottom left) between signal double b-jets and background single b-jets. The background jet rejection as function of signal jet efficiency using different algorithm configurations are also shown in the bottom right: Blue curve represents the case using two-track vertices as input primitive vertices; Red curve represents the case using MSV as input primitive vertices; Black curve represents the case using MSV as input, and with outliers being removed in an iterative way as described above.

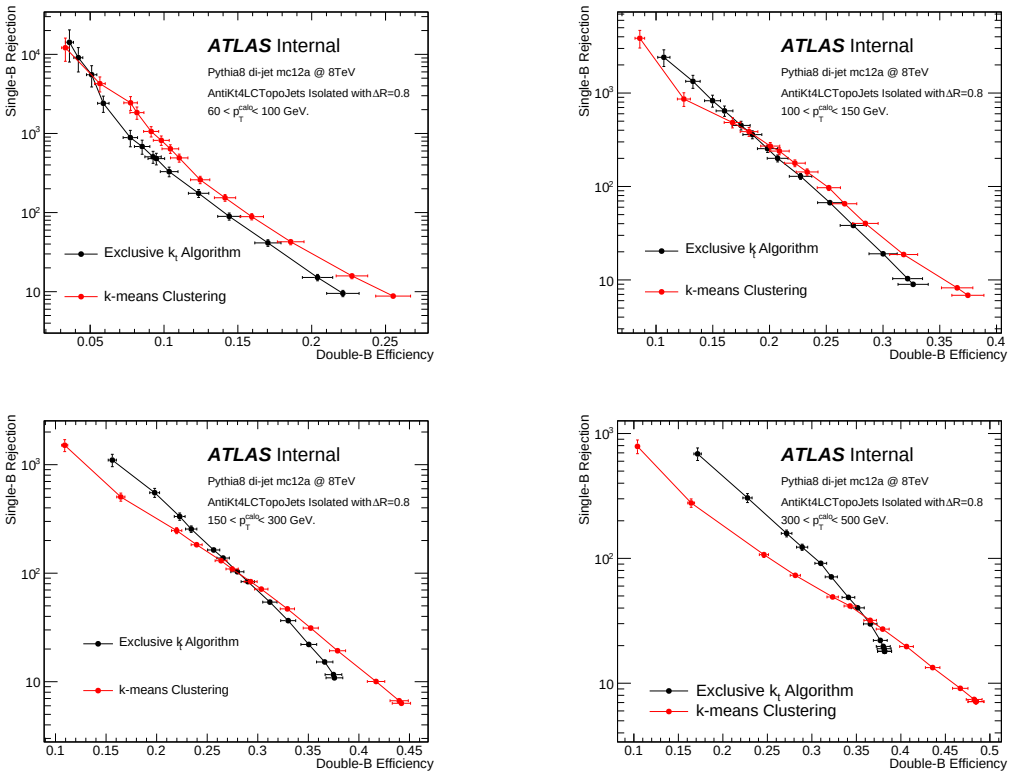


Figure B.13: Background single b-jet rejection as function of double b-jet efficiency between *k-means* and exclusive-k_t algorithms in $60 < p_{\mathrm{T}} < 100$ GeV (top left), $100 < p_{\mathrm{T}} < 150$ GeV (top right), $150 < p_{\mathrm{T}} < 300$ GeV (bottom left) and $300 < p_{\mathrm{T}} < 500$ GeV (bottom right)

that it has much smaller angular limitations in ΔR measurement, in particular in the low p_{T} region, suggesting a better reconstruction efficiency by using *k-means* algorithm. Furthermore, double secondary vertices reconstructed by *k-means* algorithm has better angular resolution, as shown in Figure B.15. In all p_{T} bins, *k-means* algorithm is able to provide a better angular resolution in terms of measurement of the ΔR between double secondary vertices.

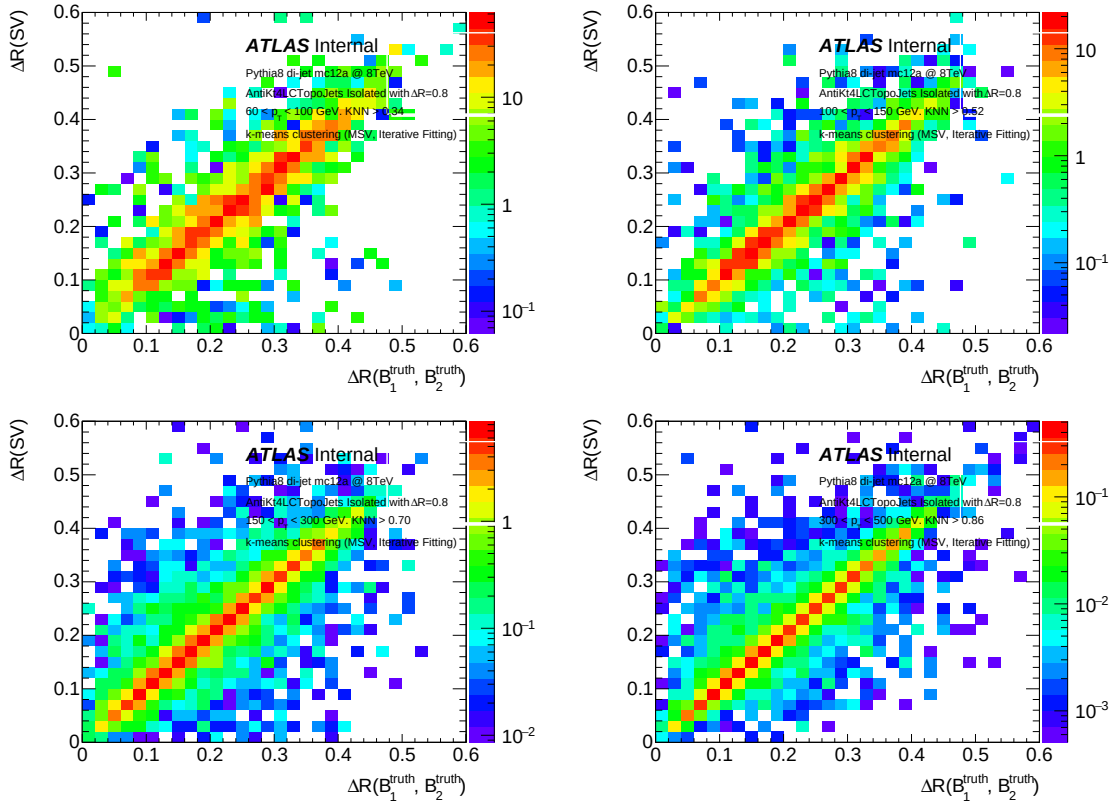


Figure B.14: Correlation between reconstructed and truth ΔR between secondary vertices in signal double b-jets using *k-means* algorithm for $60 < p_{\mathrm{T}} < 100$ GeV (top left), $100 < p_{\mathrm{T}} < 150$ GeV (top right), $150 < p_{\mathrm{T}} < 300$ GeV (bottom left) and $300 < p_{\mathrm{T}} < 500$ GeV (bottom right). The z-axis is in log-scale.

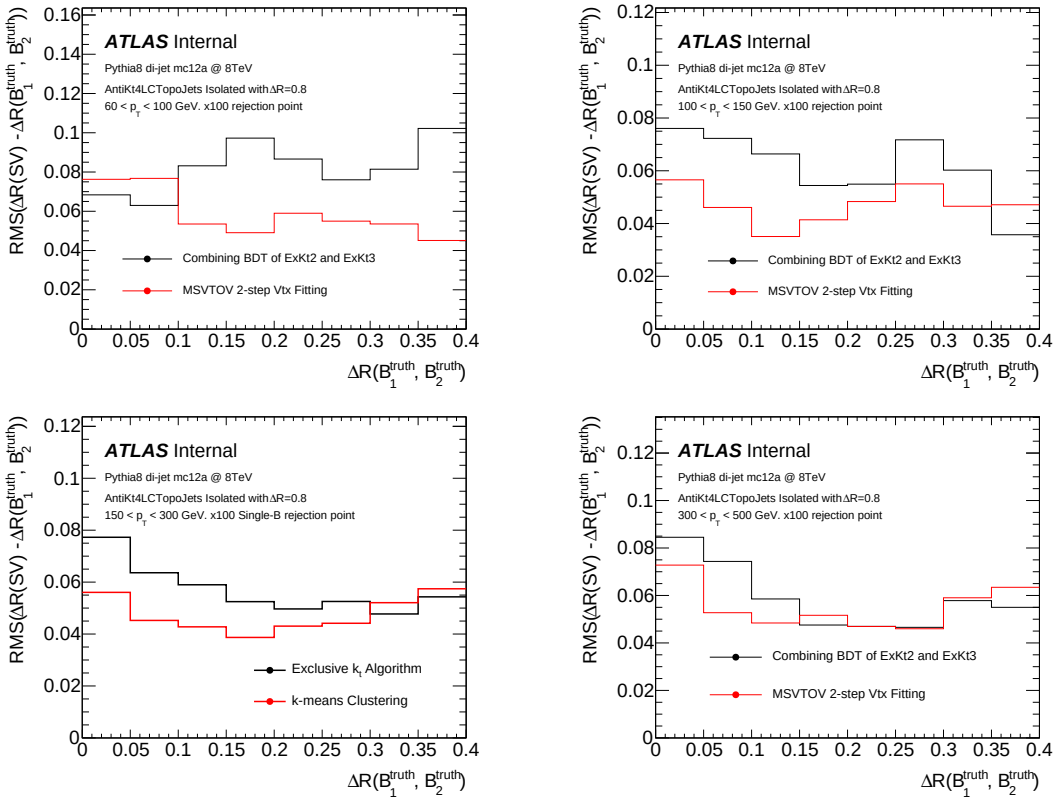


Figure B.15: RMS of the distribution of $\Delta R_{recon} - \Delta R_{truth}$ in signal double b-jets for $60 < p_{\mathrm{T}} < 100$ GeV (top left), $100 < p_{\mathrm{T}} < 150$ GeV (top right), $150 < p_{\mathrm{T}} < 300$ GeV (bottom left) and $300 < p_{\mathrm{T}} < 500$ GeV (bottom right)

Bibliography

[1] ATLAS Collaboration, *Observation of a new particle in the search for the Standard Model Higgs boson with the ATLAS detector at the LHC*, Phys. Lett. B **716** (2012) 1, arXiv:1207.7214 [hep-ex].

[2] CMS Collaboration, *Observation of a new boson at a mass of 125 GeV with the CMS experiment at the LHC*, Phys. Lett. B **716** (2012) 30, arXiv:1207.7235 [hep-ex].

[3] A. Abdesselam et al., *Boosted objects: A Probe of beyond the Standard Model physics*, Eur. Phys. J. **C71** (2011) 1661, arXiv:1012.5412 [hep-ph].

[4] A. Altheimer et al., *Jet Substructure at the Tevatron and LHC: New results, new tools, new benchmarks*, J. Phys. **G39** (2012) 063001, arXiv:1201.0008 [hep-ph].

[5] A. Altheimer et al., *Boosted objects and jet substructure at the LHC. Report of BOOST2012, held at IFIC Valencia, 23rd-27th of July 2012*, Eur. Phys. J. **C74** (2014) 2792, arXiv:1311.2708 [hep-ex].

[6] D. Adams et al., *Towards an Understanding of the Correlations in Jet Substructure*, Eur. Phys. J. **C75** (2015) 409, arXiv:1504.00679 [hep-ph].

[7] M. Gell-Mann, *A schematic model of baryons and mesons*, Physics Letters **8** (1964) 214 – 215, http://www.sciencedirect.com/science/article/pii/S0031916364920013.

[8] G. Zweig, *An SU(3) model for strong interaction symmetry and its breaking. Version 1*,.

[9] S. L. Glashow, *Partial-symmetries of weak interactions*, Nuclear Physics **22** (1961) 579–588.

[10] F. Englert and R. Brout, *Broken Symmetry and the Mass of Gauge Vector Mesons*, Phys. Rev. Lett. **13** (1964) 321–323, https://link.aps.org/doi/10.1103/PhysRevLett.13.321.

[11] P. W. Higgs, *Broken Symmetries and the Masses of Gauge Bosons*, Phys. Rev. Lett. **13** (1964) 508–509, https://link.aps.org/doi/10.1103/PhysRevLett.13.508.

[12] G. S. Guralnik, C. R. Hagen, and T. W. B. Kibble, *Global Conservation Laws and Massless Particles*, Phys. Rev. Lett. **13** (1964) 585–587, https://link.aps.org/doi/10.1103/PhysRevLett.13.585.

[13] S. Weinberg, *A model of leptons*, Physical review letters **19** (1967) 1264.

[14] S. Abdus, *Weak and Electromagnetic Interactions, Conf*, Proc. C **680519** (1968) 367–377.

[15] H. D. Politzer, *Reliable Perturbative Results for Strong Interactions?*, Phys. Rev. Lett. **30** (1973) 1346–1349, https://link.aps.org/doi/10.1103/PhysRevLett.30.1346.

[16] D. J. Gross and F. Wilczek, *Asymptotically Free Gauge Theories. I*, Phys. Rev. D **8** (1973) 3633–3652, https://link.aps.org/doi/10.1103/PhysRevD.8.3633.

[17] D. J. Gross and F. Wilczek, *Ultraviolet Behavior of Non-Abelian Gauge Theories*, Phys. Rev. Lett. **30** (1973) 1343–1346, https://link.aps.org/doi/10.1103/PhysRevLett.30.1343.

[18] M. E. Peskin and D. V. Schroeder, *An Introduction to quantum field theory*. 1995. http://www.slac.stanford.edu/spires/find/books/www?cl=QC174.45%3AP4.

[19] M. D. Schwartz, *Quantum Field Theory and the Standard Model*. Cambridge University Press, 2014. http://www.cambridge.org/us/academic/subjects/physics/theoretical-physics-and-mathematical-physics/quantum-field-theory-and-standard-model.

[20] CERN, . CERN, Geneva, 2010. https://cds.cern.ch/record/1119304. Comments: 7 lectures, 234 pages, published as CERN Yellow Report http://cdsweb.cern.ch/record/1119304.

[21] *Standard Model*, https://en.wikipedia.org/wiki/Standard_Model.

[22] L. Alvarez-Gaume and J. Ellis, *Eyes on a prize particle*, Nature Phys. **7** (2011) 2–3, https://cds.cern.ch/record/1399903, Editorial Material.

[23] L. Randall and R. Sundrum, *A Large mass hierarchy from a small extra dimension*, Phys. Rev. Lett. **83** (1999) 3370–3373, arXiv:hep-ph/9905221 [hep-ph].

[24] I. Antoniadis, N. Arkani-Hamed, S. Dimopoulos, and G. R. Dvali, *New dimensions at a millimeter to a Fermi and superstrings at a TeV*, Phys. Lett. **B436** (1998) 257–263, arXiv:hep-ph/9804398 [hep-ph].

[25] Maxime Gabella, *The Randall-Sundrum Model*, 2006, https://www-thphys.physics.ox.ac.uk/people/MaximeGabella/rs.pdf.

[26] W. D. Goldberger and M. B. Wise, *Modulus stabilization with bulk fields*, Phys. Rev. Lett. **83** (1999) 4922–4925, arXiv:hep-ph/9907447 [hep-ph].

[27] H. Davoudiasl, J. L. Hewett, and T. G. Rizzo, *Experimental probes of localized gravity: On and off the wall*, Phys. Rev. **D63** (2001) 075004, arXiv:hep-ph/0006041 [hep-ph].

[28] A. Oliveira, *Gravity particles from Warped Extra Dimensions, predictions for LHC*, arXiv:1404.0102 [hep-ph].

[29] K. Agashe, H. Davoudiasl, G. Perez, and A. Soni, *Warped Gravitons at the LHC and Beyond*, Phys. Rev. D **76** (2007) 036006, arXiv:hep-ph/0701186.

[30] LHC New Physics Working Group Collaboration, D. Alves, *Simplified Models for LHC New Physics Searches*, J. Phys. **G39** (2012) 105005, arXiv:1105.2838 [hep-ph].

[31] D. Pappadopulo, A. Thamm, R. Torre, and A. Wulzer, *Heavy Vector Triplets: Bridging Theory and Data*, JHEP **09** (2014) 060, arXiv:1402.4431 [hep-ph].

[32] V. D. Barger, W.-Y. Keung, and E. Ma, *A Gauge Model With Light W and Z Bosons*, Phys. Rev. **D22** (1980) 727.

[33] R. Contino, D. Marzocca, D. Pappadopulo, and R. Rattazzi, *On the effect of resonances in composite Higgs phenomenology*, JHEP **10** (2011) 081, arXiv:1109.1570 [hep-ph].

[34] Lyndon Evans and Philip Bryant, *LHC Machine*, Journal of Instrumentation **3** (2008) S08001, http://stacks.iop.org/1748-0221/3/i=08/a=S08001.

[35] LHC Study Group Collaboration, T. S. Pettersson and P. Lefvre, *The Large Hadron Collider: Conceptual Design*, Tech. Rep. CERN-AC-95-05-LHC, Oct, 1995. https://cds.cern.ch/record/291782.

[36] O. S. Brning, P. Collier, P. Lebrun, S. Myers, R. Ostojic, J. Poole, and P. Proudlock, *LHC Design Report*. CERN Yellow Reports: Monographs. CERN, Geneva, 2004. https://cds.cern.ch/record/782076.

[37] J. P. Blewett, *200-GeV Intersecting Storage Accelerators*, eConf **C710920** (1971) 501.

[38] *Interim Summary Report on the Analysis of the 19 September 2008 Incident at the LHC*, Tech. Rep. Document EDMS 973073, CERN/AT/PhL. https://edms.cern.ch/ui/file/973073/1/Report_on_080919_incident_at_LHC__2_.pdf.

[39] M. Lamont, *Status of the LHC*, Journal of Physics: Conference Series **455** (2013) 012001, http://stacks.iop.org/1742-6596/455/i=1/a=012001.

[40] ATLAS Collaboration, *ATLAS Luminosity Public Results (Run 1)*, https://twiki.cern.ch/twiki/bin/view/AtlasPublic/LuminosityPublicResults.

[41] R. Bruce, G. Arduini, H. Bartosik, R. De Maria, M. Giovannozzi, G. Iadarola, J. Jowett, K. S. B. Li, M. Lamont, A. Lechner, E. Metral, D. Mirarchi, T. Pieloni, S. Redaelli, G. Rumolo, B. Salvant, R. Tomas Garcia, and J. Wenninger, *LHC Run 2: Results and Challenges* , Tech. Rep. CERN-ACC-2016-0103, CERN, Geneva, Jul, 2016. https://cds.cern.ch/record/2201447.

[42] ATLAS Collaboration, *ATLAS Luminosity Public Results (Run 2)*, https://twiki.cern.ch/twiki/bin/view/AtlasPublic/LuminosityPublicResultsRun2.

[43] ATLAS Collaboration, *The ATLAS Experiment at the CERN Large Hadron Collider*, JINST **3** (2008) S08003.

[44] *ATLAS Fact Sheets*, http://atlasexperiment.org/fact-sheets-1-view.html.

[45] ATLAS Collaboration, *ATLAS detector and physics performance: Technical Design Report, 1.* Technical Design Report ATLAS. CERN, Geneva, 1999. https://cds.cern.ch/record/391176.

[46] ATLAS Collaboration, *ATLAS detector and physics performance: Technical Design Report, 2.* Technical Design Report ATLAS. CERN, Geneva, 1999. https://cds.cern.ch/record/391177.

[47] ATLAS Collaboration, *Expected performance of the ATLAS experiment: detector, trigger and physics.* CERN, Geneva, 2009. https://cds.cern.ch/record/1125884.

[48] E. Hines, *Performance of Particle Identification with the ATLAS Transition Radiation Tracker*, Tech. Rep. ATL-INDET-PROC-2011-017, CERN, Geneva, Sep, 2011. https://cds.cern.ch/record/1385059. Comments: 8 pages, 7 figures. Conference proceedings for the Meeting of the Division of Particles and Fields of the American Physical Society (DPF), 2011.

[49] G. A. et al., *ATLAS pixel detector electronics and sensors*, Journal of Instrumentation **3** (2008) P07007, http://stacks.iop.org/1748-0221/3/i=07/a=P07007.

[50] M. Capeans, G. Darbo, K. Einsweiller, M. Elsing, T. Flick, M. Garcia-Sciveres, C. Gemme, H. Pernegger, O. Rohne, and R. Vuillermet, *ATLAS Insertable B-Layer Technical Design Report*, Tech. Rep. CERN-LHCC-2010-013. ATLAS-TDR-19, Sep, 2010. https://cds.cern.ch/record/1291633.

[51] ATLAS Collaboration, *ATLAS Insertable B-Layer Technical Design Report Addendum*, Tech. Rep. CERN-LHCC-2012-009. ATLAS-TDR-19-ADD-1, May, 2012. https://cds.cern.ch/record/1451888. Addendum to CERN-LHCC-2010-013, ATLAS-TDR-019.

[52] H. Spieler, *Introduction to Radiation Detectors and Electronics*, http://www-physics.lbl.gov/~spieler/physics_198_notes/, Lecture Notes - Physics 198, Spring Semester 1998 - UC Berkeley.

[53] M. erv, *The ATLAS Diamond Beam Monitor*, Journal of Instrumentation **9** (2014) C02026, http://stacks.iop.org/1748-0221/9/i=02/a=C02026.

[54] V. Cindro, D. Dobos, I. Dolenc, H. Frais-Klbl, A. Goriek, E. Griesmayer, H. Kagan, G. Kramberger, B. Macek, I. Mandi, M. Miku, M. Niegl, H. Pernegger, D. Tardif, W. Trischuk, P. Weilhammer, and M. Zavrtanik, *The ATLAS Beam Conditions Monitor*, Journal of Instrumentation **3** (2008) P02004, http://stacks.iop.org/1748-0221/3/i=02/a=P02004.

[55] M. Kronberger, C. W. Fabjan, and P. Lecoq, *Optimization of the light extraction from heavy inorganic scintillators*. PhD thesis, Vienna, Tech. U., Vienna, 2008. https://cds.cern.ch/record/1105938. Presented on 18 Jun 2008.

[56] A. Lounis, D. Martinot, G. Calderini, G. Marchiori, M. Benoit, and N. Dinu, *TCAD Simulations of ATLAS Pixel Guard Ring and Edge Structure for SLHC Upgrade*, Tech. Rep. ATL-UPGRADE-PUB-2010-001, CERN, Geneva, Jan, 2010. https://cds.cern.ch/record/1233750.

[57] S. Parker, C. Kenney, and J. Segal, *3D A proposed new architecture for solid-state radiation detectors*, Nuclear Instruments and Methods in Physics Research Section A: Accelerators, Spectrometers, Detectors and Associated Equipment **395** (1997) 328 – 343, http://www.sciencedirect.com/science/article/pii/S0168900297006943.

[58] G. Darbo, *Experience on 3D Silicon Sensors for ATLAS IBL*, Tech. Rep. arXiv:1411.6937. ATL-INDET-PROC-2014-017, CERN, Geneva, Nov, 2014. https://cds.cern.ch/record/1971961. Comments: 9 pages, 7 figures, conference proceedings for International Workshop on Semiconductor Pixel Detectors for Particles and Imaging (PIXEL2014), will be published on JINST.

[59] G. Giacomini, A. Bagolini, M. Boscardin, G.-F. Dalla Betta, F. Mattedi, M. Povoli, E. Vianello, and N. Zorzi, *Development of double-sided full-passing-column 3D sensors at FBK*, IEEE Transactions on Nuclear Science **60** (2013) 2357–2366.

[60] G. Pellegrini, J. Balbuena, D. Bassignana, E. Cabruja, C. Fleta, C. Guardiola, M. Lozano, D. Quirion, and M. Ullán, *3D double sided detector fabrication at IMB-CNM*, Nuclear Instruments and Methods in Physics Research Section A: Accelerators, Spectrometers, Detectors and Associated Equipment **699** (2013) 27–30.

[61] T. A. I. collaboration, *Prototype ATLAS IBL modules using the FE-I4A front-end readout chip*, Journal of Instrumentation **7** (2012) P11010, http://stacks.iop.org/1748-0221/7/i=11/a=P11010.

[62] A. A. et al., *The silicon microstrip sensors of the {ATLAS} semiconductor tracker*, Nuclear Instruments and Methods in Physics Research Section A: Accelerators, Spectrometers, Detectors and Associated Equipment **578** (2007) 98 – 118, http://www.sciencedirect.com/science/article/pii/S0168900207007644.

[63] T. A. T. collaboration, *The ATLAS Transition Radiation Tracker (TRT) proportional drift tube: design and performance*, Journal of Instrumentation **3** (2008) P02013, http://stacks.iop.org/1748-0221/3/i=02/a=P02013.

[64] David Barney, *Particle Detectors: Calorimetry*, May, 2016, https://indico.cern.ch/event/526766/, CERN Academic Trainign Lecture Regular Programme.

[65] ATLAS Collaboration Collaboration,, *ATLAS liquid-argon calorimeter: Technical Design Report*. Technical Design Report ATLAS. CERN, Geneva, 1996. https://cds.cern.ch/record/331061.

[66] ATLAS Collaboration Collaboration,, *ATLAS tile calorimeter: Technical Design Report*. Technical Design Report ATLAS. CERN, Geneva, 1996. https://cds.cern.ch/record/331062.

[67] ATLAS Collaboration Collaboration,, *ATLAS muon spectrometer: Technical Design Report*. Technical Design Report ATLAS. CERN, Geneva, 1997. https://cds.cern.ch/record/331068.

[68] Kerstin Hoepfner, *Particle Detectors: Muon Detectors*, May, 2016, https://indico.cern.ch/event/526767/, CERN Academic Trainign Lecture Regular Programme.

[69] ATLAS Collaboration, *Commissioning of the ATLAS Muon Spectrometer with cosmic rays*, Eur. Phys. J. C **70** (2010) 875, arXiv:1006.4384 [hep-ex].

[70] G. Cattani and the RPC group, *The Resistive Plate Chambers of the ATLAS experiment: performance studies*, Journal of Physics: Conference Series **280** (2011) 012001, http://stacks.iop.org/1742-6596/280/i=1/a=012001.

[71] P. Jenni and M. Nessi, *ATLAS Forward Detectors for Luminosity Measurement and Monitoring*, Tech. Rep. CERN-LHCC-2004-010. LHCC-I-014, CERN, Geneva, Mar, 2004. `https://cds.cern.ch/record/721908`. revised version number 1 submitted on 2004-03-22 14:56:11.

[72] P. Jenni, M. Nordberg, M. Nessi, and K. Jon-And, *ATLAS Forward Detectors for Measurement of Elastic Scattering and Luminosity*. Technical Design Report ATLAS. CERN, Geneva, 2008. `https://cds.cern.ch/record/1095847`.

[73] ATLAS Collaboration Collaboration, P. Jenni, M. Nessi, and M. Nordberg, *Zero Degree Calorimeters for ATLAS*, Tech. Rep. LHCC-I-016. CERN-LHCC-2007-001, CERN, Geneva, Jan, 2007. `https://cds.cern.ch/record/1009649`.

[74] ATLAS Collaboration, *Improved luminosity determination in pp collisions at $\sqrt{s} = 7$ TeV using the ATLAS detector at the LHC*, Eur. Phys. J. C **73** (2013) 2518, `arXiv:1302.4393 [hep-ex]`.

[75] ATLAS Collaboration, *Luminosity determination in pp collisions at $\sqrt{s} = 8$ TeV using the ATLAS detector at the LHC*, Eur. Phys. J. C **76** (2016) 653, `arXiv:1608.03953 [hep-ex]`.

[76] Frank Winklmeier, *Particle Detectors: Trigger/DAQ for Particle Physics Detectors*, May, 2016, `https://indico.cern.ch/event/526768/`, CERN Academic Trainign Lecture Regular Programme.

[77] van UdenR. G. H., R. A. Correa, E. A. Lopez, H. M., XiaC., LiG., SchülzgenA., de WaardtH., K. M. J., and O. M., *Ultra-high-density spatial division multiplexing with a few-mode multicore fibre*, Nat Photon **8** (2014) 865–870, `http://dx.doi.org/10.1038/nphoton.2014.243`.

[78] ATLAS Collaboration Collaboration, ATLAS Collaboration, *Technical Design Report for the Phase-I Upgrade of the ATLAS TDAQ System*, Tech. Rep. CERN-LHCC-2013-018. ATLAS-TDR-023, Sep, 2013. `https://cds.cern.ch/record/1602235`. Final version presented to December 2013 LHCC.

[79] ATLAS Collaboration, *Performance of the ATLAS Trigger System in 2015*, `arXiv:1611.09661 [hep-ex]`.

[80] ATLAS Collaboration, *2015 start-up trigger menu and initial performance assessment of the ATLAS trigger using Run-2 data*, ATL-DAQ-PUB-2016-001, 2016, `https://cds.cern.ch/record/2136007/`.

[81] ATLAS Collaboration, *Performance of the ATLAS Trigger System in 2010*, Eur. Phys. J. C **72** (2012) 1849, `arXiv:1110.1530 [hep-ex]`.

[82] T. A. T. Collaboration, *The ATLAS Data Acquisition and High Level Trigger system*, Journal of Instrumentation **11** (2016) P06008, http://stacks.iop.org/1748-0221/11/i=06/a=P06008.

[83] R. Achenbach, P. Adragna, V. Andrei, P. Apostologlou, B. sman, C. Ay, B. M. Barnett, B. Bauss, M. Bendel, C. Bohm, J. R. A. Booth, I. P. Brawn, P. B. Thomas, D. G. Charlton, N. J. Collins, C. J. Curtis, A. Dahlhoff, A. O. Davis, S. Eckweiler, J. P. Edwards, E. Eisenhandler, P. J. W. Faulkner, J. Fleckner, F. Fhlisch, J. Garvey, C. N. P. Gee, A. R. Gillman, P. Hanke, R. P. Hatley, S. Hellman, A. Hidvgi, S. J. Hillier, K. Jakobs, M. Johansen, E. E. Kluge, M. Landon, V. Lendermann, J. N. Lilley, K. Mahboubi, G. Mahout, A. Mass, K. Meier, T. Moa, E. Moyse, F. Mller, A. Neusiedl, C. Nding, B. Oltmann, J. M. Pentney, V. J. O. Perera, U. Pfeiffer, D. P. F. Prieur, W. Qian, D. L. Rees, S. Rieke, F. Rhr, D. P. C. Sankey, U. Schfer, K. Schmitt, H. C. Schultz-Coulon, C. Schumacher, S. Silverstein, R. J. Staley, R. Stamen, M. C. Stockton, S. Tapprogge, J. P. Thomas, T. Trefzger, P. M. Watkins, A. Watson, P. Weber, and E. E. Woehrling, *The ATLAS Level-1 Calorimeter Trigger*, Journal of Instrumentation **3** (2008) P03001, http://stacks.iop.org/1748-0221/3/i=03/a=P03001.

[84] S. Ask, D. Berge, P. Borrego-Amaral, D. Caracinha, N. Ellis, P. Farthouat, P. Glln, S. Haas, J. Haller, P. Klofver, A. Krasznahorkay, A. Messina, C. Ohm, T. Pauly, M. Perantoni, H. P. L. Junior, G. Schuler, D. Sherman, R. Spiwoks, T. Wengler, J. M. de Seixas, and R. T. Teixeira, *The ATLAS central level-1 trigger logic and TTC system*, Journal of Instrumentation **3** (2008) P08002, http://stacks.iop.org/1748-0221/3/i=08/a=P08002.

[85] ATLAS Collaboration, *Search for light dijet resonances with the ATLAS detector using a Trigger-object Level Analysis in LHC pp collisions at* $\sqrt{s} = 13$ *TeV*, ATLAS-CONF-2016-030, 2016, https://cds.cern.ch/record/2161135.

[86] ATLAS Collaboration, *Electron efficiency measurements with the ATLAS detector using the 2012 LHC proton–proton collision data*, ATLAS-CONF-2014-032, 2014, https://cds.cern.ch/record/1706245.

[87] ATLAS Collaboration, *Muon reconstruction performance of the ATLAS detector in proton–proton collision data at* $\sqrt{s} = 13$ *TeV*, Eur. Phys. J. C **76** (2016) 292, arXiv:1603.05598 [hep-ex].

[88] ATLAS Collaboration, *Performance of missing transverse momentum reconstruction with the ATLAS detector in the first proton–proton collisions at* $\sqrt{s} = 13$ *TeV*, ATL-PHYS-PUB-2015-027, 2015, https://cds.cern.ch/record/2037904.

[89] T. G. Cornelissen, N. Van Eldik, M. Elsing, W. Liebig, E. Moyse, N. Piacquadio, K. Prokofiev, A. Salzburger, and A. Wildauer, *Updates of the ATLAS Tracking Event Data*

Model (Release 13), Tech. Rep. ATL-SOFT-PUB-2007-003. ATL-COM-SOFT-2007-008, CERN, Geneva, Jun, 2007. http://cds.cern.ch/record/1038095.

[90] M. Limper, S. Bentvelsen, and A. P. Colijn, *Track and vertex reconstruction in the ATLAS inner detector*. PhD thesis, Amsterdam U., Amsterdam, 2009. http://cds.cern.ch/record/1202457. Presented on 12 Oct 2009.

[91] A. Rosenfeld and J. L. Pfaltz, *Sequential Operations in Digital Picture Processing*, J. ACM **13** (1966) 471–494, http://doi.acm.org/10.1145/321356.321357.

[92] ATLAS Collaboration, *A neural network clustering algorithm for the ATLAS silicon pixel detector*, JINST **9** (2014) P09009, arXiv:1406.7690 [hep-ex].

[93] Andreas Salzburger, *Inner Detector Reconstruction I – Tracking*, September, 2008, https://indico.cern.ch/event/34087/contributions/802944/attachments/669263/919934/IDTracking_A_Salzburger.pdf, Artemis School on Calibration and Performance of ATLAS Detectors.

[94] T. Cornelissen, M. Elsing, S. Fleischmann, W. Liebig, E. Moyse, and A. Salzburger, *Concepts, Design and Implementation of the ATLAS New Tracking (NEWT)*, Tech. Rep. ATL-SOFT-PUB-2007-007. ATL-COM-SOFT-2007-002, CERN, Geneva, Mar, 2007. https://cds.cern.ch/record/1020106.

[95] ATLAS Collaboration, *Performance of the ATLAS Silicon Pattern Recognition Algorithm in Data and Simulation at* $\sqrt{s} = 7$ *TeV*, ATLAS-CONF-2010-072, 2010, https://cds.cern.ch/record/1281363.

[96] ATLAS Collaboration, *The Optimization of ATLAS Track Reconstruction in Dense Environments*, ATL-PHYS-PUB-2015-006, 2015, https://cds.cern.ch/record/2002609.

[97] R. Fruhwirth, *Application of Kalman filtering to track and vertex fitting*, Nucl. Instrum. Meth. **A262** (1987) 444–450.

[98] ATLAS Collaboration, *Performance of primary vertex reconstruction in proton–proton collisions at* $\sqrt{s} = 7$ *TeV in the ATLAS experiment*, ATLAS-CONF-2010-069, 2010, https://cds.cern.ch/record/1281344.

[99] ATLAS Collaboration, *Vertex Reconstruction Performance of the ATLAS Detector at*$\sqrt{s} = 13$ *TeV*, ATL-PHYS-PUB-2015-026, 2015, https://cds.cern.ch/record/2037717.

[100] G. Piacquadio and K. Jakobs, *Identification of b-jets and investigation of the discovery potential of a Higgs boson in the* $WH \to l\nu b\bar{b}$ *channel with the ATLAS experiment*. PhD thesis, Freiburg U., Freiburg, 2010. https://cds.cern.ch/record/1243771. Presented on 11 Jan 2010.

[101] W. Waltenberger, R. Frhwirth, and P. Vanlaer, *Adaptive vertex fitting*, Journal of Physics G: Nuclear and Particle Physics **34** (2007) N343, http://stacks.iop.org/0954-3899/34/i=12/a=N01.

[102] ATLAS Collaboration, *2016 Primary Vertex Performance Plots*, https://atlas.web.cern.ch/Atlas/GROUPS/PHYSICS/PLOTS/IDTR-2016-007/.

[103] https://theory.slac.stanford.edu/our-research/simulations.

[104] ATLAS Collaboration, *Topological cell clustering in the ATLAS calorimeters and its performance in LHC Run 1*, arXiv:1603.02934 [hep-ex].

[105] ATLAS Collaboration, *Jet energy measurement with the ATLAS detector in proton–proton collisions at* $\sqrt{s} = 7$ *TeV*, Eur. Phys. J. C **73** (2013) 2304, arXiv:1112.6426 [hep-ex].

[106] ATLAS Collaboration, M. Aaboud et al., *Jet energy scale measurements and their systematic uncertainties in proton-proton collisions at* $\sqrt{s} = 13$ *TeV with the ATLAS detector*, arXiv:1703.09665 [hep-ex].

[107] ATLAS Collaboration, *Jet energy measurement and its systematic uncertainty in proton–proton collisions at* $\sqrt{s} = 7$ *TeV with the ATLAS detector*, Eur. Phys. J. C **75** (2015) 17, arXiv:1406.0076 [hep-ex].

[108] M. Cacciari, G. P. Salam, and G. Soyez, *FastJet User Manual*, Eur. Phys. J. **C72** (2012) 1896, arXiv:1111.6097 [hep-ph].

[109] M. Cacciari, G. P. Salam, and G. Soyez, *The Anti-k(t) jet clustering algorithm*, JHEP **04** (2008) 063, arXiv:0802.1189 [hep-ph].

[110] S. Catani, Y. Dokshitzer, M. Seymour, and B. Webber, *Longitudinally-invariant k-clustering algorithms for hadron-hadron collisions*, Nuclear Physics B **406** (1993) 187 – 224, http://www.sciencedirect.com/science/article/pii/055032139390166M.

[111] S. D. Ellis and D. E. Soper, *Successive combination jet algorithm for hadron collisions*, Phys. Rev. **D48** (1993) 3160–3166, arXiv:hep-ph/9305266 [hep-ph].

[112] Y. L. Dokshitzer, G. D. Leder, S. Moretti, and B. R. Webber, *Better jet clustering algorithms*, JHEP **08** (1997) 001, arXiv:hep-ph/9707323 [hep-ph].

[113] M. Wobisch and T. Wengler, *Hadronization corrections to jet cross-sections in deep inelastic scattering*, 1998, arXiv:hep-ph/9907280 [hep-ph], https://inspirehep.net/record/484872/files/arXiv:hep-ph_9907280.pdf.

[114] M. Cacciari, G. P. Salam, and G. Soyez, *The Catchment Area of Jets*, JHEP **04** (2008) 005, arXiv:0802.1188 [hep-ph].

[115] M. Cacciari and G. P. Salam, *Pileup subtraction using jet areas*, Phys. Lett. **B659** (2008) 119–126, arXiv:0707.1378 [hep-ph].

[116] ATLAS Collaboration, *Expected performance of the ATLAS b-tagging algorithms in Run-2*, ATL-PHYS-PUB-2015-022, 2015, https://cds.cern.ch/record/2037697.

[117] ATLAS Collaboration, *Optimisation of the ATLAS b-tagging performance for the 2016 LHC Run*, ATL-PHYS-PUB-2016-012, 2016, https://cds.cern.ch/record/2160731.

[118] ATLAS Collaboration, *Performance of b-Jet Identification in the ATLAS Experiment*, JINST **11** (2016) P04008, arXiv:1512.01094 [hep-ex].

[119] ATLAS Collaboration Collaboration,, *Identification of Jets Containing b-Hadrons with Recurrent Neural Networks at the ATLAS Experiment*, Tech. Rep. ATL-PHYS-PUB-2017-003, CERN, Geneva, Mar, 2017. http://cds.cern.ch/record/2255226.

[120] ATLAS Collaboration, *Properties of jets measured from tracks in proton–proton collisions at center-of-mass energy $\sqrt{s} = 7$ TeV with the ATLAS detector*, Phys. Rev. D **84** (2011) 054001, arXiv:1107.3311 [hep-ex].

[121] ATLAS Collaboration, *Flavor Tagging with Track-Jets in Boosted Topologies with the ATLAS Detector*, ATL-PHYS-PUB-2014-013, 2014, https://atlas.web.cern.ch/Atlas/GROUPS/PHYSICS/PUBNOTES/ATL-PHYS-PUB-2014-013.

[122] ATLAS Collaboration, *Search for Higgs boson pair production in the $b\bar{b}b\bar{b}$ final state from pp collisions at $\sqrt{s} = 8$ TeV with the ATLAS detector*, Eur. Phys. J. C **75** (2015) 412, arXiv:1506.00285 [hep-ex].

[123] ATLAS Collaboration, *Expected Performance of Boosted Higgs ($\to b\bar{b}$) Boson Identification with the ATLAS Detector at $\sqrt{s} = 13$ TeV*, ATL-PHYS-PUB-2015-035, 2015, https://cds.cern.ch/record/2042155.

[124] ATLAS Collaboration, *Boosted Higgs ($\to b\bar{b}$) Boson Identification with the ATLAS Detector at $\sqrt{s} = 13$ TeV*, ATLAS-CONF-2016-039, 2016, https://cds.cern.ch/record/2206038.

[125] A. Schwartzman, Q. Zeng, M. Kagan, and G. Piacquadio, *Performance of Track Jet based b-tagging in Monte Carlo at $\sqrt{s} = 8$ TeV with the ATLAS Detector*, Tech. Rep. ATL-COM-PHYS-2015-1323, CERN, Geneva, Oct, 2015. https://cds.cern.ch/record/2062412.

[126] W. Van Den Wollenberg, M. Kagan, E. Thompson, and L. Zhou, *Measurement of the Track-Jet b-Tagging Efficiency of the MV1 algorithm in pp Collisions at $\sqrt{s} = 8$ TeV using*

eμ Dilepton $t\bar{t}$ events, Tech. Rep. ATL-COM-PHYS-2015-009, CERN, Geneva, Jan, 2015. https://cds.cern.ch/record/1981533.

[127] ATLAS Collaboration, *b-tagging in dense environments*, ATL-PHYS-PUB-2014-014, 2014, https://atlas.web.cern.ch/Atlas/GROUPS/PHYSICS/PUBNOTES/ATL-PHYS-PUB-2014-014.

[128] ATLAS Collaboration, *Early Inner Detector Tracking Performance in the 2015 Data at $\sqrt{s} = 13$ TeV*, ATL-PHYS-PUB-2015-051, 2015, https://cds.cern.ch/record/2110140.

[129] ATLAS Collaboration, *Tagging and suppression of pileup jets with the ATLAS detector*, ATLAS-CONF-2014-018, 2014, https://cds.cern.ch/record/1700870.

[130] P. Nef and A. Schwartzman, *Tagging and suppression of pileup jets*, Tech. Rep. ATLAS-COM-CONF-2014-025, CERN, Geneva, Apr, 2014. https://cds.cern.ch/record/1697147.

[131] ATLAS Collaboration, *Performance of jet substructure techniques for large-R jets in proton–proton collisions at $\sqrt{s} = 7$ TeV using the ATLAS detector*, JHEP **09** (2013) 076, arXiv:1306.4945 [hep-ex].

[132] ATLAS Collaboration, *Identification of Boosted, Hadronically Decaying W Bosons and Comparisons with ATLAS Data Taken at $\sqrt{s} = 8$ TeV*, Eur. Phys. J. C **76** (2016) 154, arXiv:1510.05821 [hep-ex].

[133] D. Krohn, J. Thaler, and L.-T. Wang, *Jet Trimming*, JHEP **02** (2010) 084, arXiv:0912.1342 [hep-ph].

[134] S. D. Ellis, C. K. Vermilion, and J. R. Walsh, *Recombination Algorithms and Jet Substructure: Pruning as a Tool for Heavy Particle Searches*, Phys. Rev. **D81** (2010) 094023, arXiv:0912.0033 [hep-ph].

[135] J. M. Butterworth, A. R. Davison, M. Rubin, and G. P. Salam, *Jet substructure as a new Higgs search channel at the LHC*, Phys. Rev. Lett. **100** (2008) 242001, arXiv:0802.2470 [hep-ph].

[136] A. J. Larkoski, G. P. Salam, and J. Thaler, *Energy Correlation Functions for Jet Substructure*, JHEP **06** (2013) 108, arXiv:1305.0007 [hep-ph].

[137] A. J. Larkoski, I. Moult, and D. Neill, *Power Counting to Better Jet Observables*, JHEP **12** (2014) 009, arXiv:1409.6298 [hep-ph].

[138] A. J. Larkoski, I. Moult, and D. Neill, *Analytic Boosted Boson Discrimination*, JHEP **05** (2016) 117, arXiv:1507.03018 [hep-ph].

[139] L. G. Almeida, S. J. Lee, G. Perez, G. F. Sterman, I. Sung, and J. Virzi, *Substructure of high-p_T Jets at the LHC*, Phys. Rev. **D79** (2009) 074017, arXiv:0807.0234 [hep-ph].

[140] J. M. Butterworth, B. E. Cox, and J. R. Forshaw, WW, Phys. Rev. D **65** (2002) 096014, https://link.aps.org/doi/10.1103/PhysRevD.65.096014.

[141] J. Thaler and K. Van Tilburg, *Identifying Boosted Objects with N-subjettiness*, JHEP **03** (2011) 015, arXiv:1011.2268 [hep-ph].

[142] J. Thaler and K. Van Tilburg, *Maximizing Boosted Top Identification by Minimizing N-subjettiness*, JHEP **02** (2012) 093, arXiv:1108.2701 [hep-ph].

[143] A. Hook, M. Jankowiak, and J. G. Wacker, *Jet Dipolarity: Top Tagging with Color Flow*, JHEP **04** (2012) 007, arXiv:1102.1012 [hep-ph].

[144] ATLAS Collaboration, *Measurement of the cross-section of high transverse momentum vector bosons reconstructed as single jets and studies of jet substructure in pp collisions at $\sqrt{s} = 7$ TeV with the ATLAS detector*, New J. Phys. **16** (2014) 113013, arXiv:1407.0800 [hep-ex].

[145] S. D. Ellis, A. Hornig, T. S. Roy, D. Krohn, and M. D. Schwartz, *Qjets: A Non-Deterministic Approach to Tree-Based Jet Substructure*, Phys. Rev. Lett. **108** (2012) 182003, arXiv:1201.1914 [hep-ph].

[146] ATLAS Collaboration, *Performance and Validation of Q-jets at the ATLAS Detector in pp Collisions at $\sqrt{s} = 8$ TeV in 2012*, ATLAS-CONF-2013-087, 2013, https://cds.cern.ch/record/1572981.

[147] ATLAS Collaboration, *Identification of Boosted, Hadronically-Decaying W and Z Bosons in $\sqrt{s} = 13$ TeV Monte Carlo Simulations for ATLAS*, ATL-PHYS-PUB-2015-033, 2015, https://cds.cern.ch/record/2041461.

[148] ATLAS Collaboration Collaboration,, *Search for Dark Matter Produced in Association with a Higgs Boson Decaying to $b\bar{b}$ at $\sqrt{s} = 13$ TeV with the ATLAS Detector*, Tech. Rep. ATLAS-CONF-2017-028, CERN, Geneva, Apr, 2017. http://cds.cern.ch/record/2259066.

[149] ATLAS Collaboration, *Search for new resonances decaying to a W or Z boson and a Higgs boson in the $\ell^+\ell^- b\bar{b}$, $\ell\nu b\bar{b}$, and $\nu\bar{\nu}b\bar{b}$ channels with pp collisions at $\sqrt{s} = 13$ TeV with the ATLAS detector*, Phys. Lett. B **765** (2017) 32, arXiv:1607.05621 [hep-ex].

[150] ATLAS Collaboration, *Measurements of Higgs boson production and couplings in diboson final states with the ATLAS detector at the LHC*, Phys. Lett. B **726** (2013) 88, arXiv:1307.1427 [hep-ex].

[151] CMS Collaboration, *Measurement of the properties of a Higgs boson in the four-lepton final state*, Phys. Rev. D **89** (2014) 092007, arXiv:1312.5353 [hep-ex].

[152] S. Dawson, S. Dittmaier, and M. Spira, *Neutral Higgs-boson pair production at hadron colliders: QCD corrections*, Phys. Rev. D **58** (1998) 115012, arXiv:hep-ph/9703387.

[153] J. Grigo, J. Hoff, K. Melnikov, and M. Steinhauser, *On the Higgs boson pair production at the LHC*, Nucl. Phys. B **875** (2013) 1, arXiv:1305.7340.

[154] D. de Florian and J. Mazzitelli, *Higgs Boson Pair Production at Next-to-Next-to-Leading Order in QCD*, Phys. Rev. Lett. **111** (2013) 201801, arXiv:1309.6594.

[155] L. Fitzpatrick, J. Kaplan, L. Randall, and L.-T. Wang, *Searching for the Kaluza-Klein graviton in bulk RS models*, JHEP **09** (2007) 013, arXiv:hep-ph/0701150.

[156] G. Branco et al., *Theory and phenomenology of two-Higgs-doublet models*, Phys. Rept. **516** (2012) 1, arXiv:1106.0034.

[157] G. D. Kribs and A. Martin, *Enhanced di-Higgs production through light colored scalars*, Phys. Rev. D **86** (2012) 095023, arXiv:1207.4496.

[158] R. Grober and M. Muhlleitner, *Composite Higgs Boson Pair Production at the LHC*, JHEP **06** (2011) 020, arXiv:1012.1562.

[159] R. Contino et al., *Anomalous Couplings in Double Higgs Production*, JHEP **08** (2012) 154, arXiv:1205.5444.

[160] ATLAS Collaboration, *Searches for Higgs boson pair production in the $hh \to bb\tau\tau, \gamma\gamma WW^*, \gamma\gamma bb, bbbb$ channels with the ATLAS detector*, Phys. Rev. D **92** (2015) 092004, arXiv:1509.04670 [hep-ex].

[161] B. Cooper, N. Konstantinidis, L. Lambourne, and D. Wardrope, *Boosted $hh \to b\bar{b}b\bar{b}$: A new topology in searches for TeV-scale resonances at the LHC*, Phys. Rev. D **88** (2013) 114005, arXiv:1307.0407.

[162] M. Gouzevitch et al., *Scale-invariant resonance tagging in multijet events and new physics in Higgs pair production*, JHEP **07** (2013) 148, arXiv:1303.6636.

[163] D. de Lima, A. Papaefstathiou, and M. Spannowsky, *Standard model Higgs boson pair production in the $\left(b\bar{b}\right)\left(b\bar{b}\right)$ final state*, JHEP **08** (2014) 030, arXiv:1404.7139.

[164] D. Wardrope et al., *Non-resonant Higgs pair production in the $b\bar{b}b\bar{b}$ final state at the LHC* , arXiv:1410.2794.

[165] ATLAS Collaboration, *Search for pair production of Higgs bosons in the $b\bar{b}b\bar{b}$ final state using proton–proton collisions at $\sqrt{s} = 13$ TeV with the ATLAS detector*, Phys. Rev. D **94** (2016) 052002, arXiv:1606.04782 [hep-ex].

[166] ATLAS Collaboration, *Search for pair production of Higgs bosons in the $b\bar{b}b\bar{b}$ final state using proton–proton collisions at $\sqrt{s} = 13$ TeV with the ATLAS detector*, ATLAS-CONF-2016-049, 2016, https://cds.cern.ch/record/2206131.

[167] T. Sjostrand, S. Mrenna, and P. Z. Skands, *A Brief Introduction to PYTHIA 8.1*, Comput. Phys. Commun. **178** (2008) 852, arXiv:0710.3820.

[168] ATLAS Collaboration,, *Summary of ATLAS Pythia 8 tunes*, http://cdsweb.cern.ch/record/1474107.

[169] D. J. Lange, *The EvtGen particle decay simulation package*, Nucl. Instrum. Meth. A **462** (2001) 152.

[170] GEANT4 Collaboration, S. Agostinelli et al., *GEANT4: A simulation toolkit*, Nucl. Instrum. Meth. A **506** (2003) 250.

[171] ATLAS Collaboration, *The ATLAS Simulation Infrastructure*, Eur. Phys. J. C **70** (2010) 823, arXiv:1005.4568 [hep-ex].

[172] J. Alwall et al., *The automated computation of tree-level and next-to-leading order differential cross sections, and their matching to parton shower simulations*, JHEP **07** (2014) 079, arXiv:1405.0301 [hep-ph].

[173] R. D. Ball et al., *Parton distributions with LHC data*, Nucl. Phys. B **867** (2013) 244, arXiv:1207.1303 [hep-ph].

[174] ATLAS Collaboration, *ATLAS Pythia 8 tunes to 7 TeV data*, ATL-PHYS-PUB-2014-021, 2014, https://cds.cern.ch/record/1966419.

[175] H.-L. Lai, M. Guzzi, J. Huston, Z. Li, P. M. Nadolsky, J. Pumplin, and C. P. Yuan, *New parton distributions for collider physics*, Phys. Rev. D **82** (2010) 074024, arXiv:1007.2241 [hep-ph].

[176] M. Bahr et al., *Herwig++ Physics and Manual*, Eur. Phys. J. C **58** (2008) 639–707, arXiv:0803.0883 [hep-ph].

[177] P. M. Nadolsky et al., *Implications of CTEQ global analysis for collider observables*, Phys. Rev. D **78** (2008) 013004, arXiv:0802.0007 [hep-ph].

[178] S. Gieseke, C. Rohr, and A. Siodmok, *Colour reconnections in Herwig++*, Eur. Phys. J. C **72** (2012) 2225, arXiv:1206.0041 [hep-ph].

[179] T. Sjöstrand, S. Mrenna, and P. Z. Skands, *PYTHIA 6.4 Physics and Manual*, JHEP **05** (2006) 026, arXiv:hep-ph/0603175.

[180] P. Z. Skands, *Tuning Monte Carlo Generators: The Perugia Tunes*, Phys. Rev. D **82** (2010) 074018, arXiv:1005.3457 [hep-ph].

[181] M. Czakon and A. Mitov, *Top++: A Program for the Calculation of the Top-Pair Cross-Section at Hadron Colliders*, arXiv:1112.5675 [hep-ph].

[182] ATLAS Collaboration, *Auxiliary Figures and Tables of EXOT-2015-11*, https://twiki.cern.ch/twiki/bin/view/AtlasPublic/LuminosityPublicResultsRun2.

[183] http://twiki.cern.ch/twiki/bin/view/AtlasProtected/JetSubstructureRecommendations.

[184] A. Davison and I. Ochoa, *Validating the ATLAS Large R-parameter Jet Mass Scale and Resolution with Hadronically Decaying Boosted W Bosons Using the 2012 Dataset*, http://cds.cern.ch/record/1557901.

[185] ATLAS Collaboration,, *Estimation of the Systematic Uncertainties on the b-Tagging of close by b-Jets in pp Collisions at $\sqrt{s} = 8$ TeV using Multi-Jet Events*, Tech. Rep. ATL-COM-PHYS-2014-1561, August, 2014. https://cds.cern.ch/record/1975945.

[186] G. Cowan, K. Cranmer, E. Gross, and O. Vitells, *Asymptotic formulae for likelihood-based tests of new physics*, Eur. Phys. J. C **71** (2011) 1554, arXiv:1007.1727 [physics.data-an].

[187] The ATLAS Collaboration, The CMS Collaboration, The LHC Higgs Combination Group Collaboration,, *Procedure for the LHC Higgs boson search combination in Summer 2011*, Tech. Rep. CMS-NOTE-2011-005. ATL-PHYS-PUB-2011-11, CERN, Geneva, Aug, 2011. https://cds.cern.ch/record/1379837.

[188] E. Gross and O. Vitells, *Trial factors or the look elsewhere effect in high energy physics*, Eur. Phys. J. C **70** (2010) 525–530, arXiv:1005.1891 [physics.data-an].

[189] M. J. Dugan, H. Georgi, and D. B. Kaplan, *Anatomy of a Composite Higgs Model*, Nucl. Phys. **B254** (1985) 299–326.

[190] K. Agashe, R. Contino, and A. Pomarol, *The Minimal composite Higgs model*, Nucl. Phys. **B719** (2005) 165–187, arXiv:hep-ph/0412089 [hep-ph].

[191] M. Schmaltz and D. Tucker-Smith, *Little Higgs review*, Ann. Rev. Nucl. Part. Sci. **55** (2005) 229–270, arXiv:hep-ph/0502182 [hep-ph].

[192] ATLAS Collaboration, *Search for a new resonance decaying to a W or Z boson and a Higgs boson in the $\ell\ell/\ell\nu/\nu\nu + b\bar{b}$ final states with the ATLAS detector*, Eur. Phys. J. C **75** (2015) 263, arXiv:1503.08089 [hep-ex].

[193] CMS Collaboration, *Search for a massive resonance decaying into a Higgs boson and a W or Z boson in hadronic final states in proton–proton collisions at $\sqrt{s} = 8$ TeV*, JHEP **02** (2016) 145, arXiv:1506.01443 [hep-ex].

[194] CMS Collaboration, *Search for massive WH resonances decaying into the $\ell\nu b\bar{b}$ final state at $\sqrt{s} = 8$ TeV*, Eur. Phys. J. C **76** (2016) 237, arXiv:1601.06431 [hep-ex].

[195] CMS Collaboration, *Search for narrow high-mass resonances in proton–proton collisions at $\sqrt{s} = 8$ TeV decaying to a Z and a Higgs boson*, Phys. Lett. B **748** (2015) 255, arXiv:1502.04994 [hep-ex].

[196] ATLAS Collaboration, *Searches for heavy diboson resonances in pp collisions at $\sqrt{s} = 13$ TeV with the ATLAS detector*, JHEP **09** (2016) 173, arXiv:1606.04833 [hep-ex].

[197] ATLAS Collaboration, *ATLAS Exotics Public Results*, https://twiki.cern.ch/twiki/bin/view/AtlasPublic/ExoticsPublicResults.

[198] ATLAS Collaboration, *A Search for Resonances Decaying to a W or Z Boson and a Higgs Boson in the $q\bar{q}^{(\prime)}b\bar{b}$ Final State*, ATLAS-CONF-2016-083, 2016, https://cds.cern.ch/record/2206276.

[199] ATLAS Collaboration, *Search for Heavy Resonances Decaying to a W or Z Boson and a Higgs Boson in the $q\bar{q}^{(\prime)}b\bar{b}$ Final State in pp Collisions at $\sqrt{s} = 13$ TeV with the ATLAS Detector*, ATLAS-CONF-2017-018, 2017, https://cds.cern.ch/record/2258132.

[200] S. Frixione and B. R. Webber, *Matching NLO QCD computations and parton shower simulations*, JHEP **0206** (2002) 029, arXiv:hep-ph/0204244 [hep-ph].

[201] J. Pumplin, D. Stump, J. Huston, H. Lai, P. M. Nadolsky, et al., *New generation of parton distributions with uncertainties from global QCD analysis*, JHEP **0207** (2002) 012, arXiv:hep-ph/0201195 [hep-ph].

[202] ATLAS Collaboration, *Comparison of Monte Carlo generator predictions for gap fraction and jet multiplicity observables in $t\bar{t}$ events*, ATL-PHYS-PUB-2014-005, 2014, https://cds.cern.ch/record/1703034.

[203] T. Gleisberg, S. Hoeche, F. Krauss, M. Schonherr, S. Schumann, et al., *Event generation with SHERPA 1.1*, JHEP **0902** (2009) 007, arXiv:0811.4622 [hep-ph].

[204] ATLAS Collaboration, *Jet mass reconstruction with the ATLAS Detector in early Run 2 data*, ATLAS-CONF-2016-035, 2016, `https://cds.cern.ch/record/2200211`.

[205] R. Camacho Toro, M. Campanelli, J. S. Ennis, Y. Gao, V. Ippolito, R. Jansky, E. Kajomovitz, A. Martyniuk, Z. A. Meadows, B. Murray, A. Picazio, S. Schramm, A. Vaidya, S. Willocq, and B. Wynne, *Search for diboson resonances with jets in 36.7 fb $^{-1}$ of pp collisions at $\sqrt{s} = 13$ TeV with the ATLAS detector*, Tech. Rep. ATL-COM-PHYS-2016-1490, CERN, Geneva, Oct, 2016. `https://cds.cern.ch/record/2225991`.

[206] ATLAS Collaboration, *Selection of jets produced in* 13 *TeV proton–proton collisions with the ATLAS detector*, ATLAS-CONF-2015-029, 2015, `https://cds.cern.ch/record/2037702`.

[207] ATLAS Collaboration, *Search for low-scale gravity signatures in multi-jet final states with the ATLAS detector at ?s = 13 TeV*, Tech. Rep. ATL-COM-PHYS-2015-536, CERN, Geneva, Jun, 2015. `https://cds.cern.ch/record/2026080`.

[208] ATLAS Collaboration, *Search for high-mass diboson resonances with boson-tagged jets in proton–proton collisions at $\sqrt{s} = 8$ TeV with the ATLAS detector*, JHEP **12** (2015) 055, `arXiv:1506.00962 [hep-ex]`.

[209] ATLAS Collaboration, *Measurement of the differential cross-section of highly boosted top quarks as a function of their transverse momentum in $\sqrt{s} = 8$ TeV proton–proton collisions using the ATLAS detector*, Phys. Rev. D **93** (2016) 032009, `arXiv:1510.03818 [hep-ex]`.

[210] ATLAS Collaboration, *Measurement of large radius jet mass reconstruction performance at $\sqrt{s} = 8$ TeV using the ATLAS detector*, ATLAS-CONF-2016-008, 2016, `https://cds.cern.ch/record/2139642`.

[211] ATLAS Collaboration, *Calibration of b-tagging using dileptonic top pair events in a combinatorial likelihood approach with the ATLAS experiment*, ATLAS-CONF-2014-004, 2014, `https://cds.cern.ch/record/1664335`.

[212] Luca Cadamuro, *Search and prospects for HH production*, `https://indico.in2p3.fr/event/13763/session/0/contribution/53/material/slides/0.pdf`.

[213] CMS Collaboration Collaboration,, *Search for heavy resonances decaying into a vector boson and a Higgs boson in hadronic final states with 2016 data*, Tech. Rep. CMS-PAS-B2G-17-002, CERN, Geneva, 2017. `https://cds.cern.ch/record/2256742`.

[214] S. Meehan, N. L. Whallon, Q. Zeng, D. Guest, M. Kagan, S.-C. Hsu, N. Norjoharuddeen, C. Issever, J. Frost, S. Prell, J. Yu, C. Chen, and A. Schwartzman, *Advanced Subjet Techniques for Higgs($\to b\bar{b}$) Boson Tagging at 13 ATLAS*, Tech. Rep.

ATL-COM-PHYS-2016-703, CERN, Geneva, Jun, 2016.
https://cds.cern.ch/record/2158510.

[215] Qi Zeng, *Pixel Digi Updates*, https://indico.cern.ch/event/508652/.

[216] Qi Zeng, *Status of New Pixel Digitization (Bichsel Model) for Rel21*, https://indico.cern.ch/event/506065/.

[217] Qi Zeng, *Update of Bichsel model*, https://indico.cern.ch/event/502082/.

[218] Qi Zeng, *Update on Bichsel model*, https://indico.cern.ch/event/509876/.

[219] Qi Zeng, *Pixel Ionization Model*, https://indico.cern.ch/event/539749/.

[220] Bill Murray, *Tracking*, https://indico.cern.ch/event/575287/.

[221] Qi Zeng, *Status of Bichsel model validation*, https://indico.cern.ch/event/562569/.

[222] Ben Nachman, *First Results on Pixel NN Training for R21*, https://indico.cern.ch/event/587900/.

[223] Alex Kastanas, Ben Nachman, *Clustering and Tracking In Dense Environments*, https://indico.cern.ch/event/589444/.

[224] Mutiple Authors, *R21 tracking condition validation*, https://indico.cern.ch/event/590646/.

[225] Marco Battaglia, *MC16 validation update*, https://indico.cern.ch/event/588927/.

[226] Alex Kastanas, *Status of NN training*, https://indico.cern.ch/event/590913/.

[227] Alessandro Calandri, *MV2 training in release 21.0.8*, https://indico.cern.ch/event/571869/.

[228] M. INOKUTI, *Inelastic Collisions of Fast Charged Particles with Atoms and Molecules¯The Bethe Theory Revisited*, Rev. Mod. Phys. **43** (1971) 297–347, https://link.aps.org/doi/10.1103/RevModPhys.43.297.

[229] Particle Data Group Collaboration, K. A. Olive et al., *Review of Particle Physics*, Chin. Phys. **C38** (2014) 090001.

[230] H. Bichsel, *Straggling in thin silicon detectors*, Rev. Mod. Phys. **60** (1988) 663–699, https://link.aps.org/doi/10.1103/RevModPhys.60.663.

[231] Dong Su, *Landau Fluctuation*, https://indico.cern.ch/event/523323/.

[232] ATLAS Collaboration, *Measurement of the $b\bar{b}$ dijet cross section in pp collisions at $\sqrt{s} = 7$ TeV with the ATLAS detector*, Eur. Phys. J. C **76** (2016) 670, `arXiv:1607.08430 [hep-ex]`.

[233] ATLAS Collaboration, *Identification and Tagging of Double b-hadron jets with the ATLAS Detector*, ATLAS-CONF-2012-100, 2012, `https://cds.cern.ch/record/1462603`.